Max-Planck-Institut
für Polymerforschung

Max Planck Institute
for Polymer Research

Unfolding of Natural Macromolecules and Folding of Synthetic Polymers: Bioinspired Strategies for Constructing Precision Nanomaterials

Dissertation zur Erlangung des Doktorgrades Doctor rerum naturalium (Dr. rer. nat.) der Fakultät für Naturwissenschaften der Universität Ulm

vorgelegt von

Chaojian Chen

aus Anhui, China

2020

Dissertation der Universität Ulm

Amtierender Dekan: Prof. Dr. Thorsten Bernhardt
1. Gutachter: Prof. Dr. Tanja Weil
2. Gutachter: Prof. Dr. Mika Lindén

Tag der Promotion: November 9, 2020
Universität Ulm, Fakultät für Naturwissenschaften

Max-Planck-Institut
für Polymerforschung

Max Planck Institute
for Polymer Research

Unfolding of Natural Macromolecules and Folding of Synthetic Polymers: Bioinspired Strategies for Constructing Precision Nanomaterials

Dissertation to obtain the degree Doctor rerum naturalium (Dr. rer. nat.) of the Faculty of Natural Sciences of the University of Ulm

submitted by

Chaojian Chen

from Anhui, China

2020

Dedicated to my parents.

Dissertation of Ulm University

Dean of the Faculty: Prof. Dr. Thorsten Bernhardt
Reviewer 1: Prof. Dr. Tanja Weil
Reviewer 2: Prof. Dr. Mika Lindén

Day of the promotion: November 9, 2020
Faculty of Natural Sciences, Ulm University

Abstract

Through billions of years of evolution, the unique three-dimensional hierarchical structures of biomacromolecules generated in living matter represent the highest level of precision and complexity of matter. The creation of synthetic polymers and nanomaterials with biomolecule-inspired architectures and functions is a rapidly expanding field in materials science. This thesis is inspired by the perfect structure of proteins regarding their defined polypeptide sequence and the controlled folding process to build the hierarchical precision architecture. Conceptually, three-dimensional protein structures can be unfolded into precision linear polypeptides, and alternatively, linear synthetic polymers can be folded into compact states, mimicking the hierarchical structure of biomacromolecules. This thesis employs these two opposite yet complementary strategies to prepare a diverse range of functional materials with controlled structures, including anisotropic brush polymers, various metal nanostructures, poly(bis-sulfone) bioconjugates, and wormlike polymer assemblies, for applications in different fields ranging from site-specific assembly to catalysis and biomedicine.

By unfolding native proteins into linear polypeptides, the first part of the thesis focuses on the templated synthesis of well-defined nanomaterials using unfolded proteins. Anisotropic brush polymers with monodisperse lengths were first prepared by attaching initiators to the backbone and then growing polymers via activators regenerated by electron transfer atom transfer radical polymerization (ARGET ATRP). By varying polymerization conditions and the initiator density on the backbone, the size and shape of brush polymers could be controlled. Importantly, different functional entities were introduced onto an absolute position of brush polymers located asymmetrically along the backbone by taking advantage of the site-specific modification of proteins. Combining biotin—streptavidin interactions, higher ordered constructs were fabricated, which may find applications in both biomedicine and nanoscience. Beyond soft polymer architectures, stable and water-soluble noble metal nanostructures, including spherical gold and platinum nanoparticles as well as gold nanoflowers, were also fabricated by using denatured proteins as templates. Moreover, the reduction of metal ions and ARGET ATRP were combined in one pot as they both involve the use of reducing agents. Poly(*N*-isopropylacrylamide)-coated gold

nanoflowers with controllable sizes, shapes, and shell thickness were obtained and applied as smart catalysts for the hydrogenation of *p*-nitrophenol.

The second part of this thesis demonstrates that bioinspired hierarchical structures can be constructed via folding and assembly of synthetic polymers. In this aspect, we first synthesized a thiol-reactive copolymer based on poly(bis-sulfone), which was conjugated with an endogenous peptide that targets C-X-C chemokine receptor type 4. The obtained conjugate folded and self-assembled into narrowly dispersed nanoparticles in aqueous solutions with functional peptides on the surface. Due to the multivalent effect, the conjugate revealed enhanced antiviral activity and the ability to inhibit cancer stem cell migration. However, the folding process of the polymer—peptide conjugate is dictated by random hydrophobic collapse of the polymer. To increase the level of structural control, we further folded linear poly(2-hydroxyethyl methacrylate) (PHEMA) into the cyclic topology via a highly efficient click reaction and compared its self-assembly behavior with that of linear PHEMA. Interestingly, the cyclic PHEMA formed wormlike structures as observed from TEM images. Based on their structural similarity, macrocyclic brush polymers with amphiphilic block side chains were designed and synthesized, which could form stable wormlike assemblies and higher-ordered structures. This work not only points out the vital role of polymer folding in macromolecular self-assembly, but also establishes a versatile approach for constructing bioinspired hierarchical structures from synthetic polymers.

In summary, unfolding of natural macromolecules and folding of synthetic polymers have been developed in this thesis as two unique biomolecule-inspired strategies for the fabrication of various nanomaterials with controlled structures. These strategies not only significantly expand the applications of biomacromolecules in various fields, but also provide new directions for the fabrication of the next generation biomolecule-inspired architectures.

Table of Contents

List of Figures

List of Abbreviations

1D	one-dimensional
2D	two-dimensional
3D	three-dimensional
AEMA	2-aminoethyl methacrylate
ARGET	activators regenerated by electron transfer
ATRP	atom transfer radical polymerization
$AuCl_4^-$	chloroauric anions
AuNFs	gold nanoflowers
AuNPs	gold nanoparticles
BCB	benzocyclobutene
BSA	bovine serum albumin
BTA	benzene-1,3,5-tricarboxamide
C10-bi	sebacic acid bis(N-succinimidyl) ester
CB[8]	cucurbit[8]uril
CDSA	crystallization-driven self-assembly
CuAAC	copper-catalyzed azide—alkyne cycloaddition
CXCR4	C-X-C chemokine receptor type 4
Cys-34	cysteine-34
DLS	dynamic light scattering
DNA	deoxyribonucleic acid
DTT	dithiothreitol
eATRP	electrochemically mediated ATRP
EDS	energy dispersive spectrometer
FITC	fluorescein isothiocyanate
FNDs	fluorescent nanodiamonds
FTIR	Fourier-transform infrared
FU	5-fluorouracil
Gd-DTPA	Gadolinium-diethylenetriamine pentacetate
GPC	gel permeation chromatography
$HAuCl_4$	chloroauric acid
HEMA	2-hydroxyethyl methacrylate
HHHs	hexagonally packed hollow hoops

HSA	human serum albumin
ICAR	initiators for continuous activator regeneration
LCMs	large compound micelles
LCST	lower critical solution temperature
MOEGMA	oligo (ethylene glycol) methyl ether methacrylate
MRI	magnetic resonance imaging
NMR	nuclear magnetic resonance
OEGMA	oligo(ethylene glycol)methacrylate
P4VP	poly(4-vinylpyridine)
PAA	poly(acrylic acid)
PB	phosphate buffer
PCL	polycaprolactone
PCR	polymerase chain reaction
PDAC	pancreatic ductal adenocarcinoma
PDMAEMA	poly(2-(dimethylamino)ethyl methacrylate)
PEG	poly(ethylene glycol)
PFS	polyferrocenylsilane
PHEMA	poly(2-hydroxyethyl methacrylate)
PI-DPELi	(1,1-diphenylethylene) end-capped polyisoprenyllithium
PMeO$_2$MA-*b*-PTA	poly[2-(2-methoxyethoxy)ethyl methacrylate]-*block*-poly[2-(*tert*-butylaminoethyl) methacrylate]
PMMA	poly(methyl methacrylate)
PNIPAM	poly(*N*-isopropylacrylamide)
POEGMA	poly[oligo(ethylene glycol) methyl methacrylate]
PS	polystyrene
PS-DPELi	(1,1-diphenylethylene) end-capped polystyryllithium
P*t*BA	poly(*tert*-butyl acrylate)
PTMSPMA	poly(3-(trimethoxysilyl)propyl methacrylate)
PtNPs	platinum nanoparticles
QDs	quantum dots
RAFT	reversible addition—fragmentation chain transfer
***R*$_h$**	hydrodynamic radius
RNA	ribonucleic acid
ROMP	ring-opening metathesis polymerization

SARA	supplemental activators and reducing agents
SCPNs	single-chain polymer nanoparticles
SE	secondary-electron image
SEM	scanning electron microscope
ssDNA	single-stranded DNA
SST	somatostatin
St	styrene
TA	thioctic acid
***t*BA**	*tert*-butyl acrylate
TCEP	tris(2-carboxyethyl) phosphine
TEM	transmission electron microscopy
U-DPy	uracil-diamidopyridine
UPy	2-ureidopyrimidinone

Chapter 1 Introduction

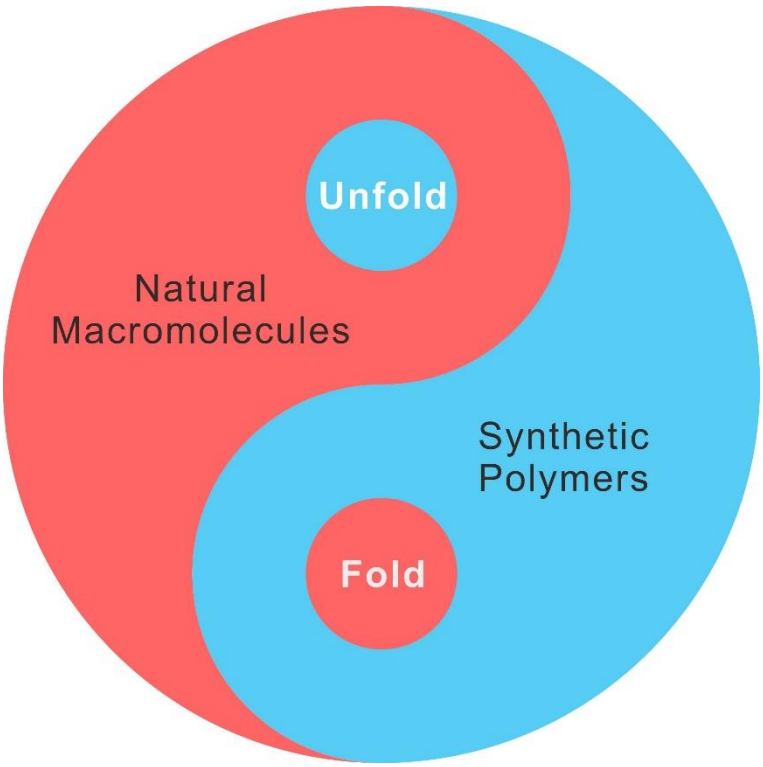

Parts of this thesis (section 1.4) are already published in the following journal article:

Chen CJ, Ng DYW, Weil T. Polymer bioconjugates: Modern design concepts toward precision hybrid materials, *Prog. Polym. Sci.* **2020**, *105*, 101241.

https://doi.org/10.1016/j.progpolymsci.2020.101241

1.1 Biomacromolecules and their hierarchical precision structures

Biomacromolecules, also known as biopolymers, are polymers generated by living organisms, which serve as fundamental structural and functional units of life. In comparison to synthetic polymers, biomacromolecules such as proteins and nucleic acids, possess defined monomer sequences that fold and self-assemble into uniform and absolute three-dimensional (3D) hierarchical structures. The precise structure formation is of great significance for their various biological functions including biorecognition, molecular transport, enzymatic catalysis as well as the storage, replication and transcription of genetic information.

Proteins are linear polypeptides typically composed of 20 canonical amino acids, which form unique 3D hierarchical architectures via folding and self-assembly under specific physiological conditions [1, 2] (Figure 1-1A). The amino acid sequence linked by amide bonds is defined as the primary structure [3]. The secondary structure, such as α-helix and β-sheet, refers to the local spatial arrangement of the polypeptide chain primarily formed from the hydrogen bond interactions between intrachain amide bonds [4]. Further folding of the secondary structure domains form the tertiary structure. Finally, the quaternary structure can be obtained by assembling individual proteins into supramolecular biological units. In particular, highly complex yet precise protein cages of symmetric shapes are widely formed in Nature [5, 6] (Figure 1-1B).

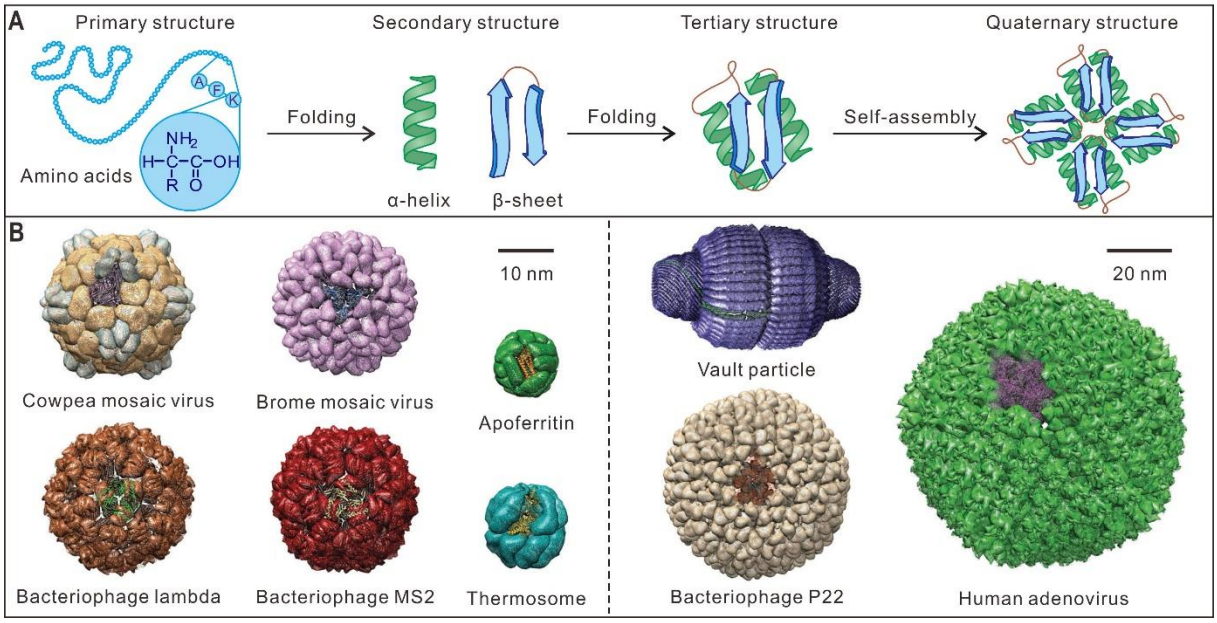

Figure 1-1 | Hierarchical structures of proteins. (A) Folding and self-assembly of polypeptides into hierarchical protein structures. (B) Selected protein cages with symmetric structures [6]. Copyright 2016. Adapted with permission from the Royal Society of Chemistry.

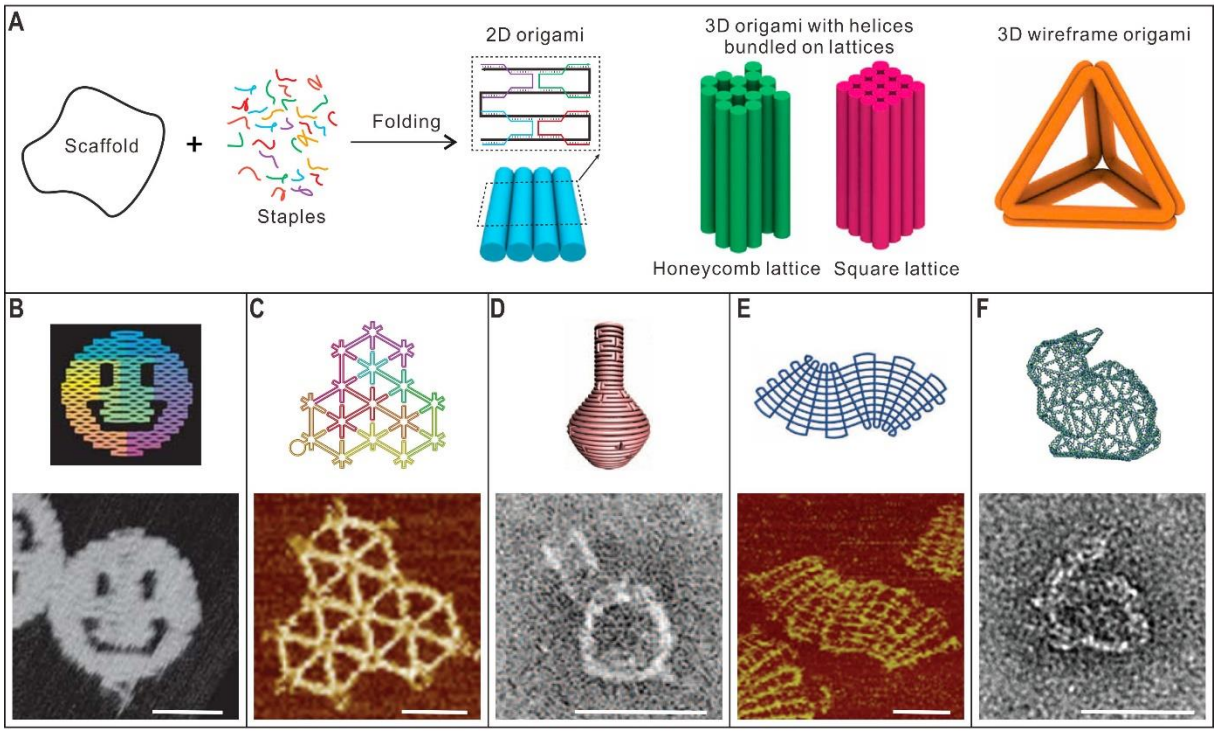

Figure 1-2 | Programming DNA chains into arbitrary structures. (A) DNA origami for the fabrication of 2D and 3D nanoobjects [7]. Copyright 2017. Adapted with permission from Elsevier Inc. (B) A smiley face [8]. Copyright 2006. Reproduced with permission from Springer Nature. (C) A 2D wireframe DNA origami pattern [9]. Copyright 2015. Reproduced with permission from Springer Nature. (D) A nanoflask [10]. Copyright 2011. Reproduced with permission from the American Association for the Advancement of Science. (E) An S-shaped gridiron structure [11]. Copyright 2013. Reproduced with permission from the American Association for the Advancement of Science. (F) A wireframe Stanford bunny [12]. Copyright 2015. Reproduced with permission from Springer Nature. All scale bars indicate 50 nm.

Nucleic acids, polymers composed of nucleotides, are another important class of biomacromolecules. As carriers of genetic information, deoxyribonucleic acid (DNA) chains form double helixes with their complementary sequences and ribonucleic acid (RNA) single chains fold into sophisticated tertiary structures. Pioneered by Seeman in the 1980s, DNA has been explored as an emerging building block for preparation of precision nanostructures in material science [13-15]. More recently, DNA origami, which refers to the folding of DNA chains, has provided the vast possibility to design and construct arbitrary two-dimensional (2D) and 3D nanoobjects [16-18]. As shown in Figure 1-2A, this technique involves the arrangement of a long single-stranded DNA (scaffold) with the help of hundreds of short complementary sequences (staples) [7]. In 2006, Rothemund demonstrated the DNA origami technique by folding DNA into a series of different 2D shapes including a smiley face (Figure 1-2B) [8]. Since then, this field has been progressed rapidly and various 2D and 3D precision nanostructures

have been reported (Figure 1-2C to F), showing the great versatility of the technique for constructing hierarchical nanomaterials [9-12].

Collectively, both polypeptides and DNA chains provide some advantages over synthetic polymers. On the one hand, they possess controlled lengths and defined monomer sequences. On the other hand, these biomacromolecules can both be programmed into precise 3D hierarchical nanostructures, which are often the molecular basis of their biological functions. Very importantly, folding and self-assembly are two basic principles to drive the formation of these structures.

1.2 Synthetic approaches to structurally defined polymers

The synthesis of polymers with similar features of biomacromolecules, including controlled molecular weights, narrow molecular weight distributions, and controlled monomer sequences, has been a long-standing goal for synthetic chemists. In this regard, controlled polymerization techniques have been developed to synthesize well-defined polymers with high control over the molecular weight and the size distribution [19-21]. In addition, much efforts have been devoted for the preparation of sequence-controlled polymers via different approaches. In this section, two of the most prominent controlled radical polymerization techniques, atom transfer radical polymerization (ATRP) and reversible addition—fragmentation chain transfer (RAFT) polymerization, are first introduced followed by a brief overview on the synthesis of sequence-controlled polymers.

1.2.1 Controlled radical polymerizations

ATRP is a versatile living radical polymerization technique that enables the synthesis of polymers with controlled molecular weights, low molecular weight distributions, and desired functionalities. It was independently discovered by the research groups of Matyjaszewski [22] and Sawamoto [23] in 1995. As displayed in Figure 1-3A, the ATRP process relies on an equilibrium between a large number of dormant species (P_n-X) and a low concentration of active propagating species ($P_n^{\bullet}$). A transition metal complex in its low oxidation state (Mt^m-Y/Ligand) is used as catalyst to activate the dormant species via an inner sphere electron transfer process [24-27]. Polymer chains grow after the addition of monomers to the generated intermediate radicals. The metal complex in its high oxidation state (X-Mt^{m+1}-Y/Ligand) is able to rapidly react with

radicals to reform the activator and the dormant species. This ensures the low concentration of the active propagating species and a well-controlled ATRP. Due to its tolerance to a wide range of monomers, solvents, and polymerization conditions, ATRP has been intensively used to synthesize structurally defined polymers with different compositions, topologies, and functionalities. These novel "precision" polymeric materials have found applications in various fields, such as nanomaterial synthesis, photonics, and biomedicine [24, 25]. In addition to normal ATRP, some new ATRP techniques, for example, activators regenerated by electron transfer (ARGET) ATRP [28, 29], initiators for continuous activator regeneration (ICAR) ATRP [30, 31], supplemental activators and reducing agents (SARA) ATRP [32], and electrochemically mediated ATRP (eATRP) [33], have also been developed, allowing polymer synthesis with only ppm amounts of metal catalysts (Figure 1-3A).

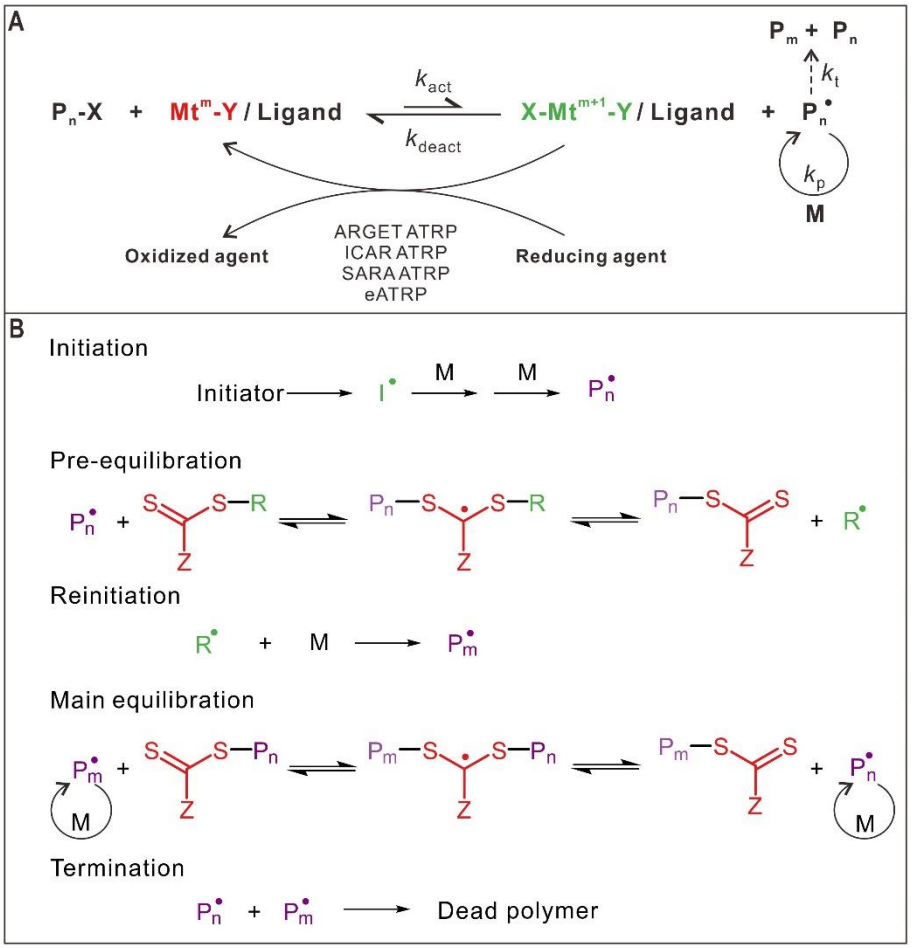

Figure 1-3 | Controlled radical polymerizations. (A) Scheme of the ATRP equilibrium with details also showing the regeneration of active catalysts in various non-conventional ATRP techniques. Adapted with permission from [25]. Copyright 2014 American Chemical Society. (B) The proposed mechanism of RAFT polymerization. Reproduced with permission from [34]. Copyright 2017 American Chemical Society.

RAFT polymerization, first reported in 1998, is another controlled radical polymerization technique for the synthesis of polymers with narrow molecular weight distributions as well as tailored molecular weights and architectures [35]. In comparison to ATRP, RAFT polymerization does not require transition metal catalysts. Instead, chain transfer agents, typically thiocarbonylthio compounds, are used to mediate the polymerization via a reversible chain transfer process [36, 37]. The mechanism of RAFT polymerization is depicted in Figure 1-3B. In an effective RAFT reaction, the chain transfer process is faster than the propagation, ensuring similar chances for growth and growth rates for all polymer chains. The growing radical chains are kept in a low concentration and the chain termination is highly restricted. Due to its compatibility with a variety of reaction conditions and monomers, RAFT polymerization has been widely adopted to produce functional polymeric materials for many applications in materials science and biomedicine [38, 39].

1.2.2 Sequence control of synthetic polymers

The development of controlled radical polymerizations has greatly improved the control over the molecular weight and molecular weight distribution of synthetic polymers. However, the sequential arrangement of monomers, which is another crucial feature of biomacromolecules, is still very challenging in a non-natural polymer chain [40]. In Nature, the monomer sequence of biopolymers is of great importance because it determines their biofunctions, higher order structures, and often macroscopic properties. To better understand structure—property relationships of polymers, the preparation of synthetic polymers with defined monomer sequences has emerged as a recent research interest for synthetic chemists [41].

The major efforts to achieve this goal can be categorized into two strategies [42]. The first strategy takes advantage of biological entities, such as DNA templates, enzymes, and ribosomes, to regulate the sequence of non-natural monomers. For example, Liu et al. reported the enzyme-free synthesis of sequence-defined peptide nucleic acids [43, 44] and non-nucleic acid polymers [45] by using DNA templates. The polymerase chain reaction (PCR) and genetic engineering are two routinely used techniques for the synthesis of nucleic acids and structural proteins based on natural base pairs and amino acids, respectively [46, 47]. They can also be applied for non-natural monomers to prepare sequence-controlled polymers [48-50].

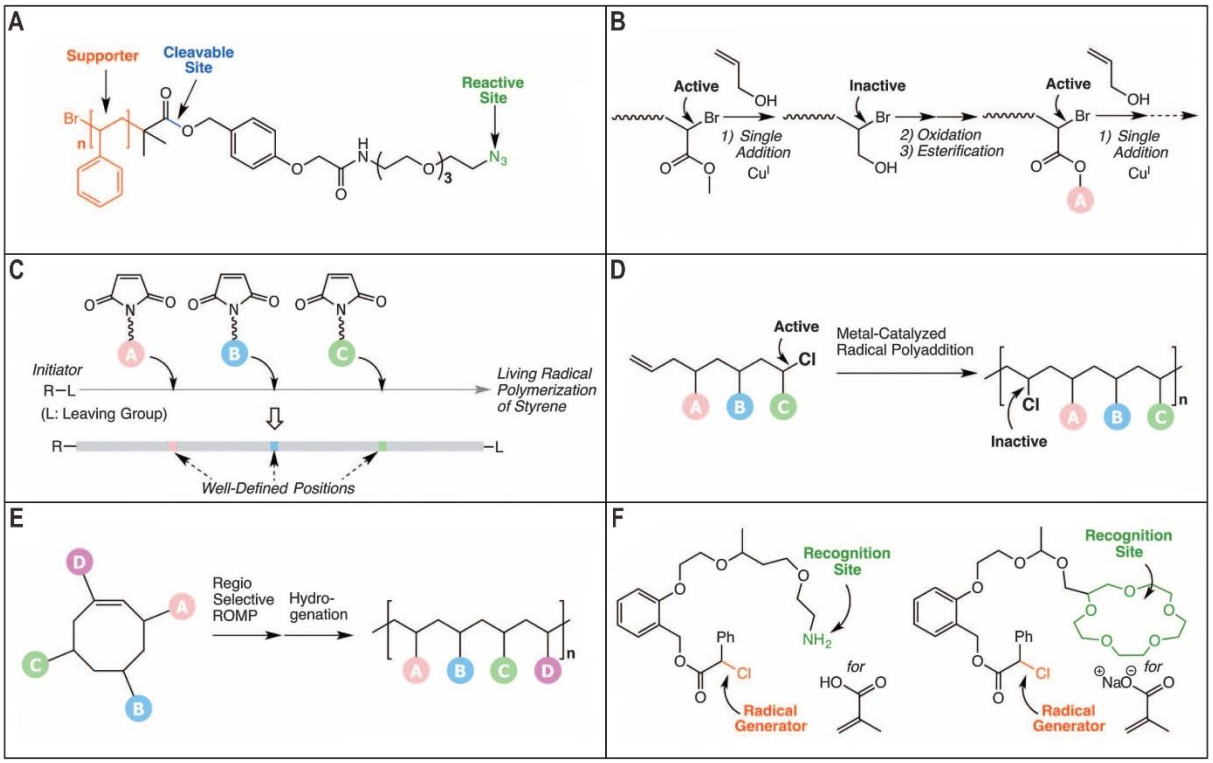

Figure 1-4 | Synthesis of sequence-controlled polymers by chemical approaches. (A) Soluble polystyrene supporter with a reactive azide end for iterative synthesis. (B) Single-monomer addition in ATRP of allyl alcohol. (C) Time-controlled additions of functional comonomers in living radical polymerization of styrene. (D) Preparation of sequence-controlled vinyl polymers via metal-catalyzed radical polyaddition between a carbon—chlorine bond and nonconjugated olefin. (E) Regioselective ring-opening metathesis polymerization (ROMP) of asymmetric substituted cyclooctenes for the synthesis of sequence-specific vinyl copolymers. (F) Template initiators for living radical polymerization. [42], Copyright 2013. Reproduced with permission from the American Association for the Advancement of Science.

The second strategy is based on chemical approaches, which may allow large-scale synthesis of sequence-controlled polymers with diverse structures [40, 42]. An evident method is to link monomers one by one in a designed sequence. The solid-phase synthesis of peptides is a famous example using this method. In addition to amino acids, this method can also be used for other monomers. However, the accessibility of reaction sites in solid supports is often restricted, which may lower the coupling efficiency. To address this issue, soluble polystyrene supports containing reactive azide end groups have been prepared for iterative synthesis (Figure 1-4A) [51]. The sequence regulation in chain-growth or step-growth polymerizations is more difficult but some progress has been achieved. Huang et al. reported single-monomer addition in ATRP of allyl alcohol due to inactivity of the resulting halogen end for radical formation or chain propagation (Figure 1-4B) [52]. However, another allyl alcohol can be added to the terminus when the hydroxyl methyl side chain is oxidized and

functionalized by esterification, allowing iterative addition of functional groups in a controlled sequence. Lutz et al. used time-controlled additions of acceptor comonomers during the controlled radical polymerization of styrene and realized site-directed functionalization of polymer chains (Figure 1-4C) [53, 54]. Step-growth polymerizations, such as metal-catalyzed radical polyaddition (Figure 1-4D) [55, 56] and regioselective ROMP (Figure 1-4E) [57], have also been used for the synthesis of sequence-controlled polymers and they are particularly suitable for preparing periodic polymers [42]. In addition, Sawamoto et al. reported template initiators that can recognize specific monomers, allowing selective monomer insertion and sequence control in living radical polymerizations (Figure 1-4F) [58, 59].

The preparation of sequence-controlled polymers has become a prominent topic in fundamental polymer science over the past decade. These novel polymer materials have also created new possibilities to tune the structure and broaden the application of synthetic polymers [41]. For a full overview of this emerging field, a recently published book [60] and some excellent reviews [40, 42] can be referred.

1.3 Biotemplated preparation of well-defined nanostructures

As mentioned above, biomacromolecules such as polypeptides and nucleic acids not only possess defined monomer sequences and monodisperse sizes, but also form well-defined 3D hierarchical structures under specific conditions. Therefore, these biomacromolecules and their higher order assemblies can be used as precision templates for the construction of various structurally defined nanomaterials [61].

Self-assembled protein nanostructures offer fascinating structural features for biotemplated synthesis of nanomaterials. For instance, microtubules, which are cylindrical protein filaments from the cytoskeleton, were used as a template for the preparation of temperature-responsive nanopatterned poly(*N*-isopropylacrylamide) (PNIPAM) brushes [62]. Wang and Koley et al. demonstrated the synthesis of one-dimensional (1D) conductive polyaniline and polypyrrole nanowires using rod-like tobacco mosaic virus as the template [63]. Functional nanohybrids have also been prepared by directly grafting polymers from highly symmetrical protein cages [64, 65]. Particularly, Douglas et al. reported the site-specific ATRP from the inner surface of the bacteriophage P22-based virus-like particles to form a scaffold, which was used for high-density loading of different functional small molecules (Figure 1-5A) [66].

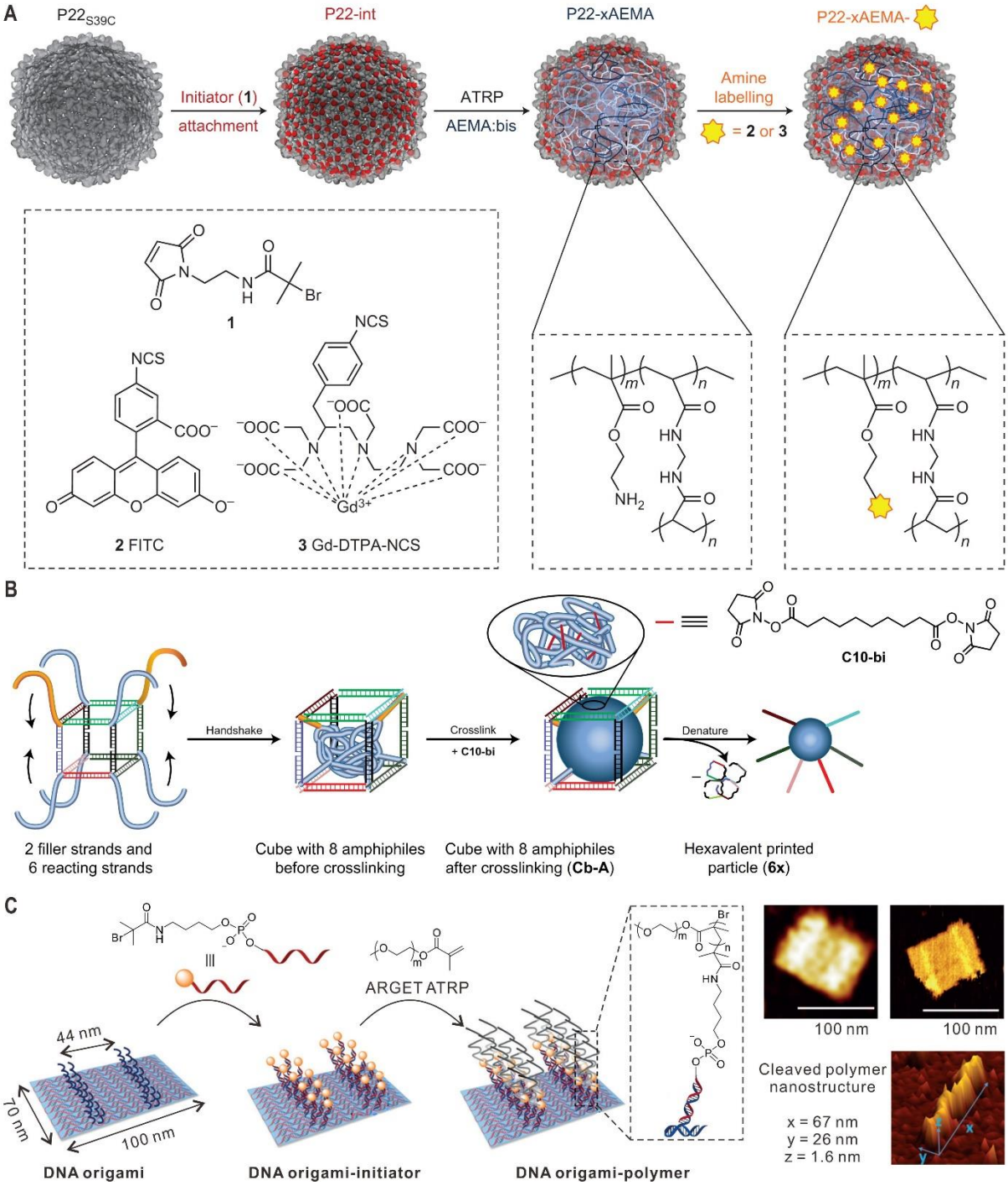

Figure 1-5 | Biotemplated synthesis of precision polymer nanostructures. (A) Site-specific ATRP of 2-aminoethyl methacrylate (AEMA) from the interior cavity of the P22 capsid. After crosslinking, functional small molecules, fluorescein isothiocyanate (FITC) or the magnetic resonance imaging (MRI) contrast agent Gd-DTPA-NCS (Gd: Gadolinium; DTPA: diethylenetriamine pentacetate), were further loaded into the polymer scaffold [66]. Copyright 2012. Reproduced with permission from Springer Nature. (B) Monodisperse polymer nanoparticles with prescribed DNA-strand patterns templated by a DNA cube scaffold. Sebacic acid bis(N-succinimidyl) ester (C10-bi) was used to crosslink the hydrophobic core [67]. Copyright 2018. Reproduced with permission from Springer Nature. (C) DNA origami-templated synthesis of polymer nanostructures by in situ ATRP [68]. Copyright 2016. Adapted with permission from John Wiley and Sons.

In addition to protein assemblies, nucleic acids that can be programmed into arbitrary 2D and 3D nanostructures are also excellent biotemplates for nanomaterial synthesis. For example, O'Reilly et al. employed a synthetic nucleic acid analogue [poly(styrene-*b*-vinylbenzyl thymine)] to prepare monodisperse micelles, which could serve as a template for the radical polymerization of a complementary adenine monomer based on a biomimetic segregation/templating approach [69]. As shown in Figure 1-5B, Sleiman et al. described the preparation of monodisperse polymer nanoparticles with a tunable number of different DNA strands in predetermined orientations by using DNA cube structures as the template [67]. The DNA-imprinted nanoparticles were able to assemble into well-defined hierarchical nanostructures by DNA base pairing. The Weil group reported the first example of in situ ATRP from a DNA origami template to prepare patterned polymeric nanostructures (Figure 1-5C) [68]. Importantly, the polymer nanostructures after cross-linking were stable in solution when the DNA origami template was removed. In addition, this DNA origami-templated technology was also employed to prepare polydopamine nanostructures of different shapes and sizes [70, 71].

Inorganic and/or metallic nanomaterials with desired architectures, which have applications in broad fields ranging from biomedicine and catalysis to electronics and energy, can also be fabricated using biological templates [61]. For instance, McMillan and coworkers fabricated ordered nanoparticle arrays of metal and semiconductor quantum dots using genetically engineered chaperonin protein templates, via either site-selective particle immobilization [72] or in situ constrained synthesis [73]. Tobacco mosaic virus has also been used as robust protein templates for the preparation of solution-stable gold nanoparticle rings [74] and rod-shaped core—shell hybrids based on metal—organic frameworks [75]. The development of DNA origami technology has improved the control over the synthesis of nanostructures to an unprecedented level [76-78]. Recently, Fan and Yan et al. reported the synthesis of biomimetic silica nanocomposites with a wide range of different shapes using frame-like, curved and porous DNA origami nanostructures as templates (Figure 1-6A and B) [79]. In addition to proteins and nucleic acids, carbohydrates have also been used as biotemplates for the synthesis of inorganic nanomaterials [80, 81]. As an example, Lin et al. reported the templated preparation of a wide range of 1D nanocrystals including plain nanorods, core—shell nanorods and nanotubes by using cylindrical cellulose-based bottlebrush polymers as nanoreactors (Figure 1-6C to F) [82].

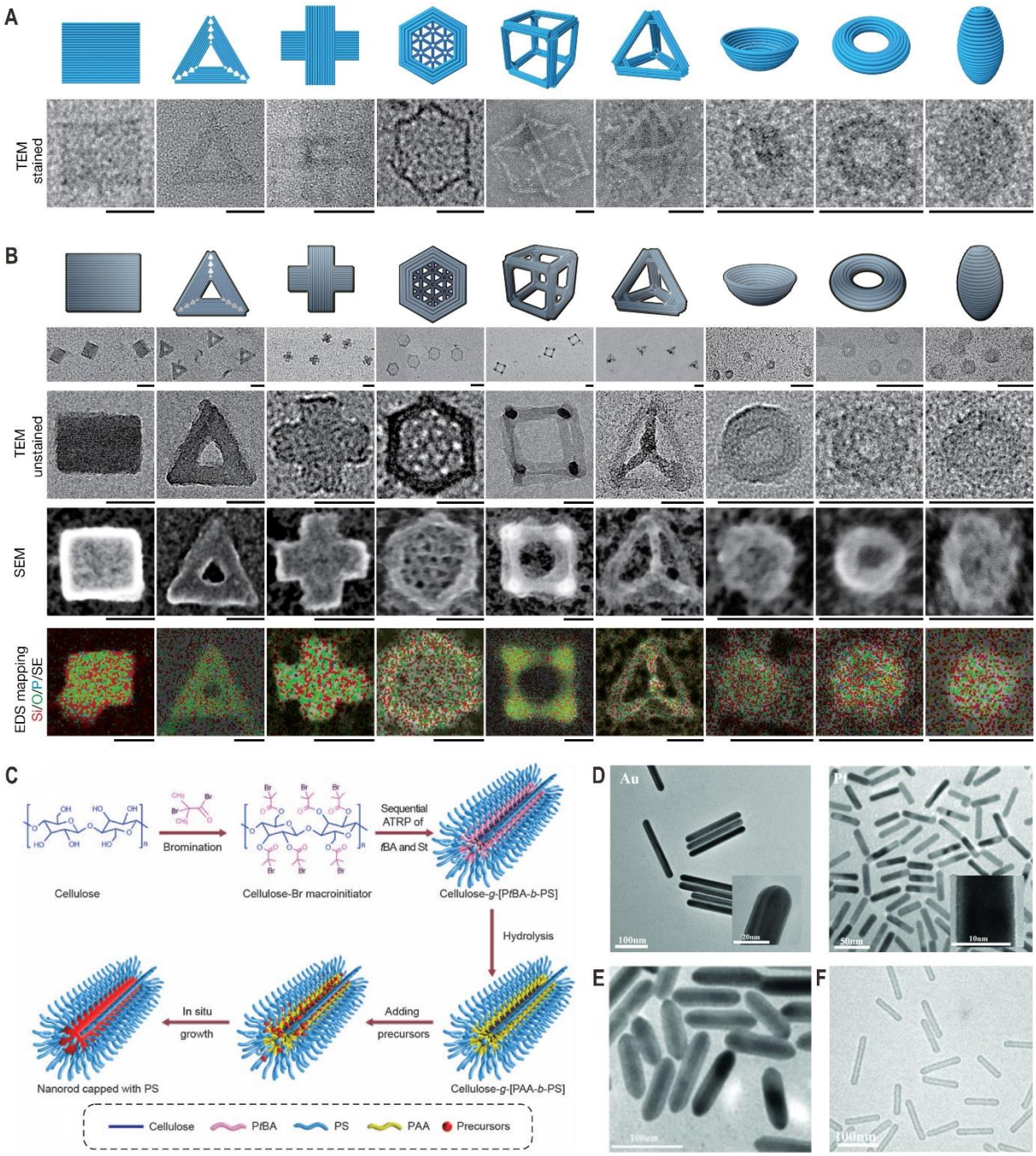

Figure 1-6 | Biotemplated synthesis of inorganic nanostructures. (A) Designed models and corresponding transmission electron microscopy (TEM) images of the 2D and 3D DNA origami templates. (B) TEM images, scanning electron microscope (SEM) images and energy dispersive spectrometer (EDS) mapping images (Red: Si, green: O, blue: P; SE, secondary-electron image) of the corresponding DNA origami silicification nanostructures. [79], Copyright 2018. Reproduced with permission from Springer Nature. (C) Scheme for the templated synthesis of plain nanorods by using cellulose-*g*-(PAA-*b*-PS) as nanoreactors. St, styrene; PS, polystyrene; PAA, poly(acrylic acid); *t*BA, *tert*-butyl acrylate. (D) TEM images of Au and Pt plain nanorods. (E) TEM image of Au-Fe_3O_4 core–shell nanorods templated by cellulose-*g*-(P4VP-*b*-P*t*BA-*b*-PS). P4VP, poly(4-vinylpyridine). (F) TEM image of Au nanotubes templated by cellulose-*g*-(PS-*b*-PAA-*b*-PS). [82], Copyright 2016. Reproduced with permission from the American Association for the Advancement of Science.

1.4 Precision nanomaterials based on unfolded proteins

1.4.1 Synthesis of precision protein-derived polymers

Globular proteins can be denatured by external stress such as solvents, inorganic salts, exposure to acids or bases, and by heat, which alters their secondary and tertiary structures but retains the peptide bonds of the primary structure between the amino acids [83]. Since all structural levels of the protein determine its function, the protein is usually no longer bioactive once it has been denatured. However, unfolded proteins could be regarded as monodispersed biopolymers providing well-defined contour length and various functional groups at determined positions along the main chain. In 2003, Whitesides et al. pioneered an approach for preparing linear polymers with determined chain lengths and functional groups at defined locations along the chain by acylation of denatured proteins [84]. In the past decade, the Weil group has explored denatured proteins as a unique polymer platform for the construction of defined nano-architectures for various applications [85]. For protein denaturation, protein aggregation during the denaturation process needs to be strictly avoided as it is very challenging to disaggregate the protein agglomerates once they have precipitated, which reduces yields and makes purification more difficult. Typically, chaotropic agents such as urea to break hydrogen bonds and other supramolecular forces and mild reducing agents such as tris(2-carboxyethyl) phosphine (TCEP) are added. Stabilizing hydrophilic polymer chains can be attached to the polypeptide backbone before or after the denaturation step to prevent aggregation of the denatured polypeptide chains [85]. In this regard, poly(ethylene glycol) (PEG) chains of different molecular weights (2000–5000 Da) have been linked through either thiol–maleimide chemistry or amine–*N*-hydroxysuccinimide ester chemistry. PEG chains provide sufficient stability under the denaturing conditions as well as biocompatibility and they alter the hydrophilic–hydrophobic balance of the denatured polypeptide chain consisting of hydrophilic and lipophilic sequence patterns preventing undesirable supramolecular interactions within the chains also due to the steric effect [86]. Figure 1-7A shows typical procedures for unfolding of blood plasma proteins human/bovine serum albumin (HSA/BSA, 66 kDa) by 5 M urea–phosphate buffer (PB) in the presence of TCEP followed by PEG conjugation. Thiol groups of the unpaired cysteines and reduced disulfide bonds are typically exposed during the denaturation step and they can be capped by different maleimides such as PEG–maleimide and *N*-(2-aminoethyl)maleimide to avoid

reformation of disulfide bonds. Noteworthy, the optimal denaturing conditions need to be carefully identified as each protein has a different inherent stability based on its folding as well as the number and location of the disulfide bridges. In this way, hen egg white lysozyme with a molecular weight of 14 kDa requires more drastic denaturation conditions, i.e., 8 M guanidine and excess of the reducing agent dithiothreitol (DTT) for denaturation compared to HSA (Figure 1-7B) [87]. By reacting single accessible thiol groups of BSA with PEG–bismaleimide to synthesize a protein-dimer precursor, a giant polypeptide–PEG–polypeptide triblock copolymer with a very high molecular weight of about 400 kDa has also been reported via the denaturation and PEGylation strategy (Figure 1-7C) [88].

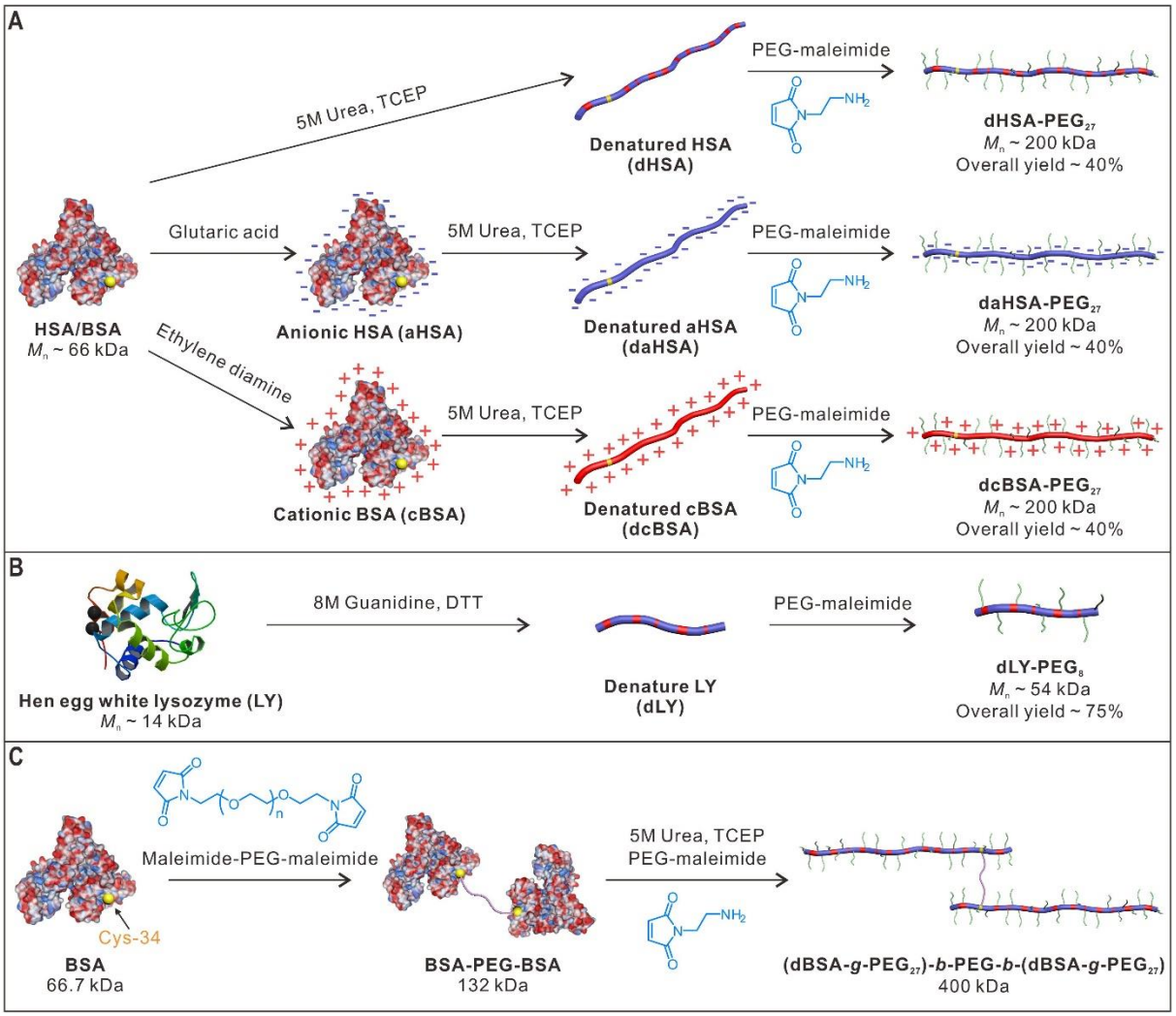

Figure 1-7 | Synthesis of precision protein-derived polymers. (A) Unfolding of HSA/BSA by 5 M urea–PB in the presence of TCEP. (B) Unfolding of lysozyme by 8 M guanidine and excess of DTT. Adapted with permission from [87]. Copyright 2012 American Chemical Society. (C) A giant polypeptide–PEG–polypeptide triblock copolymer by protein dimerization and denaturation [88]. Copyright 2012. Reproduced with permission from John Wiley and Sons.

1.4.2 Applications of denatured protein-derived polymers

The denatured protein–PEG conjugates provide several attractive characteristics: (1) biocompatibility; (2) biodegradability by proteases; (3) defined peptide sequence; (4) the final polymers offer narrow molecular weight distributions that can be characterized by mass spectrometry ensuring the quality control of products; (5) various functionalities in specific positions which allow the realization of complex tasks such as cellular uptake; and (6) tunable transition between globular, collapsed and extended architectures. In addition, the PEG side chains could reduce protein binding and provide “stealth properties” by shielding the immunogenic recognition sites (epitopes) [89]. Therefore, polypeptide–PEG conjugates based on denatured proteins offer various attractive features for biomedical applications and as precision substrates for templated synthesis of well-defined nanomaterials.

Because of their unique optical properties, quantum dots (QDs) and fluorescent nanodiamonds (FNDs) are two promising probes for tracking biological processes i.e. with super-resolution microscopy and drug delivery applications [90, 91]. However, the applications of the “bare” nanoparticles are severely limited by their poor solubility in various biological environments. In addition, other challenges include the toxicity of QDs [92] and the surface modification of FNDs that provide undefined surface functionalities with high batch-to-batch variations [93]. Denatured protein–PEG conjugates serve as attractive nanoparticle coatings due to the availabilities of many reactive amino-, carboxylic acid and thiol groups that could interact with various nanoparticle surfaces though electrostatic interactions or hydrogen bonds as well as the presence of hydrophobic amino acids that bind hydrophobic surfaces by van der Waals interactions. For example, denatured HSA–PEG conjugates functionalized with multivalent thioctic acid (TA) groups stabilize the surface of CdSe–CdZnS QDs (Figure 1-8A) [94]. The coated QDs gain improved water solubility and as well as unique pH-responsiveness, which was attributed to conformational rearrangements of the polypeptide coating at different pH. This could alter the capacity of the polymer to efficiently passivate and protect the nanoparticle surface. Based on this strategy, a polycationic polypeptide–PEG conjugate based on denatured BSA was achieved that encapsulated QDs and enabled their cellular uptake and allowed DNA complexation (Figure 1-8A) [95]. In these systems, the QD core served as an in situ reporter for pH changes, DNA complexation and ultimately even DNA transfection because its

photoluminescence dropped significantly with increasing quantities of complexed DNA. Similarly, the cationized and denatured protein–PEG conjugates could also offer excellent colloidal stability to FNDs so that they remained stable even in the presence of high ionic strength buffers required for DNA folding (Figure 1-8B). In this way, the first DNA origami-assembled FND nanostructures were formed, which is a critical step to study the coherent coupling of ordered spin arrays [96]. Moreover, the biopolymer-coated FNDs remained stable even after encapsulating high amounts of hydrophobic doxorubicin drug molecules and revealed high uptake into human lung adenocarcinoma A549 cells and in vivo efficacy attractive for cancer therapy [97].

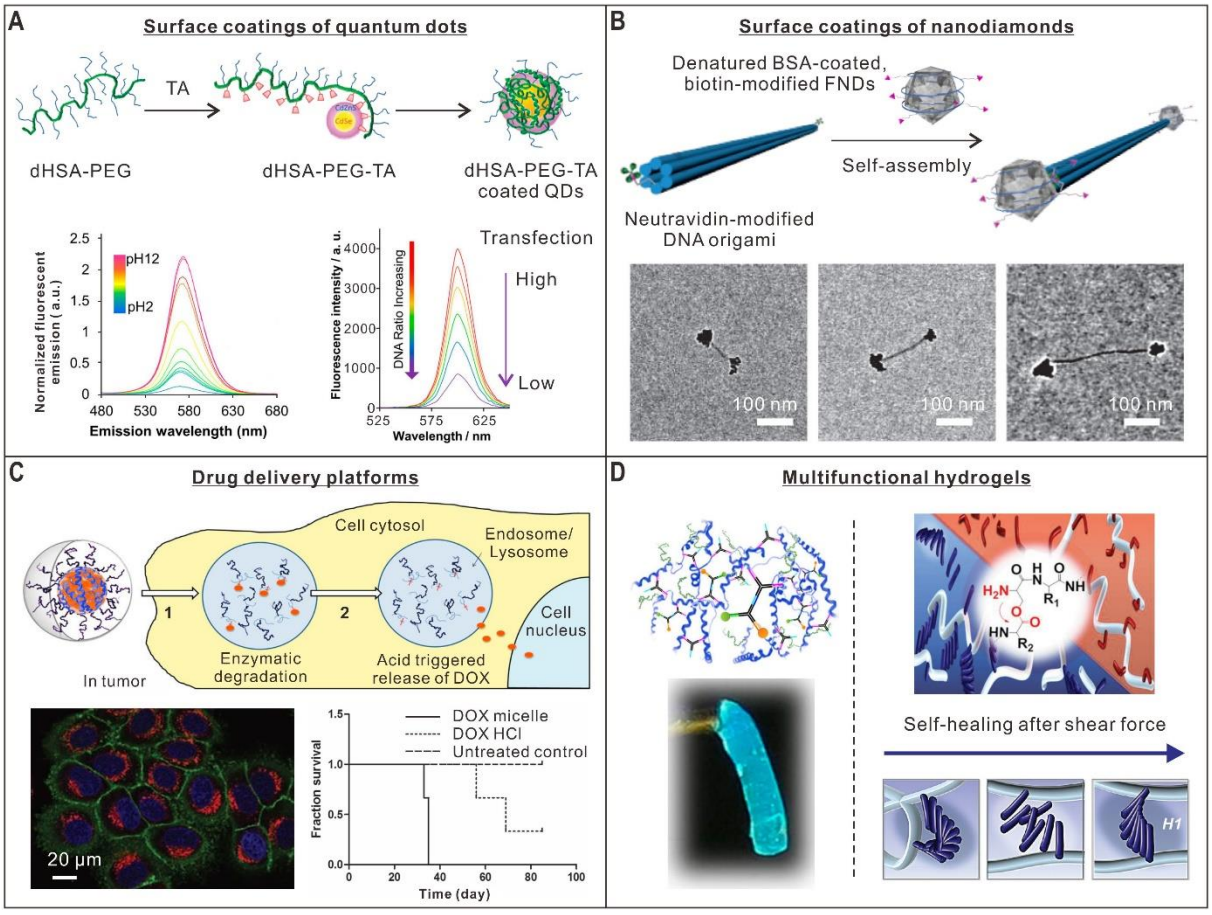

Figure 1-8 | Applications of protein-derived polymers. (A) QDs coated with denatured protein—PEG conjugates as pH (bottom left) and DNA (bottom right) sensors. [94, 95], Copyright 2010 and 2012. Adapted with permission from the American Chemical Society and John Wiley and Sons, respectively. (B) FNDs coated with denatured protein–PEG conjugates for self-assembly. Adapted with permission from [96]. Copyright 2015 American Chemical Society. (C) Core–shell nanocarriers formed from denatured cHSA–PEG conjugates for drug delivery [98]. Copyright 2013. Adapted with permission from John Wiley and Sons. (D) Denatured protein–PEG conjugates as multifunctional and degradable backbones to prepare hybrid hydrogels. [99, 100]. Copyright 2014 and 2019. Adapted with permission from the Royal Society of Chemistry and John Wiley and Sons, respectively.

The architecture of denatured protein–PEG conjugates responds to changes of the balance of hydrophilic and groups along the polypeptide backbone. These changes could either be lipophilic functionalities that are covalently attached or the presence of hydrophobic guest moieties that interact with the lipophilic amino acid side chains via supramolecular interactions. In this way, well-defined core–shell nanostructures were formed suitable for catalysis and delivery of lipophilic molecules into cells. When the cationized and denatured BSA–PEG conjugate was modified with just a few hydrophobic groups such as alkynes, stable nano-sized micelles were formed spontaneously [101]. Complexation with the hydrophobic chromophore perylenetetracarboxydiimide, a denatured HSA–PEG conjugate functionalized with folic acid groups, has been shown to form globular micelles, which were uptaken into cells via receptor-mediated endocytosis [102]. The lipophilic drug doxorubicin has also been encapsulated into these micelles by complexation [103] or covalent conjugation [101] and efficient delivery into various cancer cells has been shown. To achieve selectivity and better control over the drug release profile, a pH-responsive hydrazone linker has been introduced to conjugate doxorubicin to the denatured protein backbone that potentially allows release in the acidic microenvironments of tumor tissue as well as in acidic endosomal vesicle [98]. As shown in Figure 1-8C, a core–shell delivery system composed of a polypeptide core with doxorubicin drug molecules and a PEG shell adopts a two-step drug release based on proteolytic degradation of the backbone and acid-induced drug release. In vitro test of the drug-loaded micelles revealed high cytotoxicities against Hela cells and leukemia cell lines. More importantly, 100% survival rates of mice that received ex vivo transplantation of engrafted leukemic tumor cells after 12 weeks were demonstrated [98].

In combination with various crosslinking chemistries, the denatured protein–PEG conjugate served as biocompatible and biodegradable scaffold to prepare injectable hydrogels. As crosslinkers, multi-arm DNA [99] as well as self-assembling peptide sequences [100] have been applied. Denatured HSA–PEG conjugates were functionalized with single-stranded DNA (ssDNA) sequences that could hybridize with complementary Y-shaped DNA [99]. The formed hydrogel was used to immobilize active proteins, which were released by proteases as well as nucleases independently (Figure 1-8D, left). Furthermore, conjugation of a recombinant Rho-inhibiting C3 toxin that inhibits growth and migration of bone degrading osteoclast cells to the multi-arm DNA linker allows the toxin-loaded hydrogel to reduce osteoclast formation and bone

resorption without affecting differentiation and mineralization of bone forming osteoblast cells [104]. In another example, self-assembling peptides that spontaneously form cross β-sheet fibrillary structures were grafted to the backbone of denatured HSA–PEG conjugate. To control fibril formation of the peptides, they were masked as depsi-precursor peptides. The depsi peptide sequences do not aggregate at acidic pH until an intramolecular *O*,*N*-acyl shift occurs at higher pH values affording the formation of peptide nanofibers, which served as pH-responsive gelators (Figure 1-8D, right). The obtained hydrogels are cytocompatible, biodegradable, reveal rapid self-healing abilities and cells migrated into this porous matrix, rendering them attractive for 3D tissue engineering [100].

1.5 Biomolecule-inspired folding of synthetic polymers

For biomacromolecules, folding is a fundamental strategy to construct 3D hierarchical structures and to perform their biofunctions such as enzyme catalysis, information storage, and energy conversion [105]. Could synthetic polymers accomplish the same task? Inspired by the structure of folded biomolecules, the folding of synthetic polymers into single-chain nanoparticles and topological polymers with desired architectures has attracted much attention in recent years [106-108]. This section highlights some examples of single-chain polymer folding via different chemistries.

1.5.1 Single-chain polymer nanoparticles

Three different methods, homofunctional collapse, heterobifunctional collapse, and crosslinker-mediated collapse, are often used for intramolecular folding of synthetic polymers to prepare single-chain polymer nanoparticles (SCPNs) (Figure 1-9A) [107]. These approaches can be achieved via various chemistries including irreversible covalent bonds, dynamic covalent bonds, and supramolecular interactions.

A wide range of irreversible covalent chemistries, such as free radical coupling [109], benzocyclobutene (BCB) dimerization [110], benzosulfone dimerization [111], azide—alkyne click chemistry [112], thiol—yne click chemistry [113], Michael addition reaction [114], and oxidative polymerization of thiophene [115], have been used for making SCPNs. For example, Hawker et al. reported the intramolecular folding of BCB-functionalized linear PS and SCPNs in multigram quantities were prepared by using a continuous addition strategy (Figure 1-9B) [110].

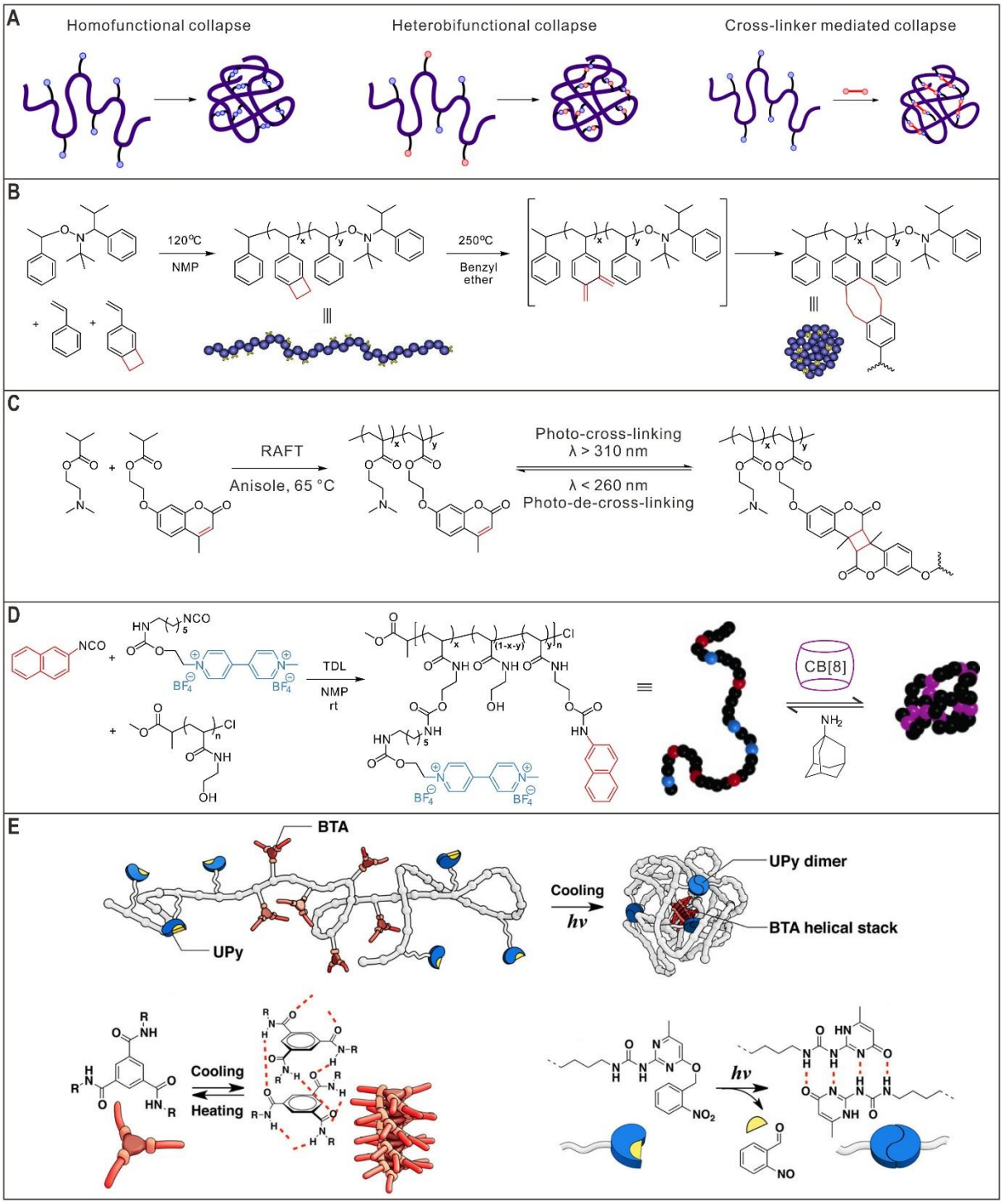

Figure 1-9 | Synthesis of SCPNs via different approaches and chemistries. (A) Three main approaches for preparing SCPNs. Reproduced with permission from [107]. Copyright 2016 American Chemical Society. (B) BCB dimerization-mediated intramolecular folding of PS. Reproduced with permission from [110]. Copyright 2002 American Chemical Society. (C) SCPNs prepared via the reversible photodimerization of coumarin groups [116]. Copyright 2011. Reproduced with permission from the Royal Society of Chemistry. (D) Formation of SCPNs in water through the CB[8]-based host—guest interaction [117]. Copyright 2012. Reproduced with permission from John Wiley and Sons. (E) Orthogonal folding of ABA triblock copolymers with BTA and UPy moieties in to SCPNs. Reproduced with permission from [118]. Copyright 2013 American Chemical Society.

SCPNs formed via irreversible covalent bonds have good stability under various conditions, which is a unique advantage for some applications but also can be a disadvantage in other cases. To mimic the dynamic nature of biomolecules, SCPNs that can respond to external stimuli have been prepared by using dynamic covalent bonds and supramolecular interactions [119, 120]. Zhao et al. synthesized coumarin-containing random copolymers via RAFT polymerization, which could be folded into well-defined SCPNs by the intrachain photodimerization of coumarin groups under UV irradiation at $\lambda > 310$ nm (Figure 1-9C). This transition was partially reversible after exposing the generated SCPNs to UV light at $\lambda < 260$ nm [116]. Using the strategy of crosslinker-mediated collapse, Fulton et al. prepared thermoresponsive dynamic covalent SCPNs based on functional copolymers with aromatic aldehyde groups, which form acyl hydrazone cross-links after adding dihydrazide [121]. These SCPNs were able to transform into a hydrogel after heating their aqueous solution at mildly acidic pH. Similarly, Scherman et al. reported the preparation of SCPNs in water via the cucurbit[8]uril (CB[8])-based host-guest chemistry [117]. As shown in Figure 1-9D, water soluble poly(*N*-hydroxyethyl acrylamide) was functionalized with viologen and napthyl guest moieties, and the obtained copolymer can be folded intramolecularly via formation of ternary complex with cucurbit[8]uril.

In addition to the polymer folding based on a single chemical interaction, two or more orthogonal interactions can be combined in one system for the stepwise folding of synthetic polymers mimicking the hierarchical structures of biomacromolecules [107]. For instance, Meijer and Palmans et al. reported the orthogonal folding of ABA triblock copolymers containing two different functional groups, *o*-nitrobenzyl-protected 2-ureidopyrimidinone (UPy) and benzene-1,3,5-tricarboxamide (BTA), in the A and B blocks [118]. While BTA groups undergo reversible self-assembly into helical aggregates when temperature is tuned, the deprotected UPy moieties form dimers after UV light irradiation (Figure 1-9E). Lutz et al. reported the successive compaction of a sequence-controlled polymer which bears pentafluorophenyl-activated ester and triisopropylsilyl-protected alkyne functions. The former group can be easily crosslinked by ethylenediamine, whereas the latter moiety self-reacts by Eglinton coupling [122]. Barner-Kowollik and Altintas et al. prepared well-defined tetrablock copolymers and studied their orthogonal folding and unfolding behaviors based on multiple hydrogen bonds and host-guest interactions [123].

1.5.2 Folded polymers with controlled topologies

For most reported SCPNs, synthetic polymers are folded into compact states in a random way. However, the folding process in biopolymers is precisely controlled. Therefore, the controlled folding of synthetic polymers into designed topologies is recognized as a grand challenge. In this regard, the preparation of cyclic polymers via intramolecular folding has attracted special attention [124, 125]. Grayson et al. pioneered the synthesis of well-defined macrocyclic polymers via copper-catalyzed azide—alkyne cycloaddition (CuAAC) [126]. They synthesized polystyrene precursors by ATRP using an alkyne-containing initiator propargyl 2-bromoisobutyrate. Because the bromine end could be easily transformed into an azide group, the linear polymer with two complementary terminal groups, alkyne and azide, was then folded intramolecularly under dilute conditions using a continuous addition technology. Importantly, both the azidation and the cyclization showed high yields and further separation was not required [126]. This simple strategy has also been used to fold other linear polymers, such as PNIPAM [127], poly(methyl methacrylate) [128], and even block copolymers [129, 130], into cyclic forms.

Like the formation of SCPNs, other covalent and non-covalent interactions have also been used as ring-closure techniques for the folding of linear polymers. For example, cyclic poly(lactide)s were prepared via the Michael addition of thiols to maleimides [131] and Glaser coupling reaction of alkynyl groups was used to cyclize linear PEG and polystyrene [132]. Deffieux et al. demonstrated the reversible folding of homotelechelic linear polystyrene with porphyrin end groups into the cyclic form [133]. Similarly, Yamamoto et al. reported the light- and heat-induced switching of linear and cyclic PEG telechelics with anthryl end groups [134].

In addition to the simple monocyclic shape, Lutz et al. reported the controlled folding of linear polymers into four different topologies, including P-shape, Q-shape, 8-shape, and α-shape (Figure 1-10A). This strategy was based on the synthesis of well-defined polystyrene chains with reactive alkyne functions at desired positions [135]. As shown in Figure 1-10B, all folded polymers showed clear decrease of the apparent molecular weight. Harada et al. studied the reversible conversion of different shapes of PEG-substituted β-cyclodextrin with an azobenzene end [136]. Tezuka et al. reported a pentacyclic quadruply fused polymer topology via polymer folding through different reactions including CuAAC and olefin metathesis [137].

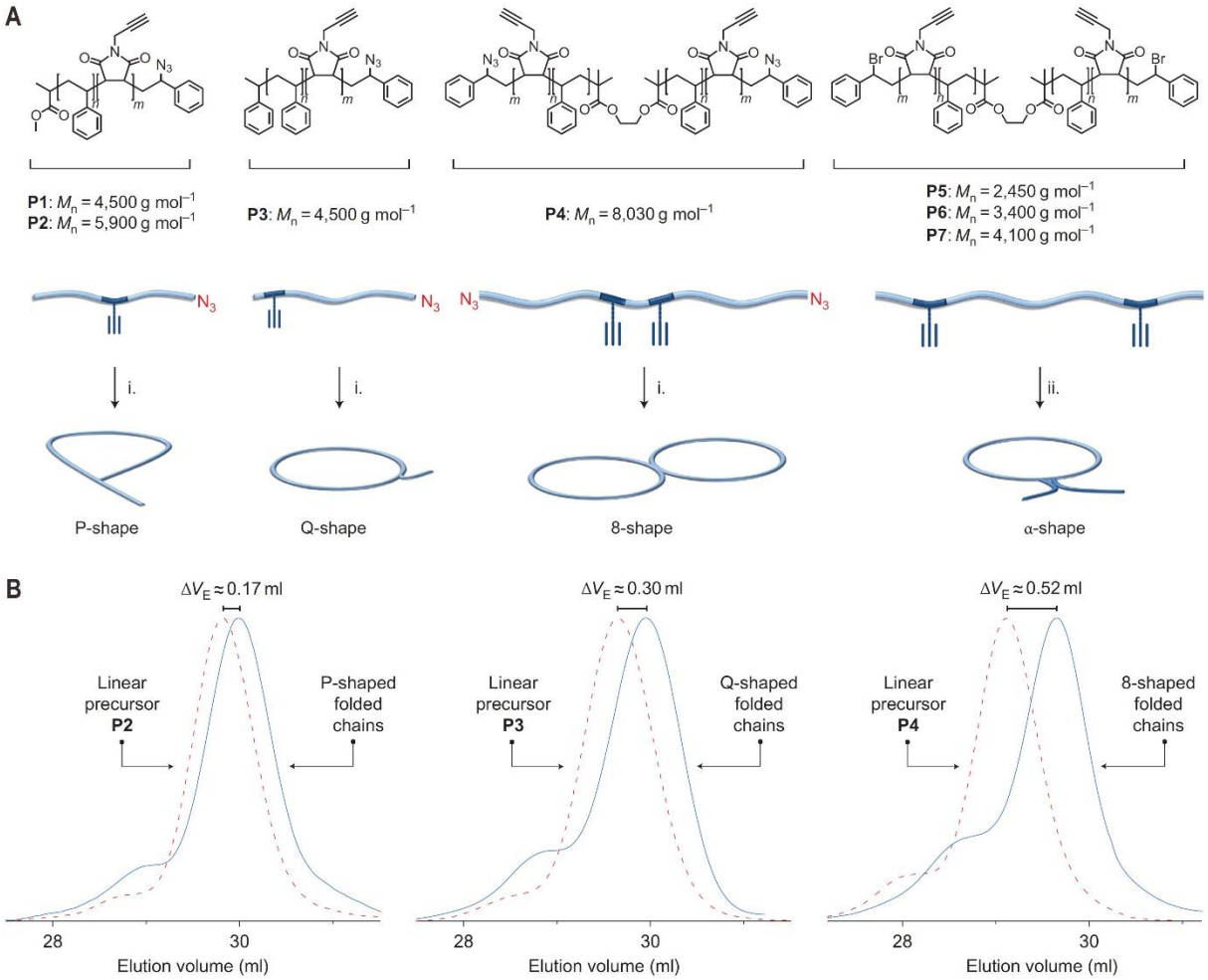

Figure 1-10 | Folding of linear polymers into controlled topologies. (A) Molecular structures and schematic illustration of polystyrene chains with position-defined reactive alkyne groups that can be folded into four different shapes: P-shape, Q-shape, 8-shape, and α-shape. Folding reactions i and ii represent CuAAC and Glaser coupling, respectively. (B) Size-exclusion chromatograms showing reduced hydrodynamic volume of polymers after folding. [135], Copyright 2011. Reproduced with permission from Springer Nature.

1.6 Controlled nanostructures via macromolecular self-assembly

1.6.1 Self-assembly of linear block copolymers

The self-assembly of amphiphilic block copolymers in selective solvents has gained considerable attention over the past decades for the construction of various polymeric nanostructures [138]. Owing to the development of controlled polymerization techniques, substantial advances have been made to the synthesis of polymeric building blocks with precisely controlled compositions and architectures, providing easy access to the manipulation of morphology and size of assemblies. These assemblies have found a broad range of applications from drug delivery and bioimaging to nanoreactors and artificial organelles [139, 140].

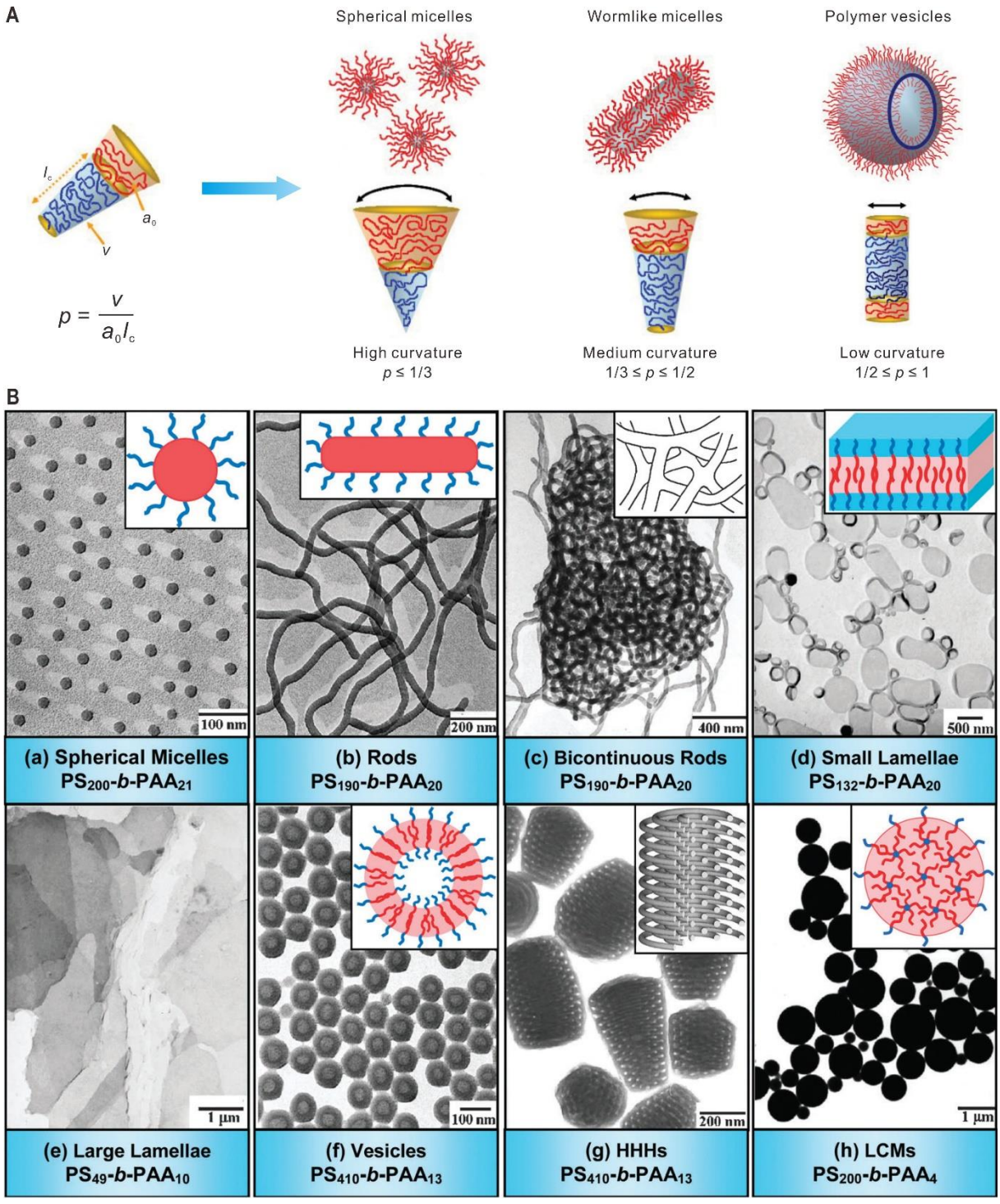

Figure 1-11 | Macromolecular self-assembly in selective solvents. (A) Three most common polymer nanostructures including spherical micelles, wormlike micelles, and vesicles via self-assembly of amphiphilic block copolymers. The morphology is primarily determined by the packing parameter, *p*, as shown in the formula. [139], Copyright 2009. Adapted with permission from John Wiley and Sons. (B) TEM images and corresponding schematic illustrations of various assemblies formed from amphiphilic PS_m-*b*-PAA_n copolymers. Note: *m* and *n* refer to numbers of repeating units of PS and PAA, respectively. HHHs: hexagonally packed hollow hoops; LCMs: large compound micelles. [138], Copyright 2012. Reproduced with permission from the Royal Society of Chemistry.

Amphiphilic block copolymers undergo self-assembly in selective solvents to minimize enthalpically unfavorable interactions between insoluble blocks and the solvent. As displayed in Figure 1-11A, the morphology is primarily determined by the packing parameter, $p = v/a_0l_c$, where v is the volume of the hydrophobic block, a_0 is the area of the head group, and l_c is the length of the hydrophobic tail [139]. Typically, vesicles (also called polymersomes) are favored when $1/2 \leq p \leq 1$, wormlike micelles when $1/3 \leq p \leq 1/2$, and spherical micelles when $p \leq 1/3$. Simple "star-like" spherical micelles are the most common morphology reported in the literature, which has been intensively used as nanocarriers for drug and gene delivery [141, 142]. Polymer vesicles, which possess an aqueous interior and a hydrophobic membrane with both inner and outer surfaces formed by hydrophilic polymers, have also been widely reported for therapeutic applications, cell mimicking and nanoreactors [143, 144]. As another thermodynamically stable structure, wormlike micelles have attracted special interests due to their anisotropic shapes and applications for biomedicine and nanomaterial synthesis [145]. In addition to these common morphologies, a diverse range of other more sophisticated structures have also been reported. For example, Eisenberg et al. systematically studied the solution self-assembly of PS-*b*-PAA, various morphologies, including spherical micelles, rods, different scales of lamellae, vesicles, HHHs, and LCMs, were observed (Figure 1-11B) [138].

Although early studies of macromolecular solution self-assembly were focused on amorphous core-forming blocks, an increasing number of crystallizable core-forming building blocks has also been investigated [140]. In this regard, the living crystallization-driven self-assembly (CDSA), based on polyferrocenylsilane (PFS)-containing block copolymers, pioneered by Manners and coworkers can be used to fabricate 1D and 2D structures with desired dimensions, providing excellent control over the formation of anisotropic polymeric structures [146]. Figure 1-12A shows cylindrical micelles prepared via CDSA of PFS-*b*-polyisoprene using small and uniform PFS-*b*-poly(dimethylsiloxane) crystallites as initiators. The process was found to be analogous to that of living polymerization reactions and monodisperse cylindrical micelles of controlled lengths were obtained [147]. Based on the robust living CDSA technique, other more complex nanostructures, including branched micelles [148], multiblock micelles [149], hierarchical supermicelles [150, 151], and 2D assemblies [152, 153], have also been reported (Figure 1-12B to G). More details about this field have been summarized in some excellent reviews [140, 146].

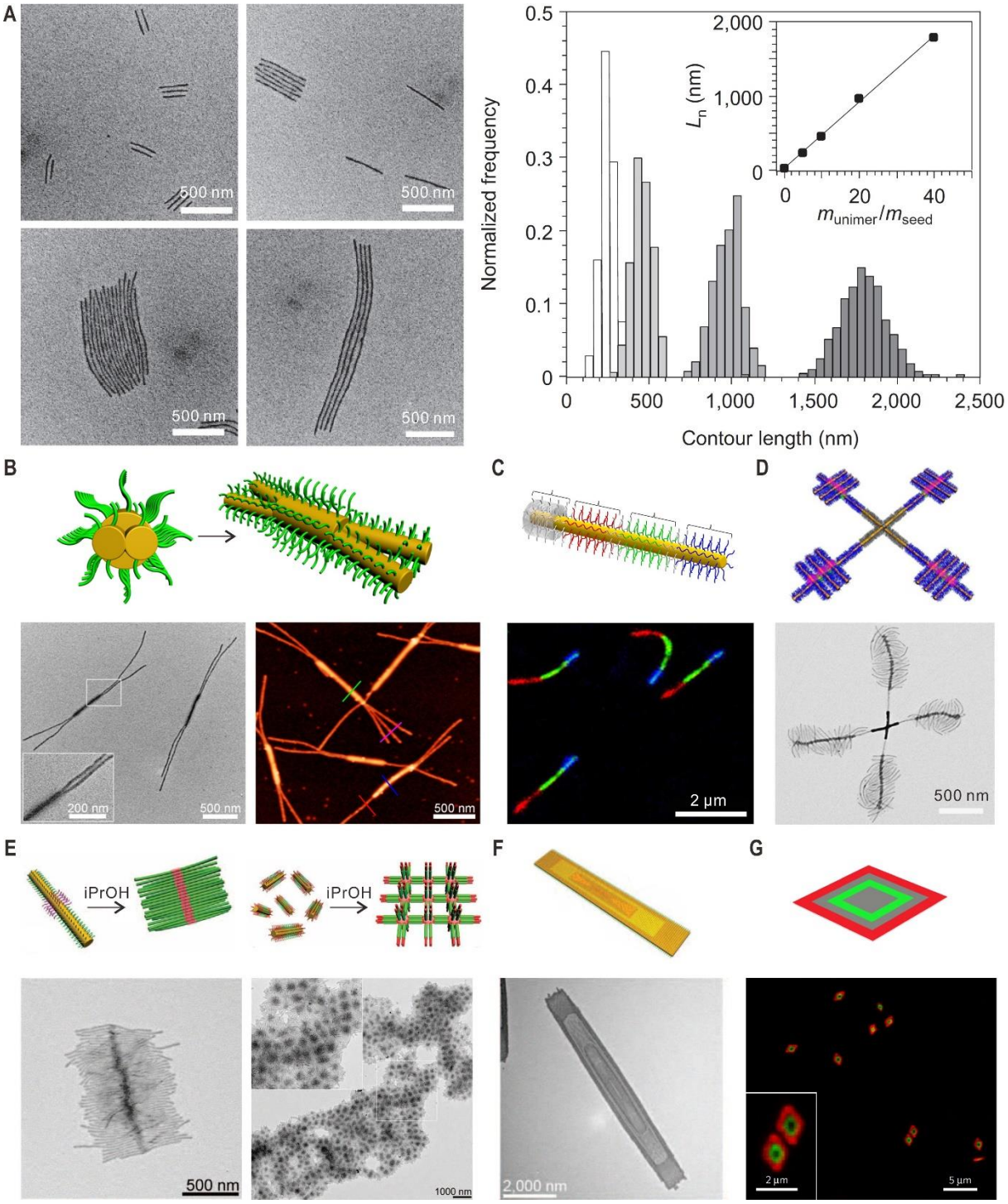

Figure 1-12 | Various precision polymer nanostructures via CDSA. (A) Monodisperse cylindrical micelles with controlled lengths formed of PFS-*b*-polyisoprene [147]. (B) Branched cylindrical micelles [148]. (C) Fluorescent multiblock micelles [149]. (D) "Windmill"-like supermicelles [150]. (E) Hierarchical self-assembly of amphiphilic cylindrical block micelles into 1D supermicelles and 3D superlattices [151]. (F) Rectangular platelet micelles [152]. (G) 2D assemblies formed from crystallizable homopolymers [153]. [A, C, D and G], Copyright 2010, 2014, 2015 and 2017. Reproduced with permission from Springer Nature. [B], Copyright 2013. Reproduced with permission from the American Chemical Society. [E and F], Copyright 2015 and 2016. Reproduced with permission from the American Association for the Advancement of Science.

1.6.2 Self-assembly of folded synthetic polymers

As mentioned in section 1.1, the precision 3D hierarchical structures of biopolymers are generated via folding and self-assembly. For synthetic polymers, the self-assembly of linear block copolymers has been intensively investigated since 1990s. Particularly, highly complex yet precise anisotropic structures can be constructed via CDSA of block copolymers. However, only little attention has been paid to the self-assembly behavior of folded polymers. Zhao and Liu et al. prepared poly(2-(dimethylamino)ethyl methacrylate)-*block*-polystyrene (PDMAEMA-*b*-PS) via RAFT polymerization and folded the PDMAEMA block intramolecularly into SCPNs [154]. By tuning length of the PDMAEMA block, the amphiphilic PS-tethered SCPNs self-assembled into different structures including strawberry-like micelles, vesicles, and bunchy micelles in selective solvents. Similarly, He et al. reported the synthesis of PEG-*block*-[poly(methyl methacrylate)-*co*-poly(3-(trimethoxysilyl)propyl methacrylate)] [PEG-*b*-P(MMA-*co*-TMSPMA)] in which the silane moieties were used for intramolecular cross-linking [155]. The self-assembly structures of both linear and folded polymers with different hydrophobic segments were compared, showing the significant role of intramolecular folding on the self-assembly behavior (Figure 1-13A).

Cyclic polymers have also been used as building blocks in macromolecular self-assembly [156]. For example, Borsali et al. reported the self-assembly of cyclic PS-*b*-polyisoprene diblock copolymers into giant wormlike micelles [157]. Grayson et al. synthesized heterotelechelic PEG-*b*-polycaprolactone (PEG-*b*-PCL) and cyclized it via CuAAC [158]. Both linear and cyclic PEG-*b*-PCL self-assembled into spherical micelles in water and the micelles formed of cyclic polymers were notably smaller (Figure 1-13B). Deffieux et al. prepared a triblock copolymer A**B**C in which **B** is a long central block and the short A and C sequences were used for cyclizing the copolymer [159]. Then, (1,1-diphenylethylene) end-capped polystyryllithium (PS-DPELi) and (1,1-diphenylethylene) end-capped polyisoprenyllithium (PI-DPELi) were grafted to the cyclic backbone. This macrocyclic brush self-assembled into cylindrical tubes in a selective solvent for polyisoprene (Figure 1-13C). It should be mentioned that most studies on the self-assembly of cyclic polymers were driven by the interest of researchers on polymer topologies. The importance of using molecular folding as a strategy to control the self-assembly behavior has not been fully realized and understood by the polymer community and there is still great potential to be explored.

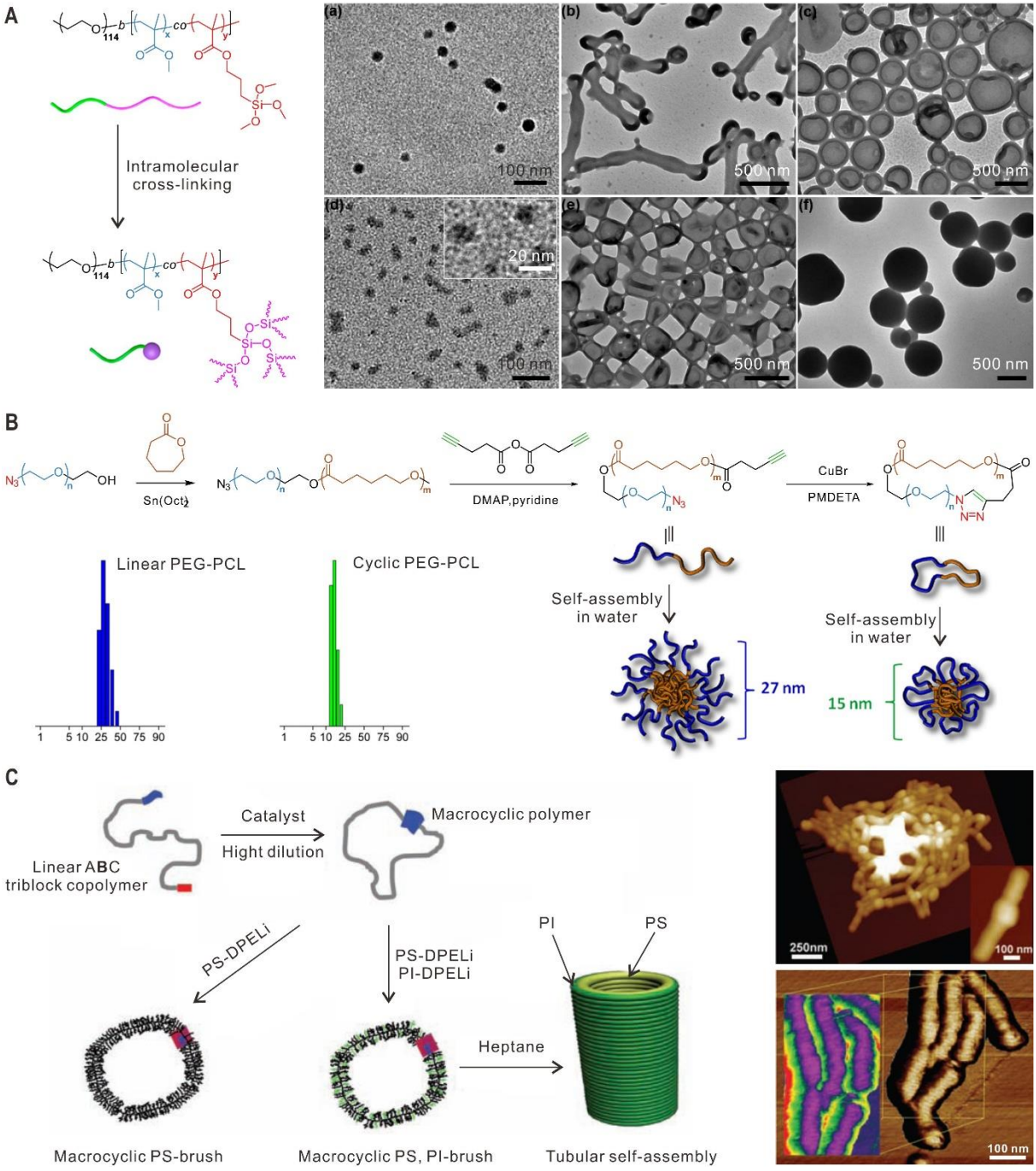

Figure 1-13 | Self-assembly of folded synthetic polymers. (A) Chemical structure of amphiphilic PEG-*b*-P(MMA-*co*-TMSPMA) and its intramolecular folding into PEG-tethered SCPNs. TEM images on the right show the different self-assembly structures of linear block copolymers (a-c) and folded PEG-tethered SCPNs (d-f) with different hydrophobic segments: (a, d) PEG_{114}-*b*-$P(MMA_{55}$-*co*-$TMSPMA_{32})$; (b, e) PEG_{114}-*b*-$P(MMA_{290}$-*co*-$TMSPMA_{111})$; and (c, f) PEG_{114}-*b*-$P(MMA3_{81}$-*co*-$TMSPMA_{124})$. Reproduced with permission from [155]. Copyright 2014 American Chemical Society. (B) Comparison of the self-assembly behaviors of linear and cyclic PEG-*b*-PCL in water. Reproduced with permission from [158]. Copyright 2013 American Chemical Society. (C) Synthesis of macrocyclic brush copolymers and their self-assembly into supramolecular tubes [159]. Copyright 2008. Reproduced with permission from the American Association for the Advancement of Science.

1.7 Applications of biomolecule-inspired nanomaterials

In the above sections, various biomolecule-inspired strategies that are used to prepare precision polymers and nanomaterials have been introduced, which include controlled polymerizations, biotemplated synthesis, polymer folding, and macromolecular self-assembly. The obtained well-controlled nanostructures can be used in numerous fields. While some exciting applications have been mentioned during the introduction of the synthetic approaches, this section highlights more examples in biomedical fields such as drug delivery, bioimaging and biosensing, as well as in non-biological fields such as energy, catalysis, and information storage.

1.7.1 Biological applications

Biomolecule-inspired nanomaterials including SCPNs and polymer assemblies have been widely used as carriers for delivery of various bioactive agents for therapeutic applications [160]. For example, Cheng et al. synthesized a copolymer with uracil-diamidopyridine (U-DPy) side moieties based on poly[oligo(ethylene glycol) methyl methacrylate] (POEGMA), which was folded into SCPNs via the formation of sextuple hydrogen bonds (Figure 1-14A). The SCPNs were successfully employed as carrier to load the hydrophilic anticancer drug 5-fluorouracil (FU) with a high loading content of 19.6% and the FU-loaded SCPNs exhibited temperature and pH dual responsive drug release profiles [161]. Paulusse et al. prepared water-soluble SCPNs with comparable physicochemical characteristics in aqueous and organic environments, which can load functional agents with different hydrophobicity. As a proof of concept, Nile red and the antibiotic rifampicin were loaded into the SCPNs, and a controlled release of rifampicin was demonstrated [162].

Due to the growing resistance of bacteria to conventional antibiotics, bio-inspired polymer nanoparticles with controlled sizes and structures have also been developed as novel antibacterial agents [163]. Du and Yuan et al. synthesized a thermo- and pH-responsive diblock copolymer poly[2-(2-methoxyethoxy)ethyl methacrylate]-*block*-poly[2-(*tert*-butylaminoethyl) methacrylate] (PMeO$_2$MA-*b*-PTA), which self-assembled into vesicles upon direct dissolution in water (Figure 1-14B). The polymer vesicles showed good antibacterial activities against both Gram-negative and Gram-positive bacteria [164]. In addition, SCPNs have also been developed as new antimicrobial agents to kill planktonic and biofilm bacteria [165].

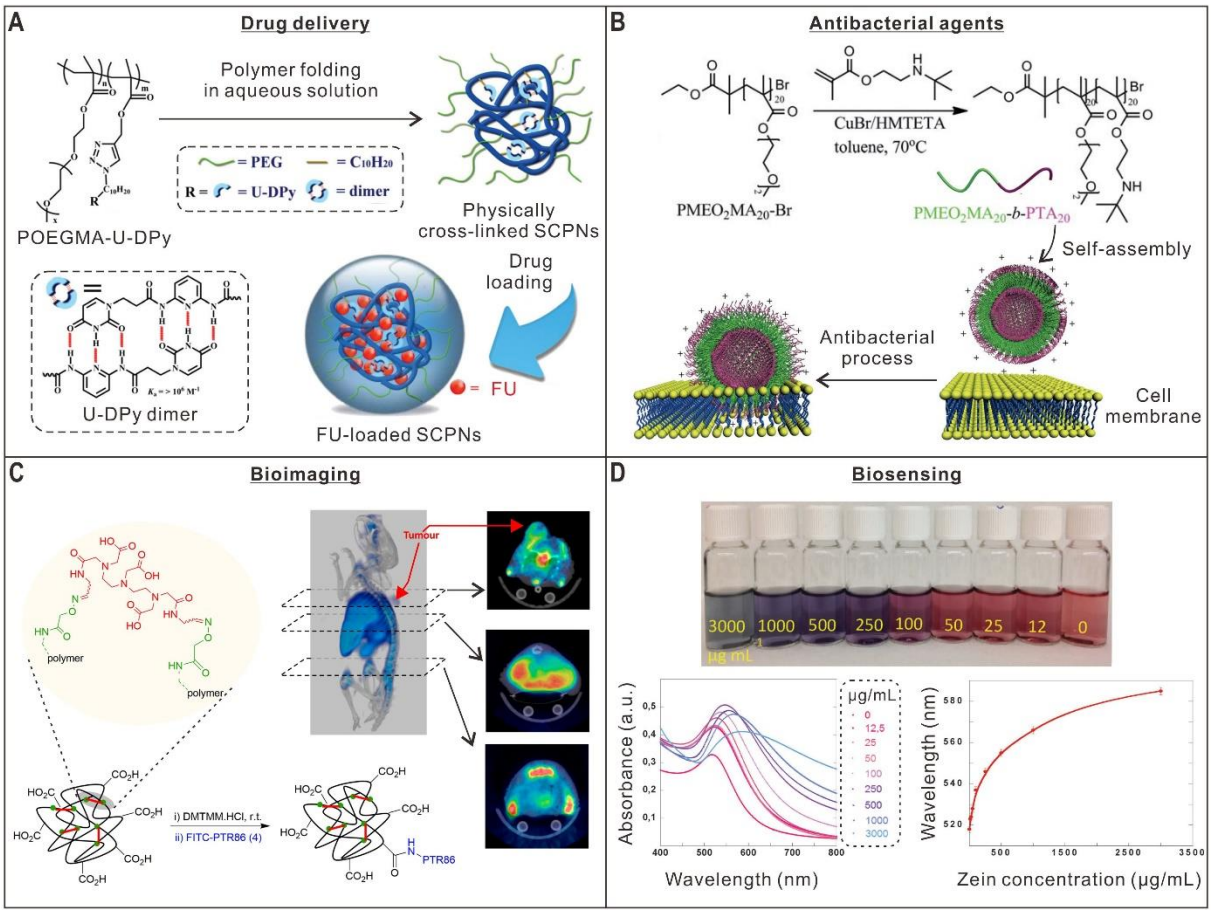

Figure 1-14 | Biomolecule-inspired nanomaterials for biological applications. (A) Stimuli-responsive SCPNs formed via self-complementary multiple hydrogen-bonding interaction of water-soluble POEGMA-U-DPy polymers for the controlled delivery of FU [161]. Copyright 2016. Reproduced with permission from the Royal Society of Chemistry. (B) Direct dissolution of a thermo- and pH-responsive diblock copolymer in water to form polymer vesicles for enhanced antibacterial activities [164]. Copyright 2013. Reproduced with permission from the Royal Society of Chemistry. (C) Biocompatible SCPNs functionalized with PTR86 for in vivo imaging of pancreatic tumors. Adapted with permission from [166]. Copyright 2016 American Chemical Society. (D) Pyridine-functionalized SCPNs for the fast and sensitive colorimetric detection of zein in aqueous ethanol [167]. Copyright 2015. Reproduced with permission from the Royal Society of Chemistry.

The early detection and post-therapy monitoring for some types of disease, such as pancreatic adenocarcinoma, are of great significance to increase the success rate of treatment [166]. In this regard, bio-inspired polymer nanoparticles have emerged as novel imaging probes. Using a diethylenetriaminepentaacetic acid-containing cross-linker, Odriozola et al. folded acrylic copolymers into water-soluble SCPNs, which could be used as MRI contrast agents after loading with Gd(III) ions [168]. Loinaz et al. reported biocompatible SCPNs based on poly(methacrylic acid) [166]. After further functionalization with the tumor targeting peptide PTR86 and the gamma emitter ^{67}Ga,

the multifunctional nanoparticle was employed for in vivo imaging using single photon emission computerized tomography, showing enhanced accumulation of targeted SCPNs in the tumor of a mouse model (Figure 1-14C).

Biosensing is another interesting field for applications of biomolecule-inspired nanomaterials. Pomposo et al. combined gold nanoparticles and pyridine-containing SCPNs for the rapid and sensitive colorimetric detection of zein in aqueous ethanol covering a concentration range of 10 ~ 3000 μg mL^{-1} [167] (Figure 1-14D). Liu et al. employed genetically engineered phages as templates to prepare MnO_2 nanowires, which were further used for glucose sensing at neutral pH [169].

1.7.2 Non-biological applications

In addition to biomedical applications, bioinspired polymers and nanomaterials can also be used in other fields such as catalysis, energy, and information storage. Inspired by enzymes, numerous efforts have been devoted to the preparation of water-soluble SCPNs for catalytic applications [170]. Meijer and Palmans et al. reported a series of functional SCPNs carrying different metal-based catalytic sites for reactions including the transfer hydrogenation of ketones [171], depropargylation reactions [172], and the carbamate cleavage reaction of rhodamine-based substrates [173] in aqueous solution. Zimmerman et al. also prepared water-soluble SCPNs with Cu centers via intramolecular folding of aspartate-containing polyolefins (Figure 1-15A). After reduction with sodium ascorbate, the obtained Cu(I)-bearing SCPNs were used to catalyze CuAAC reactions in water and in cells [174]. Apart from SCPNs, hierarchical nanomaterials formed of metals and metal oxides via biotemplated synthesis have also been frequently used as efficient catalysts for various reactions such as decomposition of dyes [175, 176] and the reduction of 4-nitrophenol [177].

Recently, the scope of applications for biomolecule-inspired nanomaterials has been extended to more emerging areas including energy conversion and functional surfaces [178]. For example, Belcher et al. employed genetically engineered M13 virus as a template to mineralize strontium titanate and bismuth ferrite, forming perovskite nanomaterials with for solar energy conversion (Figure 1-15B) [179]. Lattuada et al. prepared silica nanofibers with controlled thickness and surface roughness by templated synthesis using amyloid fibrils as a template (Figure 1-15C). The silica nanofibers were used for the creation of superhydrophobic surfaces [180].

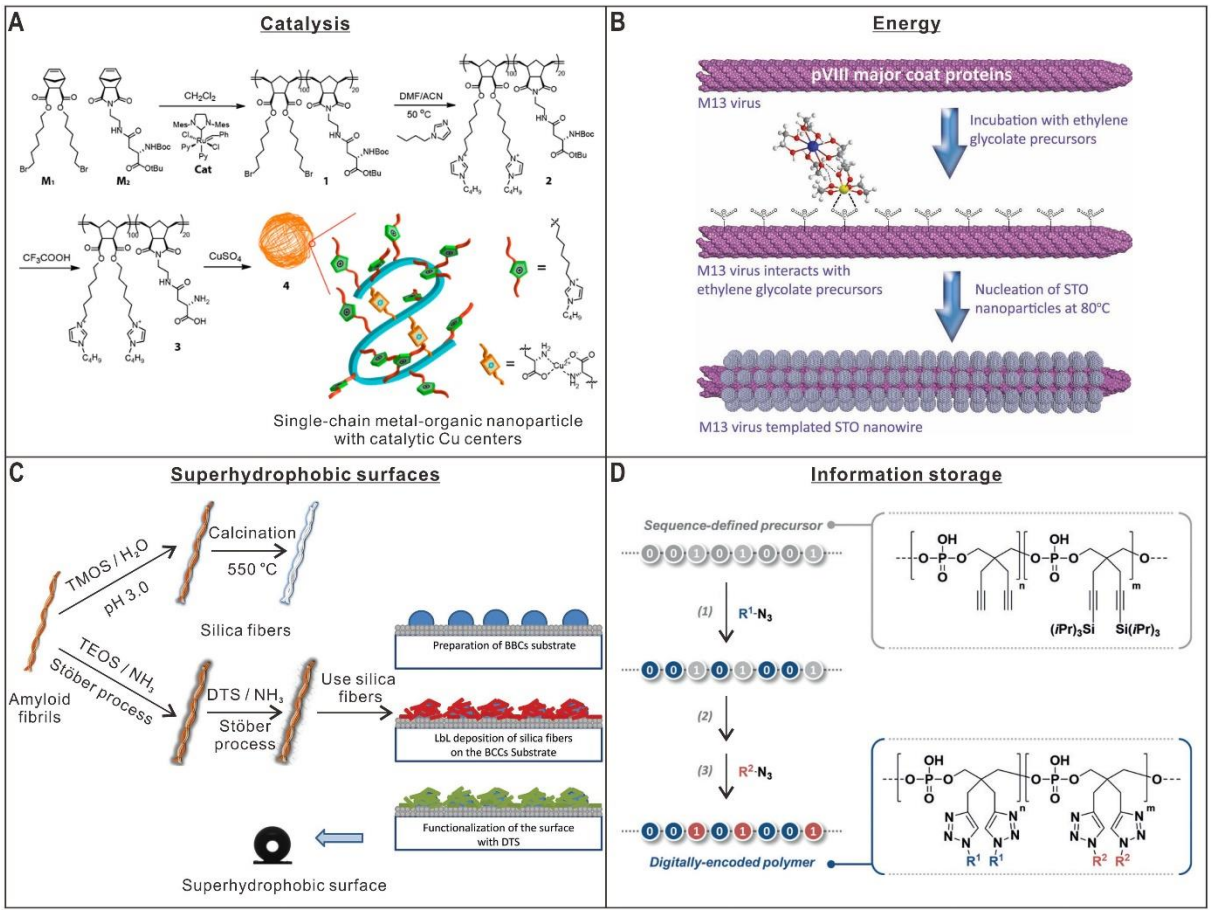

Figure 1-15 | Biomolecule-inspired nanomaterials for non-biological applications. (A) SCPNs with catalytic Cu centers for biocompatible alkyne-azide click reactions in aqueous conditions. Reproduced with permission from [174]. Copyright 2016 American Chemical Society. (B) M13 virus-templated synthesis of perovskite nanomaterials for solar energy conversion [179]. Copyright 2012. Reproduced with permission from John Wiley and Sons. (C) Amyloid fibrils-templated synthesis of long silica fibers for the preparation of superhydrophobic surfaces [180]. Copyright 2018. Reproduced with permission from John Wiley and Sons. (D) Design and preparation of digitally-encoded poly(phosphodiester)s with controlled side groups via CuAAC modification [181]. Copyright 2017. Reproduced with permission from John Wiley and Sons.

In Nature, DNA is the storage medium of genetic information. This feature has also been recreated, although currently at the proof-of-concept stage, in sequence-controlled synthetic polymers [182]. The Lutz group proposed that binary information can be implemented in a synthetic polymer using two comonomers defined as 0 and 1 bits [183]. They have made significant progress in this field by developing different synthetic polymer systems, including poly(triazole amide)s, poly(phosphodiester)s, poly(alkoxyamine phosphodiester)s, poly(alkoxyamine amide)s, and polyurethanes, as digital polymers to store information [184-189]. Recently, they reported a simple modification strategy for controlling side groups of digital poly(phosphodiester)s, which may improve the storage density and readability (Figure 1-15D) [181].

As a short summary, the unique structural features of biomacromolecules can be introduced into polymer structures and nanomaterials via different approaches. The obtained bio-inspired materials, which cannot be achieved by traditional methods, have been used for broad applications ranging from bio-related drug delivery and bioimaging to more novel applications such as catalysis, energy conversion and information storage.

1.8 Conceptual design and motivation

Biomacromolecules are an important source of innovation for material scientists to create synthetic polymers and nanomaterials with unique architectures for various applications. Particularly, this thesis is inspired by the perfect structure of proteins in which their defined polypeptide sequence and the folding process can be exploited to

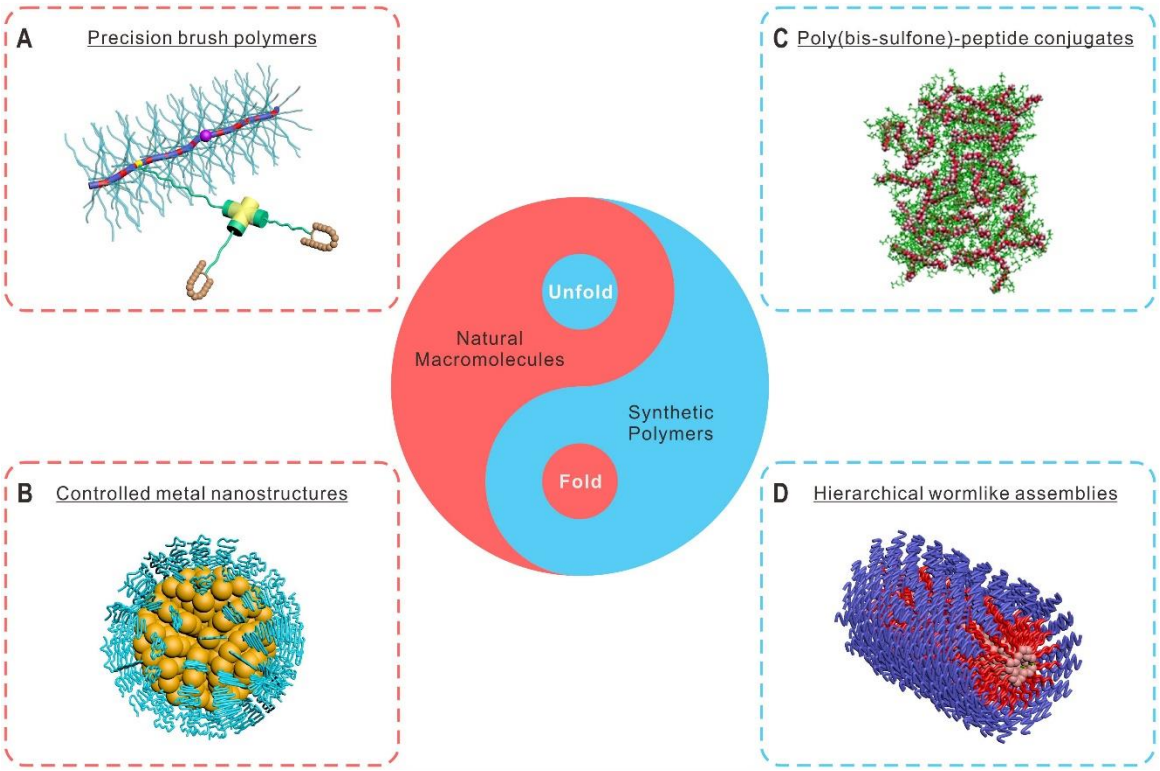

Figure 1-16 | Unfolding of natural macromolecules and folding of synthetic polymers as bioinspired strategies for preparing precision nanostructures. (A) Precision brush polymers templated by unfolded proteins [190]. Copyright 2020 The Authors. Published by the American Chemical Society. (B) Protein-templated synthesis of controlled metal nanostructures [191]. Copyright 2019 The Authors. Published by the Royal Society of Chemistry and the Chinese Chemical Society. (C) Self-assembly of poly(bis-sulfone)-peptide conjugates into micelles. Reproduced with permission from [192]. Copyright 2017 American Chemical Society. (D) Hierarchical wormlike polymer nanostructures via polymer folding and assembly.

build precise hierarchical 3D structure. From a materials science perspective, the peptide sequence after unfolding can be regarded as a precision linear polymer and used for templated synthesis of well-defined nanomaterials. On the contrary, linear synthetic polymers can also be folded into compact states, which may possess new properties such as unique self-assembly behavior. This thesis adopts these two opposite yet complementary strategies to construct a wide range of functional materials with defined structures, including precision brush polymers, controlled metal nanostructures, poly(bis-sulfone)—peptide conjugates, and hierarchical wormlike polymer assemblies for various applications, which are discussed in detail as follows (Figure 1-16).

By unfolding endogenous proteins into linear polymers, the main focus of chapter 2 of the thesis is on synthesis of well-defined nanomaterials using unfolded proteins as precision templates. Anisotropic brush polymers with monodisperse lengths were first prepared by introducing ATRP initiators to the unfolded protein backbone and then growing polymers via the grafting-from strategy (Figure 1-16A). By varying polymerization conditions and the initiator density on the polypeptide backbone, the size and shape of brush polymers were tuned. Very importantly, various functional entities can be introduced onto an absolute position located asymmetrically along the polypeptide backbone of brush polymers by taking advantage of site-specific modifications of proteins. Combining biotin—streptavidin interactions, novel higher ordered constructs were fabricated via site-specific assembly, which may find potential applications in both biomedicine and nanoscience.

Beyond soft polymer architectures, the potential of denatured protein backbone was also explored for templated synthesis of metal nanomaterials. As introduced in section 1.4.2, denatured protein–PEG conjugates have been successfully employed as attractive coatings to stabilize and functionalize various nanoparticles due to various supramolecular interactions between nanoparticle surfaces and the functional groups of proteins. These works serve as an important inspiration for the templated synthesis of functional nanoparticles for different applications. Stable and water-soluble noble metal nanostructures including spherical gold and platinum nanoparticles as well as gold nanoflowers (AuNFs) were prepared using sodium borohydride or ascorbic acid as the reducing agent. Moreover, because the reduction of metal ions and polymer synthesis via ARGET ATRP both involve the use of reducing agents, these two types of reactions with dramatically different characteristics were combined, for the first time,

in one pot (Figure 1-16B). PNIPAM-coated AuNFs with controllable sizes, shapes, and shell thickness were obtained and applied as temperature-controlled catalysts for the hydrogenation of *p*-nitrophenol, which offer great prospects for achieving “green” catalysis in aqueous media.

The aim of chapter 3 of the thesis is to construct bioinspired hierarchical polymer structures via folding and assembly of synthetic polymers. In this regard, we first designed and synthesized a thiol-reactive copolymer based on poly(bis-sulfone) via ATRP. Two oligopeptides, glutathione and an endogenous 12-mer peptide named WSC02 that targets C-X-C chemokine receptor type 4 (CXCR4), were conjugated to the copolymer. The functional polymer—WSC02 conjugate folded and assembled into narrowly dispersed nanoparticles in aqueous solutions (Figure 1-16C). Due to the multivalent effect, the conjugate demonstrated enhanced and specific antiviral activity on X4 tropic HIV-1 infection and also the ability to inhibit cancer stem cell migration.

However, the folding process of the poly(bis-sulfone)—peptide conjugate is dictated by random hydrophobic collapse of the polymer. To instill a higher level of control, the last system of the thesis investigates the defined folding of linear polymers into cyclic secondary structure via CuAAC click reaction. The self-assembly behaviors of linear and cyclic poly(2-hydroxyethyl methacrylate) (PHEMA) of different designed molecular weights were compared. It is very interesting that the folded PHEMA could form stable assemblies, which was confirmed by different techniques and wormlike assemblies were observed from TEM images for folded PHEMA. Encouraged by these results, macrocyclic brush polymers with amphiphilic block side chains were further synthesized, which could form stable wormlike assemblies and higher-ordered structures (Figure 1-16D). This work not only points out the profound influence of polymer folding in macromolecular self-assembly, but also establishes a robust and versatile approach for the construction of hierarchical bioinspired structures from synthetic polymers.

Collectively, this thesis aims to develop two unique strategies to fabricate precision nanomaterials with controlled structures for various applications. The first approach takes advantage of the precision primary structure of proteins. By unfolding proteins into linear forms, the obtained polypeptides are used as precision templates for preparing anisotropic brush polymers and controlled metal nanostructures. Learning from the folding process for the formation of 3D protein architectures, the second strategy combines the folding and self-assembly of synthetic polymers as a

general route for preparing higher ordered constructs. Particularly, a novel route is developed to fabricate stable wormlike assemblies which may find potential applications in various fields. The two strategies described in this thesis not only expand the applications of biomolecules in materials science, but also provide new directions for the fabrication of the next generation biomolecule-inspired architectures.

1.9 References

[1] Balchin D, Hayer-Hartl M, Hartl FU. In vivo aspects of protein folding and quality control. Science 2016;353:aac4354.

[2] Gething MJ, Sambrook J. Protein Folding in the Cell. Nature 1992;355:33-45.

[3] Caetano-Anolles G, Wang MW, Caetano-Anolles D, Mittenthal JE. The origin, evolution and structure of the protein world. Biochemical Journal 2009;417:621-637.

[4] Heim M, Romer L, Scheibel T. Hierarchical structures made of proteins. The complex architecture of spider webs and their constituent silk proteins. Chemical Society Reviews 2010;39:156-164.

[5] Aumiller WM, Uchida M, Douglas T. Protein cage assembly across multiple length scales. Chemical Society Reviews 2018;47:3433-3469.

[6] Rother M, Nussbaumer MG, Renggli K, Bruns N. Protein cages and synthetic polymers: a fruitful symbiosis for drug delivery applications, bionanotechnology and materials science. Chemical Society Reviews 2016;45:6213-6249.

[7] Wang PF, Meyer TA, Pan V, Dutta PK, Ke YG. The Beauty and Utility of DNA Origami. Chem 2017;2:359-382.

[8] Rothemund PWK. Folding DNA to create nanoscale shapes and patterns. Nature 2006;440:297-302.

[9] Zhang F, Jiang SX, Wu SY, Li YL, Mao CD, Liu Y, et al. Complex wireframe DNA origami nanostructures with multi-arm junction vertices. Nature Nanotechnology 2015;10:779-784.

[10] Han DR, Pal S, Nangreave J, Deng ZT, Liu Y, Yan H. DNA Origami with Complex Curvatures in Three-Dimensional Space. Science 2011;332:342-346.

[11] Han DR, Pal S, Yang Y, Jiang SX, Nangreave J, Liu Y, et al. DNA Gridiron Nanostructures Based on Four-Arm Junctions. Science 2013;339:1412-1415.

[12] Benson E, Mohammed A, Gardell J, Masich S, Czeizler E, Orponen P, et al. DNA rendering of polyhedral meshes at the nanoscale. Nature 2015;523:441-444.

[13] Seeman NC. Nucleic-Acid Junctions and Lattices. Journal of Theoretical Biology 1982;99:237-247.

[14] Aldaye FA, Palmer AL, Sleiman HF. Assembling materials with DNA as the guide. Science 2008;321:1795-1799.

[15] Seeman NC, Sleiman HF. DNA nanotechnology. Nature Reviews Materials 2018;3:1-23.

[16] Hong F, Zhang F, Liu Y, Yan H. DNA Origami: Scaffolds for Creating Higher Order Structures. Chemical Reviews 2017;117:12584-12640.

[17] Sacca B, Niemeyer CM. DNA Origami: The Art of Folding DNA. Angewandte Chemie-International Edition 2012;51:58-66.

[18] Torring T, Voigt NV, Nangreave J, Yan H, Gothelf KV. DNA origami: a quantum leap for self-assembly of complex structures. Chemical Society Reviews 2011;40:5636-5646.

[19] Braunecker WA, Matyjaszewski K. Controlled/living radical polymerization: Features, developments, and perspectives. Progress in Polymer Science 2007;32:93-146.

[20] Hawker CJ, Bosman AW, Harth E. New polymer synthesis by nitroxide mediated living radical polymerizations. Chemical Reviews 2001;101:3661-3688.

[21] Zetterlund PB, Thickett SC, Perrier S, Bourgeat-Lami E, Lansalot M. Controlled/Living Radical Polymerization in Dispersed Systems: An Update. Chemical Reviews 2015;115:9745-9800.

[22] Wang JS, Matyjaszewski K. Controlled Living Radical Polymerization - Atom-Transfer Radical Polymerization in the Presence of Transition-Metal Complexes. Journal of the American Chemical Society 1995;117:5614-5615.

[23] Kato M, Kamigaito M, Sawamoto M, Higashimura T. Polymerization of Methyl Methacrylate with the Carbon Tetrachloride/Dichlorotris-(triphenylphosphine)ruthenium(II) Methylaluminum Bis(2,6-di-tert-butylphenoxide) Initiating System: Possibility of Living Radical Polymerization. Macromolecules 1995;28:1721-1723.

[24] Matyjaszewski K. Advanced Materials by Atom Transfer Radical Polymerization. Advanced Materials 2018;30:1706441.

[25] Matyjaszewski K, Tsarevsky NV. Macromolecular Engineering by Atom Transfer Radical Polymerization. Journal of the American Chemical Society 2014;136:6513-6533.

[26] Matyjaszewski K, Xia JH. Atom transfer radical polymerization. Chemical Reviews 2001;101:2921-2990.

[27] Siegwart DJ, Oh JK, Matyjaszewski K. ATRP in the design of functional materials for biomedical applications. Progress in Polymer Science 2012;37:18-37.

[28] Jakubowski W, Matyjaszewski K. Activators regenerated by electron transfer for atom-transfer radical polymerization of (meth)acrylates and related block copolymers. Angewandte Chemie-International Edition 2006;45:4482-4486.

[29] Jakubowski W, Min K, Matyjaszewski K. Activators regenerated by electron transfer for atom transfer radical polymerization of styrene. Macromolecules 2006;39:39-45.

[30] Mueller L, Jakubowski W, Tang W, Matyjaszewski K. Successful chain extension of polyacrylate and polystyrene macroinitiators with methacrylates in an ARGET and ICAR ATRP. Macromolecules 2007;40:6464-6472.

[31] Plichta A, Li WW, Matyjaszewski K. ICAR ATRP of Styrene and Methyl Methacrylate with Ru(Cp*)Cl(PPh3)(2). Macromolecules 2009;42:2330-2332.

[32] Konkolewicz D, Wang Y, Zhong MJ, Krys P, Isse AA, Gennaro A, et al. Reversible-Deactivation Radical Polymerization in the Presence of Metallic Copper. A Critical Assessment of the SARA ATRP and SET-LRP Mechanisms. Macromolecules 2013;46:8749-8772.

[33] Chmielarz P, Fantin M, Park S, Isse AA, Gennaro A, Magenau AJD, et al. Electrochemically mediated atom transfer radical polymerization (eATRP). Progress in Polymer Science 2017;69:47-78.

[34] Perrier S. 50th Anniversary Perspective: RAFT Polymerization-A User Guide. Macromolecules 2017;50:7433-7447.

[35] Chiefari J, Chong YK, Ercole F, Krstina J, Jeffery J, Le TPT, et al. Living free-radical polymerization by reversible addition-fragmentation chain transfer: The RAFT process. Macromolecules 1998;31:5559-5562.

[36] Moad G, Rizzardo E, Thang SH. Living radical polymerization by the RAFT process. Australian Journal of Chemistry 2005;58:379-410.

[37] Moad G, Rizzardo E, Thang SH. Radical addition-fragmentation chemistry in polymer synthesis. Polymer 2008;49:1079-1131.

[38] Boyer C, Bulmus V, Davis TP, Ladmiral V, Liu JQ, Perrier S. Bioapplications of RAFT Polymerization. Chemical Reviews 2009;109:5402-5436.

[39] Keddie DJ. A guide to the synthesis of block copolymers using reversible-addition fragmentation chain transfer (RAFT) polymerization. Chemical Society Reviews 2014;43:496-505.

[40] Badi N, Lutz JF. Sequence control in polymer synthesis. Chemical Society Reviews 2009;38:3383-3390.

[41] Lutz JF. Defining the Field of Sequence-Controlled Polymers. Macromolecular Rapid Communications 2017;38:1700582.

[42] Lutz JF, Ouchi M, Liu DR, Sawamoto M. Sequence-Controlled Polymers. Science 2013;341:1238149.

[43] Kleiner RE, Brudno Y, Birnbaum ME, Liu DR. DNA-templated polymerization of side-chain-functionalized peptide nucleic acid aldehydes. Journal of the American Chemical Society 2008;130:4646-4659.

[44] Rosenbaum DM, Liu DR. Efficient and sequence-specific DNA-templated polymerization of peptide nucleic acid aldehydes. Journal of the American Chemical Society 2003;125:13924-13925.

[45] Niu J, Hili R, Liu DR. Enzyme-free translation of DNA into sequence-defined synthetic polymers structurally unrelated to nucleic acids. Nature Chemistry 2013;5:282-292.

[46] Mcgrath KP, Fournier MJ, Mason TL, Tirrell DA. Genetically Directed Syntheses of New Polymeric Materials - Expression of Artificial Genes Encoding Proteins with Repeating (Alagly)3proglugly Elements. Journal of the American Chemical Society 1992;114:727-733.

[47] Saiki RK, Gelfand DH, Stoffel S, Scharf SJ, Higuchi R, Horn GT, et al. Primer-Directed Enzymatic Amplification of DNA with a Thermostable DNA-Polymerase. Science 1988;239:487-491.

[48] Kool ET. Replacing the nucleobases in DNA with designer molecules. Accounts of Chemical Research 2002;35:936-943.

[49] Piccirilli JA, Krauch T, Moroney SE, Benner SA. Enzymatic Incorporation of a New Base Pair into DNA and Rna Extends the Genetic Alphabet. Nature 1990;343:33-37.

[50] Noren CJ, Anthonycahill SJ, Griffith MC, Schultz PG. A General-Method for Site-Specific Incorporation of Unnatural Amino-Acids into Proteins. Science 1989;244:182-188.

[51] Pfeifer S, Zarafshani Z, Badi N, Lutz JF. Liquid-Phase Synthesis of Block Copolymers Containing Sequence-Ordered Segments. Journal of the American Chemical Society 2009;131:9195-9197.

[52] Tong XM, Guo BH, Huang YB. Toward the synthesis of sequence-controlled vinyl copolymers. Chemical Communications 2011;47:1455-1457.

[53] Lutz JF, Schmidt BVKJ, Pfeifer S. Tailored Polymer Microstructures Prepared by Atom Transfer Radical Copolymerization of Styrene and N-substituted Maleimides. Macromolecular Rapid Communications 2011;32:127-135.

[54] Pfeifer S, Lutz JF. A facile procedure for controlling monomer sequence distribution in radical chain polymerizations. Journal of the American Chemical Society 2007;129:9542-9543.

[55] Satoh K, Mizutani M, Kamigaito M. Metal-catalyzed radical polyaddition as a novel polymer synthetic route. Chemical Communications 2007:1260-1262.

[56] Satoh K, Ozawa S, Mizutani M, Nagai K, Kamigaito M. Sequence-regulated vinyl copolymers by metal-catalysed step-growth radical polymerization. Nature Communications 2010;1:6.

[57] Zhang JH, Matta ME, Hillmyer MA. Synthesis of Sequence-Specific Vinyl Copolymers by Regioselective ROMP of Multiply Substituted Cyclooctenes. ACS Macro Letters 2012;1:1383-1387.

[58] Ida S, Ouchi M, Sawamoto M. Template-Assisted Selective Radical Addition toward Sequence-Regulated Polymerization: Lariat Capture of Target Monomer by Template Initiator. Journal of the American Chemical Society 2010;132:14748-14750.

[59] Ida S, Terashima T, Ouchi M, Sawamoto M. Selective Radical Addition with a Designed Heterobifunctional Halide: A Primary Study toward Sequence-Controlled Polymerization upon Template Effect. Journal of the American Chemical Society 2009;131:10808-10809.

[60] Lutz JF. Sequence-Controlled Polymers. Weinheim: Wiley-VCH; 2018.

[61] Sotiropoulou S, Sierra-Sastre Y, Mark SS, Batt CA. Biotemplated nanostructured materials. Chemistry of Materials 2008;20:821-834.

[62] Ionov L, Bocharova V, Diez S. Biotemplated synthesis of stimuli-responsive nanopatterned polymer brushes on microtubules. Soft Matter 2009;5:67-71.

[63] Niu Z, Liu J, Lee LA, Bruckman MA, Zhao D, Koley G, et al. Biological templated synthesis of water-soluble conductive polymeric nanowires. Nano Letters 2007;7:3729-3733.

[64] Abedin MJ, Liepold L, Suci P, Young M, Douglas T. Synthesis of a Cross-Linked Branched Polymer Network in the Interior of a Protein Cage. Journal of the American Chemical Society 2009;131:4346-4354.

[65] Pokorski JK, Breitenkamp K, Liepold LO, Qazi S, Finn MG. Functional Virus-Based Polymer-Protein Nanoparticles by Atom Transfer Radical Polymerization. Journal of the American Chemical Society 2011;133:9242-9245.

[66] Lucon J, Qazi S, Uchida M, Bedwell GJ, LaFrance B, Prevelige PE, et al. Use of the interior cavity of the P22 capsid for site-specific initiation of atom-transfer radical polymerization with high-density cargo loading. Nature Chemistry 2012;4:781-788.

[67] Trinh T, Liao CY, Toader V, Barlog M, Bazzi HS, Li JN, et al. DNA-imprinted polymer nanoparticles with monodispersity and prescribed DNA-strand patterns. Nature Chemistry 2018;10:184-192.

[68] Tokura Y, Jiang YY, Welle A, Stenzel MH, Krzemien KM, Michaelis J, et al. Bottom-Up Fabrication of Nanopatterned Polymers on DNA Origami by In Situ Atom-Transfer Radical Polymerization. Angewandte Chemie-International Edition 2016;55:5692-5697.

[69] McHale R, Patterson JP, Zetterlund PB, O'Reilly RK. Biomimetic radical polymerization via cooperative assembly of segregating templates. Nature Chemistry 2012;4:491-497.

[70] Tokura Y, Harvey S, Chen CJ, Wu YZ, Ng DYW, Weil T. Fabrication of Defined Polydopamine Nanostructures by DNA Origami-Templated Polymerization. Angewandte Chemie-International Edition 2018;57:1587-1591.

[71] Tokura Y, Harvey S, Xu XM, Chen CJ, Morsbach S, Wunderlich K, et al. Polymer tube nanoreactors via DNA-origami templated synthesis. Chemical Communications 2018;54:2808-2811.

[72] McMillan RA, Paavola CD, Howard J, Chan SL, Zaluzec NJ, Trent JD. Ordered nanoparticle arrays formed on engineered chaperonin protein templates. Nature Materials 2002;1:247-252.

[73] McMillan RA, Howard J, Zaluzec NJ, Kagawa HK, Mogul R, Li YF, et al. A self-assembling protein template for constrained synthesis and patterning of nanoparticle arrays. Journal of the American Chemical Society 2005;127:2800-2801.

[74] Zahr OK, Blum AS. Solution Phase Gold Nanorings on a Viral Protein Template. Nano Letters 2012;12:629-633.

[75] Li SB, Dharmarwardana M, Welch RP, Ren YX, Thompson CM, Smaldone RA, et al. Template-Directed Synthesis of Porous and Protective Core-Shell Bionanoparticles. Angewandte Chemie-International Edition 2016;55:10691-10696.

[76] Hung AM, Micheel CM, Bozano LD, Osterbur LW, Wallraff GM, Cha JN. Large-area spatially ordered arrays of gold nanoparticles directed by lithographically confined DNA origami. Nature Nanotechnology 2010;5:121-126.

[77] Schreiber R, Do J, Roller EM, Zhang T, Schuller VJ, Nickels PC, et al. Hierarchical assembly of metal nanoparticles, quantum dots and organic dyes using DNA origami scaffolds. Nature Nanotechnology 2014;9:74-78.

[78] Urban MJ, Dutta PK, Wang PF, Duan XY, Shen XB, Ding BQ, et al. Plasmonic Toroidal Metamolecules Assembled by DNA Origami. Journal of the American Chemical Society 2016;138:5495-5498.

[79] Liu XG, Zhang F, Jing XX, Pan MC, Liu P, Li W, et al. Complex silica composite nanomaterials templated with DNA origami. Nature 2018;559:593-598.

[80] Cung K, Han BJ, Nguyen TD, Mao S, Yeh YW, Xu SY, et al. Biotemplated Synthesis of PZT Nanowires. Nano Letters 2013;13:6197-6202.

[81] Pang XC, Zhao L, Han W, Xin XK, Lin ZQ. A general and robust strategy for the synthesis of nearly monodisperse colloidal nanocrystals. Nature Nanotechnology 2013;8:426-431.

[82] Pang XC, He YJ, Jung JH, Lin ZQ. 1D nanocrystals with precisely controlled dimensions, compositions, and architectures. Science 2016;353:1268-1272.

[83] Kauzmann W. Some Factors in the Interpretation of Protein Denaturation. Advances in Protein Chemistry 1959;14:1-63.

[84] Yang J, Gitlin I, Krishnamurthy VM, Vazquez JA, Costello CE, Whitesides GM. Synthesis of monodisperse polymers from proteins. Journal of the American Chemical Society 2003;125:12392-12393.

[85] Kuan SL, Wu YZ, Weil T. Precision Biopolymers from Protein Precursors for Biomedical Applications. Macromolecular Rapid Communications 2013;34:380-392.

[86] Ng DYW, Wu YZ, Kuan SL, Weil T. Programming Supramolecular Biohybrids as Precision Therapeutics. Accounts of Chemical Research 2014;47:3471-3480.

[87] Wu YZ, Pramanik G, Eisele K, Weil T. Convenient Approach to Polypeptide Copolymers Derived from Native Proteins. Biomacromolecules 2012;13:1890-1898.

[88] Wu YZ, Weil T. An Efficient Approach for Preparing Giant Polypeptide Triblock Copolymers by Protein Dimerization. Macromolecular Rapid Communications 2012;33:1304-1309.

[89] Veronese FM. Peptide and protein PEGylation: a review of problems and solutions. Biomaterials 2001;22:405-417.

[90] Alivisatos AP, Gu WW, Larabell C. Quantum dots as cellular probes. Annual Review of Biomedical Engineering 2005;7:55-76.

[91] Kuo Y, Hsu TY, Wu YC, Chang HC. Fluorescent nanodiamond as a probe for the intercellular transport of proteins in vivo. Biomaterials 2013;34:8352-8360.

[92] Hardman R. A toxicologic review of quantum dots: Toxicity depends on physicochemical and environmental factors. Environmental Health Perspectives 2006;114:165-172.

[93] Wu YZ, Jelezko F, Plenio MB, Weil T. Diamond Quantum Devices in Biology. Angewandte Chemie-International Edition 2016;55:6586-6598.

[94] Wu YZ, Chakrabortty S, Gropeanu RA, Wilhelmi J, Xu Y, Er KS, et al. pH-Responsive Quantum Dots via an Albumin Polymer Surface Coating. Journal of the American Chemical Society 2010;132:5012-5014.

[95] Wu YZ, Eisele K, Doroshenko M, Algara-Siller G, Kaiser U, Koynov K, et al. A Quantum Dot Photoswitch for DNA Detection, Gene Transfection, and Live-Cell Imaging. Small 2012;8:3465-3475.

[96] Zhang T, Neumann A, Lindlau J, Wu YZ, Prarnanik G, Naydenov B, et al. DNA-Based Self-Assembly of Fluorescent Nanodiamonds. Journal of the American Chemical Society 2015;137:9776-9779.

[97] Wu YZ, Ermakova A, Liu WN, Pramanik G, Vu TM, Kurz A, et al. Programmable Biopolymers for Advancing Biomedical Applications of Fluorescent Nanodiamonds. Advanced Functional Materials 2015;25:6576-6585.

[98] Wu YZ, Ihme S, Feuring-Buske M, Kuan SL, Eisele K, Lamla M, et al. A Core-Shell Albumin Copolymer Nanotransporter for High Capacity Loading and Two-Step Release of Doxorubicin with Enhanced Anti-Leukemia Activity. Advanced Healthcare Materials 2013;2:884-894.

[99] Wu YZ, Li C, Boldt F, Wang YR, Kuan SL, Tran TT, et al. Programmable protein-DNA hybrid hydrogels for the immobilization and release of functional proteins. Chemical Communications 2014;50:14620-14622.

[100] Gacanin J, Hedrich J, Sieste S, Glasser G, Lieberwirth I, Schilling C, et al. Autonomous Ultrafast Self-Healing Hydrogels by pH-Responsive Functional Nanofiber Gelators as Cell Matrices. Advanced Materials 2019;31:1805044.

[101] Wu YZ, Wang T, Ng DYW, Weil T. Multifunctional Polypeptide-PEO Nanoreactors via the Hydrophobic Switch. Macromolecular Rapid Communications 2012;33:1474-1481.

[102] Eisele K, Gropeanu R, Musante A, Glasser G, Li C, Muellen K, et al. Tailored Albumin-based Copolymers for Receptor-Mediated Delivery of Perylenediimide Guest Molecules. Macromolecular Rapid Communications 2010;31:1501-1508.

[103] Wu YZ, Shih EK, Ramanathan A, Vasudevan S, Weil T. Nano-Sized Albumin-Copolymer Micelles for Efficient Doxorubicin Delivery. Biointerphases 2012;7:5.

[104] Gacanin J, Kovtun A, Fischer S, Schwager V, Quambusch J, Kuan SL, et al. Spatiotemporally Controlled Release of Rho-Inhibiting C3 Toxin from a Protein-DNA Hybrid Hydrogel for Targeted Inhibition of Osteoclast Formation and Activity. Advanced Healthcare Materials 2017;6:1700392.

[105] Guichard G, Huc I. Synthetic foldamers. Chemical Communications 2011;47:5933-5941.

[106] Gonzalez-Burgos M, Latorre-Sanchez A, Pomposo JA. Advances in single chain technology. Chemical Society Reviews 2015;44:6122-6142.

[107] Mavila S, Eivgi O, Berkovich I, Lemcoff NG. Intramolecular Cross-Linking Methodologies for the Synthesis of Polymer Nanoparticles. Chemical Reviews 2016;116:878-961.

[108] Stals PJM, Li YC, Burdynska J, Nicolay R, Nese A, Palmans ARA, et al. How Far Can We Push Polymer Architectures? Journal of the American Chemical Society 2013;135:11421-11424.

[109] Mecerreyes D, Lee V, Hawker CJ, Hedrick JL, Wursch A, Volksen W, et al. A novel approach to functionalized nanoparticles: Self-crosslinking of macromolecules in ultradilute solution. Advanced Materials 2001;13:204-208.

[110] Harth E, Van Horn B, Lee VY, Germack DS, Gonzales CP, Miller RD, et al. A facile approach to architecturally defined nanoparticles via intramolecular chain collapse. Journal of the American Chemical Society 2002;124:8653-8660.

[111] Croce TA, Hamilton SK, Chen ML, Muchalski H, Harth E. Alternative o-quinodimethane cross-linking precursors for intramolecular chain collapse nanoparticles. Macromolecules 2007;40:6028-6031.

[112] Oria L, Aguado R, Pomposo JA, Colmenero J. A Versatile "Click" Chemistry Precursor of Functional Polystyrene Nanoparticles. Advanced Materials 2010;22:3038-3041.

[113] Perez-Baena I, Asenjo-Sanz I, Arbe A, Moreno AJ, Lo Verso F, Colmenero J, et al. Efficient Route to Compact Single-Chain Nanoparticles: Photoactivated Synthesis via Thiol-Yne Coupling Reaction. Macromolecules 2014;47:8270-8280.

[114] Sanchez-Sanchez A, Akbari S, Etxeberria A, Arbe A, Gasser U, Moreno AJ, et al. "Michael" Nanocarriers Mimicking Transient-Binding Disordered Proteins. ACS Macro Letters 2013;2:491-495.

[115] Dirlam PT, Kim HJ, Arrington KJ, Chung WJ, Sahoo R, Hill LJ, et al. Single chain polymer nanoparticles via sequential ATRP and oxidative polymerization. Polymer Chemistry 2013;4:3765-3773.

[116] He J, Tremblay L, Lacelle S, Zhao Y. Preparation of polymer single chain nanoparticles using intramolecular photodimerization of coumarin. Soft Matter 2011;7:2380-2386.

[117] Appel EA, Dyson J, del Barrio J, Walsh Z, Scherman OA. Formation of Single-Chain Polymer Nanoparticles in Water through Host-Guest Interactions. Angewandte Chemie-International Edition 2012;51:4185-4189.

[118] Hosono N, Gillissen MAJ, Li YC, Sheiko SS, Palmans ARA, Meijer EW. Orthogonal Self-Assembly in Folding Block Copolymers. Journal of the American Chemical Society 2013;135:501-510.

[119] Murray BS, Fulton DA. Dynamic Covalent Single-Chain Polymer Nanoparticles. Macromolecules 2011;44:7242-7252.

[120] Foster EJ, Berda EB, Meijer EW. Metastable Supramolecular Polymer Nanoparticles via Intramolecular Collapse of Single Polymer Chains. Journal of the American Chemical Society 2009;131:6964-6966.

[121] Whitaker DE, Mahon CS, Fulton DA. Thermoresponsive Dynamic Covalent Single-Chain Polymer Nanoparticles Reversibly Transform into a Hydrogel. Angewandte Chemie-International Edition 2013;52:956-959.

[122] Roy RK, Lutz JF. Compartmentalization of Single Polymer Chains by Stepwise Intramolecular Cross-Linking of Sequence-Controlled Macromolecules. Journal of the American Chemical Society 2014;136:12888-12891.

[123] Fischer TS, Schulze-Sunninghausen D, Luy B, Altintas O, Barner-Kowollik C. Stepwise Unfolding of Single-Chain Nanoparticles by Chemically Triggered Gates. Angewandte Chemie-International Edition 2016;55:11276-11280.

[124] Josse T, De Winter J, Gerbaux P, Coulembier O. Cyclic Polymers by Ring-Closure Strategies. Angewandte Chemie-International Edition 2016;55:13944-13958.

[125] Laurent BA, Grayson SM. Synthetic approaches for the preparation of cyclic polymers. Chemical Society Reviews 2009;38:2202-2213.

[126] Laurent BA, Grayson SM. An efficient route to well-defined macrocyclic polymers via "Click" cyclization. Journal of the American Chemical Society 2006;128:4238-4239.

[127] Xu J, Ye J, Liu SY. Synthesis of well-defined cyclic poly(N-isopropylacrylamide) via click chemistry and its unique thermal phase transition behavior. Macromolecules 2007;40:9103-9110.

[128] Ren JM, Satoh K, Goh TK, Blencowe A, Nagai K, Ishitake K, et al. Stereospecific Cyclic Poly(methyl methacrylate) and Its Topology-Guided Hierarchically Controlled Supramolecular Assemblies. Angewandte Chemie-International Edition 2014;53:459-464.

[129] Eugene DM, Grayson SM. Efficient preparation of cyclic poly(methyl acrylate)-block-poly(styrene) by combination of atom transfer radical polymerization and click cyclization. Macromolecules 2008;41:5082-5084.

[130] Ge ZS, Zhou YM, Xu J, Liu HW, Chen DY, Liu SY. High-Efficiency Preparation of Macrocyclic Diblock Copolymers via Selective Click Reaction in Micellar Media. Journal of the American Chemical Society 2009;131:1628-1629.

[131] Stanford MJ, Pflughaupt RL, Dove AP. Synthesis of Stereoregular Cyclic Poly(lactide)s via "Thiol-Ene" Click Chemistry. Macromolecules 2010;43:6538-6541.

[132] Zhang YN, Wang GW, Huang JL. Synthesis of Macrocyclic Poly(ethylene oxide) and Polystyrene via Glaser Coupling Reaction. Macromolecules 2010;43:10343-10347.

[133] Schappacher M, Deffieux A. Reversible Switching between Linear and Ring Polystyrenes Bearing Porphyrin End Groups. Journal of the American Chemical Society 2011;133:1630-1633.

[134] Yamamoto T, Yagyu S, Tezuka Y. Light- and Heat-Triggered Reversible Linear-Cyclic Topological Conversion of Telechelic Polymers with Anthryl End Groups. Journal of the American Chemical Society 2016;138:3904-3911.

[135] Schmidt BVKJ, Fechler N, Falkenhagen J, Lutz JF. Controlled folding of synthetic polymer chains through the formation of positionable covalent bridges. Nature Chemistry 2011;3:234-238.

[136] Inoue Y, Kuad P, Okumura Y, Takashima Y, Yamaguchi H, Harada A. Thermal and photochemical switching of conformation of poly(ethylene glycol)-substituted cyclodextrin with an azobenzene group at the chain end. Journal of the American Chemical Society 2007;129:6396-6397.

[137] Heguri H, Yamamoto T, Tezuka Y. Folding Construction of a Pentacyclic Quadruply fused Polymer Topology with Tailored kyklo-Telechelic Precursors. Angewandte Chemie-International Edition 2015;54:8688-8692.

[138] Mai YY, Eisenberg A. Self-assembly of block copolymers. Chemical Society Reviews 2012;41:5969-5985.

[139] Blanazs A, Armes SP, Ryan AJ. Self-Assembled Block Copolymer Aggregates: From Micelles to Vesicles and their Biological Applications. Macromolecular Rapid Communications 2009;30:267-277.

[140] Tritschler U, Pearce S, Gwyther J, Whittell GR, Manners I. 50th Anniversary Perspective: Functional Nanoparticles from the Solution Self-Assembly of Block Copolymers. Macromolecules 2017;50:3439-3463.

[141] Nishiyama N, Kataoka K. Current state, achievements, and future prospects of polymeric micelles as nanocarriers for drug and gene delivery. Pharmacology & Therapeutics 2006;112:630-648.

[142] Tyrrell ZL, Shen YQ, Radosz M. Fabrication of micellar nanoparticles for drug delivery through the self-assembly of block copolymers. Progress in Polymer Science 2010;35:1128-1143.

[143] Liu GY, Chen CJ, Ji J. Biocompatible and biodegradable polymersomes as delivery vehicles in biomedical applications. Soft Matter 2012;8:8811-8821.

[144] Palivan CG, Goers R, Najer A, Zhang XY, Car A, Meier W. Bioinspired polymer vesicles and membranes for biological and medical applications. Chemical Society Reviews 2016;45:377-411.

[145] Chu ZL, Dreiss CA, Feng YJ. Smart wormlike micelles. Chemical Society Reviews 2013;42:7174-7203.

[146] Hailes RLN, Oliver AM, Gwyther J, Whittell GR, Manners I. Polyferrocenylsilanes: synthesis, properties, and applications. Chemical Society Reviews 2016;45:5358-5407.

[147] Gilroy JB, Gadt T, Whittell GR, Chabanne L, Mitchels JM, Richardson RM, et al. Monodisperse cylindrical micelles by crystallization-driven living self-assembly. Nature Chemistry 2010;2:566-570.

[148] Qiu HB, Du V, Winnik MA, Manners I. Branched Cylindrical Micelles via Crystallization-Driven Self-Assembly. Journal of the American Chemical Society 2013;135:17739-17742.

[149] Hudson ZM, Lunn DJ, Winnik MA, Manners I. Colour-tunable fluorescent multiblock micelles. Nature Communications 2014;5:3372.

[150] Li XY, Gao Y, Boott CE, Winnik MA, Manners I. Non-covalent synthesis of supermicelles with complex architectures using spatially confined hydrogen-bonding interactions. Nature Communications 2015;6:8127.

[151] Qiu HB, Hudson ZM, Winnik MA, Manners I. Multidimensional hierarchical self-assembly of amphiphilic cylindrical block comicelles. Science 2015;347:1329-1332.

[152] Qiu HB, Gao Y, Boott CE, Gould OEC, Harniman RL, Miles MJ, et al. Uniform patchy and hollow rectangular platelet micelles from crystallizable polymer blends. Science 2016;352:697-701.

[153] He XM, Hsiao MS, Boott CE, Harniman RL, Nazemi A, Li XY, et al. Two-dimensional assemblies from crystallizable homopolymers with charged termini. Nature Materials 2017;16:481-488.

[154] Wen JG, Yuan L, Yang YF, Liu L, Zhao HY. Self-Assembly of Monotethered Single-Chain Nanoparticle Shape Amphiphiles. ACS Macro Letters 2013;2:100-106.

[155] Li WK, Kuo CH, Kanyo I, Thanneeru S, He J. Synthesis and Self-Assembly of Amphiphilic Hybrid Nano Building Blocks via Self-Collapse of Polymer Single Chains. Macromolecules 2014;47:5932-5941.

[156] Williams RJ, Dove AP, O'Reilly RK. Self-assembly of cyclic polymers. Polymer Chemistry 2015;6:2998-3008.

[157] Minatti E, Viville P, Borsali R, Schappacher M, Deffieux A, Lazzaroni R. Micellar morphological changes promoted by cyclization of PS-b-PI copolymer: DLS and AFM experiments. Macromolecules 2003;36:4125-4133.

[158] Zhang BY, Zhang H, Li YJ, Hoskins JN, Grayson SM. Exploring the Effect of Amphiphilic Polymer Architecture: Synthesis, Characterization, and Self-Assembly of Both Cyclic and Linear Poly(ethylene gylcol)-b-polycaprolactone. ACS Macro Letters 2013;2:845-848.

[159] Schappacher M, Deffieux A. Synthesis of macrocyclic copolymer brushes and their self-assembly into supramolecular tubes. Science 2008;319:1512-1515.

[160] Kroger APP, Paulusse JMJ. Single-chain polymer nanoparticles in controlled drug delivery and targeted imaging. Journal of Controlled Release 2018;286:326-347.

[161] Cheng CC, Lee DJ, Liao ZS, Huang JJ. Stimuli-responsive single-chain polymeric nanoparticles towards the development of efficient drug delivery systems. Polymer Chemistry 2016;7:6164-6169.

[162] Kroger APP, Hamelmann NM, Juan A, Lindhoud S, Paulusse JMJ. Biocompatible Single-Chain Polymer Nanoparticles for Drug Delivery A Dual Approach. ACS Applied Materials & Interfaces 2018;10:30946-30951.

[163] Lam SJ, Wong EHH, Boyer C, Qiao GG. Antimicrobial polymeric nanoparticles. Progress in Polymer Science 2018;76:40-64.

[164] Zhang C, Zhu YQ, Zhou CC, Yuan WZ, Du JZ. Antibacterial vesicles by direct dissolution of a block copolymer in water. Polymer Chemistry 2013;4:255-259.

[165] Nguyen TK, Lam SJ, Ho KKK, Kumar N, Qiao GG, Egan S, et al. Rational Design of Single-Chain Polymeric Nanoparticles That Kill Planktonic and Biofilm Bacteria. ACS Infectious Diseases 2017;3:237-248.

[166] Benito AB, Aiertza MK, Marradi M, Gil-Iceta L, Zahavi TS, Szczupak B, et al. Functional Single-Chain Polymer Nanoparticles: Targeting and Imaging Pancreatic Tumors in Vivo. Biomacromolecules 2016;17:3213-3221.

[167] Latorre-Sanchez A, Pomposo JA. A simple, fast and highly sensitive colorimetric detection of zein in aqueous ethanol via zein-pyridine-gold interactions. Chemical Communications 2015;51:15736-15738.

[168] Perez-Baena I, Loinaz I, Padro D, Garcia I, Grande HJ, Odriozola I. Single-chain polyacrylic nanoparticles with multiple Gd(III) centres as potential MRI contrast agents. Journal of Materials Chemistry 2010;20:6916-6922.

[169] Han L, Shao CX, Liang B, Liu AH. Genetically Engineered Phage-Templated MnO2 Nanowires: Synthesis and Their Application in Electrochemical Glucose Biosensor Operated at Neutral pH Condition. ACS Applied Materials & Interfaces 2016;8:13768-13776.

[170] ter Huurne GM, Palmans ARA, Meijer EW. Supramolecular Single-Chain Polymeric Nanoparticles. CCS Chemistry 2019;1:64–82.

[171] Terashima T, Mes T, De Greef TFA, Gillissen MAJ, Besenius P, Palmans ARA, et al. Single-Chain Folding of Polymers for Catalytic Systems in Water. Journal of the American Chemical Society 2011;133:4742-4745.

[172] Liu YL, Pauloehrl T, Presolski SI, Albertazzi L, Palmans ARA, Meijer EW. Modular Synthetic Platform for the Construction of Functional Single-Chain Polymeric Nanoparticles: From Aqueous Catalysis to Photosensitization. Journal of the American Chemical Society 2015;137:13096-13105.

[173] Liu YL, Pujals S, Stals PJM, Paulohrl T, Presolski SI, Meijer EW, et al. Catalytically Active Single-Chain Polymeric Nanoparticles: Exploring Their Functions in Complex Biological Media. Journal of the American Chemical Society 2018;140:3423-3433.

[174] Bai YG, Feng XX, Xing H, Xu YH, Kim BK, Baig N, et al. A Highly Efficient Single-Chain Metal Organic Nanoparticle Catalyst for Alkyne-Azide "Click" Reactions in Water and in Cells. Journal of the American Chemical Society 2016;138:11077-11080.

[175] Zhao YF, Wei M, Lu J, Wang ZL, Duan X. Biotemplated Hierarchical Nanostructure of Layered Double Hydroxides with Improved Photocatalysis Performance. ACS Nano 2009;3:4009-4016.

[176] Xiao G, Huang X, Liao XP, Shi B. One-Pot Facile Synthesis of Cerium-Doped TiO2 Mesoporous Nanofibers Using Collagen Fiber As the Biotemplate and Its Application in Visible Light Photocatalysis. Journal of Physical Chemistry C 2013;117:9739-9746.

[177] Behrens S, Heyman A, Maul R, Essig S, Steigerwald S, Quintilla A, et al. Constrained Synthesis and Organization of Catalytically Active Metal Nanoparticles by Self-Assembled Protein Templates. Advanced Materials 2009;21:3515-3519.

[178] Gong CC, Sun SW, Zhang YJ, Sun L, Su ZQ, Wu AG, et al. Hierarchical nanomaterials via biomolecular self-assembly and bioinspiration for energy and environmental applications. Nanoscale 2019;11:4147-4182.

[179] Nuraje N, Dang XN, Qi JF, Allen MA, Lei Y, Belcher AM. Biotemplated Synthesis of Perovskite Nanomaterials for Solar Energy Conversion. Advanced Materials 2012;24:2885-2889.

[180] Rima S, Lattuada M. Protein Amyloid Fibrils as Template for the Synthesis of Silica Nanofibers, and Their Use to Prepare Superhydrophobic, Lotus-Like Surfaces. Small 2018;14:1802854.

[181] Konig NF, Al Ouahabi A, Poyer S, Charles L, Lutz JF. A Simple Post-Polymerization Modification Method for Controlling Side-Chain Information in Digital Polymers. Angewandte Chemie-International Edition 2017;56:7297-7301.

[182] Rutten MGTA, Vaandrager FW, Elemans JAAW, Nolte RJM. Encoding information into polymers. Nature Reviews Chemistry 2018;2:365-381.

[183] Lutz JF. Coding Macromolecules: Inputting Information in Polymers Using Monomer-Based Alphabets. Macromolecules 2015;48:4759-4767.

[184] Al Ouahabi A, Charles L, Lutz JF. Synthesis of Non-Natural Sequence-Encoded Polymers Using Phosphoramidite Chemistry. Journal of the American Chemical Society 2015;137:5629-5635.

[185] Roy RK, Meszynska A, Laure C, Charles L, Verchin C, Lutz JF. Design and synthesis of digitally encoded polymers that can be decoded and erased. Nature Communications 2015;6:7237.

[186] Trinh TT, Oswald L, Chan-Seng D, Charles L, Lutz JF. Preparation of Information-Containing Macromolecules by Ligation of Dyad-Encoded Oligomers. Chemistry-A European Journal 2015;21:11961-11965.

[187] Cavallo G, Al Ouahabi A, Oswald L, Charles L, Lutz JF. Orthogonal Synthesis of "Easy-to-Read" Information-Containing Polymers Using Phosphoramidite and Radical Coupling Steps. Journal of the American Chemical Society 2016;138:9417-9420.

[188] Gunay US, Petit BE, Karamessini D, Al Ouahabi A, Amalian JA, Chendo C, et al. Chemoselective Synthesis of Uniform Sequence-Coded Polyurethanes and Their Use as Molecular Tags. Chem 2016;1:114-126.

[189] Laure C, Karamessini D, Milenkovic O, Charles L, Lutz JF. Coding in 2D: Using Intentional Dispersity to Enhance the Information Capacity of Sequence-Coded Polymer Barcodes. Angewandte Chemie-International Edition 2016;55:10722-10725.

[190] Chen CJ, Wunderlich K, Mukherji D, Koynov K, Heck AJ, Raabe M, et al. Precision Anisotropic Brush Polymers by Sequence Controlled Chemistry. Journal of the American Chemical Society 2020;142:1332-1340.

[191] Chen CJ, Ng DYW, Weil T. Polymer-grafted gold nanoflowers with temperature-controlled catalytic features by in situ particle growth and polymerization. Materials Chemistry Frontiers 2019;3:1449-1453.

[192] Riegger A, Chen CJ, Zirafi O, Daiss N, Mukherji D, Walter K, et al. Synthesis of Peptide-Functionalized Poly(bis-sulfone) Copolymers Regulating HIV-1 Entry and Cancer Stem Cell Migration. ACS Macro Letters 2017;6:241-246.

Chapter 2 Unfolding of Natural Macromolecules for the Synthesis of Precision Nanomaterials

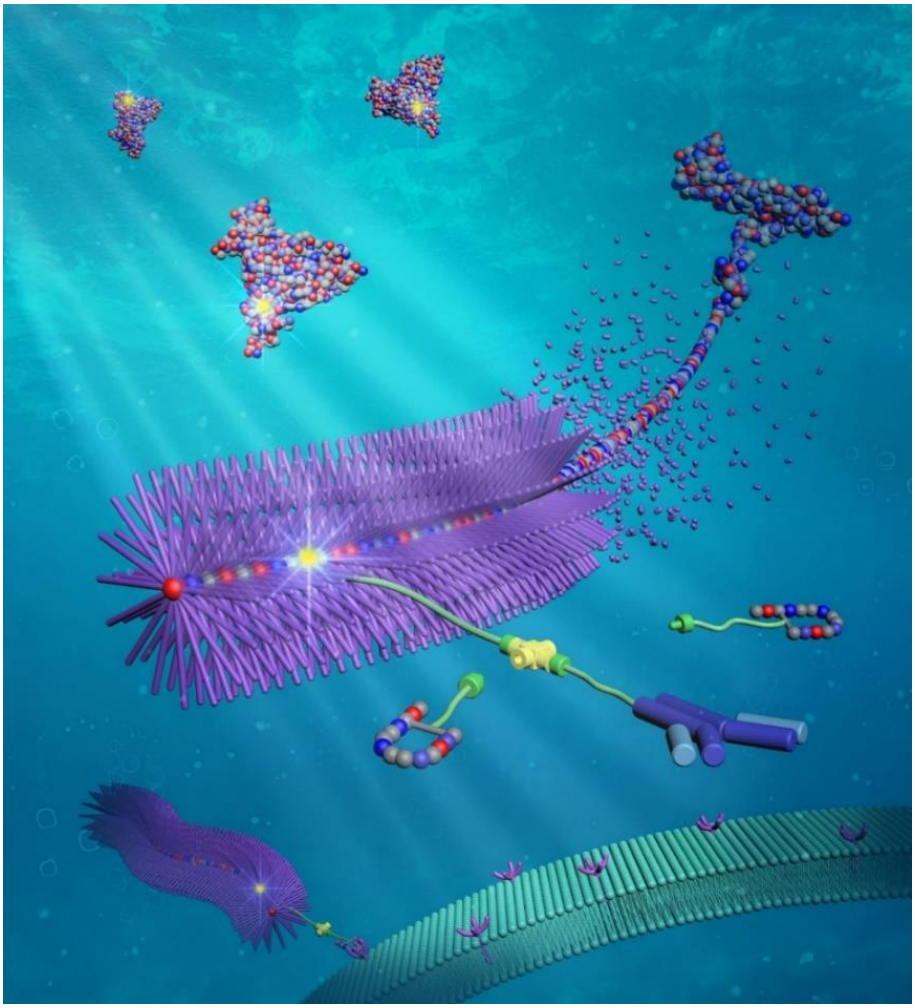

The figure is a journal cover picture of the issue: *J. Am. Chem. Soc.* **2020**, 142, 3.

2.1 Precision anisotropic brush polymers grafted from unfolded proteins

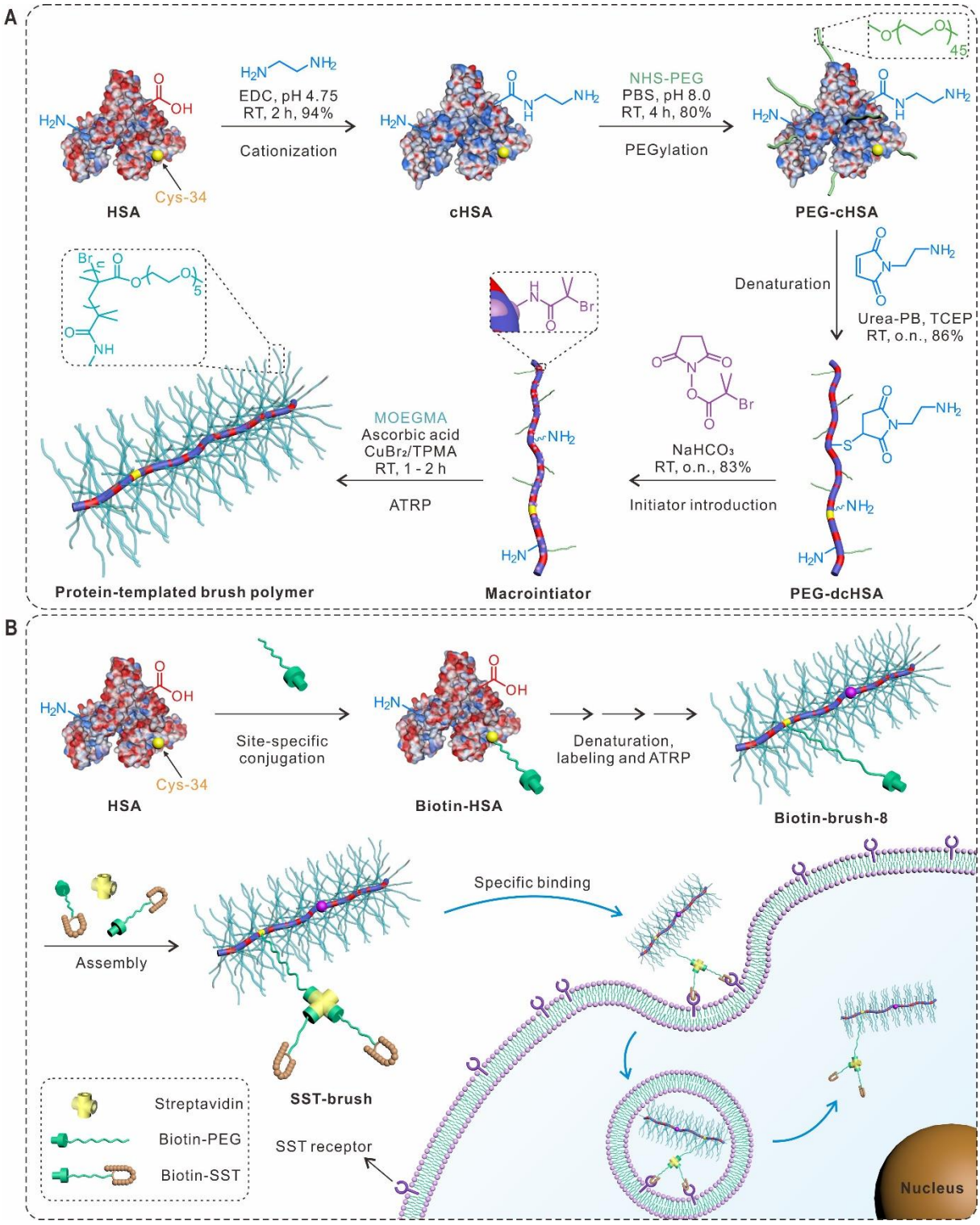

Figure 2-1 | Protein-templated precision brush polymers and their site-specific assembly. (A) Synthesis of brush polymers by grafting polymer chains from unfolded HSA via ATRP. (B) Site-specific conjugation of biotin-PEG to cysteine-34 (Cys-34) of HSA for preparation of biotin-containing brush polymers, which were further used for the site-specific assembly with biotin-somatostatin (Biotin-SST) for mediating cellular uptake by receptor mediated endocytosis. [1], Copyright 2020 The Authors. Published by the American Chemical Society.

Brush polymers constitute a unique polymer class characterized by large numbers of side chains attached to a polymer backbone [2]. Due to their compact architectures and high aspect ratios, brush polymers provide various fascinating features including wormlike shapes, notable chain-end effects, as well as unusual mechanical properties and rheological behaviors [3, 4]. Therefore, they have been considered “ideal” model systems for many experimental studies of polymers. The design and synthesis of functional brush polymers with narrow size distributions, high molecular weights, and controlled morphologies is crucial to elucidate relationships between molecular structures and physical properties of these unique macromolecules [5]. In addition, brush polymers have received considerable attention for a wide range of applications in nanoscience and biomedical fields. They have been successfully employed as templates for the fabrication of various nanomaterials such as nanotubes [6, 7], nanowires [8], nanoscale networks [9], and nonporous materials [10]. Wormlike brush polymers have been applied as photonic crystals, for tumor imaging and as delivery vehicles for therapeutics [11-14]. However, there is still no polymerization technique available that provides precise control over size, architecture, and functionality, which is essential to expand the application of brush polymers as precise macromolecular tools.

Generally, brush polymers can be achieved by three strategies: (1) *grafting through*, (2) *grafting to*, and (3) *grafting from*. The *grafting from* strategy is based on the macroinitiator comprising a distinct number of initiation sites from which the polymer side chains can be grown via various polymerization techniques [2]. Since the polymer backbone defines the contour lengths of the resulting brush polymer, much effort has been directed towards achieving well-defined and narrowly dispersed polymers. Although controlled radical polymerization reactions such as atom transfer radical polymerization (ATRP) [15] and reversible addition-fragmentation chain transfer (RAFT) [16] polymerization have been greatly advanced in the past two decades, it is still very challenging to synthesize polymer backbones with ultrahigh molecular weights and narrow distributions. Ionic polymerizations allow the synthesis of very narrowly dispersed polymers. However, this technique requires very strict reaction conditions such as inert atmosphere and degassed organic solvents as obtained in a glove box [17]. Therefore, the preparation of narrowly dispersed and ideally monodisperse polymer backbones under ambient conditions without organic solvents is highly attractive for various emerging applications in biomedical fields.

In contrast to synthetic polymers, natural biopolymers such as proteins could serve as attractive, monodisperse precursors to create brush polymers with molecular definition of the backbone. As described in chapter 1, the perfect three-dimensional structures and shapes of proteins are based on their precisely defined amino acid monomer sequences [18]. Intuitively, it would be elegant to achieve monodisperse backbones such as polypeptide chains generated from proteins for the synthesis of brush polymers with well-defined and narrowly dispersed structures [19].

By integrating protein chemistry into polymer science, we demonstrate herein a novel strategy for preparing brush polymers with monodisperse backbones by introducing high numbers of initiators into unfolded proteins. The polypeptide chains could serve as monodisperse templates, which allow the growth of polymer side chains with a tunable length via controlled polymerization techniques. In this way, well-defined brush polymers with narrow distributions, high grafting densities and long polymer side chains are obtained. Very importantly, various functional entities can be asymmetrically equipped to the backbone of the brush polymer by taking advantage of site-specific protein modification, allowing the creation of higher ordered architectures.

As a proof of concept, we selected HSA, a major blood plasma protein as a representative scaffold. In order to obtain a precision macromolecular backbone, a sequence of selective chemical and physical transformations was conducted on the protein (Figure 2-1A). First, the protein was cationized with ethylenediamine and conjugated with short poly(ethylene glycol) (PEG) chains with a M_n of 2000 g mol^{-1}. Subsequently, HSA was unfolded in 5 M urea-phosphate buffer (urea-PB) in the presence of tris(2-carboxyethyl) phosphine hydrochloride (TCEP) and *N*-(2-aminoethyl)maleimide trifluoroacetate. The obtained polypeptide backbone was then functionalized with different numbers of ATRP initiators, resulting in two protein-derived macroinitiators with varying initiator densities.

Using the *grafting from* strategy, oligo (ethylene glycol) methyl ether methacrylate (MOEGMA) as a water-soluble monomer was polymerized via activators regenerated by electron transfer atom transfer radical polymerization (ARGET ATRP). By tuning the polymerization time and monomer concentration, four brush polymers with different chain lengths and grafting densities were prepared from two macroinitiators. Gel permeation chromatography (GPC) results confirmed the successful synthesis and the brush polymers showed tunable molecular weights (M_n = 221 ~ 441 kDa) and narrow size distributions ($Đ$ = 1.16 ~1.47). Transmission electron microscopy (TEM) was

further used to directly image the morphology of the brush polymers. We found that the shape of brush polymers could be controlled by tuning the polymerization conditions. Anisotropic wormlike structures were observed when a high monomer concentration and a long polymerization time were applied. In addition, systematic light scattering and molecular simulation studies were performed to further investigate the brush polymers in the solution state. Light scattering results suggested monodisperse structures for all synthesized brush polymers. Both experiment and simulation studies also revealed anisotropic shapes for brush polymers with high grafting densities.

We further demonstrated the site-specific functionalization and assembly of protein-templated brush polymers. As shown in Figure 2-1B, HSA has only one free thiol in its native form, which is precisely located as the 34th amino acid, a cysteine (Cys-34) from the *N*-terminal of the protein. We introduced a biotin-PEG under chemoselective conditions on HSA and then synthesized biotin-functionalized brush polymers following the above described approach. Based on the biotin−streptavidin interaction, different functional entities, including AF647-labelled streptavidin, streptavidin-conjugated gold nanoparticles (5 nm), biotinylated somatostatin (biotin-SST), and a biotinylated antibody, were then assembled with the biotin-containing brush polymer in a site-specific fashion. For the functional brush polymers assembled with somatostatin, receptor-mediated uptake was observed, showing potential of this approach for drug delivery applications.

In summary, we have presented a unique approach exploiting the architecture of proteins to construct precision anisotropic brush polymers. To the best of our knowledge, the strategy described herein represents the first example of brush polymers based on monodisperse polypeptide backbones derived from natural proteins. Compared to traditional synthesis methods, this simple, straightforward and highly efficient approach proceeds in water and does not require strict reaction conditions. More importantly, brush polymers obtained from proteins provide a portfolio of functional groups of natural diversity that allow multiple functionalizations in a site-specific fashion applying state-of-the-art protein bioconjugation techniques, which is extremely challenging to achieve and has never been realized in purely synthetic brush polymers.

These results are presented comprehensively in section 5.1.

2.2 Well-defined noble metal nanostructures templated by unfolded proteins

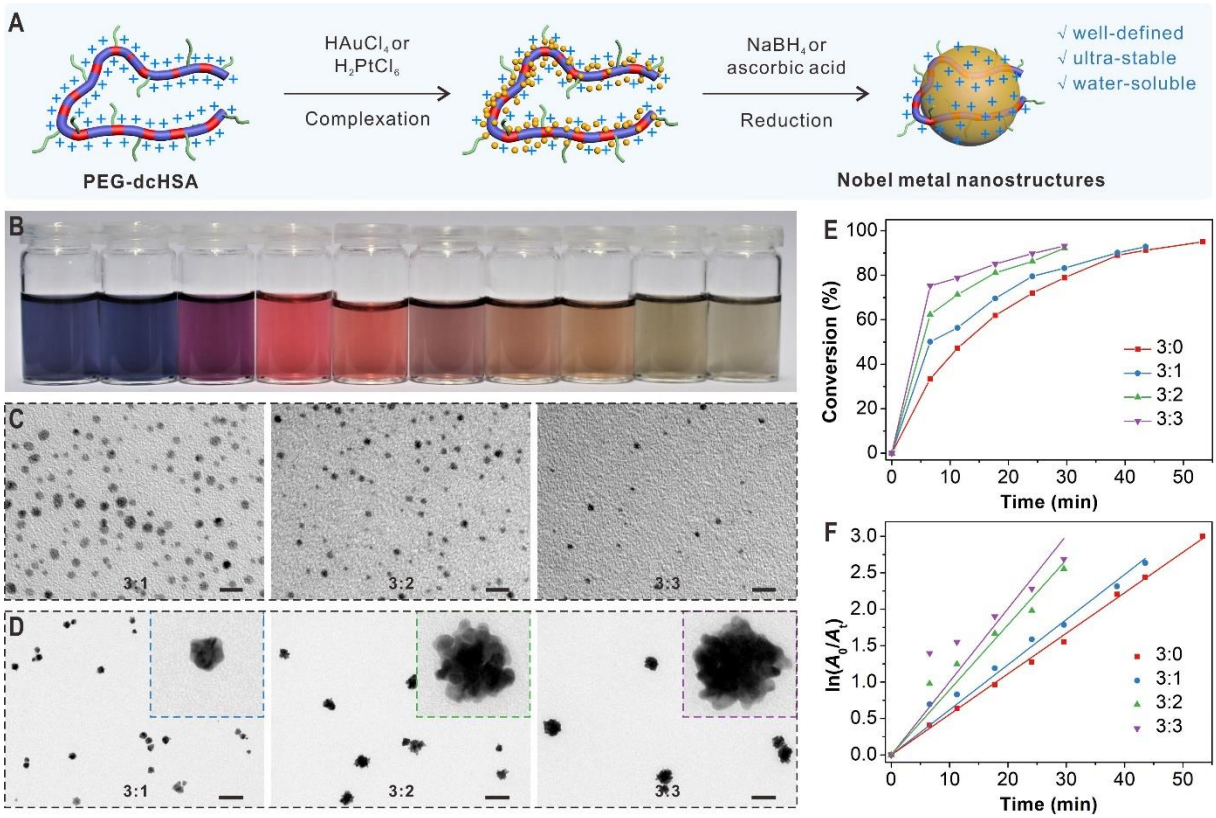

Figure 2-2 | Denatured proteins as a novel template for the synthesis of noble metal nanoparticles for catalytic applications. (A) Schematic illustration for the templated synthesis of metal nanoparticles using denatured protein PEG-dcHSA as a template. (B) Digital photo showing solutions of various noble metal nanoparticles including spherical gold nanoparticles (AuNPs), gold nanoflowers (AuNFs), and platinum nanoparticles (PtNPs) prepared by templated synthesis. (C) TEM images of ultrasmall AuNPs prepared using $NaBH_4$ as the reducing agent with different molar ratios of chloroauric anions to amino groups in the denatured protein. Scale bars: 10 nm. (D) TEM images of AuNFs prepared using ascorbic acid as the reducing agent with different molar ratios of chloroauric anions to amino groups in the denatured protein. Scale bars: 100 nm. (E) Conversion *versus* reaction time for the hydrogenation reaction of *p*-nitrophenol catalyzed by ultrasmall AuNPs prepared with $NaBH_4$ using different $HAuCl_4$/–NH_2 molar ratios. (F) Plots of $\ln(A_0/A_t)$ at 400 nm *versus* reaction time for the hydrogenation reaction catalyzed by these ultrasmall AuNPs.

Noble metal nanostructures which possess unique optical, thermal, and chemical properties have attracted great research interest in recent years [20]. They have been widely used in various fields such as catalysis, sensing and biomedicine [21]. However, metal nanoparticles aggregate easily which largely restricts their applications. Therefore, a broad range of functional surfactants and polymers have been developed for templated synthesis or post-synthesis modification of metal nanoparticles to afford long-term stable and well-dispersed nanoparticles [22, 23]. Recently, the templated

preparation and stabilization of metal nanostructures using natural polymers has been a new trend [24]. For example, chitosan [25] and cellulose [26] have been reported for templated synthesis of AuNPs to facilitate their usage in different fields.

In section 2.1, we have demonstrated the templated synthesis of precision brush polymers using unfolded proteins. In addition, unfolded proteins with various unique features, such as narrow size distribution and excellent biocompatibility, have also been employed as functional coatings for nanoparticles [27, 28], and as building blocks for functional assemblies and hydrogels [29, 30]. Due to the presence of abundant primary amino groups that can bind metal-containing anions, they serve as novel templates in this work for the synthesis of noble metal nanostructures (Figure 2-2A and B). Different template concentrations and reducing agents are selected to study their influence on the structure of obtained nanoparticles. The stability and catalytic properties of the metal nanoparticles are also evaluated.

By mixing the denatured protein template with chloroauric acid ($HAuCl_4$) aqueous solution, we firstly investigated the templated synthesis of AuNPs using sodium borohydride as the reducing agent. Ultrasmall AuNPs with the diameter of 2 ~ 5 nm were obtained (Figure 2-2C). Both TEM images and the UV-vis spectra indicate decreased particle sizes when the template concentration became higher. The reducing agent has a great impact on the size and shape of the gold nanostructures generated by templated synthesis. By replacing sodium borohydride with a mild reducing agent L-ascorbic acid, AuNFs with many branches were obtained (Figure 2-2D). The diameter of AuNFs could be controlled between 30 ~ 70 nm by varying the amount of the template. Importantly, both AuNFs and ultrasmall AuNPs demonstrated excellent stability even after vigorous centrifugation or storage at room temperature for one year. In addition, water-soluble PtNPs with an average size of ~ 3 nm were also prepared using a similar protocol, showing the broad applicability of this unique template. Lastly, all synthesized noble metal nanostructures were used as efficient catalysts for the hydrogenation of *p*-nitrophenol to *p*-aminophenol (Figure 2-2E and F). The AuNPs with an average size of 2 nm showed the highest catalytic efficiency with a rate constant of 1.026×10^{-2} L s^{-1} mg^{-1}. These metal nanoparticles with tunable size and shape, as well as good stability, dispersity and water-solubility may find broad applications in catalysis, sensors, and biomedicine.

These results are presented comprehensively in section 5.2.

2.3 One-pot concurrent polymerization and particle growth for the preparation of polymer-grafted gold nanoflowers

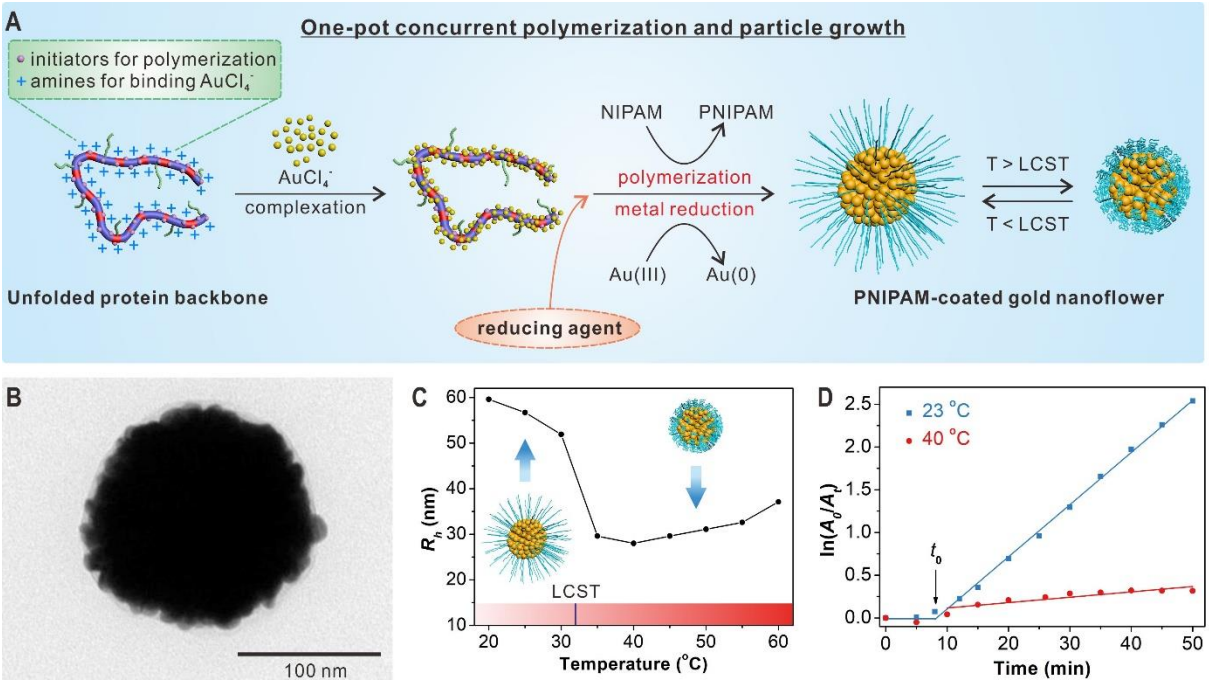

Figure 2-3 | One-pot concurrent polymerization and particle growth for the preparation of polymer-grafted gold nanoflowers for temperature-controlled catalysis. (A) Schematic illustration for the complexation of a protein-derived macroinitiator with chloroauric anions, followed by the preparation of PNIPAM-coated gold nanoflowers (PNIPAM-AuNFs) by combining activator regenerated by electron transfer atom transfer radical polymerization (ARGET ATRP) and the reduction of metal ions in a one-pot fashion. (B) TEM image of a representative PNIPAM-coated gold nanoflower prepared with an $-NH_2/HAuCl_4$ molar ratio of 6:1 at 23 °C for 2h. (C) Thermo-responsiveness of PNIPAM-AuNFs ($-NH_2/HAuCl_4$ 3:1, 40 °C, 2h) tracked by DLS at increased temperature from 20 °C to 60 °C. (D) Catalytic performances of PNIPAM-AuNFs for the hydrogenation of *p*-nitrophenol at different temperatures. [31], Copyright 2019 The Authors. Published by the Royal Society of Chemistry and the Chinese Chemical Society.

Polymer—gold hybrid nanomaterials that combine the tunable features of functional polymers and the optical, electronic, and chemical characteristics of nano-sized gold have attracted widespread interest over the past two decades [32]. Particularly, gold nanoflowers (AuNFs) with large numbers of branches and high surface-to-volume ratios have demonstrated great potential for various applications which include catalysis, drug loading, photothermal therapy, and surface enhanced Raman scattering [33, 34]. In order to introduce additional features such as water-solubility and stimuli-responsiveness to AuNFs, the preparation of AuNFs with surface-coated functional polymers is therefore a commonly-used strategy. Generally, polymer-coated

AuNFs can be obtained by either templated synthesis or grafting polymers to/from already formed AuNFs [35]. However, these approaches lack of control over the structures of polymers and AuNFs and they involve multiple synthesis and purification steps. Therefore, it would be appealing to develop a simple and general method to prepare multifunctional polymer-coated AuNFs.

In sections 2.1 and 2.2, unfolded proteins were used as precision templates for preparing brush polymers and metal nanostructures, respectively. Although the two reactions have different mechanisms and characteristics, reducing agents are required for both the ARGET ATRP and the reduction of metal ions. In this work, a simple strategy combining these two reactions in one pot for the preparation of polymer-grafted AuNFs is presented. Denatured proteins functionalized with ATRP initiators are used as a template to bind chloroauric anions ($AuCl_4^-$) and also a macroinitiator for ARGET ATRP. Ascorbic acid as the reducing agent is used to reduce metal ions and to activate the polymerization. Poly(*N*-isopropylacrylamide)-coated gold nanoflowers (PNIPAM-AuNFs) with controlled sizes and shapes are obtained and applied as a smart catalyst for the hydrogenation of *p*-nitrophenol.

Following the protocol described in section 2.1, we synthesized a macroinitiator which possesses 61 initiation sites for ARGET ATRP and high numbers of amino groups facilitating the binding of $AuCl_4^-$ (Figure 2-3A). In a typical process for one-pot synthesis of polymer-grafted AuNFs, the macroinitiator, the monomer NIPAM, the $HAuCl_4$ aqueous solution, and the $Cu^{II}Br_2$-containing catalyst complex were dissolved in deionized water. After removing oxygen, the solution was further stirred for one hour ensuring the complexation of $AuCl_4^-$ by the polypeptide template. Degassed ascorbic acid was then added continuously at a slow speed into the system to activate ATRP catalyst precursors and to reduce $AuCl_4^-$. After polymerization, the product was easily purified via centrifugation to remove unreacted monomers.

Three factors including the $-NH_2/HAuCl_4$ molar ratio, the reaction temperature, and the reaction time, were investigated and six reaction conditions were applied. TEM revealed the formation of AuNFs with rough surfaces and a layer of polymer shell under most conditions (Figure 2-3B). By adding more $HAuCl_4$ into the reaction solution, the average AuNF size increased from 148 nm to 219 nm when the molar ratio changed from 6:1 to 3:1. Further varying the $-NH_2/HAuCl_4$ molar ratio to 1:1 resulted in irregular AuNFs which was, most likely, caused by the insufficient template that can hardly bind all $AuCl_4^-$ and stabilize the AuNFs. The reaction temperature also has significant

influence on the formation of PNIPAM-AuNFs. Employing a constant $–NH_2/HAuCl_4$ molar ratio of 3:1, the average diameter of AuNFs decreased from 219 nm to 61 nm when the temperature was tuned from 23 °C to 40 °C. In addition, some evidence was observed showing increased shell thickness when the reaction time became longer.

Dynamic light scattering (DLS) was further used to investigate the thermo-responsiveness of the prepared PNIPAM-AuNFs (Figure 2-3C). The hydrodynamic radius (R_h) of the hybrid nanostructure was tracked during temperature increase from 20 °C to 60 °C. When the temperature was below 30 °C, the R_h of PNIPAM-AuNFs remained constant within the range of 52 ~ 60 nm. However, a pronounced drop to less than 30 nm was detected when the temperature increased from 30 °C to 35 °C. This temperature correlates to the reported lower critical solution temperature (LCST) of PNIPAM in the literature [36]. Importantly, this process is reversible.

The thermo-responsive nanohybrids were then employed as catalysts for the hydrogenation of *p*-nitrophenol to *p*-aminophenol (Figure 2-3D). At 23 °C, PNIPAM-AuNFs demonstrated efficient catalytic activity for the hydrogenation reaction and an apparent rate constant of 1.02×10^{-3} s^{-1} was recorded when an extremely low gold concentration of 1.52 mg L^{-1} was used. In contrast, a significant drop in the rate constant down to about 10% was observed after increasing the temperature to 40 °C. Here, the PNIPAM shell in the collapsed form serves as a diffusion barrier for *p*-nitrophenol resulting in a significantly decreased catalytic performance.

In summary, we have demonstrated a simple one-pot strategy for the preparation of polymer-coated metal nanostructures by combining ARGET ATRP and the reduction of metal ions. PNIPAM-AuNFs with controllable sizes, shapes and thermo-responsiveness have been achieved and applied as smart nanoparticle catalysts for the hydrogenation of *p*-nitrophenol. We believe this novel strategy can be expanded for the synthesis of polymer-metal hybrid nanomaterials based on various functional polymers and different noble metal structures, which may find broad applications in catalysis, sensing, and biomedicine.

These results are presented comprehensively in section 5.3.

2.4 References

[1] Chen CJ, Wunderlich K, Mukherji D, Koynov K, Heck AJ, Raabe M, et al. Precision Anisotropic Brush Polymers by Sequence Controlled Chemistry. Journal of the American Chemical Society 2020;142:1332-1340.

[2] Verduzco R, Li XY, Pesek SL, Stein GE. Structure, function, self-assembly, and applications of bottlebrush copolymers. Chemical Society Reviews 2015;44:2405-2420.

[3] Feng C, Li YJ, Yang D, Hu JH, Zhang XH, Huang XY. Well-defined graft copolymers: from controlled synthesis to multipurpose applications. Chemical Society Reviews 2011;40:1282-1295.

[4] Vatankhah-Varnosfaderani M, Daniel WFM, Everhart MH, Pandya AA, Liang HY, Matyjaszewski K, et al. Mimicking biological stress-strain behaviour with synthetic elastomers. Nature 2017;549:497-501.

[5] Dziezok P, Sheiko SS, Fischer K, Schmidt M, Moller M. Cylindrical molecular brushes. Angewandte Chemie-International Edition 1997;36:2812-2815.

[6] Huang K, Rzayev J. Well-Defined Organic Nanotubes from Multicomponent Bottlebrush Copolymers. Journal of the American Chemical Society 2009;131:6880-6885.

[7] Mullner M, Yuan JY, Weiss S, Walther A, Fortsch M, Drechsler M, et al. Water-Soluble Organo-Silica Hybrid Nanotubes Templated by Cylindrical Polymer Brushes. Journal of the American Chemical Society 2010;132:16587-16592.

[8] Yuan JY, Xu YY, Walther A, Bolisetty S, Schumacher M, Schmalz H, et al. Water-soluble organo-silica hybrid nanowires. Nature Materials 2008;7:718-722.

[9] Wu DC, Nese A, Pietrasik J, Liang YR, He HK, Kruk M, et al. Preparation of Polymeric Nanoscale Networks from Cylindrical Molecular Bottlebrushes. ACS Nano 2012;6:6208-6214.

[10] Bolton J, Bailey TS, Rzayev J. Large Pore Size Nanoporous Materials from the Self-Assembly of Asymmetric Bottlebrush Block Copolymers. Nano Letters 2011;11:998-1001.

[11] Sowers MA, McCombs JR, Wang Y, Paletta JT, Morton SW, Dreaden EC, et al. Redox-responsive branched-bottlebrush polymers for in vivo MRI and fluorescence imaging. Nature Communications 2014;5:5460.

[12] Fouz MF, Mukumoto K, Averick S, Molinar O, McCartney BM, Matyjaszewski K, et al. Bright Fluorescent Nanotags from Bottlebrush Polymers with DNA-Tipped Bristles. ACS Central Science 2015;1:431-438.

[13] Liberman-Martin AL, Chu CK, Grubbs RH. Application of Bottlebrush Block Copolymers as Photonic Crystals. Macromolecular Rapid Communications 2017;38:1700058.

[14] Luo HY, Szymusiak M, Garcia EA, Lock LL, Cui HG, Liu Y, et al. Solute-Triggered Morphological Transitions of an Amphiphilic Heterografted Brush Copolymer as a Single-Molecule Drug Carrier. Macromolecules 2017;50:2201-2206.

[15] Wang JS, Matyjaszewski K. Controlled Living Radical Polymerization - Atom-Transfer Radical Polymerization in the Presence of Transition-Metal Complexes. Journal of the American Chemical Society 1995;117:5614-5615.

[16] Chiefari J, Chong YK, Ercole F, Krstina J, Jeffery J, Le TPT, et al. Living free-radical polymerization by reversible addition-fragmentation chain transfer: The RAFT process. Macromolecules 1998;31:5559-5562.

[17] Rieger E, Gleede T, Weber K, Manhart A, Wagner M, Wurm FR. The living anionic polymerization of activated aziridines: a systematic study of reaction conditions and kinetics. Polymer Chemistry 2017;8:2824-2832.

[18] Heim M, Romer L, Scheibel T. Hierarchical structures made of proteins. The complex architecture of spider webs and their constituent silk proteins. Chemical Society Reviews 2010;39:156-164.

[19] Ng DYW, Wu YZ, Kuan SL, Weil T. Programming Supramolecular Biohybrids as Precision Therapeutics. Accounts of Chemical Research 2014;47:3471-3480.

[20] Jain PK, Huang XH, El-Sayed IH, El-Sayed MA. Noble Metals on the Nanoscale: Optical and Photothermal Properties and Some Applications in Imaging, Sensing, Biology, and Medicine. Accounts of Chemical Research 2008;41:1578-1586.

[21] Sau TK, Rogach AL, Jackel F, Klar TA, Feldmann J. Properties and Applications of Colloidal Nonspherical Noble Metal Nanoparticles. Advanced Materials 2010;22:1805-1825.

[22] Jana NR, Gearheart L, Murphy CJ. Seed-mediated growth approach for shape-controlled synthesis of spheroidal and rod-like gold nanoparticles using a surfactant template. Advanced Materials 2001;13:1389-1393.

[23] Sasidharan M, Nakashima K. Core-Shell-Corona Polymeric Micelles as a Versatile Template for Synthesis of Inorganic Hollow Nanospheres. Accounts of Chemical Research 2014;47:157-167.

[24] Yang WT, Guo WS, Chang J, Zhang BB. Protein/peptide-templated biomimetic synthesis of inorganic nanoparticles for biomedical applications. Journal of Materials Chemistry B 2017;5:401-417.

[25] Liu GY, Luo QQ, Wang HB, Zhuang WH, Wang YB. In situ synthesis of multidentate PEGylated chitosan modified gold nanoparticles with good stability and biocompatibility. RSC Advances 2015;5:70109-70116.

[26] Zhang KT, Shen MG, Liu H, Shang SB, Wang D, Liimatainen H. Facile synthesis of palladium and gold nanoparticles by using dialdehyde nanocellulose as template and reducing agent. Carbohydrate Polymers 2018;186:132-139.

[27] Wu YZ, Chakrabortty S, Gropeanu RA, Wilhelmi J, Xu Y, Er KS, et al. pH-Responsive Quantum Dots via an Albumin Polymer Surface Coating. Journal of the American Chemical Society 2010;132:5012-5014.

[28] Wu YZ, Ermakova A, Liu WN, Pramanik G, Vu TM, Kurz A, et al. Programmable Biopolymers for Advancing Biomedical Applications of Fluorescent Nanodiamonds. Advanced Functional Materials 2015;25:6576-6585.

[29] Gacanin J, Hedrich J, Sieste S, Glasser G, Lieberwirth I, Schilling C, et al. Autonomous Ultrafast Self-Healing Hydrogels by pH-Responsive Functional Nanofiber Gelators as Cell Matrices. Advanced Materials 2019;31:1805044.

[30] Wu YZ, Ihme S, Feuring-Buske M, Kuan SL, Eisele K, Lamla M, et al. A Core-Shell Albumin Copolymer Nanotransporter for High Capacity Loading and Two-Step Release of Doxorubicin with Enhanced Anti-Leukemia Activity. Advanced Healthcare Materials 2013;2:884-894.

[31] Chen CJ, Ng DYW, Weil T. Polymer-grafted gold nanoflowers with temperature-controlled catalytic features by in situ particle growth and polymerization. Materials Chemistry Frontiers 2019;3:1449-1453.

[32] Wu XJ, Gao YQ, Dong CM. Polymer/gold hybrid nanoparticles: from synthesis to cancer theranostic applications. RSC Advances 2015;5:13787-13796.

[33] Yang DP, Liu X, Teng CP, Owh C, Win KY, Lin M, et al. Unexpected formation of gold nanoflowers by a green synthesis method as agents for a safe and effective photothermal therapy. Nanoscale 2017;9:15753-15759.

[34] Ye SJ, Benz F, Wheeler MC, Oram J, Baumberg JJ, Cespedes O, et al. One-step fabrication of hollow-channel gold nanoflowers with excellent catalytic performance and large single-particle SERS activity. Nanoscale 2016;8:14932-14942.

[35] Xu D, Gu JJ, Wang WN, Yu XC, Xi K, Jia XD. Development of chitosan-coated gold nanoflowers as SERS-active probes. Nanotechnology 2010;21:375101.

[36] Li BS, Smilgies DM, Price AD, Huber DL, Clem PG, Fan HY. Poly(N-isopropylacrylamide) Surfactant-Functionalized Responsive Silver Nanoparticles and Superlattices. ACS Nano 2014;8:4799-4804.

Chapter 3 Folding of Synthetic Polymers for the Preparation of Biomimetic Hierarchical Structures

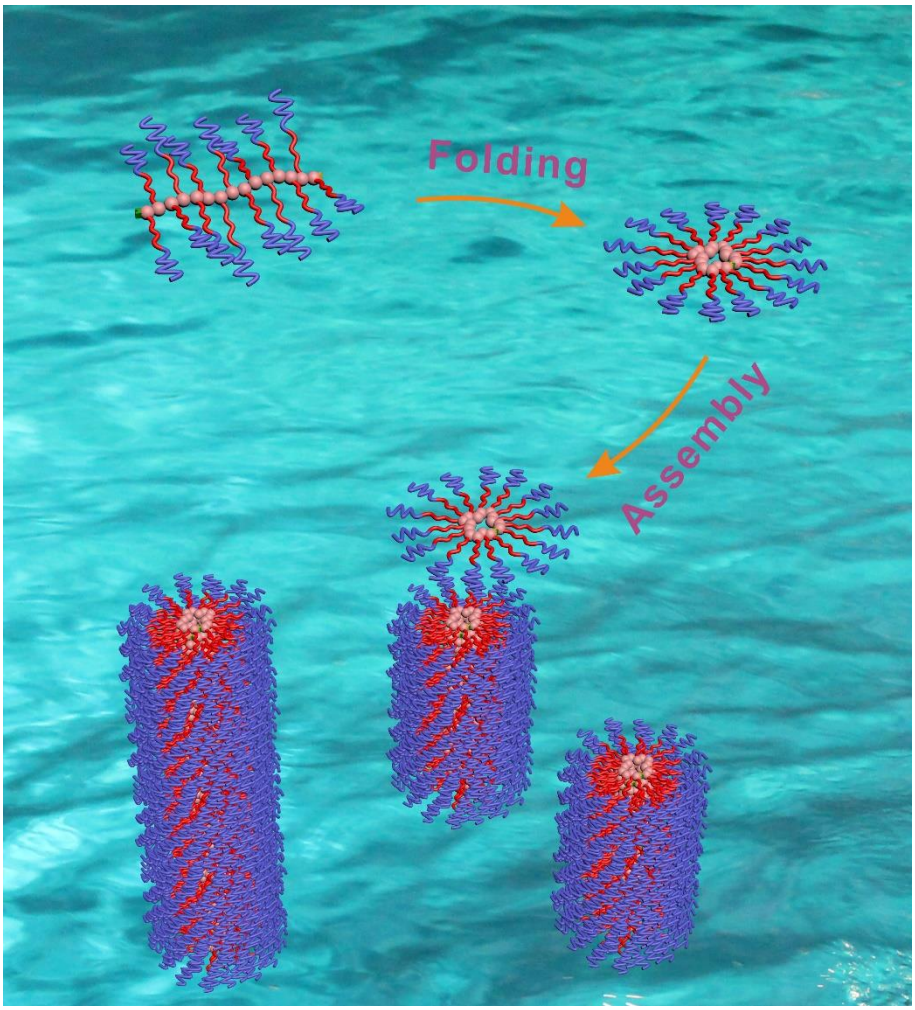

3.1 Peptide-functionalized poly(bis-sulfone) copolymers for regulating HIV-1 entry and cancer stem cell migration

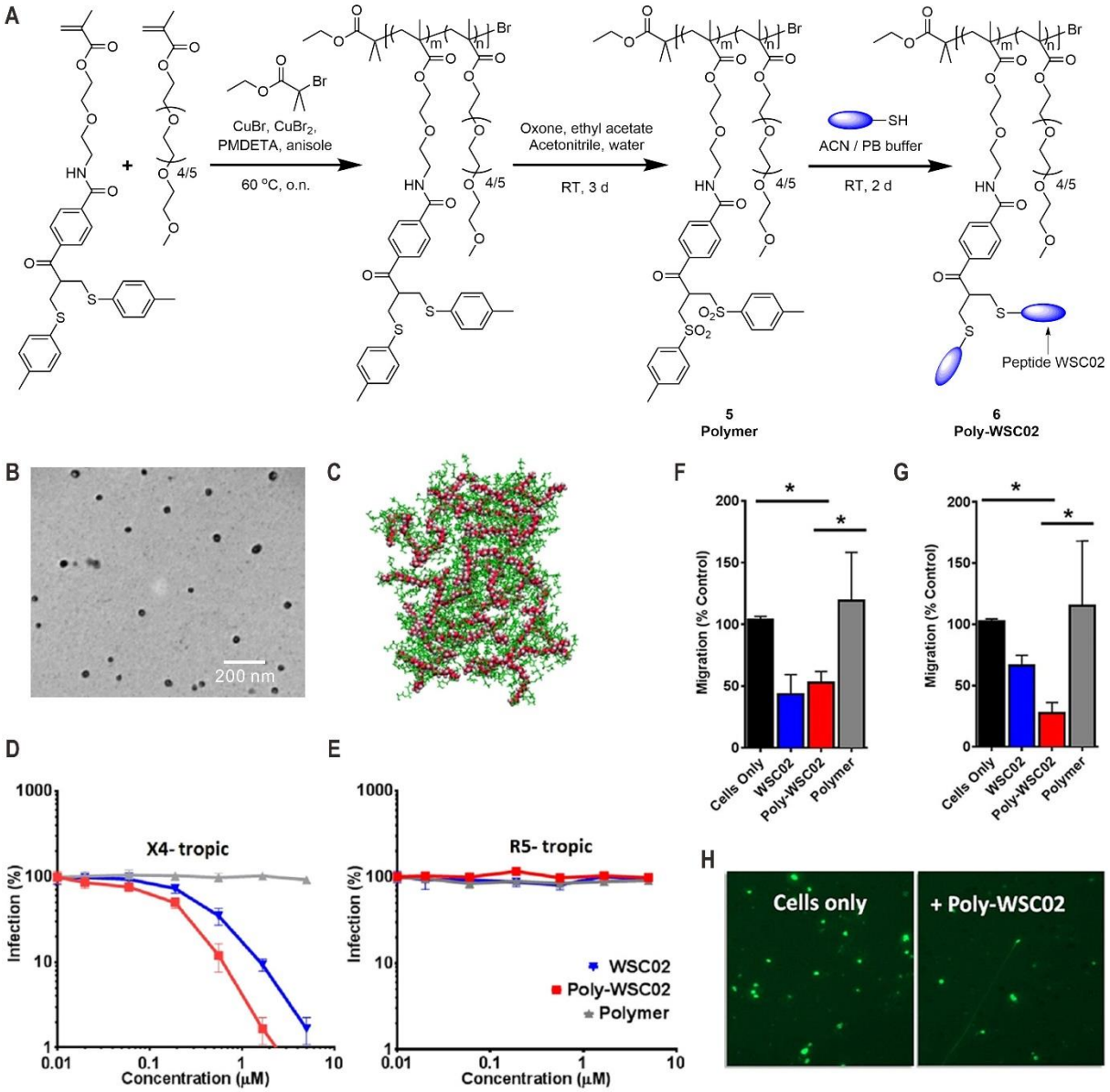

Figure 3-1 | Peptide-functionalized poly(bis-sulfone) copolymers for regulating HIV-1 entry and cancer stem cell migration. (A) Synthesis of thiol-reactive poly[oligo(ethylene glycol) methacrylate-*co*-(bis-sulfone)] (**5**). The copolymer was functionalized with the thiol-containing peptide WSC02, yielding the bioactive conjugate Poly-WSC02 (**6**) (B) TEM image of assemblies formed by Poly-WSC02. (C) Simulation snapshot showing the self-folding of an analogue of Poly-WSC02, where each chain consists of a hydrocarbon (red spheres) backbone with tri(ethylene glycol) (green bonds) side chains. (D-E) HIV infection assay of polymer **5**, native WSC02, and Poly-WSC02 (**6**) in (D) X4-tropic and in (E) R5-tropic cells. (F-G) Impact of native WSC02 and Poly-WSC02 on cancer cell migration in vitro. Cancer cells were isolated from human (PANC354, F) and mouse (CHX, G) primary tumors. (H) Representative microscope pictures of the migrated cancer cells after staining with DAPI. Adapted with permission from [1]. Copyright 2017 American Chemical Society.

Polymer-peptide conjugates that integrate unique features of synthetic polymers and functional peptides have found numerous applications in biomedical areas [2-4]. Although various synthetic approaches have been established for bioconjugation, the development of suitable chemistries for specific biomolecules is still an important topic. Particularly, a series of thiol-based reactions, including thiol–ene, thiol–yne, thiol–vinylsulfone, and thiol–parafluoro reactions, have attracted special attention as they can selectively address cysteines of polypeptides under mild conditions [5]. However, these interactions are mainly applied for small molecules and there are limited studies reporting the synthesis of thiol-reactive polymers that can be used as multivalent scaffolds [6, 7]. Therefore, it is very important to synthesize functional polymers with multiple thiol-reactive groups for conjugation with biomolecules.

In chapter 2, I have described the strategy of using unfolded proteins as novel templates for preparing precision brush polymers and noble metal nanostructures. As an opposite strategy, linear synthetic polymers can also be folded and assembled into compact states via different interactions mimicking the 3D hierarchical structure of biopolymers. In collaboration with Andreas Riegger, we synthesized novel thiol-reactive copolymers with functional bis-sulfone moieties and demonstrated their application for peptide conjugation [1]. The peptide-functionalized poly(bis-sulfone) copolymers fold and assemble into spherical aggregates in aqueous solution, which were further used for inhibition of HIV-1 entry and cancer cell migration.

In 2006, Brocchini and Shaunak et al. reported a bis-sulfone containing reagent, which can intercalate into native disulfide bonds in proteins and peptides by site-specific bisalkylation of two cysteine sulfur atoms to form a three-carbon bridge [8, 9]. This bis-sulfone functionality was further developed by the Weil group as a multifunctional platform for various applications [10] such as cross-conjugation of different biomolecules [11] and cancer targeted photodynamic therapy [12]. Here, we designed and synthesized a bis-sulfide monomer, which was then copolymerized with water-soluble oligo(ethylene glycol)methacrylate (OEGMA) via ATRP. The resulting copolymer was oxidized to afford thiol-reactive poly[oligo(ethylene glycol) methacrylate-*co*-(bis-sulfone)] (**5**). The structure and synthetic route of the bis-sulfone-containing copolymer are illustrated in Figure 3-1A. The GPC measurement of **5** revealed a M_n of 15100 g mol^{-1} with a molecular weight dispersity of 1.11, indicating a very narrow distribution. Based on further MALDI-ToF mass spectra analysis, the copolymer provides around five bis-sulfone groups per polymer chain. Because a

single bis-sulfone can be functionalized with two thiol containing peptides, up to 10 peptides can be introduced via Michael reactions to each polymer backbone.

Different thiol-containing oligopeptides, including a tripeptide glutathione and a 12-mer peptide termed WSC02, were attached to the bis-sulfone copolymer **5**. Among them, WSC02 is a peptide that targets C-X-C chemokine receptor type 4 (CXCR4) which plays crucial roles in several diseases including cancer metastasis, immuno-deficiencies, and HIV [13, 14]. The obtained conjugate (Poly-WSC02) showed high tendency for self-organization in aqueous solution as indicated by DLS. Spherical assemblies with narrow dispersity were observed by TEM (Figure 3-1B). To complement the observed morphology, all atom molecular dynamics simulations were performed for a simplified analogue of Poly-WSC02, showing the formation of nano-sized aggregates via molecular folding and self-assembly (Figure 3-1C).

To study whether the peptides were localized on the surface, we tested the inhibitory effect of Poly-WSC02 against CXCR4 (X4) and CCR5 (R5) tropic HIV-1 infection using TZM-bl cells. X4-tropic viruses infect cells by specific interaction with the membrane receptors CXCR4 and CD4, whereas R5-tropic variants utilize CD4 and CCR5 [15]. As shown in Figure 3-1D, Poly-WSC02 revealed an enhanced antiviral activity (IC_{50} = 150 ± 60 nM) than the native WSC02 (IC_{50} = 360 ± 70 nM). In contrast, both WSC02 and Poly-WSC02 had no effect on R5-tropic virus infection (Figure 3-1E), confirming the specificity of the peptide for X4-tropic HIV infection. As CXCR4 is also involved in leucocyte trafficking and the metastasis of pancreatic ductal adenocarcinoma (PDAC), we tested the inhibitory effect of the conjugate on the migration of primary PDAC cells isolated from human or mouse tumors (Figure 3-1F to H). Both Poly-WSC02 and native WSC02 inhibited human cancer cell migration by ~ 50%, while for mouse cancer cells the conjugate showed an enhanced effect.

In summary, we have presented the synthesis of a novel thiol-reactive copolymer containing functional bis-sulfone groups and demonstrated its application as a platform for peptide conjugation. As a CXCR4 antagonist, WSC02 was successfully conjugated to the poly(bis-sulfone) copolymer resulting a functional polymer bioconjugate that folded and assembled into narrowly dispersed spherical aggregates in aqueous media. The hybrid nanomaterial demonstrated both antiviral effects against HIV-1 and the ability to inhibit cancer cell migration as a result of the folded architecture providing the targeting groups at the outer surface.

These results are presented comprehensively in section 5.4.

3.2 Biomolecule-inspired self-assembly of folded synthetic polymers into wormlike hierarchical structures

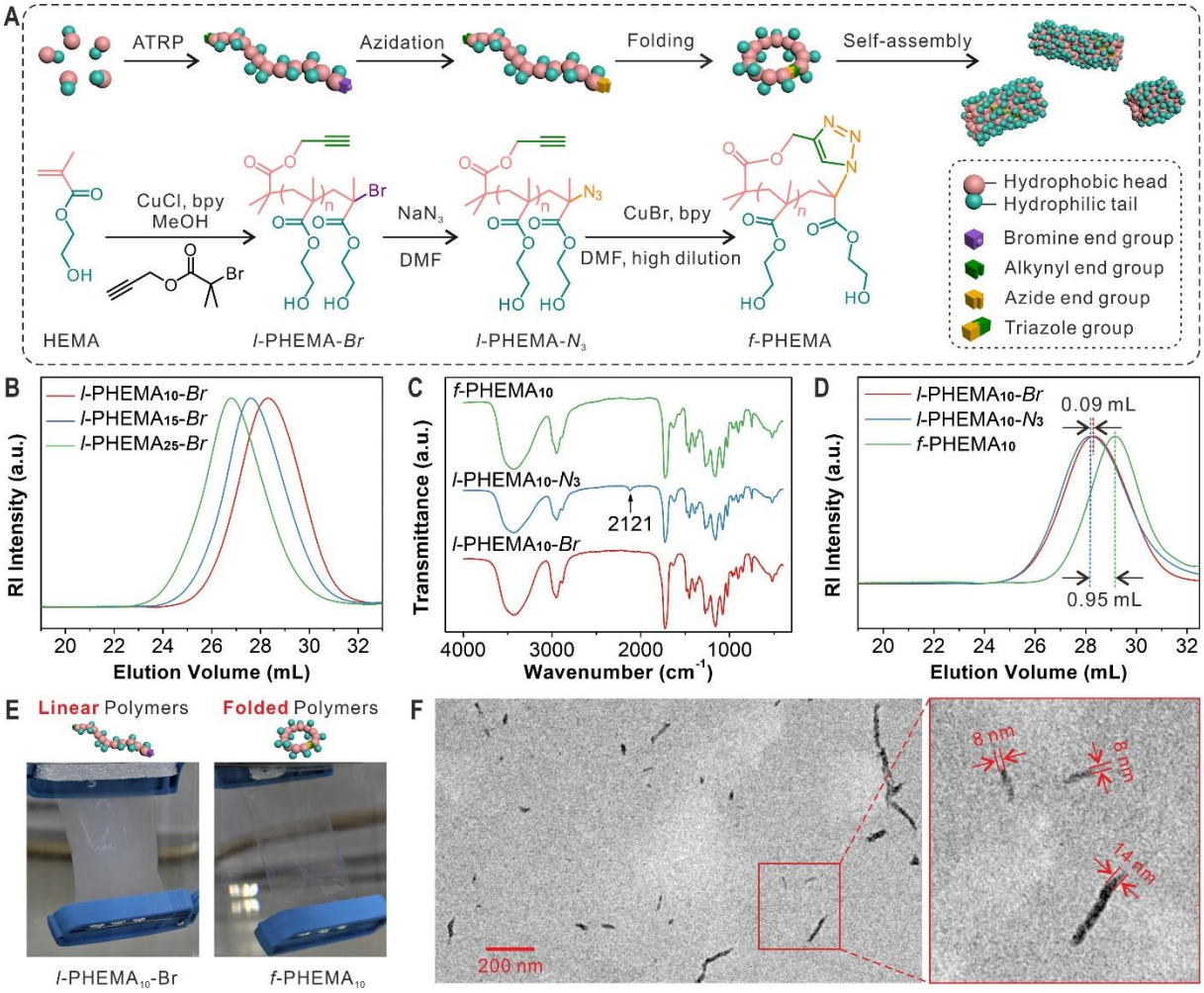

Figure 3-2 | Biomolecule-inspired self-assembly of folded synthetic polymers. (A) Schematic illustration for the synthesis of linear PHEMA and its folding-induced self-assembly into wormlike hierarchical structures. (B) GPC elution curves (eluent: DMF; standard: PMMA) of three linear PHEMA with different designed repeating units. (C) FTIR spectra, and (D) GPC curves of *l*-PHEMA$_{10}$-*Br*, *l*-PHEMA$_{10}$-*N*$_3$, and *f*-PHEMA$_{10}$. (E) Digital images showing the self-assembly solutions of linear polymer *l*-PHEMA$_{10}$-*Br* and folded ring polymer *f*-PHEMA$_{10}$ after dialysis against deionized water for 1 h. (F) TEM images showing the formation of wormlike structures via self-assembly of *f*-PHEMA$_{10}$.

In section 3.1, I have demonstrated the synthesis of poly(bis-sulfone) copolymers and its formation of bioactive spherical nanostructures via polymer folding and self-assembly. However, the folding of synthetic polymers in this system by noncovalent interactions proceeds in a random manner. As mentioned in the introduction, proteins in Nature are polypeptides that form highly precise 3D structures through first folding of linear polypeptides into ordered secondary structures such as α-helix and β-sheets,

followed by folding and assembly of these secondary structures into tertiary and quaternary structures [16, 17]. In addition, DNA chains can also be folded into various complex yet precise 2D and 3D nanoarchitectures using the so-called DNA origami technique pioneered by Rothemund [18-20]. For both proteins and nucleic acids, the precise folding of linear biopolymer chains is a fundamental step towards the formation of their 3D hierarchical structures, as well as the realization of their biological functions and applications in material fields [16, 21].

The preparation of biomimetic nanostructures with different levels of controlled structures especially with anisotropic shapes represents a great challenge in polymer science. Self-assembly of amphiphilic block copolymers has gained much attention over the past 30 years for the preparation of polymer nanoobjects with various morphologies such as spherical micelles, wormlike micelles, and vesicles [22]. These structures can be made from a wide variety of synthetic polymers, making them attractive for many applications including catalysis, tumor imaging, drug delivery [23-27]. However, the preparation of wormlike assemblies requires very strict control over the hydrophilic-hydrophobic ratio of the polymer and well-defined hierarchical structures are difficult to achieve. Intramolecular folding of synthetic polymer chains into single chain nanoparticles or topological polymers is another emerging technique for the construction of functional polymer nanoobjects [28, 29]. This field is in its early stage. Although various interactions including covalent bonds and noncovalent chemistries have already been developed for single chain folding, the self-assembly of folded polymers is still considered an unexplored area.

In this section, we report a biomolecule-inspired strategy for constructing wormlike hierarchical structures by combining single chain folding and macromolecular self-assembly. First, we synthesize and fold linear polymers of different molecular weights into cyclic polymers. Second, the self-assembly behavior of these folded polymers is compared with their linear counterparts. Due to the rearrangement of the hydrophobic backbone and hydrophilic side groups during the folding step, hierarchical wormlike structures are obtained via self-assembly of cyclic polymers. Furthermore, we synthesize macrocyclic brush polymers with amphiphilic block chains that can self-assemble into stable wormlike nanoobjects and higher-ordered structures. This work reports for the first time the self-assembly of folded homopolymers into wormlike hierarchical nanostructures. Our simple strategy also points out the possibility to fabricate other hierarchical structures by folding of synthetic polymers.

Using propargyl 2-bromoisobutyrate as an initiator, we polymerized 2-hydroxyethyl methacrylate (HEMA) and prepared three linear poly(2-hydroxyethyl methacrylate) (PHEMA) samples with different molecular weights (*l*-PHEMA$_{10}$-*Br*, *l*-PHEMA$_{15}$-*Br*, and *l*-PHEMA$_{25}$-*Br*) via ATRP (Figure 3-2A). These polymers were characterized by proton nuclear magnetic resonance (^{1}H NMR) spectroscopy and GPC, showing designed molecular weights and narrow size distributions (Figure 3-2B). Then, the bromine termini of these polymers were transferred to azide groups by reacting with sodium azide. The Fourier-transform infrared (FTIR) spectrum in Figure 3-2C shows the characteristic peak of azide group at 2121 cm^{-1}, indicating the successful azidation reaction. Subsequently, linear PHEMA polymers with functional azide ends were folded into cyclic polymers via click chemistry under high dilution conditions. The disappearance of the azide peak in FTIR spectra (Figure 3-2C) and a new signal of triazole at 8.5 ppm in the ^{1}H NMR spectrum of the product confirmed the click reaction between azide and alkyne end groups. To further elucidate whether the reaction happened intramolecularly or intermolecularly, we compared the GPC elution curves of the polymers before and after the reaction (Figure 3-2D). In addition, 2D diffusion ordered NMR spectra were collected using an 850 MHz spectrometer. Both characterizations showed decreased hydrodynamic volumes of the folded polymers, excluding the possibility of intermolecular reactions. Therefore, we can conclude that the linear polymers were successfully folded into the ring secondary structure.

In order to compare the self-assembly behavior of linear and folded polymers, the samples were firstly dissolved in methanol and then dialyzed against deionized water. As shown in Figure 3-2E, the self-assembly solution for linear polymers turned turbid after dialysis for 1 h. By further increasing the dialysis time to three days, methanol was completely replaced by water which resulted in the formation some gel-like precipitates. Interestingly, the solution of folded polymers was transparent during the dialysis process, indicating that the folded polymers have higher colloidal stability. We then employed DLS to characterize the self-assembly solution of folded PHEMA and the results suggest the formation of nanoscale assemblies in the range of 30 ~ 60 nm for all three folded ring polymers. For linear PHEMA, DLS experiment was not possible due to the presence of large aggregates.

We further studied the self-assembly of folded polymers by loading Nile Red with different concentrations of assemblies. Nile Red is a fluorescent probe that shows low fluorescence emission in aqueous solution. However, its fluorescent intensity becomes

much stronger if the probe is encapsulated into a hydrophobic environment [30-32]. For the assemblies of folded polymers, the characteristic emission peak of Nile Red can be clearly observed when the concentration is high such as 0.5 mg mL^{-1}, indicating the formation of a hydrophobic environment. By plotting the emission intensity at 654 nm over the concentration of the solutions, the critical aggregation concentration of *f*-$PHEMA_{10}$ was determined as 0.008 mg mL^{-1}, indicating that it starts forming a hydrophobic internal environment at this concentration. As shown in Figure 3-2F, the formation of wormlike structures with a diameter of ~ 10 nm was observed by TEM, which is direct evidence that tertiary structures were formed from folded polymers. For comparison, linear polymers only formed irregular aggregates, demonstrating the important role of polymer folding in the self-assembly. We also performed ^1H NMR measurements of folded polymers in a series of solvent mixtures of MeOD and D_2O. The peaks of the methylene groups in the side chains gradually shift when the amount of D_2O increases while the peaks of methyl groups in the backbone do not change. This indicates that the backbone of the folded polymers was packed in the core and the side chains on the surface during the self-assembly process. In addition, molecular dynamic simulation results suggest the formation of wormlike micelles by packing of folded polymers in a layer-by-layer manner with hydrophilic side chains on the surface.

Moreover, we designed and synthesized macrocyclic brush polymers with amphiphilic PS-*b*-PAA side chains via consecutive ATRP growth of polystyrene (PS) and poly(*tert*-butyl acrylate) (P*t*BA) from cyclic PHEMA. The hydrophobic P*t*BA block was then hydrolyzed into hydrophilic poly(acrylic acid) (PAA). We found that the polymer concentration and the hydrophilic-hydrophobic ratio are two important factors on the assembly. At a low concentration of 0.1 mg mL^{-1}, discrete structures were obtained. When the concentration increased to 0.4 mg mL^{-1}, TEM and atomic force microscopy (AFM) images show the formation of wormlike assemblies and higher-ordered structures. For cyclic brush polymers with similar side chain lengths, the wormlike assemblies became longer with the decrease of the PAA mass fraction. By customizing the block constituents, proportion and length, the architectural outcome can be tuned.

In summary, we have established a convenient strategy to prepare wormlike hierarchical structures by self-assembly of folded polymers. Compared to traditional fabrication methods, the wormlike structures obtained by this approach possess a cyclic secondary structure. This work not only provides a versatile approach for the

construction of wormlike structures from synthetic polymers, but also points out a novel avenue to arrange atoms by combining polymer folding and macromolecular self-assembly for fabricating other hierarchical structures of different shapes which are not possible by traditional self-assembly approaches.

These results are presented comprehensively in section 5.5.

3.3 References

[1] Riegger A, Chen CJ, Zirafi O, Daiss N, Mukherji D, Walter K, et al. Synthesis of Peptide-Functionalized Poly(bis-sulfone) Copolymers Regulating HIV-1 Entry and Cancer Stem Cell Migration. ACS Macro Letters 2017;6:241-246.

[2] Gauthier MA, Klok HA. Peptide/protein-polymer conjugates: synthetic strategies and design concepts. Chemical Communications 2008:2591-2611.

[3] Canalle LA, Lowik DWPM, van Hest JCM. Polypeptide-polymer bioconjugates. Chemical Society Reviews 2010;39:329-353.

[4] Cobo I, Li M, Sumerlin BS, Perrier S. Smart hybrid materials by conjugation of responsive polymers to biomacromolecules. Nature Materials 2015;14:143-159.

[5] Stenzel MH. Bioconjugation Using Thiols: Old Chemistry Rediscovered to Connect Polymers with Nature's Building Blocks. ACS Macro Letters 2013;2:14-18.

[6] Arslan M, Gevrek TN, Lyskawa J, Szunerits S, Boukherroub R, Sanyal R, et al. Bioinspired Anchorable Thiol-Reactive Polymers: Synthesis and Applications Toward Surface Functionalization of Magnetic Nanoparticles. Macromolecules 2014;47:5124-5134.

[7] Gevrek TN, Bilgic T, Klok HA, Sanyal A. Maleimide-Functionalized Thiol Reactive Copolymer Brushes: Fabrication and Post-Polymerization Modification. Macromolecules 2014;47:7842-7851.

[8] Shaunak S, Godwin A, Choi JW, Balan S, Pedone E, Vijayarangam D, et al. Site-specific PEGylation of native disulfide bonds in therapeutic proteins. Nature Chemical Biology 2006;2:312-313.

[9] Brocchini S, Balan S, Godwin A, Choi JW, Zloh M, Shaunak S. PEGylation of native disulfide bonds in proteins. Nature Protocols 2006;1:2241-2252.

[10] Wang T, Wu YZ, Kuan SL, Dumele O, Lamla M, Ng DYW, et al. A Disulfide Intercalator Toolbox for the Site-Directed Modification of Polypeptides. Chemistry-A European Journal 2015;21:228-238.

[11] Wang T, Pfisterer A, Kuan SL, Wu YZ, Dumele O, Lamla M, et al. Cross-conjugation of DNA, proteins and peptides via a pH switch. Chemical Science 2013;4:1889-1894.

[12] Wang T, Zabarska N, Wu YZ, Lamla M, Fischer S, Monczak K, et al. Receptor selective ruthenium-somatostatin photosensitizer for cancer targeted photodynamic applications. Chemical Communications 2015;51:12552-12555.

[13] Peled A, Wald O, Burger J. Development of novel CXCR4-based therapeutics. Expert Opinion on Investigational Drugs 2012;21:341-353.

[14] Webster RM. Combination therapies in oncology. Nature Reviews Drug Discovery 2016;15:81-82.

[15] Berger EA, Doms RW, Fenyo EM, Korber BTM, Littman DR, Moore JP, et al. A new classification for HIV-1. Nature 1998;391:240-240.

[16] Heim M, Romer L, Scheibel T. Hierarchical structures made of proteins. The complex architecture of spider webs and their constituent silk proteins. Chemical Society Reviews 2010;39:156-164.

[17] Balchin D, Hayer-Hartl M, Hartl FU. In vivo aspects of protein folding and quality control. Science 2016;353:aac4354.

[18] Sacca B, Niemeyer CM. DNA Origami: The Art of Folding DNA. Angewandte Chemie-International Edition 2012;51:58-66.

[19] Hong F, Zhang F, Liu Y, Yan H. DNA Origami: Scaffolds for Creating Higher Order Structures. Chemical Reviews 2017;117:12584-12640.

[20] Rothemund PWK. Folding DNA to create nanoscale shapes and patterns. Nature 2006;440:297-302.

[21] Wang PF, Meyer TA, Pan V, Dutta PK, Ke YG. The Beauty and Utility of DNA Origami. Chem 2017;2:359-382.

[22] Mai YY, Eisenberg A. Self-assembly of block copolymers. Chemical Society Reviews 2012;41:5969-5985.

[23] Palivan CG, Goers R, Najer A, Zhang XY, Car A, Meier W. Bioinspired polymer vesicles and membranes for biological and medical applications. Chemical Society Reviews 2016;45:377-411.

[24] Blanazs A, Armes SP, Ryan AJ. Self-Assembled Block Copolymer Aggregates: From Micelles to Vesicles and their Biological Applications. Macromolecular Rapid Communications 2009;30:267-277.

[25] Tritschler U, Pearce S, Gwyther J, Whittell GR, Manners I. 50th Anniversary Perspective: Functional Nanoparticles from the Solution Self-Assembly of Block Copolymers. Macromolecules 2017;50:3439-3463.

[26] Nishiyama N, Kataoka K. Current state, achievements, and future prospects of polymeric micelles as nanocarriers for drug and gene delivery. Pharmacology & Therapeutics 2006;112:630-648.

[27] Tyrrell ZL, Shen YQ, Radosz M. Fabrication of micellar nanoparticles for drug delivery through the self-assembly of block copolymers. Progress in Polymer Science 2010;35:1128-1143.

[28] Mavila S, Eivgi O, Berkovich I, Lemcoff NG. Intramolecular Cross-Linking Methodologies for the Synthesis of Polymer Nanoparticles. Chemical Reviews 2016;116:878-961.

[29] Gonzalez-Burgos M, Latorre-Sanchez A, Pomposo JA. Advances in single chain technology. Chemical Society Reviews 2015;44:6122-6142.

[30] Chen CJ, Liu GY, Liu XS, Pang SP, Zhu CS, Lv LP, et al. Photo-responsive, biocompatible polymeric micelles self-assembled from hyperbranched polyphosphate-based polymers. Polymer Chemistry 2011;2:1389-1397.

[31] Sackett DL, Wolff J. Nile Red as a Polarity-Sensitive Fluorescent-Probe of Hydrophobic Protein Surfaces. Analytical Biochemistry 1987;167:228-234.

[32] Greenspan P, Fowler SD. Spectrofluorometric Studies of the Lipid Probe, Nile Red. Journal of Lipid Research 1985;26:781-789.

Chapter 4 Summary and Outlook

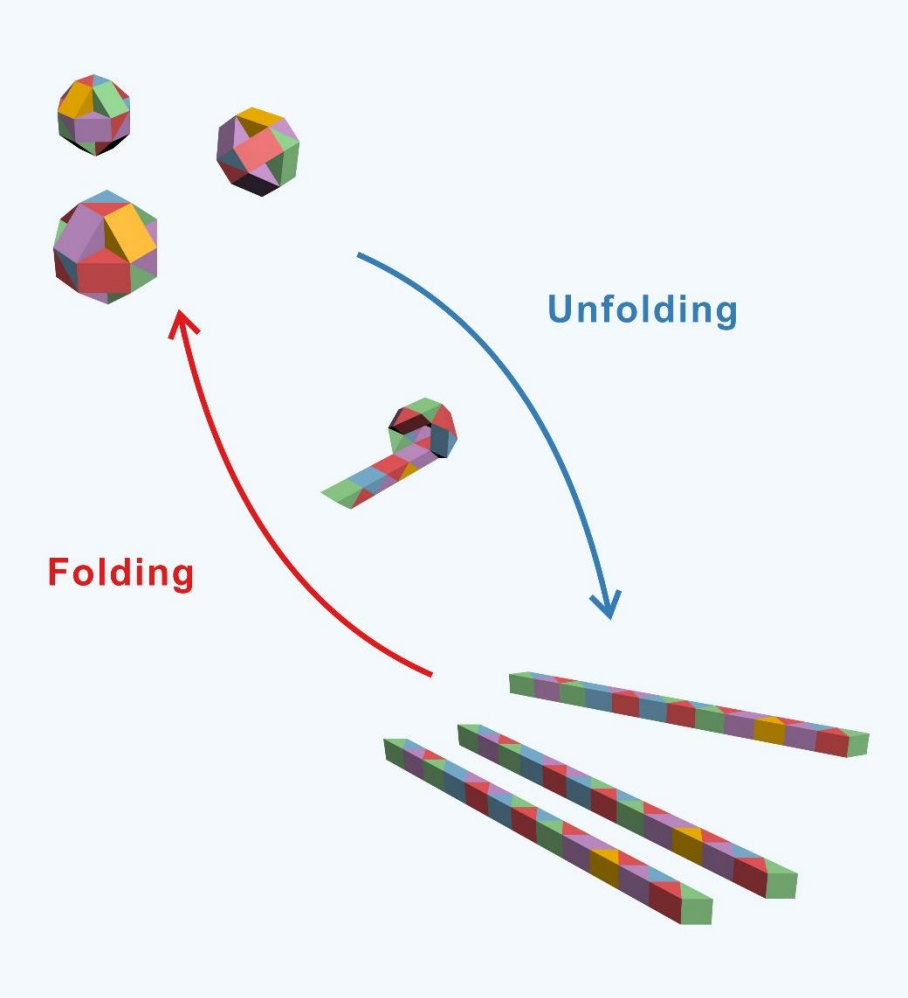

The preparation of bioinspired materials with controlled architectures has attracted rapidly growing attention over the past decades. In this field, the precision structures of biomacromolecules are undoubtedly an important source of innovation. Inspired by the programmability and hierarchical structures of biomolecules such as proteins and nucleic acids, I have developed two complementary strategies for constructing a diverse spectrum of precision nanomaterials for different applications range from site-specific assembly to catalysis and biomedicine.

In the first system, linear polypeptides unfolded from native proteins have been employed as precision templates for the synthesis of anisotropic brush polymers with monodisperse lengths. By first introducing initiators and then grafting polymer chains from the polypeptide backbone, the size and shape of brush polymers have been controlled by tuning (1) the initiator density on the backbone, or (2) polymerization conditions such as monomer concentration and polymerization time. Different functional entities have been introduced onto an absolute position of brush polymers located asymmetrically along the backbone by taking advantage of the site-specific modification of proteins. This positional mono-functionalization strategy has been combined with biotin—streptavidin interactions to demonstrate the capabilities for site-specific assembly to construct higher ordered architectures, showing great potential of the brush polymers for applications in biomedicine and nanoscience.

In addition, unfolded proteins have also been used for the templated fabrication of stable and water-soluble noble metal nanostructures due to the strong metal ion binding ability of amino groups on the polypeptide backbone. This environmentally friendly procedure, which is completed in aqueous solution at room temperature and involves the use of natural polymer-derived templates, has been successfully showed for preparing spherical gold and platinum nanoparticles as well as gold nanoflowers using two different reducing agents. More significantly, the reduction of metal ions and polymer synthesis by ARGET ATRP have been combined in one pot because the same reducing agent, ascorbic acid, can activate both reactions. Thermo-responsive PNIPAM-coated gold nanoflowers with controllable sizes, shapes, and shell thickness have been obtained and applied as water-soluble and temperature-controlled catalyst for the hydrogenation of *p*-nitrophenol. The combination of ARGET ATRP and the in situ reduction of metal ions in one pot, which simplifies reaction and purification procedures, can be extended to prepare other polymer-metal hybrid materials for various applications in sensing, catalysis, and biomedicine.

Above, I have demonstrated that the unfolding of 3D protein architectures into precision linear polymers can be employed as a general strategy for the templated preparation of different precision nanomaterials. As an opposite and complementary approach, folding of linear synthetic polymers into compact states has also been developed as a universal method to construct bioinspired 3D hierarchical structures. In this aspect, I have collaborated with Andreas Riegger and reported a thiol-reactive copolymer based on poly(bis-sulfone) with narrow molecular weight distribution. We have demonstrated the efficient conjugation of the copolymer with different peptides including an endogenous peptide that targets C-X-C chemokine receptor type 4. The obtained polymer—peptide conjugate could fold and self-assemble into narrowly dispersed nanoparticles in aqueous solutions with functional peptides on the surface. Due to the multivalent effect, the hybrid has revealed potent antiviral effects against HIV-1 and the ability to inhibit cancer stem cell migration, offering a therapeutic platform to simultaneously address two different classes of diseases.

In the last system, the structural control of folded polymers has been increased to a higher level. I have synthesized linear PHEMA polymers with varied molecular weights and folded them into cyclic polymers via the highly efficient CuAAC click reaction. Surprisingly, the folded cyclic PHEMA polymers have demonstrated obviously different self-assembly behavior in comparison to their linear counterparts, which was confirmed by several different techniques. Wormlike assemblies formed by the cyclic PHEMA have been observed from TEM images. Encouraged by these results, we have further synthesized macrocyclic brush polymers with amphiphilic block side chains, which could form stable wormlike assemblies and higher-ordered structures. This work not only shows the significant role of polymer folding in macromolecular assembly, but also establishes a novel approach for the construction of bioinspired hierarchical structures via self-assembly of folded synthetic polymers.

In summary, unfolding of natural macromolecules and folding of synthetic polymers have been developed as two powerful biomolecule-inspired strategies for the fabrication of various nanomaterials with defined architectures. Although a first applicability of these concepts has already been demonstrated in this thesis, it is apparent that they have far greater potential for preparing more complex architectures to meet the needs of different applications. For example, the preparation of protein-derived brush polymers can be extended in many aspects such as the backbone, chemical strategy, polymerization techniques and design. Significantly, genetical

engineering methods can be used to introduce bioorthogonal chemical handles into any location of the protein backbone. Therefore, it is possible to stoichiometrically functionalize brush polymers with different theranostic agents, generating a multifunctional platform with many attractive features such as size uniformity, biodegradability, and synergistic therapeutic effects (Figure 4-1A). One can also envision that multiple metal nanoparticles or fluorescent nanodiamonds can be precisely arranged along the brush polymers, forming plasmonic nanostructures or ordered spin arrays with designed distances (Figure 4-1B). In addition, both the anisotropic brush polymers and wormlike polymer assemblies are ideal templates for the synthesis of 1D nanocrystals, which have broad applications in optics, electronics, sensors, and catalysis (Figure 4-1C). Most importantly, the controlled folding of synthetic polymers into defined 3D architectures has always been an exciting goal. With the progress in the design and synthesis of sequence-defined polymers, I believe it will be possible in one day to program synthetic polymers with various covalent and supramolecular interactions into arbitrary 3D hierarchical structures (Figure 4-1D). Collectively, the strategies developed in this thesis not only significantly expand the applications of biomacromolecules in various fields, but also provide new directions for the fabrication of the next generation biomolecule-inspired architectures.

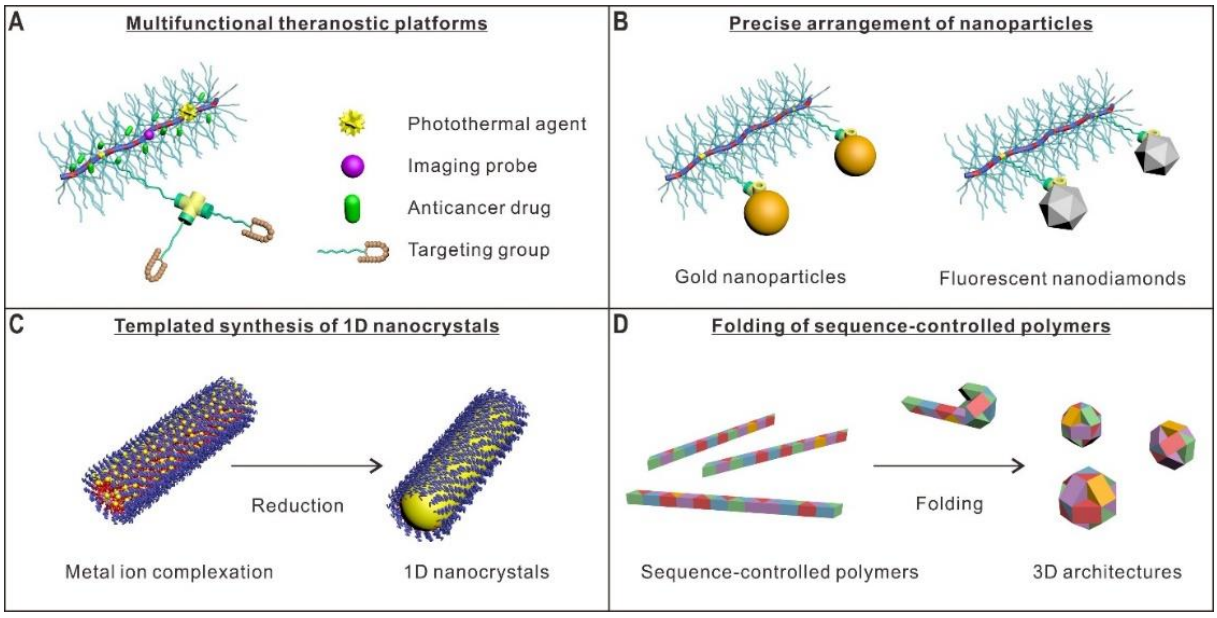

Figure 4-1 | Outlook of the biomolecule-inspired strategies for preparing more complex and precise nanoarchitectures.

Chapter 5 Publications

In the following are the reprints of manuscripts. The reprints were made with permission of the relative journal. Furthermore, the copyrights are given on the respective cover and information of the contribution of the respective authors is listed.

5.1 Precision anisotropic brush polymers by sequence controlled chemistry

Chaojian Chen, Katrin Wunderlich, Debashish Mukherji, Kaloian Koynov,
Astrid Johanna Heck, Marco Raabe, Matthias Barz, George Fytas, Kurt Kremer,
David Yuen Wah Ng,* and Tanja Weil*

* Corresponding authors
Published in *J. Am. Chem. Soc.* **2020**, *142*, 1332−1340.

Contribution of the respective authors:

Chaojian Chen: Design and conduction of the experiments, results analysis and interpretation, figure design and writing of the manuscript.
Katrin Wunderlich and George Fytas: Interpretation and discussion on the light scattering data.
Debashish Mukherji and Kurt Kremer: Molecular simulations.
Kaloian Koynov: FCS experiments and interpretation.
Astrid Johanna Heck: Supply of biotin-SST, gel experiments.
Marco Raabe: Supply of PEG-cHSA.
Matthias Barz: Discussion on the results.
David Yuen Wah Ng: Cell experiments, design and discussion of the concept and results, writing of the manuscript.
Tanja Weil: Acquiring funding for the project, design and discussion of the concept and results, correcting the manuscript.

JACS JOURNAL OF THE AMERICAN CHEMICAL SOCIETY

Article

Cite This: J. Am. Chem. Soc. 2020, 142, 1332−1340

pubs.acs.org/JACS

Precision Anisotropic Brush Polymers by Sequence Controlled Chemistry

Chaojian Chen,[†,‡] Katrin Wunderlich,[†] Debashish Mukherji,[†,§] Kaloian Koynov,[†] Astrid Johanna Heck,[†] Marco Raabe,[†,‡] Matthias Barz,[∥] George Fytas,[†,⊥] Kurt Kremer,[†] David Yuen Wah Ng,*[,†] and Tanja Weil*[,†,‡]

[†]Max Planck Institute for Polymer Research, Ackermannweg 10, 55128 Mainz, Germany

[‡]Ulm University, Albert-Einstein-Allee 11, 89081 Ulm, Germany

[§]Stewart Blusson Quantum Matter Institute, University of British Columbia, Vancouver V6T 1Z4, Canada

[∥]Johannes Gutenberg University Mainz, Duesbergweg 10-14, 55128 Mainz, Germany

[⊥]Institute of Electronic Structure and Laser, Foundation for Research and Technology, P.O. Box 1527, 71110 Heraklion, Greece

Supporting Information

ABSTRACT: The programming of nanomaterials at molecular length-scales to control architecture and function represents a pinnacle in soft materials synthesis. Although elusive in synthetic materials, Nature has evolutionarily refined macromolecular synthesis with perfect atomic resolution across three-dimensional space that serves specific functions. We show that biomolecules, specifically proteins, provide an intrinsic macromolecular backbone for the construction of anisotropic brush polymers with monodisperse lengths via grafting-from strategy. Using human serum albumin as a model, its sequence was exploited to chemically transform a single cysteine, such that the expression of said functionality is asymmetrically placed along the backbone of the eventual brush polymer. This positional monofunctionalization strategy was connected with biotin−streptavidin interactions to demonstrate the capabilities for site-specific self-assembly to create higher ordered architectures. Supported by systematic experimental and computational studies, we envisioned that this macromolecular platform provides unique avenues and perspectives in macromolecular design for both nanoscience and biomedicine.

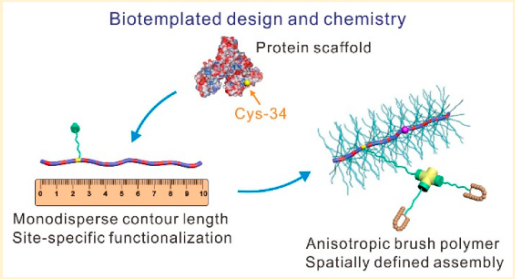

INTRODUCTION

Chemistry at the macromolecular level is often radically challenged by the exposure of target functional groups as they are inevitably subjected to the influences of structural conformation in solution. Although synthetic methods such as ultrafast click chemistry and bio-orthogonal reactions do alleviate these problems significantly,[1,2] the subject of conformational factors cannot be solved by fast reaction kinetics alone. The access toward a chemical moiety is dictated by numerous noncovalent intramolecular forces and is further amplified especially for any site-oriented chemistry. For synthetic macromolecules such as polymers, it is seemingly an unsurmountable task to map accessibility of each functional side chain due to its dispersity as well as the pseudorandomness of its sequence. Hence, the resolution of molecular engineering on polymers has been broadly restricted on a statistical basis despite impressive advances in controlled living polymerization methodologies.[3−5] Nonetheless, polymer-based methods have, in fact, contributed a fast-track route to probe different aspects of nanoscience, i.e., size, shape, and surfaces due to its facile synthesis.

In the repertoire of nanotechnology, the shape or anisotropy of an object was the most recent addition to the facet of nanoengineering, as their unique material properties as well as biological behavior have intrigued the community in both disciplines.[6] Among various anisotropic synthetic architectures, brush polymers constitute a dominant proportion where they have demonstrated unusual mechanical properties and rheological behavior[7−11] as well as being successfully employed as templates for the fabrication of nanotubes,[12,13] nanowires,[14] networks,[15] and nanoporous materials.[16] In biomedicine, wormlike brush polymers have been applied for tumor imaging and as delivery vehicles for therapeutics due to their unique pharmacokinetics.[17−19] In view of these broad applications, a deeper understanding would necessitate structure−function relationships with molecular information. However, pure polymer chemistry alone does not adequately resolve these recurring questions due to its limitations in providing accurate information on the distribution of chemical functionalities.

Received: September 29, 2019
Published: December 12, 2019

DOI: 10.1021/jacs.9b10491
J. Am. Chem. Soc. 2020, 142, 1332−1340

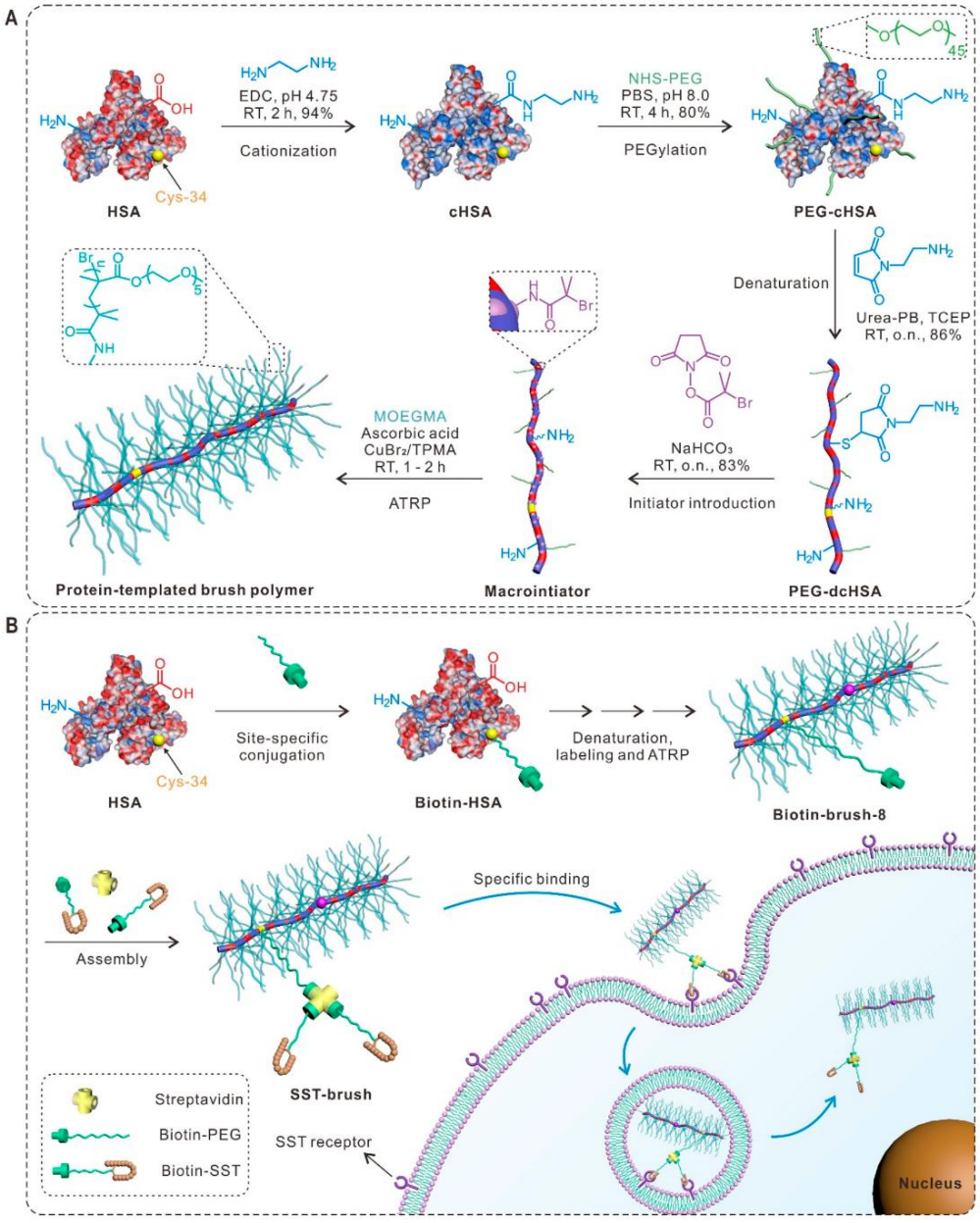

Figure 1. Synthesis and site-specific functionalization of protein-templated brush polymers. (A) Scheme for the synthesis of protein-templated brush polymers by grafting polymer chains from unfolded human serum albumin (HSA) via ATRP. (B) Site-specific conjugation of biotin-PEG to cysteine-34 (Cys-34) of HSA for preparation of the functional brush polymer (**biotin-brush-8**) with a spatially defined biotin group. The biotin group can be used as a versatile handle for the assembly with different functional objects in combination with the adapter protein streptavidin. For example, biotinylated somatostatin (biotin-SST) was introduced for mediating cellular uptake by receptor-mediated endocytosis.

Unlike synthetic chemistry, Nature produces biopolymers such as proteins in which the exact information on each atom's location on the polymer chain is known and invariable. We show herein that by tapping into the vast proteome in biology, the polypeptide chain of proteins is an extraordinary macromolecular backbone that presents far-reaching perspectives in the development of precision nanomaterials. Physically, proteins are monodispersed, and therefore, have absolute lengths which can be tuned by simply choosing a desired protein class.[20] The exact sequence of amino acids is known easily from online databases allowing rational chemical design directly from its macromolecular blueprint. Hence, chemical modifications on side chains of lysines ($-NH_2$), cysteines ($-SH$), and aspartic/glutamic acids ($-COOH$) result in well-positioned functionalities at specific loci along the polypeptide backbone. These modifications can be characterized by well-

DOI: 10.1021/jacs.9b10491
J. Am. Chem. Soc. 2020, 142, 1332−1340

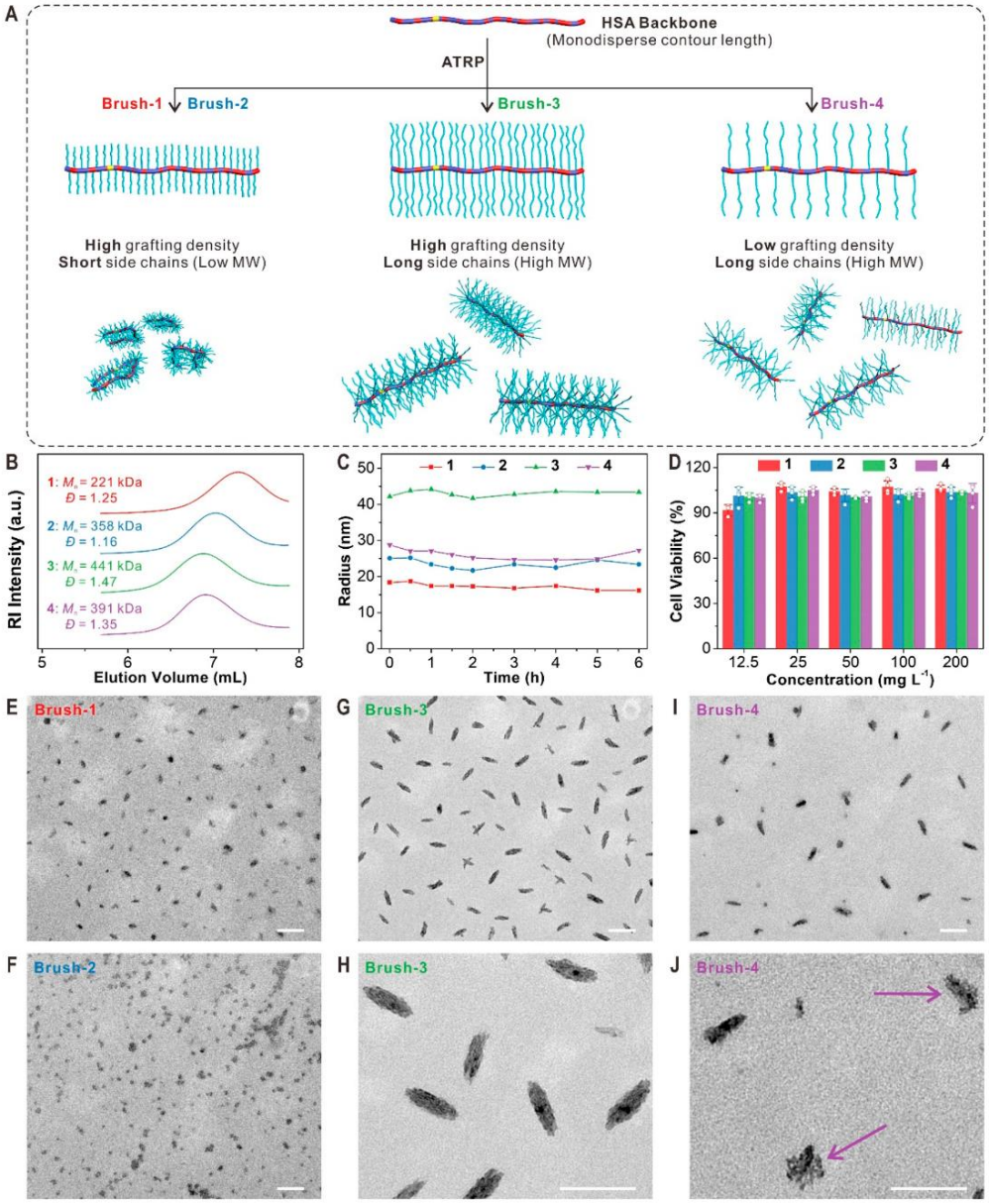

Figure 2. Characterization of **brush-1** to **brush-4**. (A) Schematic illustration of brush polymers synthesized with different grafting densities and side chain lengths from two macroinitiators. (B) GPC curves of **brush-1** to **brush-4**. (C) Size changes of **brush-1** to **brush-4** after mixing with the protease trypsin tracked by DLS. (D) Cell viability (24 h, 37 °C, 5% CO_2) test of **brush-1** to **brush-4** against A549 cells at various concentrations. (E) TEM image of **brush-1**. (F) TEM image of **brush-2**. (G) Low and (H) high magnification TEM images of **brush-3**. (I) Low and (J) high magnification TEM images of **brush-4**. Scale bars: 200 nm.

established mass fingerprinting technology unavailable to synthetic polymers. Furthermore, conformational perturbations affecting synthetic macromolecular chemistry are, conversely, minimized in proteins. Each protein molecule of the same type, as synthesized in biology, is folded identically in a rigid manner with a highly regular exposure of functional groups on its accessible surface. Importantly, by a subsequent denaturation of the globular protein in urea,[21,22] the originally hidden side chains can become accessible and therefore be modified independently.[23,24]

To realize the implementation of Nature's technology in polymer chemistry, we use human serum albumin (HSA), a major blood plasma protein as a representative scaffold, on which a sequence of selective chemical and physical transformations are performed. These chemical reactions (e.g., functional group conversion, grafting "to" and "from" methods of polymer conjugation, supramolecular assembly) are

DOI: 10.1021/jacs.9b10491
J. Am. Chem. Soc. 2020, 142, 1332−1340

Table 1. Polymerization Conditions and Characterization of Brush-1 to Brush-4

category	parameter	brush-1	brush-2	brush-3	brush-4
polymerization	number of initiators	61	61	61	39
	monomer (vol %)	5%	10%	10%	10%
	time (h)	2	1	2	2
GPC[a]	M_n (kDa)	221	358	441	391
	M_w (kDa)	277	415	650	528
	M_p (kDa)	241	382	495	467
	$Đ$	1.25	1.16	1.47	1.35
TEM	length (nm)	56 ± 12	53 ± 13	139 ± 18	116 ± 24
	aspect ratio	1.83	1.51	2.85	2.51
light scattering	R_g[b] (nm)	19 ± 0.5	24 ± 0.5	32 ± 1	22 ± 1 (28)[d]
	R_h[c] (nm)	23 ± 0.4	30 ± 0.3	38 ± 1	37 ± 1
	R_g/R_h	0.83	0.8	0.84	0.59
	a (nm)	26	32	38	28 (35)[d]
	b (nm)	20	24	34	20 (29)[d]
	R_h*[e] (nm)	22	27	35	23 (31)[d]

[a]Measured by GPC using deionized water containing 0.1 M $NaNO_3$ as the mobile phase and linear PEG standards for calibration. [b]Measured by SLS. [c]Measured by DLS in aqueous solution (1 mg mL^{-1}). [d]The numbers in parentheses correspond to the scaling prediction (inset of Figure S13). [e]Computed for ellipsoidal shape using the listed a and b values.

conducted on a single protein chain to show their compatibility as well as the broad applicability of the system. By taking advantage of how functional groups are exposed differently in the native and denatured forms of HSA and the order in which the above reactions are conducted, the protein backbone can provide a large chemical space for structural design. While simpler statistical "grafting to" approaches on denatured proteins have been performed by our group,[23,25] these conjugates lack structural definition and do not incorporate site specificity that takes full advantage of the protein sequence. Herein, we present the synthesis of an anisotropic molecular brush with monodispersed contour length while asymmetrically equipping the brush with a target function with atomic precision (specifically at cysteine-34). In this way, we would like to demonstrate that proteins can efficiently act as a molecularly ordered template to create large anisotropic nanoobjects with chemical functions at precise loci.

RESULTS AND DISCUSSION

Protein-Templated Brush Polymers. The amino-acid sequence and relative solvent accessibility of native human serum albumin (HSA) can be extracted from Uniprot database and PyMOL (Figure S1 and Table S1 in the Supporting Information, SI). At the macromolecular design stage, we allocated specific roles to different amino acid side chains for the synthesis of a brush polymer: (1) a high density of amine moieties of lysine side chains is necessary to graft polymers from the protein backbone to provide shape anisotropy (Figure 1A); and (2) a specific amino acid side chain such as cysteine-34 to serve as an orthogonal focal point for assembling complex functions (Figure 1B).

First, the potential of using a protein backbone for the brush polymer synthesis was investigated. HSA was cationized with ethylenediamine to convert the surface carboxylic acid groups into amino functionalities for the conjugation reactions at a later stage. Sequentially, approximately 32 polyethylene glycol (PEG, 2000 g mol^{-1}) chains were grafted onto cationized HSA (cHSA) using standard *N*-hydroxysuccinimide chemistry (Figure 1A). These chains were necessary to stabilize the protein backbone in the following denaturation step in which the PEG-cHSA was unfolded and linearized in 5 M urea-phosphate buffer (urea-PB) in the presence of tris(2-carboxyethyl) phosphine hydrochloride (TCEP) as a mild reducing agent. The reduced thiols were capped with *N*-(2-aminoethyl)maleimide trifluoroacetate to prevent refolding as well as increasing, further, the number of reactive amino groups on the protein backbone. Subsequently, the resulting denatured polypeptide (PEG-dcHSA) was modified with 2-bromoisobutanoic acid *N*-hydroxysuccinimide ester in different stoichiometries to afford two HSA macroinitiators with varying initiator densities. The products were characterized by matrix-assisted laser desorption/ionization time-of-flight (MALDI-ToF) mass spectrometry to show the extent of modifications, on average 39 and 61 initiators, respectively (PEG-dcHSA-Br_{39}, PEG-dcHSA-Br_{61}) (Figure S2).

While the growth of polymers from native proteins has been developed extensively, particularly as functional polymer–protein conjugates,[26−30] the application of protein scaffolds in their denatured form opens new possibilities that have not been investigated before. We selected activators regenerated by electron transfer atom transfer radical polymerization (ARGET ATRP) for the "grafting from" strategy, which has been shown to be particular suitable for the synthesis of brush-like polymers of high molecular weights in aqueous media.[31−33] Oligo (ethylene glycol) methyl ether methacrylate (MOEG-MA, $M_n \approx 300$ g mol^{-1}) was polymerized in the presence of copper(II) bromide/tris(2-pyridylmethyl)amine ($CuBr_2$/TPMA) under deoxygenated and inert conditions. Thereafter, the brush polymer was isolated and purified by ultrafiltration using a Vivaspin 6 centrifugal concentrator.

To demonstrate the effects of different chain lengths and grafting densities, four brush polymers (denoted as **brush-1** to **brush-4**) were prepared from two macroinitiators by varying the monomer concentration and polymerization time (Figure 2A, Table 1). The formation of the brush polymers was confirmed by gel permeation chromatography (GPC) with peak molecular weights M_p between 241 and 495 kDa using linear PEG as calibration standards (Figure 2B). As the brush polymers were highly branched, an important consideration is that the molecular weight interpretation from GPC could very well be underestimated. Among all four different polymerization conditions, **brush-3**, which was grafted from PEG-

DOI: 10.1021/jacs.9b10491
J. Am. Chem. Soc. 2020, 142, 1332−1340

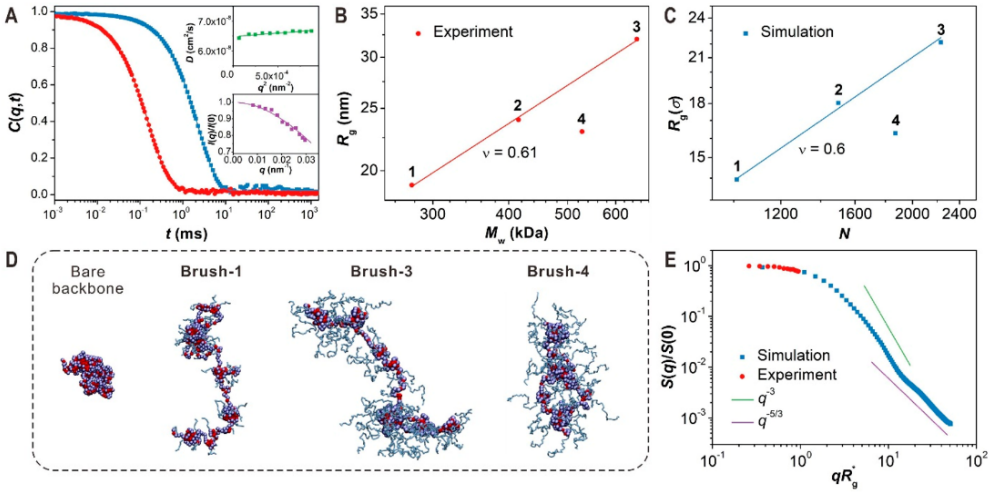

Figure 3. Light scattering and molecular simulation studies of **brush-1** to **brush-4** in solution. (A) Relaxation functions $C(q,t)$ for the translational diffusion dynamics in aqueous solution of **brush-3** (1 mg mL^{-1}) at 293 K at two scattering wave vectors (blue filled squares, q = 0.008 nm^{-1} and red filled circles, q = 0.030 nm^{-1}) represented by a single exponential decay (solid lines). Upper inset: The diffusion coefficient, D as a function of q^2 with the solid line indicating a linear representation. Lower inset: Normalized light scattering intensity $I(q)/I(0)$ as a function of q, where the solid line denotes the representation by the form factor of a solid prolate ellipsoid with semiaxes, a = 38 nm and b = 34 nm. (B and C) Chain gyration radius R_g as a function of overall molecular weight of brush polymers obtained from experiment (B) and simulation (C). A clear good solvent scaling is observed for both cases for the polymers with same grafting densities. (D) Simulation snapshots of the bare backbone and **brush-1**, **brush-3**, and **brush-4**. (E) Double-logarithmic plot of $S(q)/S(0)$ as a function of qR_g*. Here, $S(0)$ is the total molecular weight of the brush polymer system, which is the total number of monomers in the simulation. Red filled circles and blue squares represent the experimental and simulated data, respectively.

dcHSA-Br$_{61}$ by applying the highest monomer concentration and longest polymerization time revealed a number-average molecular weight M_n of 441 kDa with a dispersity $Đ$ of 1.47. Other variations by lowering the monomer concentrations or shortening polymerization time result in lower molecular weights and demonstrate significantly narrower dispersities. In comparison to other brush polymers grafted from pure synthetic polypeptide backbones of similar molecular weights, much larger dispersities in the range of 1.66−3.04 have been reported.[34,35] Moreover, these brush polymers were shelf stable and resistant toward rigorous proteolytic digestion by trypsin over 6 h, confirming the successful growth of a dense and protecting PEG shell (Figures 2C and S3). The cytotoxicity profile of these conjugates suggests their potential for drug delivery as these hybrids remain biocompatible to cells up to 0.2 g L^{-1} (Figure 2D).

Structural Anisotropy. The brush polymers (**brush-1** to **brush-4**) were imaged using transmission electron microscopy (TEM) to correlate the morphology with the grafted polymer chains (Figures 2E−J and S5−S9, Table 1). **Brush-1** synthesized with a lower monomer concentration (5%) and **brush-2** prepared with a shorter polymerization time (1 h) display elliptical and spherical shapes (Figures 2E,F). These observations strongly imply a plausible structural collapse as the shorter PMOEGMA side chains could not provide sufficient steric stabilization to linearize the backbone. Once the PMOEGMA side chains become longer, i.e., **brush-3** and **brush-4**, anisotropic worm-like structures were observed (Figure 2G−J). Statistically, the narrow size distributions of these elongated polymers serve as direct evidence that the 3D structure of HSA was successfully unfolded and stabilized in the extended form. However, it is interesting to note on **brush-4** that some spherical and irregular nanostructures coexisted as well as some indications of a more spreaded PEG side chains (Figure 2J purple arrows). In order to investigate these morphologies without the influences of sample preparation in TEM conducted in the dry state, we reveal the structure of **brush-1** to **brush-4** in the absence of interactions in dilute solutions utilizing light scattering techniques.

Dynamic and static light scattering (DLS/SLS) experiments on dilute aqueous solutions of **brush-1** to **brush-4** yield size and shape information harnessing both the diffusion dynamics and the intensity dependence on the scattering wave vector (q). The relaxation functions $C(q,t)$ were virtually single exponential as depicted exemplarily for **brush-3** in Figure 3A suggesting monodisperse structures in all four systems (Figures S10−S12). The hydrodynamic radius R_h was calculated from the diffusion coefficient (at q = 0) for all four brush polymers. The value of R_h increases in the range 20 to 40 nm (Table 1) being significantly larger than the corresponding value, R_h = 2 nm, for the macroinitiator PEG-dcHSA-Br$_{61}$. For all four polymers, the light scattering intensity $I(q)$ displayed a q-dependence that led to the calculation of the radius of gyration R_g (Figure S11B). Both R_h and R_g, summarized in Table 1 (Figure S13), showed a positive correlation between their respective sizes in solution to the extent of polymerization and/or grafting densities. For **brush-1** to **brush-3**, the ratio R_g/R_h conforms to that of ellipsoid structures with values of this ratio ranging from 0.775 to 4.[36] Only for **brush-4**, R_g/R_h decreases below the limit, suggesting that the HSA core is more compact in this variation (Figure 3D). While the PMOEGMA chains increase R_h, the lower grafting density have a smaller effect on the R_g than for **brush-1** to **brush-3**, leading to a very small R_g/R_h of 0.59. Such a small value has been observed as well for PNIPAM microgels[37] or cross-linked polystyrene nanoparticles.[38] Consequently, to obtain further

DOI: 10.1021/jacs.9b10491
J. Am. Chem. Soc. 2020, 142, 1332−1340

Journal of the American Chemical Society Article

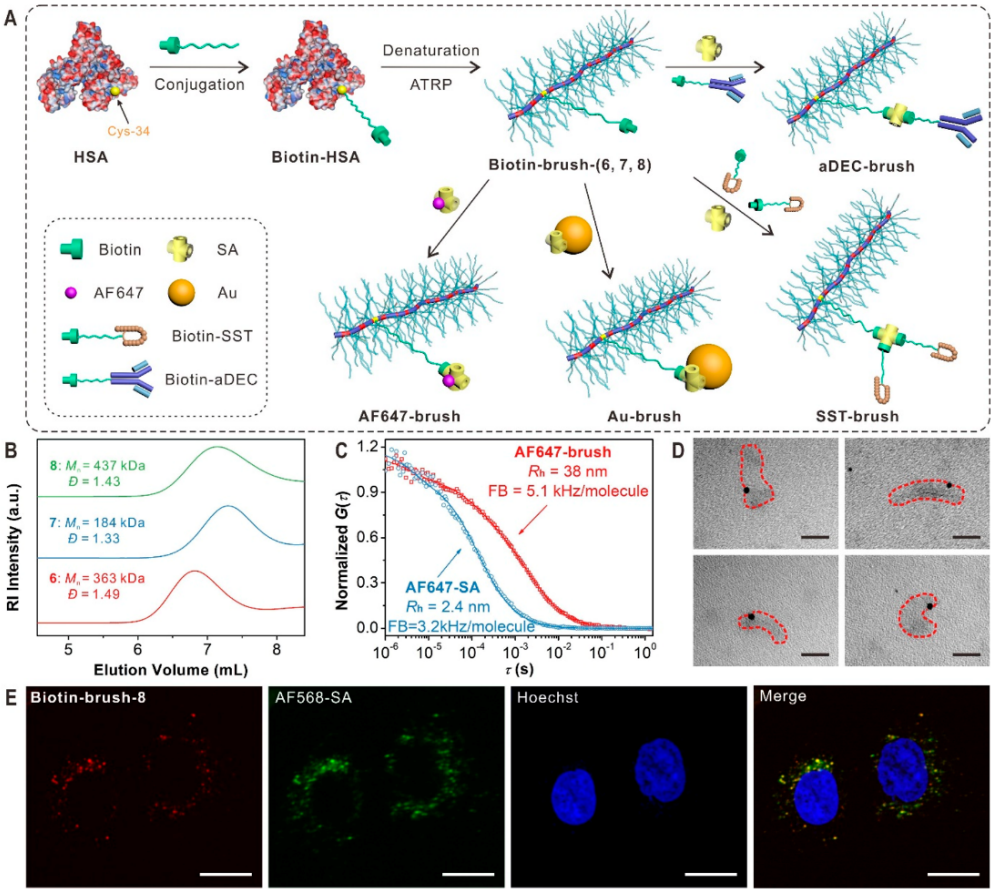

Figure 4. Brush polymers equipped with a biotin group for site-directed assembly. (A) Site-specific conjugation of biotin-PEG to Cys-34 of HSA for synthesis of brush polymers with a spatially defined biotin group, and their assembly with a spectrum of different functional objects: (1) AF647 labeled streptavidin (AF647-SA), (2) streptavidin-conjugated gold nanoparticles (Au-SA), (3) biotinylated somatostatin (biotin-SST) and streptavidin (SA), and (4) biotinylated aDEC205 antibody (biotin-aDEC) and SA. (B) GPC curves of biotin-functionalized brush polymers **biotin-brush-6**, **biotin-brush-7**, and fluorescent **biotin-brush-8**. (C) Normalized FCS autocorrelation curves measured in ~2 nM aqueous solutions of AF647-SA (blue circles) and its assembly with **biotin-brush-6** (AF647-brush, red squares). The solid lines represent the corresponding fits with eq S10. The fits yield the values of the hydrodynamic radius R_h and the fluorescence brightness (FB) of the studied species as indicated. (D) TEM images showing the assembly of **biotin-brush-7** with Au-SA. Scale bars: 20 nm. (E) Confocal laser scanning microscopy images showing the somatostatin-mediated cell uptake of **biotin-brush-8** after assembly with biotin-SST and AF568 labeled streptavidin (AF568-SA). The colocalization of **biotin-brush-8** and AF568-SA confirms the assembly process. Scale bars: 20 μm.

shape information, $I(q)$ is represented by the form factor of an ellipsoid with semiaxes a and b (Figures 3A and S13). The listed values suggest a prolate ($a > b$) ellipsoid. To prove the self-consistency of the data analysis, the computed hydrodynamic radii (R_h*) of the ellipsoid using Perrin's theory[39] (SI) were compared against the experimental R_h values (Table 1). The agreement of these values from **brush-1** to **brush-3** represents unambiguous anisotropy in their solution structures. Nonetheless, it is interesting to note that for **brush-4**, a discrepancy (R_h*, R_g, and R_g/R_h) (Figures 3B and S13) was observed. This might be attributed to differences in intramolecular packing of HSA and the grafted PMOEGMA chains in **brush-4**. Previously, significant change in the polymer packing due to the lower grafting density was also reported for tethered colloids.[40]

We seek to address the importance of how each macromolecule is intramolecularly packed by performing DLS/SLS and molecular dynamic simulations using a generic bead–spring model (Figure 3B–E).[41] For this purpose, we have simulated a model brush polymer directly replicating the experiments in terms of backbone sequence/length, side chain lengths, and grafting densities (Table S2). The variations on the side chain lengths and grafting densities have a profound impact on the conformation of the brush polymers, whereas their resultant anisotropy as a prolate ellipsoid is consistent with DLS/SLS experimental observations. A closer inspection of Figure 3B,C illustrates that, for the same grafting density and varying side chain length (**brush-1** to **brush-3**), both SLS and simulation data show a good solvent scaling with the change in total molecular weight of the brush polymer. The deviation for **brush-4** is a result of lower grafting density which is consistent with literature.[42] We further illustrate simulation snapshots for three different systems (**brush 1**, **brush 3**, and **brush 4**) in comparison with a folded configuration of the bare protein

DOI: 10.1021/jacs.9b10491
J. Am. Chem. Soc. 2020, 142, 1332−1340

backbone (Figure 3D). More specifically, for **brush-1** and **brush-3**, a pearl necklace type configuration is observed, consisting of collapsed hydrophobic core and hairy hydrophilic side chains exposed to the solvent. Alternatively, because of the low grafting density, **brush-4** shows a more compact, rather distorted spherical configuration. It has been reported for uncharged brush polymers with flexible backbones that the lower the grafting density, the less elongated the main chain becomes.[42]

As the chain structures do not show the typical self-avoiding random walk configurations known for standard good solvent cases (Figures 3B,C), we further investigate this rather contradictory behavior. A quantity that best describes the overall conformation of a chain is the single chain structure factor $S(q)$. The simulation data of normalized structure factor $S(q)/S(0)$ is shown in Figure 3E for **brush-3**, with $S(0)$ being the total molecular weight of **brush-3**. The simulation result is in good agreement with the experimental data within the Gruinier regime (i.e., $q \rightarrow 0$). Note that the experimental data were obtained from SLS and therefore are only available for the long wavelength limit. Interestingly, we find that for small length scales (or large q values), **brush-3** behaves as if in a good solvent condition (represented by $q^{-5/3}$ power law) while globally it remains somewhat collapsed, showing a scaling q^{-3}. Note that if the chain was fully collapsed, as in the case of the bare backbone (Figure 3D), the system would show a perfect spherical scattering with the corresponding scaling q^{-4} instead. Although the system remains overall globular, it consists of rather large, good solvent blobs with sizes comparable to R_g (Figures 3B and Figure S16).

Site-Specific Functionalization and Assembly. While we have shown extensively that the monodispersity of proteins is a principle physical feature toward architectural design and anisotropy, the chemistry associated with its amino acid sequence is where diversification of functions takes root. To directly challenge the frontier of macromolecular chemistry, we designated the installation of a target functional moiety, precisely located on a single monomer unit in an asymmetrical position (No. 34 of 585 amino acids) along the protein backbone. The highlight would be that only one additional synthetic step is necessary by simply addressing an orthogonal functionality (Figure 4A).

Solvent accessible free thiols or disulfide bridges, characteristic of cysteines, are very often located on the surface of proteins and, in this case, HSA possesses a single thiol group in its native form. This thiol moiety is, without ambiguity, exactly located as the 34th amino acid, a cysteine (Cys-34), from the *N*-terminal of the protein. It can be projected that, after unfolding, any chemistry targeting Cys-34 would afford a function that is asymmetrically located along the 585-amino acid long protein backbone. Using this to our advantage, we performed a Michael reaction separately with Alexa Fluor 647 C_2 maleimide (AF647-MI) and maleimide end-capped biotin-PEG (biotin-PEG-MI) under chemoselective conditions on HSA (Figures S17–S18 and S24–S26). The respective monofunctionalized HSA (F-HSA, Biotin-HSA) follows the synthesis protocols for **brush-3** to afford the asymmetrically functionalized counterpart. By design, the inclusion of the fluorophore to afford **brush-5** represents a proof of concept and as a reporter for single particle fluorescence measurements (Figures S19–S21). However, the brush polymer equipped with a biotin-PEG extension aims to demonstrate the potential of the system to enable site-directed self-assembly (Figure 4A).

The brush polymer site-specifically functionalized with one AF647 group (**brush-5**) was characterized first with GPC (M_n = 409 kDa) as a quality control that the synthetic protocols are in line with **brush-3** (Figure S19). Visualization by TEM was similarly achieved and the expected anisotropic particles were observed (Figure S20). In order to probe the chemistry and the success of the concept, fluorescence correlation spectroscopy (FCS) was employed. While FCS operates on similar principles as DLS, it has the advantage to quantify and correlate single fluorophores with its connected nanostructure. Referenced against free AF647 (FB = 19 kHz/molecule), the fluorescence brightness of each molecule of **brush-5** (FB = 22 kHz/molecule) in combination with its measured hydrodynamic radius (R_h = 32 nm) demonstrated that each brush polymer is precisely equipped with a single fluorophore (Figures S22–S23).

Although the synthetic concepts were proven, the availability and its potential for functional capabilities (i.e., self-assembly) or ligand attachment cannot be demonstrated by a fluorophore alone. In this aspect, the biotin moiety enables a characteristic supramolecular interaction with the protein streptavidin, to showcase that the brush polymer can be further built-up with a defined spatial orientation. For this purpose, biotin-functionalized brush polymers **biotin-brush-6** (M_n = 363 kDa) and **biotin-brush-7** (M_n = 184 kDa, shorter side chains) were synthesized in anticipation of the potential steric constraints during the biotin/streptavidin binding event (Figure 4B). By adopting a similar approach using FCS, AF647-labeled streptavidin (AF647-SA) was used to quantify the assembly with **biotin-brush-6**. The increase in hydrodynamic radius from 2.4 to 38 nm monitored through the fluorophore suggests the successful binding of the small streptavidin (53 kDa) onto the brush polymer (Figure 4C). However, the fluorescence brightness indicates that, on average, slightly more than one streptavidin protein is bound to the brush polymer suggesting a minor presence of additional nonspecific adsorption of streptavidin.

We challenged the precision brush system further by the attachment of larger nanoobjects using streptavidin-conjugated gold nanoparticles (Au-SA, 5 nm) to explore its limitations as well as identify considerations from the design perspective. In addition, it provides better visualization of the binding event due to the different electron absorptivity between proteins and inorganic materials. The ligand/protein interaction was compared independently with both **biotin-brush-6** and **biotin-brush-7**. Due to the much larger steric requirements of the gold nanoparticle compared to free streptavidin protein, we observed successful binding events only with **biotin-brush-7** which has shorter side chains (Figure 4D). Notably, gold nanoparticles were observed to be positioned at the near-end of brush polymers which is consistent with the position of Cys-34 in the amino acid sequence of HSA. Hence, the TEM results suggest that the systematic built-up of higher ordered architectures can be tailored in a precise fashion using this technology.

To further demonstrate the broad applicability of the system, we expanded the system to assemble bioactive molecules. Here, we chose a hormonal targeting group, somatostatin, which targets the somatostatin receptor 2 (SSTR2) in cancer cells (Figure 1B). Using biotinylated somatostatin (biotin-SST) synthesized using an existing protocol,[43] the assembly consist of biotinylated fluorescent brush polymer **biotin-brush-8** (Figures S27), biotin-SST and

DOI: 10.1021/jacs.9b10491
J. Am. Chem. Soc. 2020, 142, 1332–1340

streptavidin (1:2:1 molar ratio). The afforded construct (500 nM) was incubated with A549 cells for 24 h where the cellular uptake was monitored with confocal laser scanning microscopy (Figure S29). In this experiment, somatostatin-mediated uptake was observed compared to the **biotin-brush-8**/streptavidin as the control. Fluorescence microscopy studies at 2 h, 6, and 24 h showed time dependent cellular uptake of the somatostatin functionalized brush (Figure S29). While receptor-mediated pathways generally possess faster uptake kinetics, we postulate that the slower internalization could be due to the large size and highly dense PEG brush. As a further confirmation, colocalization studies with an additional fluorescent label on streptavidin (AF568-SA) showed that the construct remains largely intact during the internalization process (Figures 4E and S30). As a final test to widen the biological relevance, we replace biotin-SST with biotinylated aDEC (biotin-aDEC), a model antibody, to show that the platform allows the assembly of both small peptides as well as a significantly larger protein. Here, we perform an SDS-PAGE and a Western blot to show the successful assembly process of both the somatostatin/antibody conjugated brush (Figures S31 and S32). Therefore, we have demonstrated that brush polymers site-specifically functionalized with a biotin group can be used as a powerful and versatile platform for assembly with a wide variety of functional entities.

■ CONCLUSIONS

In summary, a unique synthetic framework exploiting the architecture of proteins to construct precision anisotropic brush polymers was presented, along with a strong emphasis on its innate monodispersity and sequence controlled chemistry. The facile engineering of chemical strategies toward the control of size, contour lengths, and anisotropy was shown by simply varying (1) the initiator density on the polypeptide backbone, or (2) the polymerization conditions such as monomer concentration and polymerization time. In particular, a distinct chemical function was introduced onto an absolute position located asymmetrically along the polypeptide backbone which has, to the best of our knowledge, not been achieved before for other synthetic brush polymer systems. By exploiting this specific handle, we show its broad potential in assembling unique macromolecular conjugates from both material and biological perspectives. It should be noted that bioorthogonal chemical handles can be incorporated into any position of protein backbones through genetical engineering methods, therefore it is possible to stoichiometrically functionalize brush polymers with desired functions.

Collectively, the capacity of this platform is multiplicative in that each aspect including the backbone, chemical strategy, or polymerization techniques and design can be postulated to expand far greater than those explored within this study. Likewise, it is also conceivable to overcome the limitations presented within this study by varying the aforementioned factors. In perspective, by developing a methodical and extensive evaluation of this technology, we seek to stimulate exciting synergy with the available toolbox for site-selective protein chemistry and achieve molecular programming at the nanoscale.

■ ASSOCIATED CONTENT

Supporting Information

The Supporting Information is available free of charge at https://pubs.acs.org/doi/10.1021/jacs.9b10491.

Experimental details, characterization techniques, simulation details and further analysis, supplementary data, and discussion (PDF)

■ AUTHOR INFORMATION

Corresponding Authors

*david.ng@mpip-mainz.mpg.de
*weil@mpip-mainz.mpg.de

ORCID

Chaojian Chen: 0000-0002-2588-2447
Katrin Wunderlich: 0000-0002-8096-7427
Debashish Mukherji: 0000-0002-6242-1754
Kaloian Koynov: 0000-0002-4062-8834
Marco Raabe: 0000-0002-3677-6615
Matthias Barz: 0000-0002-1749-9034
Kurt Kremer: 0000-0003-1842-9369
David Yuen Wah Ng: 0000-0002-0302-0678
Tanja Weil: 0000-0002-5906-7205

Notes

The authors declare no competing financial interest.

■ ACKNOWLEDGMENTS

The authors acknowledge financial support from SFB 1066-Project A6, Q2. C.C. is grateful for a doctoral fellowship from Promotionskolleg Pharmaceutical Biotechnology of Ulm University funded by the state of Baden−Württemberg. G.F. is thankful for the support from ERC AdG SmartPhon No. 694977, and T.W. acknowledges support by ERC Synergy grant no. 319130-BioQ. We also thank Dr. Hans Joachim Räder for his helpful discussion on the MALDI-ToF mass spectra.

■ REFERENCES

(1) Ouchi, M.; Badi, N.; Lutz, J. F.; Sawamoto, M. Single-chain technology using discrete synthetic macromolecules. *Nat. Chem.* **2011**, *3*, 917.

(2) Schmidt, B. V. K. J.; Fechler, N.; Falkenhagen, J.; Lutz, J. F. Controlled folding of synthetic polymer chains through the formation of positionable covalent bridges. *Nat. Chem.* **2011**, *3*, 234.

(3) Wang, J. S.; Matyjaszewski, K. Controlled living radical polymerization - atom-transfer radical polymerization in the presence of transition-metal complexes. *J. Am. Chem. Soc.* **1995**, *117*, 5614.

(4) Matyjaszewski, K.; Xia, J. H. Atom transfer radical polymerization. *Chem. Rev.* **2001**, *101*, 2921.

(5) Chiefari, J.; Chong, Y. K.; Ercole, F.; Krstina, J.; Jeffery, J.; Le, T. P. T.; Mayadunne, R. T. A.; Meijs, G. F.; Moad, C. L.; Moad, G.; Rizzardo, E.; Thang, S. H. Living free-radical polymerization by reversible addition-fragmentation chain transfer: The RAFT process. *Macromolecules* **1998**, *31*, 5559.

(6) Thorkelsson, K.; Bai, P.; Xu, T. Self-assembly and applications of anisotropic nanomaterials: A review. *Nano Today* **2015**, *10*, 48.

(7) Verduzco, R.; Li, X.; Pesek, S. L.; Stein, G. E. Structure, function, self-assembly, and applications of bottlebrush copolymers. *Chem. Soc. Rev.* **2015**, *44*, 2405.

(8) Sheiko, S. S.; Sumerlin, B. S.; Matyjaszewski, K. Cylindrical molecular brushes: Synthesis, characterization, and properties. *Prog. Polym. Sci.* **2008**, *33*, 759.

(9) Feng, C.; Li, Y. J.; Yang, D.; Hu, J. H.; Zhang, X. H.; Huang, X. Y. Well-defined graft copolymers: from controlled synthesis to multipurpose applications. *Chem. Soc. Rev.* **2011**, *40*, 1282.

(10) Vatankhah-Varnosfaderani, M.; Daniel, W. F. M.; Everhart, M. H.; Pandya, A. A.; Liang, H. Y.; Matyjaszewski, K.; Dobrynin, A. V.; Sheiko, S. S. Mimicking biological stress-strain behaviour with synthetic elastomers. *Nature* **2017**, *549*, 497.

DOI: 10.1021/jacs.9b10491
J. Am. Chem. Soc. 2020, 142, 1332−1340

(11) Daniel, W. F. M.; Burdynska, J.; Vatankhah-Varnoosfaderani, M.; Matyjaszewski, K.; Paturej, J.; Rubinstein, M.; Dobrynin, A. V.; Sheiko, S. S. Solvent-free, supersoft and superelastic bottlebrush melts and networks. *Nat. Mater.* **2016**, *15*, 183.
(12) Huang, K.; Rzayev, J. Well-defined organic nanotubes from multicomponent bottlebrush copolymers. *J. Am. Chem. Soc.* **2009**, *131*, 6880.
(13) Mullner, M.; Yuan, J. Y.; Weiss, S.; Walther, A.; Fortsch, M.; Drechsler, M.; Muller, A. H. E. Water-soluble organo-silica hybrid nanotubes templated by cylindrical polymer brushes. *J. Am. Chem. Soc.* **2010**, *132*, 16587.
(14) Yuan, J. Y.; Xu, Y. Y.; Walther, A.; Bolisetty, S.; Schumacher, M.; Schmalz, H.; Ballauff, M.; Muller, A. H. E. Water-soluble organo-silica hybrid nanowires. *Nat. Mater.* **2008**, *7*, 718.
(15) Wu, D. C.; Nese, A.; Pietrasik, J.; Liang, Y. R.; He, H. K.; Kruk, M.; Huang, L.; Kowalewski, T.; Matyjaszewski, K. Preparation of polymeric nanoscale networks from cylindrical molecular bottle-brushes. *ACS Nano* **2012**, *6*, 6208.
(16) Bolton, J.; Bailey, T. S.; Rzayev, J. Large pore size nanoporous materials from the self-assembly of asymmetric bottlebrush block copolymers. *Nano Lett.* **2011**, *11*, 998.
(17) Fouz, M. F.; Mukumoto, K.; Averick, S.; Molinar, O.; McCartney, B. M.; Matyjaszewski, K.; Armitage, B. A.; Das, S. R. Bright fluorescent nanotags from bottlebrush polymers with DNA-tipped bristles. *ACS Cent. Sci.* **2015**, *1*, 431.
(18) Luo, H. Y.; Szymusiak, M.; Garcia, E. A.; Lock, L. L.; Cui, H. G.; Liu, Y.; Herrera-Alonso, M. Solute-triggered morphological transitions of an amphiphilic heterografted brush copolymer as a single-molecule drug carrier. *Macromolecules* **2017**, *50*, 2201.
(19) Sowers, M. A.; McCombs, J. R.; Wang, Y.; Paletta, J. T.; Morton, S. W.; Dreaden, E. C.; Boska, M. D.; Ottaviani, M. F.; Hammond, P. T.; Rajca, A.; Johnson, J. A. Redox-responsive branched-bottlebrush polymers for in vivo MRI and fluorescence imaging. *Nat. Commun.* **2014**, *5*, 5460.
(20) Yang, J.; Gitlin, I.; Krishnamurthy, V. M.; Vazquez, J. A.; Costello, C. E.; Whitesides, G. M. Synthesis of monodisperse polymers from proteins. *J. Am. Chem. Soc.* **2003**, *125*, 12392.
(21) Wu, Y. Z.; Chakrabortty, S.; Gropeanu, R. A.; Wilhelmi, J.; Xu, Y.; Er, K. S.; Kuan, S. L.; Koynov, K.; Chan, Y.; Weil, T. pH-responsive quantum dots via an albumin polymer surface coating. *J. Am. Chem. Soc.* **2010**, *132*, 5012.
(22) Wu, Y. Z.; Pramanik, G.; Eisele, K.; Weil, T. Convenient approach to polypeptide copolymers derived from native proteins. *Biomacromolecules* **2012**, *13*, 1890.
(23) Wu, Y. Z.; Ermakova, A.; Liu, W. N.; Pramanik, G.; Vu, T. M.; Kurz, A.; McGuinness, L.; Naydenov, B.; Hafner, S.; Reuter, R.; Wrachtrup, J.; Isoya, J.; Fortsch, C.; Barth, H.; Simmet, T.; Jelezko, F.; Weil, T. Programmable biopolymers for advancing biomedical applications of fluorescent nanodiamonds. *Adv. Funct. Mater.* **2015**, *25*, 6576.
(24) Ng, D. Y. W.; Wu, Y. Z.; Kuan, S. L.; Weil, T. Programming supramolecular biohybrids as precision therapeutics. *Acc. Chem. Res.* **2014**, *47*, 3471.
(25) Wu, Y. Z.; Ihme, S.; Feuring-Buske, M.; Kuan, S. L.; Eisele, K.; Lamla, M.; Wang, Y. R.; Buske, C.; Weil, T. A core-shell albumin copolymer nanotransporter for high capacity loading and two-step release of doxorubicin with enhanced anti-leukemia activity. *Adv. Healthcare Mater.* **2013**, *2*, 884.
(26) Bontempo, D.; Maynard, H. D. Streptavidin as a macroinitiator for polymerization: In situ protein-polymer conjugate formation. *J. Am. Chem. Soc.* **2005**, *127*, 6508.
(27) Cobo, I.; Li, M.; Sumerlin, B. S.; Perrier, S. Smart hybrid materials by conjugation of responsive polymers to biomacromolecules. *Nat. Mater.* **2015**, *14*, 143.
(28) De, P.; Li, M.; Gondi, S. R.; Sumerlin, B. S. Temperature-regulated activity of responsive polymer-protein conjugates prepared by grafting-from via RAFT polymerization. *J. Am. Chem. Soc.* **2008**, *130*, 11288.
(29) Heredia, K. L.; Bontempo, D.; Ly, T.; Byers, J. T.; Halstenberg, S.; Maynard, H. D. In situ preparation of protein - "Smart" polymer conjugates with retention of bioactivity. *J. Am. Chem. Soc.* **2005**, *127*, 16955.
(30) Lucon, J.; Qazi, S.; Uchida, M.; Bedwell, G. J.; LaFrance, B.; Prevelige, P. E.; Douglas, T. Use of the interior cavity of the P22 capsid for site-specific initiation of atom-transfer radical polymerization with high-density cargo loading. *Nat. Chem.* **2012**, *4*, 781.
(31) Averick, S.; Simakova, A.; Park, S.; Konkolewicz, D.; Magenau, A. J. D.; Mehl, R. A.; Matyjaszewski, K. ATRP under biologically relevant conditions: grafting from a protein. *ACS Macro Lett.* **2012**, *1*, 6.
(32) Oh, J. K.; Perineau, F.; Charleux, B.; Matyjaszewski, K. AGET ATRP in water and inverse miniemulsion: a facile route for preparation of high-molecular-weight biocompatible brush-like polymers. *J. Polym. Sci., Part A: Polym. Chem.* **2009**, *47*, 1771.
(33) Jakubowski, W.; Matyjaszewski, K. Activator generated by electron transfer for atom transfer radical polymerization. *Macromolecules* **2005**, *38*, 4139.
(34) Liu, Y.; Chen, P.; Li, Z. B. Molecular bottlebrushes with polypeptide backbone prepared via ring-opening polymerization of NCA and ATRP. *Macromol. Rapid Commun.* **2012**, *33*, 287.
(35) Lahasky, S. H.; Lu, L.; Huberty, W. A.; Cao, J. B.; Guo, L.; Garno, J. C.; Zhang, D. H. Synthesis and characterization of thermo-responsive polypeptoid bottlebrushes. *Polym. Chem.* **2014**, *5*, 1418.
(36) Schärtl, W. *Light Scattering from Polymer Solutions and Nanoparticle Dispersions*; Springer: Berlin/Heidelberg, 2007.
(37) Senff, H.; Richtering, W. Temperature sensitive microgel suspensions: Colloidal phase behavior and rheology of soft spheres. *J. Chem. Phys.* **1999**, *111*, 1705.
(38) Martin, H. J.; White, B. T.; Scanlon, C. J.; Saito, T.; Dadmun, M. D. Tunable synthetic control of soft polymeric nanoparticle morphology. *Soft Matter* **2017**, *13*, 8849.
(39) Zhao, J. Q.; Pearce, E. M.; Kwei, T. K.; Jeon, H. S.; Kesani, P. K.; Balsara, N. P. Micelles formed by a model hydrogen-bonding block-copolymer. *Macromolecules* **1995**, *28*, 1972.
(40) Cang, Y.; Reuss, A. N.; Lee, J.; Yan, J. J.; Zhang, J. N.; Alonso-Redondo, E.; Sainidou, R.; Rembert, P.; Matyjaszewski, K.; Bockstaller, M. R.; Fytas, G. Thermomechanical properties and glass dynamics of polymer-tethered colloidal particles and films. *Macromolecules* **2017**, *50*, 8658.
(41) Kremer, K.; Grest, G. S. Dynamics of entangled linear polymer melts - a molecular-dynamics simulation. *J. Chem. Phys.* **1990**, *92*, 5057.
(42) Kikuchi, M.; Nakano, R.; Jinbo, Y.; Saito, Y.; Ohno, S.; Togashi, D.; Enomoto, K.; Narumi, A.; Haba, O.; Kawaguchi, S. Graft density dependence of main chain stiffness in molecular rod brushes. *Macromolecules* **2015**, *48*, 5878.
(43) Wang, T.; Wu, Y. Z.; Kuan, S. L.; Dumele, O.; Lamla, M.; Ng, D. Y. W.; Arzt, M.; Thomas, J.; Mueller, J. O.; Barner-Kowollik, C.; Weil, T. A disulfide intercalator toolbox for the site-directed modification of polypeptides. *Chem. - Eur. J.* **2015**, *21*, 228.

DOI: 10.1021/jacs.9b10491
J. Am. Chem. Soc. 2020, 142, 1332−1340

Supplementary Information

Precision Anisotropic Brush Polymers by Sequence Controlled Chemistry

Chaojian Chen,[1,2] Katrin Wunderlich,[1] Debashish Mukherji,[1,3] Kaloian Koynov,[1] Astrid Johanna Heck,[1] Marco Raabe,[1,2] Matthias Barz,[4] George Fytas,[1,5] Kurt Kremer,[1] David Yuen Wah Ng,[1,] and Tanja Weil[1,2,*]*

[1]Max Planck Institute for Polymer Research, Ackermannweg 10, 55128 Mainz, Germany
[2]Ulm University, Albert-Einstein-Allee 11, 89081 Ulm, Germany
[3]Stewart Blusson Quantum Matter Institute, University of British Columbia, Vancouver V6T 1Z4, Canada
[4]Johannes Gutenberg University Mainz, Duesbergweg 10-14, 55128 Mainz, Germany
[5]Institute of Electronic Structure and Laser, Foundation for Research and Technology, P.O. Box 1527, 71110 Heraklion, Greece

Table of Contents

I. Experimental

1.1. Materials

Human serum albumin (HSA, 96%), tris(2-carboxyethyl) phosphine hydrochloride (TCEP, ≥ 98%), 2-bromoisobutanoic acid *N*-hydroxysuccinimide ester (NHS-BiB, 98%), *O*-[(*N*-succinimidyl)succinyl-aminoethyl]-*O'*-methylpolyethylene glycol (NHS-PEG, $M_n \sim 2000$), *N*-(3-Dimethylaminopropyl)-*N'*-ethylcarbodiimide hydrochloride (EDC·HCl, ≥ 98%), *N*-(2-aminoethyl)maleimide trifluoroacetate salt (MI-NH_2, 95%), trypsin (Type I from bovine pancreas, ~10,000 BAEE units/mg protein), tris(2-pyridylmethyl)amine (TPMA, 98%), copper(II) bromide ($CuBr_2$, 99%), and L-ascorbic acid (≥ 99%) were purchased from Sigma-Aldrich and used without further treatment. Ethylendiamine (> 99%), ethylenediaminetetraacetic acid (EDTA, 98%) and urea (99.5%) were purchased from Acros Organics and used as received. Oligo(ethylene glycol) methyl ether methacrylate (MOEGMA, Sigma-Aldrich, M_n ~300) was purified by passing a basic alumina column before use. Alexa Fluor 647 C_2 maleimide (AF647-MI) and Alexa Fluor™ 647 NHS ester (Succinimidyl ester) (AF647-NHS, 1250 g mol^{-1}) were purchased from Thermo Fisher Scientific and used under dark. Poly(ethylene glycol) [N-(2-maleimidoethyl)carbamoyl]methyl ether 2-(biotinylamino)ethane (biotin-PEG-maleimide or biotin-PEG-MI, $M_n \sim 5400$) was obtained from Sigma-Aldrich. Streptavidin (SA, buffer composition after restoration: 20 mM potassium phosphate, pH 6.5; Specific activity: 20.6 μg/mg protein), Alexa Fluor™ 568 labeled streptavidin (AF568-SA), and Alexa Fluor™ 647 labeled streptavidin (AF647-SA) were purchased from Thermo Fisher Scientific and used as received. Streptavidin-conjugated gold nanoparticles (Au-SA, particle size 5 nm, concentration 0.5 mg mL^{-1}, 2.5×10^{14} particles/mL) were purchased from NANOCS. Biotinylated somatostatin (Biotin-SST) was synthesized according to the literature.[1] Dulbecco's Modified Eagle's Medium (DMEM) high glucose, fetal bovine serum, penicillin/streptomycin were purchased from GE Healthcare. All other solvents and salts were obtained from commercial suppliers and used as received.

1.2. Preparation of protein-templated brush polymers (brush-1 to brush-4)

1.2.1. Synthesis of cationic HSA (cHSA)

HSA (150 mg, 2.26 μmol) was dissolved in 15 mL of degassed ethylenediamine solution (2.5 M) and the pH was tuned to 4.75 by using HCl. After adding EDC·HCl (4 mmol, 766 mg) and stirring for two hours at room temperature, acetate buffer (1 mL, 4 M, pH 4.75) was added to terminate the reaction. The obtained reaction solution was purified twice with acetate buffer (100 mM, pH 4.75) and thrice with deionized water by ultracentrifugation using a Vivaspin 20 concentrator (MWCO 30 kDa). The resulting solution was lyophilized to afford the product as a white fluffy solid (154 mg, yield: 94%, MALDI-ToF MS: 72.3 kDa).

1.2.2. Synthesis of PEGylated cHSA (PEG-cHSA)

cHSA (100 mg, 1.4 μmol) was firstly dissoleved in degassed phosphate buffer (30 mL, 50 mM, pH 8.0). NHS-PEG (105 mg, 52.4 μmol) was dissolved in 0.4 mL of DMSO and then added into the cHSA solution. After stirring at room temperature for four hours, the reaction solution was purified with deionized water for five times by ultracentrifugation using a Vivaspin 20 concentrator (MWCO 30 kDa). The resulting solution was lyophilized to obtain the product as a white fluffy solid (151 mg, yield: 80 %). The MALDI-ToF MS indicates a molecular weight of 136.6 kDa which means on average 32 PEG chains were conjugated into each cHSA backbone.

1.2.3. Synthesis of denatured PEG-cHSA (PEG-dcHSA)

Preparation of the urea-phosphate buffer (urea-PB)

Urea (150.15 g, 2.5 mol), EDTA (292.24 mg, 1 mmol), $Na_2HPO_4 \cdot 7H_2O$ (5.4276 g, 25 mmol) and NaH_2PO_4 (0.5699 g, 25 mmol) were dissolved in 0.5 L of deionized water. The urea-PB with 50 mM phosphate buffer, 5 M urea and 2 mM EDTA was then obtained by adjusting the pH to 7.4.

Synthesis of PEG-dcHSA

To a 50 mL flask, 20 mL of urea-PB was added and then degassed via bubbling for five minutes. Followed PEG-cHSA (27.2 mg, 200 nmol) was dissolved and further stirred for 15 min. TCEP (5.8 mg, 20 μmol) was added and stirred for 30 min under argon flow. Lastly, MI-NH_2 (15.24 mg, 60 μmol) was added and stirred overnight under argon protection. The obtained reaction solution was purified with urea-PB for three times and with deionized water for five times by ultracentrifugation using a Vivaspin 20 concentrator (MWCO 30 kDa). The resulting solution was lyophilized to afford the product as a white fluffy solid (24.1 mg, yield: 86%, MALDI-ToF MS: 140.4 kDa).

1.2.4. Synthesis of macroinitiators PEG-dcHSA-Br_{39} and PEG-dcHSA-Br_{61}

PEG-dcHSA-Br_{39} and PEG-dcHSA-Br_{61} were synthesized by attaching different amounts of ATRP initiators to PEG-dcHSA. In a typical experiment for the synthesis of PEG-dcHSA-Br_{39}, PEG-dcHSA (5.0 mg, 36 nmol) was dissolved in 10 mL of $NaHCO_3$ (0.1 M, pH 8.5). NHS-BiB (15.3 mg, 0.058 mmol) dissolved in 1 mL of DMSO was then added dropwise into the PEG-dcHSA solution. The reaction solution was stirred overnight at room temperature and purified with deionized water for eight times by ultracentrifugation using a Vivaspin 20 concentrator (MWCO 50 kDa). The product was obtained as a white fluffy solid after lyophilizing (4.3 mg, yield: 83%, MALDI-ToF MS: 146.2 kDa).

1.2.5. Synthesis of brush-1 to brush-4

Preparation of the stock solution of $CuBr_2$/TPMA catalyst

$CuBr_2$ (4.47 mg, 0.02 mmol) and TPMA (46.5 mg, 0.16 mmol) was dissolved in 1 mL mixture solution of water:DMF (1:1 v/v) and stored at 4 °C prior to use. Therefore, the concentration of the effective Cu^{2+} in the stock solution was 20 nmol μL^{-1}.

Preparation of the ascorbic acid solution

To a 10 mL Schlenk flask, L-ascorbic acid (4.4 mg, 25 μmol) was firstly added under argon flow. Degassed deionized water (5 mL) was then added to dissolve L-ascorbic acid. The solution was then stirred under argon flow for 40 min. Therefore, the concentration of L-ascorbic acid was 5 nmol μL^{-1}.

Atom-transfer radical polymerization (ATRP)

Protein-templated brush polymers (**brush-1** to **brush-4**) were synthesized via activator regenerated by electron transfer (ARGET) ATRP under different conditions. As a typical protocol, PEG-dcHSA-Br_{61} (0.449 mg, 3 nmol) was firstly dissolved in 0.449 mL of deionized water in a 5 mL flask. MOEGMA (52.3 μL, 183 μmol), the $CuBr_2$/TPMA catalyst solution (11 μL, 220 nmol of Cu^{2+}) and 0.5 mL of deionized water were then added. Subsequently, the mixture solution was degassed through three freeze-pump-thaw cycles and the flask was refilled with argon. The L-ascorbic acid solution was then added with a syringe pump at a speed of 0.6 $\mu L\ min^{-1}$ at room temperature for two hours. The brush polymer solution was purified with deionized water for five times by ultracentrifugation using a Vivaspin 6 concentrator (MWCO 30 kDa).

1.3. Preparation of the protein-templated brush polymer site-specifically functionalized with a dye (brush-5)

1.3.1. Synthesis of fluorescent HSA (f-HSA) via site-specific labeling

The site-specific labelling of HSA with a dye was conducted under dark. HSA (10 mg, 0.15 μmol) was dissolved in 10 mL of degassed PBS (pH 6.5). Alexa Fluor 647 C_2 maleimide (AF647-MI, 0.465 mg, 0.37 μmol) dissolved in 30 μL of DMSO was then added dropwise and the reaction was allowed to proceed under dark for 18 h at room temperature. The reaction solution was washed with deionized water by ultracentrifugation using a Vivaspin 6 concentrator (MWCO 30 kDa) for several times until no color was observed in the filtered

solution. The resultant solution was lyophilized to afford the product as a light blue fluffy solid (8.3 mg, yield: 76%, MALDI-ToF MS: 67.2 kDa).

1.3.2. Synthesis of cationic f-HSA (f-cHSA)

f-HSA (8.1 mg, 0.12 μmol) was dissolved in 1 mL of degassed ethylenediamine solution (2.5 M) and the pH was tuned to 4.75 by using HCl. EDC·HCl (0.24 mmol, 45 mg) was then added. After stirring for two hours at room temperature, acetate buffer (0.1 mL, 4 M, pH 4.75) was added to terminate the reaction. The obtained reaction solution was purified twice with acetate buffer (100 mM, pH 4.75) and thrice with deionized water by ultracentrifugation using a Vivaspin 6 concentrator (MWCO 30 kDa). The resulting solution was lyophilized to afford the product as a light blue fluffy solid (8.4 mg, yield: 96%, MALDI-ToF MS: 72.5 kDa).

1.3.3. Synthesis of PEGylated f-cHSA (f-PEG-cHSA)

f-cHSA (8.1 mg, 0.11 μmol) was firstly dissoleved in 8 mL of degassed phosphate buffer (50 mM, pH 8.0). NHS-PEG (6.9 mg, 3.45 μmol) was dissolved in 0.1 mL of DMSO and then added into the cHSA solution. After stirring overnight at room temperature, the reaction solution was purified with deionized water for eight times by ultracentrifugation using a Vivaspin 6 concentrator (MWCO 30 kDa). The resulting solution was lyophilized to obtain the product as a light blue fluffy solid (11.6 mg, yield: 96%). The MALDI-ToF MS indicates a molecular weight of 107.9 kDa which means on average 18 PEG chains were conjugated into each f-cHSA backbone.

1.3.4. Synthesis of denatured f-PEG-cHSA (f-PEG-dcHSA)

The reaction and purification were conducted under dark. To a 25 mL flask, 10 mL of urea-PB (50 mM phosphate buffer, 5 M urea and 2 mM EDTA, pH 7.4) was added and then degassed via bubbling for ten minutes. f-PEG-cHSA (11.3 mg, 105 nmol) was then dissolved and stirred for 15 min. Subsequently, TCEP (2.9 mg, 10 μmol) was added and stirred for 30 min under argon flow. Lastly, MI-NH_2 (7.62 mg, 30 μmol) was added and stirred overnight under argon

atmosphere. The obtained reaction solution was purified with urea-PB for three times and with deionized water for five times by ultracentrifugation using a Vivaspin 6 concentrator (MWCO 30 kDa). The product was obtained as a light blue fluffy solid after lyophilizing (11.6 mg, yield: 99%, MALDI-ToF MS: 110.9 kDa).

1.3.5. Synthesis of the fluorescent macroinitiator f-PEG-dcHSA-Br

The reaction and purification were conducted under dark. f-PEG-dcHSA (11.5 mg, 104 nmol) was dissolved in 15 mL of $NaHCO_3$ (0.1 M, pH 8.5). NHS-BiB (147 mg, 0.56 mmol) dissolved in 1.5 mL of DMSO was then added dropwise into the f-PEG-dcHSA solution. The reaction solution was stirred overnight at room temperature and then washed with deionized water for eight times by ultracentrifugation using a Vivaspin 20 concentrator (MWCO 30 kDa). The purified solution was then lyophilized to afford the product as a light blue fluffy solid (11.8 mg, yield: 91%, MALDI-ToF MS: 125.2 kDa).

1.3.6. Synthesis of brush-5

The brush polymer site-specifically functionalized with AF647 (**brush-5**) was synthesized by ARGET ATRP under dark. Briefly, f-PEG-dcHSA-Br (0.48 mg, 3.83 nmol) was firstly dissolved in 0.48 mL of deionized water in a 5 mL flask. MOEGMA (80 μL, 280 μmol), $CuBr_2$/TPMA catalyst solution (10 μL, 200 nmol of Cu^{2+}) and 0.5 mL of deionized water were then added. The mixture solution was then degassed through three freeze-pump-thaw cycles and the flask was refilled with argon. The L-ascorbic acid solution was then added with a syringe pump at a speed of 0.6 μL min^{-1} at room temperature for two hours. The fluorescent brush polymer was purified with deionized water for five times by ultracentrifugation using a Vivaspin 6 concentrator (MWCO 30 kDa).

1.4. Preparation of protein-templated brush polymers site-specifically functionalized with biotin (biotin-brush-6 and biotin-brush-7) and their assembly

110.6 kDa which means in average 17 PEG chains were conjugated into each Biotin-cHSA backbone.

1.4.4. Synthesis of denatured biotin-PEG-cHSA (biotin-PEG-dcHSA)

To a 15 mL flask, 6 mL of urea-PB (50 mM phosphate buffer, 5 M urea and 2 mM EDTA, pH 7.4) was added and then degassed via bubbling for 15 minutes. Biotin-PEG-cHSA (8.3 mg, 75 nmol) was then dissolved and stirred for 15 min. Subsequently, TCEP (2.15 mg, 7.5 μmol) was added and stirred for 30 min under argon flow. Lastly, MI-NH_2 (5.72 mg, 22.5 μmol) was added and stirred overnight under argon atmosphere. The obtained reaction solution was purified with urea-PB for three times and with deionized water for five times by ultracentrifugation using a Vivaspin 6 concentrator (MWCO 30 kDa). The product was obtained as a white fluffy solid after lyophilizing (8.5 mg, yield: 99%, MALDI-ToF MS: 113.7 kDa).

1.4.5. Synthesis of biotin-functionalized macroinitiator biotin-PEG-dcHSA-Br

Biotin-PEG-dcHSA (8.5 mg, 75 nmol) was dissolved in 10 mL of $NaHCO_3$ (0.1 M, pH 8.5). NHS-BiB (160 mg, 0.61 mmol) dissolved in 1.6 mL of DMSO was then added dropwise into the biotin-PEG-dcHSA solution. The reaction solution was stirred overnight at room temperature and then washed with deionized water for eight times by ultracentrifugation using a Vivaspin 20 concentrator (MWCO 30 kDa). The purified solution was then lyophilized to afford the product as a white fluffy solid (6.3 mg, yield: 64%, MALDI-ToF MS: 131.7 kDa).

1.4.6. Synthesis of biotin-brush-6 and biotin-brush-7

Protein-templated brush polymers site-specifically functionalized with biotin (**biotin-brush-6** and **biotin-brush-7**) were synthesized by ARGET ATRP. In a typical example for the synthesis of **biotin-brush-6**, biotin-PEG-dcHSA-Br (0.53 mg, 4 nmol) was firstly dissolved in 0.53 mL of deionized water in a 5 mL flask. MOEGMA (139.4 μL, 488 μmol), $CuBr_2$/TPMA catalyst solution (14 μL, 280 nmol of Cu^{2+}) and 0.7 mL of deionized water were then added. The mixture solution was then degassed through three freeze-pump-thaw cycles and the flask was refilled with argon. The L-ascorbic acid solution was then added with a syringe pump at a speed of 0.6

μL min^{-1} at room temperature for one hour. The biotin-functionalized brush polymer was purified with deionized water for five times by ultracentrifugation using a Vivaspin 6 concentrator (MWCO 30 kDa).

1.4.7. Assembly with AF647-labeled streptavidin (AF647-SA)

AF647-SA (1.8 mg mL^{-1}, 10 μL) was mixed with **biotin-brush-6** (1 mL, ~0.3 nmol) and stirred overnight. The sample was then sent for FCS measurement.

1.4.8. Assembly with streptavidin-conjugated Au nanoparticles (Au-SA)

Streptavidin-conjugated gold nanoparticles (Au-SA, 0.096 mL, 5 nm, 0.5 mg mL^{-1}, 2.5×10^{14} particles mL^{-1}) was mixed with a biotin-containing brush polymer (0.1 mL, 0.04 nmol) with a molar ratio of 1:1 in water. The solution was gently shaken for two hours and then used for TEM characterization.

1.5. Preparation of the protein-templated fluorescent brush polymer site-specifically functionalized with biotin (biotin-brush-8) and its assembly

1.5.1. Synthesis of biotin-functionalized fluorescent macroinitiator biotin-PEG-f-dcHSA-Br

Biotin-PEG-dcHSA-Br (2.74 mg, 20 nmol) was dissolved in 4 mL of $NaHCO_3$ (0.1 M, pH 8.5). AF647-NHS (0.25 mg, 200 nmol) dissolved in 0.1 mL of DMSO was then added dropwise into the biotin-PEG-dcHSA-Br solution. The reaction solution was stirred overnight under dark at room temperature and then washed with deionized water for eight times by ultracentrifugation using a Vivaspin 6 concentrator (MWCO 30 kDa). The purified solution was then lyophilized to afford the product as a blue fluffy solid (2.3 mg, yield: 84 %, MALDI-ToF MS: 132.1 kDa).

1.5.2. Synthesis of biotin-brush-8

The protein-templated fluorescent brush polymer site-specifically functionalized with biotin (**biotin-brush-8**) was synthesized by ARGET ATRP. Briefly, biotin-PEG-f-dcHSA-Br (0.54 mg, 4 nmol) was firstly dissolved in 0.54 mL of deionized water in a 5 mL flask. MOEGMA (139.4 μL, 488 μmol), $CuBr_2$/TPMA catalyst solution (14 μL, 280 nmol of Cu^{2+}) and 0.7 mL of deionized water were then added. The mixture solution was then degassed through three freeze-pump-thaw cycles and the flask was refilled with argon. The L-ascorbic acid solution was then added with a syringe pump at a speed of 0.6 μL min^{-1} at room temperature for one hour. The biotin-functionalized fluorescent brush polymer was purified with deionized water for five times by ultracentrifugation using a Vivaspin 20 concentrator (MWCO 30 kDa).

1.5.3. Assembly with biotinylated somatostatin (biotin-SST) and streptavidin (SA)

SA or AF568-SA (32 μg, 0.6 nmol) was firstly dissolved in Milli-Q water to 1 mg mL^{-1} and then mixed with **biotin-brush-8** (2 mL, 0.3 μM) in a 5 mL tube. After stirring at room temperature for 8 h, biotin-SST (2.964 μL, 1 mg mL^{-1}) was added into the tube, and the mixture was stirred further for 10 h. The final solution was purified with PBS for five times by ultracentrifugation using a Vivaspin 6 concentrator (MWCO 30 kDa) and the final construct concentration was tuned to 2 μM.

1.5.4. Assembly with biotinylated aDEC205 antibody (biotin-aDEC) and streptavidin (SA)

Self-assembly of **biotin-brush-8** with biotin-aDEC was performed by dissolving 0.1 mg (1.8 nmol, 1 equiv) SA in 500 μL phosphate buffer (50 mM, pH 7.4) and subsequent addition of 0.27 mg (1.8 nmol, 1 equiv) biotin-aDEC and 0.78 mg (1.8 nmol, 1 equiv) **biotin-brush-8**. The mixture was incubated for 30 min under shaking and purified by rigorous ultrafiltration using a Vivaspin 500 (MWCO 30kDa, 3 × 500 μL of 50 mM phosphate buffer pH 7.4).

II. Characterization

2.1. Matrix-assisted laser desorption/ionization (MALDI) mass spectrometry

MALDI time-of-flight (MALDI-ToF) mass spectrometry was performed on Bruker rapifleX spectrometer. Saturated solution of sinapinic acid dissolved in a 50:50 water/acetonitrile with 0.2% TFA (trifloroacetic acid) was used as the matrix solution.

2.2. Gel permeation chromatography (GPC)

The molecular weight and molecular weight distribution were determined by GPC. Deionized water containing 0.1 M $NaNO_3$ was used as eluent at a flow rate of 1 mL min^{-1}. Shodex RI 101 detector was used. Linear PEG standards were used for calibration.

2.3. Dynamic light scattering (DLS)

Dilute solutions of the macroinitiator PEG-dcHSA-Br_{61} and brush polymers (**brush-1** to **brush-4**) were prepared in water and filtered through a 450 nm filter (Millipore HA) into optical cells with 20 mm diameter. The experiment was performed on an ALV5000 setup with a 194 mW laser at λ = 532 nm, at different scattering angles θ defining the scattering wave vector $q = \frac{4\pi n}{\lambda}\sin\frac{\theta}{2}$ with n = 1.333 being the water refractive index. The relaxation function, $C(q,t) = [G(q,t_0^{-1})]^{1/2}$ computed from the experimental scattering intensity autocorrelation function $G(q,t)$ was represented either by an inverse Laplace transform (ILT) analysis using the CONTIN algorithmor the stretched exponential function of the form: α

$$C(q,t) = \alpha e^{-(\frac{t}{\tau})^{\beta}} \qquad \text{(S1)}$$

where α is the amplitude, τ the relaxation time and $\beta \leqslant 1$ the stretching parameter. ILT was employed in the case of more than one relaxation process in $C(q,t)$, whereas Equation S1 can amount for the presence of one process deviating from the ideal single exponential shape. In dilute solutions, the relaxation rate $\Gamma(q) = 1/\tau(q)$ is usually diffusive defining the diffusion coefficient $D = \Gamma(q)/q^2$. For species with small size R i.e., both the scattering intensity $I(q)$ and

$D = D_0$ are q-independent with $I \sim cM$ and $D_0 = \frac{k_B T}{6\pi\eta_0 R_h}$ where c, M, R_h, η_0, k_B, and T are the probed species concentration, its molecular weight and hydrodynamic ratio, the solvent viscosity, the Boltzmann constant and the absolute temperature, respectively. For $qR \sim 1$, both $I(q)$ and $D(q)$ depend on q defining the probing length ($2\pi/q$). The former, known as the form factor, yields (at low qR_g) the radius of gyration R_g,

$$I(q)^{-1}=I(0)^{-1}(1+q^2R_g^2/3) \quad \text{(S2)}$$

whereas the effective D is given by,

$$D = D_0(1 + Aq^2) \quad \text{(S3)}$$

with A is a parameter characterizing the shape of the diffusing species.

Equations for prolate ellipsoids (Perrin)[2]

$$R_h = a/f(b/a) \quad \text{(S4)}$$

$$f(b/a) = \frac{\ln\left[\frac{1+(1-b^2/a^2)^{1/2}}{b/a}\right]}{(1-b^2/a^2)^{1/2}} \quad \text{(S5)}$$

for $a > b$ (prolate)

Static scattering:

$$I(q) = \frac{9\pi}{2}\int_0^{\pi/2}\frac{[J_{3/2}(u)]^2}{u^3}cos\beta d\beta \quad \text{(S6)}$$

$$u = qa(cos^2\beta + \frac{b^2}{a^2}sin^2\beta)^{1/2} \quad \text{(S7)}$$

$$J_{\frac{3}{2}}(u) = \left(\frac{2u}{\pi}\right)^{1/2}\left(\frac{sinu}{u^2} - \frac{cosu}{u}\right) \quad \text{(S8)}$$

Equation for Gaussian coils (Pecora)[3]

$$P(x) = \frac{2}{x^4}\left(e^{-x^2} - 1 + x^2\right) \quad \text{(S9)}$$

2.4. Stability test against trypsin

Trypsin was dissolved in deionized water to prepare a 3 mg mL^{-1} solution and then passed through a syringe filter with the pore size of 220 nm. The solution (1 mL) was then mixed with 2 mL of brush polymer solution (0.3 μM) in a clean hood at room temperature. Therefore, the final concentrations of trypsin and the brush polymer were 1 mg mL^{-1} and 0.2 μM, respectively.

DLS was then used to track the size change of the mixture solution immediately and after different time intervals until six hours.

2.5. Cell viability test

A549 mammalian lung adenocarcinoma cells were cultured in standard T-75 flasks using high glucose DMEM fortified with 10% fetal bovine serum, 1% penicillin/streptomycin and 1% MEM non-essential amino acids. The cells were split at near confluency and incubated at 37 °C, 5% CO_2 prior to each experiment.

Pre-cultured A549 cells were seeded (6,500 cells per well) in a white 96-well plate (half area, Greiner BioOne®) and allowed to adhere overnight at 37 °C, 5% CO_2. The brush polymers (**brush-1** to **brush-4**) were prepared at various concentrations (12.5 – 200 mg L^{-1}) in DMEM and introduced as independent replicates for 24 h at 37 °C, 5% CO_2. CellTiter-Glo® (Promega) was employed following manufacturer's protocol and the resultant luminescence was detected using Glomax® Multi 96-well plate reader (Promega). Data is presented in Figure 2D as mean ± SEM, n = 3.

2.6. Transmission electron microscopy (TEM)

TEM samples were prepared by adding 4 µL of the brush polymer solution onto a carbon-coated copper grid. After drying in air for 10 min, the remained solution was removed by a filter paper. The samples were then stained with 2% uranyl acetate solution and dried in air. The measurement was conducted on a JEOL JEM-1400 TEM operating at an accelerating voltage of 120 kV. ImageJ software was used for the analysis of length and width of brush polymer samples.

2.7. Fluorescent spectroscopy

Fluorescent emission spectra were collected using a TECAN (Spark 20M) microplate reader at room temperature. The excitation wavelength was set as 594 nm and the emission wavelength

was monitored from 600 to 800 nm. Excitation and emission bandwidths were both maintained at 20 nm and the emission wavelength step size was 1 nm.

2.8. Fluorescent correlation spectroscopy (FCS)

Fluorescence correlation spectroscopy (FCS) experiments were performed on a commercial confocal microscope, LSM 880 (Carl Zeiss, Jena, Germany) equipped with a C-Apochromat 40x/1.2W water immersion objective. The AF647 molecules and were excited by a HeNe laser (633 nm) fiber-coupled to the microscope. Emitted fluorescence light was collected with the same objective, passed through a confocal pinhole and directed to a spectral detection unit (Quasar, Carl Zeiss). In this unit emission is spectrally separated by a grating element on a 32 channel array of GaAsP detectors operating in a single photon counting mode. In all experiments the emission in the spectral range 640-700 nm was considered. An eight-well polystyrene-chambered coverglass (Laboratory-Tek, Nalge Nunc International, Penfield, NY) was used as a sample cell for the studied solutions. For each sample series of measurements with a total duration of 5 min were performed. The time-dependent fluctuations of the fluorescent intensity $\delta I(t)$ were recorded and analyzed by an autocorrelation function $G(\tau) = 1+<\delta I(t)\delta I(t+\tau)>/<I(t)>^2$. As has been shown theoretically for an ensemble of m different types of freely diffusing identical fluorescence species, $G(\tau)$ has the following analytical form:[4]

$$G(\tau) = 1+\frac{1}{N}\left[1+\frac{f_T}{1-f_T}e^{-t/\tau_T}\right]\sum_{i=1}^{m}\frac{F_i}{\left[1+\frac{\tau}{\tau_{Di}}\right]\sqrt{1+\frac{\tau}{S^2\tau_{Di}}}} \qquad \text{(S10)}$$

Here, N is the average number of diffusing fluorescence species in the observation volume, f_T and τ_T are the fraction and the decay time of the triplet state, $S = z_0/r_0$ is the so-called structure parameter with z_0 and r_0 representing the axial and radial dimensions of the confocal volume. F_i is the fraction of the i-th species and τ_{Di} is their diffusion time through the observation volume that is related to their diffusion coefficient, D_i, through $D_i = r_0^2/4\tau_{Di}$. The experimentally obtained $G(\tau)$ were fitted with Equation S10, yielding the corresponding diffusion times and subsequently the diffusion coefficients of the fluorescent species. Finally, the hydrodynamic radii R_h were calculated (assuming spherical particles) using the Stokes-Einstein relation: $R_h =$

$\frac{k_B T}{6\pi\eta D}$ where k_B is the Boltzmann constant, T is the temperature, and η is the viscosity of the solvent. Furthermore, FCS yielded also the fluorescent brightness (*FB*) of the studied species defined as the ratio between the detected average fluorescent intensity and the mean number of fluorescent species in the observation volume, $FB=\langle I(t)\rangle/N$. As the value of r_0 depends strongly on the specific characteristics of the optical setup a calibration was done using the reference value[5] of the AF647 diffusion coefficient 3.3×10^{-10} m^2/s at 25°C.

2.9. Confocal laser scanning microscopy (CLSM)

Cell culture was performed with human lung adenocarcinoma cell line, A549, pre cultured in high glucose DMEM, supplemented with 10% Fetal Bovine Serum, 1% Penicillin/Streptomycin, 1% MEM. Cell passages used within the experiment are between 7-12.

Cells were seeded at a density of 15,000 cells/well in an Ibidi® µ-slide 8-well confocal microscopy chamber and left to adhere for 24 h. Stock solutions, prepared at 2 µM, were diluted with DMEM to a final concentration of 500 nM. From the cells, DMEM was aspirated and the samples were introduced into each individual well. The cells were then incubated for 24 h. Subsequently, the cell nuclei were stained with Hoechst for 20 min before imaging live on a Leica SP5 confocal microscope system.

For the time lapse studies at 2 h, 6 h and 24 h, the cells were seeded identically as above with the samples introduced into the cells in such a way that all three time intervals end at the same time for imaging. Each well was likewise washed and stained with Hoechst for 20 min before imaging live on a Leica SP5 confocal microscope system.

2.10. SDS-PAGE and Western blot

Electrophoresis was carried out using 10% Bis-Tris polyacrylamide resolving gels with 6% Bis-Tris polyacrylamide stacking gel. Sample preparation was performed under denaturing conditions: 3 µL of LDS sample buffer (NuPAGE, Invitrogen, Carlsbad, CA, USA) and 1 µL

of 1 M Dithiothreitol (DTT) where mixed with 8 µL of a 2 µM protein solution and incubated for 10 min at 95 °C prior to gel.

As a reference 2 µL of AppliChem Protein Marker VI® protein ladders were loaded to the gel. The gel was run using 1 × MES SDS Running Buffer (NuPAGE, Invitrogen, Carlsbad, CA, USA) with a constant 150 V for about 50 min. The bioconjugation was confirmed using Western blot analysis and immunoblot detection with a Streptavidin-Horseradish peroxidase (Strep-HRP) conjugate to detect the presence of biotin. Western Blot was performed after SDS-PAGE by blotting on a nitrocellulose membrane using Mini Trans-Blot® Cell Module (Bio-Rad Laboratory-Inc. Hercules, USA). The nitrocellulose membrane was rinsed with MeOH and equilibrated with filter paper, sponges, and gel in a blotting buffer for 10 minutes. A blotting sandwich was prepared according to the transfer charge by stacking a sponge, two filters, gel, the membrane, followed by two filters and a sponge. The transfer was performed using 90 mA overnight at 4 °C, revealing a successful transfer to the membrane, visualized by Ponceau S. Following this, the membrane was blocked using 5 % skim milk in 1 × Tris-buffered saline with Tween20 (TBS-T) for 60 minutes. After washing with TBS-T, the membrane was incubated with Strep-HRP (1:4000 in 5% skim milk/TBST) for one hour. Chemiluminescence was detected using enhanced chemiluminescence (ECL, Western Lightning Plus, PerkinElmer, Waltham, USA).

III. Supplementary Data and Discussion

3.1. The amino acid sequence and solvent accessibility of HSA

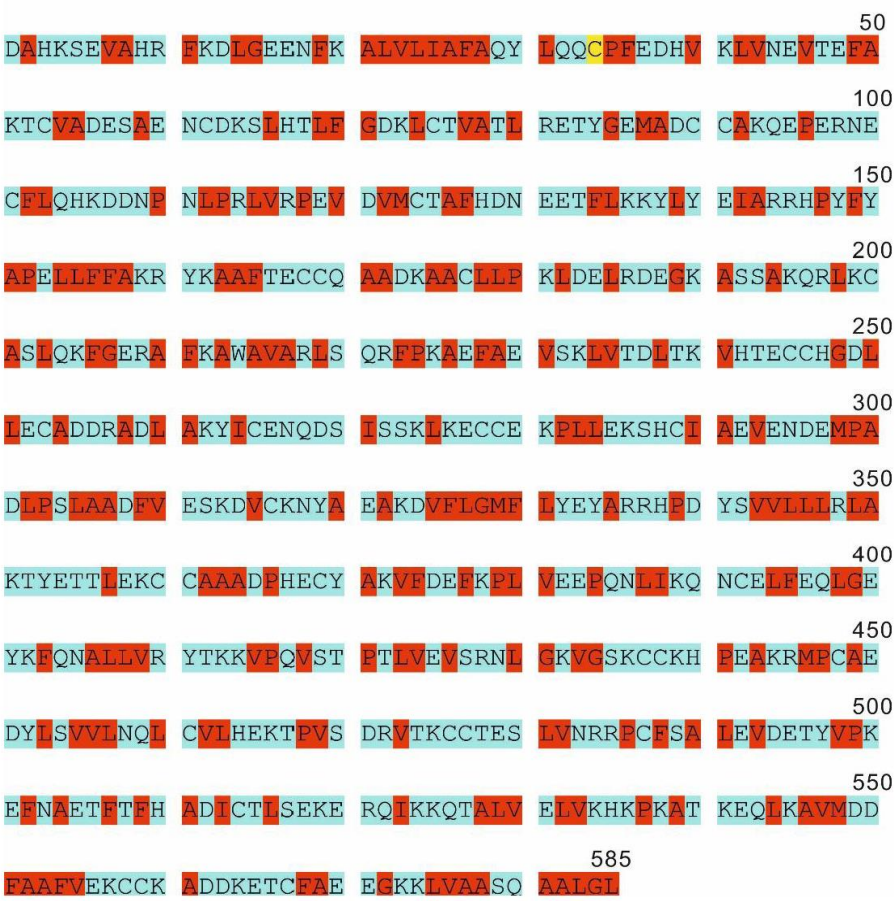

Figure S1. The full amino acid sequence of HSA. The one-letter abbreviations for amino acids are as follows: R: Arginine; K: Lysine; D: Aspartic acid; E: Glutamic acid; Q: Glutamine; N: Asparagine; H: Histidine; S: Serine; T: Threonine; Y: Tyrosine; C: Cysteine; W: Tryptophan; A: Alanine; I: Isoleucine; L: Leucine; M: Methionine; F: Phenylalanine; V: Valine; P: Proline; G: Glycine.

Table S1. Solvent accessibility of HSA (PDB: 1AO6) obtained with Pymol 2.03.

ASP`1 0% | |	LYS`41 54% |===== |	ARG`81 74% |======= |
ALA`2 0% | |	LEU`42 2% | |	GLU`82 99% |========= |
HIS`3 0% | |	VAL`43 6% | |	THR`83 82% |======== |
LYS`4 0% | |	ASN`44 48% |==== |	TYR`84 11% |= |
SER`5 23% |== |	GLU`45 32% |=== |	GLY`85 41% |==== |
GLU`6 35% |=== |	VAL`46 6% | |	GLU`86 73% |======= |
VAL`7 1% | |	THR`47 4% | |	MET`87 15% |= |
ALA`8 1% | |	GLU`48 71% |======= |	ALA`88 18% |= |
HIS`9 51% |===== |	PHE`49 28% |== |	ASP`89 68% |====== |
ARG`10 14% |= |	ALA`50 0% | |	CYS`90 0% | |
PHE`11 11% |= |	LYS`51 44% |==== |	CYS`91 39% |=== |
LYS`12 63% |====== |	THR`52 48% |==== |	ALA`92 78% |======= |
ASP`13 52% |===== |	CYS`53 0% | |	LYS`93 47% |==== |
LEU`14 23% |== |	VAL`54 34% |=== |	GLN`94 79% |======= |
GLY`15 36% |=== |	ALA`55 82% |======== |	GLU`95 31% |=== |
GLU`16 38% |=== |	ASP`56 48% |==== |	PRO`96 73% |======= |
GLU`17 85% |======== |	GLU`57 46% |==== |	GLU`97 54% |===== |
ASN`18 31% |=== |	SER`58 86% |======== |	ARG`98 7% | |
PHE`19 0% | |	ALA`59 35% |=== |	ASN`99 2% | |
LYS`20 34% |=== |	GLU`60 94% |========= |	GLU`100 57% |===== |
ALA`21 16% |= |	ASN`61 33% |=== |	CYS`101 5% | |
LEU`22 1% | |	CYS`62 0% | |	PHE`102 1% | |
VAL`23 0% | |	ASP`63 84% |======== |	LEU`103 16% |= |
LEU`24 5% | |	LYS`64 32% |=== |	GLN`104 75% |======= |
ILE`25 0% | |	SER`65 54% |===== |	HIS`105 27% |== |
ALA`26 10% | |	LEU`66 8% | |	LYS`106 11% |= |
PHE`27 1% | |	HIS`67 18% |= |	ASP`107 26% |== |
ALA`28 1% | |	THR`68 25% |== |	ASP`108 28% |== |
GLN`29 3% | |	LEU`69 14% |= |	ASN`109 51% |===== |
TYR`30 6% | |	PHE`70 10% |= |	PRO`110 20% |= |
LEU`31 5% | |	GLY`71 5% | |	ASN`111 74% |======= |
GLN`32 7% | |	ASP`72 45% |==== |	LEU`112 22% |== |
GLN`33 44% |==== |	LYS`73 26% |== |	PRO`113 79% |======= |
CYS`34 3% | |	LEU`74 2% | |	ARG`114 79% |======= |
PRO`35 46% |==== |	CYS`75 25% |== |	LEU`115 62% |====== |
PHE`36 8% | |	THR`76 59% |===== |	VAL`116 87% |======== |
GLU`37 73% |======= |	VAL`77 19% |= |	ARG`117 38% |=== |
ASP`38 36% |=== |	ALA`78 1% | |	PRO`118 53% |===== |
HIS`39 0% | |	THR`79 59% |===== |	GLU`119 63% |====== |
VAL`40 20% |== |	LEU`80 56% |===== |	VAL`120 12% |= |

ASP`121 41% |==== |	TYR`161 12% |= |	ALA`201 5% | |
VAL`122 50% |==== |	LYS`162 39% |=== |	SER`202 10% |= |
MET`123 13% |= |	ALA`163 42% |==== |	LEU`203 15% |= |
CYS`124 5% | |	ALA`164 5% | |	GLN`204 50% |==== |
THR`125 64% |====== |	PHE`165 0% | |	LYS`205 74% |======= |
ALA`126 43% |==== |	THR`166 44% |==== |	PHE`206 33% |=== |
PHE`127 2% | |	GLU`167 40% |==== |	GLY`207 26% |== |
HIS`128 59% |===== |	CYS`168 0% | |	GLU`208 51% |===== |
ASP`129 85% |======== |	CYS`169 16% |= |	ARG`209 55% |===== |
ASN`130 49% |==== |	GLN`170 70% |====== |	ALA`210 24% |== |
GLU`131 33% |=== |	ALA`171 13% |= |	PHE`211 1% | |
GLU`132 66% |====== |	ALA`172 77% |======= |	LYS`212 35% |=== |
THR`133 41% |==== |	ASP`173 43% |==== |	ALA`213 31% |=== |
PHE`134 16% |= |	LYS`174 29% |== |	TRP`214 30% |=== |
LEU`135 19% |= |	ALA`175 19% |= |	ALA`215 1% | |
LYS`136 28% |== |	ALA`176 40% |==== |	VAL`216 11% |= |
LYS`137 43% |==== |	CYS`177 30% |== |	ALA`217 0% | |
TYR`138 16% |= |	LEU`178 0% | |	ARG`218 20% |== |
LEU`139 9% | |	LEU`179 13% |= |	LEU`219 9% | |
TYR`140 5% | |	PRO`180 57% |===== |	SER`220 0% | |
GLU`141 18% |= |	LYS`181 32% |=== |	GLN`221 2% | |
ILE`142 27% |== |	LEU`182 10% | |	ARG`222 16% |= |
ALA`143 0% | |	ASP`183 29% |== |	PHE`223 3% | |
ARG`144 12% |= |	GLU`184 63% |====== |	PRO`224 3% | |
ARG`145 29% |== |	LEU`185 6% | |	LYS`225 49% |==== |
HIS`146 29% |== |	ARG`186 60% |===== |	ALA`226 1% | |
PRO`147 2% | |	ASP`187 60% |===== |	GLU`227 71% |======= |
TYR`148 14% |= |	GLU`188 31% |=== |	PHE`228 20% |= |
PHE`149 3% | |	GLY`189 12% |= |	ALA`229 66% |====== |
TYR`150 9% | |	LYS`190 39% |=== |	GLU`230 15% |= |
ALA`151 0% | |	ALA`191 38% |=== |	VAL`231 0% | |
PRO`152 7% | |	SER`192 20% |== |	SER`232 28% |== |
GLU`153 5% | |	SER`193 13% |= |	LYS`233 41% |==== |
LEU`154 1% | |	ALA`194 27% |== |	LEU`234 2% | |
LEU`155 11% |= |	LYS`195 45% |==== |	VAL`235 3% | |
PHE`156 8% | |	GLN`196 5% | |	THR`236 54% |===== |
PHE`157 2% | |	ARG`197 14% |= |	ASP`237 30% |=== |
ALA`158 12% |= |	LEU`198 20% |= |	LEU`238 18% |= |
LYS`159 39% |=== |	LYS`199 17% |= |	THR`239 5% | |
ARG`160 30% |== |	CYS`200 4% | |	LYS`240 54% |===== |

VAL`241 1% | |	LYS`281 55% |===== |	GLU`321 69% |====== |
HIS`242 2% | |	PRO`282 62% |====== |	ALA`322 47% |==== |
THR`243 39% |=== |	LEU`283 50% |===== |	LYS`323 46% |==== |
GLU`244 14% |= |	LEU`284 18% |= |	ASP`324 59% |===== |
CYS`245 11% |= |	GLU`285 28% |== |	VAL`325 51% |===== |
CYS`246 2% | |	LYS`286 20% |= |	PHE`326 6% | |
HIS`247 38% |=== |	SER`287 9% | |	LEU`327 14% |= |
GLY`248 17% |= |	HIS`288 20% |= |	GLY`328 16% |= |
ASP`249 16% |= |	CYS`289 28% |== |	MET`329 36% |=== |
LEU`250 5% | |	ILE`290 8% | |	PHE`330 1% | |
LEU`251 3% | |	ALA`291 39% |=== |	LEU`331 5% | |
GLU`252 18% |= |	GLU`292 53% |===== |	TYR`332 7% | |
CYS`253 0% | |	VAL`293 18% |= |	GLU`333 22% |== |
ALA`254 14% |= |	GLU`294 76% |======= |	TYR`334 6% | |
ASP`255 6% | |	ASN`295 40% |=== |	ALA`335 0% | |
ASP`256 24% |== |	ASP`296 10% | |	ARG`336 8% | |
ARG`257 10% |= |	GLU`297 69% |====== |	ARG`337 20% |= |
ALA`258 25% |== |	MET`298 51% |===== |	HIS`338 24% |== |
ASP`259 53% |===== |	PRO`299 26% |== |	PRO`339 35% |=== |
LEU`260 11% |= |	ALA`300 95% |========= |	ASP`340 45% |==== |
ALA`261 5% | |	ASP`301 96% |========= |	TYR`341 12% |= |
LYS`262 54% |===== |	LEU`302 29% |== |	SER`342 0% | |
TYR`263 27% |== |	PRO`303 67% |====== |	VAL`343 1% | |
ILE`264 7% | |	SER`304 71% |======= |	VAL`344 8% | |
CYS`265 24% |== |	LEU`305 11% |= |	LEU`345 0% | |
GLU`266 69% |====== |	ALA`306 22% |== |	LEU`346 1% | |
ASN`267 32% |=== |	ALA`307 44% |==== |	LEU`347 11% |= |
GLN`268 21% |== |	ASP`308 65% |====== |	ARG`348 5% | |
ASP`269 95% |========= |	PHE`309 7% | |	LEU`349 0% | |
SER`270 57% |===== |	VAL`310 15% |= |	ALA`350 19% |= |
ILE`271 2% | |	GLU`311 74% |======= |	LYS`351 56% |===== |
SER`272 10% | |	SER`312 35% |=== |	THR`352 19% |= |
SER`273 63% |====== |	LYS`313 77% |======= |	TYR`353 0% | |
LYS`274 23% |== |	ASP`314 57% |===== |	GLU`354 13% |= |
LEU`275 0% | |	VAL`315 1% | |	THR`355 49% |==== |
LYS`276 59% |===== |	CYS`316 29% |== |	THR`356 11% |= |
GLU`277 72% |======= |	LYS`317 65% |====== |	LEU`357 1% | |
CYS`278 3% | |	ASN`318 53% |===== |	GLU`358 58% |===== |
CYS`279 29% |== |	TYR`319 6% | |	LYS`359 76% |======= |
GLU`280 83% |======== |	ALA`320 78% |======= |	CYS`360 2% | |

CYS`361 43% |==== |	TYR`401 28% |== |	PRO`441 63% |====== |
ALA`362 82% |======== |	LYS`402 55% |===== |	GLU`442 82% |======== |
ALA`363 44% |==== |	PHE`403 0% | |	ALA`443 56% |===== |
ALA`364 96% |========= |	GLN`404 2% | |	LYS`444 51% |===== |
ASP`365 71% |======= |	ASN`405 11% |= |	ARG`445 20% |= |
PRO`366 19% |= |	ALA`406 34% |=== |	MET`446 6% | |
HIS`367 46% |==== |	LEU`407 5% | |	PRO`447 20% |== |
GLU`368 84% |======== |	LEU`408 0% | |	CYS`448 42% |==== |
CYS`369 47% |==== |	VAL`409 20% |= |	ALA`449 4% | |
TYR`370 1% | |	ARG`410 34% |=== |	GLU`450 0% | |
ALA`371 60% |===== |	TYR`411 10% |= |	ASP`451 20% |== |
LYS`372 61% |====== |	THR`412 1% | |	TYR`452 19% |= |
VAL`373 2% | |	LYS`413 23% |== |	LEU`453 13% |= |
PHE`374 32% |=== |	LYS`414 7% | |	SER`454 19% |= |
ASP`375 61% |====== |	VAL`415 4% | |	VAL`455 15% |= |
GLU`376 52% |===== |	PRO`416 6% | |	VAL`456 3% | |
PHE`377 2% | |	GLN`417 35% |=== |	LEU`457 3% | |
LYS`378 62% |====== |	VAL`418 6% | |	ASN`458 2% | |
PRO`379 59% |===== |	SER`419 56% |===== |	GLN`459 20% |== |
LEU`380 27% |== |	THR`420 10% | |	LEU`460 2% | |
VAL`381 12% |= |	PRO`421 68% |====== |	CYS`461 11% |= |
GLU`382 50% |==== |	THR`422 12% |= |	VAL`462 10% | |
GLU`383 44% |==== |	LEU`423 3% | |	LEU`463 14% |= |
PRO`384 0% | |	VAL`424 3% | |	HIS`464 8% | |
GLN`385 47% |==== |	GLU`425 41% |==== |	GLU`465 55% |===== |
ASN`386 51% |===== |	VAL`426 4% | |	LYS`466 49% |==== |
LEU`387 15% |= |	SER`427 1% | |	THR`467 70% |======= |
ILE`388 8% | |	ARG`428 18% |= |	PRO`468 66% |====== |
LYS`389 56% |===== |	ASN`429 15% |= |	VAL`469 53% |===== |
GLN`390 67% |====== |	LEU`430 6% | |	SER`470 4% | |
ASN`391 17% |= |	GLY`431 0% | |	ASP`471 80% |======= |
CYS`392 7% | |	LYS`432 30% |== |	ARG`472 24% |== |
GLU`393 57% |===== |	VAL`433 12% |= |	VAL`473 0% | |
LEU`394 32% |=== |	GLY`434 2% | |	THR`474 41% |==== |
PHE`395 18% |= |	SER`435 43% |==== |	LYS`475 54% |===== |
GLU`396 74% |======= |	LYS`436 50% |===== |	CYS`476 2% | |
GLN`397 71% |======= |	CYS`437 1% | |	CYS`477 12% |= |
LEU`398 18% |= |	CYS`438 17% |= |	THR`478 69% |====== |
GLY`399 43% |==== |	LYS`439 81% |======== |	GLU`479 77% |======= |
GLU`400 41% |==== |	HIS`440 31% |=== |	SER`480 32% |=== |

LEU`481 23% |== |	ARG`521 6% | |	ALA`561 50% |===== |
VAL`482 23% |== |	GLN`522 24% |== |	ASP`562 85% |======== |
ASN`483 44% |==== |	ILE`523 37% |=== |	ASP`563 34% |=== |
ARG`484 9% | |	LYS`524 51% |===== |	LYS`564 86% |======== |
ARG`485 5% | |	LYS`525 6% | |	GLU`565 68% |====== |
PRO`486 22% |== |	GLN`526 0% | |	THR`566 48% |==== |
CYS`487 38% |=== |	THR`527 33% |=== |	CYS`567 27% |== |
PHE`488 0% | |	ALA`528 4% | |	PHE`568 1% | |
SER`489 26% |== |	LEU`529 4% | |	ALA`569 52% |===== |
ALA`490 74% |======= |	VAL`530 2% | |	GLU`570 60% |====== |
LEU`491 9% | |	GLU`531 25% |== |	GLU`571 39% |=== |
GLU`492 76% |======= |	LEU`532 10% | |	GLY`572 10% | |
VAL`493 49% |==== |	VAL`533 2% | |	LYS`573 69% |====== |
ASP`494 14% |= |	LYS`534 10% | |	LYS`574 77% |======= |
GLU`495 80% |======= |	HIS`535 21% |== |	LEU`575 22% |== |
THR`496 80% |======== |	LYS`536 23% |== |	VAL`576 16% |= |
TYR`497 24% |== |	PRO`537 21% |== |	ALA`577 57% |===== |
VAL`498 95% |========= |	LYS`538 96% |========= |	ALA`578 55% |===== |
PRO`499 47% |==== |	ALA`539 58% |===== |	SER`579 17% |= |
LYS`500 72% |======= |	THR`540 19% |= |	GLN`580 62% |====== |
GLU`501 82% |======== |	LYS`541 83% |======== |	ALA`581 78% |======= |
PHE`502 38% |=== |	GLU`542 79% |======= |	ALA`582 35% |=== |
ASN`503 45% |==== |	GLN`543 39% |=== |	LEU`583 0% | |
ALA`504 60% |===== |	LEU`544 6% | |	GLY`584 0% | |
GLU`505 87% |======== |	LYS`545 52% |===== |	LEU`585 0% | |
THR`506 64% |====== |	ALA`546 54% |===== |	
PHE`507 3% | |	VAL`547 18% |= |	
THR`508 64% |====== |	MET`548 8% | |	
PHE`509 9% | |	ASP`549 61% |====== |	
HIS`510 63% |====== |	ASP`550 46% |==== |	
ALA`511 28% |== |	PHE`551 2% | |	
ASP`512 58% |===== |	ALA`552 26% |== |	
ILE`513 5% | |	ALA`553 39% |=== |	
CYS`514 32% |=== |	PHE`554 3% | |	
THR`515 37% |=== |	VAL`555 2% | |	
LEU`516 30% |== |	GLU`556 52% |===== |	
SER`517 39% |=== |	LYS`557 66% |====== |	
GLU`518 45% |==== |	CYS`558 4% | |	
LYS`519 60% |===== |	CYS`559 49% |==== |	
GLU`520 23% |== |	LYS`560 65% |====== |	

3.2. Synthesis and characterization of brush-1 to brush-4

3.2.1. MALDI-ToF mass spectra

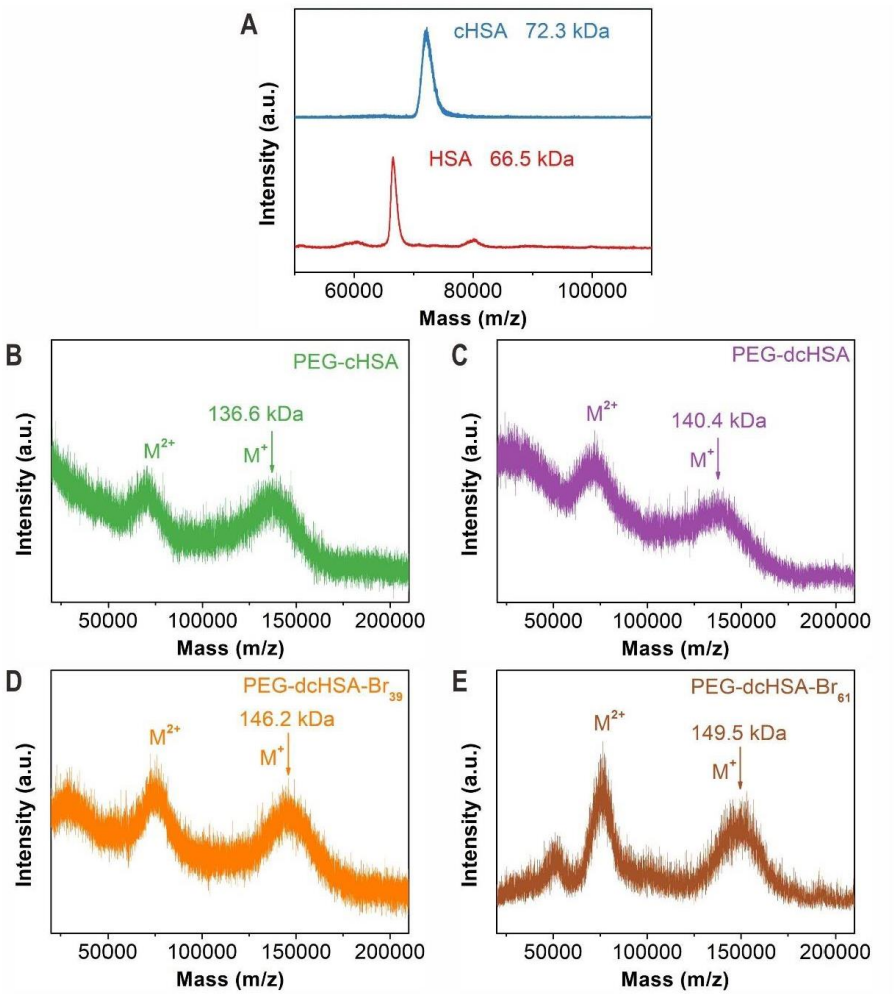

Figure S2. MALDI-ToF mass spectra of (A) HSA and cHSA, (B) PEG-cHSA, (C) PEG-dcHSA, as well as two macroinitiators (D) PEG-dcHSA-Br_{39} and (E) PEG-dcHSA-Br_{61}.

3.2.2. Stability of brush-1 to brush-4

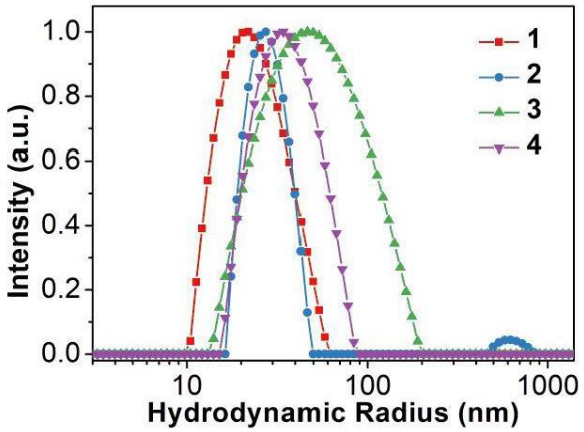

Figure S3. Size distribution of **brush-1** to **brush-4** after storage at 4 °C for two months measured by DLS.

As shown in Figure S3, the sizes of brush polymers (**brush-1** to **brush-4**) did not change during storage and they remained stable even in water solution for more than two months at 4 °C suggesting that they could be stored at low and elevated temperatures without the formation of stable aggregates and precipitates.

3.2.3. Thermo-responsiveness of the brush polymer

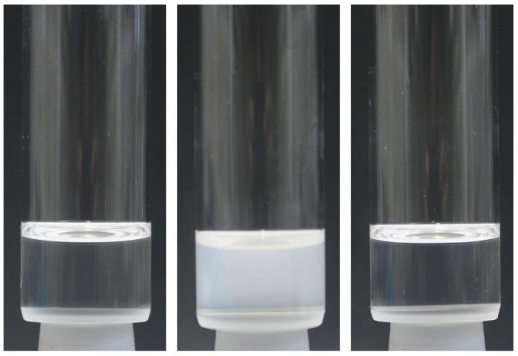

Figure S4. Digital images showing the thermal responsiveness of **brush-3**.

Brush-3 reveals high solubility in water at 25 °C. Upon temperature increase to 65 °C, the solution turned turbid immediately (Figure S4). This lower critical solution temperature (LCST) is consistent with other PMOEGMA polymers based on the monomer with a molecular weight of 300 g mol^{-1}.[6] Importantly, this behavior is fully reversible and the solution became transparent when the temperature was again decreased to 60 °C underlining that individual brush polymers were recovered and no permanent aggregation occurred. Such reversible responsiveness of the brush polymers also provides interesting future opportunities, e.g. to control their self-assembly.

3.2.4. Supplementary TEM characterization of brush polymers

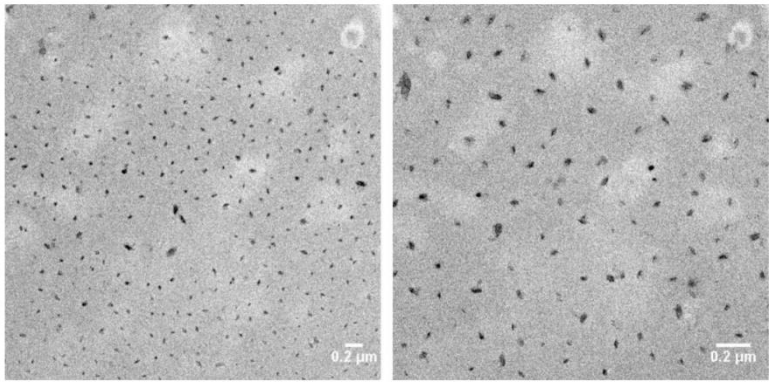

Figure S5. Additional TEM images for the statistical analysis of **brush-1**.

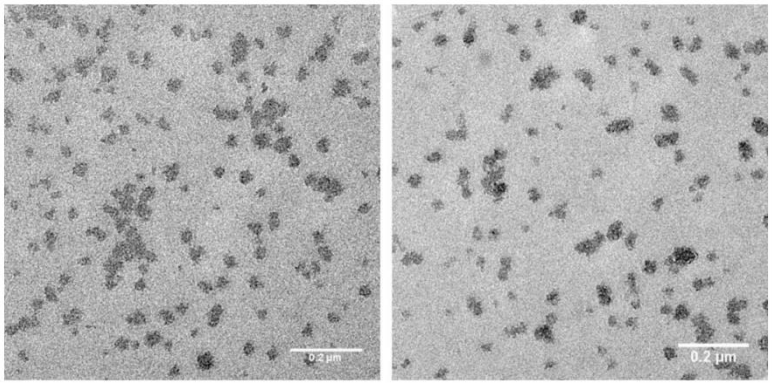

Figure S6. Additional TEM images for the statistical analysis of **brush-2**.

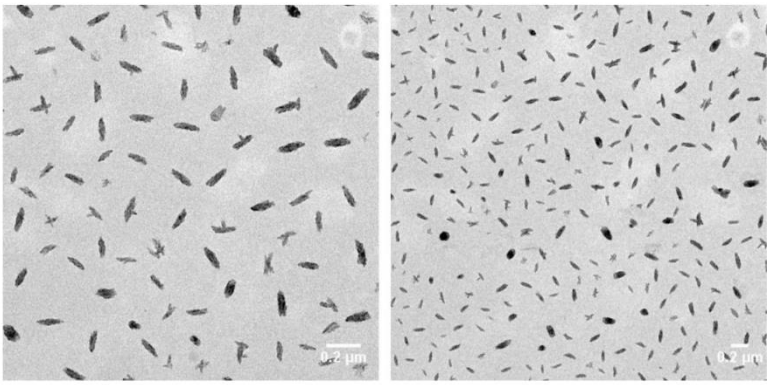

Figure S7. Additional TEM images for the statistical analysis of **brush-3**.

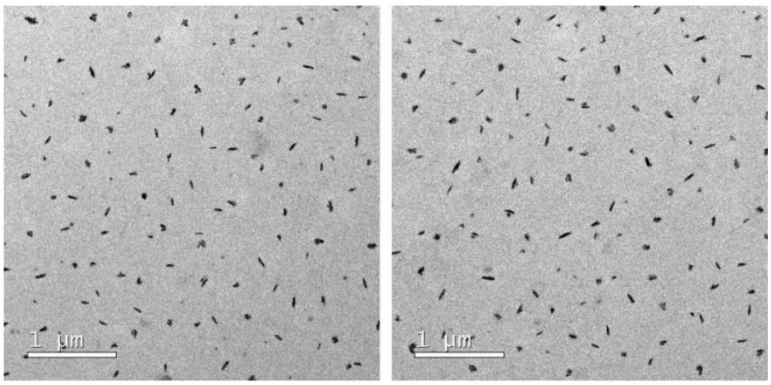

Figure S8. Additional TEM images for the statistical analysis of **brush-4**.

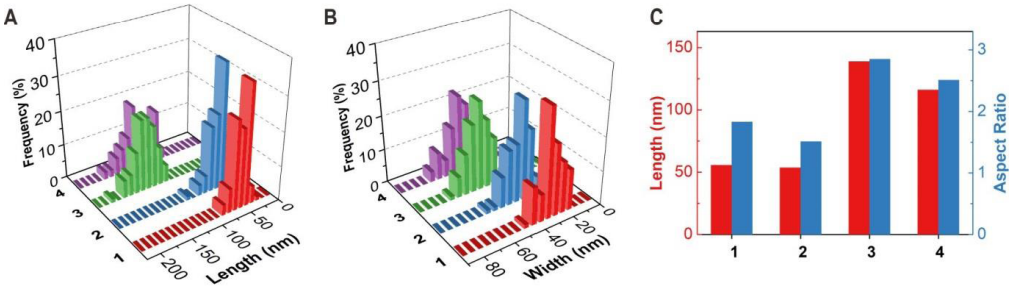

Figure S9. (A, B) Statistic analysis of length distribution (A) and width distribution (B) of **brush-1** to **brush-4**. (C) Comparison of the average length and the aspect ratio of **brush-1** to **brush-4**.

Based on TEM images in Figure 2E-J and Figures S5-S8, statistical analysis was performed for **brush-1** to **brush-4** using ImageJ software. For each polymer sample, the length and width of 100 brush polymers were analyzed based on their length (Figure S9A) and width (Figure S9B) distributions. The average lengths and aspect ratios of these structures were plotted in Figure S9C. From this graph, **brush-3** with the highest density and length of the PMOEGMA side chains displayed an average length of 139 nm and an aspect ratio of 2.85:1. **Brush-4** providing comparable PMOEGMA side chain length but lower chain density reveals an average length of 116 nm and a slightly lower aspect ratio of 2.51:1. In comparison, much lower values were obtained for **brush-1** and **brush-2** with shorter side chains, revealing average lengths of ~55 nm and aspect ratios of ~1.7:1. These results clearly indicate that architectures, molecular weights and contour lengths of bottlebrush polymers could be controlled within a wide range by simply tuning initiator densities along the polypeptide backbone or varying the polymerization conditions.

3.2.5. Supplementary light scattering analysis of brush polymers

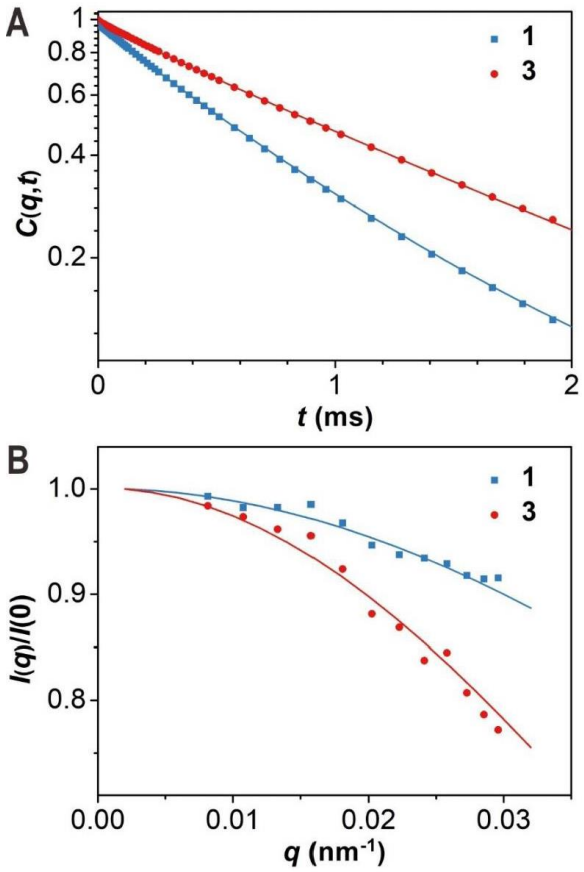

Figure S10. (A) Relaxation functions $C(q,t)$ for the translational diffusion dynamics in aqueous solution of **brush-1** (blue filled squares) and **brush-3** (red filled circles) at 20°C at two scattering wave vectors (q = 0.011 nm^{-1}). The intensities of **brush-1** (blue filled squares) and **brush-3** (red filled circles) are shown in (B). The solid lines denote the representation of the form factor of a solid prolate ellipsoid (**brush-1**: a = 26 nm, b = 20 nm; **brush-3**: a = 38 nm, b = 34 nm).

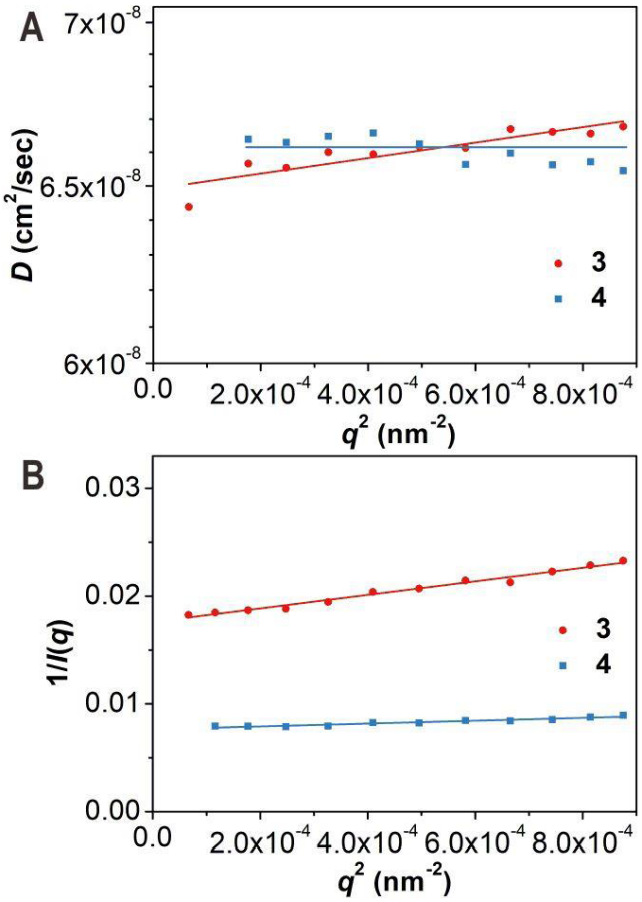

Figure S11. Diffusion coefficients and $1/I(q)$ versus q^2 for **brush-3** (red filled circles) and **brush-4** (blue filled squares) are shown in the (A) and (B), respectively.

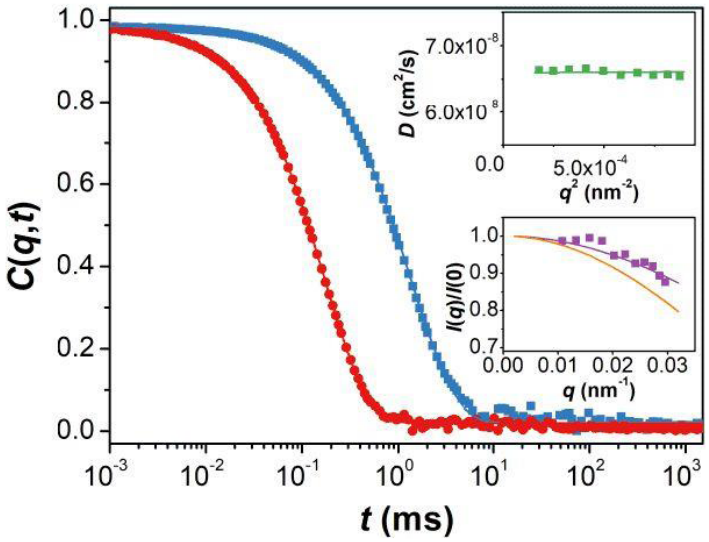

Figure S12. Relaxation functions $C(q,t)$ for the translational diffusion dynamics in aqueous solution of **brush-4** (1 mg mL^{-1}) at 293 K at two scattering wave vectors (blue filled squares, q = 0.011 nm^{-1} and red filled circles, q = 0.030 nm^{-1}) represented by a single exponential decay (solid lines). Upper inset: The diffusion coefficient, D as a function of q^2 with the solid green line indicating a linear representation. Lower inset: Normalized light scattering intensity $I(q)/I(0)$ as a function of q where the purple solid line denotes the representation by the form factor of a solid prolate ellipsoid with semi-axes, a = 28 nm and b = 20 nm. The yellow line indicates the ellipsoid form factor using a = 35 nm and b = 29 nm in case **brush-4** would conform to a brush configuration (Figure S13).

S33

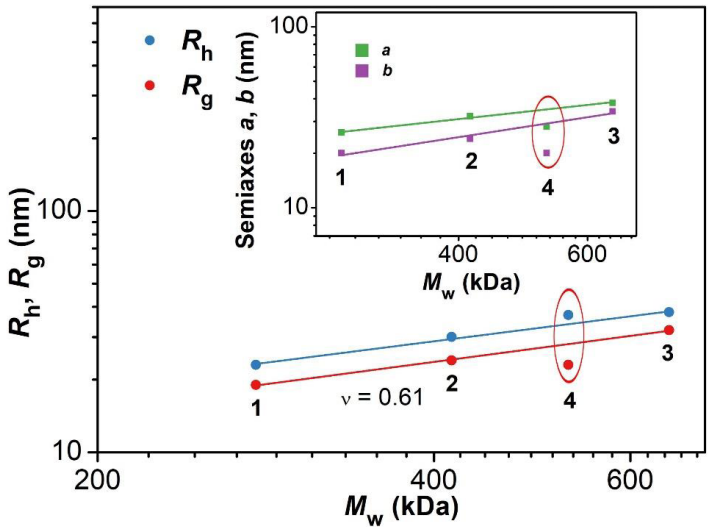

Figure S13. Experimental DLS/SLS data: double logarithmic plot of the hydrodynamic radius, R_h (blue filled circles) and the radius of gyration, R_g (red filled circles) for **brush-1** to **brush-4** as a function of the corresponding molecular weight M_w. Solid lines represent the scaling $R_h \sim M_w^{0.6}$. Inset: The semi-axes, a (green filled squares), b (purple filled squares), of a prolate ellipsoid as a function of M_w. The scaling for a and b is 0.44 and 0.62, respectively. The encircles points in the main plot and the inset deviate from the reported scaling behavior.

3.3. Simulation details and further analysis

To study the structural behavior of brush polymers with different side chain lengths and grafting densities (as shown in Table S2), we have performed molecular dynamics simulation of an implicit solvent generic bead-spring model.[7] In this model, individual monomers of in a polymer interact with each other via a 6–12 Lennard–Jones (LJ) potential. Furthermore, to model the bonded connectivity, adjacent monomers in a polymer are connected via an additional finitely extensible nonlinear elastic potential (FENE). The parameters are chosen such that a reasonably large time step can be chosen. The results are presented in units of the LJ interaction energy ε, LJ length unit σ and unit of mass m. This leads to a time unit of $\tau = \sigma(\frac{m}{\varepsilon})^{1/2}$. The specific choice of the model is motivated by the fact that we want to address rather generic polymer structural properties, without attempting to complicate our model system with specific chemical details.

Table S2. Details for molecular simulation.

brush polymer	M_w/kDa	backbone number	side chain number	repeating units of side chains
brush-1	277	585	61	7
brush-2	415	585	61	15
brush-3	650	585	61	27
brush-4	528	585	39	33

We use simplified replica of the experimental brush polymer system. Here the experimental backbone sequence of hydrophobic and hydrophilic residues (see Figure S14) are modeled with the standard Lennard-Jones (LJ) interactions, where interaction between two hydrophobic residues is chosen as attractive with interaction strength of $2k_BT$ and a cutoff of 2.5σ. The interaction between hydrophilic units is modeled as the repulsive LJ with a cutoff of $2^{1/6}\sigma$ and interaction strength of k_BT. This ensures that the native structure of bare backbone is well reproduced in our generic simulations, as known from experimental backbone structure. The backbone sequence used as an input in our simulations is shown in Figure S14. To model the

hydrophilic side chains, we again use repulsive LJ interaction. Note that in our simplified model, a one-to-one monomer mapping is done for the backbone chain.

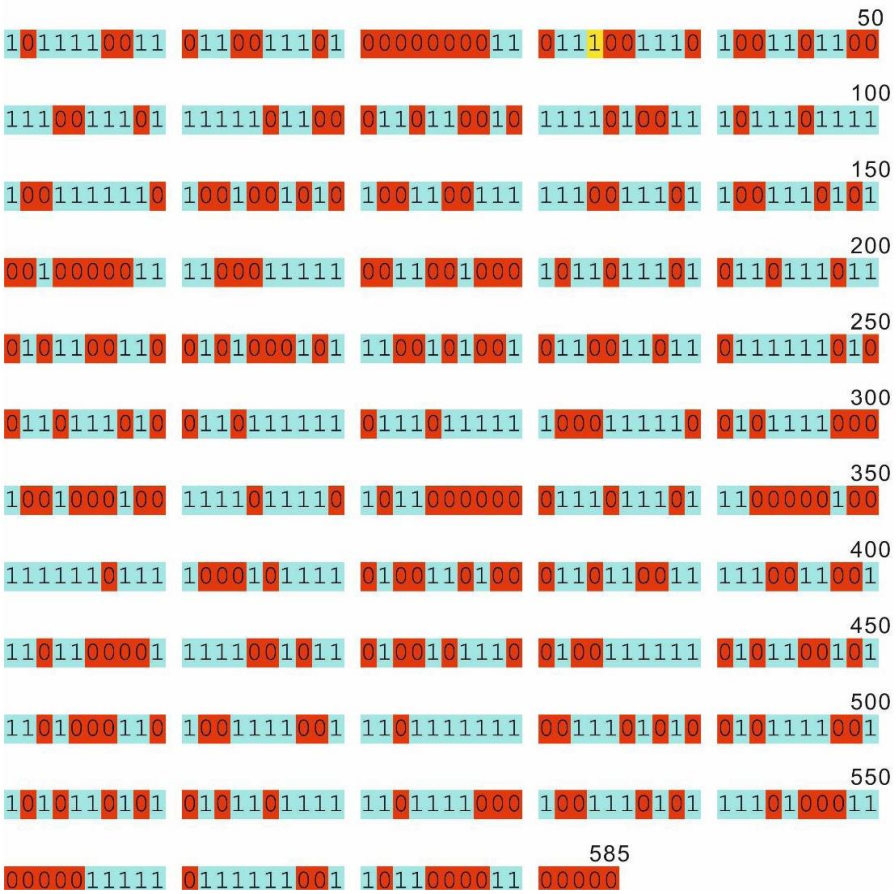

Figure S14. The hydrophobic-hydrophilic pattern of amino acid sequence of HSA for molecular simulation. Hydrophilic amino acids are represented as number "1" and hydrophobic acids are number "0" in the simulation.

We consider a chain of length $N_1 = 585$, the same as number of residues in the backbone of the experimental system. The side chain lengths and the grafting densities are again taken to be the same as the experimental system. The equations of motion are integrated using a velocity Verlet algorithm with a time step $\delta t = 0.01\tau$. The simulations were usually equilibrated for 10^7 MD time steps. The measurements are typically observed over another 5×10^9 MD steps. These values are at least one order of magnitude larger than the typical

chain end-to-end relaxation time. During this time, observables such as the gyration radius R_g and static structure factor $S(q)$ are calculated. The temperature is set using a Langevin thermostat with damping constant $\gamma = 1.0\tau^{-1}$ and the temperature is set to 1 ε/k_B.

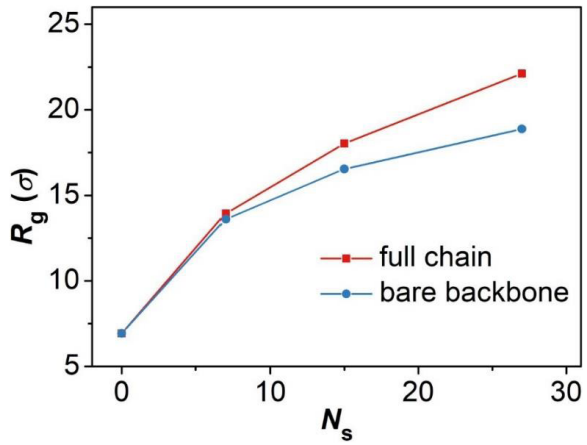

Figure S15. Polymer gyration radius R_g as a function of side chain length N_s for a given grafting density where a backbone is grafted with 61 side chains (see Table S2). Results are shown for bare backbone and also for the full brush polymer chain.

In Figure S15 we show simulation results of R_g values as a function of side chain length N_s for a given grafting density, where a backbone is grafted with 61 side chains. The data is shown for only bare backbone size and also for the full chain. As expected, a chain becomes more swollen with increasing N_s.

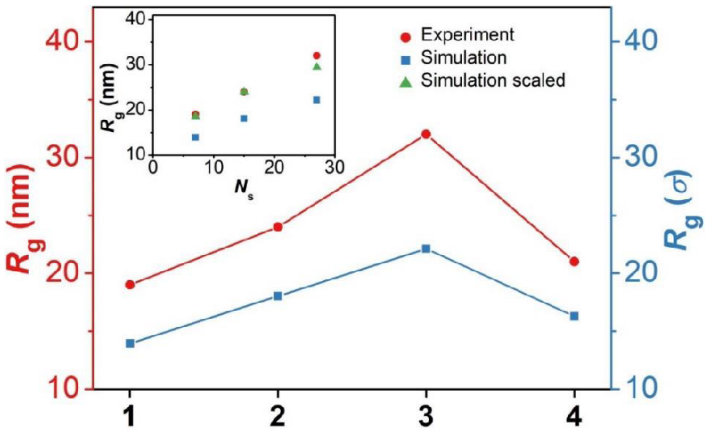

Figure S16. A comparative plot of gyration radius R_g obtained from experiments and simulations for all four brush polymer samples (**brush-1** to **brush-4**). Inset shows the same R_g with changing side chain length N_s for a given grafting density where the backbone is grafted with 61 side chains.

In the main panel of Figure S16 we present a comparative experimental and simulation data of R_g for four different bottle brush systems. It can be appreciated that rather simplified simulation model reproduces the correct trend observed in experiments. Not only that we have the same trend, simulations also give same scaling of total R_g with the side chain length N_s (see the inset of Figure S16). Interestingly, a simple shifting of the simulation data (green triangle) by a factor of ~1.33 gives a rather convincing master curve, i.e. $R_g^* \sim 1.33\ R_g$. While we do not have a direct evidence of this shifting parameter, we use it as a match between chemical specific experimental and chemically independent generic simulation data.

3.4. Synthesis and characterization of brush-5

3.4.1. Schematic illustration for the synthesis of brush-5

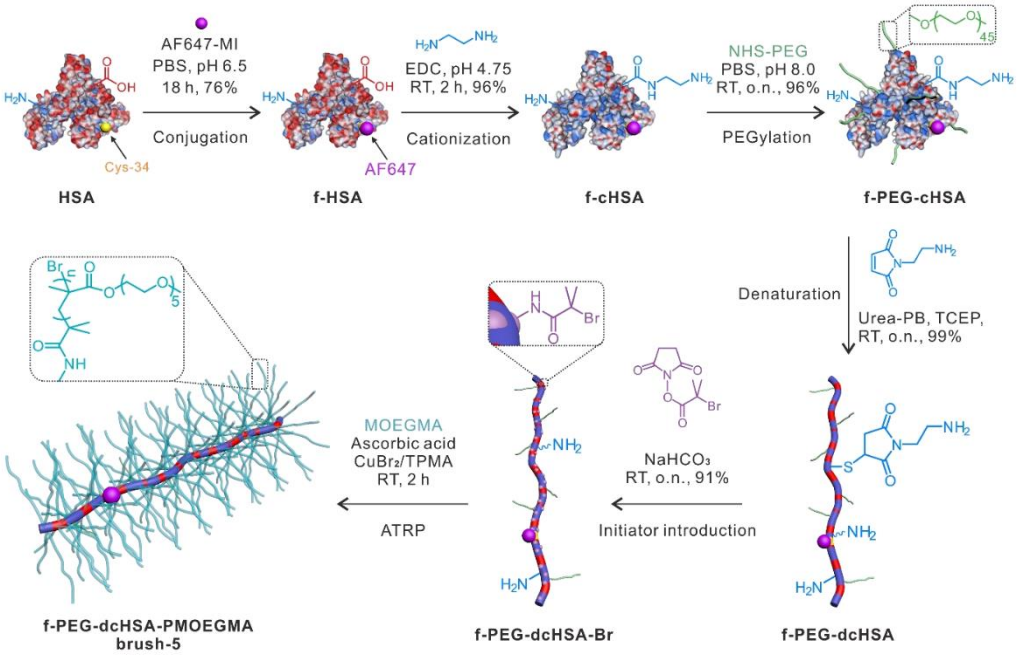

Figure S17. Schematic illustration for the synthesis of the brush polymer site-specifically functionalized with AF647 (**brush-5**).

3.4.2. MALDI-ToF mass spectra

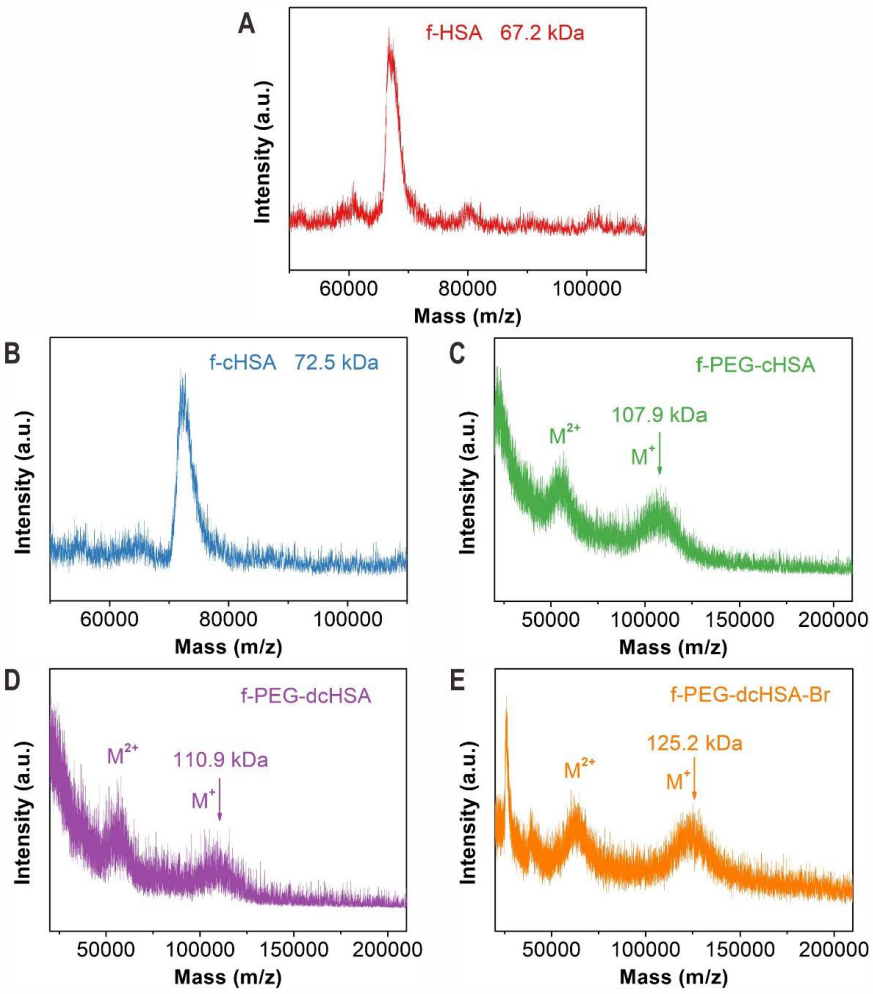

Figure S18. MALDI-ToF mass spectra of (A) f-HSA, (B) f-cHSA, (C) f-PEG-cHSA, (D) f-PEG-dcHSA, and (E) the AF647-labeled fluorescent macroinitiator f-PEG-dcHSA-Br.

3.4.3. Characterization of brush-5

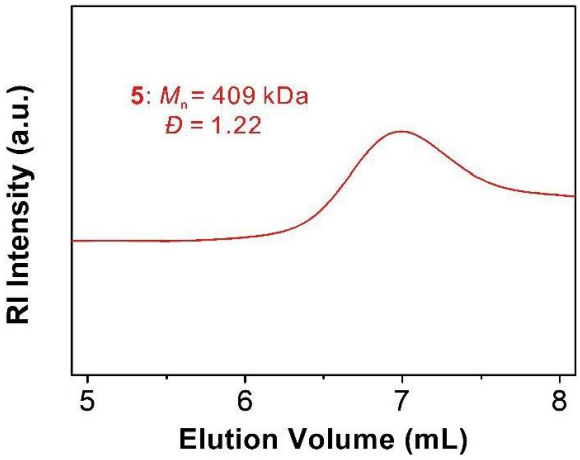

Figure S19. GPC elution curve of **brush-5**.

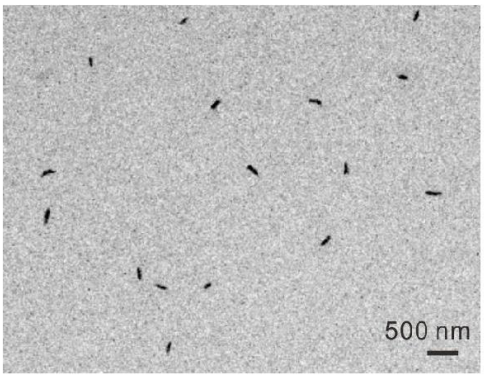

Figure S20. TEM image of **brush-5**.

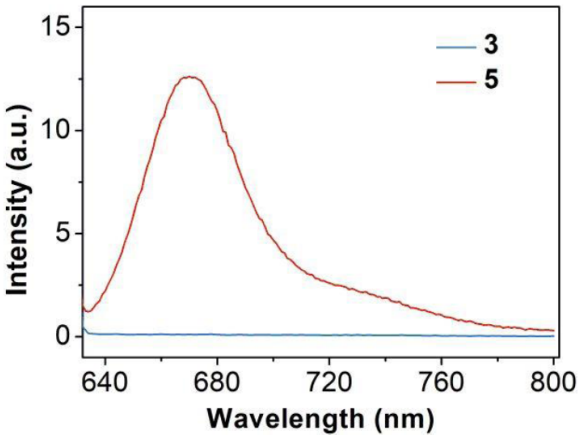

Figure S21. Comparison of fluorescent spectra of **brush-3** and **brush-5**. The characteristic peak of AF647 in the spectrum of **brush-5** confirms the successful introduction of the fluorescent dye.

3.4.4. FCS characterization and analysis

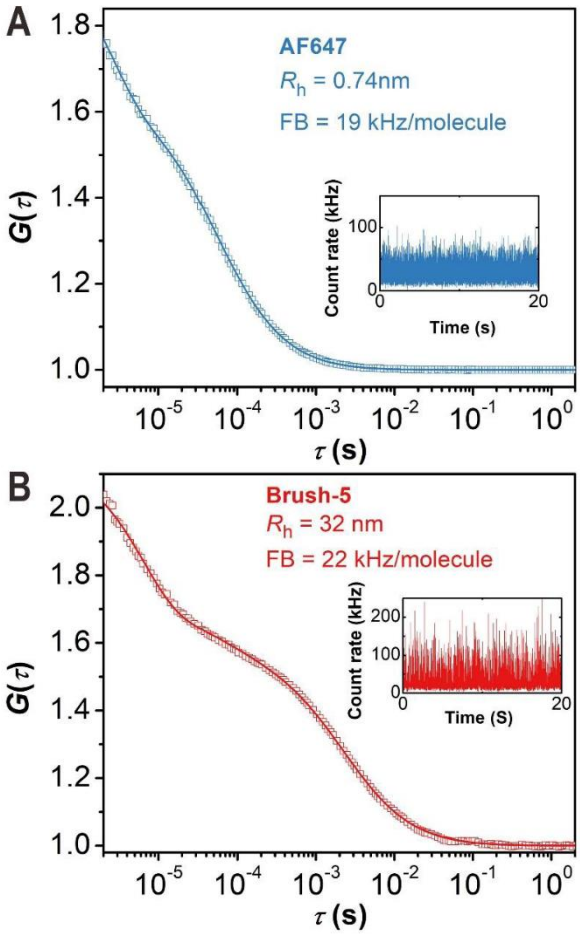

Figure S22. FCS autocorrelation curves (symbols) measured in ~2 nM aqueous solutions of AF647 (A) and the AF647-labeled polymer **brush-5** (B). The solid lines represent the corresponding fits with Equation S10. The insets show the respective intensity time trace plots.

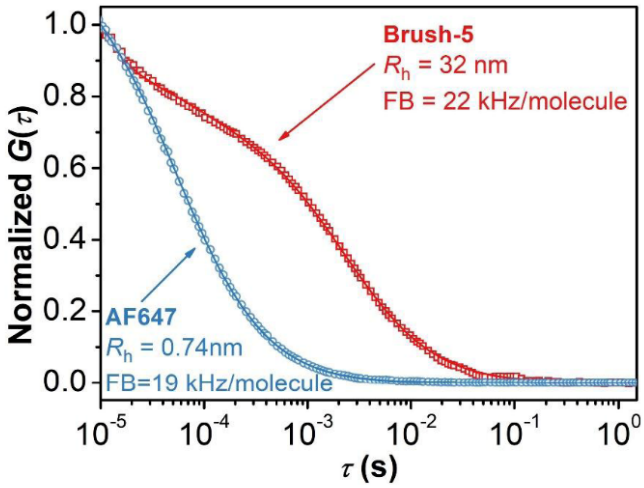

Figure S23. Normalized FCS autocorrelation curves measured in ~ 2 nM aqueous solutions of AF647 (blue circles) and the **brush-5** (red squares). The solid lines represent the corresponding fits with Equation S10. The fits yield values of $R_{h,\,AF647} \approx 0.74$ nm and $FB_{AF647} = 19$ kHz/molecule for the hydrodynamic radius and the fluorescent brightness of the individual AF647 molecules. The corresponding values for **brush-5** were $R_{h,\,\mathbf{brush\text{-}5}} \approx 32$ nm and $FB_{\mathbf{brush\text{-}5}} = 22$ kHz/molecule. The very similar fluorescent brightness values for both systems indicate that only one AF647 molecule is attached to each brush molecule.

3.5. Synthesis and characterization of biotin-brush-6 and biotin-brush-7

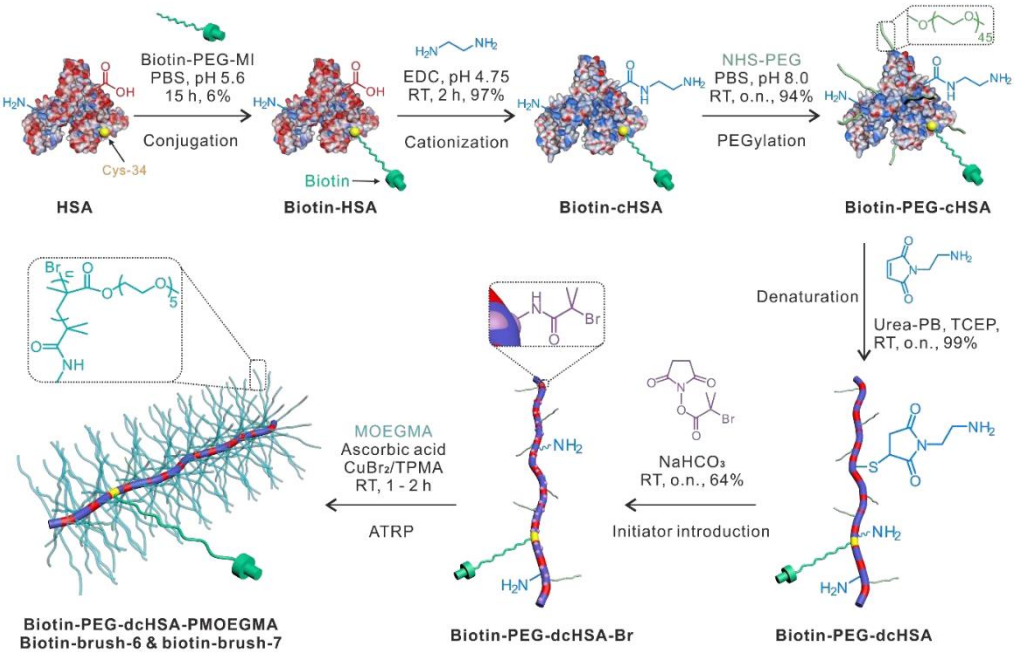

Figure S24. Schematic illustration for the synthesis of protein-templated brush polymers site-specifically functionalized with biotin (**biotin-brush-6** and **biotin-brush-7**).

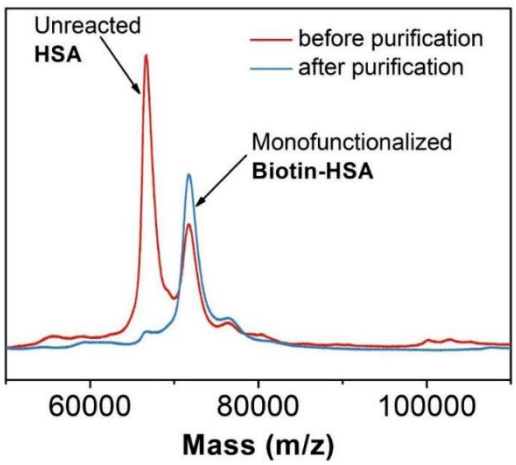

Figure S25. Comparison of the MALDI-ToF mass spectra of biotin-HSA before and after purification by a column composed of Thermo Scientific Pierce Monomeric Avidin Agarose.

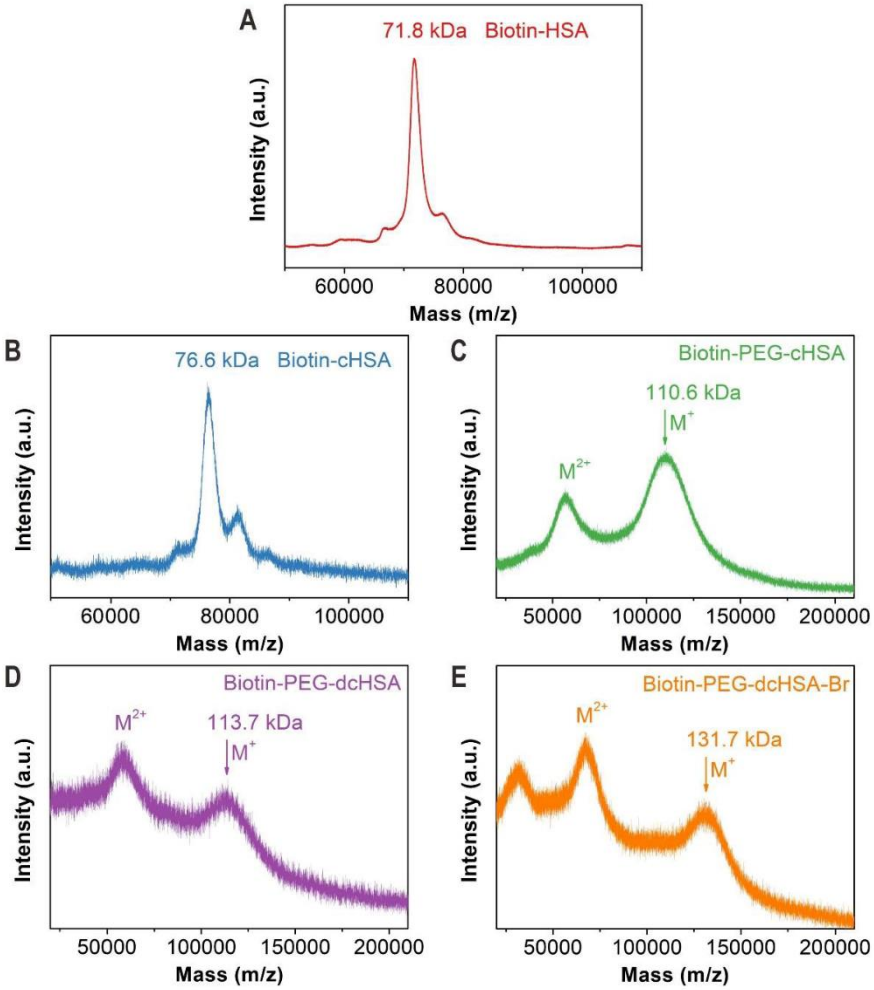

Figure S26. MALDI-ToF mass spectra of (A) biotin-HSA, (B) biotin-cHSA, (C) biotin-PEG-cHSA, (D) biotin-PEG-dcHSA, and (E) the biotin-functionalized macroinitiator biotin-PEG-dcHSA-Br.

3.6. Synthesis and characterization of biotin-brush-8

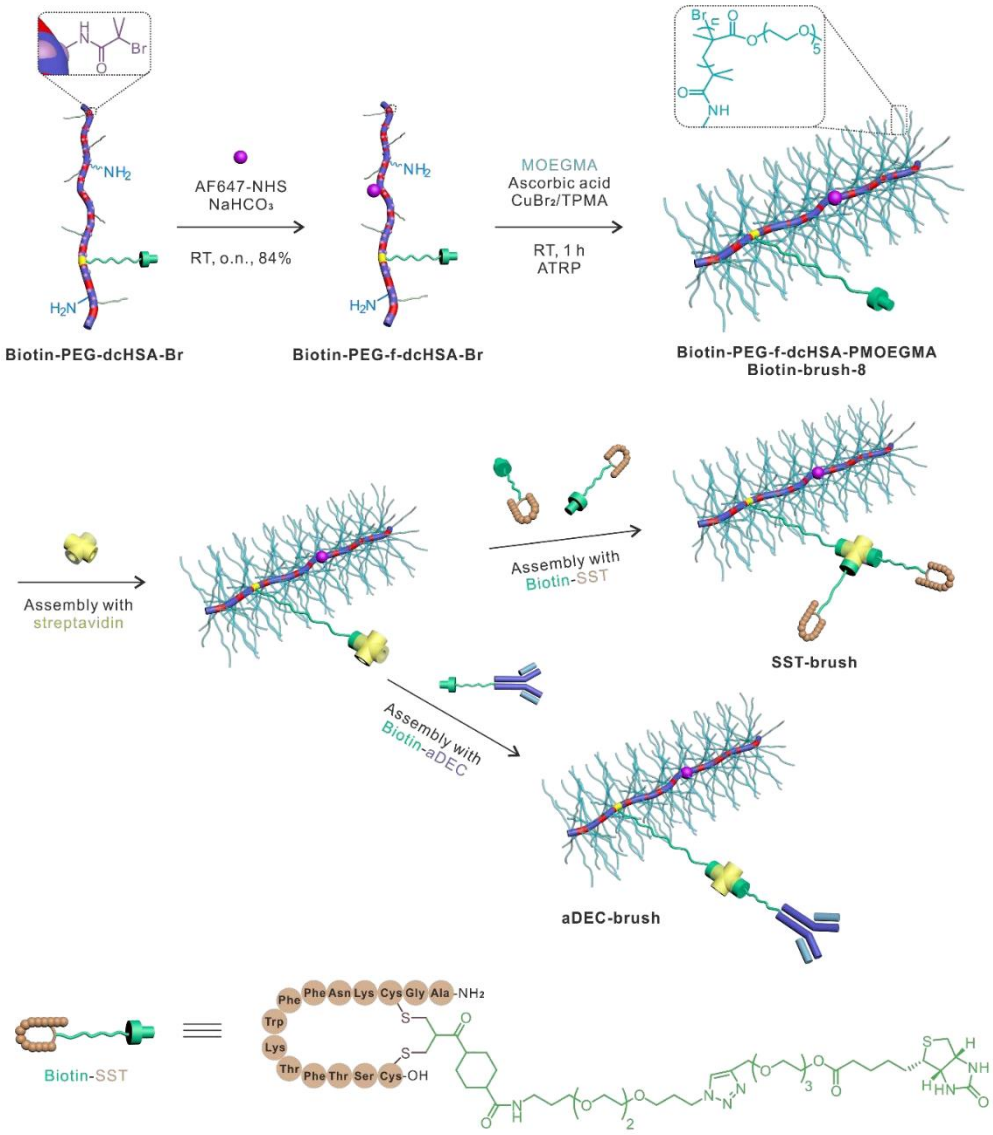

Figure S27. Synthesis of the protein-templated fluorescent brush polymer site-specifically functionalized with biotin (**biotin-brush-8**) and its stepwise assembly with (1) streptavidin and (2) biotin-SST or biotin-aDEC.

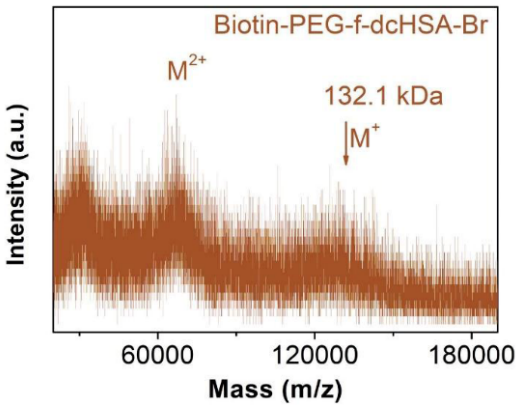

Figure S28. MALDI-ToF mass spectrum of biotin-functionalized fluorescent macroinitiator biotin-PEG-f-dcHSA-Br.

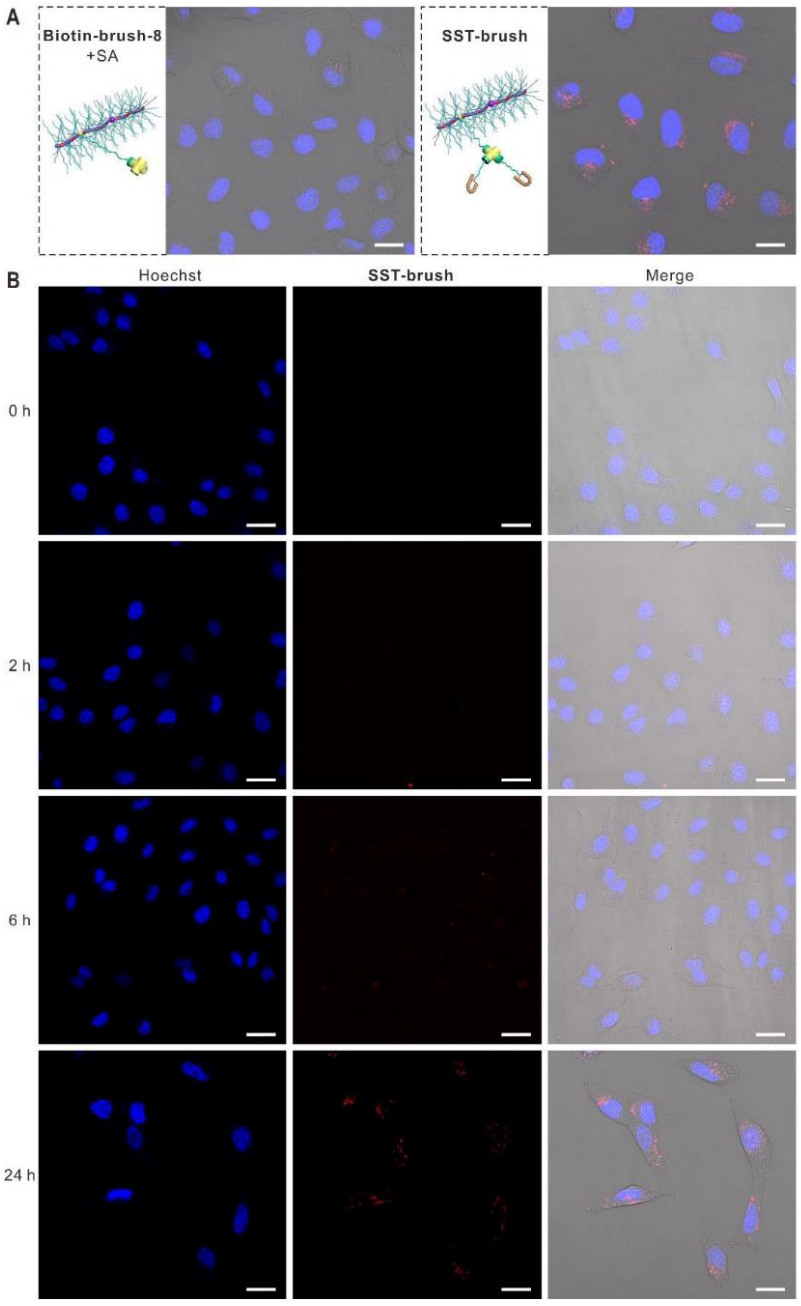

Figure S29. (A) Confocal laser scanning microscopy images showing the cellular uptake of **biotin-brush-8** after assembly with SA (left) and SA/Biotin-SST yielding SST-brush (right) after 24 h. Cellular uptake by A549 cells is only observed after the assembly of Biotin-SST. (B) Time lapse study at 2 h, 6 h and 24 h of 500 nM of SST-brush at 37 °C, 5% CO_2. Nuclei are visualized by Hoechst. Scale bars: 20 μm.

S49

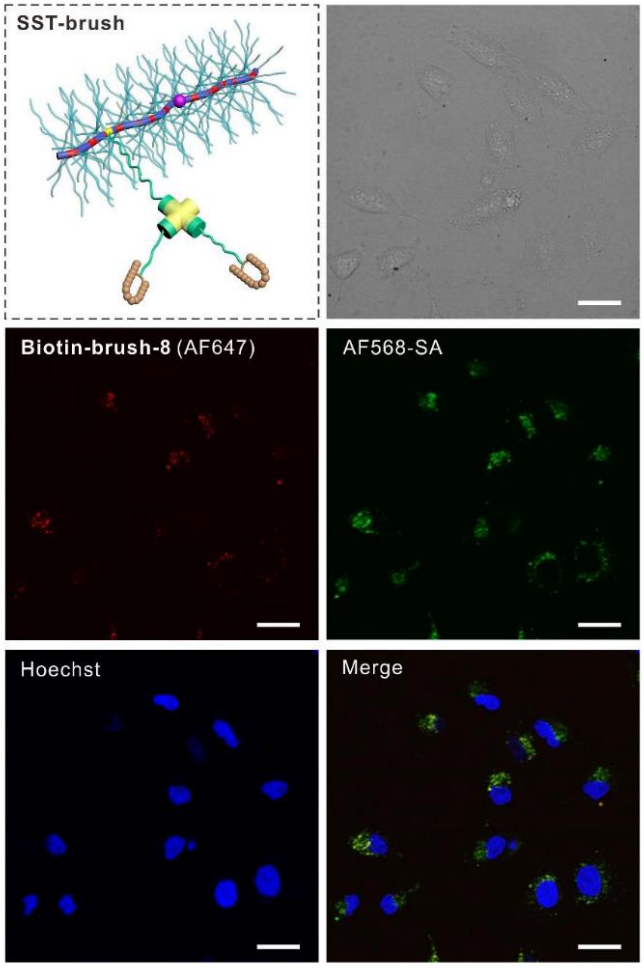

Figure S30. Confocal laser scanning microscopy images showing the cell internalization of SST-brush that has been labeled with AF647 (**biotin-brush-8** labeled with AF647) at the polypeptide backbone. Colocalization of AF568-SA and the brush polymer after 24 h were observed indicating that the SST-brush remained intact inside the A549 cells. Scale bars: 20 μm.

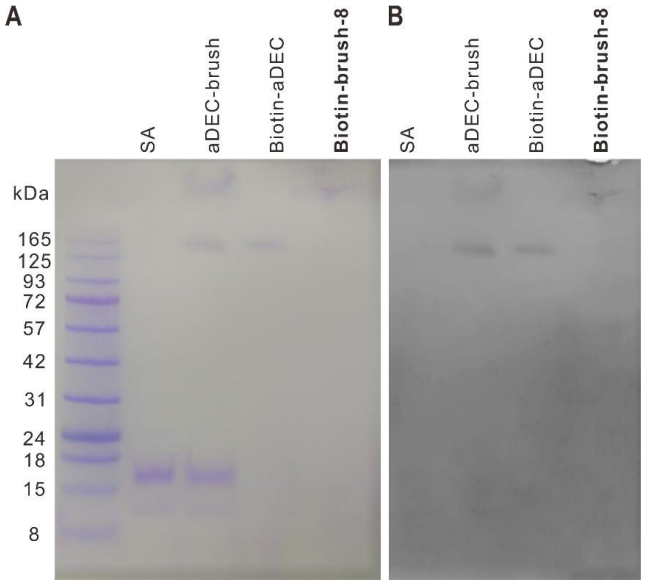

Figure S31. SDS-PAGE with coomassie staining (A) and western blot with chemiluminescence detection of SA-HRP (B) results, showing the assembly of **biotin-brush-8** with a biotinylated model antibody (biotin-aDEC) and SA generating aDEC-brush. Under heating conditions, the aDEC-brush complex can be separated in its consisting components to be visualized by coomassie stain (A) or SA-HRP (B) to detect biotinylated molecules.

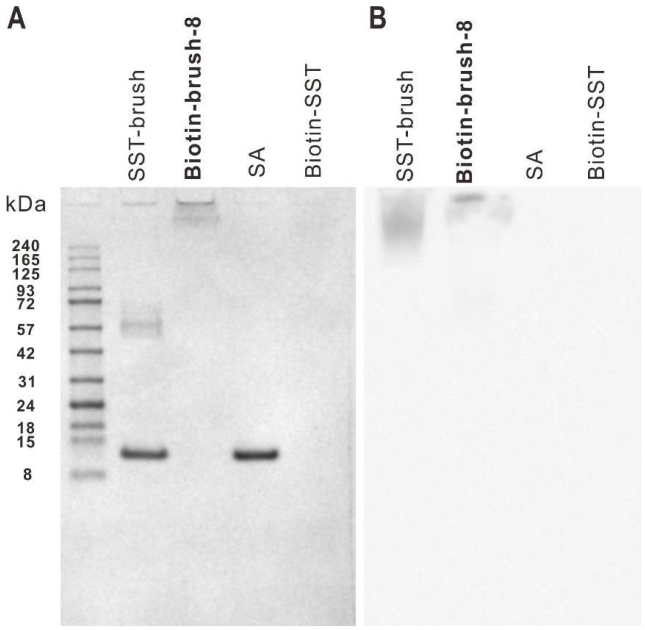

Figure S32. SDS-PAGE after coomassie staining (A) and western blot with chemiluminescence detection of SA-HRP (B) results, showing the assembly of **biotin-brush-8** with biotinylated SST and SA generating SST-brush. Under heating conditions, the SST-brush complex can be separated in its consisting components to be visualized by coomassie stain (A) or SA-HRP (B) to detect biotinylated molecules. The cyclic peptide SST consist of only 14 amino acids, which were not enough for a sufficient staining with coomassie dye. Additionally, the small size of the SST prevented retention on the nitrocellulose membrane with a pore size of 0.2 µm.

IV. References

1. Wang, T.; Wu, Y. Z.; Kuan, S. L.; Dumele, O.; Lamla, M.; Ng, D. Y. W.; Arzt, M.; Thomas, J.; Mueller, J. O.; Barner-Kowollik, C.; Weil, T., A Disulfide Intercalator Toolbox for the Site-Directed Modification of Polypeptides. *Chem-Eur J* **2015,** *21* (1), 228-238.

2. Zhao, J. Q.; Pearce, E. M.; Kwei, T. K.; Jeon, H. S.; Kesani, P. K.; Balsara, N. P., Micelles Formed by a Model Hydrogen-Bonding Block-Copolymer. *Macromolecules* **1995,** *28* (6), 1972-1978.

3. Berne, B. J.; Pecora, R., *Dynamic Light Scattering*. John Wiley: New York, 1976.

4. Rigler, R.; Elson, E. S., *Fluorescence Correlation Spectroscopy: Theory and Applications*. Springer Verlag: New York, 2001; p 487.

5. Kapusta, P., Absolute Diffusion Coefficients: Compilation of Reference Data for FCS Calibration. *Application note*.

6. Lutz, J. F., Polymerization of oligo(ethylene glycol) (meth)acrylates: Toward new generations of smart biocompatible materials. *J Polym Sci Pol Chem* **2008,** *46* (11), 3459-3470.

7. Kremer, K.; Grest, G. S., Dynamics of Entangled Linear Polymer Melts - a Molecular-Dynamics Simulation. *J Chem Phys* **1990,** *92* (8), 5057-5086.

5.2 Denatured proteins as a novel template for the synthesis of well-defined, ultra-stable and water-soluble metal nanostructures for catalytic applications

Chaojian Chen,* David Yuen Wah Ng, and Tanja Weil*

* Corresponding authors

Invited article published in *J. Leather Sci. Eng.* **2020**, *2*, 7.

Contribution of the respective authors:

Chaojian Chen: Design of the project, conduction of the experiments, results analysis and interpretation, figure design and writing of the manuscript.
David Yuen Wah Ng: Discussion on the results, correcting the manuscript.
Tanja Weil: Acquiring funding for the project, design and discussion of the concept and results, correcting the manuscript.

Chen et al. Journal of Leather Science and Engineering (2020) 2:7
https://doi.org/10.1186/s42825-020-00020-5

Journal of Leather Science and Engineering

RESEARCH Open Access

Denatured proteins as a novel template for the synthesis of well-defined, ultra-stable and water-soluble metal nanostructures for catalytic applications

Chaojian Chen[1,2*], David Yuen Wah Ng[1] and Tanja Weil[1,2*]

Abstract

The templated synthesis of noble metal nanoparticles using biomass, such as proteins and polysaccharides, has generated great interest in recent years. In this work, we report on denatured proteins as a novel template for the preparation of water-soluble metal nanoparticles with excellent stability even after high speed centrifugation or storage at room temperature for one year. Different noble metal nanoparticles including spherical gold and platinum nanoparticles as well as gold nanoflowers are obtained using sodium borohydride or ascorbic acid as the reducing agent. The particle size can be controlled by the concentration of the template. These metal nanoparticles are further used as catalysts for the hydrogenation reaction of *p*-nitrophenol to *p*-aminophenol. Especially, spherical gold nanoparticles with an average size of 2 nm show remarkable catalytic performance with a rate constant of 1.026×10^{-2} L s^{-1} mg^{-1}. These metal nanoparticles with tunable size and shape have great potential for various applications such as catalysis, energy, sensing, and biomedicine.

Keywords: Unfolded proteins, Gold nanoparticles, Gold nanoflowers, Platinum nanoparticles, Biotemplated synthesis, Catalysis

1 Introduction

Due to their high surface-to-volume ratios and quantum size effects, noble metal nanoparticles exhibit distinct optical, thermal, and chemical properties from their bulk counterparts [1, 2]. These nanoparticles with controlled sizes and shapes have received tremendous attention in a myriad of areas including catalysis, energy, optics, sensing, biomedicine, and leather industry [3–7]. For example, gold nanoparticles (AuNPs) have shown remarkable catalytic activities for many organic transformations such as addition to carbon–carbon bonds, oxidation of carbon monoxide and alcohols, selective hydrogenations, and carbon–carbon coupling reactions [8–10]. However, metal nanoparticles aggregate easily which greatly hinders their usage in catalysis, biomedicine, and many other fields. To solve this problem, a variety of substances including thiol-containing surfactants and polymers have been developed for surface functionalization of metal nanoparticles with long-term stability and dispersity [11–14]. It should be noted that this strategy may involve tedious synthetic and purification steps, harsh reaction conditions, and the use of toxic organic solvents [15, 16].

Recently, the environmentally friendly synthesis and stabilization of metal nanoparticles using biopolymers have become a trend [15–19]. For instance, chitosan [20–22], cellulose [23], gelatin [24], bovine serum albumin [25, 26], and collagen that can be extracted from leather products [27], have been reported as templates for the synthesis of gold nanoparticles at room temperature. In the past decade, our group has developed a facile synthesis route to unfold

* Correspondence: chenc@mpip-mainz.mpg.de; weil@mpip-mainz.mpg.de
[1]Max Planck Institute for Polymer Research, Ackermannweg 10, 55128 Mainz, Germany
Full list of author information is available at the end of the article

native proteins including human serum albumin (HSA) and lysozyme to well-defined linear biopolymers [28, 29]. Such protein-derived polymers offer many fascinating characteristics such as biocompatibility, biodegradability, predetermined length, narrow size distribution, and a defined number of functional groups at distinct positions along the polypeptide backbone [30]. In addition, the conjugated PEG chains can reduce protein binding and prolong circulation time in the blood stream. Therefore, these protein-derived polymers are particularly attractive for biomedical applications and as templates for preparation of precision nanomaterials. For example, multifunctional nanoparticles have been constructed by coating these protein-derived biopolymers to the surface of quantum dots, gold nanostructures, and nanodiamonds [28, 31–33]. The resulting nanohybrids which display excellent stability and biocompatibility, have been successfully used in gene transfection, cell imaging, and cancer therapy [31, 32, 34].

In this work, we report on unfolded protein backbones that possess a large number of amino groups able to bind metal ions and using them to act as novel templates for the preparation of noble metal nanoparticles with controlled sizes and shapes. Two reducing agents, ascorbic acid and sodium borohydride, are used to control the shape, and the template concentration is discovered to control the size of nanoparticles. Anisotropic gold nanoflowers (AuNFs) as well as ultrasmall spherical AuNPs and platinum nanoparticles (PtNPs) with high water solubility, excellent stability and good biocompatibility have been obtained. The template is derived from natural polymers, and the whole process is conducted in aqueous solution at room temperature. Therefore, the route can be regarded as an environmentally friendly procedure. More significantly, the well-defined nanoparticles demonstrate excellent catalytic performances for the hydrogenation reaction of *p*-nitrophenol to *p*-aminophenol. Collectively, these metal nanoparticles prepared using the novel protein-derived template may find great potential in surface-enhanced Raman spectroscopy, photothermal therapy, catalysis, biomedicine, textiles, and functional coatings for leather products.

2 Experimental section

2.1 Materials

Human serum albumin (HSA, 96%), tris(2-carboxyethyl) phosphine hydrochloride (TCEP, ≥98%), *O*-[(*N*-succinimidyl)succinyl-aminoethyl]-*O*′-methylpolyethylene glycol (NHS-PEG, M_n ~ 2000), *p*-nitrophenol (99%), *N*-(2-aminoethyl) maleimide trifluoroacetate salt (MI-NH_2, 95%), *N*-(3-dimethylaminopropyl)-*N*′-ethylcarbodiimide hydrochloride (EDC·HCl, ≥98%), and L-ascorbic acid (≥99%) were purchased from Sigma-Aldrich and used without further treatment. Gold (III) chloride trihydrate ($HAuCl_4{\cdot}3H_2O$, ≥99.5%) was obtained from Carl Roth. Ethylendiamine (> 99%), urea (99.5%), hydrogen hexachloroplatinate (IV) hydrate ($H_2PtCl_6{\cdot}xH_2O$, 99.9%, 39% Pt), and ethylenediaminetetraacetic acid (EDTA, 98%) were purchased from Acros Organics and used as received. Sodium borohydride ($NaBH_4$, > 95%) was obtained from Fisher Chemical. All other solvents and salts were obtained from commercial suppliers and used as received.

2.2 Synthesis of cationic HSA (cHSA) [32, 34]

HSA (150 mg, 2.26 μmol) was dissolved in 15 mL of degassed ethylenediamine solution (2.5 M), and the pH was tuned to 4.75 by using HCl. After adding EDC·HCl (4 mmol, 766 mg) and stirring for two hours at room temperature, acetate buffer (1 mL, 4 M, pH 4.75) was added to terminate the reaction. The obtained reaction solution was purified twice with acetate buffer (100 mM, pH 4.75) and thrice with deionized water by ultracentrifugation using a Vivaspin 20 concentrator (MWCO 30 kDa). The resulting solution was lyophilized to afford the product as a white fluffy solid (160 mg, yield: 98%, MALDI-ToF MS: 72.3 kDa).

2.3 Preparation of PEGylated cHSA (PEG-cHSA) [32, 34]

cHSA (101 mg, 1.40 μmol) was firstly dissolved in degassed phosphate buffer (30 mL, 50 mM, pH 8.0). NHS-PEG (159.6 mg, 79.8 μmol) was dissolved in 0.6 mL of DMSO and then added into the cHSA solution. After stirring at room temperature for four hours, the reaction solution was purified five times with deionized water by ultracentrifugation using a Vivaspin 20 concentrator (MWCO 30 kDa). The resulting solution was lyophilized to obtain the product as a white fluffy solid (206 mg, yield: 90%). The MALDI-ToF MS indicates a molecular weight of 164.3 kDa which means on average 46 PEG chains were conjugated into each cHSA backbone.

2.4 Synthesis of denatured PEG-cHSA (PEG-dcHSA) [32, 34]

Urea-phosphate buffer with 50 mM phosphate buffer, 5 M urea and 2 mM EDTA (urea-PB, pH 7.4) was firstly prepared by dissolving urea (150.15 g, 2.5 mol), EDTA (292.24 mg, 1 mmol), $Na_2HPO_4{\cdot}7H_2O$ (5.4276 g, 25 mmol) and NaH_2PO_4 (0.5699 g, 25 mmol) in 0.5 L of Milli-Q water. Then, 80 mL of urea-PB was added in a 250 mL flask and degassed via bubbling by argon for five minutes. Followed PEG-cHSA (100 mg, 0.61 μmol) was dissolved and further stirred for 15 min. TCEP (9.0 mg, 31 μmol) was added and stirred for 30 min under argon flow. Lastly, MI-NH_2 (46 mg, 181 μmol) was added and stirred overnight under argon protection. The obtained reaction solution was purified three times with urea-PB and five times with deionized water by ultracentrifugation using a Vivaspin 20 concentrator (MWCO 30 kDa). The resulting solution was lyophilized to afford the product as a white fluffy solid (99 mg, yield: 96%, MALDI-ToF MS: 168.5 kDa).

2.5 Synthesis of AuNPs using $NaBH_4$ as the reducing agent

The molar ratio of $HAuCl_4$ to amino groups in PEG-dcHSA for the synthesis of AuNPs was tuned from 3:0 to 3:3. Take the molar ratio of 3:3 as an example, 1.5 mg of PEG-dcHSA was dissolved in 4.4 mL of Milli-Q water and then 0.5 mL of $HAuCl_4$ aqueous solution (2 mM) was added and stirred for one hour. Afterwards, 0.1 mL of freshly prepared $NaBH_4$ solution (100 mM) was added dropwise under vigorous stirring. The color of the solution changed immediately to yellow. After stirring for one more hour, the solution was measured by UV-vis spectrometry. The product was purified five times with deionized water by ultracentrifugation using a Vivaspin 6 concentrator (MWCO 30 kDa).

2.6 Synthesis of AuNFs using ascorbic acid as the reducing agent

For the preparation of AuNFs, the reducing agent solution (100 mM) was obtained by dissolving L-ascorbic acid (176.1 mg) in 10 mL of degassed Milli-Q water. Most procedures and conditions are the same with those used for the synthesis of AuNPs in section 2.5, and the only difference is that L-ascorbic acid was used to replace $NaBH_4$ as the reducing agent.

2.7 Synthesis of PtNPs using $NaBH_4$ as the reducing agent

The procedures for the synthesis of PtNPs are similar to those used for preparing AuNPs. H_2PtCl_6 solution (2 mM) was obtained by dissolving 10 mg $H_2PtCl_6{\cdot}xH_2O$ (39% Pt) in 10 mL Milli-Q water. The molar ratios of H_2PtCl_6 to amino groups in PEG-dcHSA were 3:2 and 3:0. The solutions were stirred overnight before use.

2.8 Catalytic reduction of *p*-nitrophenol to *p*-aminophenol

To a 20 mL glass bottle, 3 mL of freshly prepare *p*-nitrophenol aqueous solution (1 mM, pH = 12) and 15 mL of $NaBH_4$ aqueous solution (50 mM dissolved in Milli-Q water) were firstly added and gently shaken. Followed 1.2 mL of the mixed solution of $NaBH_4$ and *p*-nitrophenol was added into a vial and determined amounts of metal nanocatalysts were added and the reaction was monitored by UV-vis spectrometer. The absorbance at 400 nm is subtracted from that at 500 nm to correct for background absorption and then used to calculate the conversion and apparent rate constant (k_{app}). The conversion (C) is calculated using the following equation:

$$C = \frac{A_0 - A_t}{A_0} \times 100\%$$

where A_0 and A_t are the absorbance at time 0 and t. The apparent rate constant (k_{app}) is determined as the slope of $\ln(A_0/A_t)$ at 400 nm against the reaction time.

2.9 Characterization

UV-vis absorbance spectra were collected using a TECAN (Spark 20 M) microplate reader. The samples were added in a Greiner 96 flat transparent plate. The wavelength range was set from 250 to 800 nm. Matrix-assisted laser desorption/ionization time-of-flight (MALDI-ToF) mass spectrometry was performed on Bruker rapifleX spectrometer. Saturated solution of sinapinic acid dissolved in a 1:1 water/acetonitrile with 0.2% trifluoroacetic acid was used as the matrix solution and different concentrations of samples were measured. Transmission electron microscopy (TEM) samples were prepared by adding 4 μL of the metal nanoparticle solution onto a carbon-coated copper grid. After drying in air for 10 min, the remaining solution was removed by blotting with a filter paper. The measurement was conducted on a JEOL JEM-1400 TEM operating at an accelerating voltage of 120 kV. ImageJ software was used for the analysis of particle size.

3 Results and discussion

3.1 Unfolding native proteins to well-defined biopolymers

The synthesis of protein-derived biopolymer PEG-dcHSA and its application as a novel template for the preparation of metal nanoparticles are schematically illustrated in Fig. 1a. Firstly, the native protein HSA was cationized by converting carboxyl groups on the surface to primary amino groups. In order to prevent protein aggregation during the following denaturation step, short polyethylene glycol (PEG) chains with an average molecular weight of 2000 g mol^{-1} were introduced. These biocompatible PEG chains also afford PEG-cHSA with improved solubility and stability due to the steric effect between different chains. Subsequently, PEG-cHSA was unfolded in urea-phosphate buffer in the presence of TCEP as a reducing agent. In this step, urea could break the hydrogen bonds and other supramolecular forces. The 17 disulfide bridges in the 3D structure of HSA were also destroyed by TCEP, and the generated thiol groups were capped by MI-NH_2. Therefore, the number of primary amino groups was further increased, which resulted in better solubility and metal ion binding ability of PEG-dcHSA. MALDI-ToF mass spectra in Fig. 1b show the increase of molecular mass in each step, confirming the successful synthesis of the PEGylated linear polypeptide PEG-dcHSA.

3.2 Ultrasmall AuNPs prepared using $NaBH_4$ as the reducing agent

The protein-derived linear biopolymer PEG-dcHSA which possesses abundant primary amino groups that can bind various metal-containing anions was used as a template for the in situ synthesis of different metal nanoparticles. First, we investigated the templated

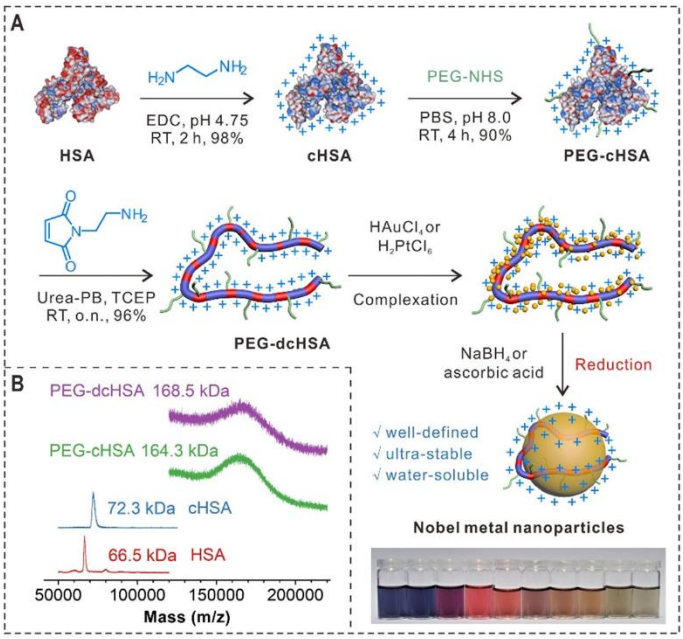

Fig. 1 **a** Schematic illustration for the preparation of denatured protein PEG-dcHSA and its application as a template for the synthesis of metal nanoparticles. **b** MALDI-ToF mass spectra showing the successful synthesis of PEG-dcHSA

synthesis of AuNPs using $NaBH_4$ as the reducing agent. In a typical procedure, PEG-dcHSA was dissolved in Milli-Q water and then mixed with $HAuCl_4$ aqueous solution for one hour. Subsequently, freshly prepared $NaBH_4$ solution was added dropwise under vigorous stirring. The reaction solution changed immediately to yellow, pink or red depending on the added amount of PEG-dcHSA. After stirring for one more hour, the product was purified by five ultracentrifugation cycles with deionized water using a Vivaspin 6 concentrator (MWCO 30 kDa). As PEG-dcHSA is a precision polymer derived from HSA, the average number of primary amino groups in PEG-dcHSA was calculated as 147 (see supplementary information for more details). The molar ratio of chloroauric acid ($HAuCl_4$) to amino groups in PEG-dcHSA was tuned from 3:0 to 3:3 by fixing the amount of $HAuCl_4$ and gradually increasing the amount of the denatured proteins. The details for the synthesis of AuNPs with different $HAuCl_4$/$-NH_2$ molar ratios are summarized in Table 1.

The reaction was very fast as indicated by the swift change of the solution color after adding the reducing agent. As displayed on the top panel of Fig. 2a, the color gradually shifts from red to light brown with the increased amount of denatured proteins. The UV-vis absorbance spectrum in Fig. 2b shows a characteristic peak at 512 nm for the sample without adding the template ($HAuCl_4$/$-NH_2$ molar ratio = 3:0). In contrast, the peaks of the other three samples are weaker and a blue shift is observed when the amount of PEG-dcHSA is increased, indicating reduction of size for these AuNPs [35, 36]. TEM was further used to directly observe the morphology of AuNPs and the results are displayed in Fig. 2c-k. We can see that AuNPs prepared under four different $HAuCl_4$/$-NH_2$ molar ratios all display good dispersity, narrow distributions, and spherical shapes. The AuNPs prepared with a $HAuCl_4$/$-NH_2$ molar ratio of 3:0 has an average diameter of 6.4 ± 2.2 nm. Ultrasmall AuNPs with the size of 2 ~ 5 nm were obtained when the denatured protein template was added to the reaction solutions. Increasing the added amount of PEG-dcHSA made the particle size smaller, which is consistent with the UV-vis spectra. Therefore, we can conclude that the protein-derived biopolymer can be used as an ideal template for the preparation of ultrasmall AuNPs together with the use of $NaBH_4$ as the reducing agent.

Table 1 Conditions for the synthesis of ultrasmall AuNPs using $NaBH_4$ as the reducing agent

$HAuCl_4$/$-NH_2$ molar ratio	$HAuCl_4$ (2 mM)	PEG-dcHSA	H_2O	$NaBH_4$ (100 mM)
3:0	0.5 mL	0 mg	4.4 mL	0.1 mL
3:1	0.5 mL	0.5 mg	4.4 mL	0.1 mL
3:2	0.5 mL	1.0 mg	4.4 mL	0.1 mL
3:3	0.5 mL	1.5 mg	4.4 mL	0.1 mL

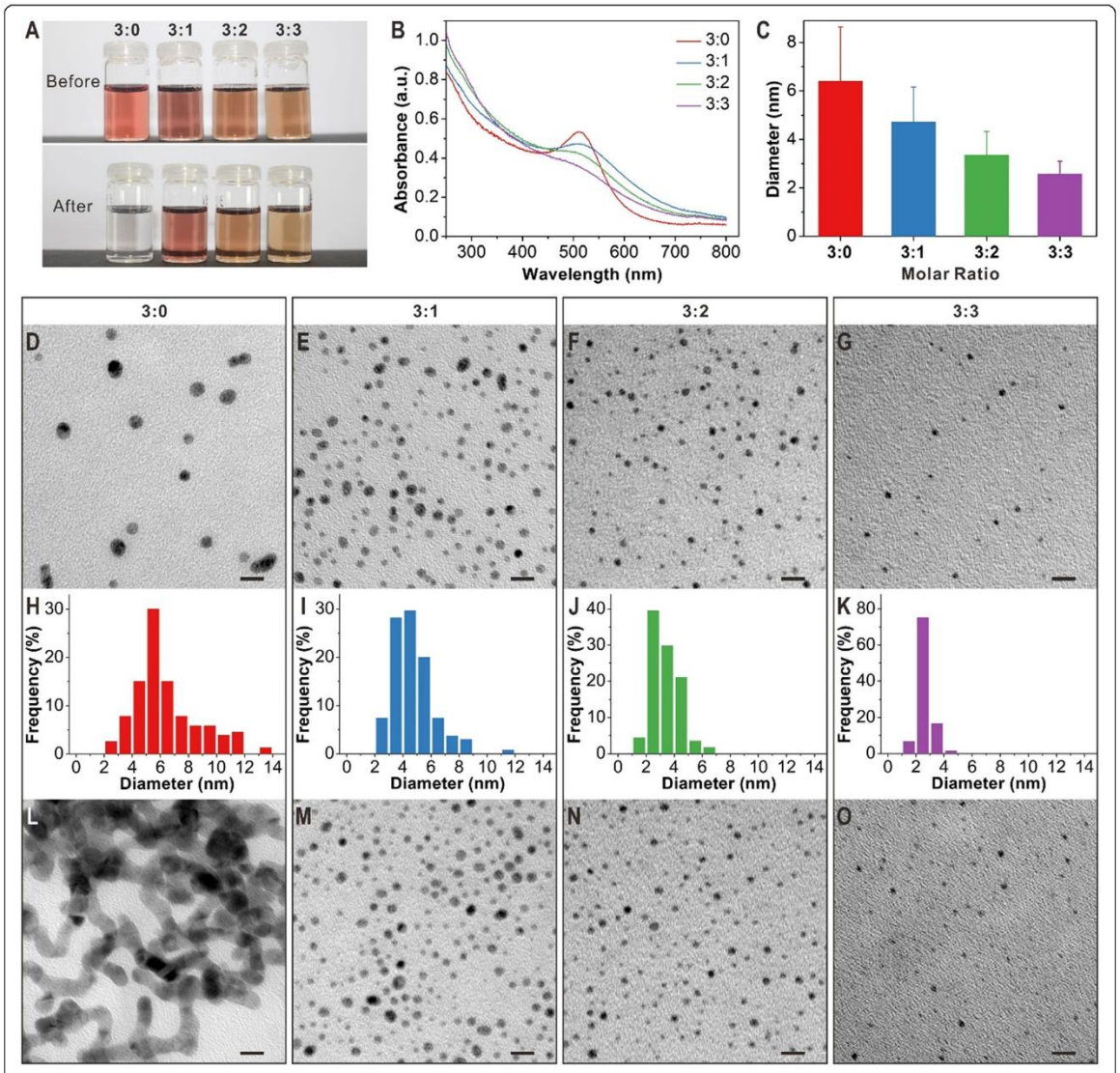

Fig. 2 Characterization of ultrasmall AuNPs prepared using $NaBH_4$ as the reducing agent. **a** Optical images comparing solutions of AuNPs before and after purification by ultracentrifugation. The AuNPs were prepared using different molar ratios of chloroauric anions to amino groups from the denatured protein. **b** UV-vis spectra of the AuNPs before purification by ultracentrifugation. **c** The average size of AuNPs obtained by analyzing more than 100 particles from TEM images. (D-K) TEM images and size distributions of AuNPs prepared using different molar ratios of chloroauric anions to amino groups in the denatured protein before purification: **d** and **h** 3:0; **e** and **i** 3:1; **f** and **j** 3:2; **g** and **k**) 3:3. **l**-**o** TEM images of AuNPs after purification by ultracentrifugation: **l** 3:0; **m** 3:1; **n** 3:2; **o** 3:3. Scale bars: 10 nm

Crucially, the samples prepared with denatured proteins demonstrated significantly enhanced stability compared to AuNPs prepared without the template ($HAuCl_4$/$-NH_2$ molar ratio 3:0). After the formation of AuNPs, the reaction solutions were purified five times by centrifugation at a high speed of 5000 rpm. As shown in the bottom panel of Fig. 2a, colors of AuNPs prepared in the presence of the biopolymer template did not change even though they were repeatedly concentrated and recovered. The solutions stayed homogeneous and there was no obvious change for the UV spectra of these solutions (Figure S1). In contrast, the solution of the AuNPs prepared in the absence of the template changed to colorless after the purification step and black precipitates were observed at the bottom (see Figure S2). As displayed in the TEM image, severe aggregation occurred for the AuNPs without protection by denatured proteins (Fig. 2l). For AuNPs prepared in the presence

of the biopolymer, all of them remained well-dispersed and no size change was observed (Fig. 2m-o). In addition, the AuNPs prepared by templated synthesis show excellent stability and dispersity even after storage at room temperature for one year (Figure S3). Therefore, the protein-derived biopolymer is indispensable for good water-solubility and excellent stability of AuNPs.

3.3 AuNFs prepared using ascorbic acid as the reducing agent

The choice of reducing agent has a great impact on the size and shape of AuNPs formed by templated synthesis. We further investigated the influence on particle morphology and size the when using L-ascorbic acid as the reducing agent and PEG-dcHSA as the template. By replacing $NaBH_4$ with L-ascorbic acid, four Au nanostructures were synthesized with similar conditions as in Table 1. As shown in Fig. 3a, the reaction solutions showed different colors from red to purple and to blue when the amount of denatured proteins was increased. UV-vis spectra in Fig. 3b show characteristic peaks of gold nanoparticles and a red shift is observed when the molar ratio of chloroauric anions to amine groups in denatured protein was changed from 3:0 to 3:3. Both the colors and UV-vis spectra indicate an increase of particle size after adding more biopolymers. Furthermore, we used TEM to directly characterize the size and morphology of these Au nanostructures (Fig. 3c-k). Very interestingly, AuNFs with multiple extrusions were obtained, indicating a different particle formation mechanism when ascorbic acid was used as the reducing agent. More specifically, some very small gold dots were firstly formed, which served as seeds for the following reduction of $HAuCl_4$. Because L-ascorbic acid is a mild reducing agent, the reactions were slower than those using $NaBH_4$. Under slow reaction kinetics, gold atoms and small dots had enough time to diffuse and meet each other. Because the added biopolymer template may favor to bind certain crystalline phases [37], the nanoparticles thus grew along specific facets and formed branched morphologies. The diameter of AuNFs was tuned in 30 ~ 70 nm by varying the amount of the denatured protein based on analysis of more than 100 nanoparticles in TEM images for each sample. The increase of biopolymer concentration leads to larger-sized AuNFs, which is a different trend in comparison to the synthesis of ultrasmall AuNPs using $NaBH_4$ as the reducing agent. The reason for this interesting phenomenon is not clear. One possible reason is the larger area covered by the presence of more PEG-dcHSA. This facilitated the anisotropic growth of flower branches and the size increased. For the sample prepared in absence of the biopolymer template, spherical AuNPs with an average size of 35.4 ± 10.0 nm were obtained. In addition, the TEM image in Fig. 3d even shows aggregation before purification for the sample prepared without the denatured protein template, indicating the poor stability of naked AuNPs. Surprisingly, all three AuNFs prepared in the presence of different amounts of denatured proteins demonstrated excellent stability despite their larger sizes compared to those ultrasmall AuNPs prepared using $NaBH_4$ as the reducing agent (Fig. 3m-o and Figure S4).

3.4 Catalytical reduction of *p*-nitrophenol by Au nanostructures

Due to their high surface-to-volume ratios, gold nanomaterials are ideal catalysts for many organic reactions [8–10]. For example, the hydrogenation reaction of *p*-nitrophenol to *p*-aminophenol by $NaBH_4$, which can be easily monitored by UV-vis spectroscopy, is a model reaction to evaluate the catalytic performance of noble metal catalysts [38]. Here, both ultrasmall AuNPs and AuNFs prepared under different conditions were used for the catalytical reduction of *p*-nitrophenol. As displayed in Fig. 4a-d, the characteristic peaks at 400 nm decreased for all spherical AuNPs prepared using $NaBH_4$ as the reducing agent, indicating their catalytic activity for the hydrogenation reaction. More importantly, there is a clear trend that the reaction became faster when the AuNPs were prepared in the presence of more PEG-dcHSA. The time to convert 90% catalyzed by AuNPs prepared without the biopolymer template ($HAuCl_4$/$-NH_2$ molar ratio = 3:0) is more than 40 min. In contrast, it took only 24 min for the AuNPs prepared with a $HAuCl_4$/$-NH_2$ molar ratio of 3:3 (Fig. 4e). By plotting $\ln(A_0/A_t)$ at 400 nm against the reaction time, the apparent rate constant (k_{app}) is determined as the slope of fitted lines. As shown in Fig. 4f, the AuNPs prepared with a $HAuCl_4$/$-NH_2$ molar ratio of 3:3 show the highest k_{app} of $1.673 \times 10^{-3}\,s^{-1}$. The apparent rate constants for AuNPs prepared with $HAuCl_4$/$-NH_2$ molar ratios of 3:0, 3:1, 3:2 are $9.273 \times 10^{-4}\,s^{-1}$, $1.032 \times 10^{-3}\,s^{-1}$, $1.488 \times 10^{-3}\,s^{-1}$, respectively. The higher catalytic activity of AuNPs synthesized with more templates is attributed to their smaller size and therefore higher surface-to-volume ratio to provide more catalytically active sites. Although the biopolymer coating may have a negative influence on the catalytic performance, it seems that the size effect is more significant. As the Au concentration (C_{Au}) in this catalytic reaction is only $0.163\,mg\,L^{-1}$, the rate constant (k_{app}/C_{Au}) of the AuNPs prepared with a $HAuCl_4$/$-NH_2$ molar ratio of 3:3 is as high as $1.026 \times 10^{-2}\,L\,s^{-1}\,mg^{-1}$.

UV-vis spectra showing the catalytic properties of AuNPs and AuNFs prepared with ascorbic acid for the hydrogenation of *p*-nitrophenol are depicted in Fig. 5a-d. By plotting the conversion against the time, we can see that the reaction catalyzed by spherical AuNPs showed a relatively high speed (Fig. 5e). However,

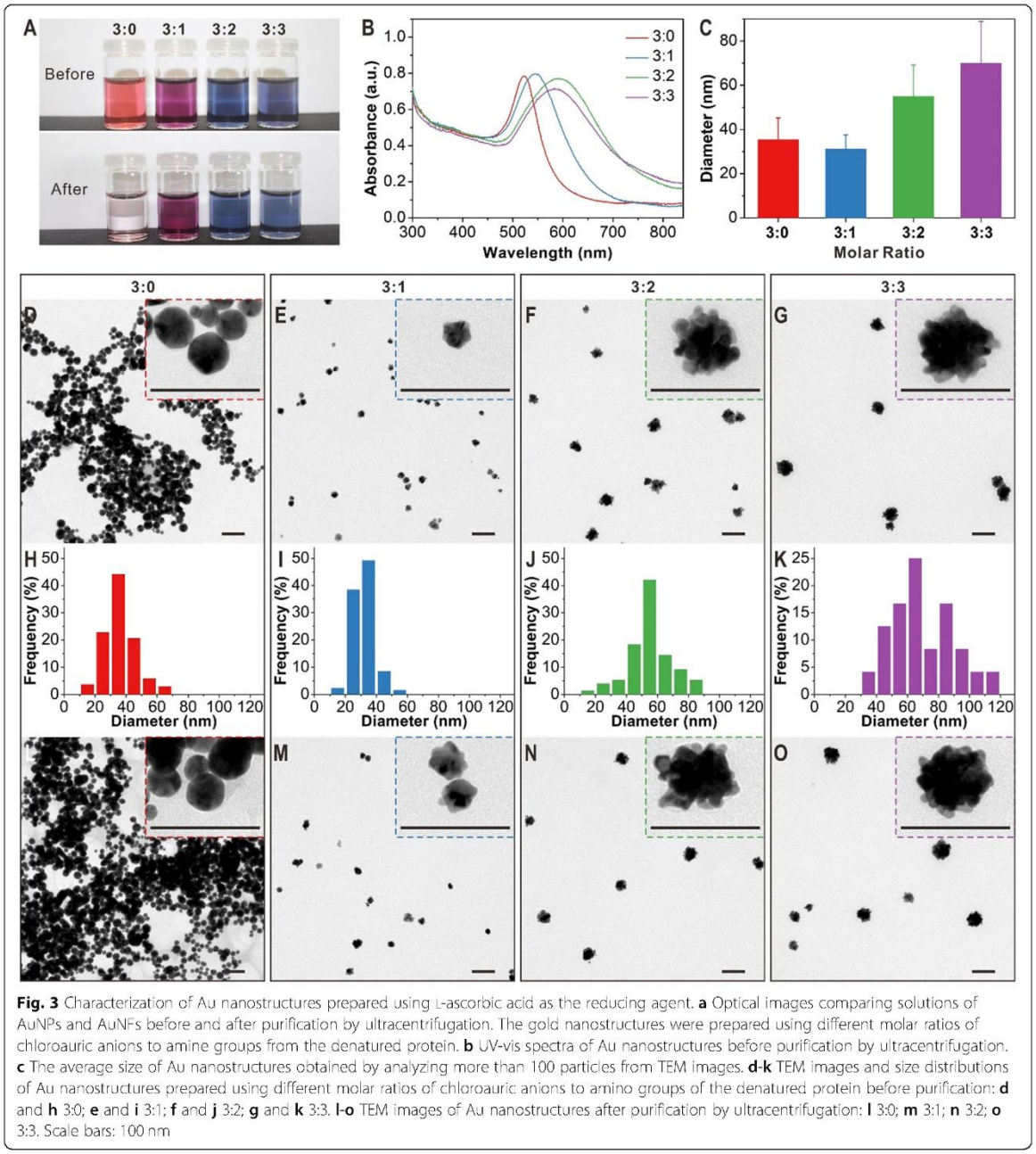

Fig. 3 Characterization of Au nanostructures prepared using L-ascorbic acid as the reducing agent. **a** Optical images comparing solutions of AuNPs and AuNFs before and after purification by ultracentrifugation. The gold nanostructures were prepared using different molar ratios of chloroauric anions to amine groups from the denatured protein. **b** UV-vis spectra of Au nanostructures before purification by ultracentrifugation. **c** The average size of Au nanostructures obtained by analyzing more than 100 particles from TEM images. **d**-**k** TEM images and size distributions of Au nanostructures prepared using different molar ratios of chloroauric anions to amino groups of the denatured protein before purification: **d** and **h** 3:0; **e** and **i** 3:1; **f** and **j** 3:2; **g** and **k** 3:3. **l**-**o** TEM images of Au nanostructures after purification by ultracentrifugation: **l** 3:0; **m** 3:1; **n** 3:2; **o** 3:3. Scale bars: 100 nm

AuNFs prepared in the presence of PEG-dcHSA demonstrate slower reaction kinetics especially in the beginning stages. This phenomenon probably is due to the biopolymer coating of AuNFs, which took some time for small molecules to diffuse. Fig. 5f shows the plot of $\ln(A_0/A_t)$ at 400 nm against the reaction time, the k_{app} of spherical AuNPs ($HAuCl_4$/$-NH_2$ molar ratios of 3:0) was determined as $1.518 \times 10^{-3}\,s^{-1}$. For AuNFs, we also calculated the k_{app} for the period after diffusion. As the Au concentration (C_{Au}) here is $2.627\,mg\,L^{-1}$, the rate constants (k_{app}/C_{Au}) catalyzed by AuNFs prepared with $HAuCl_4$/$-NH_2$ molar ratios of 3:1, 3:2, 3:3 are $3.64 \times 10^{-4}\,L\,s^{-1}\,mg^{-1}$, $4.21 \times 10^{-4}\,L\,s^{-1}\,mg^{-1}$, and $4.69 \times 10^{-4}\,L\,s^{-1}\,mg^{-1}$, respectively. Although the catalytic activity is not as high as ultrasmall AuNPs, they are still among the very effective Au catalysts in the literature [39–42].

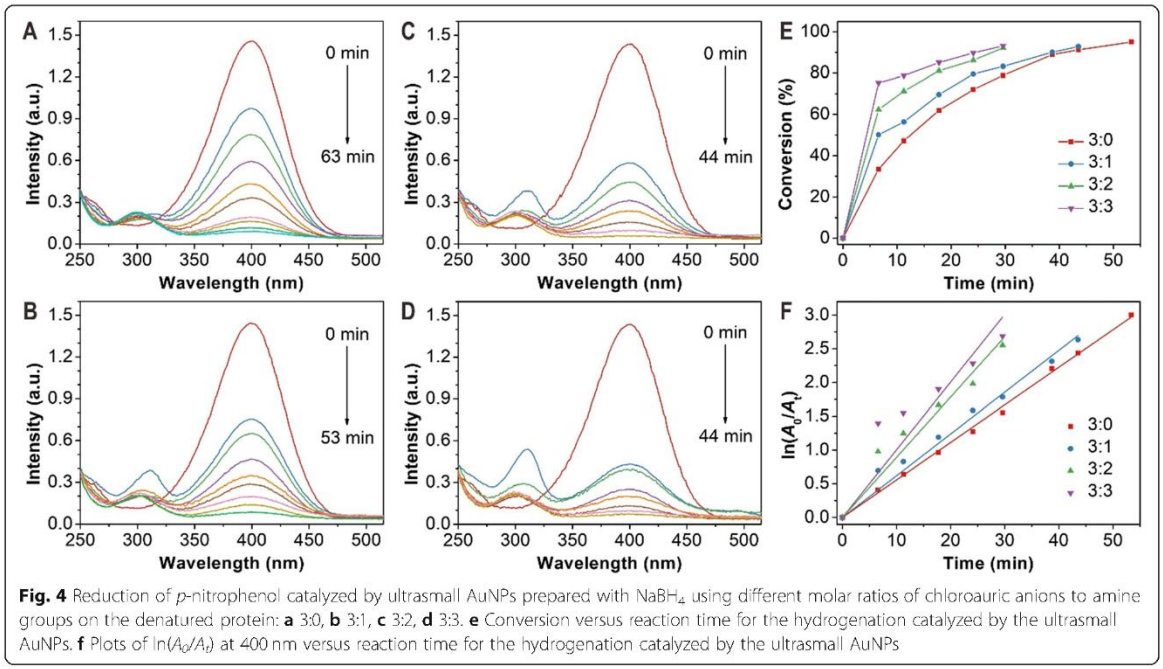

Fig. 4 Reduction of *p*-nitrophenol catalyzed by ultrasmall AuNPs prepared with $NaBH_4$ using different molar ratios of chloroauric anions to amine groups on the denatured protein: **a** 3:0, **b** 3:1, **c** 3:2, **d** 3:3. **e** Conversion versus reaction time for the hydrogenation catalyzed by the ultrasmall AuNPs. **f** Plots of $\ln(A_0/A_t)$ at 400 nm versus reaction time for the hydrogenation catalyzed by the ultrasmall AuNPs

3.5 Synthesis of PtNPs and their catalytic performance

In addition to well-defined AuNPs and AuNFs, other noble metal nanoparticles can also be prepared using the protein-derived biopolymer as template. For example, PtNPs have also attracted broad attention in catalysis and nanomedicine [43–46]. We further explored the preparation of PtNPs in the presence of PEG-dcHSA by reducing H_2PtCl_6 with $NaBH_4$. The molar ratio of $PtCl_6^{2-}$ anions to amine groups of PEG-dcHSA in the solution was set as 3:2. As shown in Fig. 6a, water-soluble PtNPs

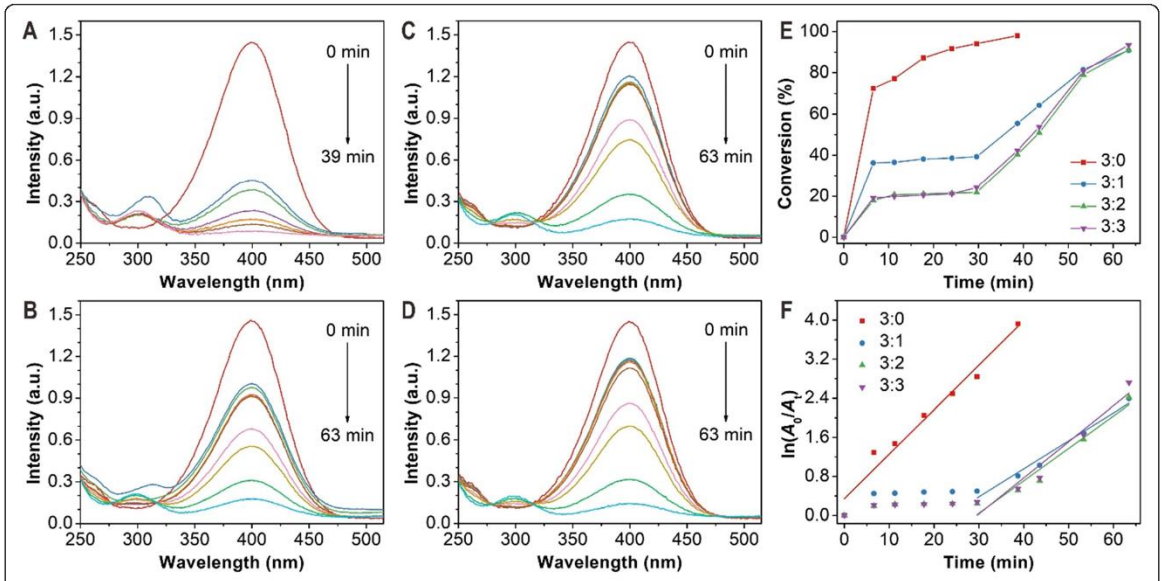

Fig. 5 Reduction of *p*-nitrophenol catalyzed by gold nanostructures prepared with L-ascorbic acid using different molar ratios of chloroauric anions to amine groups on the denatured protein: **a** 3:0, **b** 3:1, **c** 3:2, **d** 3:3. **e** Conversion versus reaction time for the hydrogenation catalyzed by these Au nanostructures. **f** $\ln(A_0/A_t)$ at 400 nm versus reaction time for the hydrogenation catalyzed by these Au nanostructures

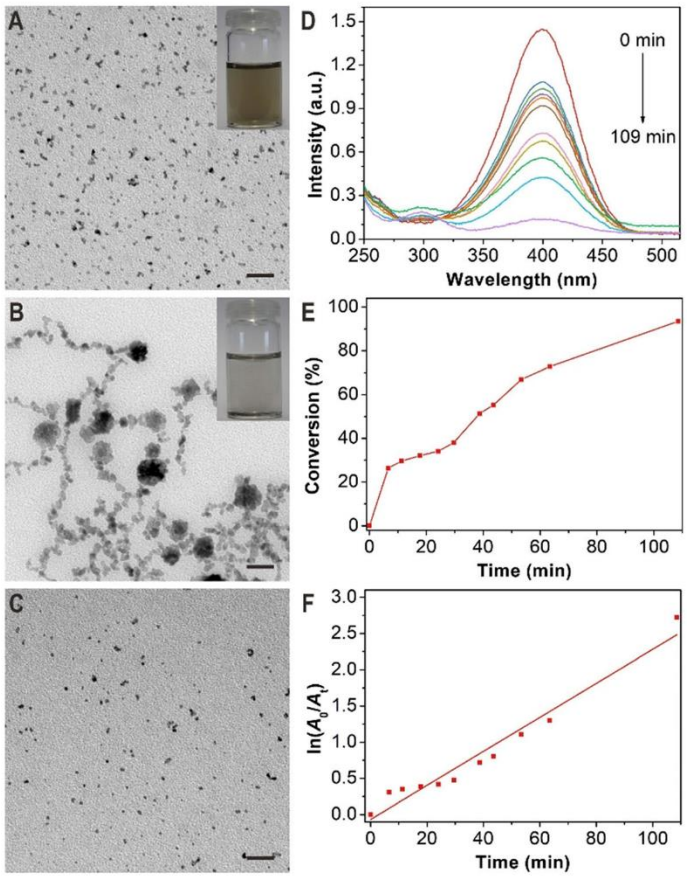

Fig. 6 **a** TEM image of PtNPs prepared using a molar ratio of $PtCl_6^{2-}$ anions to amine groups of PEG-dcHSA of 3:2. **b** TEM image of Pt aggregates prepared in the absence of the template. **c** TEM image of PdNPs after purification by ultracentrifugation. **d** Reduction of *p*-nitrophenol catalyzed by PtNPs. **e** Conversion versus reaction time for the hydrogenation catalyzed by PtNPs. **f** Plot of $\ln(A_0/A_t)$ at 400 nm versus reaction time for the hydrogenation catalyzed by these PtNPs. Scale bars: 20 nm

with good dispersity and an average size of ~ 3 nm were obtained. In a control experiment, very severe aggregation was observed for PtNPs prepared without adding the denatured protein (Fig. 6b). In addition, the size and dispersity of PtNPs by templated synthesis did not change even after purification several times by ultracentrifugation at a high speed of 5000 rpm, indicating their excellent stability (Fig. 6c).

We further evaluated the catalytic performance of PtNPs using the same hydrogenation reaction. As shown in Fig. 6d, the characteristic peak at 400 nm of *p*-nitrophenol gradually decreased in two hours. The conversion reaches 90% after reacting for 100 min (Fig. 6e). By plotting $\ln(A_0/A_t)$ at 400 nm against the reaction time, the k_{app} was obtained as $3.913 \times 10^{-4}\,s^{-1}$ (Fig. 6f). Therefore, PtNPs synthesized and stabilized with PEG-dcHSA can also serve as an effective catalyst for the hydrogenation reaction. In comparison, a catalytic study for PtNPs prepared without the biopolymer template was not possible because the particles were difficult to purify and the amount could not be determined.

4 Conclusion

In summary, denatured proteins have been reported as a novel template for the synthesis of water-soluble, ultrastable, and well-defined noble metal nanoparticles (AuNPs, AuNFs, PtNPs). Au nanostructures of different shapes (spherical and flower-like) have been prepared using $NaBH_4$ or ascorbic acid as the reducing agent. The sizes of Au nanostructures have been controlled by tuning the molar ratio of metal ions to amino groups of the template. Compared to nanoparticles prepared without the template, these metal nanoparticles prepared by templated synthesis demonstrated much better stability even after high speed centrifugation or storage at room temperature for one year. Moreover, these nanoparticles

have been used as efficient catalysts for the hydrogenation of *p*-nitrophenol to *p*-aminophenol. AuNPs with an average size of 2 nm show the highest catalytic efficiency with a rate constant of $1.026 \times 10^{-2}\,L\,s^{-1}\,mg^{-1}$. These metal nanoparticles with tunable size and shape, as well as good stability, dispersity and water-solubility may find great potentials in catalysis, sensors, biomedicine and many other fields.

5 Supplementary information

Supplementary information accompanies this paper at https://doi.org/10.1186/s42825-020-00020-5.

Additional file 1: Figure S1. UV-vis spectra of ultrasmall AuNPs after purification by ultracentrifugation. **Figure S2.** Enlarged photo of AuNPs prepared in the absence of the biopolymer template after purification five times by ultracentrifugation. **Figure S3.** Digital photo (A) and TEM images (B-D) showing the excellent stability and dispersity of AuNPs after storage for one year at room temperature. **Figure S4.** Digital photo (A) and TEM images (B-D) showing the excellent stability and dispersity of AuNFs after storage for one year at room temperature.

Abbreviations

AuNFs: Gold nanoflowers; AuNPs: Gold nanoparticles; cHSA: Cationic HSA; EDC·HCl: *N*-(3-Dimethylaminopropyl)-*N*′-ethylcarbodiimide hydrochloride; EDTA: Ethylenediaminetetraacetic acid; $HAuCl_4{\cdot}3H_2O$: Gold (III) chloride trihydrate; $H_2PtCl_6xH_2O$: Hydrogen hexachloroplatinate (IV) hydrate; HSA: Human serum albumin; k_{app}: Apparent rate constant; MALDI-ToF: Matrix-assisted laser desorption/ionization time-of-flight; MI-NH_2: *N*-(2-aminoethyl) maleimide trifluoroacetate salt; $NaBH_4$: Sodium borohydride; NHS-PEG: *O*-[(*N*-succinimidyl)succinyl-aminoethyl]-*O*′-methylpolyethylene glycol; PEG: Polyethylene glycol; PEG-cHSA: PEGylated cHSA; PEG-dcHSA: Denatured PEG-cHSA; PtNPs: Platinum nanoparticles; TCEP: Tris(2-carboxyethyl) phosphine hydrochloride; TEM: Transmission electron microscopy

Acknowledgements

The authors thank Julius Gemen for his assist with part of the experiments. Christopher Synatschke and Nicole Kirsch-Pietz are gratefully acknowledged for critically reading the manuscript.

Authors' contributions

C.C. performed the experiments and wrote the manuscript. D.Y.W.N. and T.W. supervised the project and revised the manuscript. All authors discussed the results and commented on the manuscript. The author(s) read and approved the final manuscript.

Funding

The authors acknowledge financial support by the Deutsche Forschungsgemeinschaft (DFG, German Research Foundation) – Project number 213555243 SFB 1066 (A06). C.C. is grateful for a doctoral fellowship from Promotionskolleg Pharmaceutical Biotechnology of Ulm University funded by the state of Baden–Württemberg.

Availability of data and materials

All data generated or analyzed during this study are included in this published article and its supplementary information.

Competing interests

The authors declare that they have no competing interests.

Author details

[1]Max Planck Institute for Polymer Research, Ackermannweg 10, 55128 Mainz, Germany. [2]Ulm University, Albert-Einstein-Allee 11, 89081 Ulm, Germany.

Received: 9 January 2020 Accepted: 18 March 2020
Published online: 23 March 2020

References

1. Eustis S, El-Sayed MA. Why gold nanoparticles are more precious than pretty gold: Noble metal surface plasmon resonance and its enhancement of the radiative and nonradiative properties of nanocrystals of different shapes. Chem Soc Rev. 2006;35:209.
2. Sau TK, Rogach AL. Nonspherical Noble metal nanoparticles: colloid-chemical synthesis and morphology control. Adv Mater. 2010;22:1781.
3. Zhou W, Gao X, Liu DB, Chen XY. Gold nanoparticles for in vitro diagnostics. Chem Rev. 2015;115:10575.
4. Sau TK, Rogach AL, Jackel F, Klar TA, Feldmann J. Properties and applications of colloidal nonspherical Noble metal nanoparticles. Adv Mater. 2010;22:1805.
5. Arvizo RR, Bhattacharyya S, Kudgus RA, Giri K, Bhattacharya R, Mukherjee P. Intrinsic therapeutic applications of noble metal nanoparticles: past, present and future. Chem Soc Rev. 2012;41:2943.
6. Zeng J, Huang JL, Lu W, Wang XP, Wang B, Zhang SY, Hou JG. Necklace-like noble-metal hollow nanoparticle chains: synthesis and tunable optical properties. Adv Mater. 2007;19:2172.
7. Bigall NC, Reitzig M, Naumann W, Simon P, van Pee KH, Eychmuller A. Fungal templates for noble-metal nanoparticles and their application in catalysis. Angew Chem Int Ed. 2008;47:7876.
8. Corma A, Garcia H. Supported gold nanoparticles as catalysts for organic reactions. Chem Soc Rev. 2008;37:2096.
9. Ide MS, Davis RJ. The important role of hydroxyl on oxidation catalysis by gold nanoparticles. Acc Chem Res. 2014;47:825.
10. Mitsudome T, Kaneda K. Gold nanoparticle catalysts for selective hydrogenations. Green Chem. 2013;15:2636.
11. Shimmin RG, Schoch AB, Braun PV. Polymer size and concentration effects on the size of gold nanoparticles capped by polymeric thiols. Langmuir. 2004;20:5613.
12. Oh E, Susumu K, Goswami R, Mattoussi H. One-phase synthesis of water-soluble gold nanoparticles with control over size and surface functionalities. Langmuir. 2010;26:7604.
13. Enciso AE, Doni G, Nifosi R, Palazzesi F, Gonzalez R, Ellsworth AA, Coffer JL, Walker AV, Pavan GM, Mohamed AA, Simanek EE. Facile synthesis of stable, water soluble, dendron-coated gold nanoparticles. Nanoscale. 2017;9:3128.
14. Salorinne K, Man RWY, Li CH, Taki M, Nambo M, Crudden CM. Water-soluble N-heterocyclic Carbene-protected gold nanoparticles: size-controlled synthesis, stability, and optical properties. Angew Chem Int Ed. 2017;56:6198.
15. Yang WT, Guo WS, Chang J, Zhang BB. Protein/peptide-templated biomimetic synthesis of inorganic nanoparticles for biomedical applications. J Mater Chem B. 2017;5:401.
16. Chakraborty I, Parak WJ. Protein-induced shape control of Noble metal nanoparticles. Adv Mater Interfaces. 2019;6:1801407.
17. Dickerson MB, Sandhage KH, Naik RR. Protein- and peptide-directed syntheses of inorganic materials. Chem Rev. 2008;108:4935.
18. Li Y, Tang ZH, Prasad PN, Knecht MR, Swihart MT. Peptide-mediated synthesis of gold nanoparticles: effects of peptide sequence and nature of binding on physicochemical properties. Nanoscale. 2014;6:3165.
19. Virkutyte J, Varma RS. Green synthesis of metal nanoparticles: biodegradable polymers and enzymes in stabilization and surface functionalization. Chem Sci. 2011;2:837.
20. Liu GY, Luo QQ, Wang HB, Zhuang WH, Wang YB. In situ synthesis of multidentate PEGylated chitosan modified gold nanoparticles with good stability and biocompatibility. RSC Adv. 2015;5:70109.
21. Sun LJ, Li J, Cai J, Zhong L, Ren GH, Ma QM. One pot synthesis of gold nanoparticles using chitosan with varying degree of deacetylation and molecular weight. Carbohydr Polym. 2017;178:105.
22. Yen HJ, Young YA, Tsai TN, Cheng KM, Chen XA, Chen YC, Chen CC, Young JJ, Hong PD. Positively charged gold nanoparticles capped with folate quaternary chitosan: synthesis, cytotoxicity, and uptake by cancer cells. Carbohydr Polym. 2018;183:140.
23. Zhang KT, Shen MG, Liu H, Shang SB, Wang D, Liimatainen H. Facile synthesis of palladium and gold nanoparticles by using dialdehyde nanocellulose as template and reducing agent. Carbohydr Polym. 2018;186:132.
24. Lu LH, Ai K, Ozaki Y. Environmentally friendly synthesis of highly monodisperse biocompatible gold nanoparticles with urchin-like shape. Langmuir. 2008;24:1058.

25. Goswami N, Saha R, Pal SK. Protein-assisted synthesis route of metal nanoparticles: exploration of key chemistry of the biomolecule. J Nanopart Res. 2011;13:5485.
26. Leng YM, Fu L, Ye LQ, Li B, Xu XM, Xing XJ, He JB, Song YL, Leng CL, Guo YM, Ji XX, Lu ZW. Protein-directed synthesis of highly monodispersed, spherical gold nanoparticles and their applications in multidimensional sensing. Sci Rep. 2016;6:28900.
27. Wei G, Wang L, Sun LL, Song YH, Sun YJ, Guo CL, Yang T, Li ZA. Type I collagen-mediated synthesis and assembly of UV-photoreduced gold nanoparticles and their application in surface-enhanced Raman scattering. J Phys Chem C. 2007;111:1976.
28. Wu YZ, Chakrabortty S, Gropeanu RA, Wilhelmi J, Xu Y, Er KS, Kuan SL, Koynov K, Chan Y, Weil T. pH-responsive quantum dots via an albumin polymer surface coating. J Am Chem Soc. 2010;132:5012.
29. Wu YZ, Pramanik G, Eisele K, Weil T. Convenient approach to polypeptide copolymers derived from native proteins. Biomacromolecules. 2012;13:1890.
30. Chen CJ, Wunderlich K, Mukherji D, Koynov K, Heck AJ, Raabe M, Barz M, Fytas G, Kremer K, Ng DYW, Weil T. Precision anisotropic brush polymers by sequence controlled chemistry. J Am Chem Soc. 2020;142:1332.
31. Wu YZ, Eisele K, Doroshenko M, Algara-Siller G, Kaiser U, Koynov K, Weil T. A quantum dot Photoswitch for DNA detection, gene transfection, and live-cell imaging. Small. 2012;8:3465.
32. Wu YZ, Ermakova A, Liu WN, Pramanik G, Vu TM, Kurz A, McGuinness L, Naydenov B, Hafner S, Reuter R, Wrachtrup J, Isoya J, Fortsch C, Barth H, Simmet T, Jelezko F, Weil T. Programmable biopolymers for advancing biomedical applications of fluorescent Nanodiamonds. Adv Funct Mater. 2015;25:6576.
33. Chen CJ, Ng DYW, Weil T. Polymer-grafted gold nanoflowers with temperature-controlled catalytic features by in situ particle growth and polymerization. Mater Chem Front. 2019;3:1449.
34. Wu YZ, Ihme S, Feuring-Buske M, Kuan SL, Eisele K, Lamla M, Wang YR, Buske C, Weil T. A Core-Shell albumin copolymer Nanotransporter for high capacity loading and two-step release of doxorubicin with enhanced anti-leukemia activity. Adv Healthc Mater. 2013;2:884.
35. Haiss W, Thanh NTK, Aveyard J, Fernig DG. Determination of size and concentration of gold nanoparticles from UV-Vis spectra. Anal Chem. 2007;79:4215.
36. ten Hove JB, Schijven LMI, Wang JY, Velders AH. Size-controlled and water-soluble gold nanoparticles using UV-induced ligand exchange and phase transfer. Chem Commun. 2018;54:13355.
37. Xia YN, Xiong YJ, Lim B, Skrabalak SE. Shape-controlled synthesis of metal Nanocrystals: simple chemistry meets complex physics? Angew Chem Int Ed. 2009;48:60.
38. Zhao PX, Feng XW, Huang DS, Yang GY, Astruc D. Basic concepts and recent advances in nitrophenol reduction by gold- and other transition metal nanoparticles. Coord Chem Rev. 2015;287:114.
39. Marcelo G, Lopez-Gonzalez M, Mendicuti F, Tarazona MP, Valiente M. Poly(N-isopropylacrylamide)/gold hybrid hydrogels prepared by catechol redox chemistry. Characterization and Smart Tunable Catalytic Activity. Macromolecules. 2014;47:6028.
40. Rashid MH, Bhattacharjee RR, Kotal A, Mandal TK. Synthesis of spongy gold nanocrystals with pronounced catalytic activities. Langmuir. 2006;22:7141.
41. Wang ML, Jiang TT, Lu Y, Liu HJ, Chen Y. Gold nanoparticles immobilized in hyperbranched polyethylenimine modified polyacrylonitrile fiber as highly efficient and recyclable heterogeneous catalysts for the reduction of 4-nitrophenol. J Mater Chem A. 2013;1:5923.
42. Ye YL, Jin M, Wan DC. One-pot synthesis of porous monolith-supported gold nanoparticles as an effective recyclable catalyst. J Mater Chem A. 2015;3:13519.
43. Cheong SS, Watt JD, Tilley RD. Shape control of platinum and palladium nanoparticles for catalysis. Nanoscale. 2010;2:2045.
44. Lara P, Philippot K. The hydrogenation of nitroarenes mediated by platinum nanoparticles: an overview. Catal Sci Technol. 2014;4:2445.
45. Pedone D, Moglianetti M, De Luca E, Bardi G, Pompa PP. Platinum nanoparticles in nanobiomedicine. Chem Soc Rev. 2017;46:4951.
46. Peng ZM, Yang H. Designer platinum nanoparticles: control of shape, composition in alloy, nanostructure and electrocatalytic property. Nano Today. 2009;4:143.

Publisher's Note

Supplementary Information

Denatured proteins as a novel template for the synthesis of well-defined, ultra-stable and water-soluble metal nanostructures for catalytic applications

Chaojian Chen, [1,2]* David Yuen Wah Ng[1] and Tanja Weil[1,2]*

[1]Max Planck Institute for Polymer Research, Ackermannweg 10, 55128 Mainz, Germany
[2]Ulm University, Albert-Einstein-Allee 11, 89081 Ulm, Germany

Calculation of the number of primary amino groups in PEG-dcHSA:

As the primary structure of HSA is known, the numbers of lysine (K), aspartic acid (D), glutamic acid (E), and cysteine (C) are 59, 36, 62, and 35, respectively. Therefore, the number of primary amino groups in native HSA is 60 (59 plus 1 from the N terminal). During the cationization step, the carboxyl groups of D and E were converted to primary amino groups. Based on the MALDI-ToF spectra, on average 46 amino groups were consumed in the PEGylation step. Finally, the cysteines were also transferred to primary amino groups in the unfolding step. Therefore, the average number of primary amino groups in PEG-dcHSA can be calculated as:

$$60 + (36+62) - 46 + 35 = 147$$

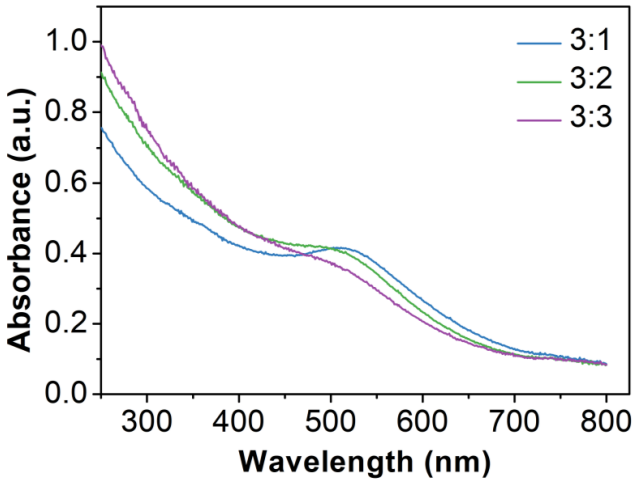

Figure S1 UV-vis spectra of ultrasmall AuNPs after purification by ultracentrifugation. $NaBH_4$ was selected as the reducing agent and different molar ratios of chloroauric anions to amino groups in PEG-dcHSA from 3:1 to 3:3 were used for the preparation of these AuNPs.

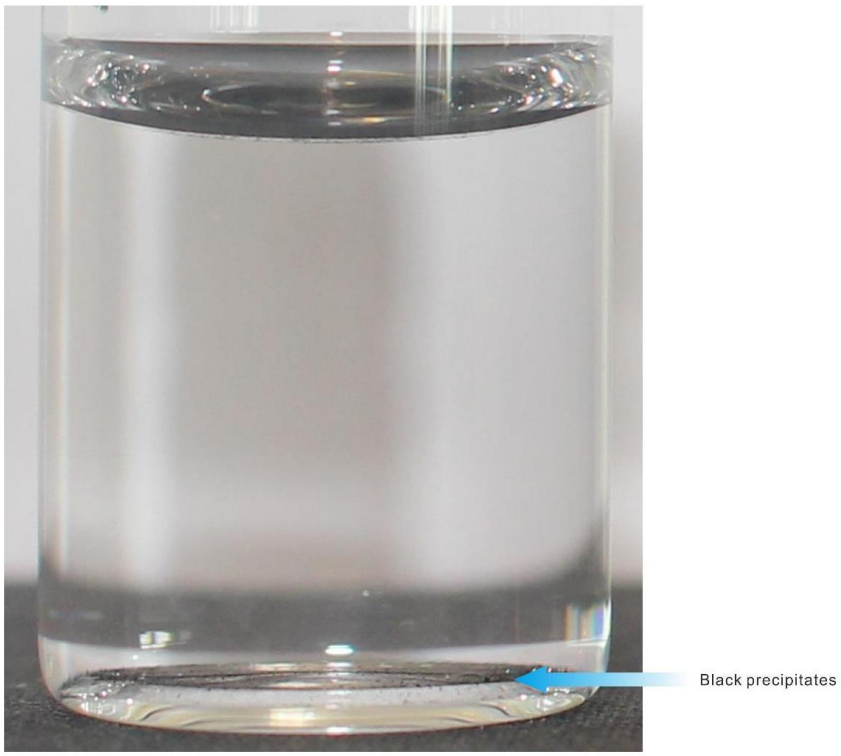

Figure S2 Enlarged photo of AuNPs prepared in the absence of the biopolymer template (molar ratio of chloroauric anions to amino groups in the denatured protein = 3:0) after purification five times by ultracentrifugation.

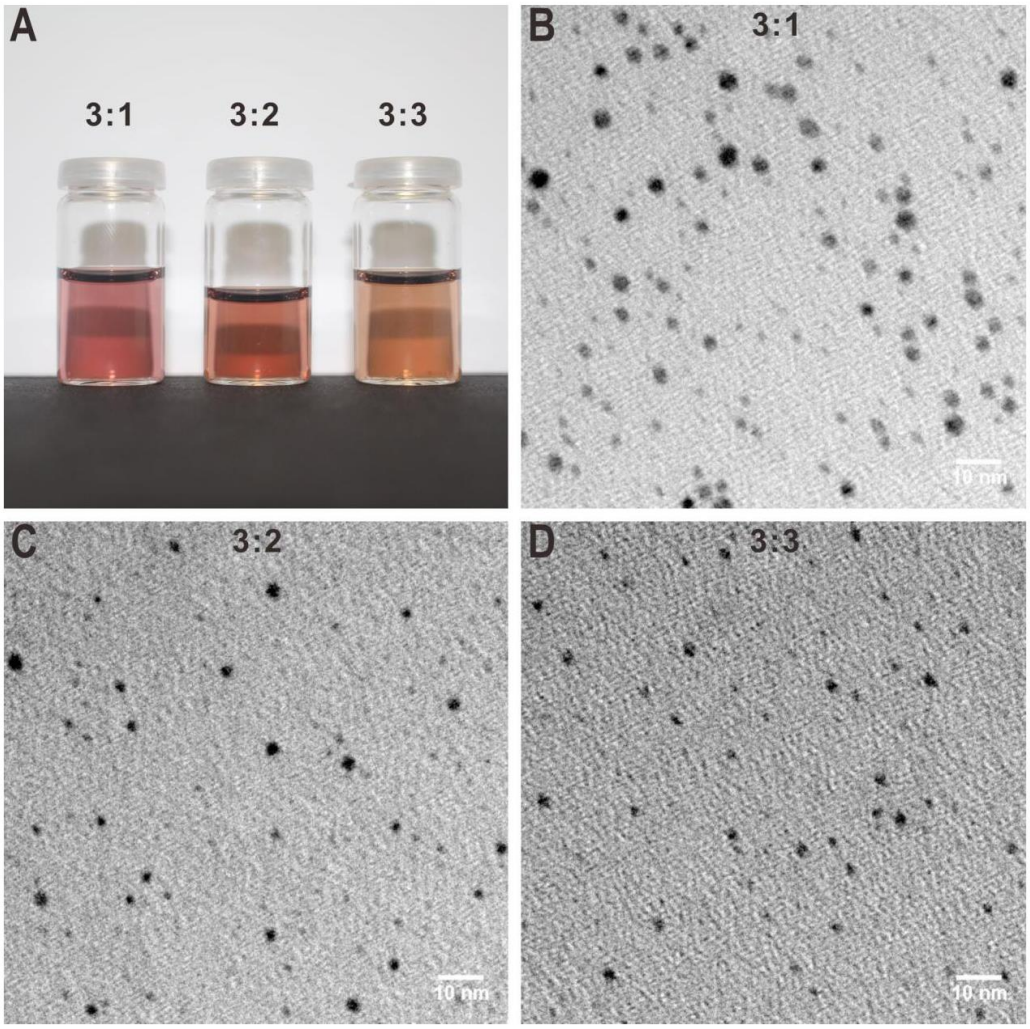

Figure S3 Digital photo (A) and TEM images (B-D) showing the excellent stability and dispersity of AuNPs after storage for one year at room temperature. The AuNPs were prepared using $NaBH_4$ as the reducing agent with different molar ratios of chloroauric anions to amino groups from the denatured protein.

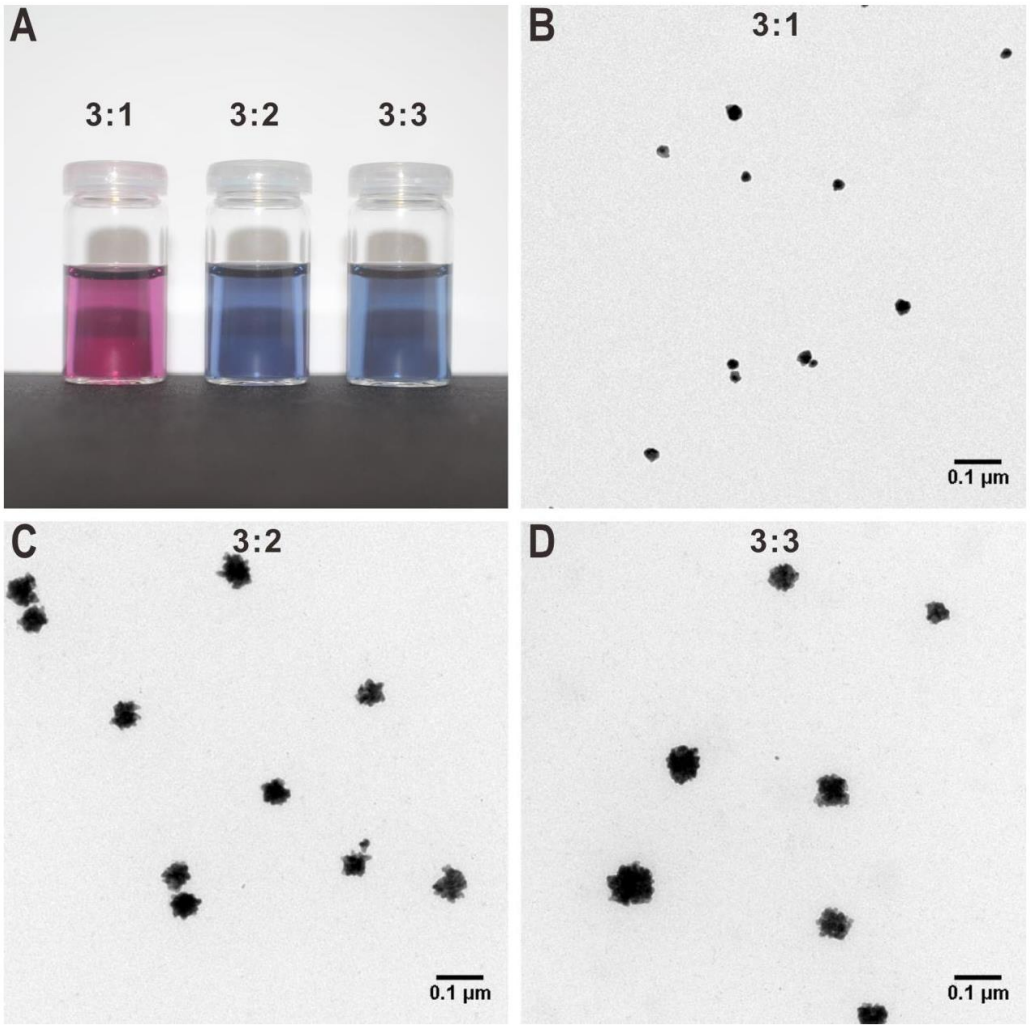

Figure S4 Digital photo (A) and TEM images (B-D) showing the excellent stability and dispersity of AuNFs after storage for one year at room temperature. The AuNFs were prepared using ascorbic acid as the reducing agent with different molar ratios of chloroauric anions to amino groups from the denatured protein.

5.3 Polymer-grafted gold nanoflowers with temperature-controlled catalytic features by *in-situ* particle growth and polymerization

Chaojian Chen, David Yuen Wah Ng,* and Tanja Weil*

* Corresponding authors

Published in *Mater. Chem. Front.* **2019**, *3*, 1449−1453.

Contribution of the respective authors:

Chaojian Chen: Design of the project, conduction of the experiments, results analysis and interpretation, figure design and writing of the manuscript.
David Yuen Wah Ng: Design and discussion of the concept and results, correcting the manuscript.
Tanja Weil: Acquiring funding for the project, design and discussion of the concept and results, correcting the manuscript.

MATERIALS CHEMISTRY FRONTIERS

RESEARCH ARTICLE

View Article Online
View Journal | View Issue

Cite this: *Mater. Chem. Front.*, 2019, 3, 1449

Received 18th April 2019,
Accepted 14th May 2019

DOI: 10.1039/c9qm00252a

rsc.li/frontiers-materials

Polymer-grafted gold nanoflowers with temperature-controlled catalytic features by *in situ* particle growth and polymerization†

Chaojian Chen, [ab] David Yuen Wah Ng *[a] and Tanja Weil *[ab]

We report a convenient strategy for the synthesis of polymer-grafted gold nanoflowers by combining an activator regenerated by electron transfer atom transfer radical polymerization (ARGET ATRP) and the reduction of metal ions in a one-pot fashion. Poly(*N*-isopropylacrylamide)-coated gold nanoflowers (PNIPAM-AuNFs) with controllable sizes, shapes, and shell thickness are obtained and applied as temperature-controlled nanoparticle catalysts for the hydrogenation of *p*-nitrophenol.

Polymer–metal hybrid nanomaterials, particularly polymer–gold nanocomposites, have attracted continuous attention over the past two decades.[1,2] The combination of chemical, optical, and electronic characteristics of nano-sized metals with tunable features of functional polymers has opened various promising applications including as components in optical and electronic devices, as well as in catalysis, sensors and biomedicine.[3,4] It is widely accepted that the properties of polymer–metal nanocomposites are largely determined by their composition, shape, size, distribution, and surface structures. Therefore, substantial efforts have been devoted to control and optimize the properties of these nanomaterials.[5,6]

Gold nanoflowers (AuNFs) are unique nanostructures with large numbers of branches.[7–10] Owning to their coarse surfaces consisting of many sharp tips, as well as high surface-to-volume ratios, 3D hierarchical AuNFs have demonstrated remarkable performances in catalysis,[11,12] surface-enhanced Raman scattering,[13–15] photothermal conversion,[16] and cell imaging.[17] AuNFs with surface-grafted functional polymers are particularly attractive as the polymer shell provides additional features such as solubility and stimuli-responsiveness.[18] Polymer–AuNFs can be achieved by *in situ* reduction of gold ions in the presence of polymer templates or by grafting polymer chains to or from already formed AuNFs.[19] However, these methods involve tedious multistep fabrication and purification processes, and there is only limited control over the structure of the metal nanoparticles and the polymers at the surface.[14] Therefore, a facile and green route for the synthesis of multifunctional polymer-coated AuNFs would be very attractive.

Atom transfer radical polymerization (ATRP) is a widely used polymerization technique for the synthesis of well-defined polymers. However, ATRP catalysts are usually sensitive to air and other oxidants. To solve this limitation, Matyjaszewski *et al.* have developed an improved technique termed activator regenerated by electron transfer (ARGET) ATRP (Fig. 1A).[20–23] Transition metal complexes in their oxidation stable state (*e.g.*, $CuBr_2$/ligand) are used as catalyst precursors in ARGET ATRP. A reducing agent such as ascorbic acid is continuously added to reduce the Cu^{II} species to the active catalyst (Cu^{I} species). The major benefits of ARGET ATRP are low amounts of catalysts, ease of preparation, storage, and handling of the ATRP catalysts in air.

We report a convenient procedure for the synthesis of catalytically active AuNFs coated by a responsive poly(*N*-isopropylacrylamide) (PNIPAM) shell by combining ARGET ATRP and the reduction of metal ions in one reaction step. The approach is based on a protein-derived biopolymer template providing (1) distinct numbers of amino groups able to bind chloroauric anions and (2) many initiation sites for ARGET ATRP. Human serum albumin (HSA) has been selected as biotemplate as it is an important physiological transporter for various metal ions[24] and metallodrugs[25] in the bloodstream. In our previous work, denatured HSA has been exploited for the stabilization of metal colloids and nanoparticles.[26–28] Herein, the HSA-derived biopolymer is equipped with ATRP initiators and combined with ascorbic acid reducing the metal ions and activating the ATRP catalyst for PNIPAM polymerization. In this way, PNIPAM-coated gold nanoflowers (PNIPAM-AuNFs) of tunable sizes and shapes with excellent stability and thermo-responsiveness have been obtained in a one-pot reaction. Temperature-responsive PNIPAM has been used for the first time to coat AuNFs, although some PNIPAM-Au nanocomposites are known.[29–31] PNIPAM-AuNFs serve as a smart catalyst,

[a] *Max Planck Institute for Polymer Research, Ackermannweg 10, 55128 Mainz, Germany. E-mail: weil@mpip-mainz.mpg.de, david.ng@mpip-mainz.mpg.de*
[b] *Ulm University, Albert-Einstein-Allee 11, 89081 Ulm, Germany. E-mail: tanja.weil@uni-ulm.de*

† Electronic supplementary information (ESI) available: Experimental details, MALDI-ToF spectra, TEM images and other characterizations of PNIPAM-AuNFs, comparison of the catalytic activity. See DOI: 10.1039/c9qm00252a

View Article Online
Research Article Materials Chemistry Frontiers

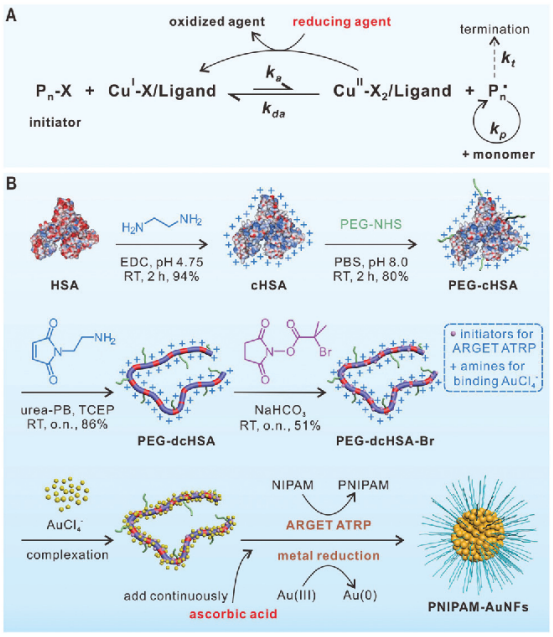

Fig. 1 (A) The mechanism of ARGET ATRP. (B) Synthesis of PEG-dcHSA-Br and its application as a substrate for preparing PNIPAM-AuNFs by one-pot concurrent ARGET ATRP and gold reduction.

whereby the temperature-responsive PNIPAM shell controls hydrogenation of *p*-nitrophenol to *p*-aminophenol. We believe that the approach could be extended to other noble metal nanoparticles and functional polymers, providing access to a variety of multifunctional polymer–metal hybrid nanomaterials.

The synthesis of the biopolymer template is schematically illustrated in Fig. 1B. First, the carboxylic acid groups of HSA are converted into amino groups by applying a large excess of ethylenediamine to afford cationized HSA (cHSA). cHSA possesses many amino groups for the attachment of ATRP initiators and facilitates the adsorption of higher amounts of $AuCl_4^-$ anions. To improve protein solubility and stability, short polyethylene glycol (PEG, $M_n \sim 2000$) chains are conjugated to cHSA to afford PEG-cHSA with about 32 PEG chains as calculated from the matrix-assisted laser desorption/ionization time-of-flight (MALDI-ToF) mass spectrum (Fig. S3, ESI†). Next, PEG-cHSA is denatured in urea-phosphate buffer using tris(2-carboxyethyl) phosphine hydrochloride as reducing agent. *N*-(2-aminoethyl)maleimide trifluoroacetate salt (MI-NH_2) is added to cap the thiol groups generated after reduction of disulfide bridges of HSA. The resulting denatured polypeptide (PEG-dcHSA) is reacted with 2-bromoisobutanoic acid *N*-hydroxysuccinimide ester, which introduces ATRP initiators with bromide end groups to the polypeptide backbone giving PEG-cHSA-Br in 51% yield. According to MALDI-ToF mass spectra in Fig. S4 and S5 (ESI†), 61 initiation sites per polypeptide backbone have been introduced.

For the preparation of the polymer-grafted AuNFs in one reaction pot, chloroauric acid ($HAuCl_4$) is selected as the metal source and *N*-isopropylacrylamide (NIPAM) as monomer to impart a thermal-responsive polymer. In a typical process, the substrate PEG-dcHSA-Br, the monomer NIPAM, the $HAuCl_4$ solution, and the stock solution of copper(II) bromide/tris-(2-pyridylmethyl)amine ($Cu^{II}Br_2$/TPMA) are first dissolved in deionized water. Oxygen is removed through three freeze–pump–thaw cycles, and the solution is stirred at room temperature for one hour to allow the complexation of $AuCl_4^-$ by the amino groups of the peptide chains. Degassed ascorbic acid solution is added *via* a syringe pump at a slow speed of 0.6 μL min^{-1}, and the reaction proceeds at predetermined time and temperature. Purification of the polymer-grafted AuNFs proceeds by simple centrifugation to remove unreacted monomers. As summarized in Table 1, six reaction conditions have been applied to study the impact of the $-NH_2/HAuCl_4$ molar ratio (-NH_2 refers to total amount of amino groups from PEG-dcHSA-Br in the reaction solution which is 300 nmol), reaction temperature and reaction time on the sizes and morphologies of the formed PNIPAM-AuNFs. The obtained AuNFs were imaged by transmission electron microscopy (TEM) and the results are shown in Fig. 2 and Fig. S6–S11 (ESI†).

Table 1 Synthesis of PNIPAM-AuNFs under different conditions

Entry	Molar ratio of $-NH_2/HAuCl_4$	T^a (°C)	t^b (h)	Diameter^c (nm)
1	6 : 1	23	2	148 ± 16
2	3 : 1	23	2	219 ± 21
3	1 : 1	23	2	179 ± 88
4	3 : 1	40	2	61 ± 9
5	3 : 1	23	1	217 ± 18
6	3 : 1	23	4	214 ± 21

[a] Reaction temperature. [b] Reaction time. [c] Average diameter determined from TEM images using ImageJ software.

As shown in Fig. 2A–D, AuNFs with rough surfaces are formed, and the enlarged TEM images in Fig. 2 and Fig. S6–S11 (ESI†) even capture the polymer shells surrounding the AuNFs. Next, the impact of the $-NH_2/HAuCl_4$ molar ratio on the size and shape of PNIPAM-AuNFs is analyzed. By increasing the amount of $HAuCl_4$ in the reaction mixture, the $-NH_2/HAuCl_4$ molar ratio changes from 6 : 1 (entry 1) to 3 : 1 (entry 2), and to 1 : 1 (entry 3) (Table 1, 23 °C, 2 h reaction time). The diameter of the AuNFs increased from 148 ± 16 nm to 219 ± 21 nm by varying the molar ratio from 6 : 1 to 3 : 1. At equimolar ratio of $-NH_2/HAuCl_4$ (entry 3), irregular AuNFs with more dispersed shapes are observed (Fig. 2C and Fig. S8, ESI†). Here, most likely, the number of primary amines from the template is not sufficient to complex the available $AuCl_4^-$ in solution and the biopolymer is not able to stabilize the resulting AuNFs well.

The reaction temperature also plays a crucial role for the formation of PNIPAM-AuNFs. At $-NH_2/HAuCl_4$ molar ratio of 3 : 1, a temperature shift from 23 °C to 40 °C results in the formation of much smaller AuNFs with an average diameter of only 61 ± 9 nm (Fig. 2D–F and Fig. S9, ESI†) compared to 219 ± 21 nm at 23 °C. The temperature-controlled AuNF growth is attributed to the thermal-responsive characteristics of the PNIPAM shell at the AuNFs surface. Below 23 °C, PNIPAM remains well soluble in water. Therefore, gold ions and nanoclusters can penetrate the PNIPAM shell, aggregate and form larger gold

View Article Online
Materials Chemistry Frontiers Research Article

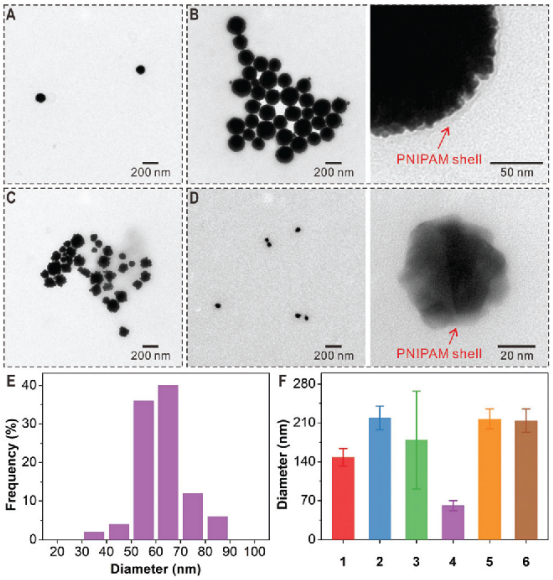

Fig. 2 TEM characterization of PNIPAM-AuNFs prepared under different conditions: (A) $-NH_2/HAuCl_4$ 6 : 1, 23 °C, 2 h; (B) $-NH_2/HAuCl_4$ 3 : 1, 23 °C, 2 h; (C) $-NH_2/HAuCl_4$ 1 : 1, 23 °C, 2 h; (D) $-NH_2/HAuCl_4$ 3 : 1, 40 °C, 2 h; (E) size distribution of PNIPAM-AuNFs (entry 4); (F) the average diameters of PNIPAM-AuNFs (entries 1–6, Table 1).

nanoparticles. However, when the temperature is increased above the lower critical solution temperature (LCST) of PNIPAM, *i.e.* to 40 °C, the PNIPAM chains collapse and form a dense shell preventing further growth of the AuNFs. Therefore, AuNF formation can be controlled *in situ* during the polymerization process by simply adjusting the temperature.

Varying the reaction time from 1 h to 2 h and 4 h does not affect the size and morphology of AuNFs and only a slight impact on the thickness of the PNIPAM shell is observed as depicted in the TEM images in Fig. S10 and S11 (ESI†). In these experiments, a $-NH_2/HAuCl_4$ molar ratio of 3 : 1 and a reaction temperature of 23 °C are selected indicating that AuNF formation is already completed within 1 h reaction time.

The thermo-responsiveness of the PNIPAM-AuNFs is studied by dynamic light scattering (DLS). The hydrodynamic radius of PNIPAM-AuNFs is monitored during temperature increase from 20 °C to 60 °C with 5 °C increments (Fig. 3 and Table S1, ESI†). When the temperature is kept below 30 °C, the hydrodynamic radius (R_h) of PNIPAM-AuNFs remains constant within the range of 52–60 nm. However, R_h reveals a pronounced drop to less than 30 nm when the temperature increases from 30 °C to 35 °C. The sizes of PNIPAM-AuNFs above 30 °C correlate to the dimensions measured by TEM as depicted in Fig. 2D. Also, the transition temperature is consistent with the LCST of PNIPAM (32 °C) reported in the literature.[29,32,33] During the experiment, the solution turns slightly turbid when the temperature increases above the LCST, indicating the formation of some minor aggregates of PNIPAM-AuNFs. This is probably the reason for the size increase when the temperature rises from 40 °C to 60 °C (Fig. 3).

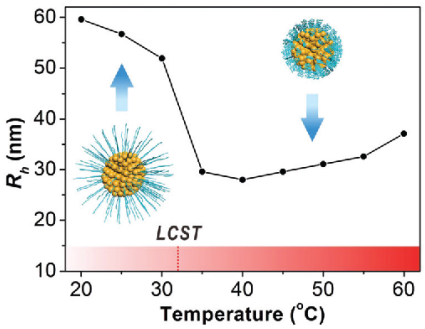

Fig. 3 Hydrodynamic radius of PNIPAM-AuNFs (entry 4) determined by DLS at increased temperature from 20 °C to 60 °C.

However, the nanohybrids can be easily re-dispersed by shaking at room temperature and the solution becomes transparent again.

PNIPAM-AuNFs with rough surfaces and a thermo-responsive polymer shell could serve as smart catalysts. As a proof of concept, the catalytic performance of PNIPAM-AuNFs is analyzed at different temperatures for the well-known hydrogenation reaction of *p*-nitrophenol to *p*-aminophenol.[34–36] This reaction allows monitoring the catalytic activity of noble metal-based nanomaterials by UV-vis spectroscopy.[37,38] Fig. 4 compares the catalytic properties of PNIPAM-AuNFs (entry 4) for the reduction of *p*-nitrophenol in the presence of $NaBH_4$ at different temperatures. At 23 °C, after PNIPAM-AuNFs have been added to the reaction solution, the characteristic peak of *p*-nitrophenol decreases gradually within 50 min reaction time (Fig. 4A). During this process, the solution changes from yellow to colorless. As a control, no absorption changes are observed after mixing $NaBH_4$ and *p*-nitrophenol for 2 h in the absence of PNIPAM-AuNFs (Fig. S13, ESI†). These results support that the PNIPAM-AuNFs possess

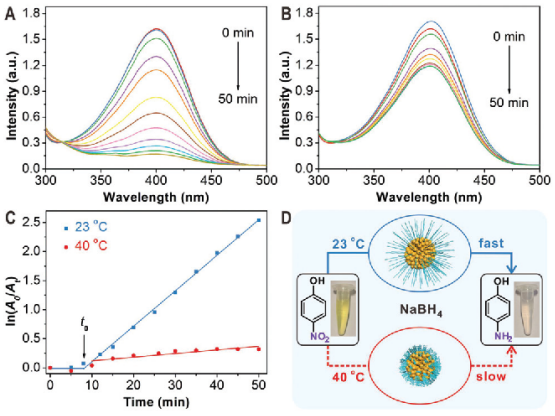

Fig. 4 Temperature-controlled catalysis by PNIPAM-AuNFs. (A and B) UV-vis spectra of the reaction solution for the hydrogenation of *p*-nitrophenol at 23 °C (A) and 40 °C (B). (C) Plots of $\ln(A_0/A_t)$ at 400 nm *versus* reaction time. (D) Scheme for the hydrogenation reaction catalyzed by PNIPAM-AuNFs at different temperatures.

View Article Online
Research Article Materials Chemistry Frontiers

catalytic activity for the hydrogenation reaction. In contrast, the characteristic peak of *p*-nitrophenol only decreases slightly within 50 min in the presence of PNIPAM-AuNFs at 40 °C (Fig. 4B). $\ln\{A_0/A_t\}$ at 400 nm is plotted against to the reaction time for both temperatures, where A_0 and A_t are the absorbance at time 0 and t. Interestingly, an induction time (t_0) is observed in the initial phase, which is ascribed to the diffusion time of *p*-nitrophenol through the PNIPAM shell.[39] After the induction time, $\ln\{A_0/A_t\}$ has a linear relationship to the reaction time, indicating that the reduction follows first-order kinetics.[40] At an extremely low gold concentration of 1.52 mg L^{-1} in the catalytic reaction solution, the PNIPAM-AuNFs show an apparent rate constant (k_{app}) of 1.02×10^{-3} s^{-1} at 23 °C, which is among the best performing nanocatalysts ever reported (see Table S2, ESI†). In contrast, by increasing the temperature to 40 °C, a significant drop in the rate constant down to about 10% is observed, as indicated by a k_{app} of 1.04×10^{-4} s^{-1} (Fig. 4C). Obviously, the PNIPAM shell serves as a diffusion barrier for *p*-nitrophenol in the collapsed form resulting in a significant reduction in catalytic activity (Fig. 4D). It is worthy of note that the polymer coating could also have an adverse impact on the catalytic performance as it acts as a physical barrier restricting the access of *p*-nitrophenol to the AuNFs.[41] There is potential to further optimize the thickness of the PNIPAM coating to increase catalytic performance while retaining high stability and stimulus-responsiveness of the nanohybrids. In addition, the nanocatalyst could be easily recycled by centrifugation but then, a slight decrease of the catalytic activity is observed (Fig. S15, ESI†).

In summary, we have reported a convenient one-pot strategy for the preparation of PNIPAM-coated AuNF catalysts by combining ARGET ATRP and the reduction of metal ions. The chloroauric anion binding capacity of cationized HSA in combination with the attached ATRP initiators provide an HSA-based macroinitiator allowing polymer growth and nanoparticle formation in a one-step reaction. The sizes and shapes of the resulting AuNFs have been controlled by varying the temperature as well as the molar ratio of the free amino groups from the biopolymer template to the chloroauric anions. The thickness of polymer shell has been adjusted by varying the reaction time. More importantly, the PNIPAM-AuNFs serve as water-soluble and temperature-responsive catalyst for the hydrogenation of *p*-nitrophenol.

The *in situ* reduction of metal ions and ARGET ATRP has not been combined before for the preparation of polymer–metal nanocomposites. Compared with conventional methods that involve nanoparticle synthesis, purification and post-modification, *in situ* growth allows the convenient synthesis of polymer-coated metal catalysts without tedious reaction and purification procedures. More significantly, smart polymers formed during the polymerization process provide additional *in situ* control over the formation of metal nanostructures, which has not been achieved yet. We believe the novel strategy could be expanded to construct other polymer–metal hybrid materials for various applications such as sensing, catalysis, controlled drug delivery, and photothermal therapy.

Conflicts of interest

There are no conflicts to declare.

Acknowledgements

The authors acknowledge financial support by the Deutsche Forschungsgemeinschaft (DFG, German Research Foundation) – Project number 213555243 SFB 1066 (A06). C. C. is grateful for a doctoral fellowship from Promotionskolleg Pharmaceutical Biotechnology of Ulm University funded by the state of Baden-Württemberg. We thank Christine Rosenauer for her help with the light scattering measurements. We also thank Christopher Synatschke and Nicole Kirsch-Pietz for critically reading the manuscript. Open Access funding provided by the Max Planck Society.

Notes and references

1 G. Palui, F. Aldeek, W. T. Wang and H. Mattoussi, *Chem. Soc. Rev.*, 2015, **44**, 193.
2 D. Kim, S. Park, J. H. Lee, Y. Y. Jeong and S. Jon, *J. Am. Chem. Soc.*, 2007, **129**, 7661.
3 P. Xu, X. J. Han, B. Zhang, Y. C. Du and H. L. Wang, *Chem. Soc. Rev.*, 2014, **43**, 1349.
4 J. Shan and H. Tenhu, *Chem. Commun.*, 2007, 4580.
5 Y. Ofir, B. Samanta and V. M. Rotello, *Chem. Soc. Rev.*, 2008, **37**, 1814.
6 G. I. Dzhardimalieva and I. E. Uflyand, *J. Polym. Res.*, 2018, **25**, 255.
7 V. M. Kariuki, J. C. Hoffmeier, I. Yazgan and O. A. Sadik, *Nanoscale*, 2017, **9**, 8330.
8 H. L. Li, Y. Yang, Y. Z. Wang, W. Li, L. H. Bi and L. X. Wu, *Chem. Commun.*, 2010, **46**, 3750.
9 W. Wang, X. Yang and H. Cui, *J. Phys. Chem. C*, 2008, **112**, 16348.
10 L. L. Zhao, X. H. Ji, X. J. Sun, J. Li, W. S. Yang and X. G. Peng, *J. Phys. Chem. C*, 2009, **113**, 16645.
11 S. J. Ye, F. Benz, M. C. Wheeler, J. Oram, J. J. Baumberg, O. Cespedes, H. K. Christenson, P. L. Coletta, L. J. C. Jeuken, A. F. Markham, K. Critchley and S. D. Evans, *Nanoscale*, 2016, **8**, 14932.
12 A. J. Wang, Y. F. Li, M. Wen, G. Yang, J. J. Feng, J. Yang and H. Y. Wang, *New J. Chem.*, 2012, **36**, 2286.
13 Q. Li, Y. Y. Jiang, R. C. Han, X. L. Zhong, S. Y. Liu, Z. Y. Li, Y. L. Sha and D. S. Xu, *Small*, 2013, **9**, 927.
14 C. Y. Song, B. Y. Yang, W. Q. Chen, Y. X. Dou, Y. J. Yang, N. Zhou and L. H. Wang, *J. Mater. Chem. B*, 2016, **4**, 7112.
15 J. P. Xie, Q. B. Zhang, J. Y. Lee and D. I. C. Wang, *ACS Nano*, 2008, **2**, 2473.
16 D. P. Yang, X. Liu, C. P. Teng, C. Owh, K. Y. Win, M. Lin, X. J. Loh, Y. L. Wu, Z. B. Li and E. Y. Ye, *Nanoscale*, 2017, **9**, 15753.
17 Q. L. Cui, F. He, X. Y. Wang, B. H. Xia and L. D. Li, *ACS Appl. Mater. Interfaces*, 2013, **5**, 213.
18 J. Virkutyte and R. S. Varma, *Chem. Sci.*, 2011, **2**, 837.
19 D. Xu, J. J. Gu, W. N. Wang, X. C. Yu, K. Xi and X. D. Jia, *Nanotechnology*, 2010, **21**, 375101.

20 W. Jakubowski and K. Matyjaszewski, *Angew. Chem., Int. Ed.*, 2006, **45**, 4482.
21 K. Min, H. F. Gao and K. Matyjaszewski, *Macromolecules*, 2007, **40**, 1789.
22 Y. Kwak, A. J. D. Magenau and K. Matyjaszewski, *Macromolecules*, 2011, **44**, 811.
23 A. Simakova, S. E. Averick, D. Konkolewicz and K. Matyjaszewski, *Macromolecules*, 2012, **45**, 6371.
24 W. Bal, M. Sokolowska, E. Kurowska and P. Faller, *Biochim. Biophys. Acta*, 2013, **1830**, 5444.
25 S. Chakrabortty, B. K. Agrawalla, A. Stumper, N. M. Veg, S. Fischer, C. Reichardt, M. Kogler, B. Dietzek, M. Feuring-Buske, C. Buske, S. Rau and T. Weil, *J. Am. Chem. Soc.*, 2017, **139**, 2512.
26 Y. Z. Wu, S. Chakrabortty, R. A. Gropeanu, J. Wilhelmi, Y. Xu, K. S. Er, S. L. Kuan, K. Koynov, Y. Chan and T. Weil, *J. Am. Chem. Soc.*, 2010, **132**, 5012.
27 Y. Z. Wu, A. Ermakova, W. N. Liu, G. Pramanik, T. M. Vu, A. Kurz, L. McGuinness, B. Naydenov, S. Hafner, R. Reuter, J. Wrachtrup, J. Isoya, C. Fortsch, H. Barth, T. Simmet, F. Jelezko and T. Weil, *Adv. Funct. Mater.*, 2015, **25**, 6576.
28 D. Y. W. Ng, Y. Z. Wu, S. L. Kuan and T. Weil, *Acc. Chem. Res.*, 2014, **47**, 3471.
29 R. A. Alvarez-Puebla, R. Contreras-Caceres, I. Pastoriza-Santos, J. Perez-Juste and L. M. Liz-Marzan, *Angew. Chem., Int. Ed.*, 2009, **48**, 138.
30 M. Tagliazucchi, M. G. Blaber, G. C. Schatz, E. A. Weiss and I. Szleifert, *ACS Nano*, 2012, **6**, 8397.
31 S. Maji, B. Cesur, Z. Y. Zhang, B. G. De Geest and R. Hoogenboom, *Polym. Chem.*, 2016, **7**, 1705.
32 R. Contreras-Caceres, A. Sanchez-Iglesias, M. Karg, I. Pastoriza-Santos, J. Perez-Juste, J. Pacifico, T. Hellweg, A. Fernandez-Barbero and L. M. Liz-Marzan, *Adv. Mater.*, 2008, **20**, 1666.
33 B. S. Li, D. M. Smilgies, A. D. Price, D. L. Huber, P. G. Clem and H. Y. Fan, *ACS Nano*, 2014, **8**, 4799.
34 J. L. Zhang, M. X. Zhang, K. J. Tang, F. Verpoort and T. L. Sun, *Small*, 2014, **10**, 32.
35 X. Y. Zhu, Z. S. Lv, J. J. Feng, P. X. Yuan, L. Zhang, J. R. Chen and A. J. Wang, *J. Colloid Interface Sci.*, 2018, **516**, 355.
36 Z. S. Lv, X. Y. Zhu, H. B. Meng, J. J. Feng and A. J. Wang, *J. Colloid Interface Sci.*, 2019, **538**, 349.
37 Y. Yu, W. Q. Xiao, T. T. Zhou, P. Zhang, C. Yan and Z. J. Zheng, *Mater. Chem. Front.*, 2017, **1**, 482.
38 X. F. Zhang, X. Y. Zhu, J. J. Feng and A. J. Wang, *Appl. Surf. Sci.*, 2018, **428**, 798.
39 Z. Chen, Z. M. Cui, C. Y. Cao, W. D. He, L. Jiang and W. G. Song, *Langmuir*, 2012, **28**, 13452.
40 S. Wunder, Y. Lu, M. Albrecht and M. Ballauff, *ACS Catal.*, 2011, **1**, 908.
41 Z. Q. Niu and Y. D. Li, *Chem. Mater.*, 2014, **26**, 72.

Electronic Supplementary Material (ESI) for Materials Chemistry Frontiers.

Supplementary Information

Polymer-grafted gold nanoflowers with temperature-controlled catalytic features by *in situ* particle growth and polymerization

Chaojian Chen,[1,2] *David Yuen Wah Ng,*[1,*] *and Tanja Weil*[1,2,*]

[1]Max Planck Institute for Polymer Research, Ackermannweg 10, 55128 Mainz, Germany

[2]Ulm University, Albert-Einstein-Allee 11, 89081 Ulm, Germany

E-mails: weil@mpip-mainz.mpg.de; david.ng@mpip-mainz.mpg.de

Table of Contents

III. SUPPLEMENTARY RESULTS

IV. REFERENCES

I. EXPERIMENTAL

1.1 Materials

Human serum albumin (HSA, 96%), tris(2-carboxyethyl) phosphine hydrochloride (TCEP, ≥98%), 2-bromoisobutanoic acid *N*-hydroxysuccinimide ester (NHS-BiB, 98%), *O*-[(*N*-succinimidyl)succinyl-aminoethyl]-*O'*-methylpolyethylene glycol (NHS-PEG, M_n ~2000), *N*-(2-aminoethyl)maleimide trifluoroacetate salt (MI-NH_2, 95%), *N*-(3-Dimethylaminopropyl)-*N'*-ethylcarbodiimide hydrochloride (EDC·HCl, ≥98%), tris(2-pyridylmethyl)amine (TPMA, 98%), copper(II) bromide ($CuBr_2$, 99%), *p*-nitrophenol (≥99%), and L-ascorbic acid (≥99%) were purchased from Sigma-Aldrich and used without further treatment. Chloroauric acid ($HAuCl_4$, >99.5%) was obtained from Carl Roth. Ethylendiamine (>99%), urea (99.5%) and ethylenediaminetetraacetic acid (EDTA, 98%) were purchased from Acros Organics and used as received. *N*-isopropylacrylamide (NIPAM, >98%) was bought from TCI. Sodium borohydride ($NaBH_4$, >95%) was obtained from Fisher Chemical. All other solvents and salts were obtained from commercial suppliers and used as received.

1.2 Preparation of cationic HSA (cHSA) [1]

HSA (150 mg, 2.26 μmol) was dissolved in 15 mL of degassed ethylenediamine solution (2.5 M) and the pH was tuned to 4.75 with HCl. After adding EDC·HCl (4 mmol, 766 mg) and stirring for two hours at room temperature, acetate buffer (1 mL, 4 M, pH 4.75) was added to terminate the reaction. The obtained reaction solution was purified twice with acetate buffer (100 mM, pH 4.75) and three times with deionized water by ultracentrifugation using a Vivaspin 20 concentrator (MWCO 30 kDa). The resulting solution was lyophilized to afford the product as a white fluffy solid (154 mg, yield: 94%, MALDI-ToF MS: 72.3 kDa).

1.3 Preparation of PEGylated cHSA (PEG-cHSA) [1]

First, cHSA (100 mg, 1.4 μmol) was dissoleved in degassed phosphate buffer (30 mL, 50 mM, pH 8.0). NHS-PEG (105 mg, 52.4 μmol) was dissolved in 0.4 mL of DMSO and then added to the cHSA solution. After stirring at room temperature for four hours, the reaction solution was purified five times with deionized water by ultracentrifugation using a Vivaspin

20 concentrator (MWCO 30 kDa). The resulting solution was lyophilized to obtain the product as a white fluffy solid (151 mg, yield: 80 %). The MALDI-ToF MS indicated a molecular weight of 136.6 kDa which means on average 32 PEG chains were conjugated to each cHSA backbone.

1.4 Synthesis of denatured PEG-cHSA (PEG-dcHSA) [2]

Preparation of the urea-phosphate buffer (urea-PB)

Urea (150.15 g, 2.5 mol), EDTA (292.24 mg, 1 mmol), $Na_2HPO_4 \cdot 7H_2O$ (5.4276 g, 25 mmol) and NaH_2PO_4 (0.5699 g, 25 mmol) were dissolved in 0.5 L of deionized water. The urea-PB with 50 mM phosphate buffer, 5 M urea and 2 mM EDTA was then obtained by adjusting the pH to 7.4.

Synthesis of PEG-dcHSA

To a 50 mL flask, 20 mL of urea-PB was added and then degassed via bubbling for five minutes. Followed PEG-cHSA (27.2 mg, 200 nmol) was dissolved and further stirred for 15 min. TCEP (0.58 mg, 2 μmol) was added and stirred for 30 min under argon flow. Lastly, MI-NH_2 (15.24 mg, 60 μmol) was added and stirred overnight under argon protection. The obtained reaction solution was purified three times with urea-PB and five times with deionized water by ultracentrifugation using a Vivaspin 20 concentrator (MWCO 30 kDa). The resulting solution was lyophilized to afford the product as a white fluffy solid (24.1 mg, yield: 86%, MALDI-ToF MS: 140.4 kDa).

1.5 Synthesis of macroinitiator PEG-dcHSA-Br

PEG-dcHSA-Br was synthesized by attaching ATRP initiators to PEG-dcHSA. In a typical procedure, PEG-dcHSA (20 mg, 145 nmol) was dissolved in 20 mL of $NaHCO_3$ (0.1 M, pH 8.5). NHS-BiB (218 mg, 0.826 mmol) dissolved in 2.18 mL of DMSO was then added dropwise into the PEG-dcHSA solution. The reaction solution was stirred overnight at room temperature and purified eight times with deionized water by ultracentrifugation using a Vivaspin 20 concentrator (MWCO 50 kDa). The product was obtained as a white fluffy solid after lyophilizing (11.1 mg, yield: 51%, MALDI-ToF MS: 149.5 kDa).

1.6 Preparation of PNIPAM-AuNFs

Preparation of the stock solution of $CuBr_2$/TPMA catalyst

$CuBr_2$ (4.47 mg, 0.02 mmol) and TPMA (46.5 mg, 0.16 mmol) was dissolved in 1 mL mixed solution of water:DMF (1:1 v/v) and stored at 4 °C prior to use. Therefore, the concentration of the effective Cu^{2+} in the stock solution was 20 nmol μL^{-1}.

Preparation of the ascorbic acid solution

To a 10 mL Schlenk flask, L-ascorbic acid (4.4 mg, 25 μmol) was firstly added under argon flow. Degassed deionized water (5 mL) was then added to dissolve L-ascorbic acid. The solution was then stirred under argon flow for 40 min. Therefore, the concentration of L-ascorbic acid was 5 nmol μL^{-1}.

Synthesis of PNIPAM-AuNFs

In a typical procedure for the synthesis of PNIPAM-AuNFs (Entry **1** in Table 1), the protein-derived substrate and macroinitiator PEG-dcHSA-Br (0.449 mg, 3 nmol with ~300 nmol of amino groups and 183 nmol of ATRP initiation sites) was first dissolved in Milli-Q water with a concentration of 1 mg mL^{-1} and then added into a 5 mL Schlenk tube. Followed $HAuCl_4$ solution (25 μL, 2 mM in Milli-Q water), the monomer NIPAM (41.4 mg, 366 μmol), the stock solution of $Cu^{II}Br_2$/TPMA catalyst (11 μL, 220 nmol of Cu^{2+}), and 0.55 mL of Milli-Q water were added. Oxygen in the mixture was then removed through three freeze-pump-thaw cycles and the solution was stirred at room temperature for one hour for the gold ions to absorb to the amino groups of PEG-dcHSA-Br. Ascorbic acid solution was then added via a syringe pump at a slow speed of 0.6 μL min^{-1}, the reaction was proceeded for 2 h at room temperature (23 °C). The final product was purified by centrifugation to remove the unreacted monomers and other impurities. For Entry **2** and **3**, the molar ratio of amino groups from PEG-dcHSA-Br to $HAuCl_4$ was tuned by increasing the added amount of $HAuCl_4$. For other reaction conditions (Entry **4-6**), the reaction temperature and time were changed respectively.

1.7 Catalytic reduction of *p*-nitrophenol

1 mL of $NaBH_4$ aqueous solution (50 mM dissolved in Milli-Q water) and 0.2 mL of freshly prepare *p*-nitrophenol aqueous solution (1 mM, pH = 12) were added to a 2 mL cuvette and mixed. The cuvette was placed in a water bath at a determined temperature. Then, 0.1 mL of PNIPAM-AuNFs solution with 0.01 μmol (1.97 μg) Au was quickly injected into the reaction cuvette and the reaction was monitored by UV-vis spectrometer. The absorbance at 400 nm was subtracted from that at 500 nm to correct for background absorption and then used to calculate the conversion and apparent rate constant (k_{app}). The conversion (C) was calculated using the following equation

$$C = \frac{A_0 - A_t}{A_0} \times 100\%$$

where A_0 and A_t are the absorbance at time 0 and t. The apparent rate constant was determined as the slope of $\ln(A_0/A_t)$ at 400 nm against to the reaction time.

II. CHARACTERIZATION

2.1 Matrix-assisted laser desorption/ionization (MALDI) mass spectrometry

MALDI time-of-flight (MALDI-ToF) mass spectrometry was performed on Bruker rapifleX spectrometer. Saturated solution of sinapinic acid dissolved in a 50:50 water/acetonitrile with 0.2% TFA (trifluoroacetic acid) was used as the matrix solution.

2.2 Transmission electron microscopy (TEM)

TEM samples were prepared by adding 4 μL of the PNIPAM-AuNFs solution onto a carbon-coated copper grid. After drying in air for 10 min, the remained solution was removed by a filter paper and the grid was then dried in air. The measurement was conducted on a JEOL JEM-1400 TEM operating at an accelerating voltage of 120 kV. ImageJ software was used for the analysis of the size of PNIPAM-AuNFs samples.

2.3 Dynamic light scattering (DLS)

The aqueous solution of PNIPAM-AuNFs was filtered through a 0.5 μm filter (Millipore LCR) into a cylindrical quartz cuvette (18 mm diameter, Hellma, Germany) after cleaning it in an acetone fountain to remove dust. The experiment was performed on an ALV spectrometer (ALV-GmbH, Germany) equipped with an He-Ne laser (λ = 632.8 nm). For temperature-controlled measurements, the light scattering instrument was equipped with a thermostat from Julabo. All experiments were performed as a triplicate measurement. Data analysis was performed using ALV5000 software.

2.4 UV-vis spectroscopy

The samples were added in a Greiner 96 flat transparent plate. UV-vis absorbance spectra were collected using a TECAN (Spark 20M) microplate reader. The wavelength range was set from 250 to 500 nm. Before measurement, the plate was shaken for three seconds with a shaking amplitude of 1 mm and frequency of 1440 rpm.

III. SUPPLEMENTARY RESULTS

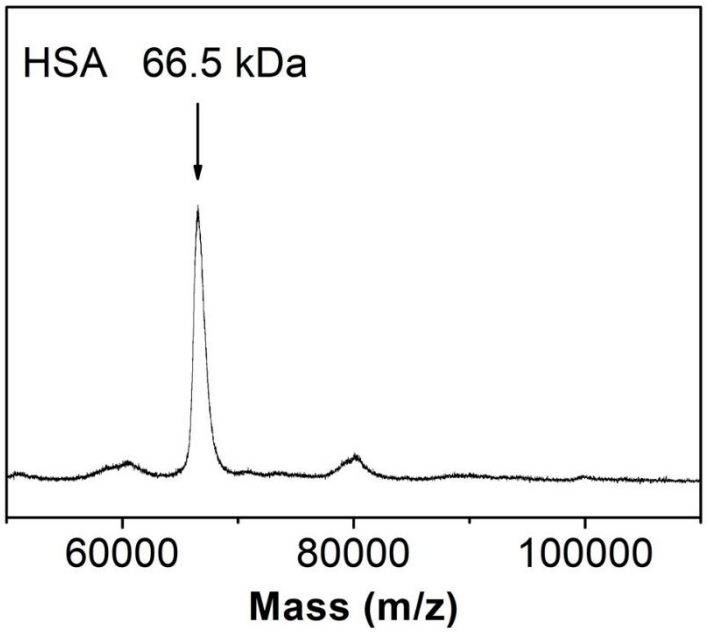

Fig. S1 MALDI-ToF mass spectrum of HSA.

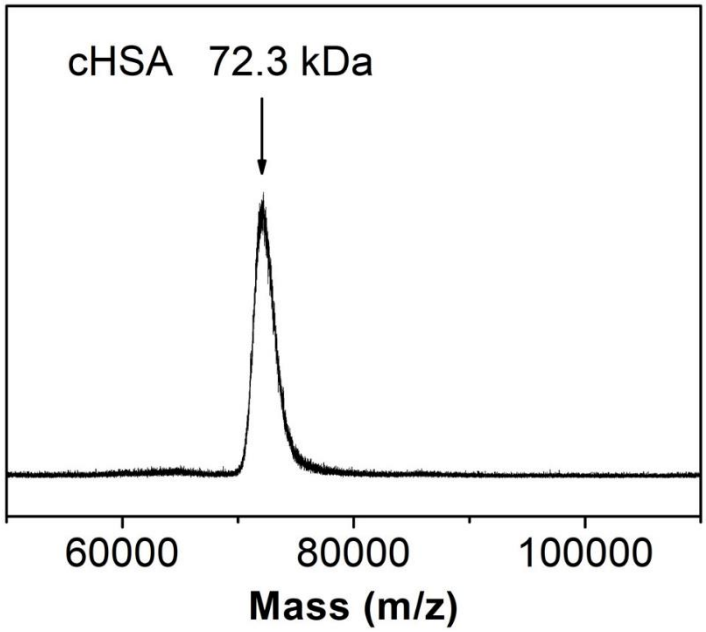

Fig. S2 MALDI-ToF mass spectrum of cHSA.

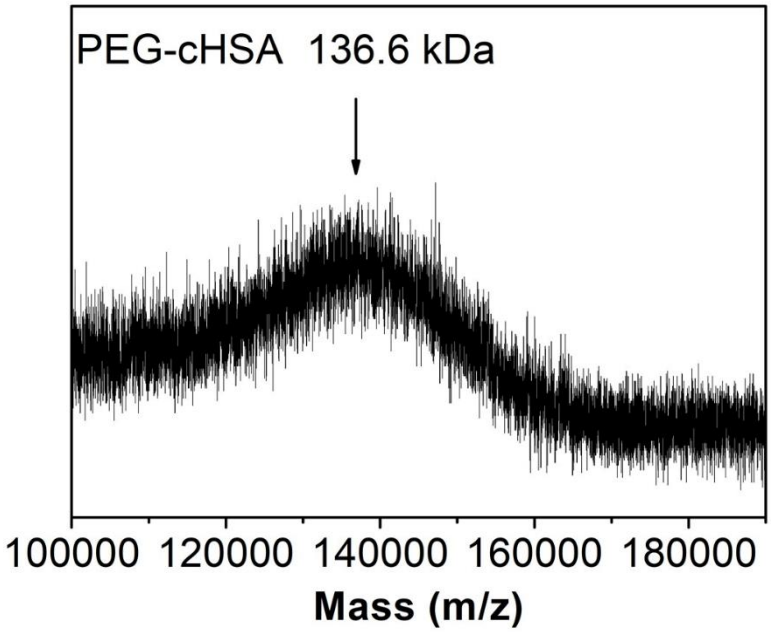

Fig. S3 MALDI-ToF mass spectrum of PEG-cHSA.

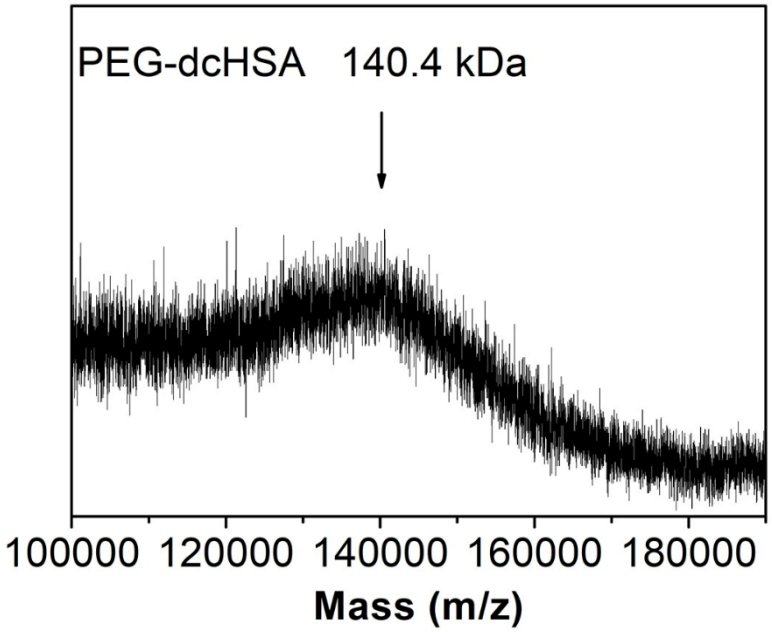

Fig. S4 MALDI-ToF mass spectrum of PEG-dcHSA.

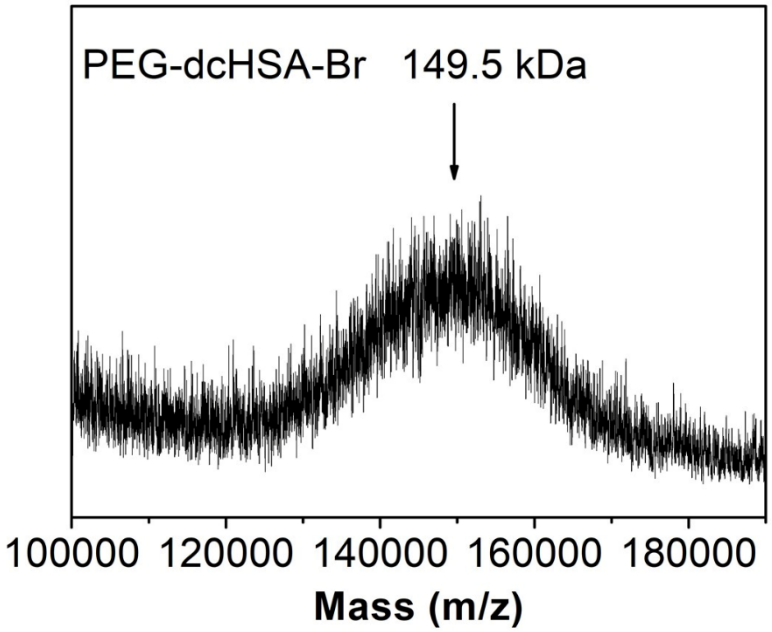

Fig. S5 MALDI-ToF mass spectrum of PEG-dcHSA-Br.

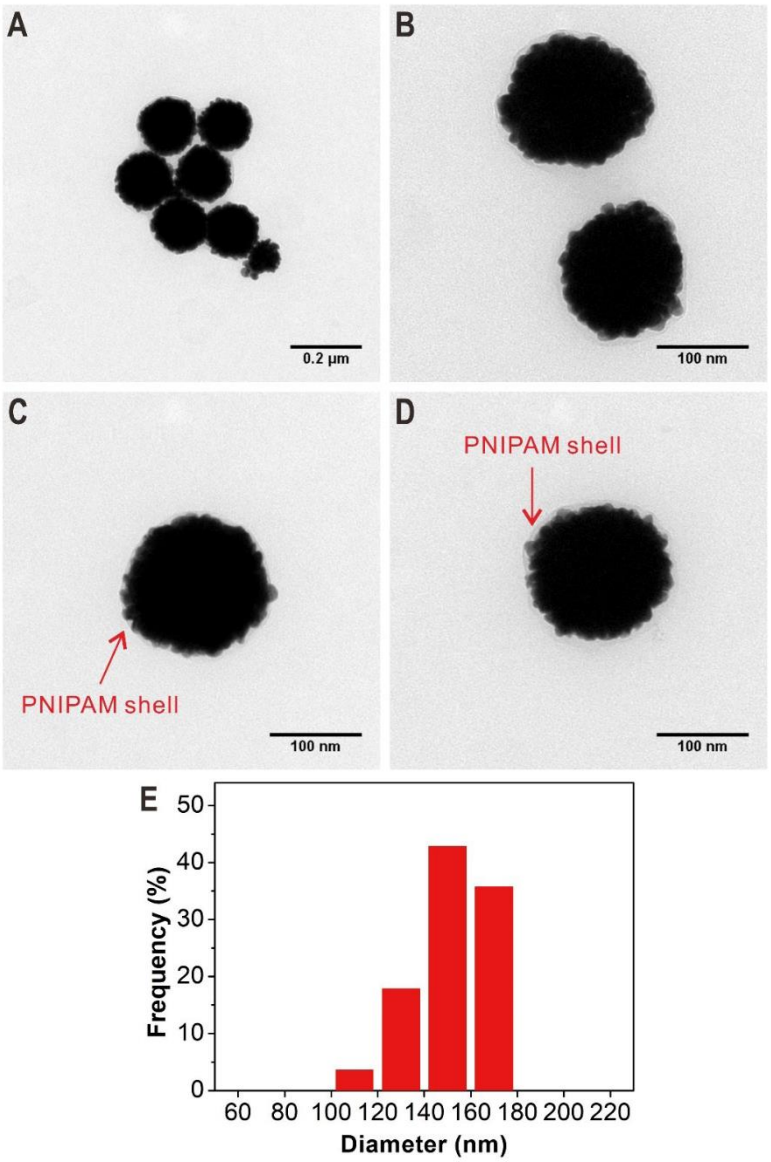

Fig. S6 TEM images (A-D) and size distribution (E) of PNIPAM-AuNFs entry 1 in Table 1 prepared with a molar ratio of $-NH_2/HAuCl_4$ = 6:1 at 23 °C for 2 h.

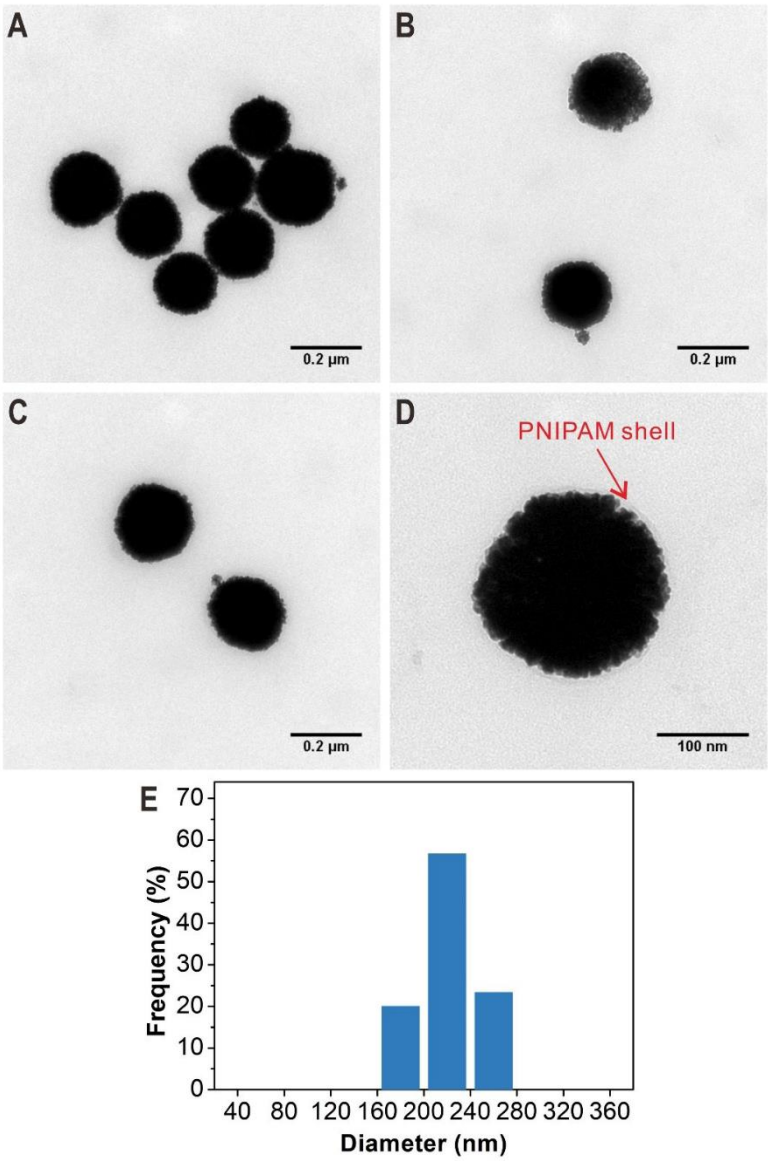

Fig. S7 TEM images (A-D) and size distribution (E) of PNIPAM-AuNFs entry **2** in Table 1 prepared with a molar ratio of $-NH_2/HAuCl_4$ = 3:1 at 23 °C for 2 h.

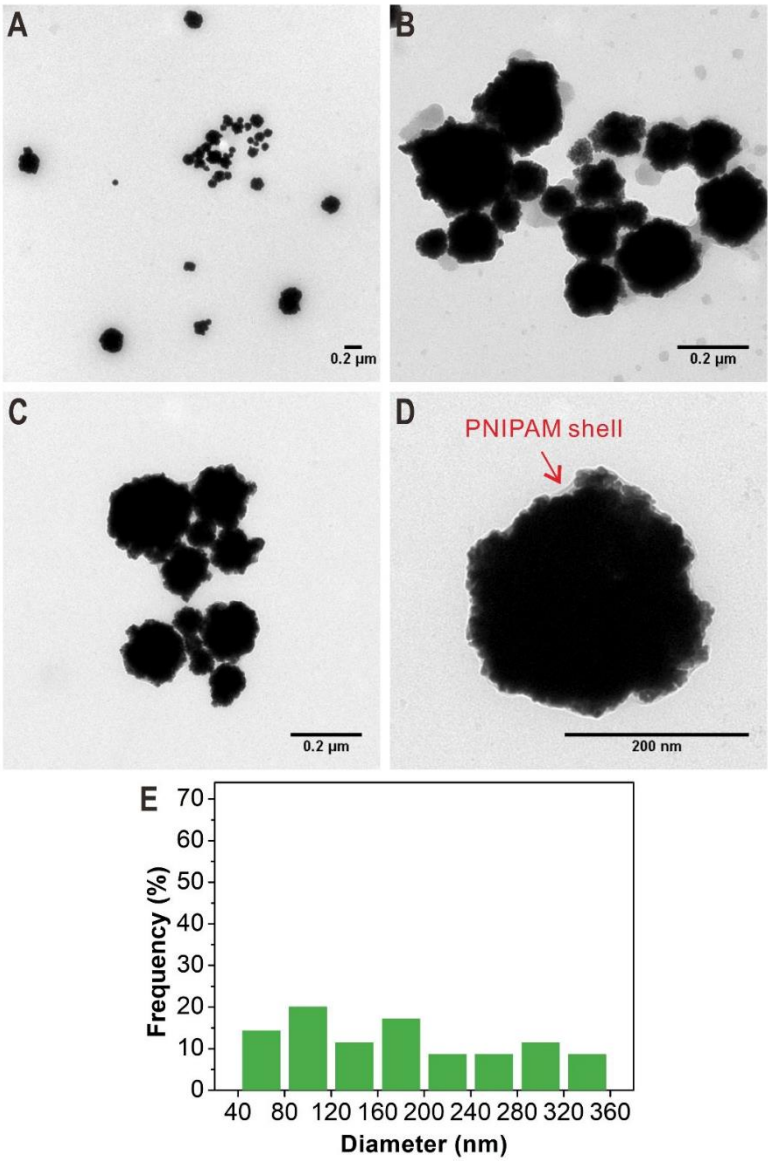

Fig. S8 TEM images (A-D) and size distribution (E) of PNIPAM-AuNFs entry **3** in Table 1 prepared with a molar ratio of $-NH_2/HAuCl_4$ = 1:1 at 23 °C for 2 h.

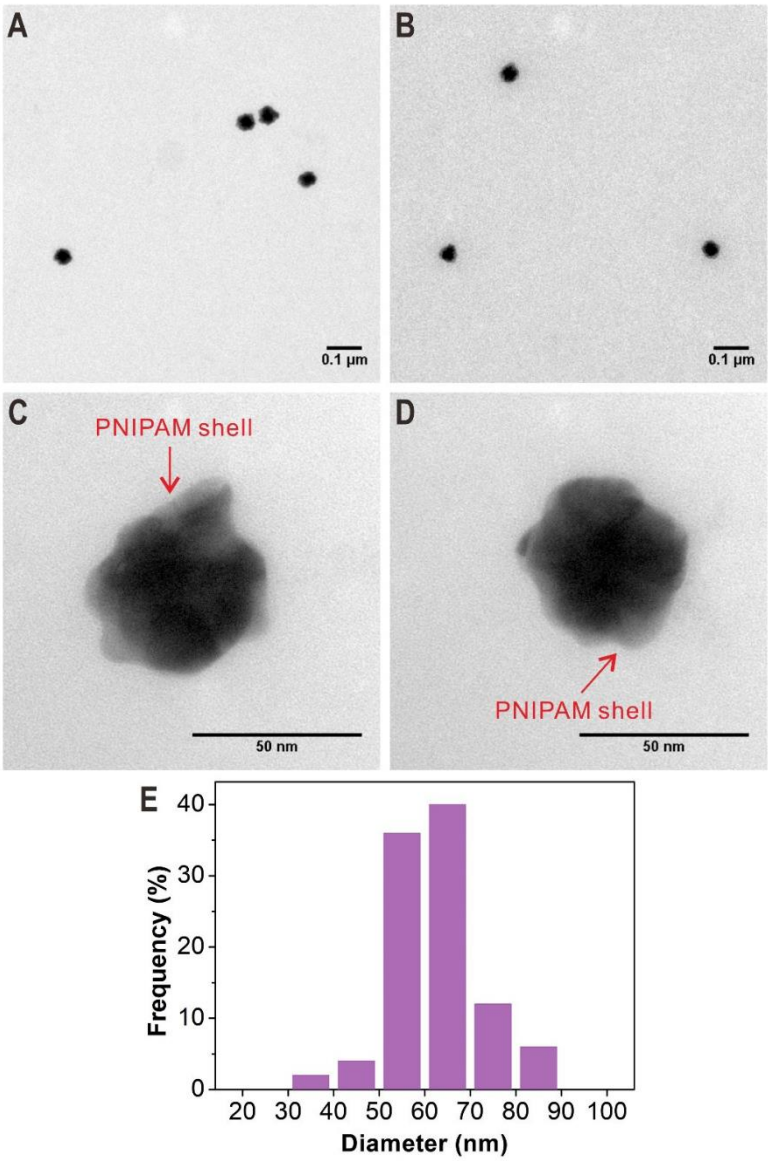

Fig. S9 TEM images (A-D) and size distribution (E) of PNIPAM-AuNFs entry **4** in Table 1 prepared with a molar ratio of $-NH_2/HAuCl_4$ = 3:1 at 40 °C for 2 h.

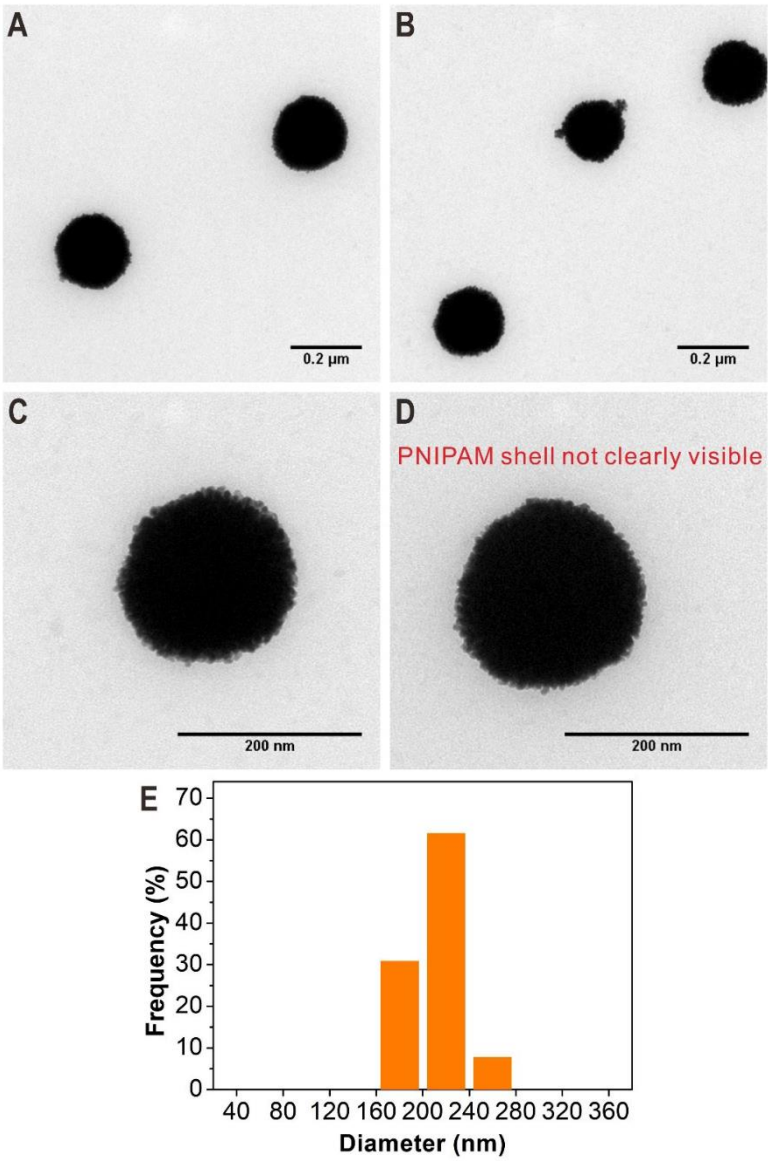

Fig. S10 TEM images (A-D) and size distribution (E) of PNIPAM-AuNFs entry **5** in Table 1 prepared with a molar ratio of $-NH_2/HAuCl_4$ = 3:1 at 23 °C for 1 h.

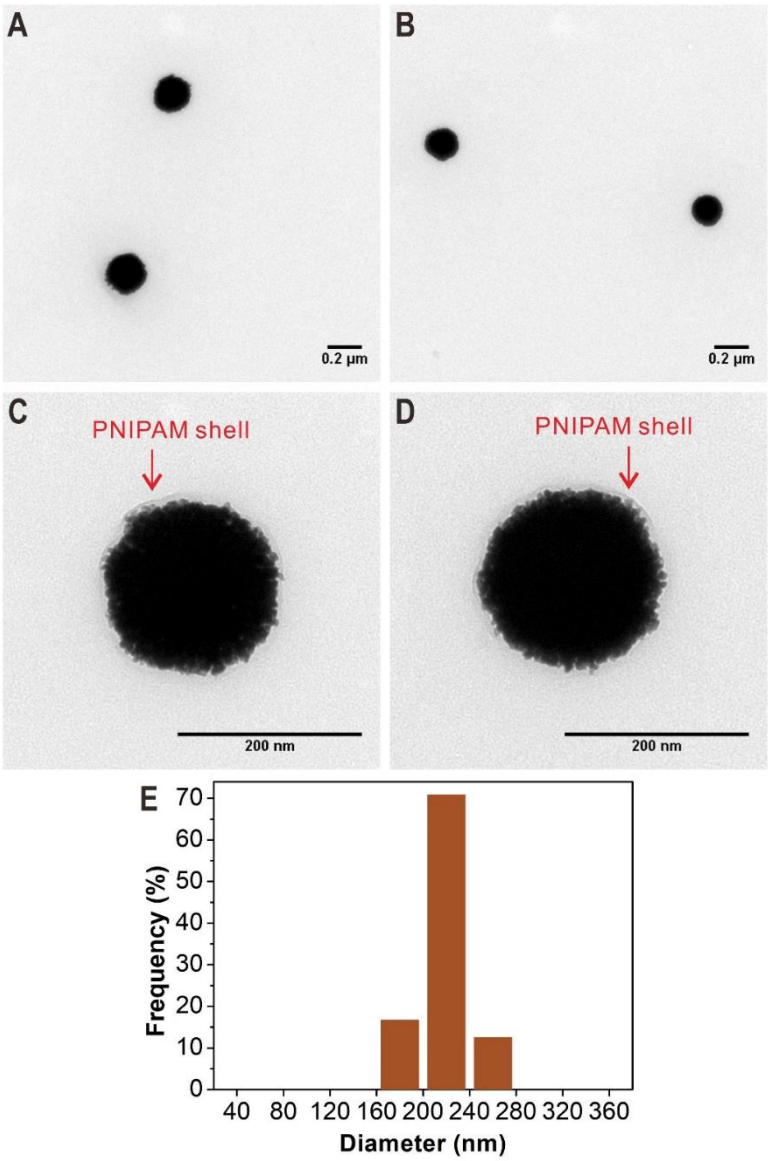

Fig. S11 TEM images (A-D) and size distribution (E) of PNIPAM-AuNFs entry **6** in Table 1 prepared with a molar ratio of $-NH_2/HAuCl_4$ = 3:1 at 23 °C for 4 h.

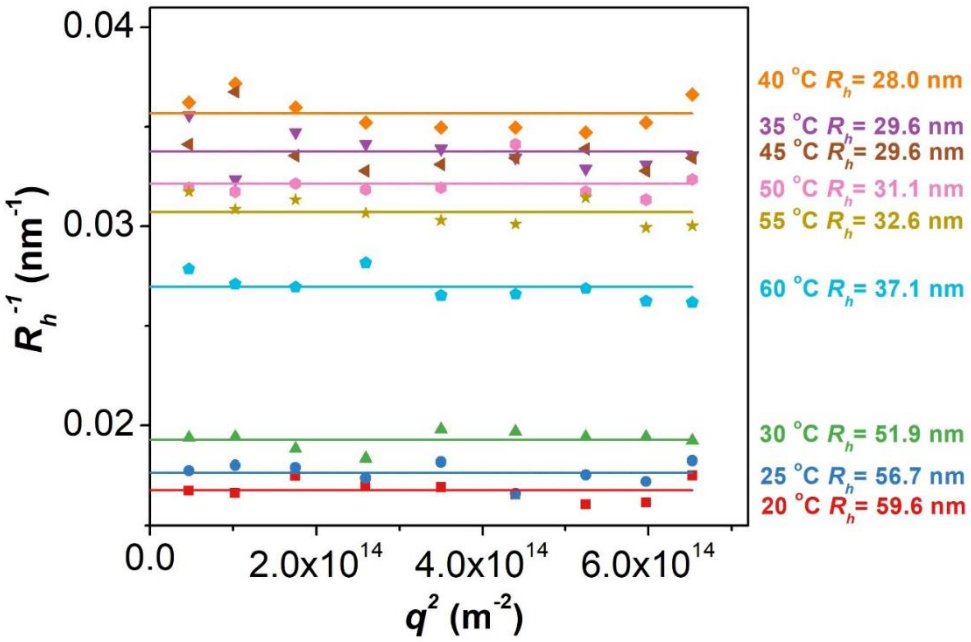

Fig. S12 DLS measurement of PNIPAM-AuNFs (entry 4 prepared under 40 °C) by tuning the temperature from 20 °C to 60 °C with a step of 5 °C.

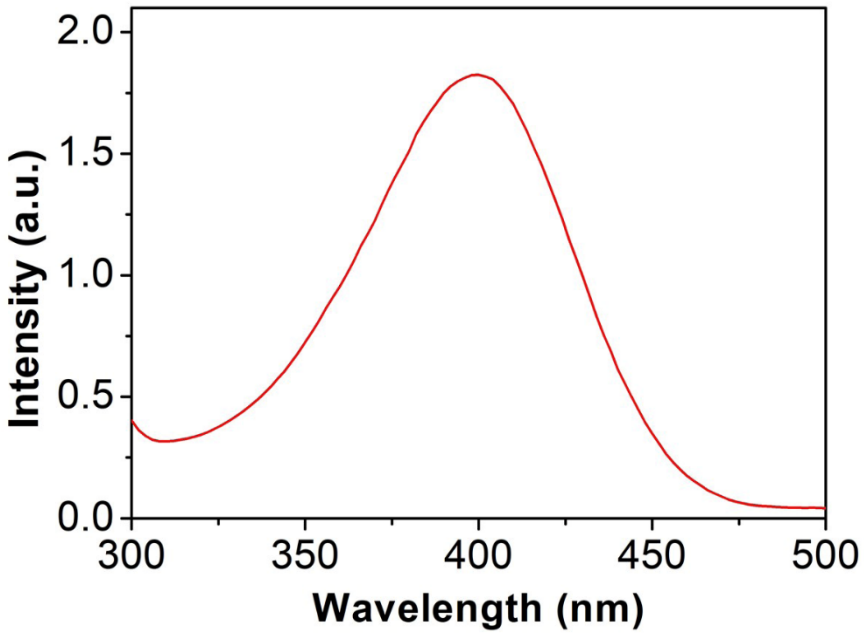

Fig. S13 UV-vis spectrum for the mixture of $NaBH_4$ and *p*-nitrophenol aqueous solution without adding PNIPAM-AuNFs after mixing 2 h.

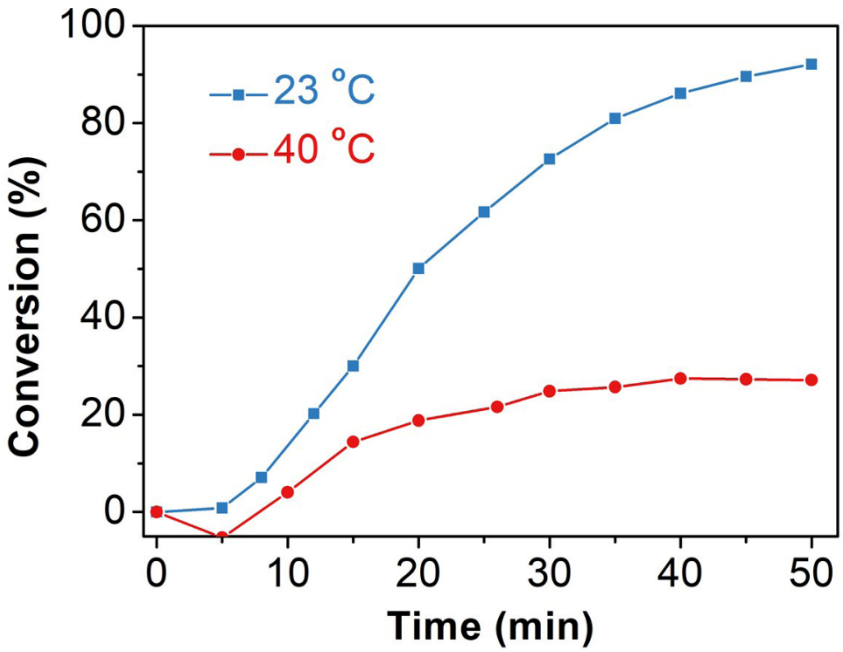

Fig. S14 Conversion *versus* reaction time for the reduction of *p*-nitrophenol using PNIPAM-AuNFs as the catalyst at different temperatures.

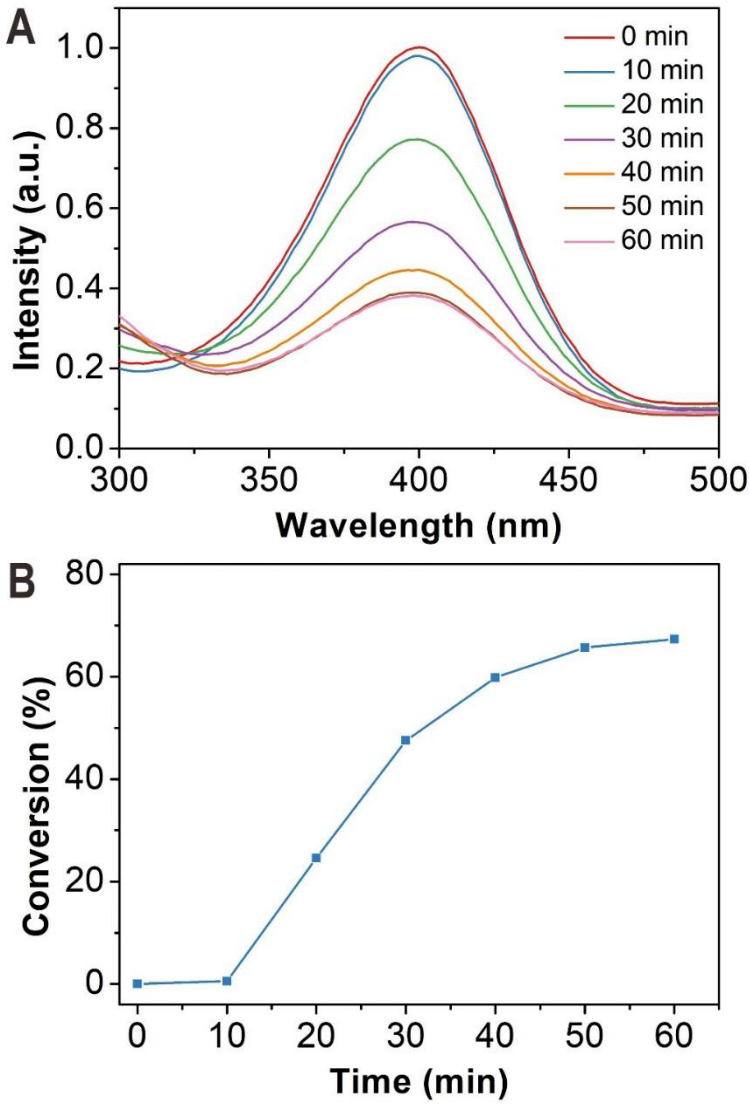

Fig. S15 Catalytic performance of recycled PNIPAM-AuNFs (entry **4**) for the hydrogenation reaction. (A) UV-vis spectra of the reaction solution for the hydrogenation of *p*-nitrophenol at different time points at room temperature. (B) Conversion *versus* reaction time for the reduction reaction catalyzed by the recycled PNIPAM-AuNFs.

Table S1 Sizes of PNIPAM-AuNFs (entry **4**) at different temperatures determined by DLS.

temperature (°C)	20	25	30	35	40	45	50	55	60
R_h (nm)	59.6	56.7	51.9	29.6	28	29.6	31.1	32.6	37.1

Table S2 Comparison of catalytic activities of various gold catalysts for the reduction of *p*-nitrophenol.

Au-based catalysts	k_{app} ($\times 10^{-3}$ s^{-1})	m_{Au}	k_{app}/m_{Au} (s^{-1} g^{-1})	M_{Au} (mg L^{-1})	k_{app}/M_{Au} ($\times 10^{-3}$ L s^{-1} mg^{-1})	activity tunability	refs
PNIPAM-AuNFs	1.02	1.97 μg	518	1.52	0.67	YES	this work
Au meso-flowers	/	/	1.56	/	/	NO	[3]
AuNFs	0.65	0.2 mg	3.25	62.5	0.01	NO	[4]
Spongy Au nanocrystals	2.1	6 mg	0.35	2000	0.001	NO	[5]
Au sponges	5.0	3 mg	1.67	274	0.018	NO	[6]
Hollow AuNFs	24.4	/	/	8	3.05	NO	[7]
Au nanospheres	/	/	/	/	0.462	NO	[7]
Au NPs@porous films	6.3	1.75 mg	3.6	88	0.072	NO	[8]
Au NPs@fiber	6-8	0.43 mg	14.0-18.6	8.6	0.70-0.93	NO	[9]
Au NPs@hydrogel	1.1	12 μg	91.7	3.87	0.28	YES	[10]
Flower-like Au nanochains	0.783	0.2 mg	3.92	62.5	0.013	NO	[11]

k_{app}: apparent rate constant

m_{Au}: amount of Au

M_{Au}: concentration of Au

/ = not mentioned

IV. REFERENCES

[1] Y. Z. Wu, S. Ihme, M. Feuring-Buske, S. L. Kuan, K. Eisele, M. Lamla, Y. R. Wang, C. Buske, T. Weil, *Adv. Healthc. Mater.* **2013**, *2*, 884-894.

[2] Y. Z. Wu, A. Ermakova, W. N. Liu, G. Pramanik, T. M. Vu, A. Kurz, L. McGuinness, B. Naydenov, S. Hafner, R. Reuter, J. Wrachtrup, J. Isoya, C. Fortsch, H. Barth, T. Simmet, F. Jelezko, T. Weil, *Adv. Funct. Mater.* **2015**, *25*, 6576-6585.

[3] H. Z. Zou, G. H. Ren, M. Y. Shang, W. Q. Wang, *Mater. Chem. Phys.* **2016**, *176*, 115-120.

[4] A. J. Wang, Y. F. Li, M. Wen, G. Yang, J. J. Feng, J. Yang, H. Y. Wang, *New J. Chem.* **2012**, *36*, 2286-2291.

[5] M. H. Rashid, R. R. Bhattacharjee, A. Kotal, T. K. Mandal, *Langmuir* **2006**, *22*, 7141-7143.

[6] Y. Yu, W. Q. Xiao, T. T. Zhou, P. Zhang, C. Yan, Z. J. Zheng, *Mater. Chem. Front.* **2017**, *1*, 482-486.

[7] S. J. Ye, F. Benz, M. C. Wheeler, J. Oram, J. J. Baumberg, O. Cespedes, H. K. Christenson, P. L. Coletta, L. J. C. Jeuken, A. F. Markham, K. Critchley, S. D. Evans, *Nanoscale* **2016**, *8*, 14932-14942.

[8] Y. L. Ye, M. Jin, D. C. Wan, *J Mater. Chem. A* **2015**, *3*, 13519-13525.

[9] M. L. Wang, T. T. Jiang, Y. Lu, H. J. Liu, Y. Chen, *J Mater. Chem. A* **2013**, *1*, 5923-5933.

[10] G. Marcelo, M. Lopez-Gonzalez, F. Mendicuti, M. P. Tarazona, M. Valiente, *Macromolecules* **2014**, *47*, 6028-6036.

[11] A. J. Wang, S. F. Qin, D. L. Zhou, L. Y. Cai, J. R. Chen, J. J. Feng, *RSC Adv.* **2013**, *3*, 14766-14773.

5.4 Synthesis of peptide-functionalized poly(bis-sulfone) copolymers regulating HIV‑1 entry and cancer stem cell migration

Andreas Riegger, Chaojian Chen, Onofrio Zirafi, Nora Daiss, Debashish Mukherji, Karolin Walter, Yu Tokura, Bettina Stöckle, Kurt Kremer, Frank Kirchhoff, David Yuen Wah Ng, Patrick Christian Hermann, Jan Münch, and Tanja Weil*

* Corresponding author

Reprinted with permission from *ACS Macro Lett.* **2017**, *6*, 241−246.

Contribution of the respective authors:

Andreas Riegger: Monomer synthesis, polymer conjugation with WSC02 peptide, manuscript preparation.
Chaojian Chen: Synthesis and characterization of the poly(bis-sulfide) and poly(bis-sulfone) copolymers, polymer conjugation with glutathione, manuscript preparation.
Onofrio Zirafi, Frank Kirchhoff, and Jan Münch: Supply of the WSC02 peptide, antiviral studies and interpretation.
Nora Daiss, Karolin Walter, and Patrick Christian Hermann: Cancer cell migration studies and interpretation.
Debashish Mukherji and Kurt Kremer: Molecular simulations.
Yu Tokura: TEM characterization.
Bettina Stöckle: Monomer synthesis and polymerization screening.
David Yuen Wah Ng: Cell viability assay, discussion on the concept and results, writing and correcting the manuscript.
Tanja Weil: Acquiring funding for the project, design and discussion of the concept and results, correcting the manuscript.

ACS Macro Letters
Letter
pubs.acs.org/macroletters

Synthesis of Peptide-Functionalized Poly(bis-sulfone) Copolymers Regulating HIV-1 Entry and Cancer Stem Cell Migration

Andreas Riegger,[†,∥] Chaojian Chen,[†,∥] Onofrio Zirafi,[‡] Nora Daiss,[§] Debashish Mukherji,[∥] Karolin Walter,[§] Yu Tokura,[†,∥] Bettina Stöckle,[†] Kurt Kremer,[∥] Frank Kirchhoff,[‡] David Yuen Wah Ng,[†,∥] Patrick Christian Hermann,[§] Jan Münch,[‡] and Tanja Weil*[,†,∥]

[†]Institute of Organic Chemistry III and [§]Department for Internal Medicine I, Ulm University, Albert-Einstein-Allee 11, 89081 Ulm, Germany

[‡]Institute of Molecular Virology, Ulm University Medical Centre, 89081 Ulm, Germany

[∥]Max Planck Institute for Polymer Research, Ackermannweg 10, 55128 Mainz, Germany

Supporting Information

ABSTRACT: Peptide−polymer conjugates have been regarded as primary stronghold in biohybrid nanomedicine, which has seen extensive development due to its intrinsic property to provide complementary functions of both the peptide material and the synthetic polymer platform. Here we present an advanced macromolecular therapeutic that targets two exclusive classes of important diseases (namely, the HIV and cancer) that are implicated by extremely different causative agents. Using a facile thiol-reactive monomer, the eventual polymer facilitates multivalent conjugation of an endogenous peptide WSC02 that targets the CXCR4 chemokine receptor. The biohybrid material demonstrated both potent antiviral effects against HIV-1 as well as inhibiting cancer stem cell migration thus establishing the foundation for multimodal nanotherapeutics that simultaneously target more than one class of disease implications.

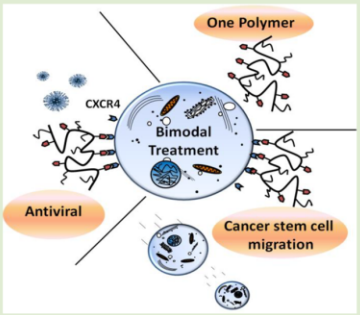

Since the inception of bioactive polymeric materials, these hybrid macromolecules have been viewed as prospective candidates for the next generation of therapeutics.[1] The rapid expansion of the field stems from the enhanced physical, chemical and pharmacokinetic properties as well as the limitless space for chemical design that a polymer platform offers. Subsequent postfunctionalization of the polymer backbone with bioactive molecules (i.e., peptides, proteins, nucleic acids, drugs, imaging agents) provides the resultant multivalent polymers that are widely studied as contemporary nanomedicine for cancer,[2] inflammatory,[3] and infectious diseases.[4] Intuitively, it is therefore critical that the bioconjugation chemistry involved in polymer postfunctionalization remains an important focus due to the stringent reaction conditions necessary for the associated biomolecules.

The frontier in thiol-based bioconjugation involves reactions with α,β unsaturated carbonyls without the necessity to apply metal catalysts occurring under mild conditions as well as being efficient, reliable, selective, and rapid.[5a,b] In this regard, thiol−halogeno, thiol−ene, thiol−yne, thiol−vinylsulfone, thiol−parafluoro, and thiol−pyridyl disulfide reactions have been extensively used to address a broad variety of material and biological applications.[5c] However, the chemistry has been widely established for small molecules and only a few number of these techniques are suitable for the site-directed bioconjugation of pH- and temperature-sensitive peptides or macromolecules. Likewise, there are also limited studies that have been published on the controlled radical polymerization of monomers containing thiol pro-reactive side chains,[6] since vinyl monomers with additional pendant sp^2 carbons are prone to cross-linking. In this context, either a furan-protected, maleimide functionalized methacrylate was polymerized and deprotected by a thermally induced retro Diels−Alder reaction at elevated temperatures (>120 °C) to unmask the thiol-reactive maleimide functionality[6a,b] or lipophilic pentafluorophenyl groups were polymerized followed by substitution of a thiol-containing molecule such as a carbohydrate.[6c] To the best of our knowledge, no sterically demanding polypeptides have been conjugated to such thiol-reactive polymers. However, polypeptides are an emerging class of macromolecular systems with diverse bioactivities often displaying high selectivities toward their protein targets. We have shown previously that the bis-sulfone functionality acts efficiently as a protected thiol reactive moiety that facilitates controlled conjugation of peptides or proteins[7] cleanly under mild conditions with the preservation of structural integrity and activity of the protein or peptide of choice.[8] In contrast to the aforementioned thiol-reactive polymers, a single bis-sulfone can be functionalized with two different or similar thiol-containing peptides in a stepwise, orthogonal fashion,[9] thus, providing high peptide

Received: January 17, 2017
Accepted: February 14, 2017
Published: February 20, 2017

DOI: 10.1021/acsmacrolett.7b00030
ACS Macro Lett. 2017, 6, 241−246

ACS Macro Letters Letter

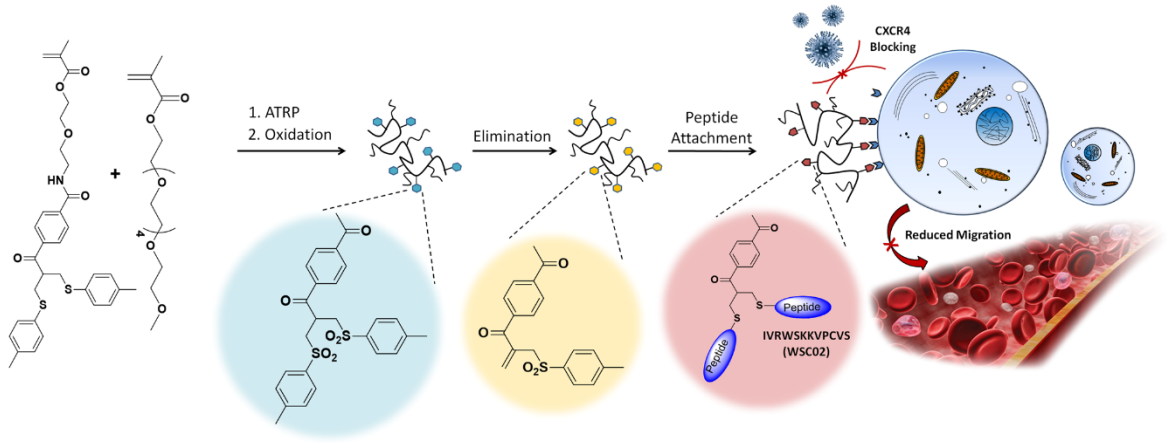

Figure 1. Synthesis of a bis-sulfide monomer, its polymerization with OEGMA by ATRP, subsequent oxidation, and thiol ligation to the peptide WSC02. The resulting multivalent copolymers binds efficiently to the chemokine membrane receptor CXCR4 and antagonizes this receptor thus inhibiting HIV-1 infection and cancer cell migration.

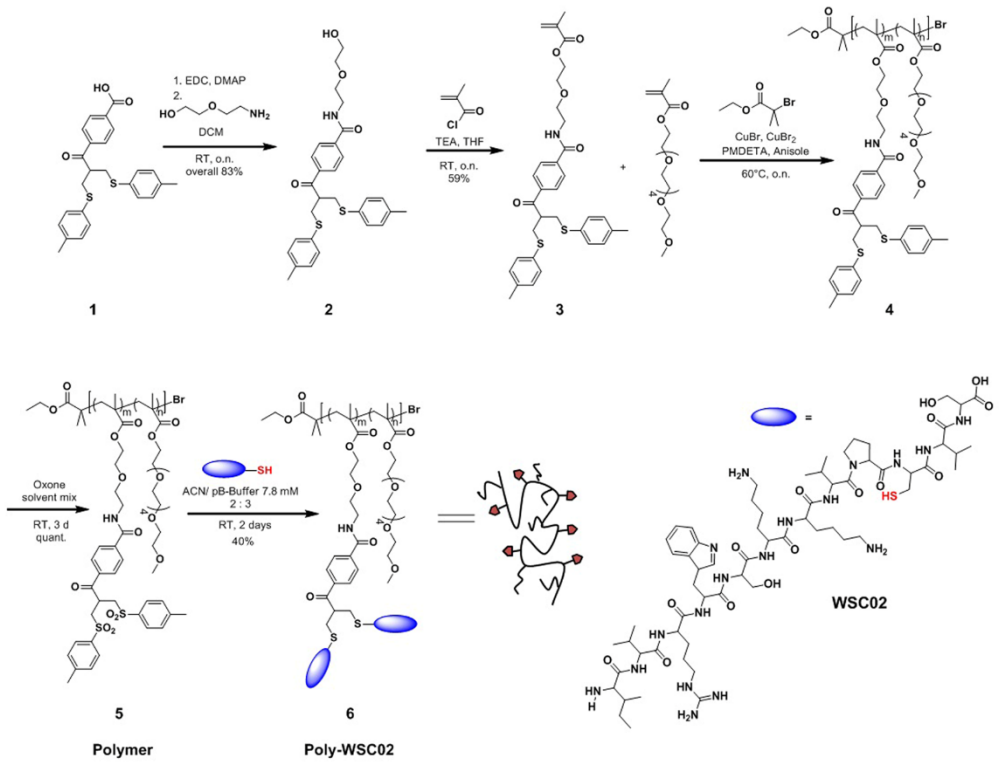

Figure 2. Synthesis of the water-soluble and thiol-reactive poly(bis-sulfone) *co*-oligo(ethylene glycol) methacrylate (OEGMA) copolymer (**5**). Polymeric scaffold was postfunctionalized with the thiol-containing peptide WSC02, yielding bioactive Poly-WSC02 (**6**).

loading densities under ambient conditions, that is, at room temperature and at neutral pH in water.

Therefore, we envisioned the creation of a novel macromolecular bis-sulfone copolymer platform that offers distinct features such as (a) narrow dispersities, (b) solubility in aqueous media, and (c) high loading capacity of bulky polypeptides that provide high specificity for their respective membrane receptor target. The resultant polypeptide-copolymer should display a broad range of bioactivities by interfering with major diseases such as virus infections and cancer. The C-X-C chemokine receptor type 4 (CXCR4), a G-protein coupled transmembrane receptor, is an excellent drug target[10] as it plays a crucial role in several important diseases such as chronic inflammatory and cardiovascular disorders, cancer progression

DOI: 10.1021/acsmacrolett.7b00030
ACS Macro Lett. 2017, 6, 241−246

ACS Macro Letters Letter

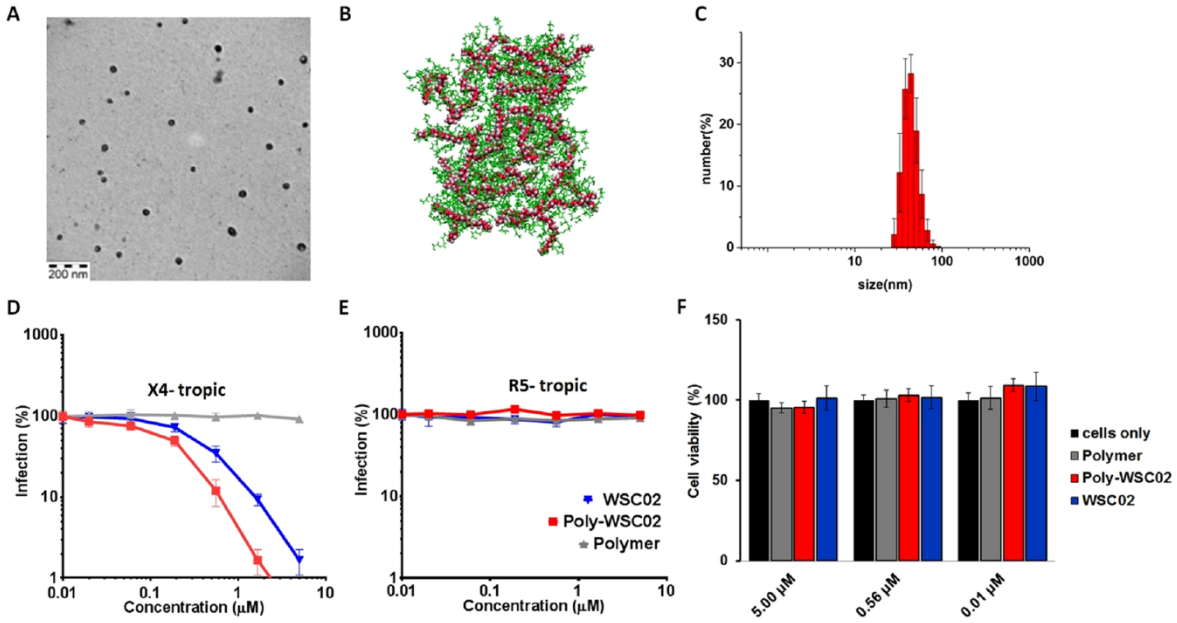

Figure 3. (A) Representative TEM image of Poly-WSC02 (**6**). (B) Simulation snapshot showing the aggregation of an analogue of Poly-WSC02, where each chain consist of a hydrocarbon (red spheres) backbone with tri(ethylene)glycol (green bonds) side chains. (C) Determination of the sphere size in water by DLS. (D) HIV infection assay of copolymer (**5**), native WSC02, and Poly-WSC02 (**6**) in X4-tropic and in (E) R5-tropic cells. (F) Cell Titer-Glo assay to TZM-bl cells up to a concentration of 5 μM. Concentrations are given with respect to the molecular weight of Poly-WSC02, Polymer, and WSC02, respectively.

and metastasis, stem cell homing and mobilization, immunodeficiencies, HIV and AIDS, or pulmonary fibrosis.[11] CXCR4 prevents viral infections such as HIV-1 as it inhibits membrane fusion and intracellular delivery of the viral payload[12] and due to its localization at the host cell, resistance development of the virus is unlikely. The small molecule CXCR4 antagonist AMD3100 is currently used in the clinics. However, due to adverse effects if administered over prolonged periods of time, it has only been approved in conjunction with G-CSF to mobilize hematopoietic stem cells to peripheral blood for certain cancer patients requiring bone marrow transplantation.[13] First polymer−CXCR4 antagonist conjugates[14] that bind to the extracellular domain of CXCR4 have just been reported, but they reveal certain disadvantages such as off-target effects of the attached drug molecules.

We have recently identified an endogenous fragment of serum albumin as a novel inhibitor of CXCR4.[15] This 16-mer peptide binds CXCR4 with an $EC_{50} \sim 10$ μM and prevents signaling via the chemokine ligand CXCL12. Furthermore, it also offers many interesting properties for clinical development since it (a) prevents inflammatory cell infiltration in vivo, (b) is not immunogenic and not cytotoxic, (c) is an inverse agonist that provides (d) high CXCR4 specificity, since it does not bind to CXCR7, suggesting less off-target effects, and (e) in contrast to AMD3100, it does not affect mitochondrial function. This initial peptide has been further optimized and the 12-mer peptide termed 408I-419_WSC02 (named WSC02 hereafter) with an EC_{50} at ~300 nM has been identified recently in our group.[15] However, like most peptide drugs, WSC02 reveals only low plasma stability,[15] thus, impeding its therapeutic application. As a consequent strategy, we envisaged combining the optimized polypeptide WSC02 with an appropriate thiol-reactive polymer scaffold to improve the inverse agonist activity of WSC02. By complementing the activity regulation of CXCR4 with the macromolecular advantages on a polymer scaffold, we will demonstrate herein new avenues to efficiently prevent both HIV-1 infection and cancer metastasis within the same macromolecular scaffold (Figure 1).

Our chemical design focused on the synthesis of a novel copolymer scaffold providing high loading of bulky polypeptides under mild conditions, solubility and biocompatibility. The carboxylic acid of literature-known bis-sulfide[16] (**1**) was activated into an NHS-ester and selectively reacted with a 2-(2-aminoethoxy)ethanol spacer to afford the highly soluble bis-sulfideamide (**2**), as depicted in Figure 2. In an esterification reaction, methacryloyl chloride was attached to the terminal alcohol to create the bis-sulfide monomer BSFI (**3**), which was characterized with MALDI-TOF MS (Supporting Information) and NMR (Figure S1). In the next step, water-soluble oligo(ethylene glycol)methacrylate (OEGMA) was copolymerized with BSFI via ATRP. The ratio of BSFI to OEGMA was designed as 1:9 to sterically accommodate the attachment of two sterically demanding WSC02 peptides per thiol reactive monomer. The resulting copolymer P(OEGMA-*co*-BSFI) (**4**) was purified by precipitation and characterized by NMR (Figure S2) and GPC (Figure S4A). In the ^{1}H NMR spectrum, the characteristic signals of the bis-sulfide groups in the aliphatic and aromatic region are clearly visible, indicating the successful incorporation of the bis-sulfide monomer into the polymer backbone. By comparing the areas of the peaks correlating to BSFI (2.35 ppm) and OEGMA (3.37 ppm), the ratio of the two monomers in the polymer chain was calculated as 1:8.9, which fits to the stoichiometric value (SI). The GPC measurement of P(OEGMA-*co*-BSFI) (**4**) revealed a number-

DOI: 10.1021/acsmacrolett.7b00030
ACS Macro Lett. 2017, 6, 241−246

average molecular weight of the polymer of 15200 g/mol with a molar mass dispersity of 1.07, indicative of a very narrow distribution.

Based on the molecular weight and the monomer ratio, on average, five bis-sulfide monomers were introduced per polymer chain. In the next step, the bis-sulfide copolymer P(OEGMA-*co*-BSFI) (**4**) was oxidized with oxone to afford P(OEGMA-*co*-BSFO) (**5**). By comparing the ^{1}H NMR spectra of **4** with **5**, the oxidation of the sulfur atoms resulted in a clear detectable shift of the signals in the aromatic region to higher ppm (Figure S3), indicating successful oxidation. The molar-mass dispersity increased slightly to 1.11 and the molecular weight remained comparable as before oxidation (GPC results, Figure S4B). Additionally, MALDI-TOF MS analysis was used to determine the molecular weight of P(OEGMA-*co*-BSFO). The MALDI-TOF MS analysis confirmed the GPC results with a deviation of only 5% (~14500 Da; Figure S8). Polymer **5** provides around five bis-sulfone monomers per polymer chain that could undergo Michael reactions with two peptides per bis-sulfone at maximum, thus, allowing the attachment of up to 10 peptides per polymer. The conjugation of the polymer with an excess of the thiol-containing CXCR4 antagonist WSC02 was accomplished by incubating the copolymer in an acetonitrile/buffer mixture at pH = 7.8. During incubation of (**5**) in the solvent mixture at pH 7.8, deprotection of the Michael acceptor occurs under the formation of the thiol-reactive monosulfone functionality as shown in Figure 1. This in situ activation of the bis-sulfone (**5**) into the monosulfone proceeds quantitatively and the formed a,ß unsaturated carbonyl can now react with nucleophilic thiols. In the next step, bioconjugation with the sterically demanding WSC02 was accomplished. To promote high conversion, 48 h reaction time was chosen. The resulting bioconjugate Poly-WSC02 (**6**) was purified with ÄKTA-SEC chromatography system (Figure S7) and analyzed via NMR, GPC/SEC. The corresponding NMR is shown in Figure S6. The molecular weight of the resulting bioconjugate (~28000 Da) was determined with MALDI-TOF-MS analysis (Figure S9). Calculating retrospectively, quantitative bioconjugation was accomplished with an average of 10 WSC02 peptides attached to the multivalent sulfone copolymer yielding Poly-WSC02 (**6**), as depicted in Figure 2. To support the broader applicability of the polymer conjugation approach, other polypeptides such as the tripeptide glutathione were also successfully attached to the in situ activated polymer (**5**), yielding a total grafting number of 8−9 glutathiones per polymer chain (see SI).

Poly-WSC02 (**6**) revealed water solubility as well as high tendency for self-organization in aqueous solution. Applying dynamic light scattering (DLS) and transmission electron microscopy (TEM), narrowly dispersed spherical aggregates were found. In water and PBS, the polymeric aggregates showed narrow size distribution of 44 ± 4 nm (Figure 3A) and 28 ± 6 nm (see SI). Similar sizes of 33 ± 7 nm were detected by TEM measurements (Figure 3A; statistical evaluation in the SI). To complement the experimentally observed morphology, we have also performed all atom molecular dynamics simulations of a simplified analogue of Poly-WSC02. Here, the polymer consists of a hydrocarbon backbone of 21 repeat units, with every alternating carbon atom attached to a tri(ethylene)glycol side chain (simulation details in Supporting Information). Simulation snapshot reveals that the aggregates are formed by spontaneous interdigitation of the side chains (Figure 3B) coupled with a corresponding decrease in the number of hydrogen bonds between the ethylene oxide and the bulk solvent (Figure S10).

In order to assess whether the WSC02 peptides were localized at the surface of the aggregates and thus available for receptor binding, HIV-1 infection assays were conducted and the cytotoxic properties of both copolymer and Poly-WSC02 (**6**) were tested using cell viability (Cell Titer-Glo) assays (see SI). Both copolymers did not display any cytotoxicity to TZM-bl cells at concentrations of up to 5 μM (Figure 3F). We have also investigated the inhibitory effect of Poly-WSC02 (**6**) against CXCR4 (X4) and CCR5 (R5) tropic HIV-1 infection using TZM-bl cells. X4-tropic viruses infect cells by specific interaction with the membrane receptors CXCR4 and CD4, whereas R5-tropic variants utilize CD4 and CCR5.[17] The native WSC02 peptide, as positive control, inhibited X4-tropic HIV-1 infection of TZM-bl cells in a dose-dependent fashion with a half-maximal inhibitory activity IC_{50} of 360 ± 70 nM, respectively (Figure 3D), confirming published data.[15] Poly-WSC02 (**6**) revealed an enhanced antiviral activity, inhibiting X4 tropic HIV-1 infection at even lower concentrations (IC_{50} = 150 ± 60 nM). As expected, both native WSC-02 and Poly-WSC02 were receptor specific for X4-tropic HIV infection but had no effect on R5-tropic virus infection. The copolymer scaffold (**5**) without WSC02 attached did not affect X4 or R5 tropic HIV-1 infection. Therefore, Poly-WSC02 reveals strong binding to CXCR4-expressing cells, and the observed enhanced effect of the multivalent conjugate could be clearly attributed to the successful attachment and exposure of the WSC02 peptides on the polymeric aggregates. CXCR4 represents a key GPCR not only facilitating HIV-1 entry into cells but it is also involved in leucocyte trafficking and the metastasis of pancreatic ductal adenocarcinoma (PDAC).[18]

Along these lines, we have shown that a population of CD133+/CXCR4+ migrating cancer stem cells is exclusively responsible for metastasis in human PDAC.[19] Depletion of CXCR4+ cells or antagonizing CXCR4 with AMD3100 or with neutralizing antibodies suppresses migration of primary pancreatic cancer cells. Furthermore, we were able to demonstrate that in patients suffering from metastatic disease, a significantly higher percentage of migrating cancer stem cells that coexpresses CXCR4 were observed. Due to this outstanding relevance of CXCR4 for migration/metastasis, we evaluated whether WSC02 peptide, Poly-WSC02 or the polymer scaffold successfully inhibit the migration of primary PDAC cells isolated from human or mouse tumors (see SI). Both WSC02 and Poly-WSC02 (**6**) inhibited human cancer cell migration by approximately 50%, whereas the copolymer (**5**) had no effect (Figure 4A). Interestingly, Poly-WSC02 (**6**) also revealed a pronounced effect on mouse cancer cells (Figure 4B); migration was even reduced to ~30%, which is well in line with higher baseline expression levels of CXCR4 as compared to human cancer cells (data not shown). For visualization, representative pictures of migrated and stained cancer cells are illustrated in Figure 4C. Therefore, Poly-WSC02 (**6**) efficiently suppresses the migration of primary pancreatic cancers cells of human and mouse origin.

In summary, we have reported the design and synthesis of a thiol-reactive bis-sulfide precursor monomer for the first time. Copolymerization of this monomer with OEGMA was successfully accomplished via ATRP and the resulting oxidized poly(bis-sulfone) copolymer (**5**) was isolated with narrow weight distribution. We have shown the applicability for efficient thiol ligation by the conjugation of the sterically

DOI: 10.1021/acsmacrolett.7b00030
ACS Macro Lett. 2017, 6, 241−246

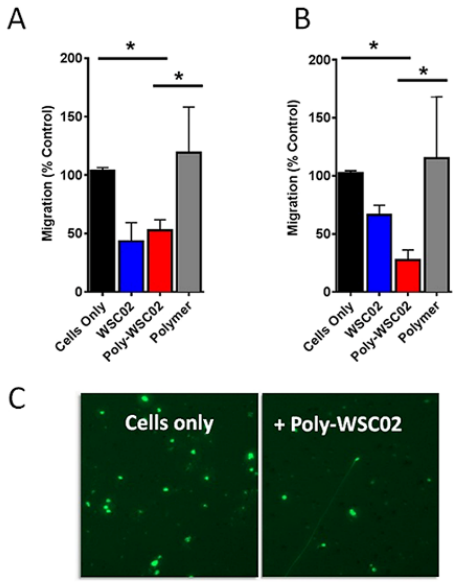

Figure 4. Native WSC02 and Poly-WSC02 (**6**) affect cancer cell migration in vitro. Cancer cells were isolated from human (PANC354, A) and mouse (CHX, B) primary tumors, $*p < 0.05$. Data is depicted as % of control. Representative microscope pictures of the migrated cancer cells after staining with DAPI (C).

demanding polypeptide WSC02, derived from the first endogenous CXCR4 antagonist, under mild reaction conditions in aqueous solution. A high loading of about ten WSCO2 peptides per polymer was achieved and the presence of the ethylene(glycol) side chains had a positive effect on solubility in aqueous media. The copolymer assembled into narrowly dispersed, bioactive aggregates with size of ~43 nm. Enhanced antiviral activity of the designated copolymer Poly-WSC02 (**6**) on X4 tropic HIV-1 infection was found, suggesting a multivalent action due to the active WSC02 peptides exposed at the surface of the spheres. Correspondingly, the second line of therapy against cancer metastasis was illustrated by the inhibition on the migration of both human and mouse primary cancer cells with high efficacy; these results are very promising and certainly merit further (pre)clinical investigations. Collectively, the combination of the CXCR4 antagonist polypeptide WSC02 on a facile macromolecular platform exhibits a strong framework in creating multimodal drugs that are molecularly specific, and yet diverse in treatment applications.

■ ASSOCIATED CONTENT

Supporting Information

The Supporting Information is available free of charge on the ACS Publications website at DOI: 10.1021/acsmacrolett.7b00030.

Materials and methods, characterizations, and supplementary figures (PDF).

■ AUTHOR INFORMATION

Corresponding Author

*E-mail: tanja.weil@uni-ulm.de.

ORCID

Tanja Weil: 0000-0002-5906-7205

Author Contributions

The manuscript was written through contributions of all authors. All authors have given approval to the final version of the manuscript.

Notes

The authors declare no competing financial interest.

■ ACKNOWLEDGMENTS

T.W., F.K. and J.M. gratefully acknowledge financial support of the Volkswagen Foundation (grant ID: 86366). J.M. was also funded by the DFG (3115-3). A.R. and K.W. are grateful for a research scholarship of the International Graduate School in Molecular Medicine Ulm funded by the Excellence Initiative of German Federal and State Government. Additionally, F.K was funded by the DFG. C.C. acknowledges support from the Promotionskolleg Pharmaceutical Biotechnology. P.C.H. acknowledges a Max Eder Fellowship of the German Cancer Aid and a Cancer Research Grant of the Hector Foundation.

■ REFERENCES

(1) Haag, R.; Kratz, F. *Angew. Chem., Int. Ed.* **2006**, *45*, 1198−1215.
(2) Duncan, R. *Nat. Rev. Cancer* **2006**, *6*, 688−701.
(3) Bridges, A. W.; García, A. J. *J. Diabetes Sci. Technol.* **2008**, *2*, 984−994.
(4) (a) Danial, M.; Klok, H.-A. *Macromol. Biosci.* **2015**, *15*, 9−35. (b) Smith, A. A. A.; Kryger, M. B. L.; Wohl, B. M.; Ruiz-Sanchis, P.; Zuwala, K.; Tolstrup, M.; Zelikin, A. N. *Polym. Chem.* **2014**, *5*, 6407−6425.
(5) (a) Lowe, A. B. *Polymer* **2014**, *55*, 5517−5549. (b) Hoyle, C. E.; Bowman, C. N. *Angew. Chem., Int. Ed.* **2010**, *49*, 1540−1573. (c) Stenzel, M. *ACS Macro Lett.* **2013**, *2*, 14−18.
(6) (a) Gevrek, T. N.; Bilgic, T.; Klok, H.-A.; Sanyal, A. *Macromolecules* **2014**, *47*, 7842−7851. (b) Arslan, M.; Gevrek, T. N.; Lyskawa, J.; Szunerits, S.; Boukherroub, R.; Sanyal, R.; Woisel, P.; Sanyal, A. *Macromolecules* **2014**, *47*, 5124−5134. (c) Noy, J.-M.; Koldevitz, M.; Roth, P. J. *Polym. Chem.* **2015**, *6*, 436−447.
(7) Wang, T.; Wu, Y.; Kuan, S. L.; Dumele, O.; Lamla, M.; Ng, D. Y. W.; Arzt, M.; Thomas, J.; Mueller, J. O.; Barner-Kowollik, C.; Weil, T. *Chem. - Eur. J.* **2015**, *21*, 228−238.
(8) Brocchini, S.; Balan, S.; Godwin, A.; Choi, J.-W.; Zloh, M.; Shaunak, S. *Nat. Protoc.* **2006**, *1*, 2241−2252.
(9) Wang, T.; Pfisterer, A.; Kuan, S. L.; Wu, Y.; Dumele, O.; Lamla, M.; Mullen, K.; Weil, T. *Chem. Sci.* **2013**, *4*, 1889−1894.
(10) Peled, A.; Wald, O.; Burger, J. *Expert Opin. Invest. Drugs* **2012**, *21*, 341−353.
(11) (a) Webster, R. M. *Nat. Rev. Drug Discovery* **2016**, *15*, 81−82. (b) Wang, Y.; Xie, Y.; Oupický, D. *Curr. Pharmacol. Rep.* **2016**, *2*, 1−10. (c) Wang, Z.; Sun, J.; Feng, Y.; Tian, X.; Wang, B.; Zhou, Y. *Tumor Biol.* **2016**, *37*, 1−14.
(12) Connell, B.; Lortat-Jacob, H. *Front. Immunol.* **2013**, *4*, 385.
(13) Lapidot, T.; Petit, I. *Exp. Hematol.* **2002**, *30*, 973−981.
(14) (a) Wang, R.-T.; Zhi, X.-Y.; Yao, S.-Y.; Zhang, Y. *Colloids Surf., B* **2015**, *133*, 43−50. (b) Wang, Y.; Hazeldine, S. T.; Li, J.; Oupický, D. *Adv. Healthcare Mater.* **2015**, *4*, 729−738.
(15) Zirafi, O.; Kim, K.-A.; Ständker, L.; Mohr, Katharina, B.; Sauter, D.; Heigele, A.; Kluge, Silvia, F.; Wiercinska, E.; Chudziak, D.; Richter, R.; Moepps, B.; Gierschik, P.; Vas, V.; Geiger, H.; Lamla, M.; Weil, T.; Burster, T.; Zgraja, A.; Daubeuf, F.; Frossard, N.; Hachet-Haas, M.; Heunisch, F.; Reichetzeder, C.; Galzi, J.-L.; Pérez-Castells, J.; Canales-Mayordomo, A.; Jiménez-Barbero, J.; Giménez-Gallego, G.; Schneider, M.; Shorter, J.; Telenti, A.; Hocher, B.; Forssmann, W.-G.; Bonig, H.; Kirchhoff, F.; Münch, J. *Cell Rep.* **2015**, *11*, 737−747.
(16) Lewis, A.; Tang, Y.; Brocchini, S.; Choi, J.-w.; Godwin, A. *Bioconjugate Chem.* **2008**, *19*, 2144−2155.

DOI: 10.1021/acsmacrolett.7b00030
ACS Macro Lett. 2017, 6, 241−246

(17) Berger, E. A.; Doms, R. W.; Fenyo, E. M.; Korber, B. T. M.; Littman, D. R.; Moore, J. P.; Sattentau, Q. J.; Schuitemaker, H.; Sodroski, J.; Weiss, R. A. *Nature* **1998**, *391*, 240−240.
(18) Saur, D.; Seidler, B.; Schneider, G.; Algül, H.; Beck, R.; Senekowitsch−Schmidtke, R.; Schwaiger, M.; Schmid, R. M. *Gastroenterology* **2005**, *129*, 1237−1250.
(19) Hermann, P. C.; Huber, S. L.; Herrler, T.; Aicher, A.; Ellwart, J. W.; Guba, M.; Bruns, C. J.; Heeschen, C. *Cell Stem Cell* **2007**, *1*, 313−323.

DOI: 10.1021/acsmacrolett.7b00030
ACS Macro Lett. 2017, 6, 241−246

Supporting Information

Synthesis of Peptide-Functionalized Poly(bis-sulfone) Copolymers Regulating HIV-1 Entry and Cancer Stem Cell Migration

*Andreas Riegger, Chaojian Chen, Onofrio Zirafi, Nora Daiss, Debashish Mukherji, Karolin Walter, Yu Tokura, Bettina Stöckle, Kurt Kremer, Frank Kirchhoff, David Yuen Wah Ng, Patrick Christian Hermann, Jan Münch, and Tanja Weil**

NMR spectra were recorded on a Bruker 400 or 500 MHz NMR spectrometer. The asterisk indicates the solvent peak. Molecular weights and molecular weight distributions of the copolymers were determined by GPC using THF as eluent. Polystyrene standards were utilized for calibration. ÄKTAPurifier FPLC and Superdex 200 10/300 GL SEC column were used for peptide copolymer analytics using pB-Buffer 7.4 (pH = 7.4, 100 mM, 50 mM NaCl) as eluent. TEM pictures were optained from JEOL-1400. DLS was measured on a Malvern Nanosizer (Malvern Ltd., Malvern, UK).The MALDI-TOF mass spectra were obtained from Bruker Reflex III MALDI-TOF spectrometer. All chemical reagents were obtained from commercial suppliers and were used without further purification unless otherwise noted. Dialysis tubings were purchased from Sigma Aldrich. Vivaspin centrifugal concentrators were purchased from GE healthcare. CellTiter-Glo Luminescent Cell Viability Assay was obtained from Promega. WSC02 (IVRWSKKVPCVS) was synthesized with a purity of 95% by ChinaPeptides (Jiangsu, China). The CXCR4 tropic molecular HIV-1 clone NL4-3 (CXCR4-tropic) and NL4-3_92TH014 (CCR5-tropic) were generated by transient transfection of 293T cells with proviral DNA.[1] Virus stocks were generated and quantified as described previously.[2] TZM-bl reporter cells encoding a lacZ gene under the control of the viral LTR promoter were obtained through the NIH AIDS Research and Reference Reagent Program and were provided by Dr. John C. Kappes, Dr. Xiaoyun Wu and Tranzyme Inc.

Experimental Procedures

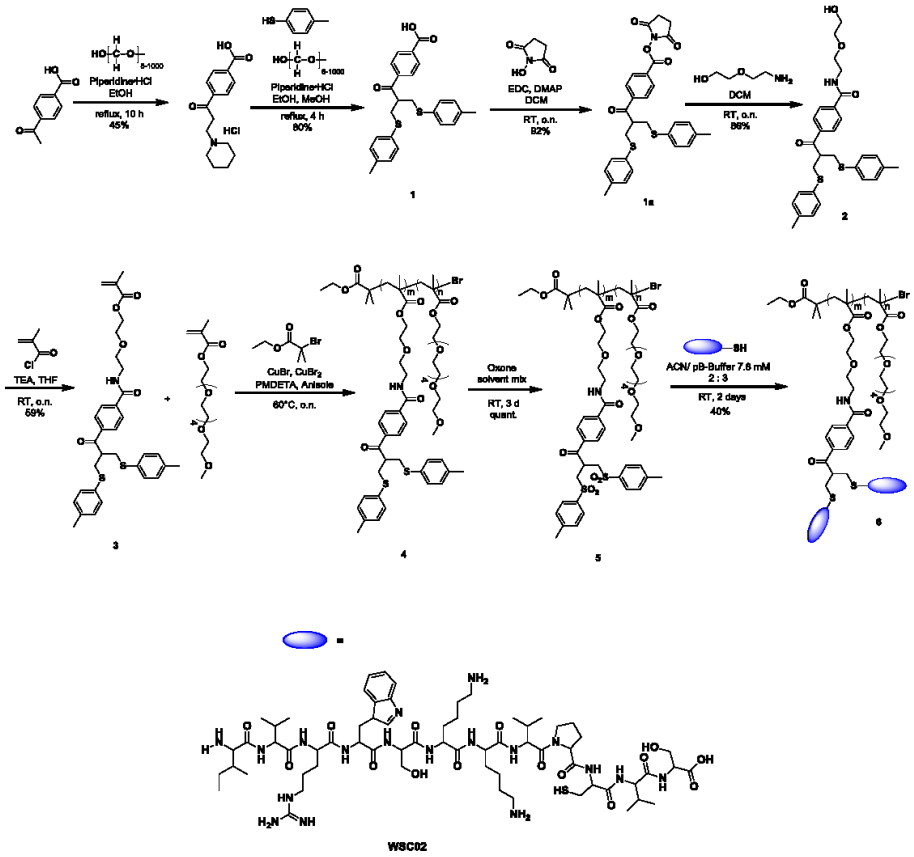

Synthesis of 1-(3-[4-Carboxy-phenyl]-3-oxo-propyl)piperidinium HCl[3]

p-acetylbenzoic acid (10 g, 60.9 mmol), piperidine HCl (7.4 g, 60.9 mmol) and paraformaldehyde (5.48 g, 183 mmol) were dissolved in 60 mL ethanol. After adding conc. hydrochloric acid (600 µL, 1.83 mmol) the reaction mixture was refluxed at 105 °C for 4 hours. Then the reaction was cooled to room temperature and a second portion paraformaldehyde (5.48 g, 183 mmol) was added. After the solution was further refluxed for 20 h, the solvent was removed under reduced pressure and the solid white product was washed with aceton (14.7 g, 49.3 mmol, yield 81%). ^{1}H-NMR (400 MHz, DMSO): δ (ppm) = 1.53-1.79 (m, 6H, -N-CH_2-CH_2-CH_2), 3.36 (t, 4H, -N-CH_2-CH_2-CH_2-), 3.48 (d, 2H, =N-CH_2-CH_2-CO-), 3.74 (t, 2H, J = 7.3 Hz, =N-CH_2-CH_2-CO-), 8.10 (m, 4H, Ar), 10.75 (s, 1H, -COOH). ^{13}C-NMR (100 MHz, DMSO): δ (ppm)

= 21.4, 22.5, 43.5, 50.9, 52.2, 128.3, 134.9, 139.0, 139.4, 167.6, 197.6. LC-MS m/z: $[M+H]^+$ calcd for $C_{15}H_{19}NO_3$, 262.3; found 262,6. Anal. calcd for $C_{15}H_{20}ClNO_3$: C 60.50, H 6.77, N 4.7; found: C 60.52, H 7.01, N 4.71.

Synthesis of Carboxylic acid bis-sulfide (1) [3]

1-(3-[4-carboxy-phenyl]-3-oxopropyl)piperidinium HCl (2 g, 6.72 mmol) and 4-methylbenzenethiol (1.68 g, 13.5 mmol) were dissolved in 80 mL ethanol. Piperidine (280 µL, 2.83 µmol) and 37% (wt/vol) aqueous formaldehyde (2 mL, 54.1 µmol) were added successive and refluxed for 1 h at 105 °C. After the mixture was cooled down to room temperature a second portion of 37% (wt/vol) aqueous formaldehyde (2 mL, 54.1 µmol) was added and further refluxed for 3 h at 105 °C. The solvent was removed under vacuum after the reaction mixture was cooled down. The residue was resolved in DCM and afterwards extracted three times with 1 N $HCl_{aq.}$ The organic layer was dried with Na_2SO_4. After the DCM was removed under vacuum, the white solid curde product was purified by column chromatography (silica gel, 2.5% methanol/DCM - 5% methanol/DCM) (2.43 g, 5.58 mmol, yield 83%). ^{1}H-NMR (400 MHz, $CDCl_3$): δ (ppm) = 2.36 (s, 6H, $-CH_3$), 3.14-3.28 (m, 4H, $-S-CH_2-$), 3.77-3.84 (m, 1H, -CO-CH-), 7.05 (d, 4H, Ar), 7.13 (d, 4H, Ar), 7.59 (d, 2H, Ar), 8.03 (d, 2H, Ar). ^{13}C-NMR (100 MHz, $CDCl_3$): δ (ppm) = 21.3, 36.5, 46.0, 128.5, 130.0, 130.5, 131.2, 131.7, 133.0, 137.4, 140.7, 170.7, 200.6. MALD-TOF MS m/z: $[M]^+$ calcd for $C_{25}H_{24}O_3S_2$, 436.6; found 436.2, $[M+H_2O]^+$ calcd for $C_{25}H_{26}O_4S_2$, 454.6; found 454.2, $[M+Na]^+$ calcd for $C_{25}H_{24}O_3S_2Na$, 459.6; found 459.2, $[M+K]^+$ calcd for $C_{25}H_{24}O_3S_2K$, 475.7; found 475.2.

Synthesis of 2,5-Dioxopyrrolidin-1-yl bis-sulfide (1a) [4]

N-hydroxysuccinimide (0.760 g, 6.61 mmol) and carboxylic acid bis-sulfide (**1**) (2.89 g, 6.61 mmol) were dried for 30 min under vacuum. After adding dry DCM (7.5 mL) the reaction mixture was stirred for 10 min at 0 °C. Then EDC·HCl (1.52 g, 7.93 mmol) and DMAP (97.0 mg, 0.794 mmol) were added to the mixture and stirred for 1.5 h at room temperature. Afterwards EDC·HCl (145 mg, 0.756 mmol) and DMAP (97 mg, 0.79 mmol) were added and further stirred for 1.5 h at room temperature. The mixture was filtered and the filtrate was diluted in DCM (45 mL), washed two times with water and the organic layer was dried with Na_2SO_4. Finally the solvent was removed under vacuum (3.23 g, 6.08 mmol, yield 92%). ^{1}H-NMR (400 MHz, $CDCl_3$):

δ (ppm) = 2.35 (s, 6H, -CH_3), 2.92 (s, 4H, -CO-CH_2-CH_2-CO-),3.13-3.25 (m, 4H, -S-CH_2-), 3.78 (m, 1H, -CO-CH-), 7.05 (d, 4H, Ar), 7.11 (d, 4H, Ar), 7.58 (d, 2H, Ar), 8.04 (d, 2H, Ar). ^{13}C-NMR (100 MHz, $CDCl_3$): δ (ppm) = 21.2, 25.8, 36.5, 45.9, 128.6, 128.9, 130.0, 130.6, 131.0, 131.7, 137.5, 141.4, 161.2, 169.1, 200.4. MALD-TOF MS m/z: $[M]^+$ calcd for $C_{29}H_{27}NO_5S_2$, 533.7; found 533.21, $[M+H_2O]^+$ calcd for $C_{29}H_{29}NO_6S_2$, 551.7; found 551.2, $[M+Na]^+$ calcd for $C_{29}H_{27}NO_5S_2Na$, 556.7; found 556.2, $[M+K]^+$ calcd for $C_{29}H_{27}NO_5S_2K$, 572.8; found 572.2.

Synthesis of N-(2-(2-Hydroxyethoxy)ethyl) bis-sulfide (2)

The 2,5-dioxopyrrolidin-1-yl bis-sulfide (**1a**) (3.23 g, 6.05 mmol) was put in a flask and purged with argon for approximately 1 min. Anhydrous DCM (15 mL) was added and 2-(2-aminoethoxyethanol) (668 µL, 6.67 mmol) was added dropwise. The reaction mixture was stirred over night at room temperature. The solvent was removed under vacuum. The residue was diluted in ethyl acetate (150 mL) and extracted three times with water, the last time with a few drops 1 N $HCl_{aq.}$, and finally with brine solution. The organic layer was dried with Na_2SO_4, the solvent was removed under vacuum. The product was purified by chromatography (silica gel, 50% acetone/n-hexane) (2.74 g, 5.20 mmol, yield 86%). ^{1}H-NMR (400 MHz, $CDCl_3$): δ (ppm) = 2.34 (s, 6H, -CH_3), 3.11-3.26 (m, 4H, -S-CH_2-), 3.62 (t, 2H, -NH-CH_2), 3.68 (s, 4H, -CH_2-CH_2-O-CH_2-CH_2-) 3.78 (m, 3H, -CO-CH-, -CH_2-OH), 7.04 (d, 4H, Ar), 7.11 (d, 4H, Ar), 7.57 (d, 2H, Ar), 7.71 (d, 2H, Ar). ^{13}C-NMR (100 MHz, $CDCl_3$): δ (ppm) = 21.2, 31.1, 36.5, 40.0, 45.7, 61.8, 69.8, 72.4, 127.4, 128.6, 130.0, 131.1, 131.6, 137.2, 138.5, 166.8, 200.5. MALD-TOF MS m/z: $[M]^+$ calcd for $C_{29}H_{33}NO_4S_2$, 523.7; found 523.2, $[M+Na]^+$ calcd for $C_{29}H_{33}NO_4S_2Na$, 546.7; found 546.2. Anal. calcd for $C_{29}H_{33}NO_4S_2$: C 66.51, H 6.35, N 2.67, S 12.25; found: C 66.40, H 6.33, N 2.63, S 11.77.

Synthesis of bis-sulfide-monomer (3)

N-(2-(2-hydroxyethoxy)ethyl) bis-sulfide (**2**) (370 mg, 0.706 mmol) and triethylamine (157 µL, 1.13 mmol) were dissolved in dry THF (7.4 mL) and afterwards cooled to 0 °C. A mixture of methacryloyl chloride (117 µL, 1.20 mmol) in dry THF (1.2 mL) was added dropwise under argon. After the addition of all reagents, the mixture was stirred at room temperature over night. The solid triethylamine hydrochloride was removed via filtration and the solvent was evaporated under vacuum. The product was purified by chromatography (silica gel, n-hexane/acetone 1/1) and a yellow-

orange high viscous product was obtained. (246 mg, 0.417 mmol, yield 59%). ^{1}H-NMR (400 MHz, $CDCl_3$): δ (ppm) = 1.89 (s, 3H), 2.35 (s, 6H), 3.14-3.26 (m, 4H), 3.69-3.77 (m, 9H), 4.33-4.35 (m, 2H), 5.53 (t, 1H), 6.08 (s, 1H), 7.04 (d, 4H, Ar), 7.12 (d, 4H, Ar), 7.58 (d, 2H, Ar), 7.72 (d, 2H, Ar). ^{13}C-NMR (100 MHz, $CDCl_3$): δ (ppm) = 18.4, 21.2, 31.0, 36.5, 40.0, 45.6, 63.5, 69.2, 69.6, 126.1, 127.3, 128.6, 130.0, 131.2, 131.6, 136.1, 137.3, 138.5, 166.6, 167.5, 200.4. MALD-TOF MS m/z: $[M]^+$ calcd for $C_{33}H_{37}NO_5S_2$, 591.8; found 591.3.

Synthesis of P(OEGMA-co-BSFI) (4)

P(OEGMA-*co*-BSFI) was synthesized by atom transfer radical polymerization (ATRP) of OEGMA and bis-sulfide monomer **(3)**. Briefly, ethyl α-bromoisobutyrate (1.95 mg, 0.01 mmol), bis-sulfide monomer (59.2 mg, 0.1 mmol), OEGMA (257 µL, 0.9 mmol), $CuBr_2$ (2.23 mg, 0.01 mmol) and PMDETA (42 µL, 0.2 mmol) were dissolved in 5 mL anisole in a 20 mL Schlenk flask under argon flow. Subsequently, the mixture was degassed through three freeze-pump-thaw cycles before CuBr (14.4 mg, 0.1 mmol) was added. The flask was then placed in a preheated oil bath and stirred at 60°C for 24 h. The resultant solution was diluted by THF and passed through a neutral Al_2O_3 column to remove the catalyst. Then the solution was concentrated, P(OEGMA-co-BSFI) **(4)** was precipitated using diethyl ether and was dried under high vacuum to obtain a white powder. Yield 31%.

Synthesis of P(OEGMA-co-BSFO) (5)

P(OEGMA-*co*-BSFI) (**4**) (15 mg, 1 µmol) was dissolved in the mixture solution of 1.5 mL ACN and 1.5 mL ethyl acetate. Oxone (25 mg, 0.04 mmol) was dissolved in 0.8 mL deionized water and then added into the copolymer solution. After stirring three days at room temperature, the organic solvent was removed by evaporation and the remained solution was dialyzed against water (MWCO = 2 kDa). The final product was obtained after freeze-drying. Yield: 99%.

Bioconjugation with glutathione

P(OEGMA-*co*-BSFO) **5** (3.1 mg, 0.2 µmol) was dissolved in 1 mL pB-Buffer (50 mM, pH 7.8, 10 mM EDTA) and incubated for 30 min. Glutathione (0.74 mg, 2.4 µmol) in 1 mL PB buffer was then added and gently shaken at room temperature for 48 h. The

aqueous solution was dialyzed against water (MWCO 3.5 kDa) for three days and lastly freeze-dried. 1.7 mg of a white solid was isolated (94.4 nmol, yield 47 %).

Bioconjugation with WSC02 (6)

11.2 mg of the peptide (7.9 µmol) was dissolved in 1.2 mL pB-Buffer (pH = 7.8, 50 mM). Then P(OEGMA-*co*-BSFO) **5** (8 mg, 0.53 µmol in 800 µL AcN) was added to the peptide solution. The mixture was incubated for 48 h at room temperature. The clear solution was transferred into an ultracentrifugation tube (vivaspin MWCO = 10000) and washed three times with water. After freeze-drying, the peptide conjugate **6** was obtained as white solid (5.6 mg, 0.2 µmol, 38%).

Preparation of TEM samples

10 uL of the sample solution (10 mg/mL) was spotted onto carbon coated TEM grids with hydrophilic surface. After 10 minutes of incubation the solvent was removed with a filter paper. Then the grid was rinsed once with 5 uL MQ water. In sequence, the samples were stained with 1% uranyl acetate solution for two minutes, washed three times with MQ water and were dried before the measurement.

Statistical evaluation was conducted by measuring the size of 62 spherical aggregates, revealing an average size of 33 ± 7 nm.

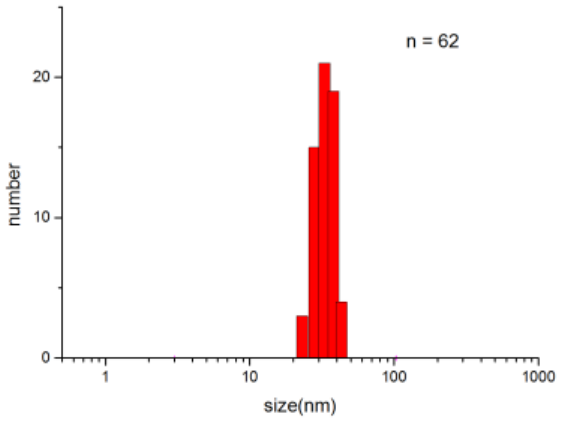

6

DLS measurements

The sample solution (10 mg/mL in H_2O/DPBS 10X) was injected into small volume cuvette (disposable UV cuvette micro; Brand). Subsequently, the samples were measured using a Malvern Nanosizer (Malvern Ltd, Malvern, UK).

Autocorrelation functions were analyzed to estimate hydrodynamic diameter. The hydrodynamic diameter distribution was presented as number distribution. DLS results are shown in main text (H_2O) and in PBS buffer:

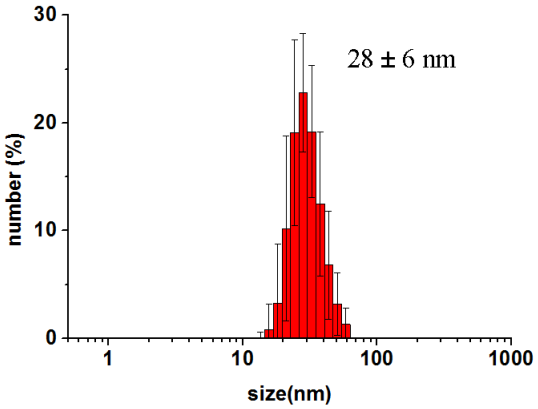

Preparation of MALDI samples

The sample solution (5 mg/ml), a matrix solution (sinapinic acid or DCTB; 10 mg/ml) and the doping salt solution silver trifluoracetate (0.1 mg/ml) were all dissolved in THF. The polymer-, matrix- and salt-solutions were mixed in the ratio 5:25:(1) and 0.5 µl were hand-spotted on a ground steel target plate.

Infection of TZM-bl cells

HIV-1 permissive TZM-bl cells expressing CD4 and CXCR4 and the second HIV-1 coreceptor CCR5 were seeded in 96 wells in 100 µl ($5x10^3$ cells/well). Next day, the medium was removed and 70 µl fresh DMEM culture medium added. Serial dilutions of Polymer, WSC02, and Poly-WSC02 (8-point dose-response curve up to 5 µM) were prepared in DPBS. Thereafter, 10 µl were added to the cells and incubated for 1 h at 37°C in a humid atmosphere of 5% CO_2/ 95% air. After incubation, 20 µl of CXCR4 (X4)-tropic or CCR5 (R5)-tropic HIV-1 (1 ng p24) were used to infect 80 µl TZM-bl cells. Three days later infection rates were determined by quantifying ß-galactosidase activities in cellular lysates using the Gal-Screen assay as

recommended by the manufacturer (Applied Biosystem, T1027). Luminescence was recorded on an Orion microplate luminometer. Values were derived from triplicate measurements. Uninfected and infected cells alone served as controls. For each compound, IC_{50} values were calculated using the dose-response inhibition model in GraphPad Prism software (version 5.03). The IC_{50} values are represented as means ± standard deviation.

Cell viability assay

TZM-bl cells were seeded in 96 wells in 100 µl ($1x10^4$ cells/well). The next day, medium was removed and 90 µl fresh DMEM culture medium added. Serial dilutions of Polymer, WSC02 and Poly-WSC02 (8-point dose-response curve up to 5 µM) were prepared in DPBS. Thereafter, 10 µl were added to the cells. Three days later cell viability was determined using the CellTiter-Glo Luminescent Cell Viability Assay (PROMEGA, G7571) as recommended by the manufacturer. Luminescence was recorded on an Orion microplate luminometer. Values were derived from triplicate measurements. Vitality rates were calculated relative to ATP levels in DPBS (no peptide) containing cells (100%).

Cancer cell migration assay

Primary cells were generated as described previously[5] maintained as adherent cultures on plastic dishes and incubated at 37°C and 5% CO_2 in RPMI medium (Invitrogen, Karlsruhe, Germany) supplemented with 10% fetal calf serum (Biochrom, Berlin, Germany), and a penicillin-streptomycin mixture (Invitrogen). A total of $5x10^5$ isolated tumor cells were re-suspended in 250 µl of RPMI media. After 30 min of incubation with the respective inhibitors, cells were seeded in the upper chamber of a transmigration insert (Cell Culture Insert, 8 µm pore size, Corning, NY). The chamber was placed in a 24-well culture dish containing 500 µl of RPMI media supplemented with 100 ng/ ml SDF-1 (PeproTech EC). After 24 h of incubation at 37°C, cells that migrated through the pores of the insert were fixated with 4% paraformaldehyde, stained with DAPI and the insert was fotographed. The number of transmigrated cells was counted using ImageJ.

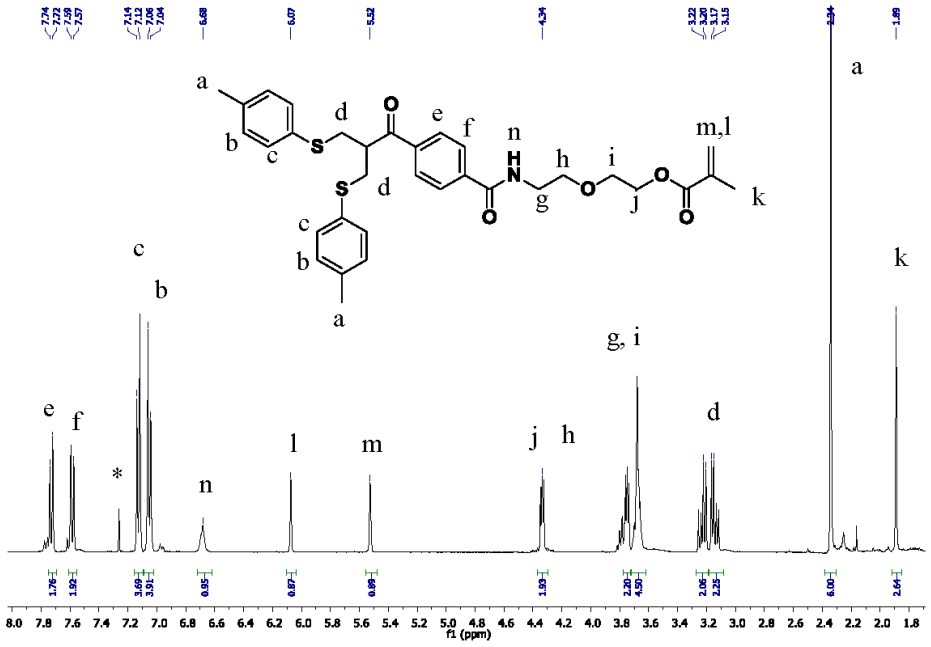

Figure S1. ^{1}H-NMR spectrum of bis-sulfide-monomer **(3)** in $CDCl_3$ (400 MHz, 298 K).

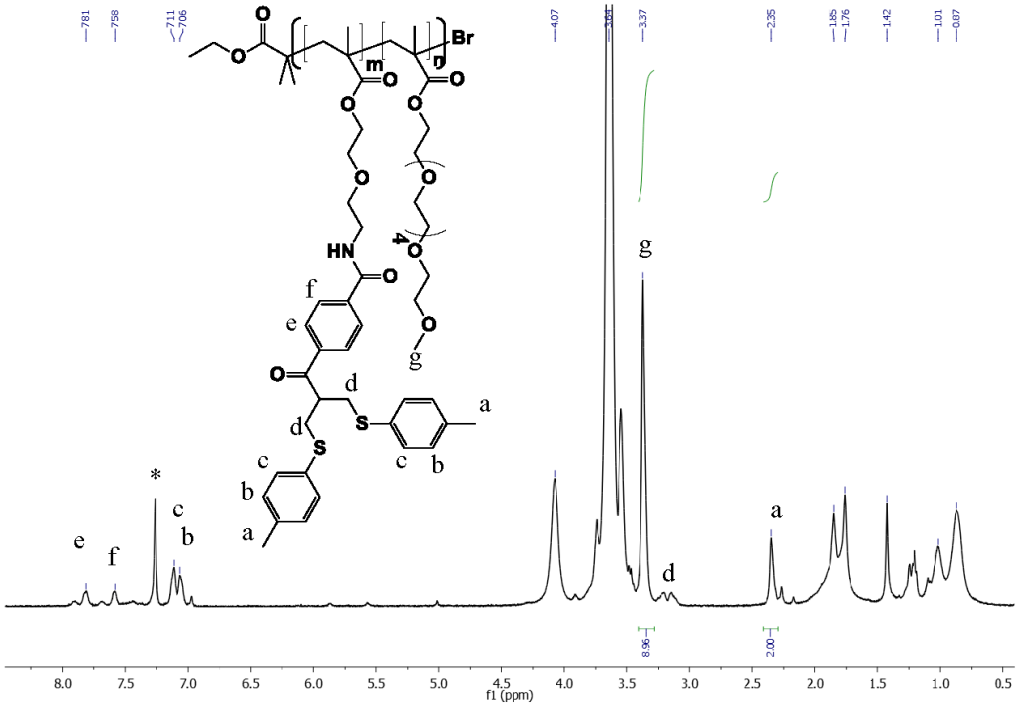

Figure S2. ^{1}H-NMR spectrum of P(OEGMA-*co*-BSFI) **(4)** in $CDCl_3$ (400 MHz, 298 K). The ratio of OEGMA and BSFI can be determined as follows: 8.9* 2.0/ 2.0 = 8.9.

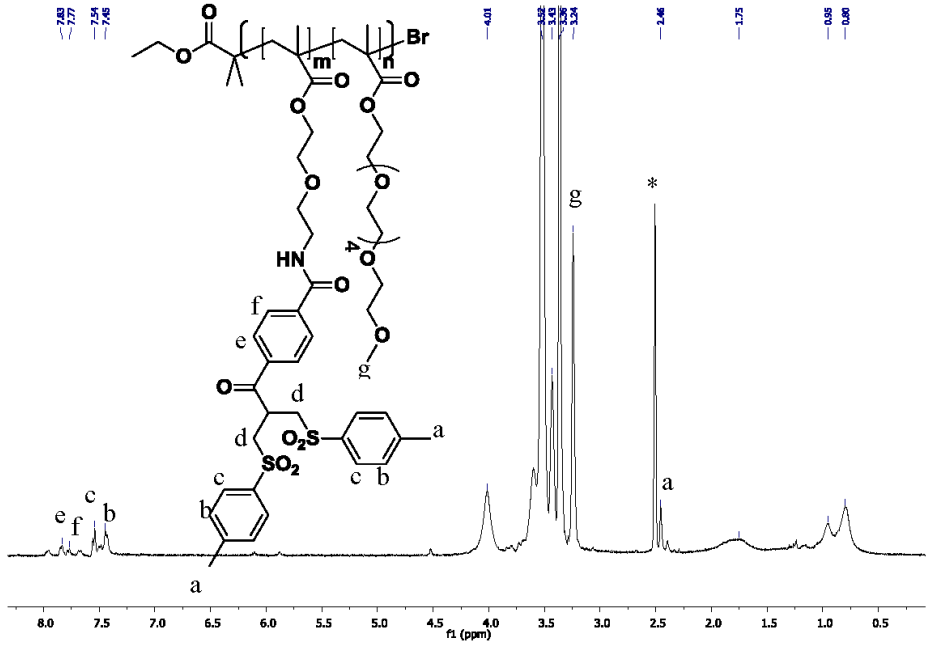

Figure S3. ^{1}H-NMR spectrum of P(OEGMA-*co*-BSFO) **(5)** in DMSO-d_6 (400 MHz, 298 K).

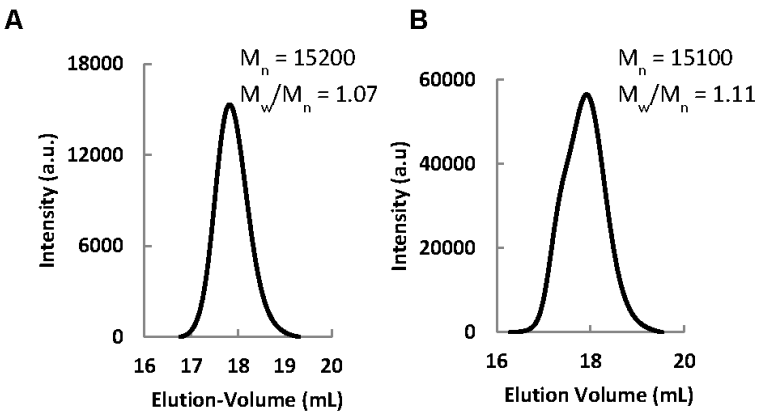

Figure S4. GPC elution peaks of the thiol reactive copolymer before (A) and after oxidation (B**),** compounds **4** and **5** respectively**.** THF was used as solvent, polystyrene standards were used for calibration.

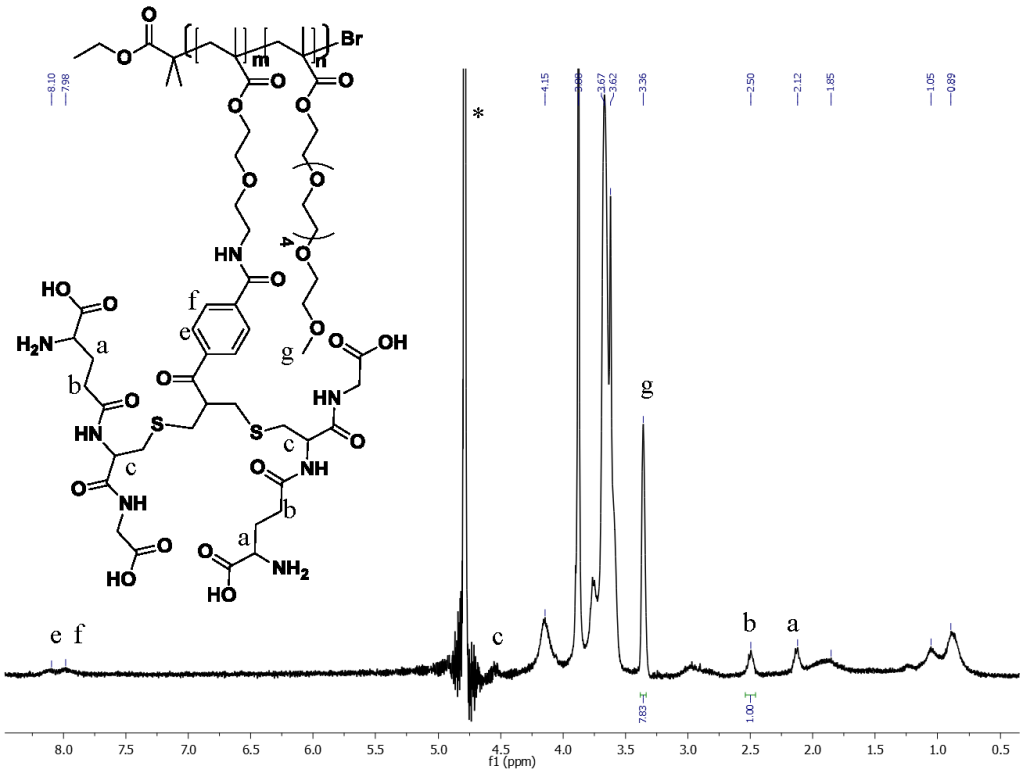

Figure S5. ^{1}H-NMR spectrum of P(OEGMA-*co*-BSFO) after post-functionalization with glutathione in D_2O (400 MHz, 298 K).

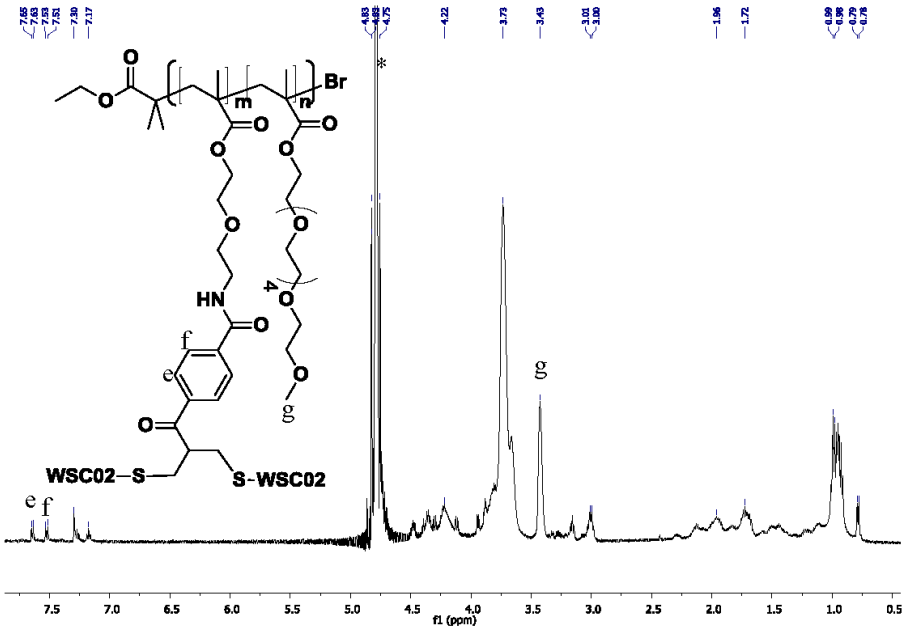

Figure S6. ^{1}H-NMR spectrum of P(OEGMA-*co*-BSFO) after post-functionalization with WSC02 **(6)** in D_2O (400 MHz, 298 K).

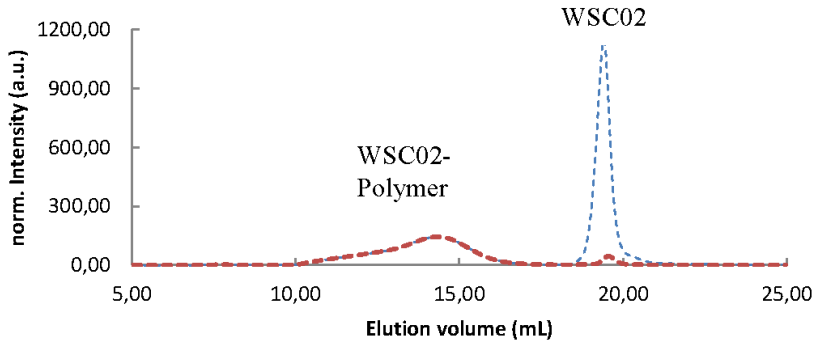

Figure S7. ÄKTA-SEC chromatograms (λ = 280 nm) after the bioconjugation to the antiviral peptide WSC02 (blue). The excess of native peptide was reduced to ~5 % (peak area) using ultracentrifugation (MWCO = 10000 g/mol).

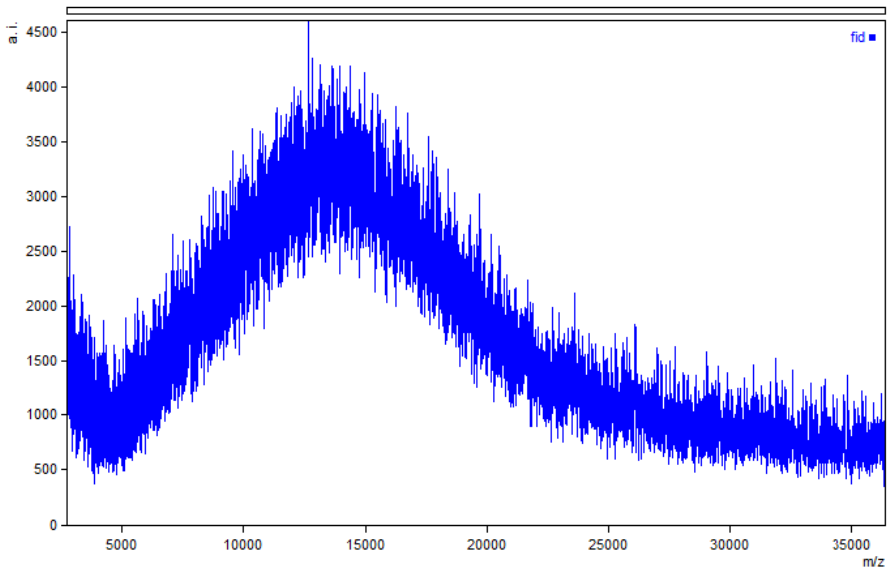

Figure S8. Measured MALDI-TOF spectrum of P(OEGMA-co-BSFO) (matrix: DCTB, doped with AgTFA).

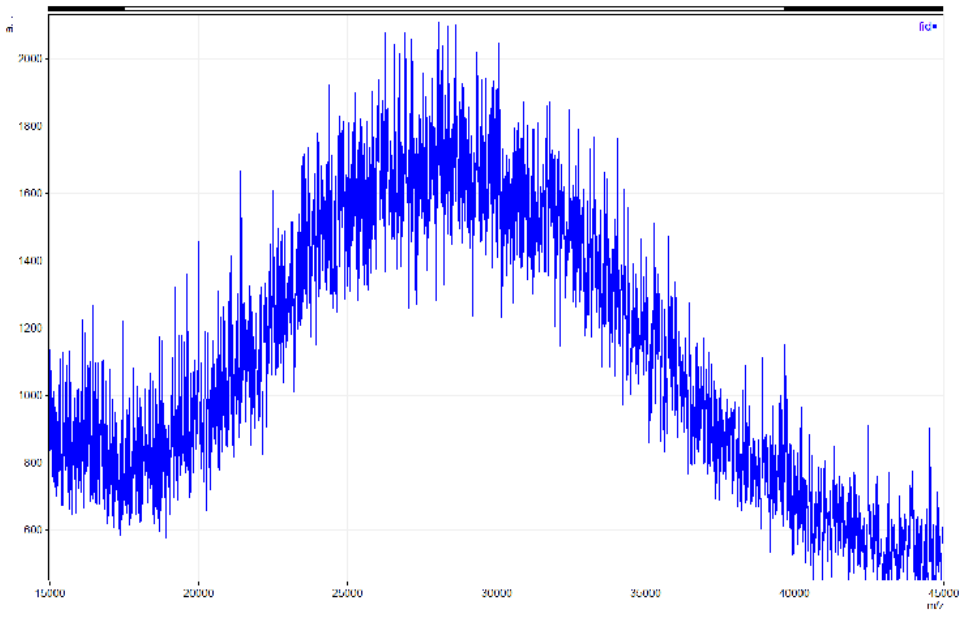

Figure S9. Measured MALDI-TOF spectrum of the WSC02-conjugated copolymer (matrix: sinapinic acid).

Theoretical Calculations Concerning the Aggregation Behavior

All atom molecular dynamics (MD) simulations are performed using the GROMACS package.[6] The temperature is set to 298 K using velocity rescaling with a coupling constant 0.5 ps.[7] The electrostatics is treated using Particle Mesh Ewald.[8] The interaction cut-off for non-bonded interactions is chosen as 1.0 nm. The time step for the simulations is 2 fs and the equations of motion are integrated using the leap-frog algorithm. LINCS algorithm is used to constraint all bond vibrations.[9]

We have chosen OPLS parameters[10] to simulate the copolymer in SPC/E water.[11] The copolymer is a simulation analogue of Poly-WSC2, which consists of a 21 units long alkane backbone with a tri(ethylene)glycol attached to every alternating carbon atom along the backbone. The initial configuration is generated by randomly distributing 40 copolymers in a solvent box consisting of 40000 water molecules. Initially 20 ns long MD run is performed in a constant pressure (NpT) ensemble, where the pressure is set at 1 bar using a Berendsen barostat [12] with a coupling time of 0.5 ps. During this time density equilibration is achieved, leading to a box dimension of 10.88 nm. This equilibrated configurations was used for a 200 ns long MD in a constant volume (NVT) ensemble. This simulation trajectory is about two times larger than the time it takes to form a well-equilibrated aggregation of the copolymer units (see Fig. S10).

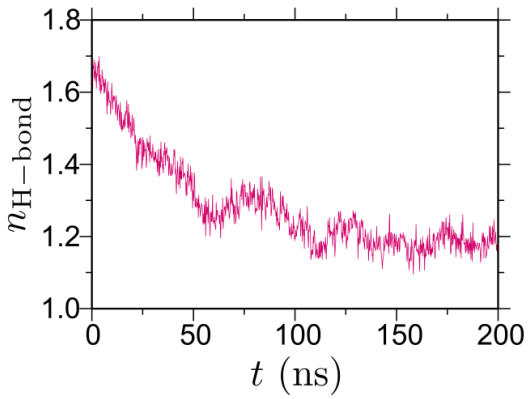

Figure S10. Time evolution of hydrogen bonds between an ethylene oxide side chain and the water molecules. For the calculations we have used the standard geometric arguments implemented in GROMACS,[6] which defines a hydrogen bond if donor-acceptor distance is ≤ 0.35 nm and the accepted-doner hydrogen angle is $\leq 30^{\circ}$.

[1] A. Papkalla, J. Münch, C. Otto, F. Kirchhoff, *J. Virol.* **2002**, *76*, 8455.

[2] J. Münch, L. Ständker, S. Pöhlmann, F. Baribaud, A. Papkalla, O. Rosorius, R. Stauber, G. Sass, N. Heveker, K. Adermann, S. Escher, E. Klüver, R. W. Doms, W.-G. Forssmann, F. Kirchhoff, *Antimicrob. Agents Chemother.* **2002**, *46*, 982.

[3] T. Wang, A. Pfisterer, S. L. Kuan, Y. Wu, O. Dumele, M. Lamla, K. Muellen, T. Weil, *Chem. Sci.* **2013**, *4*, 1889

[4] A. Lewis, Y. Tang, S. Brocchini, J. W. Choi, A. Godwin, *Bioconjug. Chem.* **2008**, *19*, 2144.

[5] P. C. Hermann, S. L. Huber, T. Herrler, A. Aicher, J. W. Ellwart, M. Guba, C. J. Bruns, C. Heeschen, *Cell Stem Cell* **2007**, *1*, 313.

[6] Pronk, S.; Pall, S.; Schulz, R.; Larsson, P.; Bjelkmar, P.; Apostolov, R.; Shirts, M.R.; Smith, J.C.; Kasson, P.M.; van der Spoel, D.; Hess, B.; Lindahl, E., *Bioinformatics* **2013**, *29*, 845.

[7] Bussi, G.; Donadio, D.; Parrinello, M., J. *Chem. Phys.* **2007**, *126*, 014101.

[8] Essmann, U.; Perera, L.; Berkowitz, M.L.; Darden, T.; Lee, H.; Pedersen, L.G., J. *Chem. Phys.* **1995**, *103*, 8577.

[9] Hess, B.; Bekker, H.; Berendsen, H.J.C.; Fraaije, J.G.E.M., *J. Comp. Chem.* **1997**, *18*, 1463.

[10] Jorgensen, W.L.; Maxwell, D.S.; Tirado-Rives, J., *J. Am. Chem. Soc.* **1996**, *118*, 11225.

[11] Berendsen, H.J.C.; Grigera, J.R.; Straatsma, T.P., *J. Phys. Chem.* **1987**, *91*, 6269.

[12] Berendsen, H.J.C.; Postma, J.P.M.; van Gunsteren, W.F.; DiNola, A.; Haak, J.R., *J. Chem. Phys.* **1984**, *81*, 3684.

5.5 Polymer cyclization as a general strategy for the emergence of hierarchical nanostructures

Chaojian Chen, Manjesh Kumar Singh, Katrin Wunderlich, Sean Harvey,
Manfred Wagner, George Fytas, Kurt Kremer, Debashish Mukherji,
David Yuen Wah Ng*, and Tanja Weil*

* Corresponding authors
Preprint posted on ChemRxiv. DOI: https://doi.org/10.26434/chemrxiv.13168139.v1.

Contribution of the respective authors:

Chaojian Chen: Design of the project, conduction of the experiments, results analysis and interpretation, figure design and writing of the manuscript.
Manjesh K. Singh, Kurt Kremer and Debashish Mukherji: Molecular simulations.
Katrin Wunderlich and George Fytas: Interpretation of the light scattering data.
Sean Harvey: AFM measurement.
Manfred Wagner: NMR experiments and interpretation.
David Yuen Wah Ng: Design and discussion of the concept and results, writing and correcting the manuscript.
Tanja Weil: Acquiring funding for the project, design and discussion of the concept and results, correcting the manuscript.

Polymer cyclization as a general strategy for the emergence of hierarchical nanostructures

Chaojian Chen[1,2], Manjesh Kumar Singh[3], Katrin Wunderlich[1], Sean Harvey[1], Manfred Wagner[1], George Fytas[1,4], Kurt Kremer[1], Debashish Mukherji[5], David Y. W. Ng[1]*, Tanja Weil[1,2]*

[1]Max Planck Institute for Polymer Research, Ackermannweg 10, 55128 Mainz, Germany

[2]Ulm University, Albert-Einstein-Allee 11, 89081 Ulm, Germany

[3]Department of Mechanical Engineering, Indian Institute of Technology Kanpur, Kanpur: 208016, Uttar Pradesh, India

[4]Institute of Electronic Structure and Laser, Foundation for Research and Technology, P.O. Box 1527, 71110 Heraklion, Greece

[5]Quantum Matter Institute, University of British Columbia, Vancouver V6T 1Z4, Canada

*Correspondence author. Email: weil@mpip-mainz.mpg.de (T.W.); david.ng@mpip-mainz.mpg.de (D.Y.W.N.)

Abstract: The creation of synthetic polymer nanoobjects with well-defined hierarchical structures is important for a wide range of applications such as nanomaterial synthesis, catalysis, and therapeutics. Inspired by the programmability and precise three-dimensional architectures of biomolecules, we report the strategy of fabricating controlled hierarchical structures through self-assembly of folded synthetic polymers. Linear poly(2-hydroxyethyl methacrylate) of different lengths are folded into cyclic polymers and their self-assembly into hierarchical structures is elucidated by various experimental techniques and molecular dynamics simulations. Based on their structural similarity, macrocyclic brush polymers with amphiphilic block side chains are synthesized, which can self-assemble into wormlike and higher-ordered structures. Our work points out the vital role of polymer folding in macromolecular self-assembly and establishes a versatile approach for constructing biomimetic hierarchical assemblies.

One Sentence Summary: Hierarchical wormlike assemblies and higher-ordered structures can be obtained via biomimetic folding and assembly of synthetic polymers.

Precise three-dimensional architectures of biomacromolecules such as proteins and DNA have stimulated various new developments in macromolecular chemistry (*1-4*). Intrigued by the programmability and specificity of intramolecular forces that enable folding of a giant molecular chain (*5, 6*), synthetic chemists have taken several approaches to recreate, in part, notable features that contribute to these unique nanostructures. A simple biomimetic model typically involves a polymer chain consisting of chemical functions that recognize their interactive partner further along the chain, such that the main backbone can fold in a predictable way (*7-10*). These functions funnel the free energy landscape of chain dynamics into, ideally, a single conformational region that would otherwise be subjected to randomness and kinetically trapped states. This led to the inception of single chain nanoparticles (SCNPs) (*11*), which focused on how polymers can be programmed to fold in a regular way akin to the chaperones of proteins (*6*). The confinement characterized by these SCNPs has discovered newfound capabilities in catalysis, biomedicine, synthetic biology and when doped, offer interesting bulk material properties (*12, 13*).

Despite these advancements, the larger perspective of how folding of a polymer chain can program higher ordered assemblies remains rare (*14, 15*). The concept of assembly driven by the regularity of macromolecules is a critical step for building sophisticated architectures that mimic the ability of proteins to form cellular nanostructures and compartments (*16-19*). Our study focuses on the emergence of structural complexity by folding of polymer chains forming specific secondary structures capable of controlled assembly into anisotropic hierarchical structures. Polymers of 2-hydroxyethyl methacrylate (HEMA) are one of the simplest polymer scaffolds possessing a hydrophobic backbone and a hydrophilic side chain that promotes inter-chain interactions through van der Waals interactions and hydrogen bonds. Folding of the polymer is directed by a single copper catalyzed azide-alkyne cycloaddition at the terminal ends (*20*). The head-to-tail bite causes the polymer chain, in aqueous solvent, to adopt a self-propagating structure consisting of a hydrophobic core surrounded by the hydroxyl groups of HEMA. The physical properties and the complexity of the propagating structures can be subsequently customized by growing a secondary block-copolymer on each HEMA side chain. Depending on the composition of the block-copolymer, higher ordered assembly morphology between the unfolded and folded form can be programmed.

To demonstrate that synthetic polymers can be folded into specific forms for constructing higher-ordered structures, polymers of HEMA (PHEMA) were folded into the cyclic topology, which is a well-established approach to fold polymers (*21*). Three linear

PHEMA samples (*l*-PHEMA$_n$-*Br*, where n represents the number of repeating units) of different lengths were synthesized via atom transfer radical polymerization (ATRP) using propargyl 2-bromoisobutyrate as the initiator (**Fig. 1**A). Their respective average molecular weights were calculated from the ^{1}H nuclear magnetic resonance (NMR) spectra as 1670 g mol^{-1} (n = 11), 2120 g mol^{-1} (n = 15), and 3040 g mol^{-1} (n = 22), which fit well to the design (figs. S1–S3, table S1). GPC results show relatively narrow molecular weight distributions of 1.36 ~ 1.39 (**Fig. 1**B). The apparent molecular weights determined by GPC are higher, which is due to the different hydrodynamic sizes of poly(methyl methacrylate) (PMMA) standards and PHEMA in DMF (*22*). Next, the bromine ends of these polymers were transformed to azide groups by reacting with sodium azide, which was confirmed by the appearance of the characteristic peak of azide at 2121 cm^{-1} in the Fourier-transform infrared (FTIR) spectra of the product (*l*-PHEMA$_n$-*N*$_3$) (**Fig. 1**C and fig. S4).

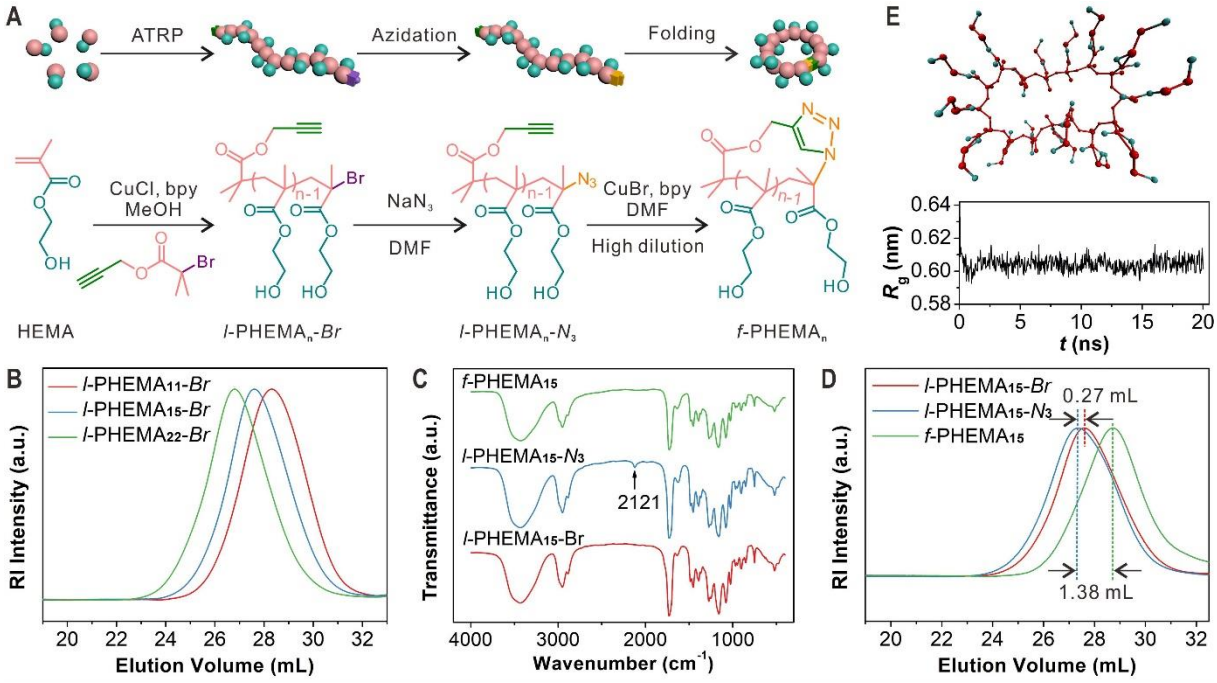

Fig. 1. Synthesis and folding of PHEMA. (A) Scheme of the synthesis of *l*-PHEMA$_n$-*Br* and its azidation and folding into the cyclic topology. (B) GPC curves (eluent: DMF; standard: PMMA) of *l*-PHEMA$_n$-*Br* with different repeating units. (C) FTIR spectra, and (D) GPC curves of *l*-PHEMA$_{15}$-*Br*, *l*-PHEMA$_{15}$-*N*$_3$, and *f*-PHEMA$_{15}$. (E) The top and bottom panels show a simulation snapshot and the time evolution of R_g of a single *f*-PHEMA$_{15}$ in pure water, respectively.

Subsequently, the heterobifunctional PHEMA with azide and alkyne ends was folded via Huisgen cycloaddition under high dilution conditions (*20*). In a typical experiment, CuBr and 2,2'-bipyridyl (bpy) were added into a Schlenk tube loaded with DMF, which was degassed

through two freeze-pump-thaw cycles. To avoid intermolecular reactions, the degassed DMF solution of *l*-PHEMA$_n$-N_3 was added into the catalyst solution at a slow speed of 0.16 mL h^{-1} via a syringe pump. As shown in **Fig. 1**C, the asymmetric stretching peak of the azide group at 2121 cm^{-1} vanished after this step. This indicates that the click reaction between azide and alkyne groups was successful, which was also proven by ^{1}H NMR (figs. S5–S7). We also proved the structure for all the products in each step by 2D ^{1}H,^{1}H correlation spectroscopy and 2D ^{1}H,^{1}H nuclear Overhauser effect spectroscopy methods (figs. S8–S16).

The obtained polymers were further characterized by GPC (**Fig. 1**D and fig. S17) and ^{1}H diffusion ordered NMR spectroscopy (figs. S18–S23). Both techniques demonstrate that the hydrodynamic volumes of all three samples decreased after the click reaction, which confirms that linear PHEMA polymers were intramolecularly folded into the cyclic topology. It should be mentioned that no shoulder peak in the higher molecular regions was observed in the GPC curves indicating no linear polymers left or oligomers formed. To investigate if a single *f*-PHEMA$_{15}$ retains its well-defined cyclic structure in pure water, we performed an all-atom molecular dynamics simulation (fig. S24). In **Fig. 1**E we show the snapshot of a *f*-PHEMA$_{15}$ and the corresponding radius of gyration (R_g). To estimate the degree of sphericity of the cyclic polymers, we also calculated the lengths of the two major axes of the structure (fig. S25). It can be appreciated that a ring remains rather stable and symmetrically cyclic in pure water.

Linear PHEMA is generally regarded as a water-swellable polymer (*23*). Using a dialysis method (*24*), we compared the self-assembly behaviors of linear and folded PHEMA. Briefly, the polymer was dissolved in methanol and then deionized water was added dropwise. The mixture solution was loaded into a dialysis membrane (MWCO = 1000 g mol^{-1}) and dialyzed against water. As shown in **Fig. 2**A and fig. S26, solutions of the linear polymers turned turbid after one hour and some gel-like precipitation was observed three days later. Surprisingly, solutions of the folded polymers remain clear, a first indication that they can stabilize themselves in pure water.

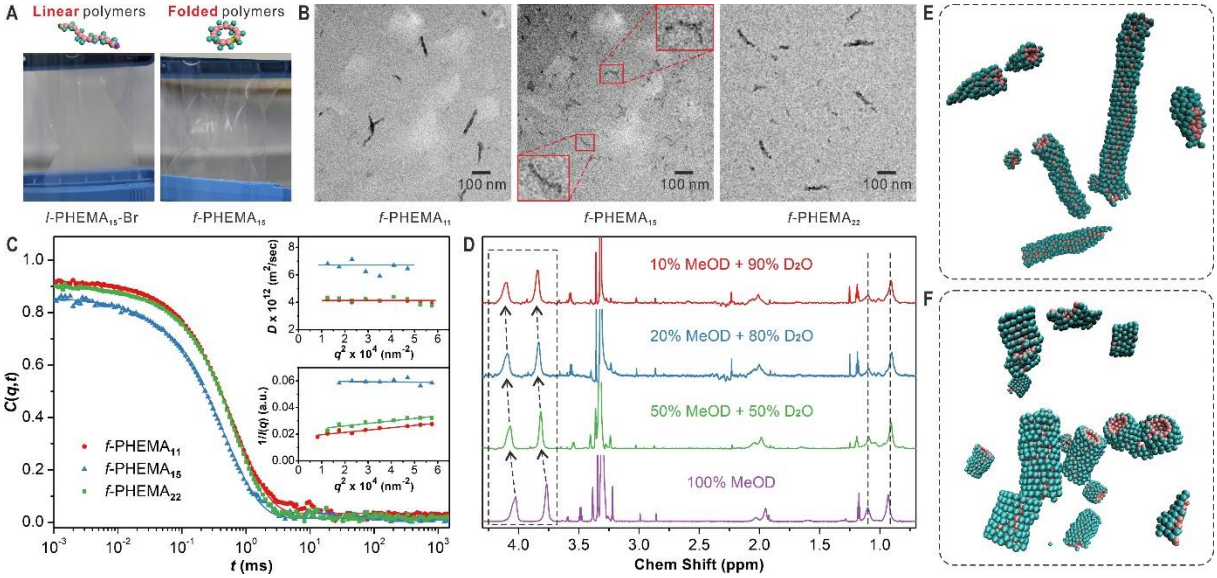

Fig. 2. Self-assembly of linear and folded polymers. (A) Solutions of *l*-PHEMA$_{15}$-*Br* and *f*-PHEMA$_{15}$ after dialysis against deionized water for one hour. (B) TEM images showing the assemblies of *f*-PHEMA$_{11}$, *f*-PHEMA$_{15}$, and *f*-PHEMA$_{22}$. (C) Relaxation functions $C(q,t)$ for the translation motion of *f*-PHEMA$_{11}$, *f*-PHEMA$_{15}$, and *f*-PHEMA$_{22}$ in water at 1 mg mL^{-1} and 293 K at a scattering angle of 90° corresponding to scattering wave vector q = 0.0187 nm^{-1}. Upper inset: The translation diffusion coefficient, D as a function of q^2 with the solid line indicating a virtually q independent D. Lower inset: $1/I(q)$ as a function of q^2. (D) ^{1}H NMR spectra (850 MHz, 298.3 K) of *f*-PHEMA$_{15}$ in mixtures of MeOD and D_2O with gradually tuned volume ratios. The chemical shifts were calibrated using tetramethylsilane as an internal standard. (E-F) Molecular dynamic simulation snapshots showing the self-assembly of a model simulation replica of *f*-PHEMA$_n$ with different ring sizes, i.e., n = 9 (E) and n = 15 (F).

Transmission electron microscopy (TEM) images reveal the formation of wormlike structures from the folded polymers (**Fig. 2**B and figs. S27–S29). For linear polymers of the same molecular weights, only irregular aggregates were observed showing the significant role of folding on the self-assembly (figs. S27–S29). We further confirmed the generation of stable assemblies from folded PHEMA by dynamic light scattering (DLS). Interestingly, both TEM and DLS results suggest *f*-PHEMA$_{15}$ with a middle ring size formed the smallest assemblies. The hydrodynamic radius R_h for assemblies of *f*-PHEMA$_{11}$, *f*-PHEMA$_{15}$, and *f*-PHEMA$_{22}$ were determined as 54 ± 2 nm, 36 ± 2 nm, and 58 ± 3 nm, respectively (**Fig. 2**C and figs. S30–S32). The large size of the *f*-PHEMA$_{11}$ and *f*-PHEMA$_{22}$ assemblies was confirmed by their measurable R_g in the Ornstein-Zernike, $I(q)^{-1}$ vs q^2 (lower inset to **Fig. 2**C): $I(q)$ of the smaller *f*-PHEMA$_{15}$ case is virtually q independent (*25*). The calculated R_g = 50 nm (59 nm) for the *f*-PHEMA$_{11}$ (*f*-PHEMA$_{22}$) assemblies are very similar to the values of R_h suggesting compact structures much larger than the single rings (**Fig. 1**E). For linear PHEMA, DLS experiment was not possible due to the presence of large aggregates.

The unique assembly behaviors of cyclic PHEMA can be ascribed to the rearrangement of the atomic distribution by polymer folding. Nile Red loading experiments indicated the formation of hydrophobic microenvironments during the assembly (fig. S33). The measured critical aggregation concentrations of *f*-PHEMA$_n$ (~0.01 mg mL^{-1}) are lower than that of many amphiphilic polymers (0.02~0.2 mg mL^{-1}) (*24*, *26*), showing the strong assembly trend of folded polymers. Furthermore, we performed NMR measurements for *f*-PHEMA$_n$ in solvent mixtures of methanol-d$_4$ (MeOD) and deuterium oxide (D_2O) with gradually tuned compositions (**Fig. 2**D and fig. S34). When the amount of D_2O increased, the signals of the methyl groups in the backbone did not change. However, the peaks from the methylene groups (3.77 and 4.03 ppm) in hydroxyethyl side chains shifted. This result indicates that the backbones of *f*-PHEMA$_n$ were packed in the core and the side chains on the surface enabling them to freely interact with the polar solvent.

To further elucidate the self-assembly, we performed molecular dynamics simulations of an implicit solvent generic model. In this model, the quantities are expressed in the units of energy ε, length σ and time τ. The choice of the generic model parameter of a ring polymer is inspired by the structural stability and the solubilities of the individual residues in pure water, as observed for a *f*-PHEMA$_{15}$ (**Fig. 1**E) (*27*, *28*). For this purpose, we investigated two ring sizes (n = 9 and 15) at the same mass density. The simulation snapshots for n = 9 and 15 show wormlike micellar structures (**Figs. 2**E and F). Here, a self-assembled structure is dictated by the competition between the entropy penalty of forming an aggregate of a particular size from the homogeneous mixture and the surface energy reduction (*29*). In our case, while we abstain from discussing the details of aggregation kinetics, we note that the sizes of the largest aggregates stabilize after a time $t \sim 10^4\tau$ in both cases. We find that the length (L), diameter (d), and R_g of the largest aggregates are $L \sim 33.5\sigma$, $d \sim 3.3\sigma$ and $R_g \sim 9.9\sigma$ for n = 9, and $L \sim 14.2\sigma$, d $\sim 4.1\sigma$ and $R_g \sim 5.0\sigma$ for n = 15. Furthermore, from L and d values of n = 9 and the analytical expression (*30*), we have estimated $R_h \sim 10.7\sigma$. It should be noted that the structures observed in our simulations reveal the microscopic picture of the single aggregates. Moreover, from the assembles in **Fig. 2**B, they typically have a diameter of 10 ~ 20 nm. Therefore, considering that the estimated diameter of a ring is about 1 nm (fig. S25), each structure in **Fig. 2**B consist of 10 ~ 20 wormlike micelles stacked sideways to form one bundle. The microscopic description of such stacking in good solvent is rather well established in the case of elongated objects attached with hydrophilic side chains (*31*).

The above results clearly show that even homopolymers with a very simple structure can assemble into higher-ordered nanostructures after molecular folding. Therefore, we believe, like polypeptides and nucleic acids, common synthetic polymers can also be programmed into controlled nanoobjects with multiple levels of defined architectures through folding and assembly. As a proof-of-concept, we designed macrocyclic brush polymers with amphiphilic polystyrene-*block*-poly(acrylic acid) (PS-*b*-PAA) side chains. PS and PAA were selected because they are broadly representative of hydrophobic and hydrophilic polymers, and PS-*b*-PAA is one of the most intensively studied systems in the field of macromolecular self-assembly (*26*).

The cyclic macroinitiator *f*-P(HEMA-*Br*)$_{22}$ was synthesized by attaching ATRP initiators to hydroxyl groups of *f*-PHEMA$_{22}$ (**Fig. 3**A). Hydrophobic PS and poly(*tert*-butyl acrylate) (P*t*BA) were consecutively grafted from the cyclic macroinitiator. The P*t*BA block was then hydrolyzed by trifluoroacetic acid into PAA, generating cyclic brush polymers with amphiphilic side chains [*f*-P(HEMA-*g*-PS$_x$-*b*-PAA$_y$)$_{22}$, where x and y represent the numbers of repeating units for PS and PAA, respectively]. These cyclic brush polymers can be regarded as the simplest folded form of the corresponding linear brush polymers. As shown in **Fig. 3B** and **C**, we synthesized four cyclic brush polymers (**CB-1** to **CB-4**). For comparison, a block copolymer (**BC**) and a linear brush polymer (**LB**) with comparable compositions were also prepared. All products in each step have been systematically characterized by NMR and FTIR spectroscopies as well as GPC (figs. S35–S49, tables S2–S4). Analysis of cyclic brush polymers by GPC shows narrow size distributions with $Đ$ in the range of 1.17 to 1.48, indicating that they can be used as uniform building blocks.

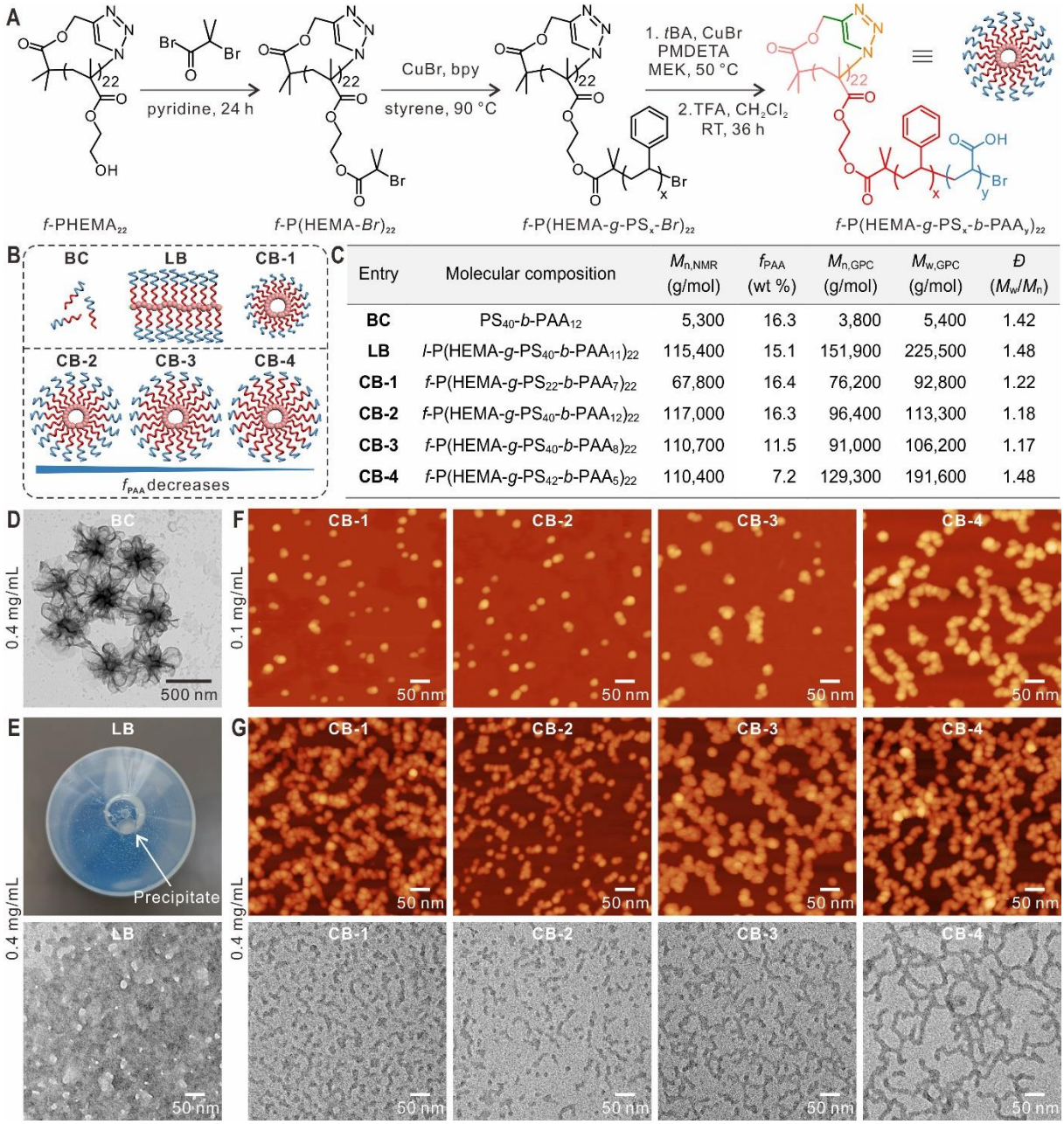

Entry	Molecular composition	$M_{n,NMR}$ (g/mol)	f_{PAA} (wt %)	$M_{n,GPC}$ (g/mol)	$M_{w,GPC}$ (g/mol)	$Đ$ (M_w/M_n)
BC	PS_{40}-*b*-PAA_{12}	5,300	16.3	3,800	5,400	1.42
LB	*l*-P(HEMA-*g*-PS_{40}-*b*-PAA_{11})$_{22}$	115,400	15.1	151,900	225,500	1.48
CB-1	*f*-P(HEMA-*g*-PS_{22}-*b*-PAA_{7})$_{22}$	67,800	16.4	76,200	92,800	1.22
CB-2	*f*-P(HEMA-*g*-PS_{40}-*b*-PAA_{12})$_{22}$	117,000	16.3	96,400	113,300	1.18
CB-3	*f*-P(HEMA-*g*-PS_{40}-*b*-PAA_{8})$_{22}$	110,700	11.5	91,000	106,200	1.17
CB-4	*f*-P(HEMA-*g*-PS_{42}-*b*-PAA_{5})$_{22}$	110,400	7.2	129,300	191,600	1.48

Fig. 3. Hierarchical self-assembly of cyclic brush polymers. (A) Scheme for the synthesis of cyclic brush polymers *f*-P(HEMA-*g*-PS_x-*b*-PAA_y)$_n$. (B) Schematic illustration and (C) molecular parameters of block copolymer **BC**, linear brush polymer **LB**, and four cyclic brush polymers (**CB-1** to **CB-4**). (D) TEM image showing the self-assembly of **BC** at 0.4 mg mL^{-1} in water. (E) Optical (top) and TEM (bottom) images showing the aggregation of **LB** in water. (F) AFM images showing the self-assembly of **CB-1** to **CB-4** at 0.1 mg mL^{-1} in water. (G) AFM (top) and TEM (bottom) images showing the self-assembly of cyclic brush polymers into 1D wormlike assemblies and hierarchical structures at 0.4 mg mL^{-1} in water.

Using a similar dialysis method, we investigated the self-assembly behavior of these amphiphilic cyclic brush polymers (**CB-1** to **CB-4**) in water and compared them with **BC** and **LB**. The polymers were first dissolved in DMF, which is a good solvent for both PS and PAA. After adding the same amount of deionized water dropwise, the mixture solutions were dialyzed

against water for three days and then tuned to desired concentrations. As shown in **Fig. 3D** and fig. S50, block copolymer **BC** self-assembled into vesicles and large compound vesicles at different concentrations due to its high weight fraction of hydrophobic PS. In comparison, the **LB** counterpart to the polymerized form of **BC** could not form ordered structures and precipitation was observed at 0.4 mg mL^{-1} (**Fig. 3E**, figs. S51–S52).

Interestingly, cyclic brush polymers with similar compositions but different topologies demonstrated drastically different self-assembly behaviors. We found that the polymer concentration and the weight fraction of PAA (f_{PAA}) are two important factors on the assembly. Discrete structures were observed by atomic force microscopy (AFM) and TEM for all samples when the concentrations were 0.1 mg mL^{-1} (**Fig. 3F**). The smallest particles in the AFM images show the same height of about 5 nm (figs. S53–S55), which corresponds with the size of single cyclic brushes. Other bigger nanoobjects can be ascribed to dimers, trimers, or oligomers of cyclic brush polymers. Importantly, the boundary between cyclic brush polymers can be visualized by AFM, which clearly shows the assembly of cyclic brush polymers in a layer-by-layer manner (**Fig. 3**F and figs. S53–S56). When the concentrations increased to 0.4 mg mL^{-1}, wormlike assemblies and hierarchical structures were obtained (**Fig. 3**G and figs. S57–S60). Unlike simple diblock copolymers that form wormlike micelles only in a narrow window of hydrophobic-hydrophilic ratios, folded polymers with a broad range of compositions can assemble into wormlike structures. More importantly, these wormlike structures are generated via stepwise folding and modular assembly, allowing the modulation of the internal structure and overall dimension in each step. For cyclic brush polymers with similar side chain lengths (**CB-2** to **CB-4**), the assemblies became longer with the decrease of f_{PAA}. By customizing the block constituents, proportion and length, the architectural outcome can be tuned.

To investigate these interesting structures, we also performed a set of generic simulations of a replica of the cyclic brush polymers for five different concentrations (c). The data for two concentrations is shown in **Fig. 4A-B** and the complete data is shown in fig. S61 and movies S1–S10. Here, the side chains greatly hinder the self-assembly. For $c = 0.0002\sigma^{-3}$, discrete oligomers are observed attaining a maximum size of ~8.5σ (**Fig. 4A**) that is smaller than the model *f*-$PHEMA_9$ (**Fig. 2E**). Moreover, for $c = 0.0009\sigma^{-3}$, the side chains can interdigitate and thus form small assemblies that are joined via the relatively large side chains (**Fig. 4B**). These observations are consistent with the trends observed in the AFM and SEM measurements.

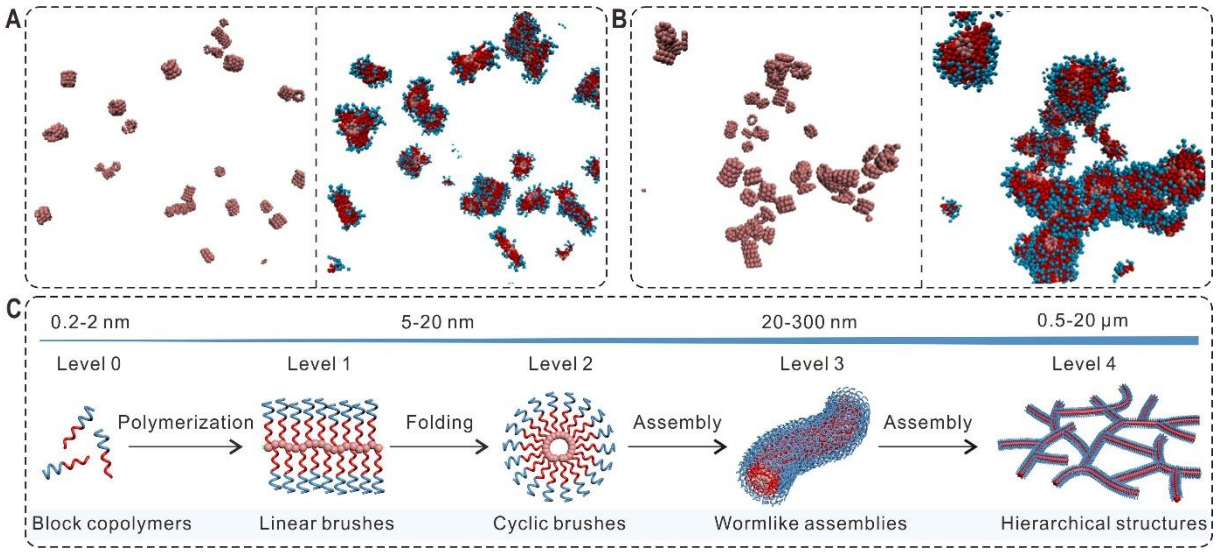

Fig. 4. Emergence of structural complexity by self-assembly of cyclic brush polymers. (A-B) Molecular simulation results showing the self-assembly of cyclic brush polymers for the two different concentrations, $c = 0.0002\sigma^{-3}$ (A) and $0.0009\sigma^{-3}$ (B). The left panels show only the hydrophobic backbones and the right panels illustrate the full molecules. (C) Formation of hierarchical structures by synthetic polymers via biomimetic folding and self-assembly.

We have therefore established a biomimetic strategy for the construction of hierarchical nanostructures via self-assembly of folded polymers. By rearranging atomic distribution of polymers to form specific preliminary structures, this modular approach is particularly powerful for preparing wormlike assemblies from synthetic polymers including common homopolymers and block copolymers. Various parameters including the polymer composition, molecular weight and primary structure can be used to manipulate the overall structure of the assemblies. The self-assembly pathway for the hierarchical structures is a versatile and stage-distinct platform to mimic the increasing complexity in the folding of polypeptides into 3D precise protein structures (**Fig. 4**C). The combination of polymer folding and self-assembly can therefore serve as a novel avenue for fabricating the next-generation hierarchical structures of unprecedentedly complex shapes which cannot be achieved by traditional methods.

References and Notes:

1. M. Heim, L. Romer, T. Scheibel, Hierarchical structures made of proteins. The complex architecture of spider webs and their constituent silk proteins. *Chem. Soc. Rev.* **39**, 156-164 (2010).
2. N. C. Seeman, H. F. Sleiman, DNA nanotechnology. *Nat. Rev. Mater.* **3**, 17068 (2018).
3. C. J. Chen, D. Y. W. Ng, T. Weil, Polymer bioconjugates: Modern design concepts toward precision hybrid materials. *Prog. Polym. Sci.* **105**, 101241 (2020).

4. C. J. Chen, K. Wunderlich, D. Mukherji, K. Koynov, A. J. Heck, M. Raabe, M. Barz, G. Fytas, K. Kremer, D. Y. W. Ng, T. Weil, Precision Anisotropic Brush Polymers by Sequence Controlled Chemistry. *J. Am. Chem. Soc.* **142**, 1332-1340 (2020).
5. P. W. K. Rothemund, Folding DNA to create nanoscale shapes and patterns. *Nature* **440**, 297-302 (2006).
6. D. Balchin, M. Hayer-Hartl, F. U. Hartl, In vivo aspects of protein folding and quality control. *Science* **353**, aac4354 (2016).
7. B. V. K. J. Schmidt, N. Fechler, J. Falkenhagen, J. F. Lutz, Controlled folding of synthetic polymer chains through the formation of positionable covalent bridges. *Nat. Chem.* **3**, 234-238 (2011).
8. N. Hosono, M. A. J. Gillissen, Y. C. Li, S. S. Sheiko, A. R. A. Palmans, E. W. Meijer, Orthogonal Self-Assembly in Folding Block Copolymers. *J. Am. Chem. Soc.* **135**, 501-510 (2013).
9. P. J. M. Stals, Y. C. Li, J. Burdynska, R. Nicolay, A. Nese, A. R. A. Palmans, E. W. Meijer, K. Matyjaszewski, S. S. Sheiko, How Far Can We Push Polymer Architectures? *J. Am. Chem. Soc.* **135**, 11421-11424 (2013).
10. Y. Tezuka, Topological Polymer Chemistry Designing Complex Macromolecular Graph Constructions. *Acc. Chem. Res.* **50**, 2661-2672 (2017).
11. S. Mavila, O. Eivgi, I. Berkovich, N. G. Lemcoff, Intramolecular Cross-Linking Methodologies for the Synthesis of Polymer Nanoparticles. *Chem. Rev.* **116**, 878-961 (2016).
12. Y. L. Liu, T. Pauloehrl, S. I. Presolski, L. Albertazzi, A. R. A. Palmans, E. W. Meijer, Modular Synthetic Platform for the Construction of Functional Single-Chain Polymeric Nanoparticles: From Aqueous Catalysis to Photosensitization. *J. Am. Chem. Soc.* **137**, 13096-13105 (2015).
13. M. Gonzalez-Burgos, A. Latorre-Sanchez, J. A. Pomposo, Advances in single chain technology. *Chem. Soc. Rev.* **44**, 6122-6142 (2015).
14. M. Schappacher, A. Deffieux, Synthesis of macrocyclic copolymer brushes and their self-assembly into supramolecular tubes. *Science* **319**, 1512-1515 (2008).
15. E. B. Trigg, T. W. Gaines, M. Marechal, D. E. Moed, P. Rannou, K. B. Wagener, M. J. Stevens, K. I. Winey, Self-assembled highly ordered acid layers in precisely sulfonated polyethylene produce efficient proton transport. *Nat. Mater.* **17**, 725-731 (2018).
16. A. H. Groschel, A. Walther, T. I. Lobling, F. H. Schacher, H. Schmalz, A. H. E. Muller, Guided hierarchical co-assembly of soft patchy nanoparticles. *Nature* **503**, 247-251 (2013).
17. H. B. Qiu, Y. Gao, C. E. Boott, O. E. C. Gould, R. L. Harniman, M. J. Miles, S. E. D. Webb, M. A. Winnik, I. Manners, Uniform patchy and hollow rectangular platelet micelles from crystallizable polymer blends. *Science* **352**, 697-701 (2016).
18. H. B. Qiu, Z. M. Hudson, M. A. Winnik, I. Manners, Multidimensional hierarchical self-assembly of amphiphilic cylindrical block comicelles. *Science* **347**, 1329-1332 (2015).
19. M. J. Huang, C. H. Hsu, J. Wang, S. Mei, X. H. Dong, Y. W. Li, M. X. Li, H. Liu, W. Zhang, T. Z. Aida, W. B. Zhang, K. Yue, S. Z. D. Cheng, Selective assemblies of giant tetrahedra via precisely controlled positional interactions. *Science* **348**, 424-428 (2015).
20. B. A. Laurent, S. M. Grayson, An efficient route to well-defined macrocyclic polymers via "Click" cyclization. *J. Am. Chem. Soc.* **128**, 4238-4239 (2006).
21. F. M. Haque, S. M. Grayson, The synthesis, properties and potential applications of cyclic polymers. *Nat. Chem.* **12**, 433-444 (2020).
22. J. V. M. Weaver, I. Bannister, K. L. Robinson, X. Bories-Azeau, S. P. Armes, M. Smallridge, P. McKenna, Stimulus-responsive water-soluble polymers based on 2-hydroxyethyl methacrylate. *Macromolecules* **37**, 2395-2403 (2004).

23. K. L. Robinson, M. A. Khan, M. V. D. Banez, X. S. Wang, S. P. Armes, Controlled polymerization of 2-hydroxyethyl methacrylate by ATRP at ambient temperature. *Macromolecules* **34**, 3155-3158 (2001).
24. C. J. Chen, G. Y. Liu, X. S. Liu, S. P. Pang, C. S. Zhu, L. P. Lv, J. Ji, Photo-responsive, biocompatible polymeric micelles self-assembled from hyperbranched polyphosphate-based polymers. *Polym. Chem.* **2**, 1389-1397 (2011).
25. K. Wunderlich, A. Larsen, J. Marakis, G. Fytas, M. Klapper, K. Mullen, Controlled Hydrogel Fiber Formation: The Unique Case of Hexaphenylbenzene-Poly(ethylene glycol) Amphiphiles. *Small* **10**, 1914-1919 (2014).
26. Y. Y. Mai, A. Eisenberg, Self-assembly of block copolymers. *Chem. Soc. Rev.* **41**, 5969-5985 (2012).
27. C. C. De Silva, P. Leophairatana, T. Ohkuma, J. T. Koberstein, K. Kremer, D. Mukherji, Sequence transferable coarse-grained model of amphiphilic copolymers. *J. Chem. Phys.* **147**, (2017).
28. Y. N. Zhao, M. K. Singh, K. Kremer, R. Cortes-Huerto, D. Mukherji, Why Do Elastin-Like Polypeptides Possibly Have Different Solvation Behaviors in Water-Ethanol and Water-Urea Mixtures? *Macromolecules* **53**, 2101-2110 (2020).
29. D. Mukherji, C. F. Abrams, Microvoid formation and strain hardening in highly cross-linked polymer networks. *Phys. Rev. E* **78**, 050801 (2008).
30. W. Vandesande, A. Persoons, The Size and Shape of Macromolecular Structures - Determination of the Radius, the Length, and the Persistence Length of Rodlike Micelles of Dodecyldimethylammonium Chloride and Bromide. *J. Phys. Chem.* **89**, 404-406 (1985).
31. H. Y. Gao, S. Bettscheider, T. Kraus, M. H. Muser, Entropy Can Bundle Nanowires in Good Solvents. *Nano Lett.* **19**, 6993-6999 (2019).

Acknowledgments:

M.K.S. thanks generous allocation of computational time at the IIT Kanpur computer facility where most generic simulations were performed. D.M. thanks the ARC Sockeye supercomputing facility where the all atom simulations were performed. **Funding**: The authors acknowledge financial support from Deutsche Forschungsgemeinschaft (DFG, German Research Foundation) – Project number 213555243 – SFB 1066 (A6). C.C. is grateful for a doctoral fellowship from Promotionskolleg Pharmaceutical Biotechnology of Ulm University funded by the state of Baden–Württemberg. D.M. thanks the Canada First Research Excellence Fund (CFREF) for the financial support. **Author contributions**: T.W. acquired funding for the project. T.W. and D.Y.W.N. supervised the project and corrected the manuscript. C.C. initiated the idea, performed the experiments, and wrote the manuscript. M.K.S., K.K. and D.M. performed the molecular simulations. K.W. and G.F. interpreted the light scattering results. S.H. performed the AFM. M.W. provided the NMR expertise. **Competing interests**: The authors declare no competing interests. **Data and materials availability**: All data is available in the main text or the supplementary materials.

Supplementary Materials:

Materials and Methods

Supplementary Text

Figures S1 to S61

Tables S1 to S4

Movies S1 to S10

Supplementary Materials for

Polymer cyclization as a general strategy for the emergence of hierarchical nanostructures

Chaojian Chen, Manjesh Kumar Singh, Katrin Wunderlich, Sean Harvey, Manfred Wagner, George Fytas, Kurt Kremer, Debashish Mukherji, David Y. W. Ng,* and Tanja Weil*

Correspondence to: weil@mpip-mainz.mpg.de (T.W.);
david.ng@mpip-mainz.mpg.de (D.Y.W.N.)

This PDF file includes:

Other Supplementary Materials for this manuscript includes the following:

Movies S1 to S10 (.mp4)

Materials and Methods

1. Materials

Propargyl 2-bromoisobutyrate (PBIB, >97%), ethyl α-bromoisobutyrate (EBIB, 98%), α-bromoisobutyryl bromide (98%), copper(I) chloride (CuCl, 99.995%), copper(I) bromide (CuBr, 99.999%), *N*,*N*,*N*′,*N*″,*N*″-pentamethyldiethylenetriamine (PMDETA, 99%), 2,2'-bipyridyl (bpy, ≥99%), methyl ethyl ketone (MEK, 99.5%) and Nile Red (technical grade) were purchased from Sigma-Aldrich and used without further treatment. Sodium azide (NaN_3, 99%) was purchased from Applichem and used as received. Trifluoroacetic acid (TFA, ≥99.9%) was obtained from Carl Roth. 2-Hydroxyethyl methacrylate (HEMA, Sigma-Aldrich, 97%, ≤250 ppm monomethyl ether hydroquinone), styrene (99%, Sigma-Aldrich), and *tert*-butyl acrylate (*t*BA, 98%, Sigma-Aldrich) were passed through basic Al_2O_3 column to remove inhibitors before use. All other solvents were obtained from commercial suppliers and used as received.

2. Synthesis and folding of linear PHEMA

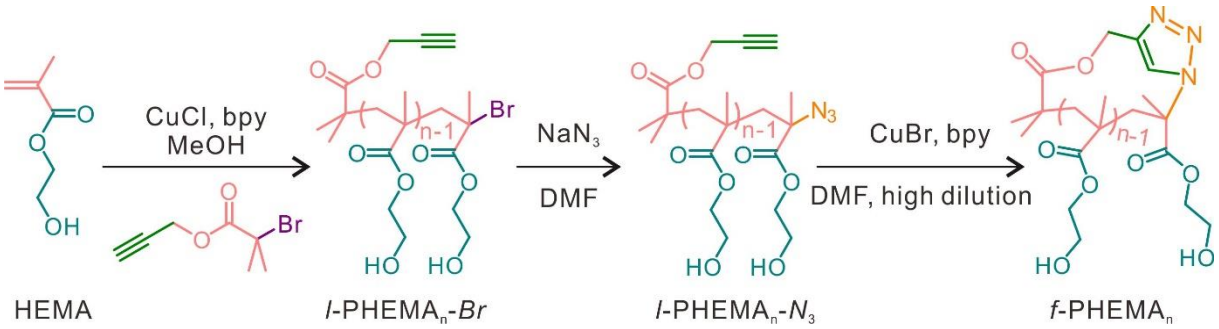

2.1 Synthesis of *l*-PHEMA$_n$-*Br* via atom transfer radical polymerization

In a typical procedure for the synthesis of *l*-PHEMA$_{22}$-*Br*, PBIB (310 µL, 2 mmol), HEMA (6.06 mL, 50 mmol) and bpy (781 mg, 5 mmol) were dissolved in 6 mL methanol in a 15 mL Schlenk flask under argon flow. Followed the mixture was degassed through three freeze-pump-thaw cycles and CuCl (238 mg, 2.4 mmol) was added to start the polymerization. After stirring at 24 °C for 5 h, the reaction mixture was quenched by exposing the reaction solution to air, followed by dilution with methanol. The solution was stirred until the color turned to blue. Then the Cu(II) catalyst was removed by passing through a silica column. The solution was concentrated and precipitated into diethyl ether. The procedure of dissolution with methanol and precipitation in diethyl ether was repeated twice. The product was obtained as a white solid after drying under high vacuum.

2.2 Synthesis of *l*-PHEMA$_n$-N_3 via azidation of *l*-PHEMA$_n$-*Br*

In a typical procedure for the synthesis of *l*-PHEMA$_{22}$-N_3, sodium azide (2.44 g, 37.5 mmol) was added to a round-bottom flask containing *l*-PHEMA$_{22}$-*Br* (2.4 g, 0.79 mmol) dissolved in mix solvent of DMF/H_2O (60 mL, 4:1 v/v). The reaction mixture was stirred at 50 °C for two days and then cooled down to room temperature. After removing most of the solvents at reduced pressure, the remaining portion was diluted with ethanol. The solid salt was removed by centrifugation. The solution was loaded into a dialysis membrane (MWCO ~ 1000 Da) and

extensively dialyzed against deionized water and methanol for two days. The product was obtained as a white solid after precipitation in diethyl ether and drying under high vacuum.

2.3 Synthesis of *f*-PHEMA$_n$ by folding *l*-PHEMA$_n$-N_3 via click chemistry

Folded PHEMA (*f*-PHEMA$_n$) with a cyclic secondary structure was synthesized by folding linear polymer *l*-PHEMA$_n$-N_3 via the azide-alkyne Huisgen cycloaddition under high dilution conditions. In a typical procedure for the folding of *l*-PHEMA$_{22}$-N_3, DMF (1 L) was added to a 2.5 L round bottomed flask and then degassed by two freeze-pump-thaw cycles. CuBr (0.86 g, 6 mmol) and bpy (1.87 g, 12 mmol) were added to the frozen DMF. The flask was resealed, evacuated, and refilled with argon. A separate flask containing 0.5 g of *l*-PHEMA$_{22}$-N_3 dissolved in 10 mL of DMF was degassed by three freeze-pump-thaw cycles. This solution was then added to the catalyst reaction solution at 120 °C via a syringe pump at a rate of 0.16 mL h^{-1}. Once the polymer was finished adding to the catalyst solution, the reaction was allowed to proceed at 120 °C for additional 24 h before cooling to room temperature. Most solvent of the reaction solution was removed under reduced pressure and the remained portion was diluted with methanol and stirred until the color changed to blue. The Cu(II) catalyst was removed by passing through a silica column. The solution was concentrated and precipitated into diethyl ether. The product was finally obtained after drying under high vacuum.

3. Self-assembly of linear and folded PHEMA

3.1 Self-assembly of linear and folded PHEMA

A dialysis method was used to prepare assemblies of folded polymers. In a typical process, 21 mg of folded PHEMA was dissolved in 7 mL of methanol at room temperature. The solution was vigorously stirred and 7 mL of deionized water was added with a speed of 0.2 mL min^{-1}. After stirring for another 2 h, the solution was loaded into a dialysis membrane (MWCO ~ 1000 Da) and dialyzed against deionized water for three days to completely remove the solvent methanol. The final concentration of polymers was tuned to 1 mg mL^{-1} by adding water. For the self-assembly of linear polymers, the same procedure was employed and precipitation was observed.

3.2 Nile Red loading and the determination of critical aggregation concentration (CAC)

The CAC of micelles was determined using Nile Red as a fluorescence probe. The concentration of polymers was varied from 1 mg mL^{-1} to 1×10^{-4} mg mL^{-1}. Nile Red solution in acetone (15 μL, 0.02 mg mL^{-1}) was then added to 1 mL of each polymer solution. After sonication for 30 min, acetone was evaporated and the final concentration of Nile Red in each sample was therefore fixed at 3×10^{-4} mg mL^{-1}. Fluorescence spectra were recorded using a TECAN system (Spark 20M) at room temperature. The excitation wavelength was set as 550 nm and the emission wavelength was monitored from 590 nm to 720 nm. Excitation and emission bandwidths were both maintained at 20 nm and the emission wavelength step size was 2 nm.

4. Synthesis of amphiphilic block copolymer PS-b-PAA

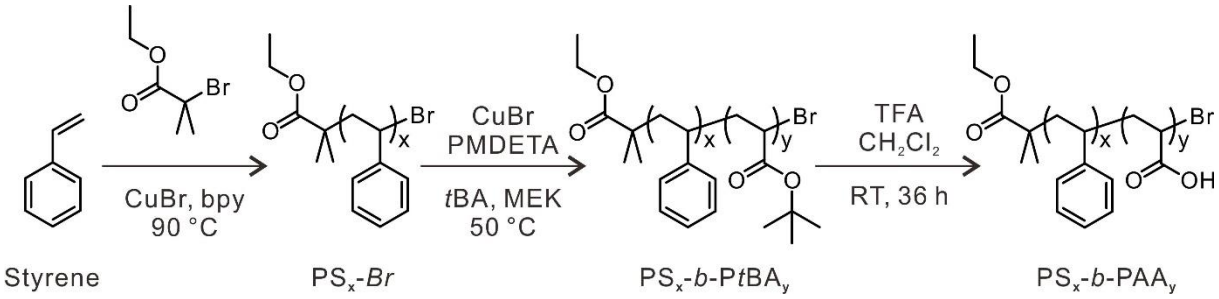

4.1 Synthesis of PS_x-*Br* via atom transfer radical polymerization

In order to synthesize PS_{40}-*Br*, EBIB (29.4 µL, 0.2 mmol), styrene (9.17 mL, 80 mmol), and bpy (62.4 mg, 0.4 mmol) were added into a 50 mL Schlenk flask and the mixture was degassed through three freeze-pump-thaw cycles. CuBr (28.6 mg, 0.2 mmol) was then added under argon flow and the polymerization was proceeded at 90 °C. After reaction for 3 h, the polymerization was stopped after putting the flask into liquid nitrogen. THF was added and the reaction mixture was then passed through a short column filled with neutral Al_2O_3 to remove the copper catalyst. The crude product was precipitated in cold methanol. The procedure of dissolution with THF and precipitation in methanol was repeated twice and the product was obtained after drying under high vacuum.

4.2 Synthesis of block copolymer PS_x-*b*-P*t*BA_y via ATRP

In a typical procedure for the synthesis of block polymer PS_{40}-*b*-P*t*BA_{12}, PS_{40}-*Br* (172 mg, 0.04 mmol initiation sites), *t*BA (2.34 mL, 16 mmol), and PMDETA (36 µL, 0.16 mmol) were dissolved in 2.34 mL MEK in a Schlenk flask and the mixture was degassed through three freeze-pump-thaw cycles. CuBr (11.5 mg, 0.08 mmol) was then added under argon flow and the polymerization was proceeded at 50 °C. After reaction for 20 min, the polymerization was stopped by putting the flask into liquid nitrogen. Acetone was added and the reaction mixture was then passed through a short column filled with neutral Al_2O_3 to remove the copper catalyst. The crude product was precipitated in methanol/water (v/v=1/1) and used for the next hydrolysis step.

4.3 Synthesis of PS_x-*b*-PAA_y by hydrolysis of *tert*-butyl ester groups of P*t*BA block

In a typical step for the synthesis of PS_{40}-*b*-PAA_{12}, 40 mg of PS_{40}-*b*-P*t*BA_{12} was dissolved in 6 mL CH_2Cl_2 followed by adding 3 mL TFA. The solution was stirred at room temperature for 36 h. After removing the solvent by evaporation, the product was dissolved in minimum amount of DMF and dialyzed against acetone and DI water (MWCO ~ 1000 Da). The final product was obtained after freeze drying.

5. Synthesis of linear brush polymers with amphiphilic block side chains

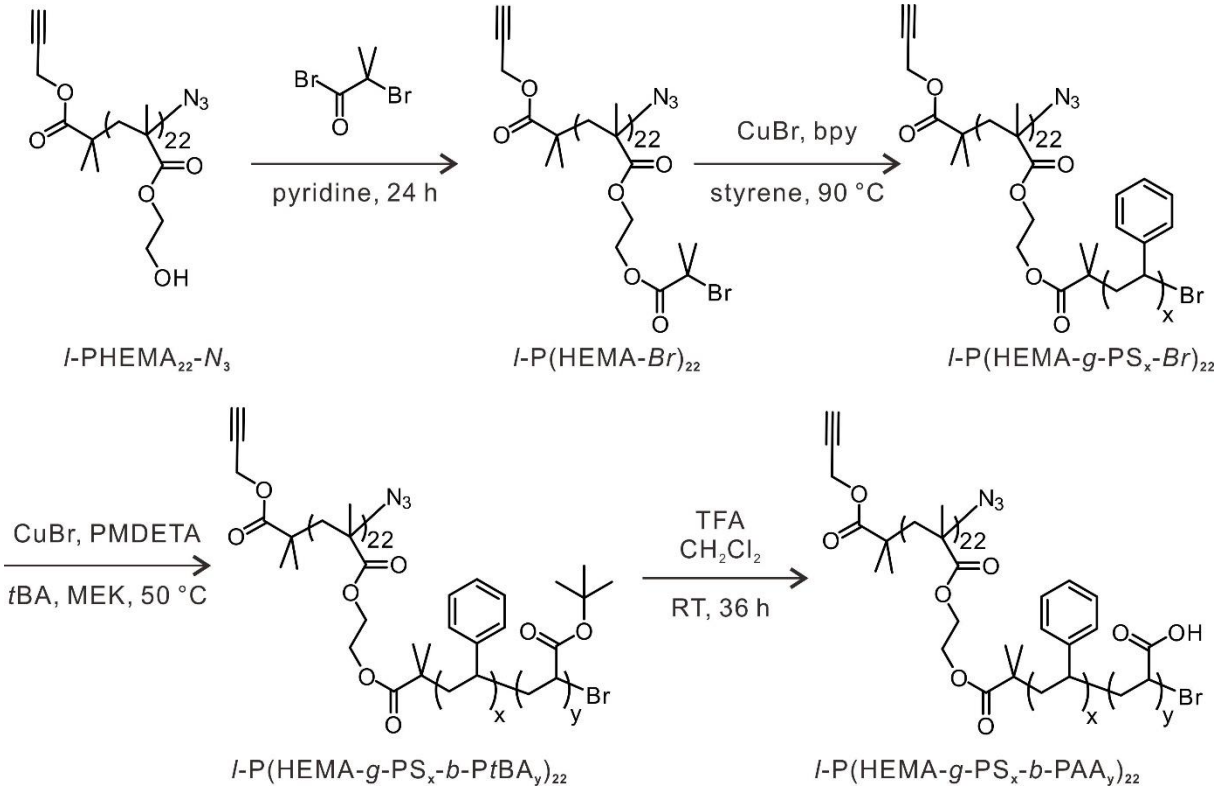

5.1 Synthesis of linear macroinitiator *l*-P(HEMA-*Br*)$_{22}$

Linear macroinitiator *l*-P(HEMA-*Br*)$_{22}$ was synthesized by esterification of *l*-PHEMA$_{22}$-*N*$_3$ with α-bromoisobutyryl bromide. Briefly, *l*-PHEMA$_{22}$-*N*$_3$ (400 mg) was dissolved in 10 mL anhydrous pyridine in a 25 mL flask. After cooling to 0 °C in an ice-water bath, α-bromoisobutyryl bromide (2 mL, 15.4 mmol) was added dropwise during 1 h. The solution was further stirred at 0 °C for 1 h, and then at room temperature for 24 h. The reaction mixture was precipitated in 100 mL cold water and then separated by centrifugation. The collected product was dissolved in a small amount of THF and reprecipitated in water. After repeating the process for two cycles, the product was obtained after drying under high vacuum.

5.2 Synthesis of linear brush polymer *l*-P(HEMA-*g*-PS$_x$-*Br*)$_{22}$

In order to synthesize linear brush polymer *l*-P(HEMA-*g*-PS$_{40}$-*Br*)$_{22}$, *l*-P(HEMA-*Br*)$_{22}$ (20 mg, 0.072 mmol initiation sites), styrene (5 mL, 43.6 mmol), and bpy (22.5 mg, 0.144 mmol) were added into a 15 mL Schlenk flask and the mixture was degassed through three freeze-pump-thaw cycles. CuBr (10.3 mg, 0.072 mmol) was then added under argon flow and the polymerization was proceeded at 90 °C. After reaction for a determined time, the polymerization was stopped after putting the flask into liquid nitrogen. THF was added and the reaction mixture was then passed through a short column filled with neutral Al_2O_3 to remove the copper catalyst. The crude product was precipitated in cold methanol. The procedure of dissolution with THF and precipitation in methanol was repeated twice and the product was obtained after drying under high vacuum.

5.3 Synthesis of linear brush polymer *l*-P(HEMA-*g*-PS_x-*b*-P*t*BA_y)$_{22}$

In a typical procedure for the synthesis of linear brush polymer *l*-P(HEMA-*g*-PS_{40}-*b*-P*t*BA_7)$_{22}$, *l*-P(HEMA-*g*-PS_{40}-*Br*)$_{22}$ (150 mg), *t*BA (1.97 mL, 13.5 mmol), and PMDETA (31 µL, 0.135 mmol) were dissolved in 1.97 mL MEK in a Schlenk flask and the mixture was degassed through three freeze-pump-thaw cycles. CuBr (10 mg, 0.067 mmol) was then added under argon flow and the polymerization was proceeded at 50 °C. After reaction for 30 min, the polymerization was stopped by putting the flask into liquid nitrogen. Acetone was added and the reaction mixture was then passed through a short column filled with neutral Al_2O_3 to remove the copper catalyst. The crude product was precipitated in methanol/water (v/v=1/1) and used for the next hydrolysis step.

5.4 Synthesis of amphiphilic linear brush polymer *l*-P(HEMA-*g*-PS_x-*b*-PAA_y)$_{22}$

In a typical step for the synthesis of *l*-P(HEMA-*g*-PS_{40}-*b*-P*t*BA_7)$_{22}$, 60 mg of *l*-P(HEMA-*g*-PS_{40}-*b*-P*t*BA_7)$_{22}$ was dissolved in 8 mL CH_2Cl_2 followed by adding 4 mL TFA. The solution was stirred at room temperature for 40 h. After removing the solvent by evaporation, the product was dissolved in minimum amount of DMF and dialyzed against acetone and DI water. The final product was obtained after freeze drying.

6. Synthesis of cyclic brush polymers with amphiphilic block side chains

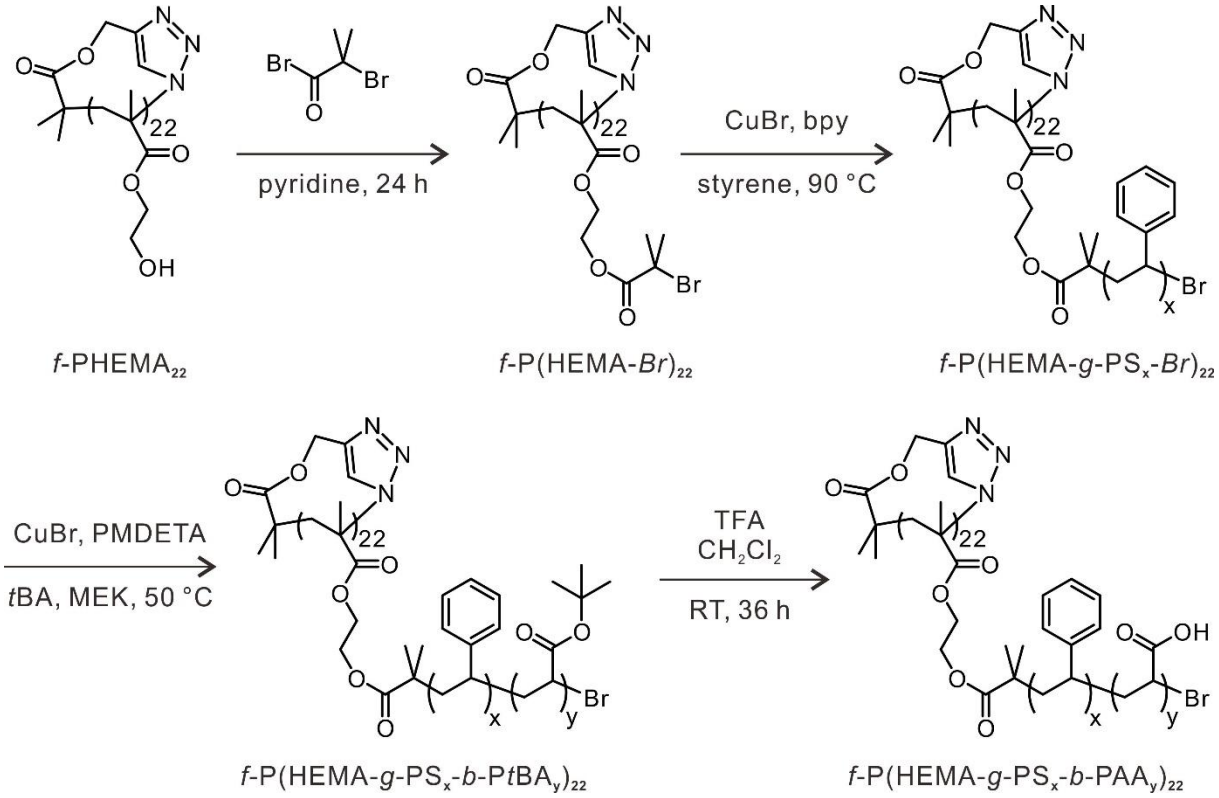

6.1 Synthesis of cyclic macroinitiator *f*-P(HEMA-*Br*)$_{22}$

Cyclic macroinitiator *f*-P(HEMA-*Br*)$_{22}$ was synthesized by esterification of *f*-$PHEMA_{22}$ with α-bromoisobutyryl bromide according to the literature (*32*). Briefly, *f*-$PHEMA_{22}$ (80 mg, ~ 0.6 mmol −OH) was dissolved in 3 mL anhydrous pyridine in a 10 mL flask. After cooling to 0 °C in an ice-water bath, α-bromoisobutyryl bromide (0.5 mL, 3.85 mmol) was added dropwise

during 20 min. The solution was further stirred at 0 °C for 1 h and then at room temperature for 24 h. The reaction mixture was precipitated in 50 mL cold water and separated by centrifugation. The collected product was dissolved in a small amount of THF and reprecipitated in water. After repeating the process for two cycles, the product was obtained after drying under high vacuum.

6.2 Synthesis of cyclic brush polymers *f*-P(HEMA-*g*-PS_x-*Br*)$_{22}$

In a typical procedure for the synthesis of cyclic brush polymer *f*-P(HEMA-*g*-PS_{40}-*Br*)$_{22}$, *f*-P(HEMA-*Br*)$_{22}$ (20 mg, 0.07 mmol initiation sites), styrene (5 mL, 43.6 mmol), and bpy (22.5 mg, 0.144 mmol) were added into a 15 mL Schlenk flask and the mixture was degassed through three freeze-pump-thaw cycles. CuBr (10.3 mg, 0.072 mmol) was then added under argon flow and the polymerization was proceeded at 90 °C. After reaction for a determined time, the polymerization was stopped after putting the flask into liquid nitrogen. THF was added and the reaction mixture was then passed through a short column filled with neutral Al_2O_3 to remove the copper catalyst. The crude product was precipitated in cold methanol. The procedure of dissolution with THF and precipitation in methanol was repeated twice and the product was obtained after drying under high vacuum.

6.3 Synthesis of cyclic brush polymers *f*-P(HEMA-*g*-PS_x-*b*-P*t*BA_y)$_{22}$

In a typical procedure for the synthesis of cyclic brush polymer *f*-P(HEMA-*g*-PS_{40}-*b*-P*t*BA_y)$_{22}$, *f*-P(HEMA-*g*-PS_{40}-*Br*)$_{22}$ (100 mg), *t*BA (1.17 mL, 8 mmol), and PMDETA (14.3 µL, 0.064 mmol) were dissolved in 1.17 mL MEK in a Schlenk flask and the mixture was degassed through three freeze-pump-thaw cycles. CuBr (2.3 mg, 0.016 mmol) was then added under argon flow and the polymerization was proceeded at 50 °C. After reaction for 30 min, the polymerization was stopped by putting the flask into liquid nitrogen. Acetone was added and the reaction mixture was then passed through a short column filled with neutral Al_2O_3 to remove the copper catalyst. The crude product was precipitated in methanol/water (v/v=1/1) and used for the next hydrolysis step.

6.4 Synthesis of amphiphilic cyclic brush polymers *f*-P(HEMA-*g*-PS_x-*b*-PAA_y)$_{22}$

In a typical step, 60 mg of *f*-P(HEMA-*g*-PS_{40}-*b*-P*t*BA_y)$_{22}$ was dissolved in 8 mL CH_2Cl_2 followed by adding 4 mL TFA. The solution was stirred at room temperature for 36 h. After removing the solvent by evaporation, the product was dissolved in minimum amount of DMF and dialyzed against acetone and DI water. The final product was obtained after freeze drying.

7. Self-assembly of block copolymers, linear and cyclic brush polymers

A dialysis method was used to prepare assemblies of block copolymers, as well as linear and cyclic brush polymers with block side chains. In a typical process, 8 mg of polymer was dissolved in 5 mL of DMF at room temperature. The solution was vigorously stirred and 5 mL of deionized water was then added with a speed of 0.2 mL min^{-1}. After stirring for another 2 h, the solution was loaded to into a dialysis membrane (MWCO ~ 1000 Da for block copolymers, MWCO ~ 3500 Da for linear and cyclic brush polymers) and dialyzed against deionized water

for three days to completely remove the solvent DMF. The final concentration of polymers was tuned to 0.4 mg mL^{-1} by adding water.

8. Characterization

8.1 Nuclear magnetic resonance (NMR) spectroscopy

Nuclear magnetic resonance (NMR) spectra were measured with a 5 mm triple resonance TXI $^{1}H/^{13}C/^{15}N$ probe equipped with a z-gradient on a 300 MHz, 700 MHz, or 850 MHz Bruker AVANCE III system.

For a proton spectrum, 128 transients were used with a 9.5 µs long 90° pulse and a 17600 Hz spectral width together with a recycling delay of 5 s. The used carbon experiment was a J-modulated spin-echo for ^{13}C-nuclei coupled to ^{1}H to determine number of attached protons (definition up (positive): C and CH_2, down (negative): CH and CH_3) with decoupling during acquisition.

The temperature was regulated at 298.3 K and calibrated with a standard ^{1}H methanol NMR sample using the Topspin 3.1 software (Bruker). The control of the temperature was realized with a VTU (variable temperature unit) and an accuracy of +/− 0.1K.

The structure prove was realized by 2D $^{1}H,^{1}H$ correlation spectroscopy (COSY) and 2D $^{1}H,^{1}H$ nuclear Overhauser effect spectroscopy (NOESY) methods. The spectroscopic widths of the homonuclear 2D-COSY and 2D-NOESY experiments were typically 14500 Hz in both dimension (f1 and f2) and the relaxation delay 2 s. The chosen mixing time for the NOESY experiment was 300 ms.

All the 2D $^{1}H,^{13}C$-HSQC-edited (heteronuclear single quantum correlations via double inept transfer and phase sensitive using Echo/Antiecho-TPPI gradient selection with decoupling during acquisition, red cross peaks are CH or CH_3 and black cross peaks are CH_2) experiments run with 2048 points in f2 (8500 Hz) and 512 points in f1 (42700 Hz) dimension. Before Fourier transformation, the data were zero filled to 1024 points in f1 and multiplied by a window function (q-sine bell or sine bell) in both dimensions.

Diffusion ordered NMR spectroscopy (DOSY NMR) experiments were performed with a gradient strength of 5,350 [G/mm] on a Bruker Avance-III 850 NMR Spectrometer. The gradient strength of probes was calibrated by analysis of a sample of $^{2}H_2O/^{1}H_2O$ at a defined temperature and compared with the theoretical diffusion coefficient of $^{2}H_2O/^{1}H_2O$ (values taken from Bruker diffusion manual) at 298.3 K.

In this work, the diffusion time (d20) was optimized for the TXI probe to 60ms while the gradient pulse length was kept at 1.8 ms. The optimization was realized by comparing the remaining intensity of the signals at 2% and 95% gradient strength. The intensity loss of the echo was in the range of 90 %.

The diffusion measurements were done with a 2D DOSY sequence (*33*) by incrementing in 32 linear steps from 2% to 100% with the TXI and the QXI probe. The 2D NMR sequences for measuring diffusion coefficient used echoes for convection compensation and longitudinal eddy current delays to store the magnetization in the z-axis, and only be dependent on T_1-relaxation. The calculation of the diffusion value was automatically calculated with the mono exponential function (*34*):

$$\ln\left(\frac{I(G)}{I(0)}\right) = -\gamma^2\delta^2G^2\left(\Delta - \frac{\delta}{3}\right)D,$$

where I(G) and I(0) are the intensities of the signals with and without gradient, γ the gyromagnetic ratio of the nucleus (^{1}H in this measurements), G is the gradient strength, δ the duration of the pulse field gradient (PFG), D the diffusion value in m^2/s and Δ the "diffusion time" between the beginning of the two gradient pulses. The relaxation delay between the scans was 3 s.

The 2D sequence for diffusion measurement used double stimulated echo with three spoil gradients for convection compensation and with an eddy current delay of 5 ms for reduction (*35*) (acronym Bruker pulse program: dstebpgp3s).

8.2 Fourier-transform infrared (FTIR) spectroscopy

Fourier-transform infrared (FTIR) spectroscopy spectra were recorded on a Bruker TENSOR II spectrometer or a Bruker Vertex 70 spectrometer at room temperature in the range of 4000 to 400 cm^{-1}. For the former, the samples were measured directly. For the latter instrument, the solid samples were thoroughly mixed with KBr and pressed into a flaky form. The spectra were collected over 32 scans with a spectral resolution of 4 cm^{-1}.

8.3 Gel permeation chromatography (GPC)

GPC was used to determine the molecular weight and molecular weight distribution. The temperature was set at 60 °C. DMF was used as eluent and the flow rate was set as 1 mL min^{-1}. Poly(methyl methacrylate) (PMMA) or polystyrene (PS) standards were used for calibration and refractive index (RI) detector was used.

8.4 Dynamic light scattering (DLS)

Folded PHEMA homopolymers were diluted to a concentration of 1 mg/mL in MilliQ water and filtered through a 450 nm filter (Millipore HA). DLS was performed on an ALV5000 setup using a coherent solid state cw laser at λ = 633 nm with a power of 194 mW. The intensity autocorrelation function $G(q,t)$ was recorded at different scattering wave vectors, $q = \frac{4\pi n}{\lambda}\sin\frac{\theta}{2}$ with n being the solvent refractive index was varied by changing the scattering angle θ between 15° ~ 150°, for water at 293 K, n = 1.333. The desired relaxation function, $C(q,t)=[G(q,t)-1]^{1/2}$, was analyzed by an inverse Laplace transformation (CONTIN algorithm).

8.5 Transmission electron microscopy (TEM)

TEM samples were prepared by adding 4 μL of the polymer self-assembly solution onto a carbon-coated copper grid. After drying in air for 10 min, the remained solution was removed by a filter paper. The measurement was conducted on a JEOL JEM-1400 TEM operating at an accelerating voltage of 120 kV.

8.6 Atomic force microscopy (AFM)

Imaging was performed with a Bruker Dimension FastScan Bio AFM equipped with the ScanAsyst mode. The sample solution was deposited onto freshly cleaved mica surface, and

left for 5 min at room temperature. The sample was scanned with the scan rates between 1 and 3 Hz. Several AFM images were acquired at different areas of the mica surface to ensure the reproducibility of the results. All images were analyzed by using the Gwyddion 2.48 software.

Supplementary Text

1. All-atom molecular dynamics simulations

To investigate the structural stability of an isolated cyclic molecule in pure water, we have performed all-atom molecular dynamics simulation of a *f*-PHEMA$_{15}$ (**Fig. 1E**). For this purpose, we have the same structure as in the experiment, without the linker used in the synthesis (fig. S24).

All-atom simulations are performed using the GROMACS molecular dynamics package (*36*) in an isobaric ensemble (NPT), where N is the number of particles, P is the isotropic pressure, and T is the temperature. T = 300 K is set using a velocity rescaling thermostat with a coupling constant of 0.1 ps (*37*). Pressure is kept at 1 bar using the Parrinello-Rahman barostat with a coupling constant of 2 ps (*38*). Electrostatics are treated with the particle mesh ewald (PME) method (*39*). The interaction cutoff for the non-bonded interactions is chosen as 1.0 nm and the equations of motions are integrated using the leap-frog integrator with a time step of δt = 1 fs. The simulation is performed for 20 ns.

For the simulation of a PHEMA ring with n = 15, the united atom GROMOS force field (*40*) is used. Water is described using the SPC/E model (*41*). For this simulation, we have used one molecule solvated in 7000 water molecules.

2. Generic molecular dynamics simulations

Generic simulations are performed using the bead spring polymer model for both systems presented in the main text (*42*). In this model, individual bonded monomers interact with each other via a combination of 6−12 Lennard-Jones potential with a cutoff distance $2^{1/6}\sigma$ and a finitely extensible nonlinear elastic (FENE) potential. The results are presented in the unit of LJ energy ε, LJ distance σ and mass *m* of the individual monomers.

The nonbonded interactions between the both hydrophobic and hydrophilic residues are also modelled using the LJ potential. The simulation is performed under the canonical ensemble with a time step of $\Delta t = 0.01\tau$ for 10^8 MD time steps. The equations of motion are integrated using the velocity Verlet algorithm. The system is thermalized via a Langevin thermostat with a damping constant $\gamma = 1\tau^{-1}$ and $T = 1\varepsilon/k_B$, where k_B is the Boltzmann constant. The generic simulations are performed by using the LAMMPS molecular dynamics packages (*43*).

2.1 Molecular dynamics simulations for the self-assembly of folded PHEMA

For the simulation of folded PHEMA, we have used a model molecule that consists of a hydrophobic backbone and one hydrophilic molecule attached to each backbone monomer. A representative structure is shown in **Fig. 1A** and fig. S24. The hydrophobic monomers interact with an attractive 6-12 LJ potential with a cut-off of 2.5σ, while the hydrophilic monomers are

modelled using a repulsive 6-12 LJ potential with a cut-off of $2^{1/6}\sigma$. The size of all monomers is taken as 1σ and the interaction energy are taken as 1ε. All other cross-monomer interactions are chosen to be repulsive 6-12 LJ potential with a cut-off of $2^{1/6}\sigma$. For these simulations, we have chosen three different backbone lengths, namely n = 9 and 15. Here, the concentration of n = 9 system is taken as $c = 0.0002\sigma^{-3}$, with c is calculated as the number of molecules per unit volume. The concentrations are adjusted such that the total mass density (or monomer number density). To keep the backbone structure flat, we have employed an additional dihedral interaction. Note that in this generic model one monomer is not equivalent of one monomer of the all atom or the experimental system.

2.2 Molecular dynamics simulations for the self-assembly of cyclic brush polymers

The system of cyclic brush polymers is similar to the above PHEMA system with a short amphiphilic block copolymer attached to each hydrophilic side monomer (**Fig. 3A**). An amphiphilic side chain consists of a 3 hydrophobic and 2 hydrophilic monomers. Like the section 2.1, the hydrophilic and the hydrophobic interactions are again modelled using a repulsive and an attractive LJ interaction, respectively. The simulations are performed for a system consists with n = 9 and for the five different concentrations, $c = 0.0002\sigma^{-3}$, $0.00035\sigma^{-3}$, $0.0005\sigma^{-3}$, $0.0009\sigma^{-3}$, and $0.0017\sigma^{-3}$. For these simulations we have used 125 molecules in a cubic box of different box dimensions. Each amphiphilic side chain consists of a flexible generic chain (*42*).

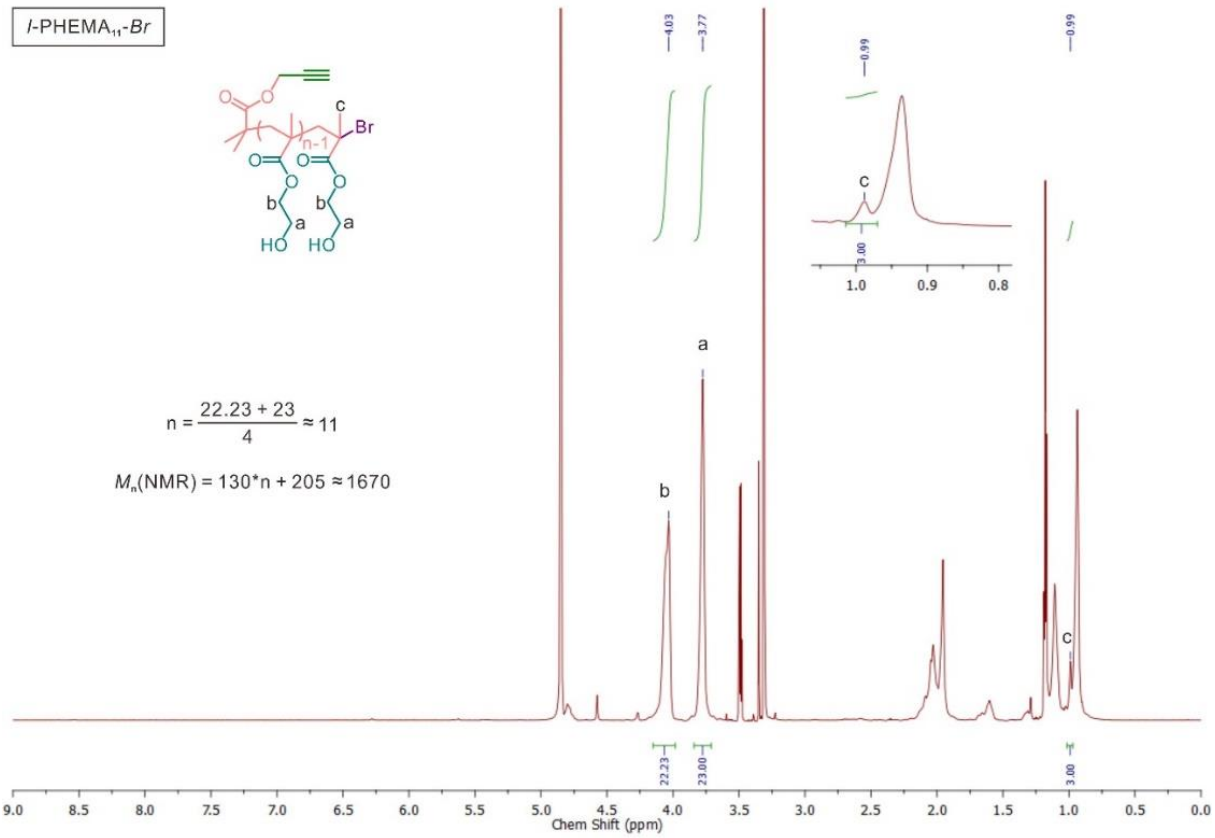

Fig. S1. ^{1}H NMR spectrum (850 MHz, 298.3 K) of *l*-PHEMA$_{11}$-*Br* in methanol-d$_4$ (MeOD). By comparing integrals of the methyl group near the bromine end (0.99 ppm) to methylene groups (3.77 ppm and 4.03 ppm) in the side chains, the average molecular weight was calculated as 1670 g mol^{-1} (n = 11).

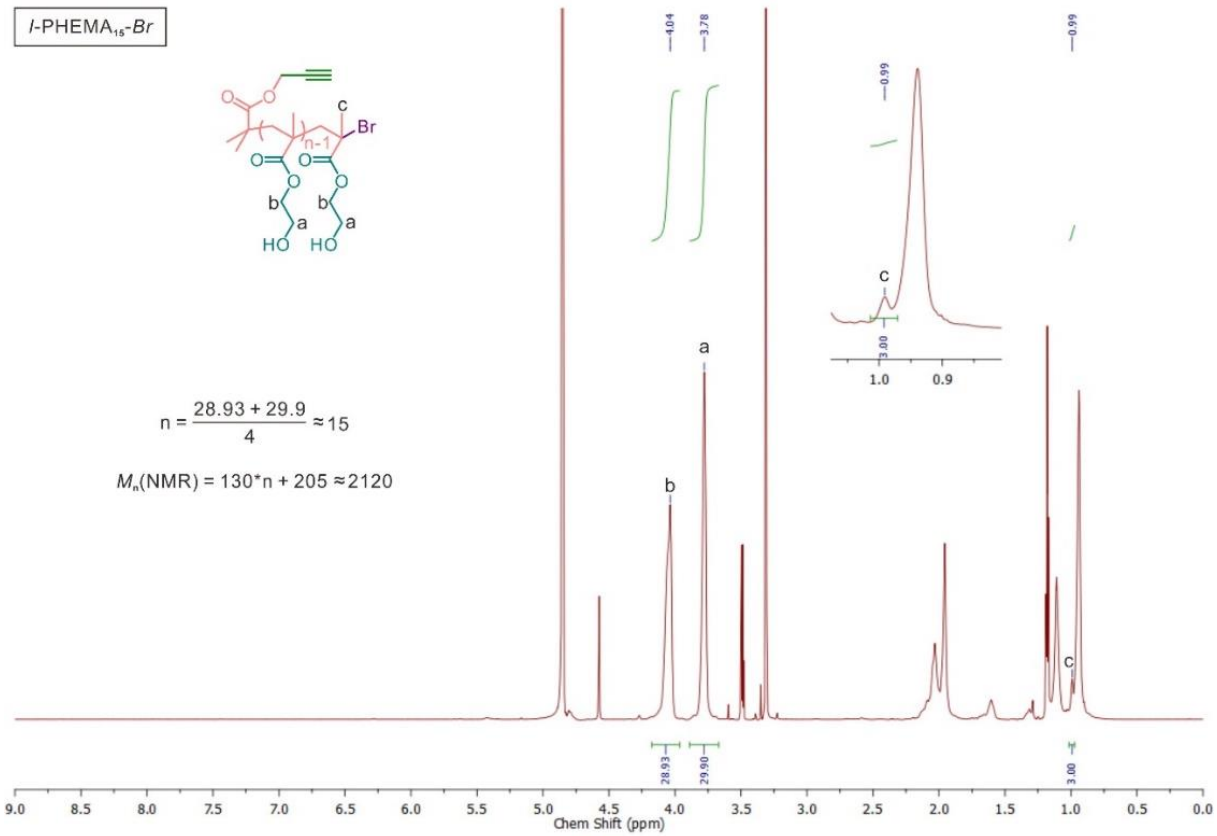

Fig. S2. ^{1}H NMR spectrum (850 MHz, 298.3 K) of *l*-PHEMA$_{15}$-*Br* in MeOD. By comparing integrals of the methyl group near the bromine end (0.99 ppm) to methylene groups (3.78 ppm and 4.03 ppm) in the side chains, the average molecular weight was calculated as 2120 g mol^{-1} (n = 15).

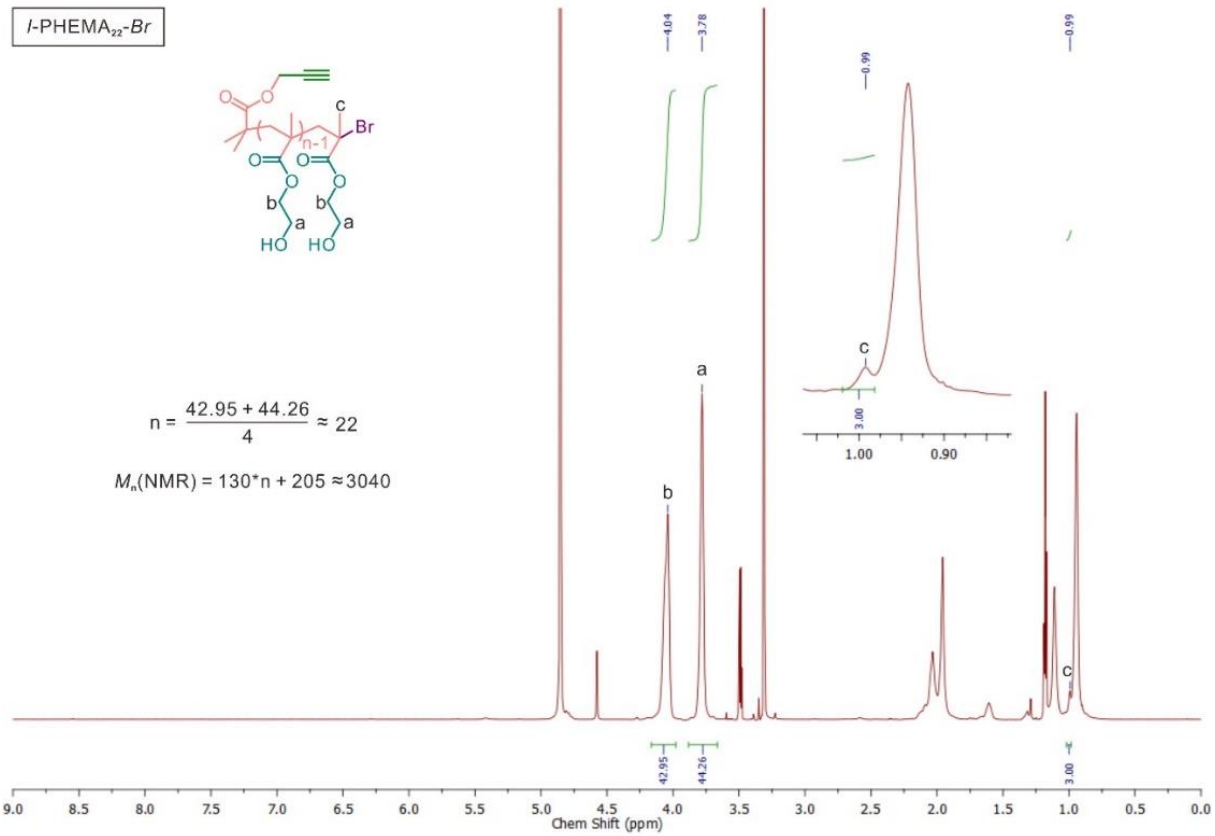

Fig. S3. ^{1}H NMR spectrum (850 MHz, 298.3 K) of *l*-PHEMA$_{22}$-*Br* in MeOD. By comparing integrals of the methyl group near the bromine end (0.99 ppm) to methylene groups (3.78 ppm and 4.03 ppm) in the side chains, the average molecular weight was calculated as 3040 g mol^{-1} (n = 22).

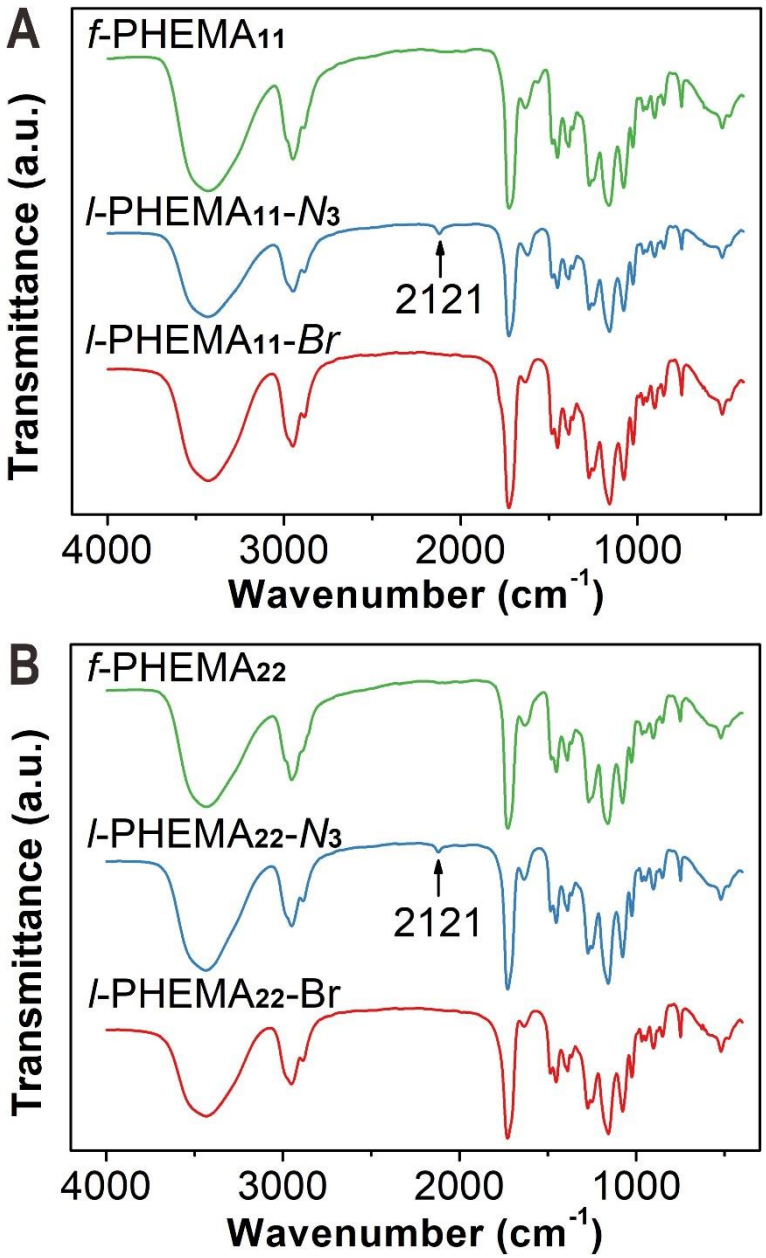

Fig. S4. (A) FTIR spectra of *l*-PHEMA$_{11}$-*Br*, *l*-PHEMA$_{11}$-*N*$_3$, and *f*-PHEMA$_{11}$. (B) FTIR spectra of *l*-PHEMA$_{22}$-*Br*, *l*-PHEMA$_{22}$-*N*$_3$, and *f*-PHEMA$_{22}$.

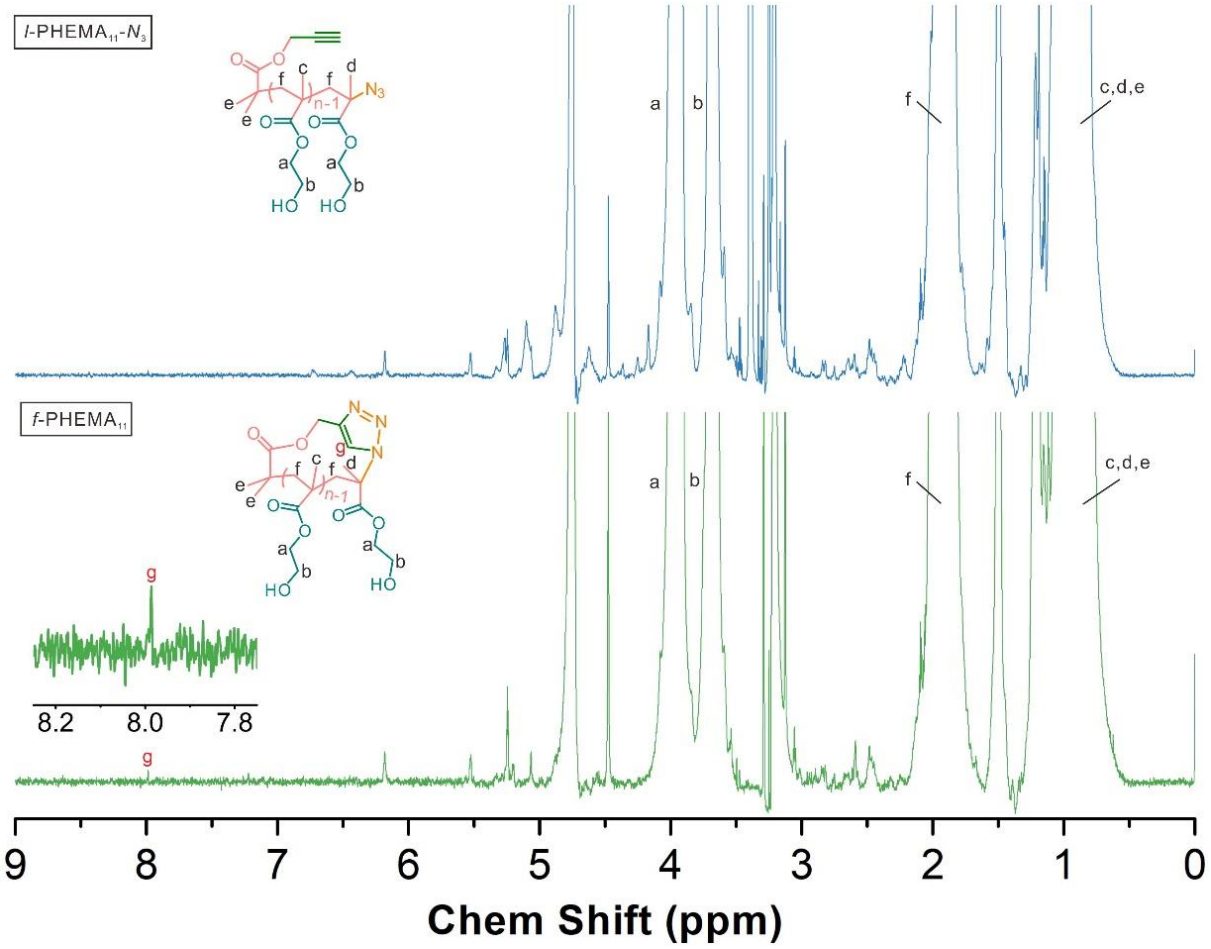

Fig. S5. Comparison of ^{1}H NMR spectra (850 MHz, MeOD, 298.3 K) of *l*-PHEMA$_{11}$-N_3 and *f*-PHEMA$_{11}$.

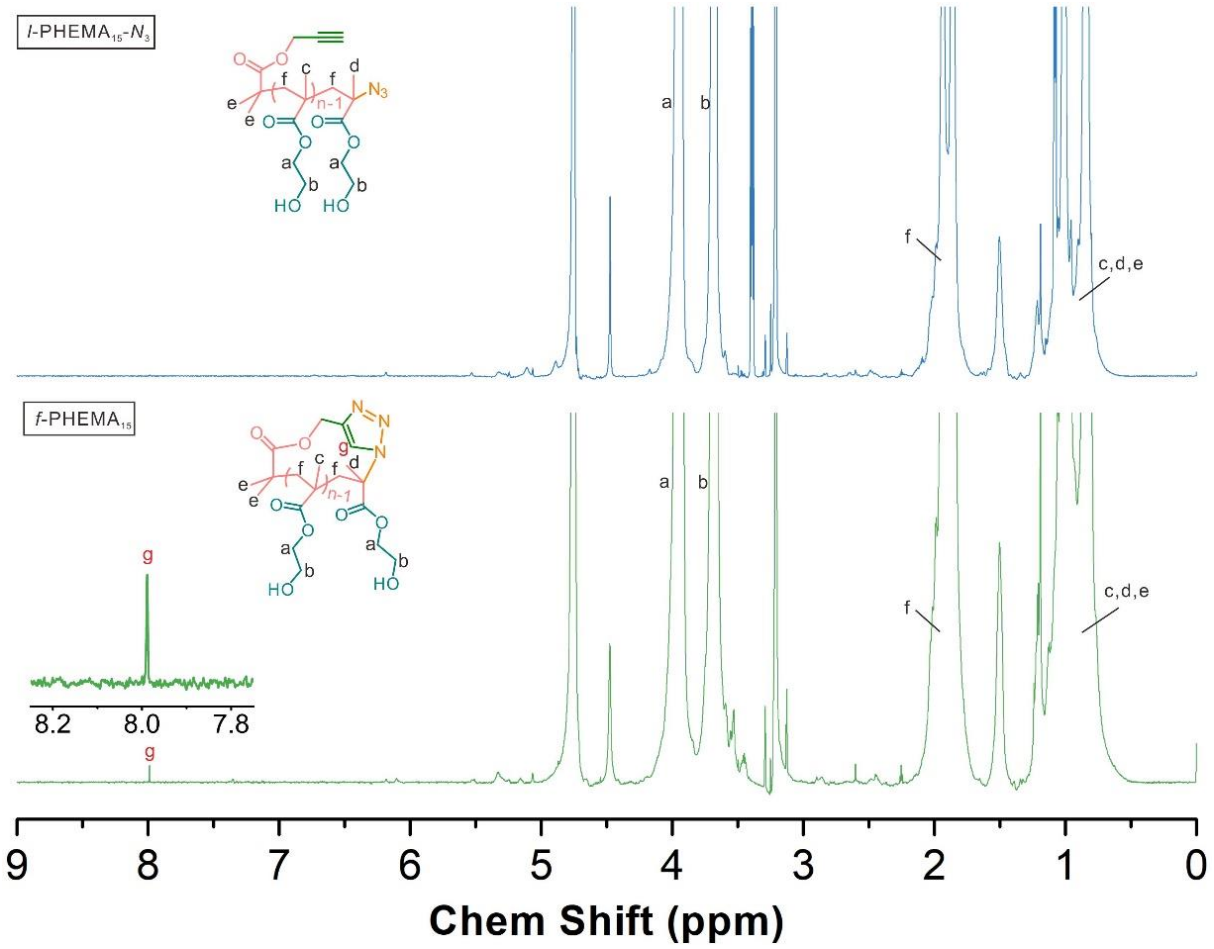

Fig. S6. Comparison of ^{1}H NMR spectra (850 MHz, MeOD, 298.3 K) of *l*-PHEMA$_{15}$-N_3 and *f*-PHEMA$_{15}$.

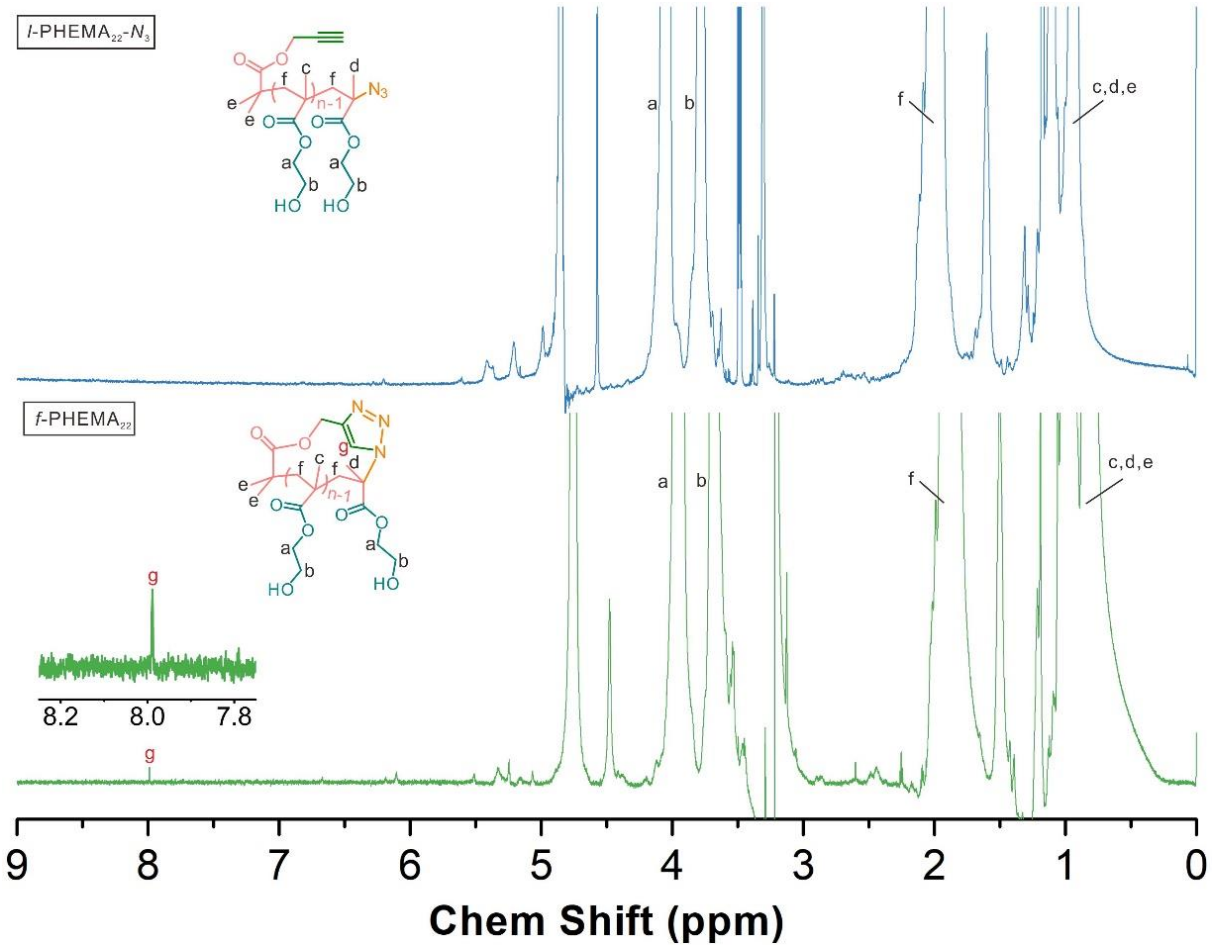

Fig. S7. Comparison of ^{1}H NMR spectra (850 MHz, MeOD, 298.3 K) of *l*-PHEMA$_{22}$-N_3 and *f*-PHEMA$_{22}$.

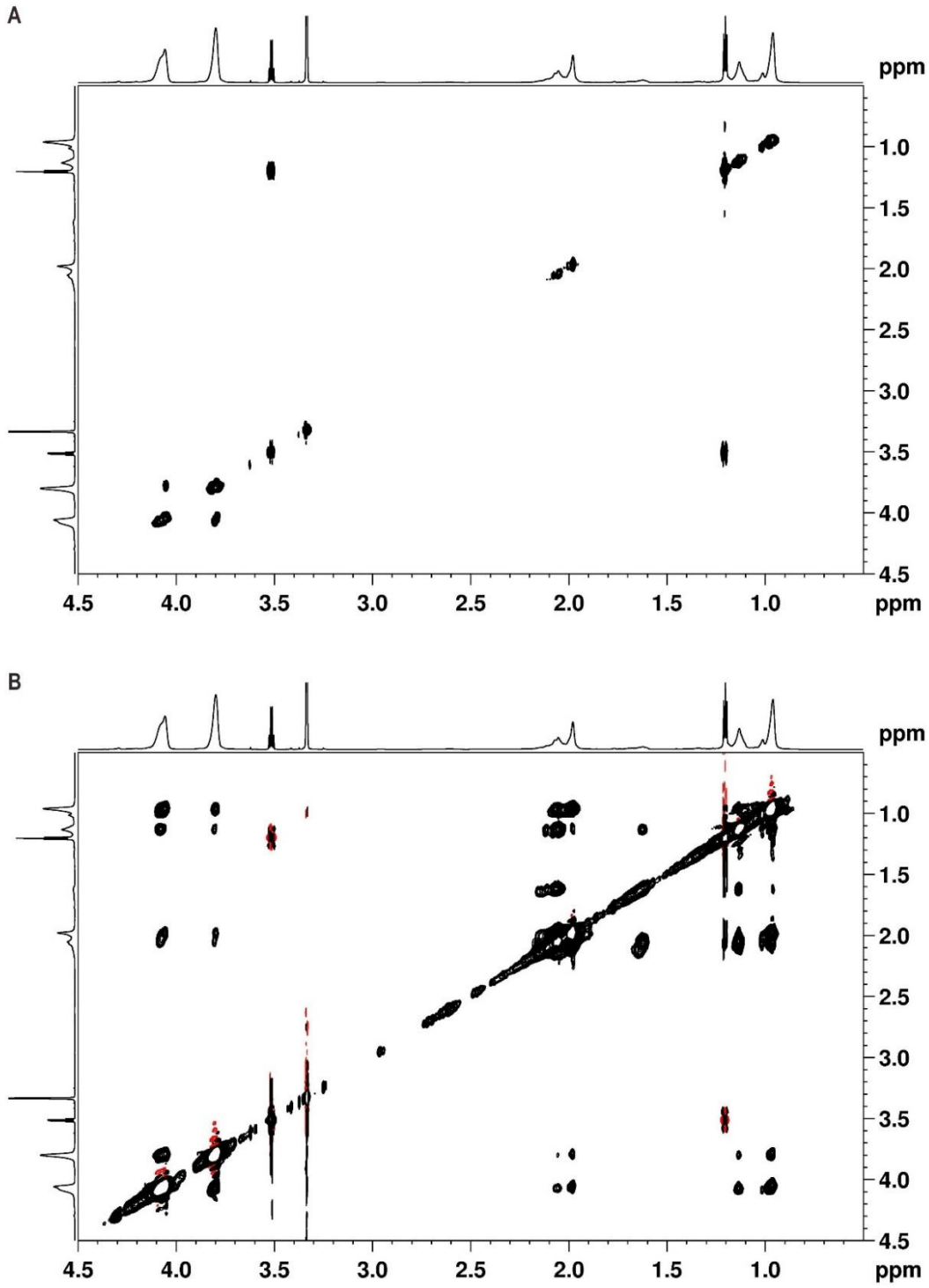

Fig. S8. 2D ^{1}H,^{1}H COSY and 2D ^{1}H,^{1}H NOESY NMR spectra (850 MHz, 298.3 K) of *l*-PHEMA$_{11}$-*Br* in MeOD.

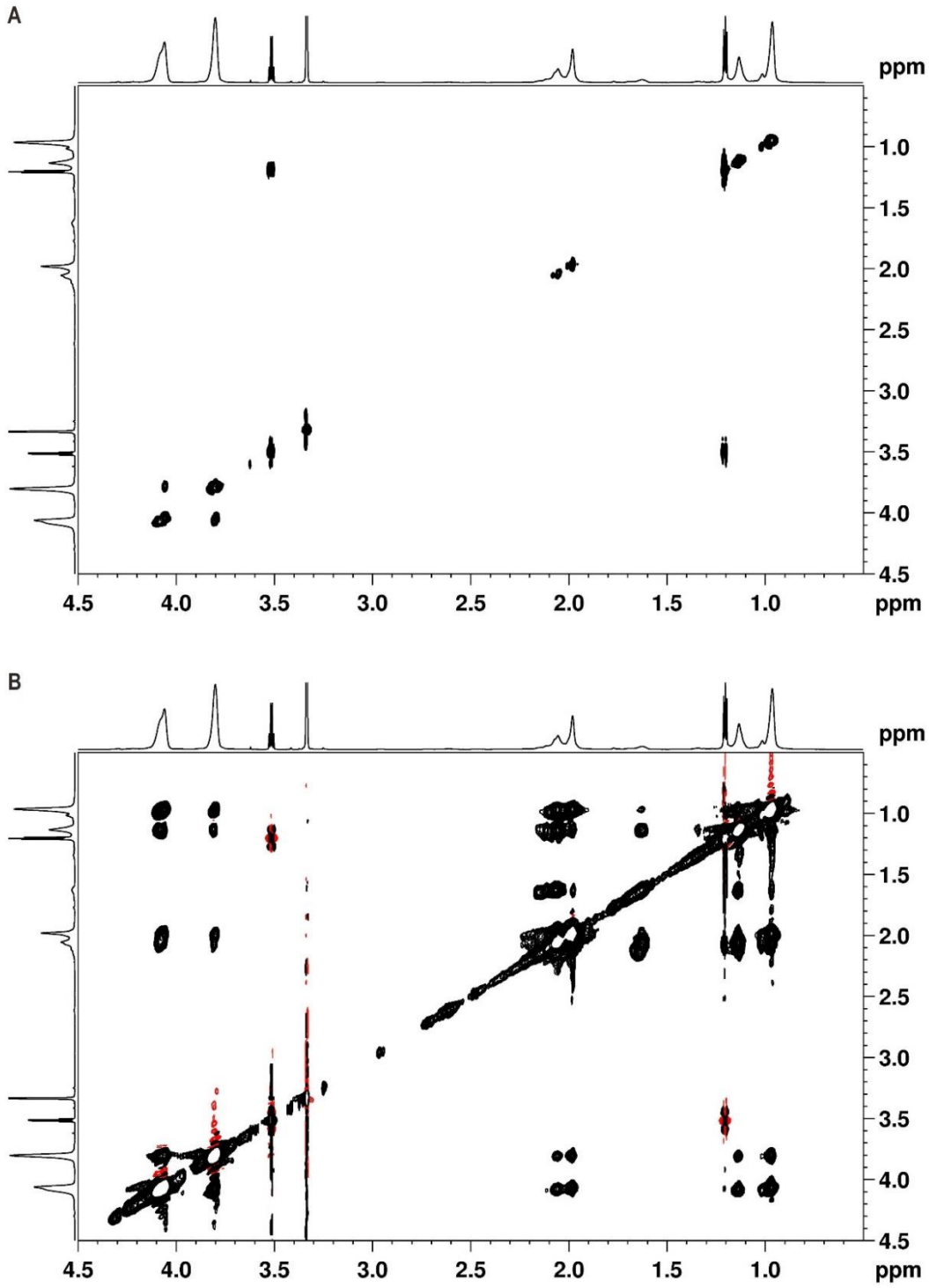

Fig. S9. 2D ^{1}H,^{1}H COSY and 2D ^{1}H,^{1}H NOESY NMR spectra (850 MHz, 298.3 K) of *l*-PHEMA$_{15}$-*Br* in MeOD.

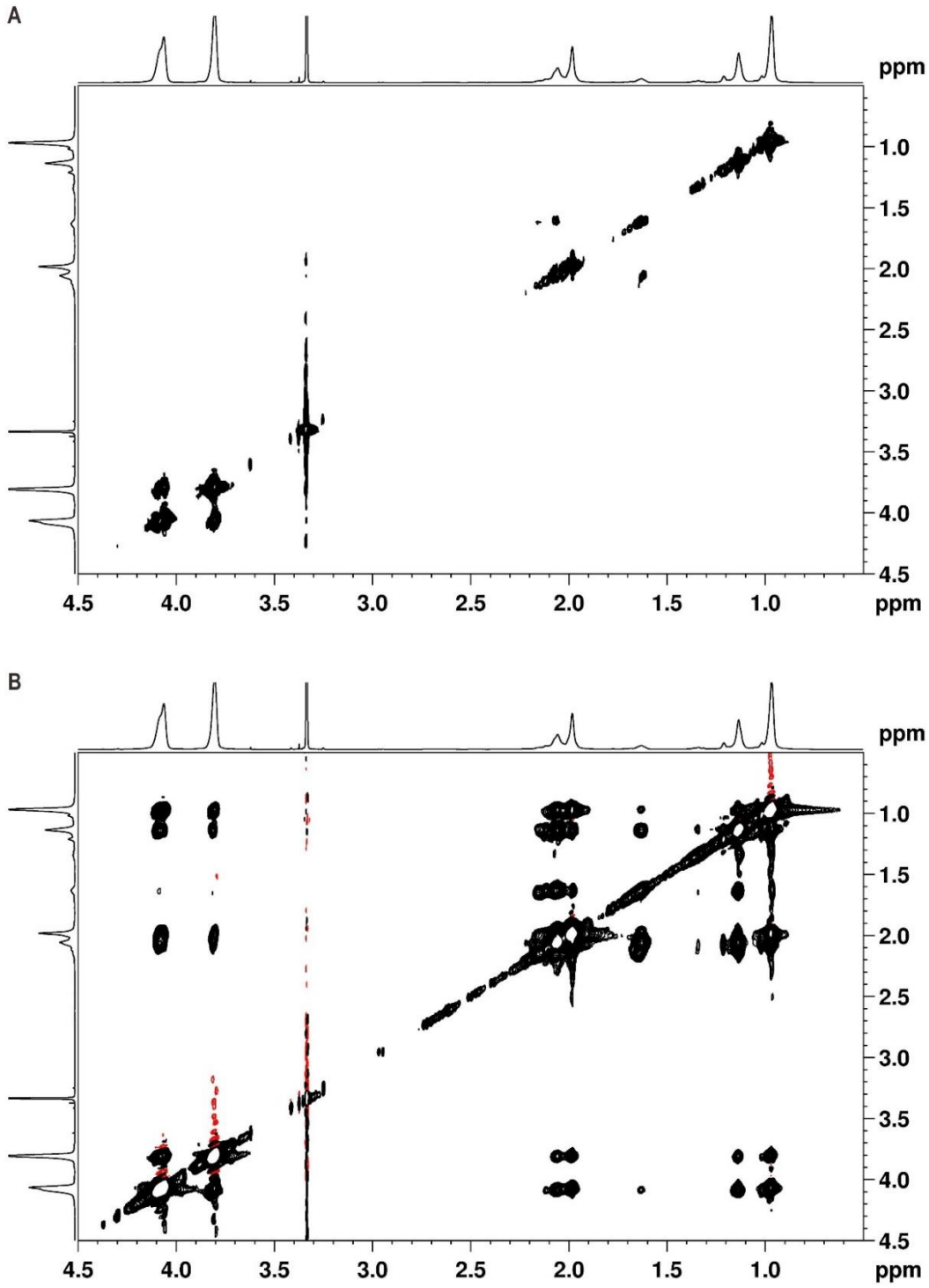

Fig. S10. 2D ^{1}H,^{1}H COSY and 2D ^{1}H,^{1}H NOESY NMR spectra (850 MHz, 298.3 K) of *l*-PHEMA$_{22}$-*Br* in MeOD.

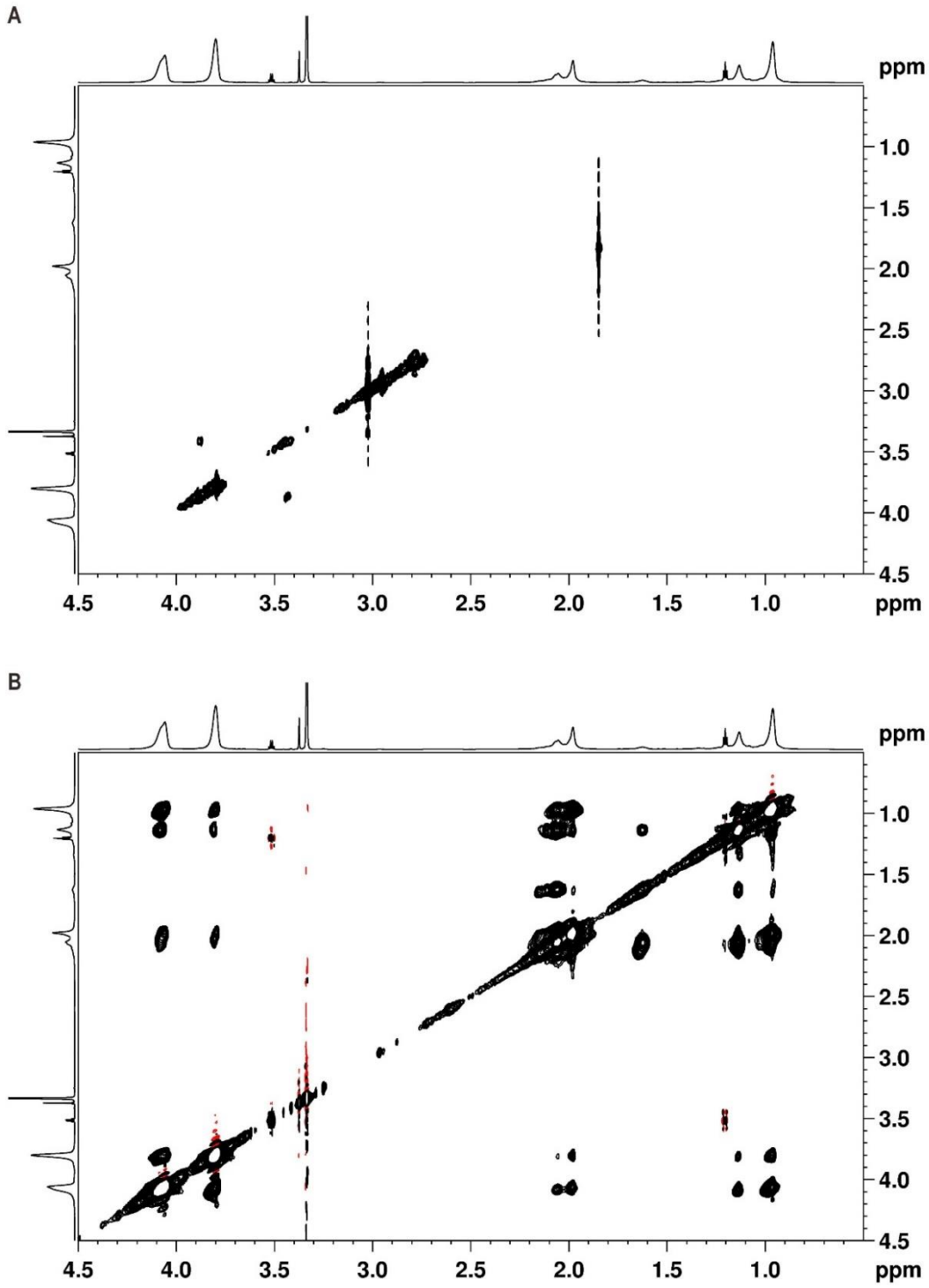

Fig. S11. 2D ^{1}H,^{1}H COSY and 2D ^{1}H,^{1}H NOESY NMR spectra (850 MHz, 298.3 K) of *l*-PHEMA$_{11}$-*N*$_3$ in MeOD.

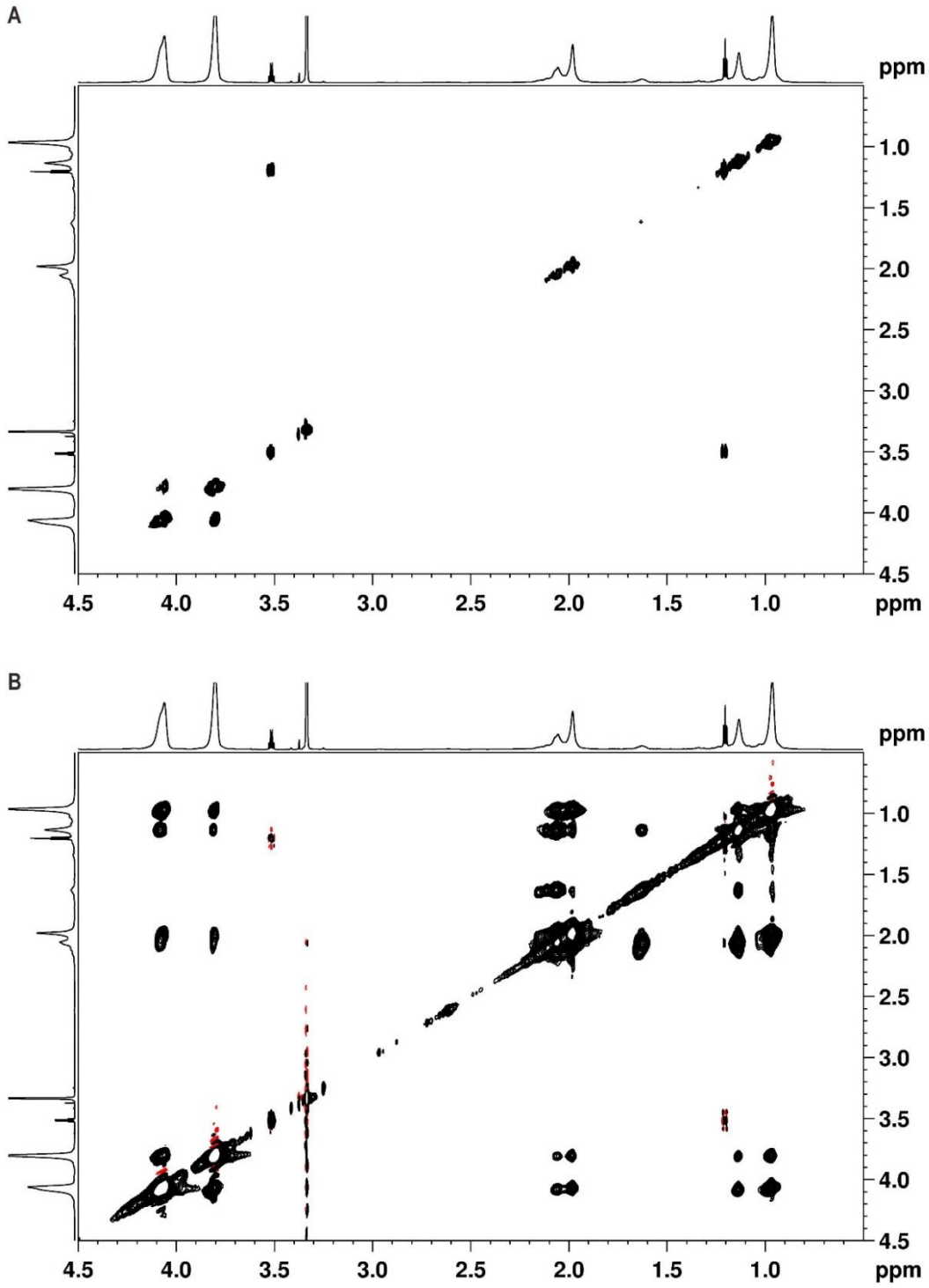

Fig. S12. 2D ^{1}H,^{1}H COSY and 2D ^{1}H,^{1}H NOESY NMR spectra (850 MHz, 298.3 K) of *l*-PHEMA$_{15}$-*N*$_3$ in MeOD.

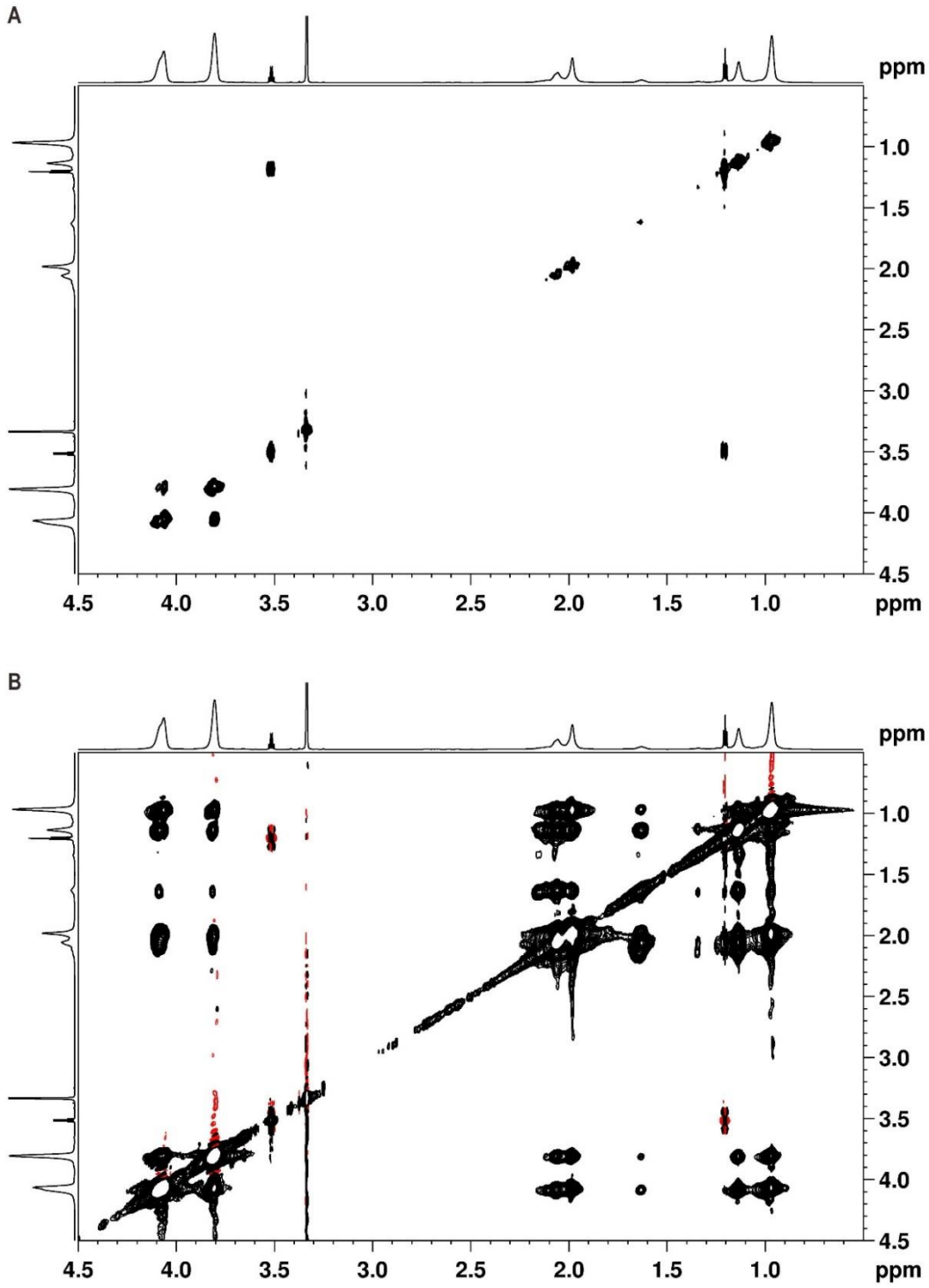

Fig. S13. 2D ^{1}H,^{1}H COSY and 2D ^{1}H,^{1}H NOESY NMR spectra (850 MHz, 298.3 K) of *l*-PHEMA$_{22}$-*N*$_3$ in MeOD.

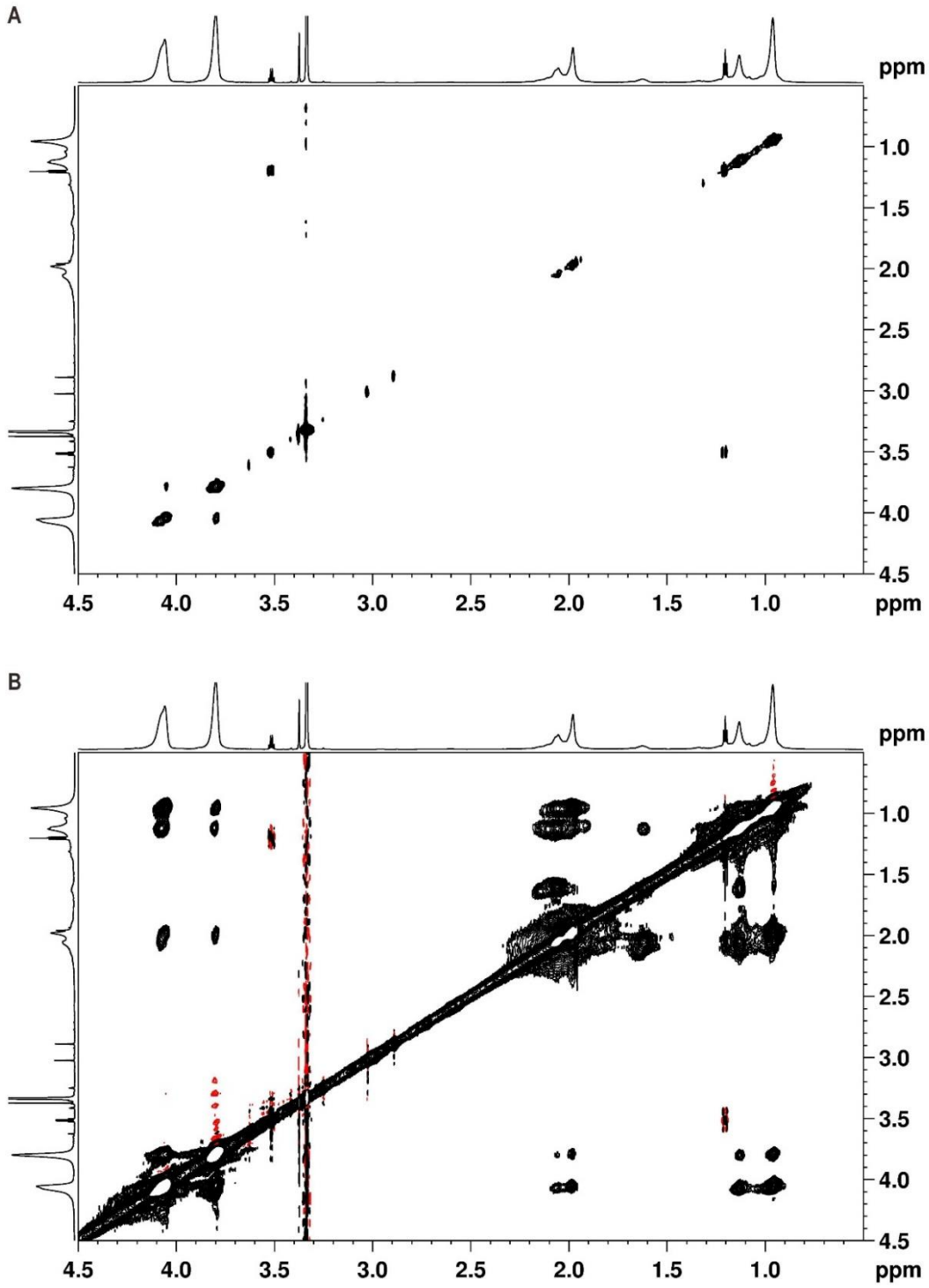

Fig. S14. 2D ^{1}H,^{1}H COSY and 2D ^{1}H,^{1}H NOESY NMR spectra (850 MHz, 298.3 K) of *f*-PHEMA$_{11}$ in MeOD.

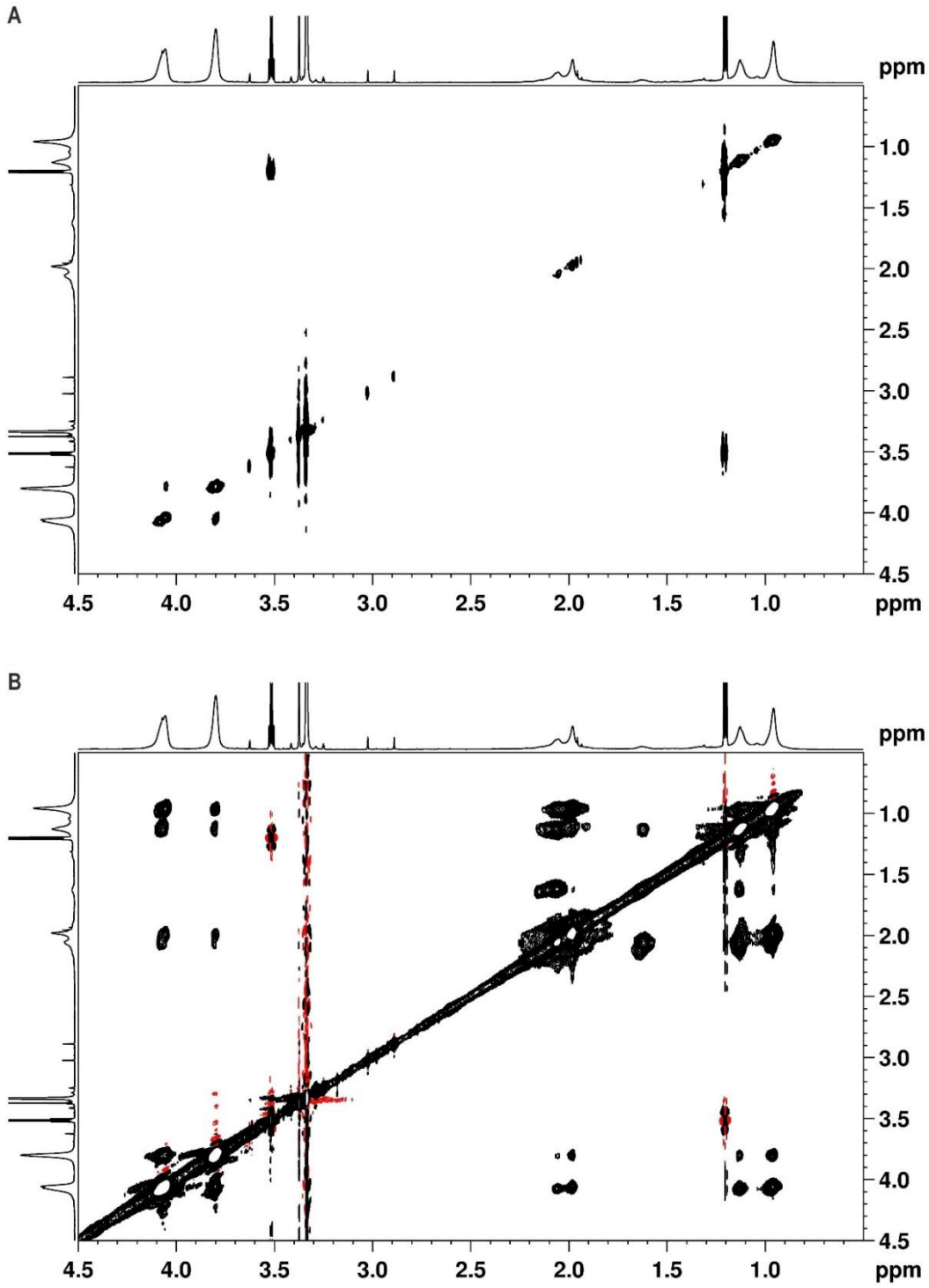

Fig. S15. 2D ^{1}H,^{1}H COSY and 2D ^{1}H,^{1}H NOESY NMR spectra (850 MHz, 298.3 K) of *f*-PHEMA$_{15}$ in MeOD.

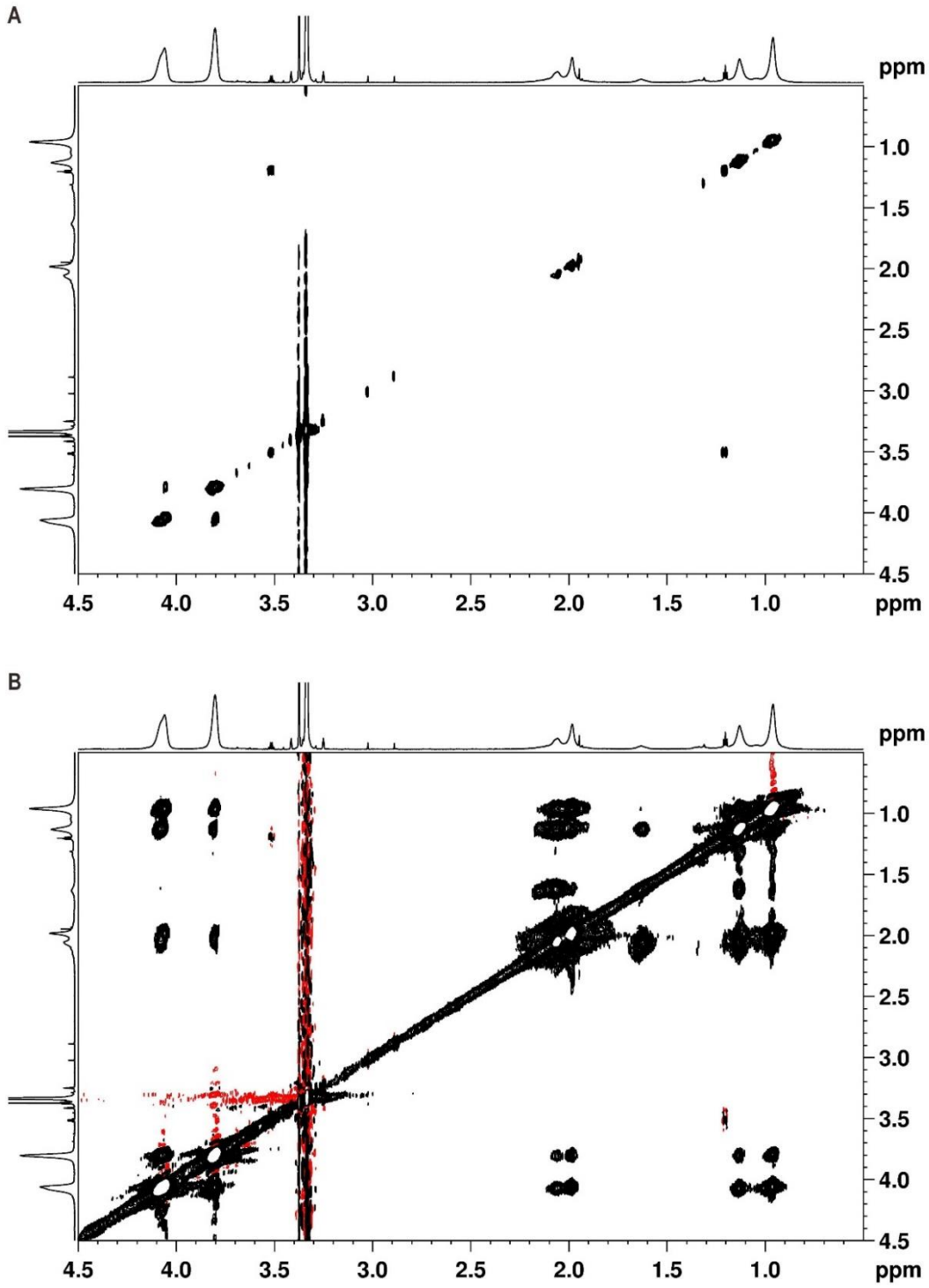

Fig. S16. 2D ^{1}H,^{1}H COSY and 2D ^{1}H,^{1}H NOESY NMR spectra (850 MHz, 298.3 K) of *f*-PHEMA$_{22}$ in MeOD.

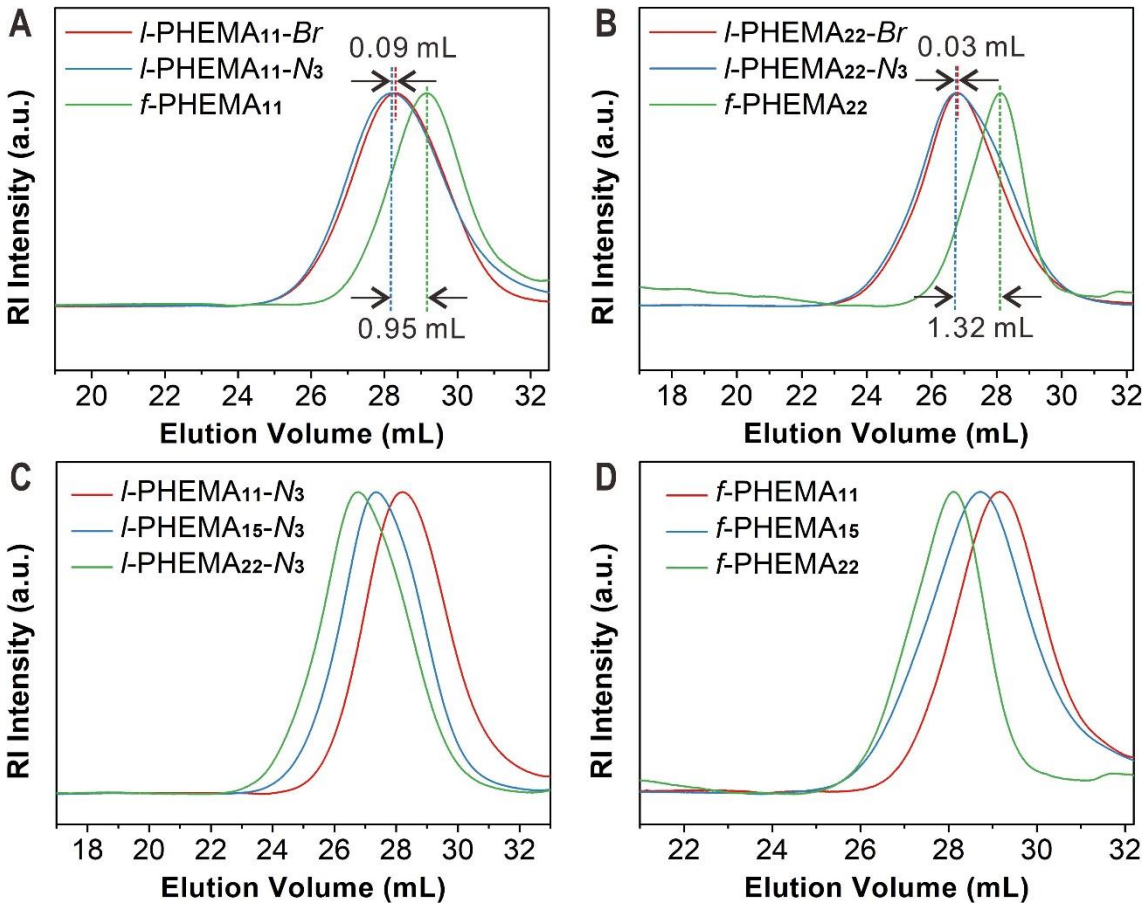

Fig. S17. (A) GPC elution curves of *l*-PHEMA$_{11}$-*Br*, *l*-PHEMA$_{11}$-*N*$_3$, and *f*-PHEMA$_{11}$. (B) GPC curves of *l*-PHEMA$_{22}$-*Br*, *l*-PHEMA$_{22}$-*N*$_3$, and *f*-PHEMA$_{22}$. (C) Comparison of the GPC elution curves of *l*-PHEMA$_n$-*N*$_3$ with different repeating units. (D) Comparison of the GPC elution curves of folded polymers *f*-PHEMA$_n$ with different ring sizes. DMF was used as the eluent and PMMA standards were employed for calibration.

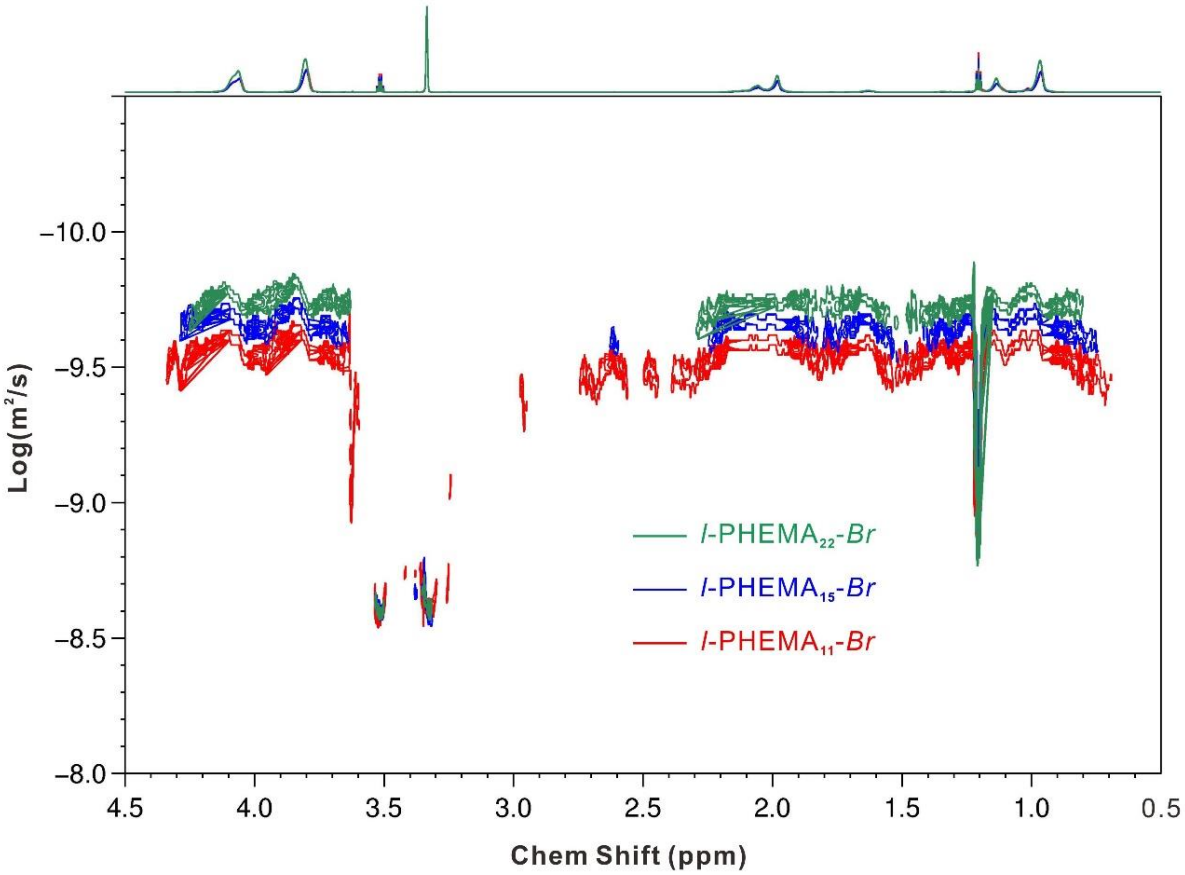

Fig. S18. ^{1}H DOSY NMR spectra (850 MHz, MeOD, 298.3 K) of *l*-PHEMA$_{11}$-*Br*, *l*-PHEMA$_{15}$-*Br*, and *l*-PHEMA$_{22}$-*Br* showing their gradually increased hydrodynamic size.

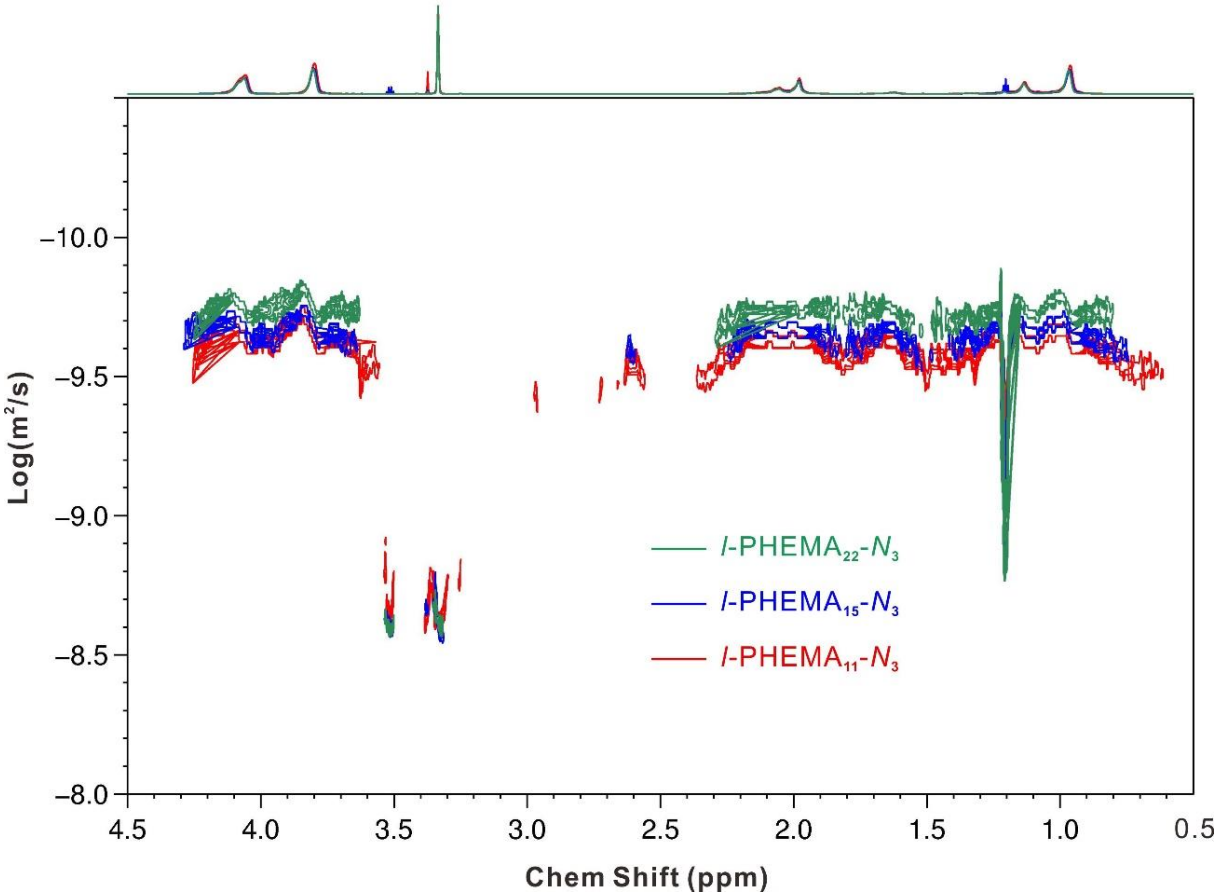

Fig. S19. ^{1}H DOSY NMR spectra (850 MHz, MeOD, 298.3 K) of *l*-PHEMA$_{11}$-N_3, *l*-PHEMA$_{15}$-N_3, and *l*-PHEMA$_{22}$-N_3 showing their gradually increased hydrodynamic size.

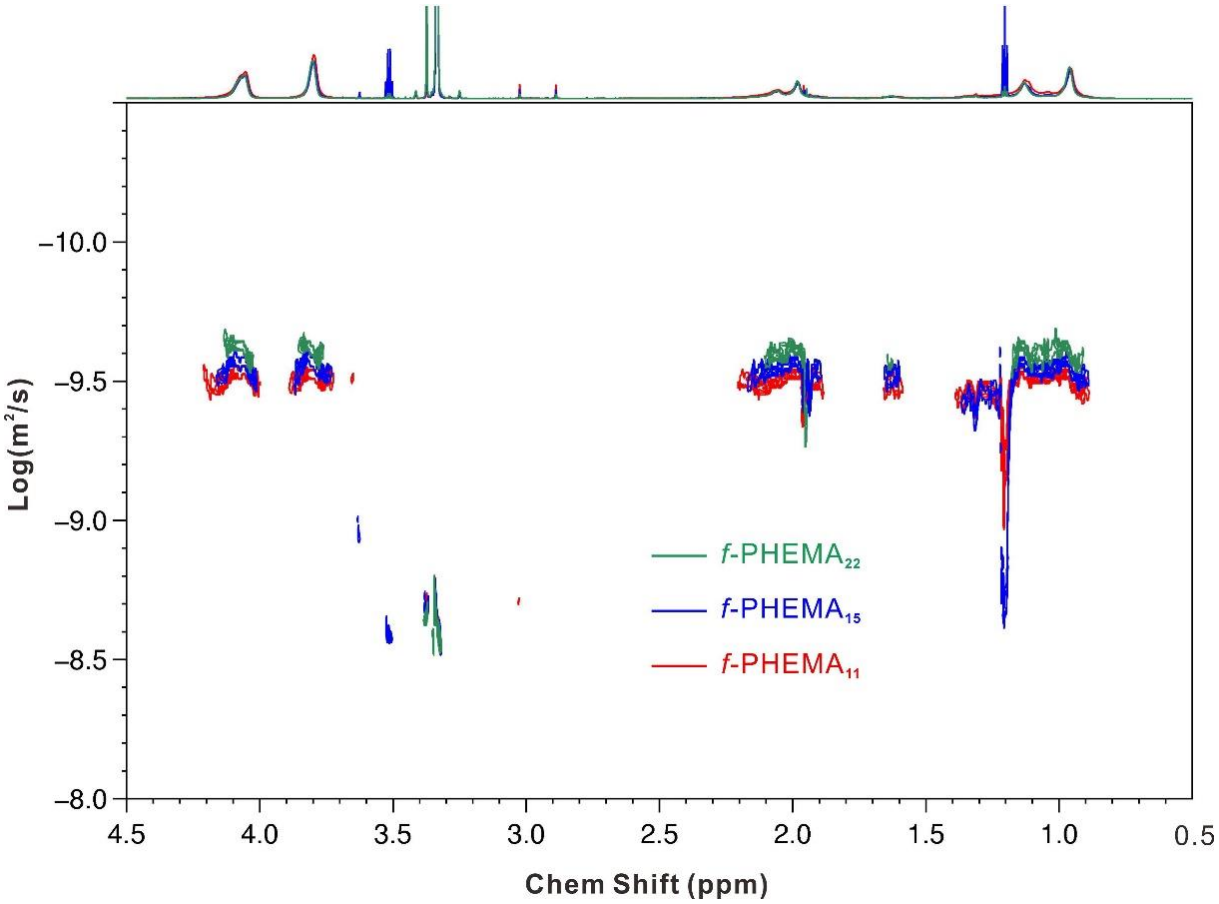

Fig. S20. ^{1}H DOSY NMR spectra (850 MHz, MeOD, 298.3 K) of *f*-PHEMA$_{11}$, *f*-PHEMA$_{15}$, and *f*-PHEMA$_{22}$ showing their gradually increased hydrodynamic size.

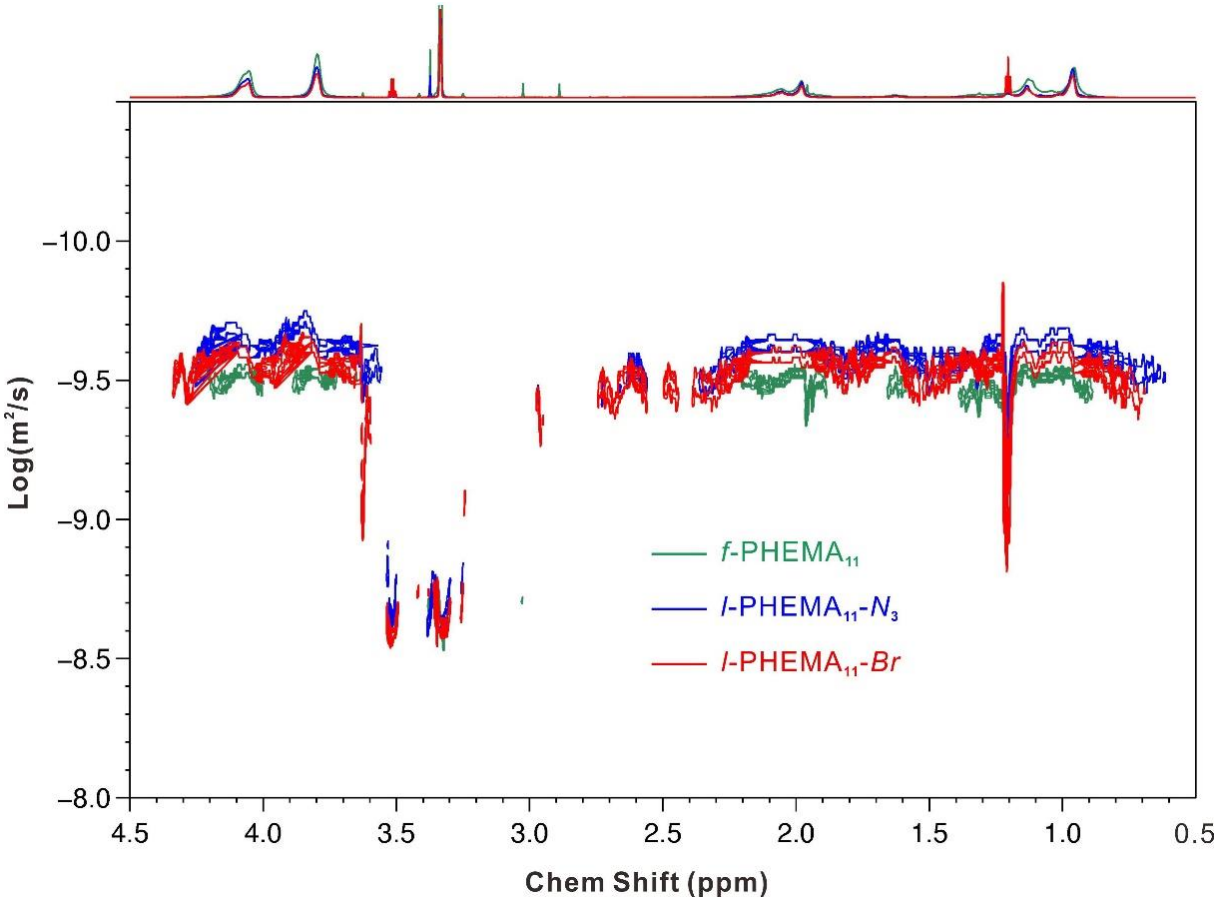

Fig. S21. ^{1}H DOSY NMR spectra (850 MHz, MeOD, 298.3 K) of *l*-PHEMA$_{11}$-*Br*, *l*-PHEMA$_{11}$-*N*$_3$, and *f*-PHEMA$_{11}$. The folded polymer *f*-PHEMA$_{11}$ diffuses faster than its linear counterparts, indicating a decreased hydrodynamic size after molecular folding.

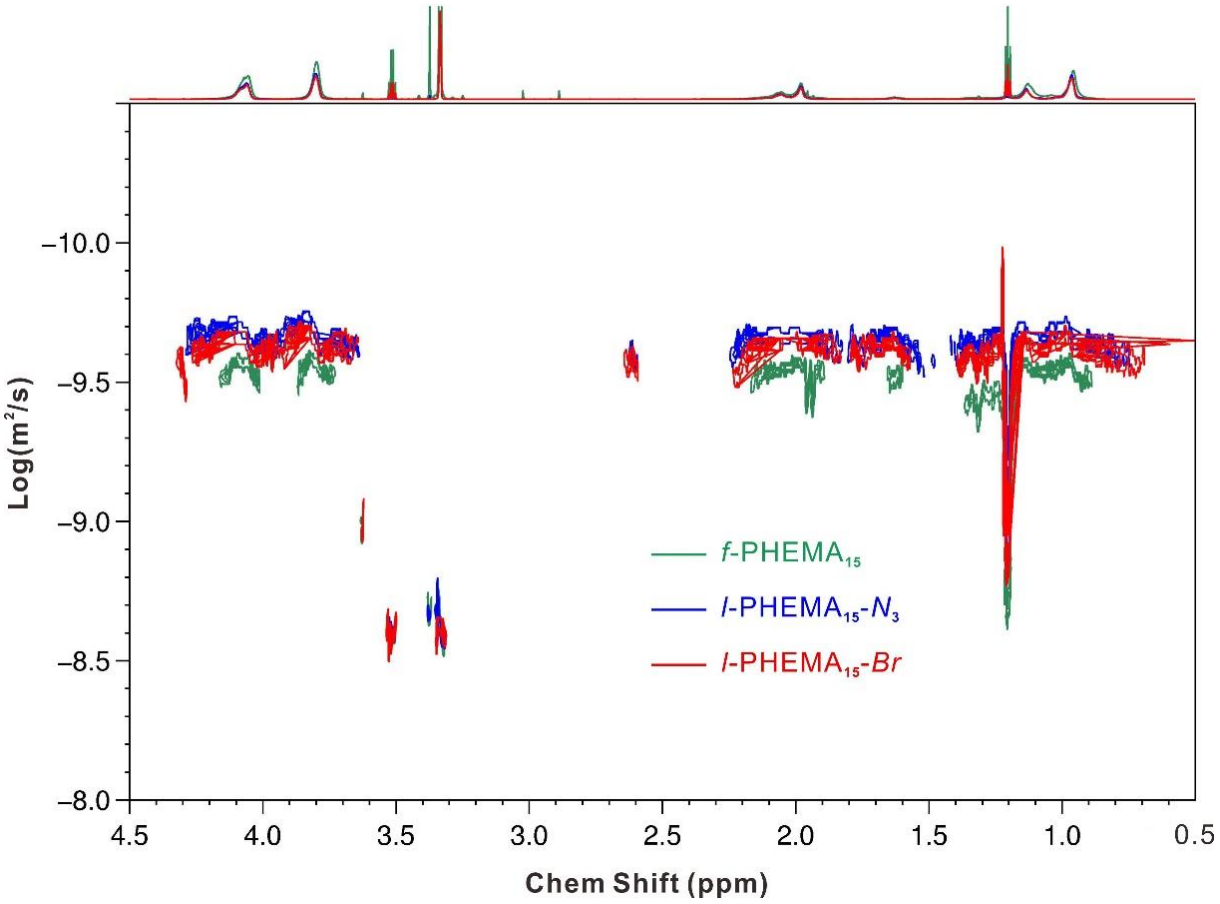

Fig. S22. ^{1}H DOSY NMR spectra (850 MHz, MeOD, 298.3 K) of *l*-PHEMA$_{15}$-*Br*, *l*-PHEMA$_{15}$-*N*$_3$, and *f*-PHEMA$_{15}$. The folded polymer *f*-PHEMA$_{15}$ diffuses faster than its linear counterparts, indicating a decreased hydrodynamic size after molecular folding.

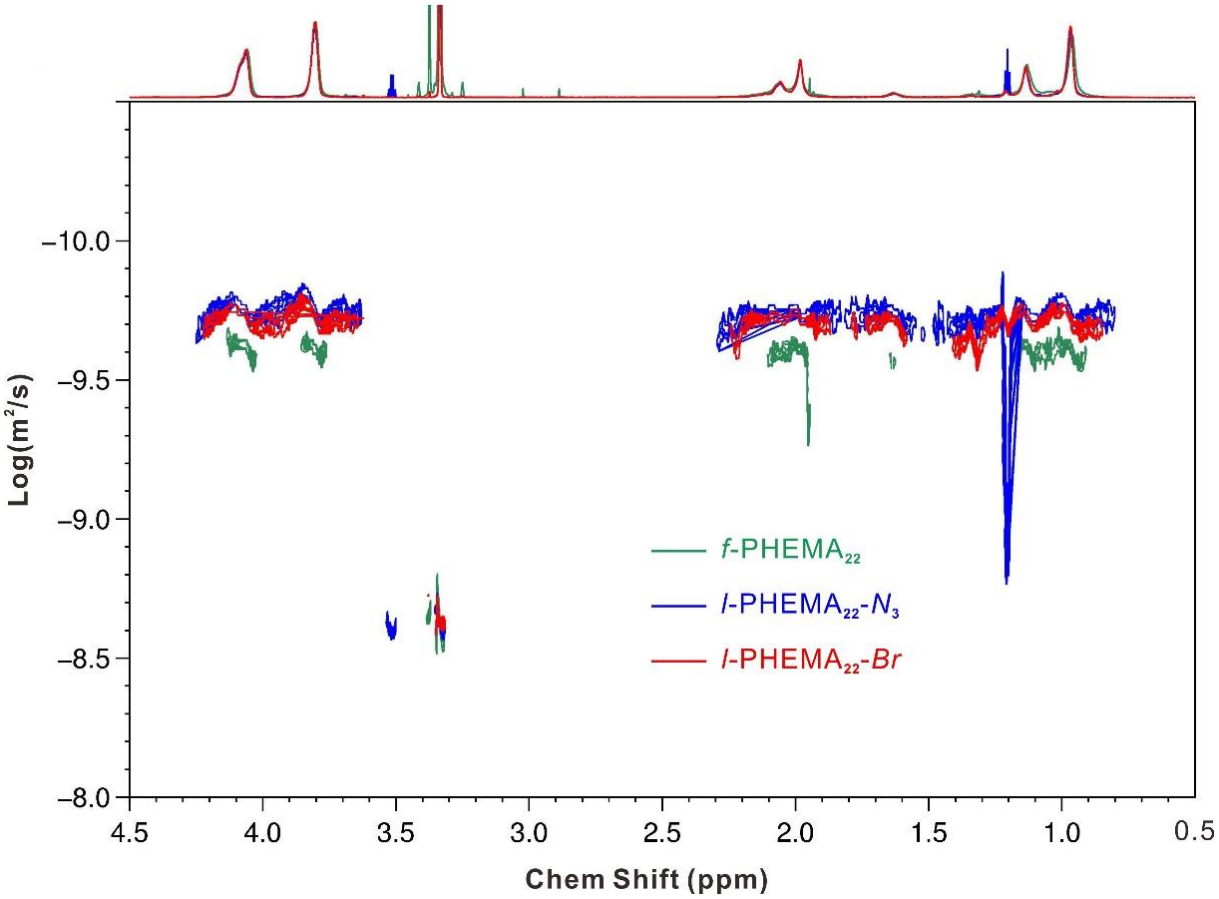

Fig. S23. ^{1}H DOSY NMR spectra (850 MHz, MeOD, 298.3 K) of *l*-PHEMA$_{22}$-*Br*, *l*-PHEMA$_{22}$-N_3, and *f*-PHEMA$_{22}$. The folded polymer *f*-PHEMA$_{22}$ diffuses faster than its linear counterparts, indicating a decreased hydrodynamic size after molecular folding.

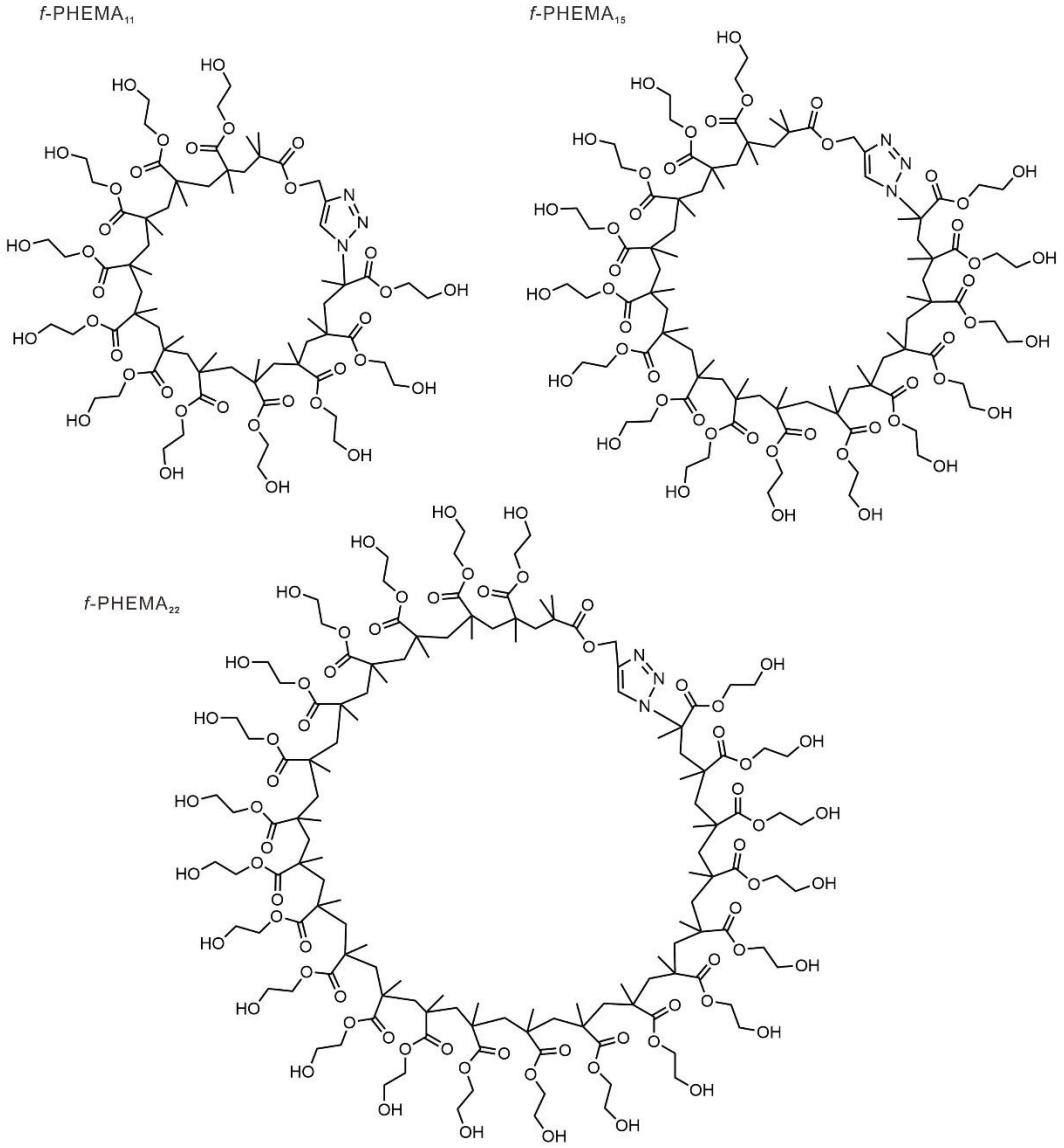

Fig. S24. Molecular structures of *f*-PHEMA$_{11}$, *f*-PHEMA$_{15}$, and *f*-PHEMA$_{22}$.

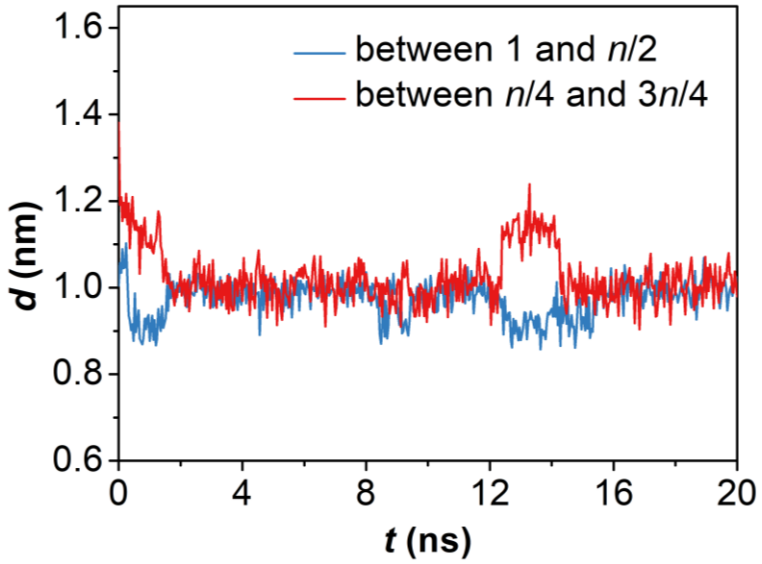

Fig. S25. Calculation of the lengths for the two major axes of a single *f*-PHEMA$_{15}$ structure in **Fig. 1E** of the main text. The distances are calculated between 1 and n/2 monomers for one axis and between n/4 and 3n/4 monomers for the second axis. These numbers are very similar over 20 ns, except for some fluctuations within the time window of 12 ~14 ns. It is another evidence that the structure indeed remains rather cyclic.

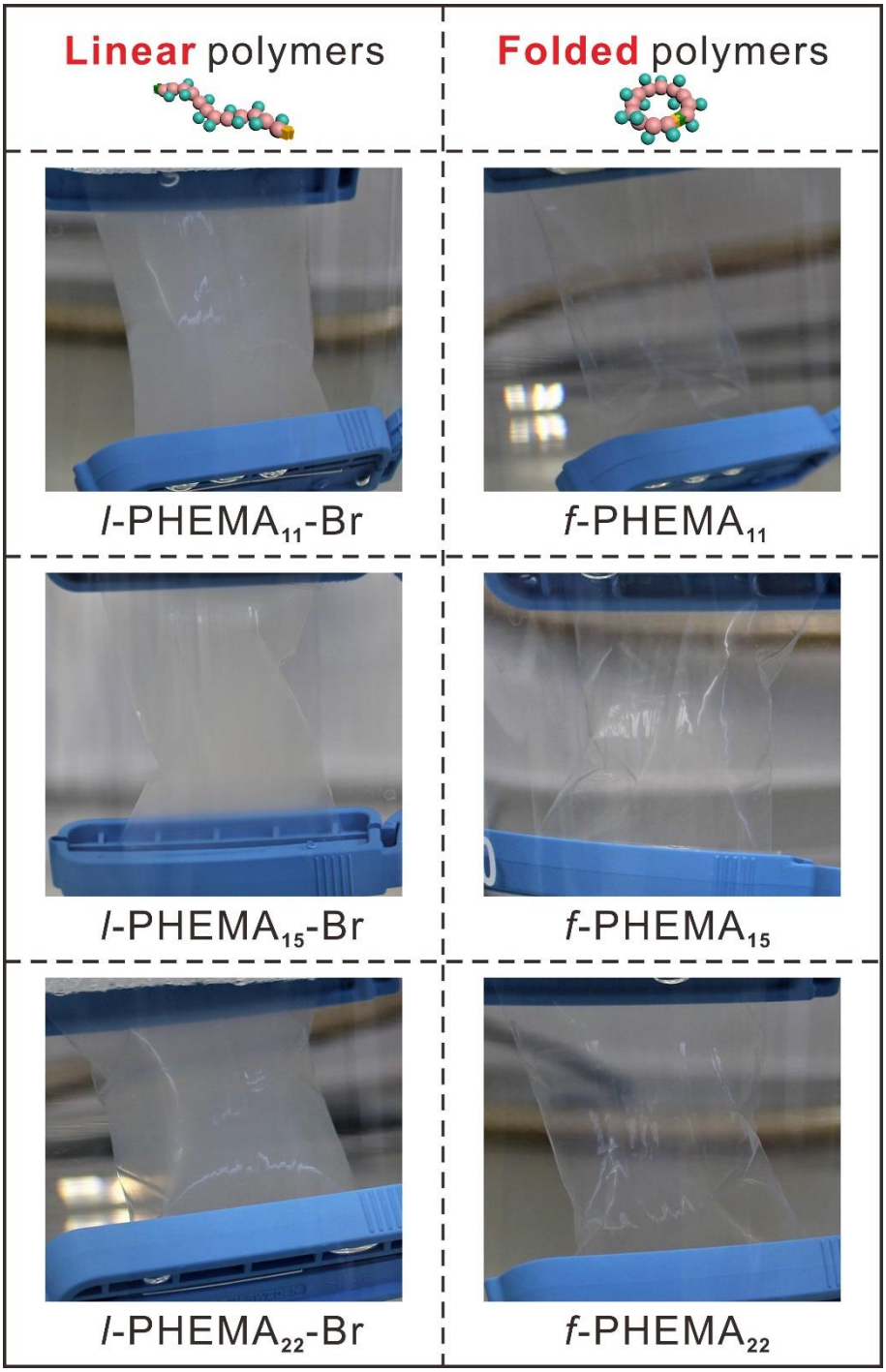

Fig. S26. Self-assembly solutions of linear polymers *l*-PHEMA$_n$-*Br* and folded polymers *f*-PHEMA$_n$ after dialysis against deionized water for 1 h.

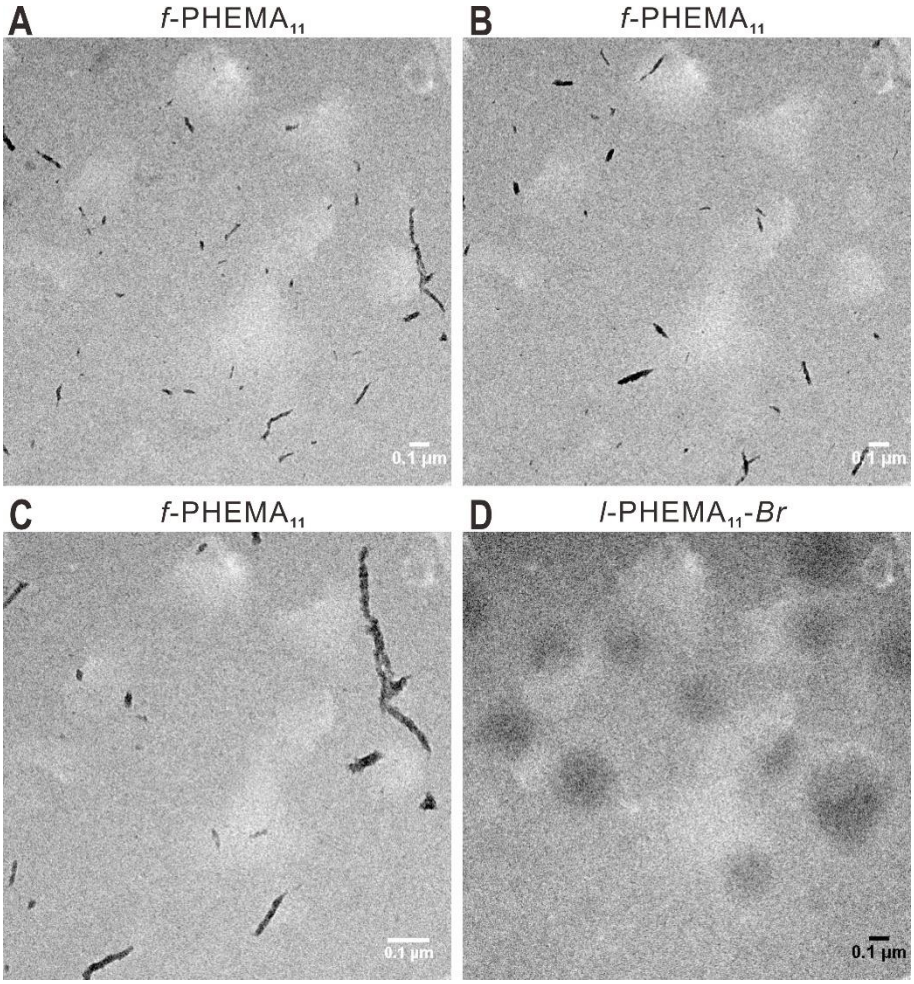

Fig. S27. TEM images for comparing the self-assembly morphologies of (A-C) folded polymer *f*-PHEMA11 and (D) linear polymer *l*-PHEMA11-*Br*.

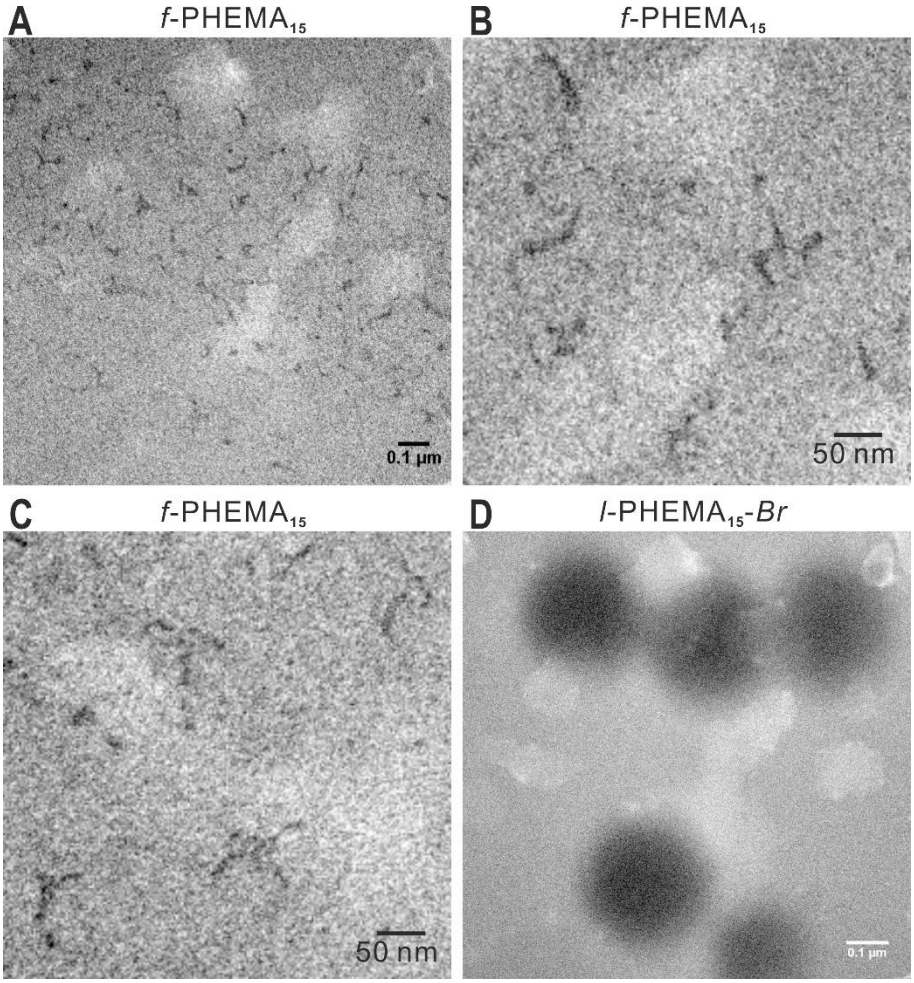

Fig. S28. TEM images for comparing the self-assembly morphologies of (A-C) folded polymer *f*-PHEMA$_{15}$ and (D) linear polymer *l*-PHEMA$_{15}$-*Br*.

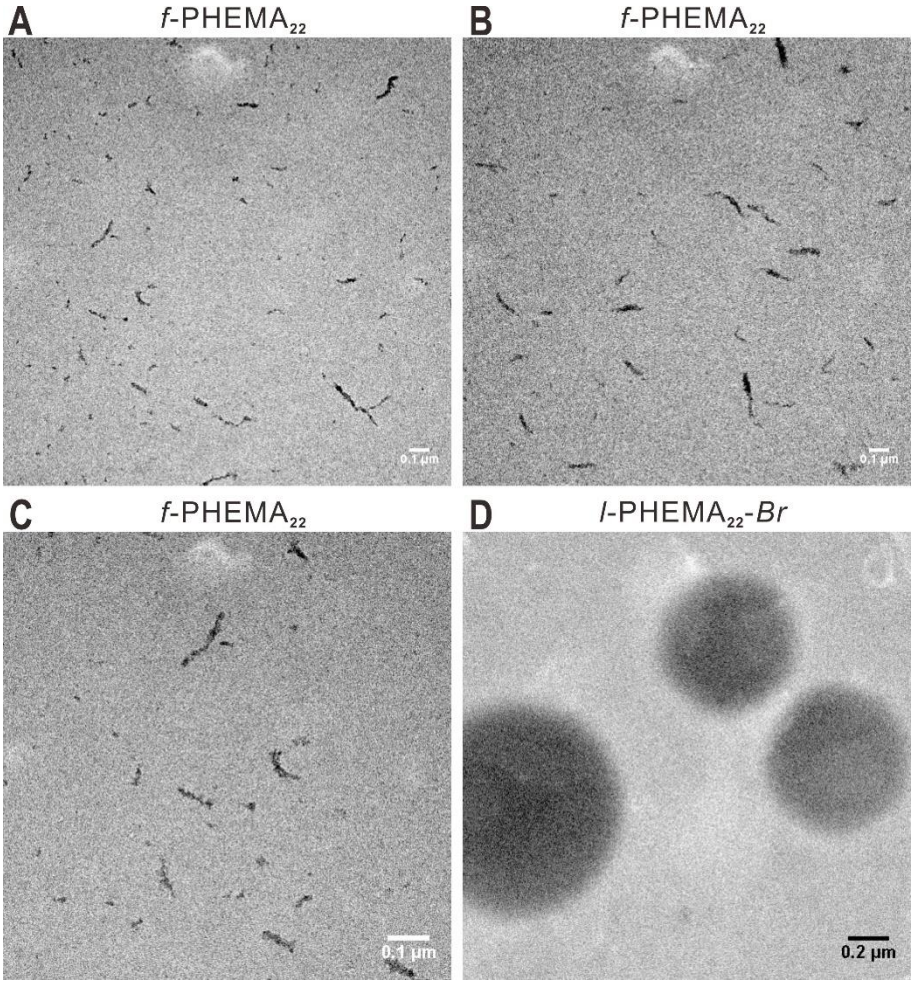

Fig. S29. TEM images for comparing the self-assembly morphologies of (A-C) folded polymer *f*-PHEMA$_{22}$ and (D) linear polymer *l*-PHEMA$_{22}$-*Br*.

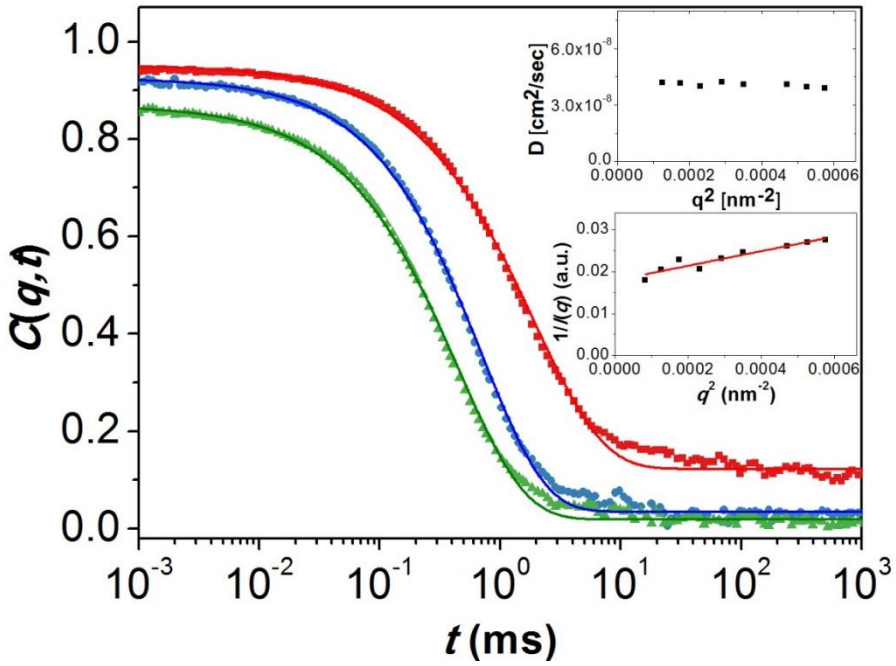

Fig. S30. Relaxation functions $C(q,t)$ for the translation motion of *f*-PHEMA$_{11}$ in water at 1 mg/mL and 293 K at different scattering angles [50° (red squares), 90° (blue circles), and 130° (green triangles)] corresponding to scattering wave vector q = 0.011 nm^{-1}, q = 0.0187 nm^{-1}, q = 0.024 nm^{-1}, respectively. Inset: $D(q = 0) = 4.34 \times 10^{-8}$ cm^2/sec; R_h = 54 ± 2 nm.

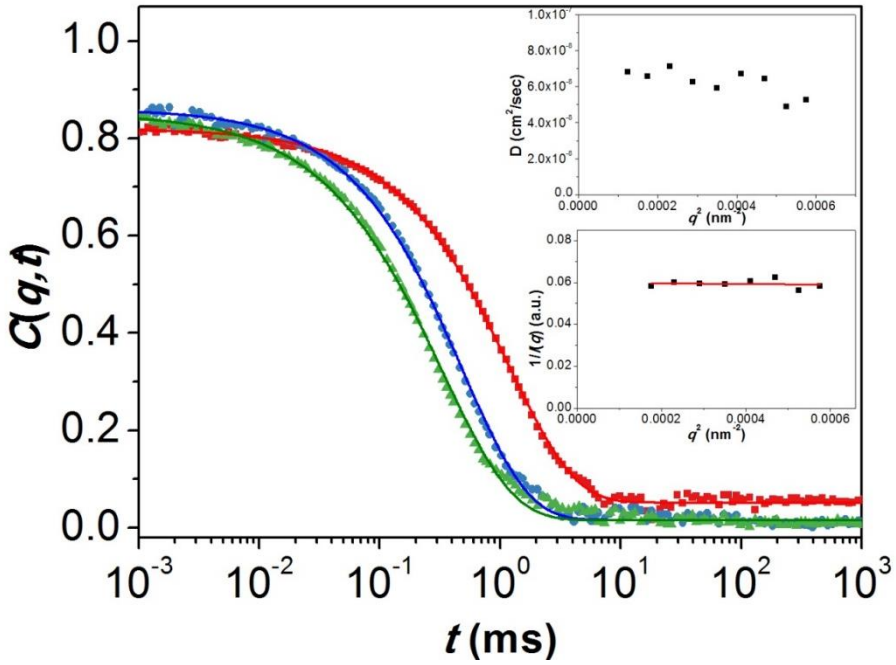

Fig. S31. Relaxation functions $C(q,t)$ for the translation motion of *f*-PHEMA$_{15}$ in water at 1 mg/mL and 293 K at different scattering angles [50° (red squares), 90° (blue circles), and 130° (green triangles)] corresponding to scattering wave vector $q = 0.011$ nm^{-1}, $q = 0.0187$ nm^{-1}, $q = 0.024$ nm^{-1}, respectively. Inset: $D(q = 0) = 6.75\times10^{-8}$ cm^2/sec; $R_h = 36 \pm 2$ nm.

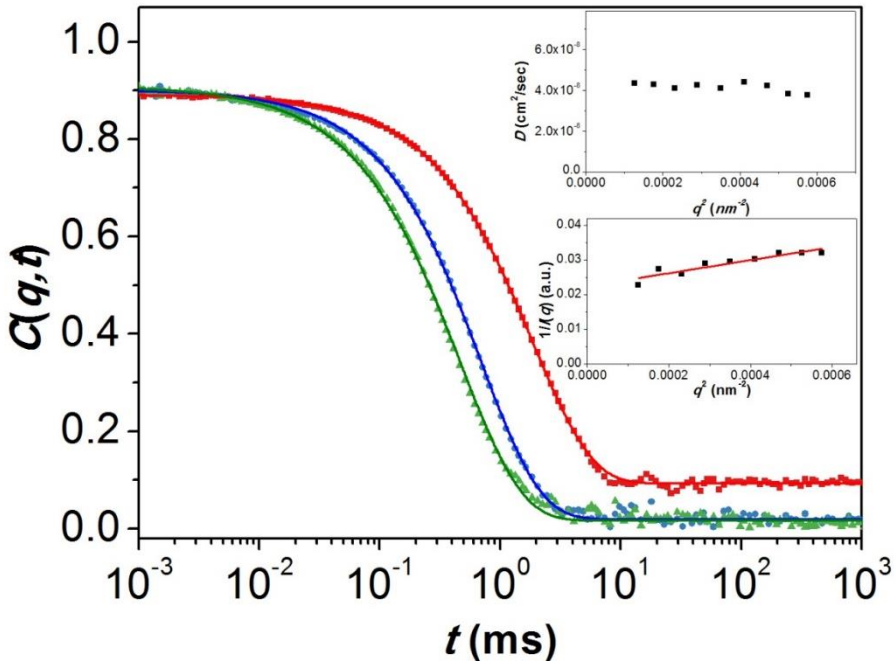

Fig. S32. Relaxation functions $C(q,t)$ for the translation motion of *f*-PHEMA$_{22}$ in water at 1 mg/mL and 293 K at different scattering angles [50° (red squares), 90° (blue circles), and 130° (green triangles)] corresponding to scattering wave vector q = 0.011 nm^{-1}, q = 0.0187 nm^{-1}, q = 0.024 nm^{-1}, respectively. Inset: $D(q = 0) = 4.21\times10^{-8}$ cm^2/sec; R_h = 58 ± 3 nm.

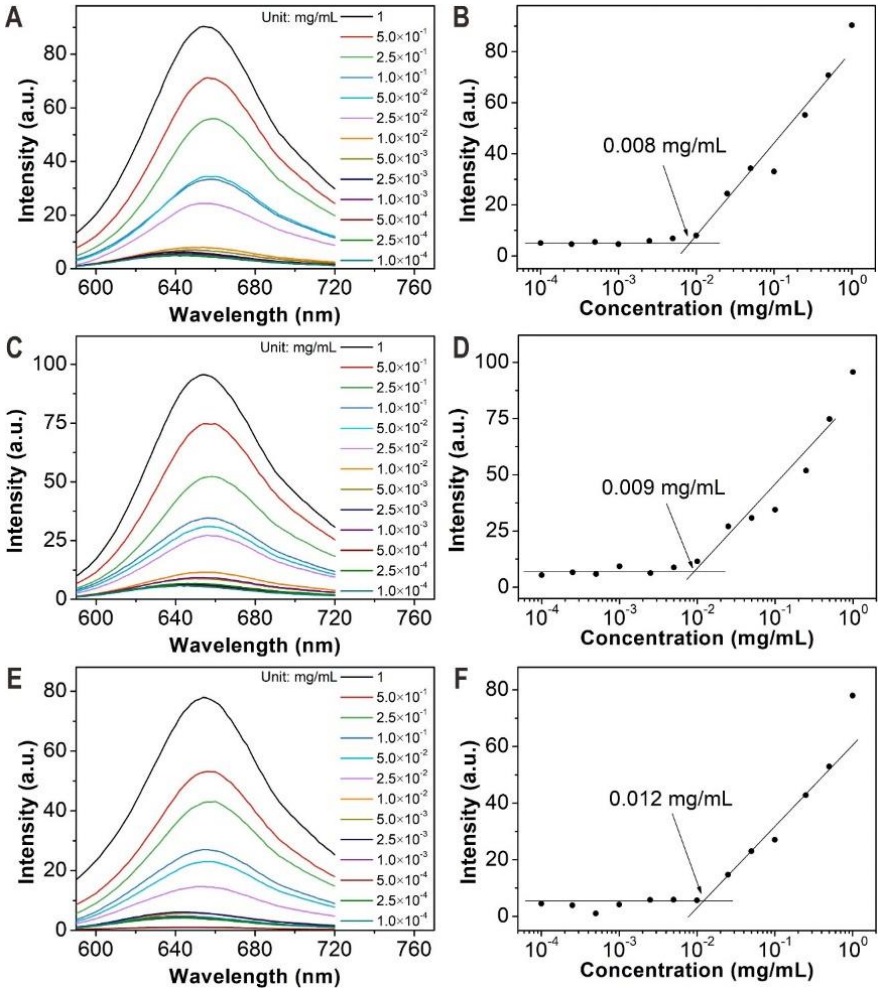

Fig. S33. (A) Fluorescence emission spectra of *f*-PHEMA$_{11}$ assemblies of varying concentrations after loading with Nile Red. Nile Red in aqueous solution shows low fluorescence emission intensity after excitation with 550 nm light. However, the intensity increases significantly if the probe is encapsulated into a hydrophobic environment. As shown in this figure, the fluorescence emission intensity is very weak when the assembly concentration is low such as 0.001 mg mL^{-1}, indicating that Nile Red molecules were dispersed in an aqueous environment. If the concentration is high, for example 0.5 mg mL^{-1}, the characteristic emission peak of Nile Red can be clearly observed, showing the encapsulation of the fluorescent probe in a hydrophobic environment. (B) Determination of the CAC of *f*-PHEMA$_{11}$ by plotting the emission intensity at 654 nm over the concentration of the assemblies. The dots can be divided into two groups connected by two straight lines based on the slope. The CAC was therefore determined from the intersection of the two lines as 0.008 mg mL^{-1}, indicating that *f*-PHEMA$_{11}$ starts to assemble and form some hydrophobic internal microenvironments at this concentration. (C) Fluorescence emission spectra of *f*-PHEMA$_{15}$ assemblies of varying concentrations after loading with Nile Red. (D) Determination of the CAC of *f*-PHEMA$_{15}$. (E) Fluorescence emission spectra of *f*-PHEMA$_{22}$ assemblies of varying concentrations after loading with Nile Red. (F) Determination of the CAC of *f*-PHEMA$_{22}$.

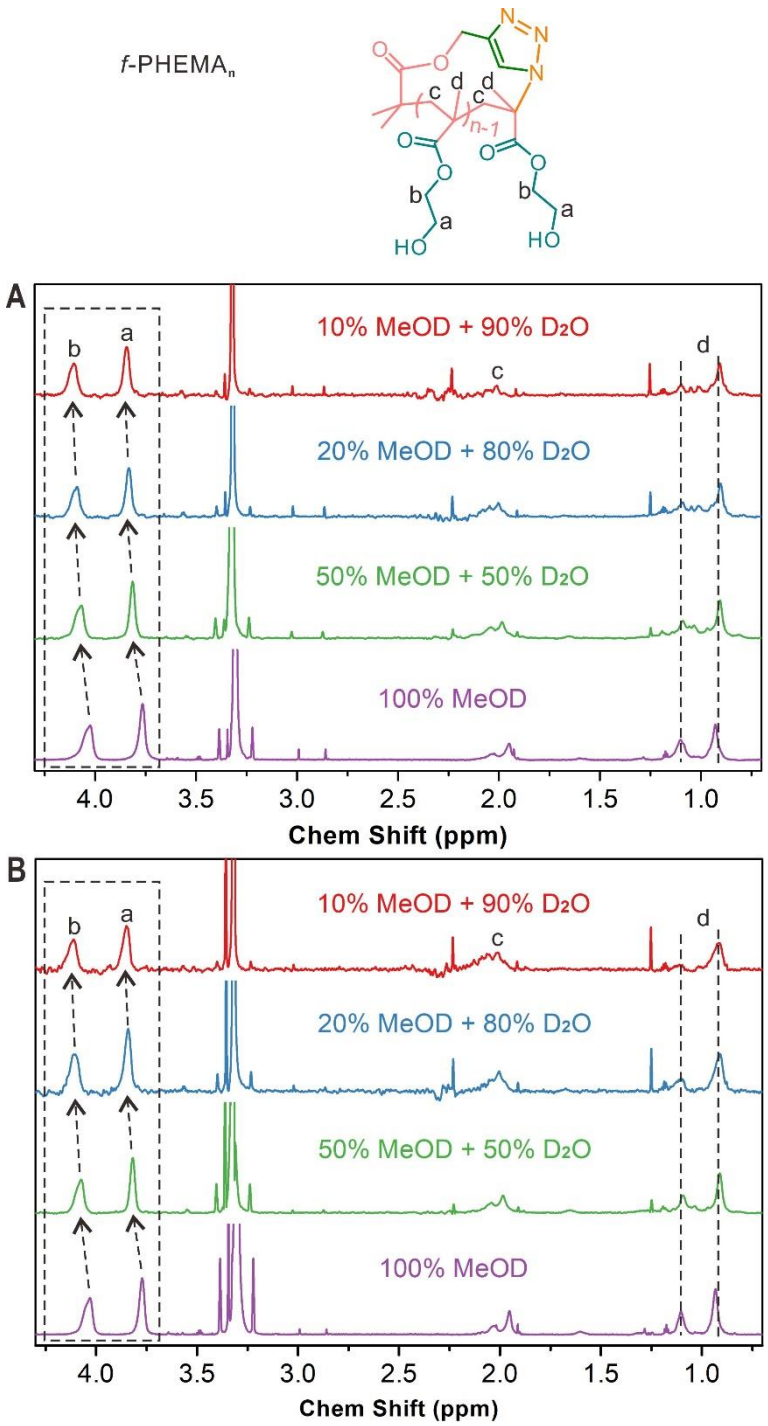

Fig. S34. (A) ^{1}H NMR spectra (850 MHz, 298.3 K) of *f*-PHEMA$_{11}$ in mixture solvents of MeOD and D_2O with gradually tuned volume ratios. (B) ^{1}H NMR spectra (850 MHz, 298.3 K) of *f*-PHEMA$_{22}$ in mixture solvents of MeOD and D_2O with gradually tuned volume ratios. Tetramethylsilane was used as an internal standard for calibrating the chemical shifts.

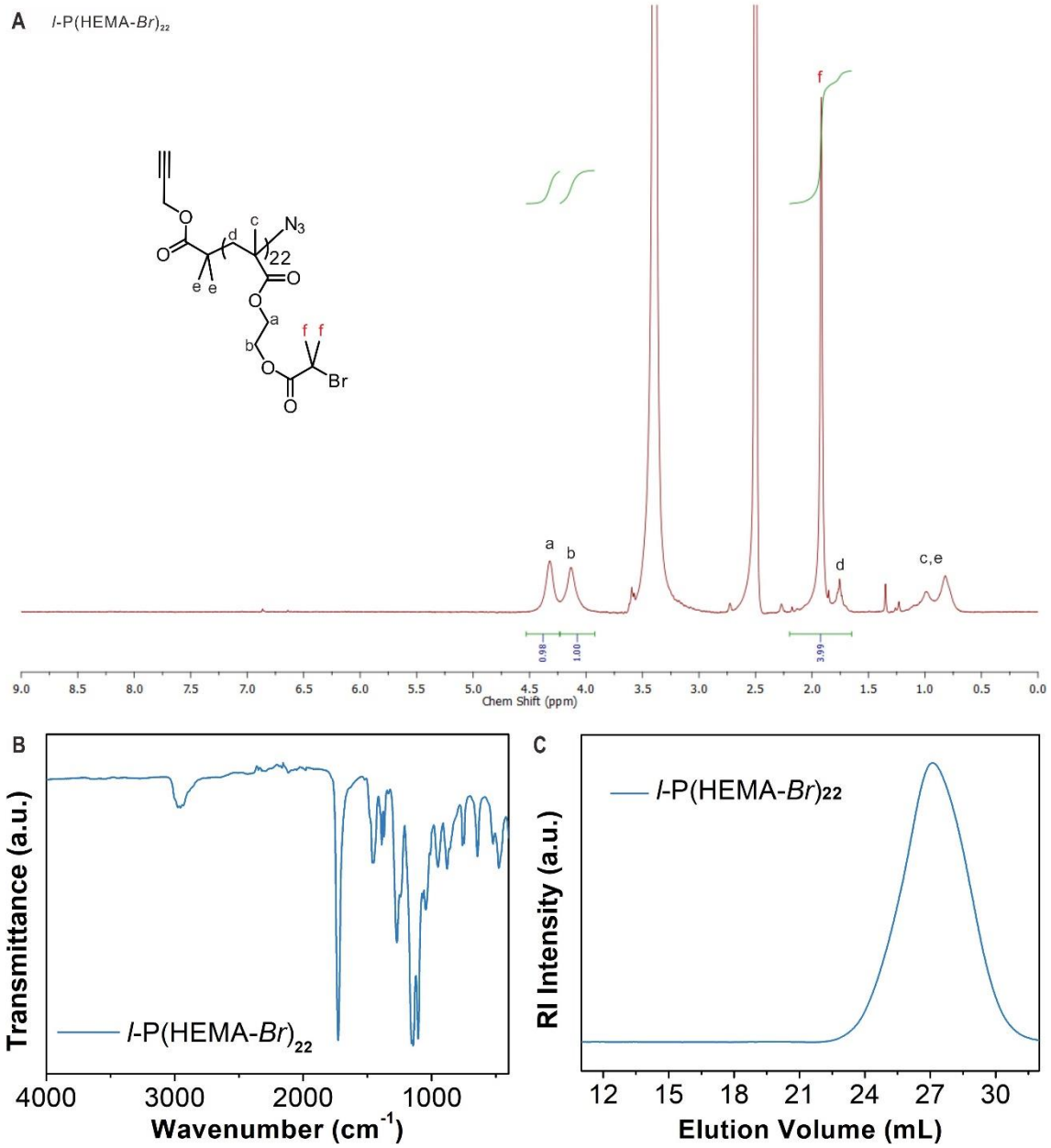

Fig. S35. Characterizations of linear macroinitiator *l*-P(HEMA-Br)$_{22}$. (A) ^{1}H NMR spectrum (300 MHz, 298.3 K) in DMSO-d$_6$. The integral ratio of signals **a** plus **b** and signals **f** plus **d** is approximately 2:4, which confirms the full conversion of hydroxyls to initiation groups. (B) FTIR spectrum. (C) GPC curve measured using DMF as the eluent with PMMA standards for calibration.

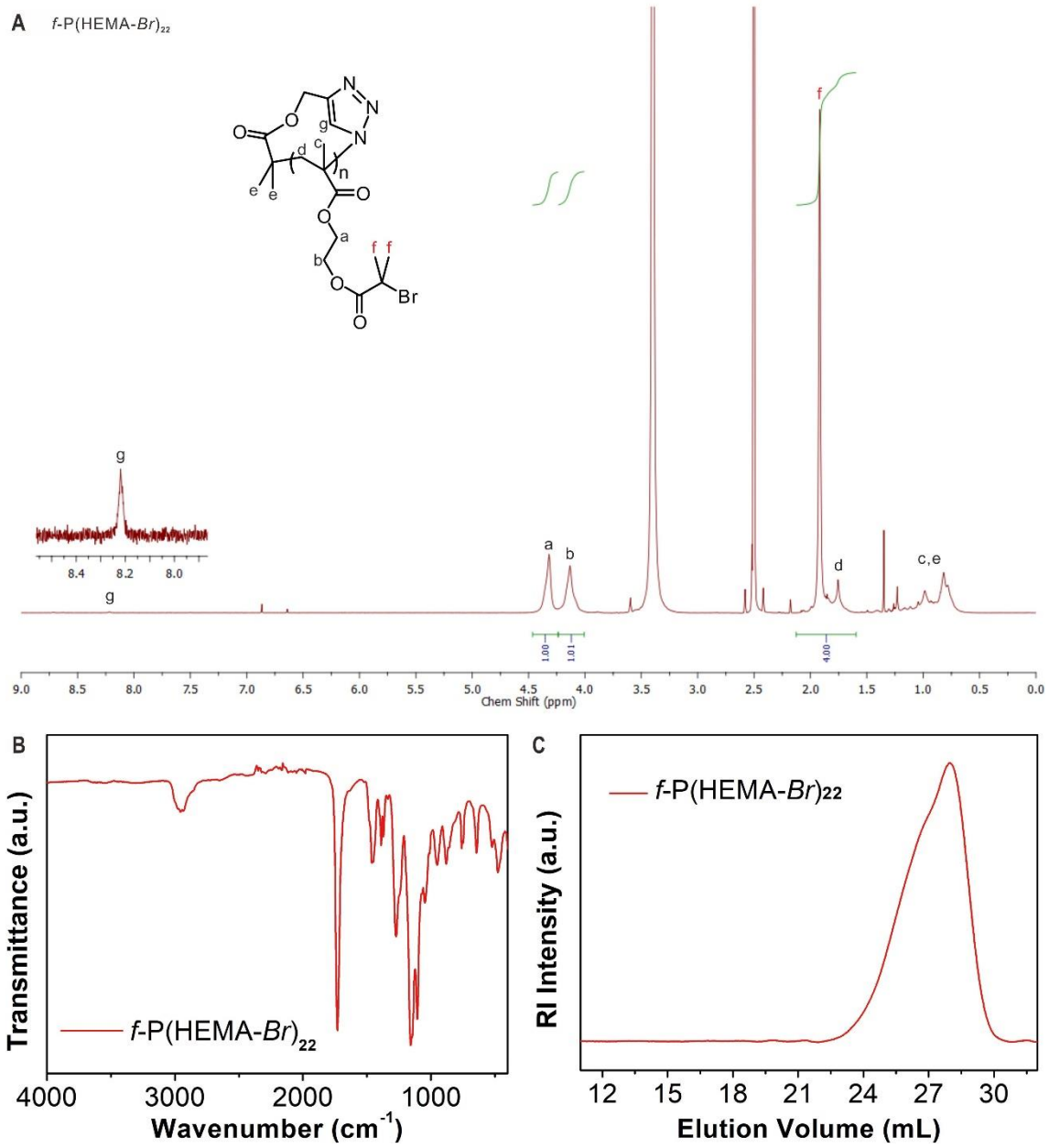

Fig. S36. Characterizations of cyclic macroinitiator *f*-P(HEMA-Br)$_{22}$. (A) ^{1}H NMR spectrum (300 MHz, 298.3 K) in DMSO-d$_6$. The integral ratio of signals **a** plus **b** and signals **f** plus **d** is approximately 2:4, which confirms the full conversion of hydroxyls to initiation groups. (B) FTIR spectrum. (C) GPC curve measured using DMF as the eluent with PMMA standards for calibration.

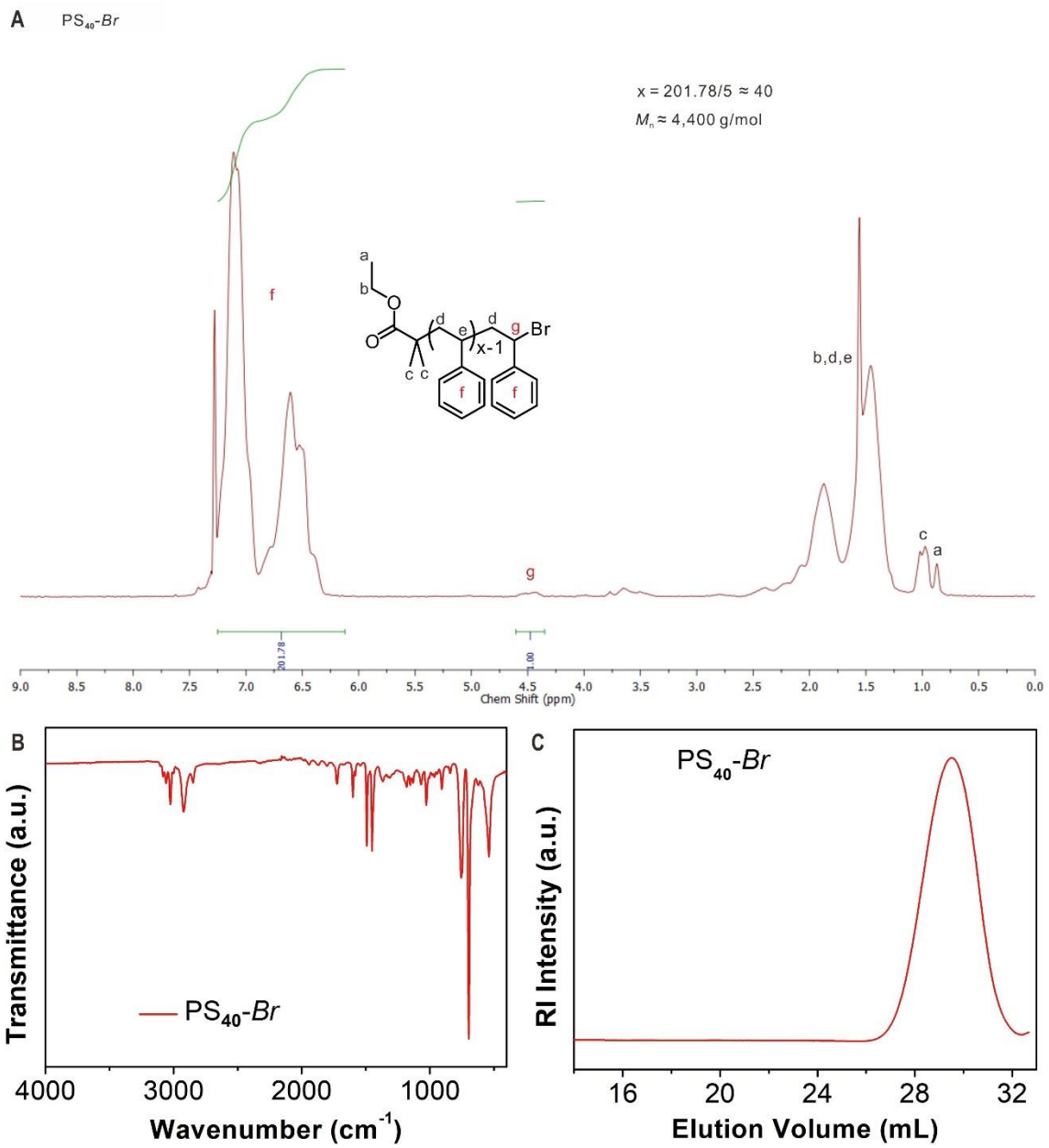

Fig. S37. Characterizations of PS40-*Br*. (A) ^{1}H NMR spectrum (300 MHz, 298.3 K) in $CDCl_3$-d. The integral ratio of signal **g** and signal **f** was used to calculated the repeating number (x) and the molecular weight ($M_{n,NMR}$). (B) FTIR spectrum. (C) GPC curve measured using DMF as the eluent with PS standards for calibration.

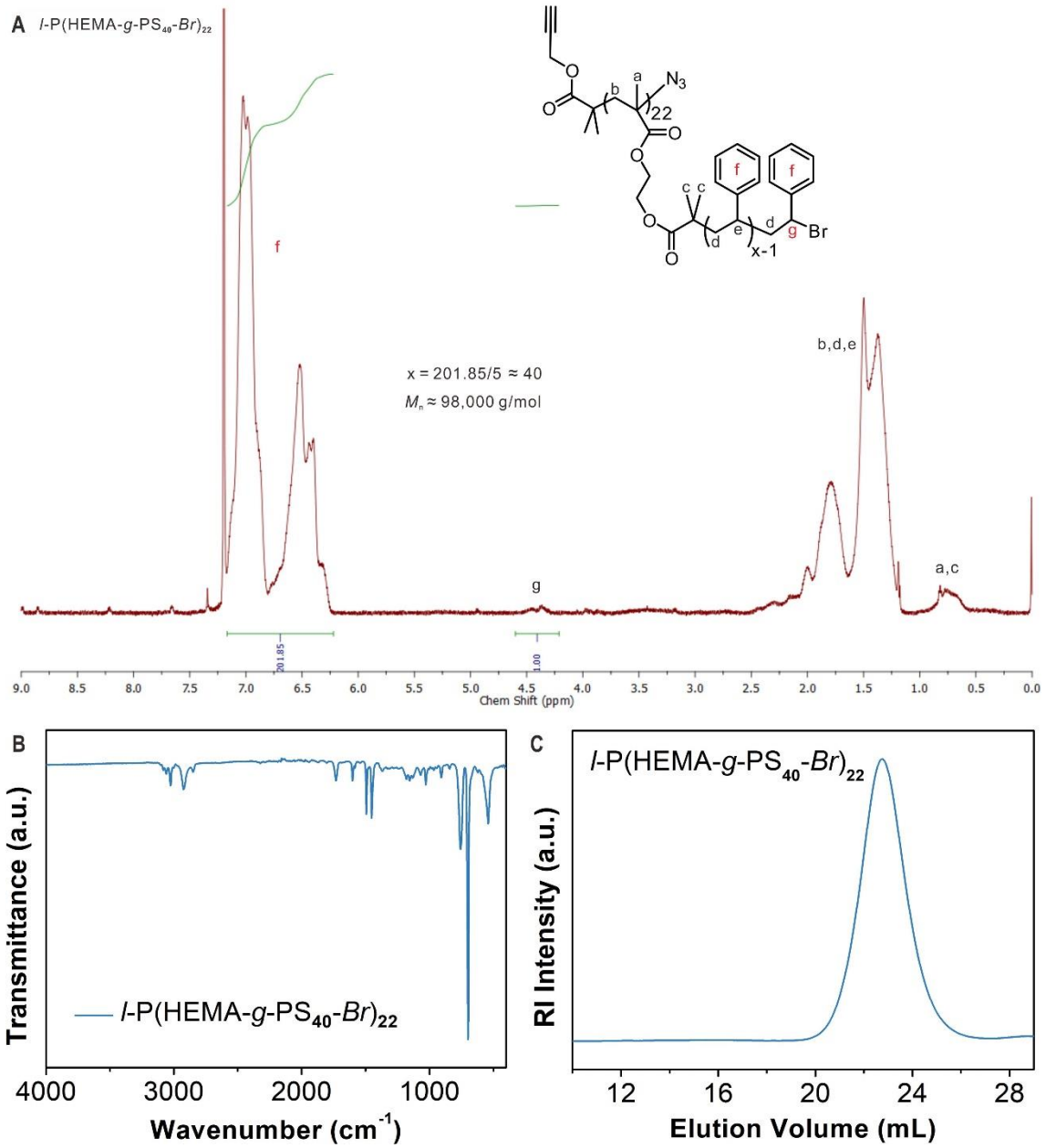

Fig. S38. Characterizations of *l*-P(HEMA-*g*-PS40-*Br*)22. (A) ^{1}H NMR spectrum (700 MHz, 298.3 K) in $CDCl_3$-d. The integral ratio of signal **g** and signal **f** was used to calculated the repeating number (x) and the molecular weight ($M_{n,NMR}$). (B) FTIR spectrum. (C) GPC curve measured using DMF as the eluent with PS standards for calibration.

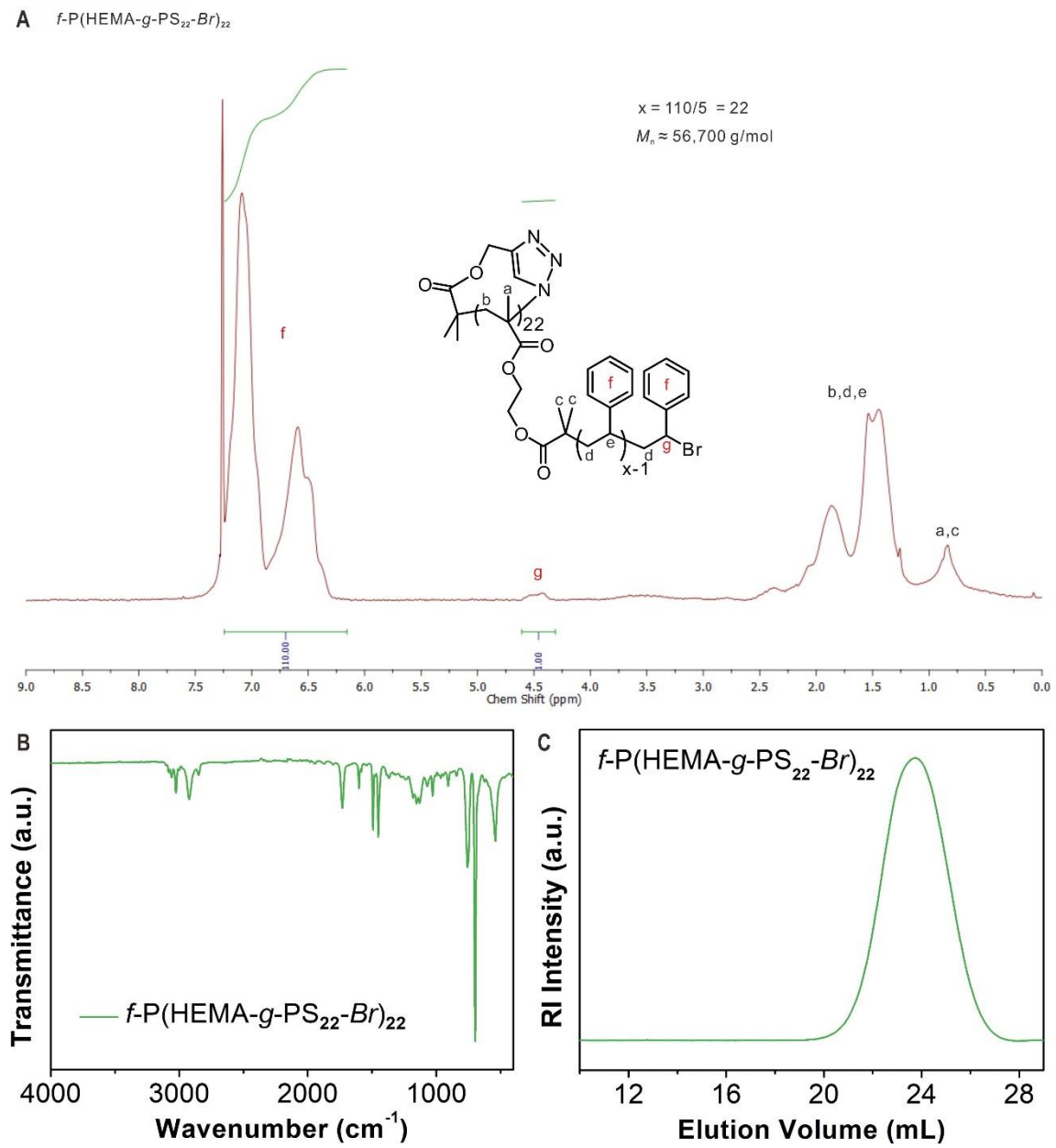

Fig. S39. Characterizations of *f*-P(HEMA-*g*-PS22-*Br*)22. (A) ^{1}H NMR spectrum (300 MHz, 298.3 K) in $CDCl_3$-d. The integral ratio of signal **g** and signal **f** was used to calculated the repeating number (x) and the molecular weight ($M_{n,NMR}$). (B) FTIR spectrum. (C) GPC curve measured using DMF as the eluent with PS standards for calibration.

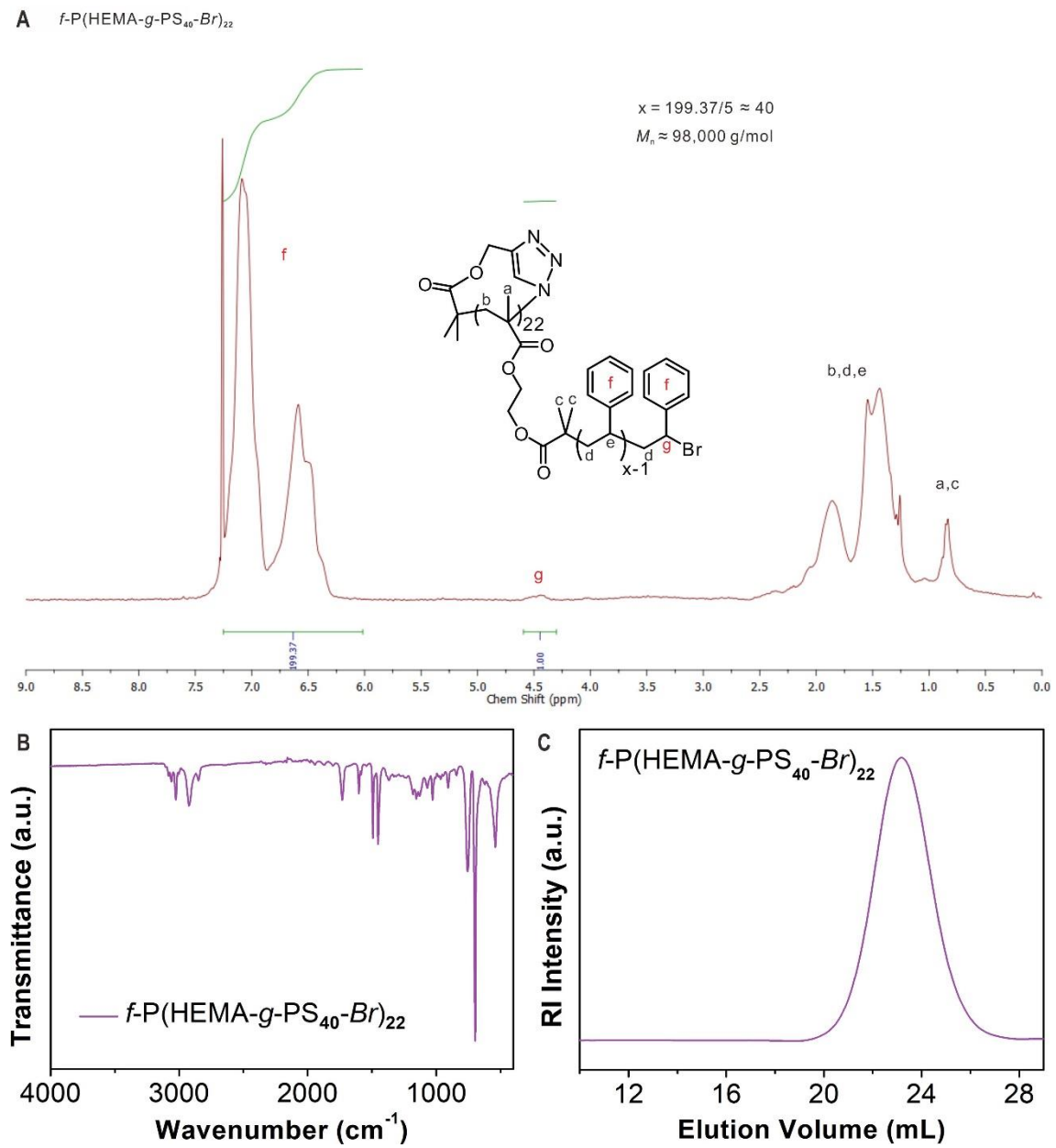

Fig. S40. Characterizations of *f*-P(HEMA-*g*-PS40-*Br*)22. (A) ^{1}H NMR spectrum (300 MHz, 298.3 K) in $CDCl_3$-d. The integral ratio of signal **g** and signal **f** was used to calculated the repeating number (x) and the molecular weight ($M_{n,NMR}$). (B) FTIR spectrum. (C) GPC curve measured using DMF as the eluent with PS standards for calibration.

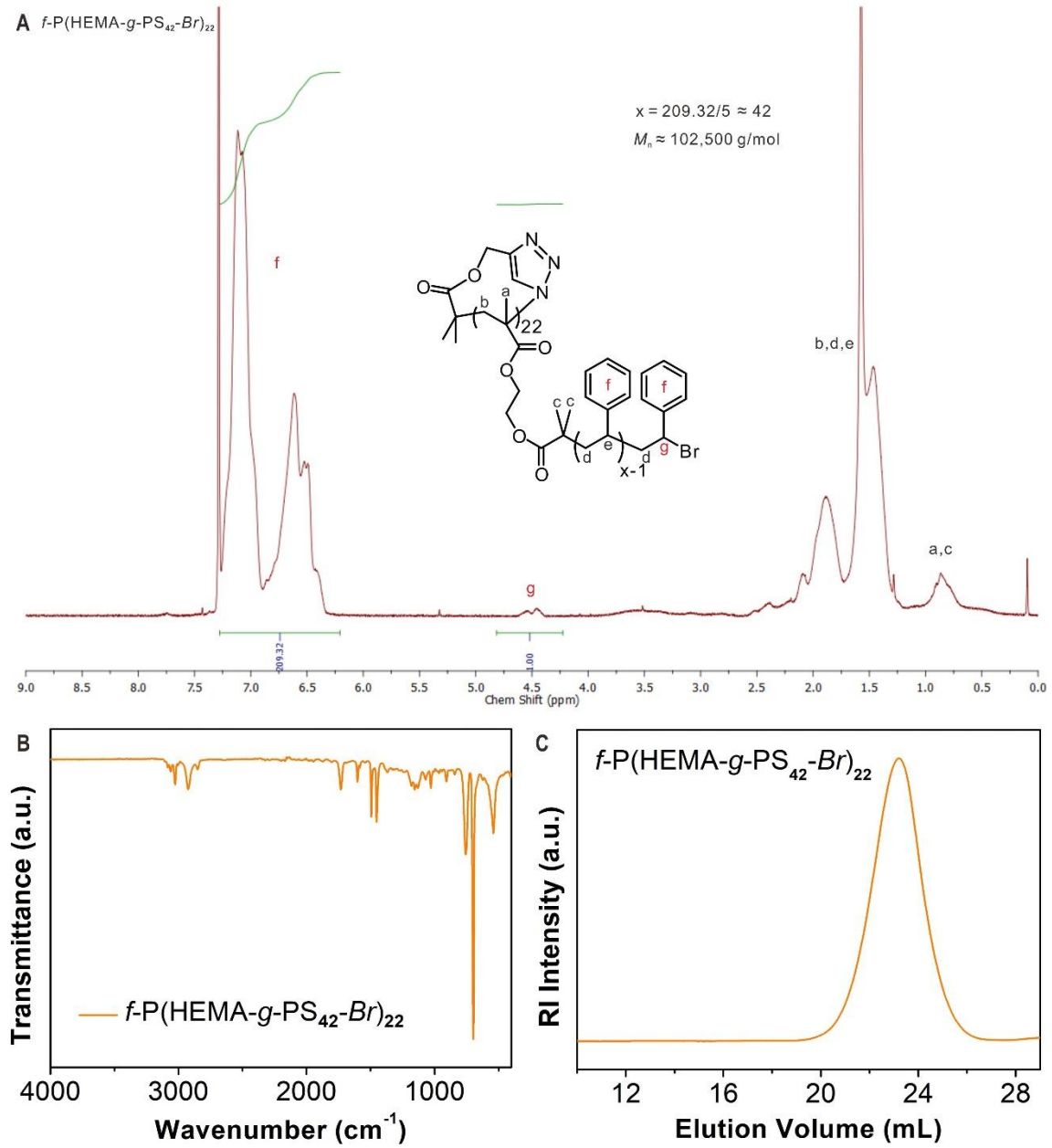

Fig. S41. Characterizations of *f*-P(HEMA-*g*-PS$_{42}$-*Br*)$_{22}$. (A) ^{1}H NMR spectrum (700 MHz, 298.3 K) in $CDCl_3$-d. The integral ratio of signal **g** and signal **f** was used to calculated the repeating number (x) and the molecular weight ($M_{n,NMR}$). (B) FTIR spectrum. (C) GPC curve measured using DMF as the eluent with PS standards for calibration.

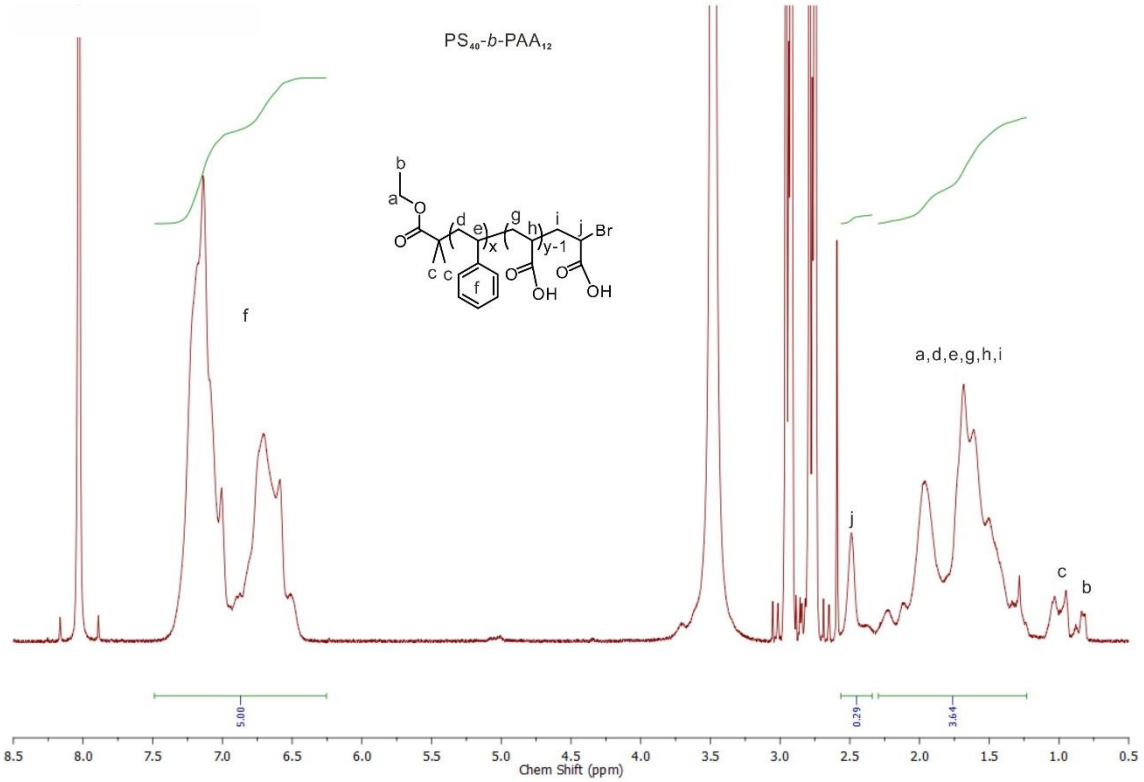

Fig. S42. ^{1}H NMR spectrum (700 MHz, 298.3 K) of PS$_{40}$-*b*-PAA$_{12}$ (**BC**) in DMF-d$_7$. The repeating number of the PAA block (*y*) was calculated by comparing the integral ratio of signal **f** with signals **a**, **d**, **e**, **g**, **h**, **i**, and **j**.

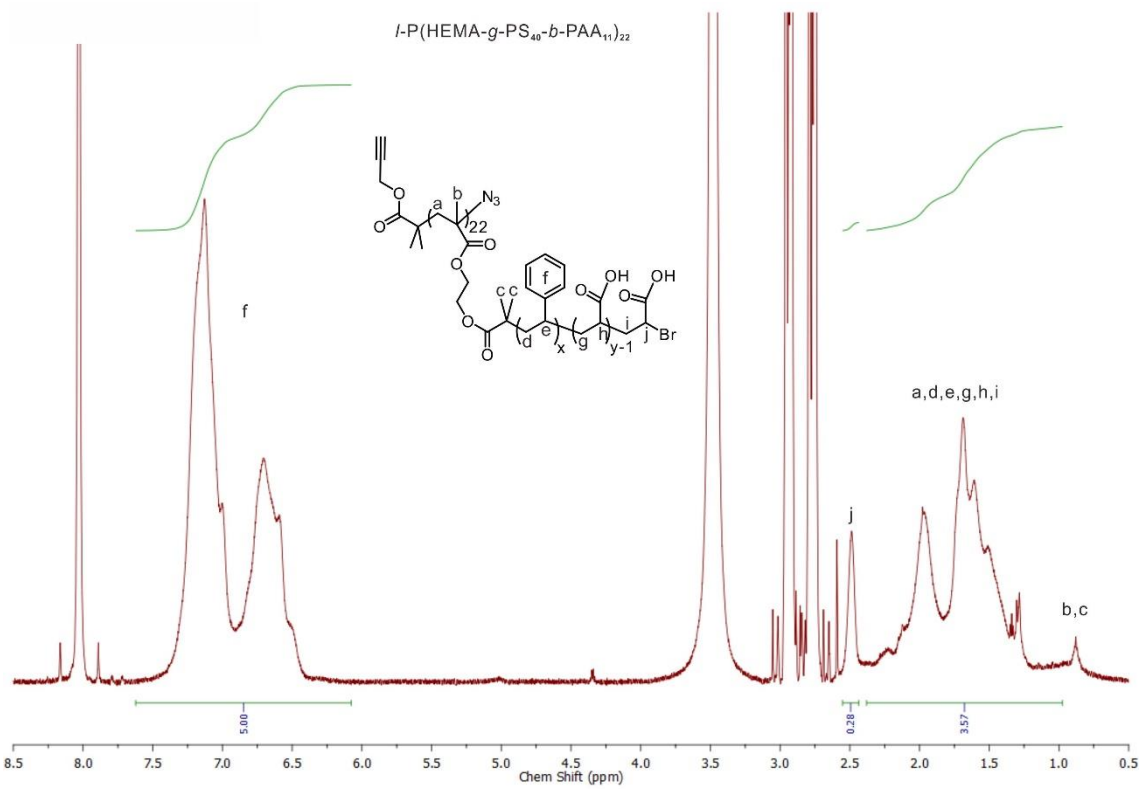

Fig. S43. ^{1}H NMR spectrum (700 MHz, 298.3 K) of *l*-P(HEMA-*g*-PS$_{40}$-*b*-PAA$_{11}$)$_{22}$ **(LB)** in DMF-d$_7$. The repeating number of the PAA block (*y*) was calculated by comparing the integral ratio of signal **f** with signals **a**, **d**, **e**, **g**, **h**, **i**, and **j**.

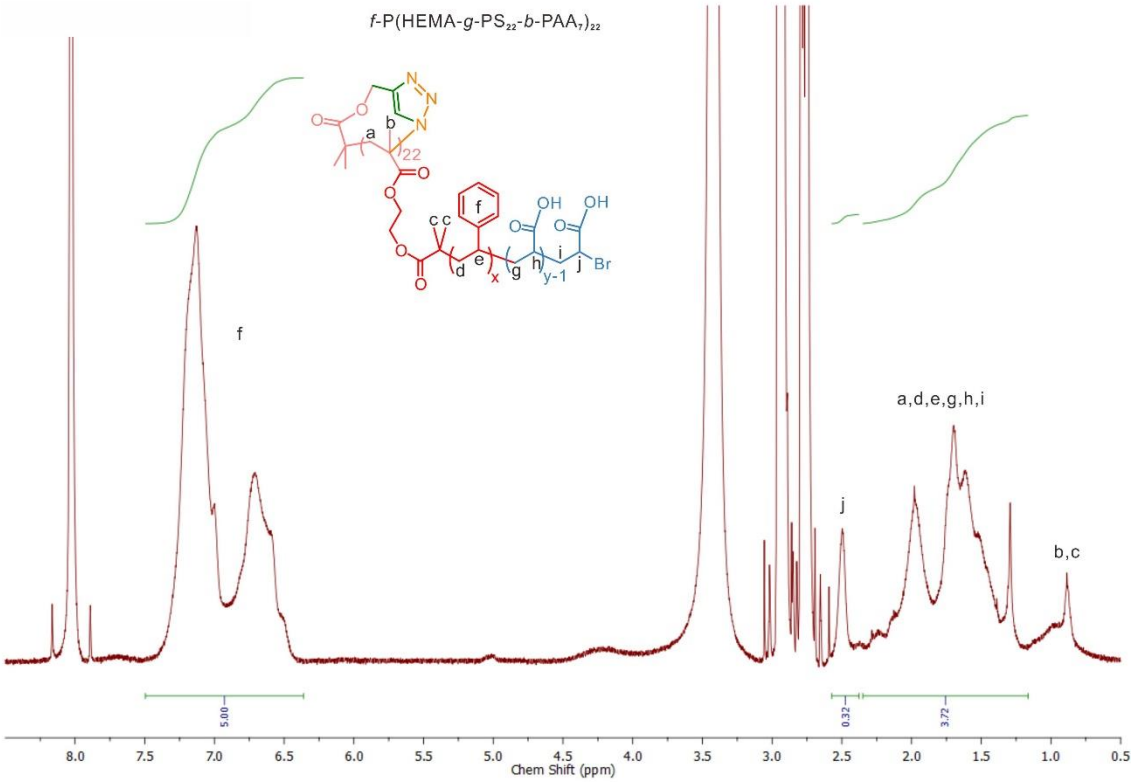

Fig. S44. ^{1}H NMR spectrum (700 MHz, 298.3 K) of *f*-P(HEMA-*g*-PS$_{22}$-*b*-PAA$_{7}$)$_{22}$ (**CB-1**) in DMF-d$_{7}$. The repeating number of the PAA block (*y*) was calculated by comparing the integral ratio of signal **f** with signals **a**, **d**, **e**, **g**, **h**, **i**, and **j**.

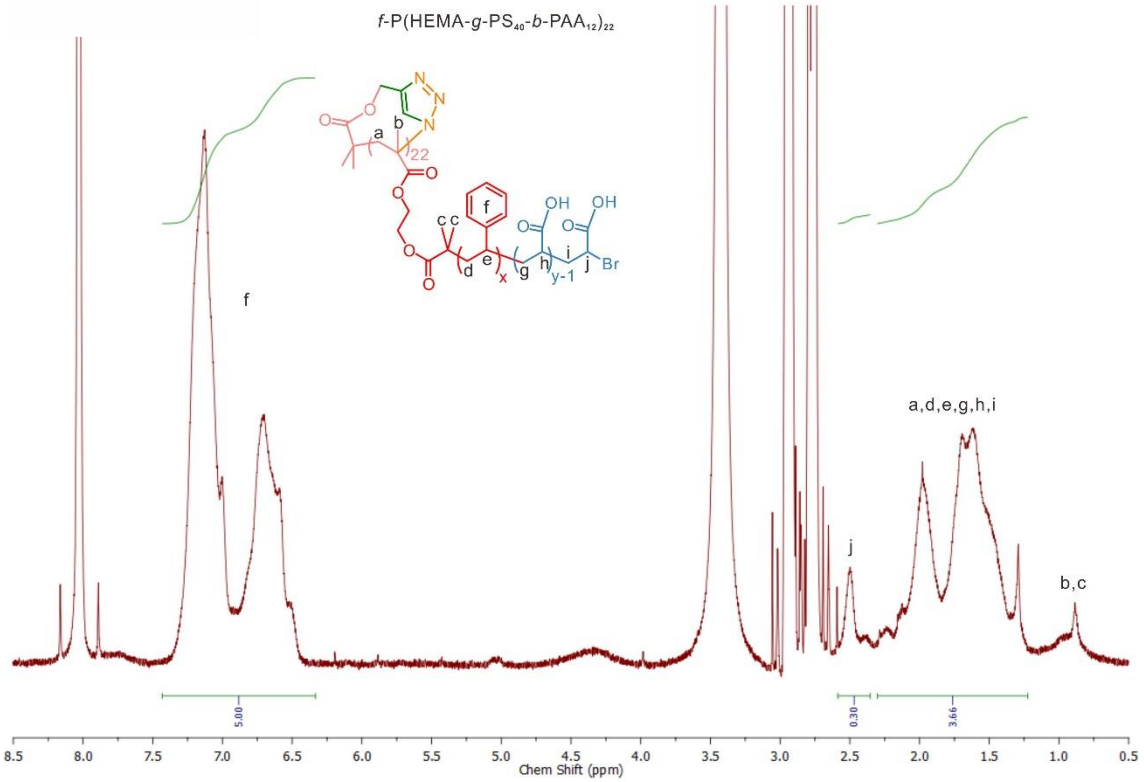

Fig. S45. ^{1}H NMR spectrum (700 MHz, 298.3 K) of *f*-P(HEMA-*g*-PS$_{40}$-*b*-PAA$_{12}$)$_{22}$ (**CB-2**) in DMF-d$_7$. The repeating number of the PAA block (*y*) was calculated by comparing the integral ratio of signal **f** with signals **a**, **d**, **e**, **g**, **h**, **i**, and **j**.

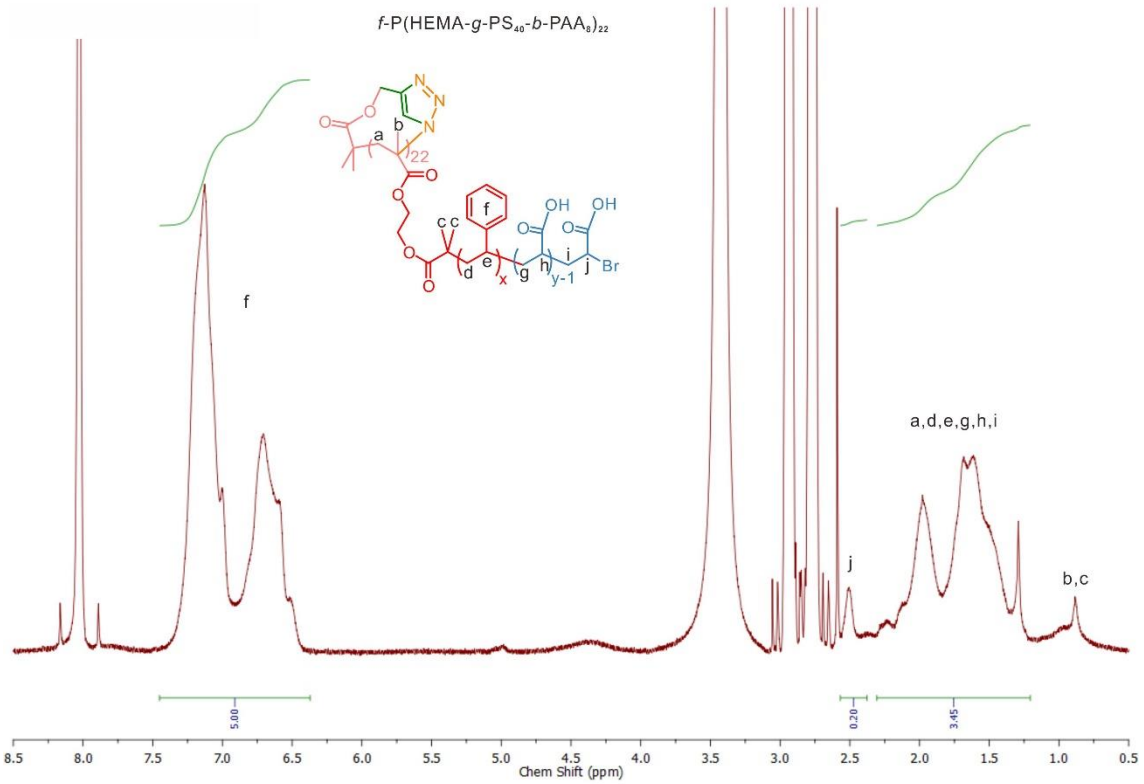

Fig. S46. ^{1}H NMR spectrum (700 MHz, 298.3 K) of *f*-P(HEMA-*g*-PS$_{40}$-*b*-PAA$_{8}$)$_{22}$ (**CB-3**) in DMF-d$_7$. The repeating number of the PAA block (*y*) was calculated by comparing the integral ratio of signal **f** with signals **a**, **d**, **e**, **g**, **h**, **i**, and **j**.

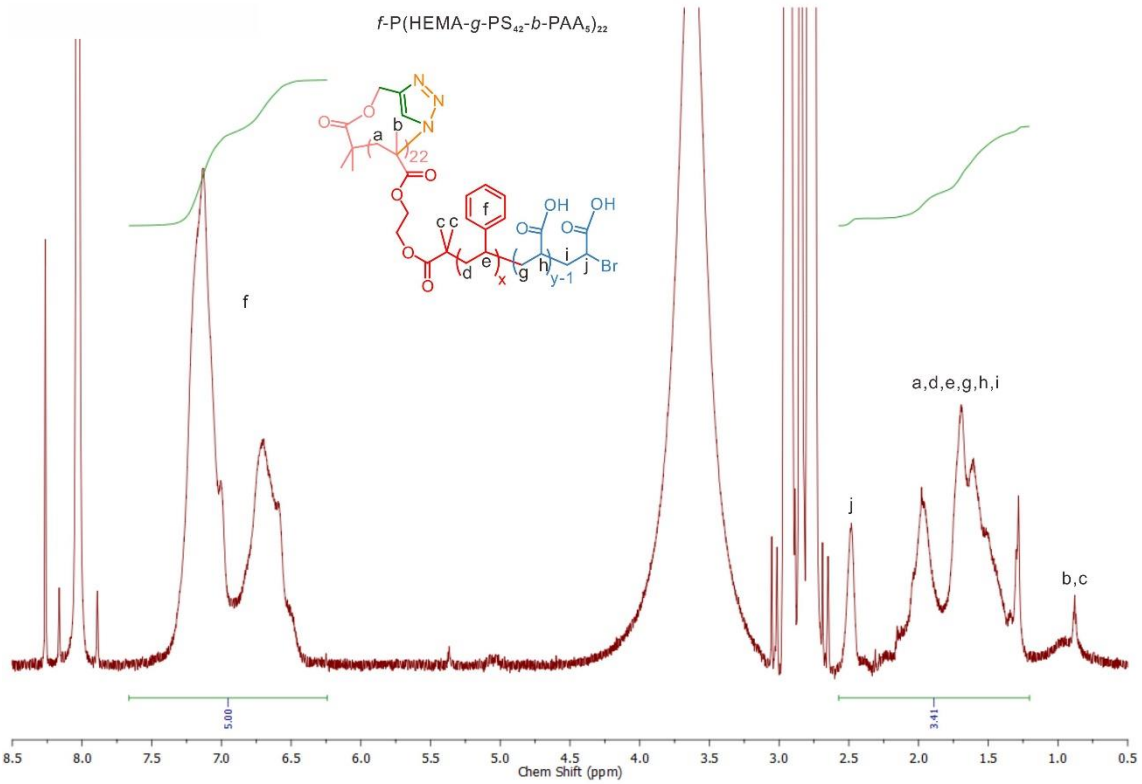

Fig. S47. ^{1}H NMR spectrum (700 MHz, 298.3 K) of *f*-P(HEMA-*g*-PS$_{42}$-*b*-PAA$_5$)$_{22}$ (**CB-4**) in DMF-d$_7$. The repeating number of the PAA block (*y*) was calculated by comparing the integral ratio of signal **f** with signals **a**, **d**, **e**, **g**, **h**, **i**, and **j**.

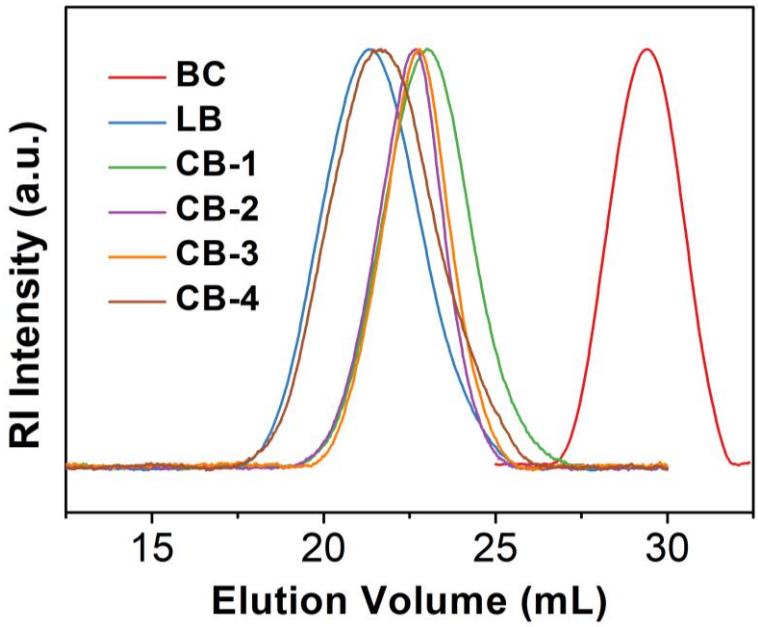

Fig. S48. GPC elution curves of block copolymer PS_{40}-*b*-PAA_{12} (**BC**), linear brush polymer *l*-P(HEMA-*g*-PS_{40}-*b*-PAA_{11})$_{22}$ (**LB**), and four cyclic brush polymers: *f*-P(HEMA-*g*-PS_{22}-*b*-PAA_7)$_{22}$ (**CB-1**), *f*-P(HEMA-*g*-PS_{40}-*b*-PAA_{12})$_{22}$ (**CB-2**), *f*-P(HEMA-*g*-PS_{40}-*b*-PAA_8)$_{22}$ (**CB-3**), and *f*-P(HEMA-*g*-PS_{42}-*b*-PAA_5)$_{22}$ (**CB-4**). DMF was used as the eluent and PS standards were employed for calibration.

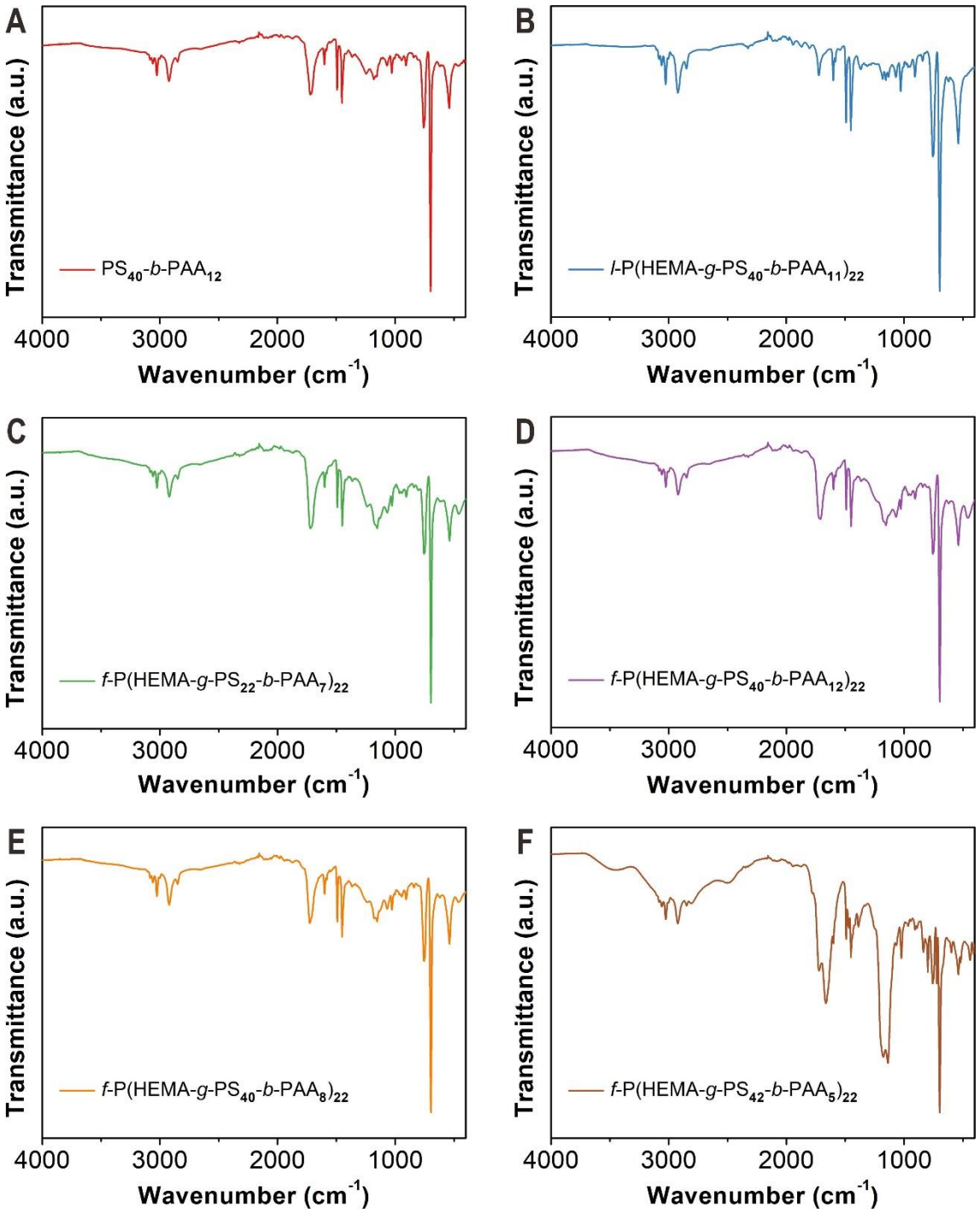

Fig. S49. FTIR spectra of (A) PS_{40}-*b*-PAA_{12} (**BC**); (B) *l*-P(HEMA-*g*-PS_{40}-*b*-PAA_{11})$_{22}$ (**LB**); (C) *f*-P(HEMA-*g*-PS_{22}-*b*-PAA_{7})$_{22}$ (**CB-1**); (D) *f*-P(HEMA-*g*-PS_{40}-*b*-PAA_{12})$_{22}$ (**CB-2**); (E) *f*-P(HEMA-*g*-PS_{40}-*b*-PAA_{8})$_{22}$ (**CB-3**); and (F) *f*-P(HEMA-*g*-PS_{42}-*b*-PAA_{5})$_{22}$ (**CB-4**).

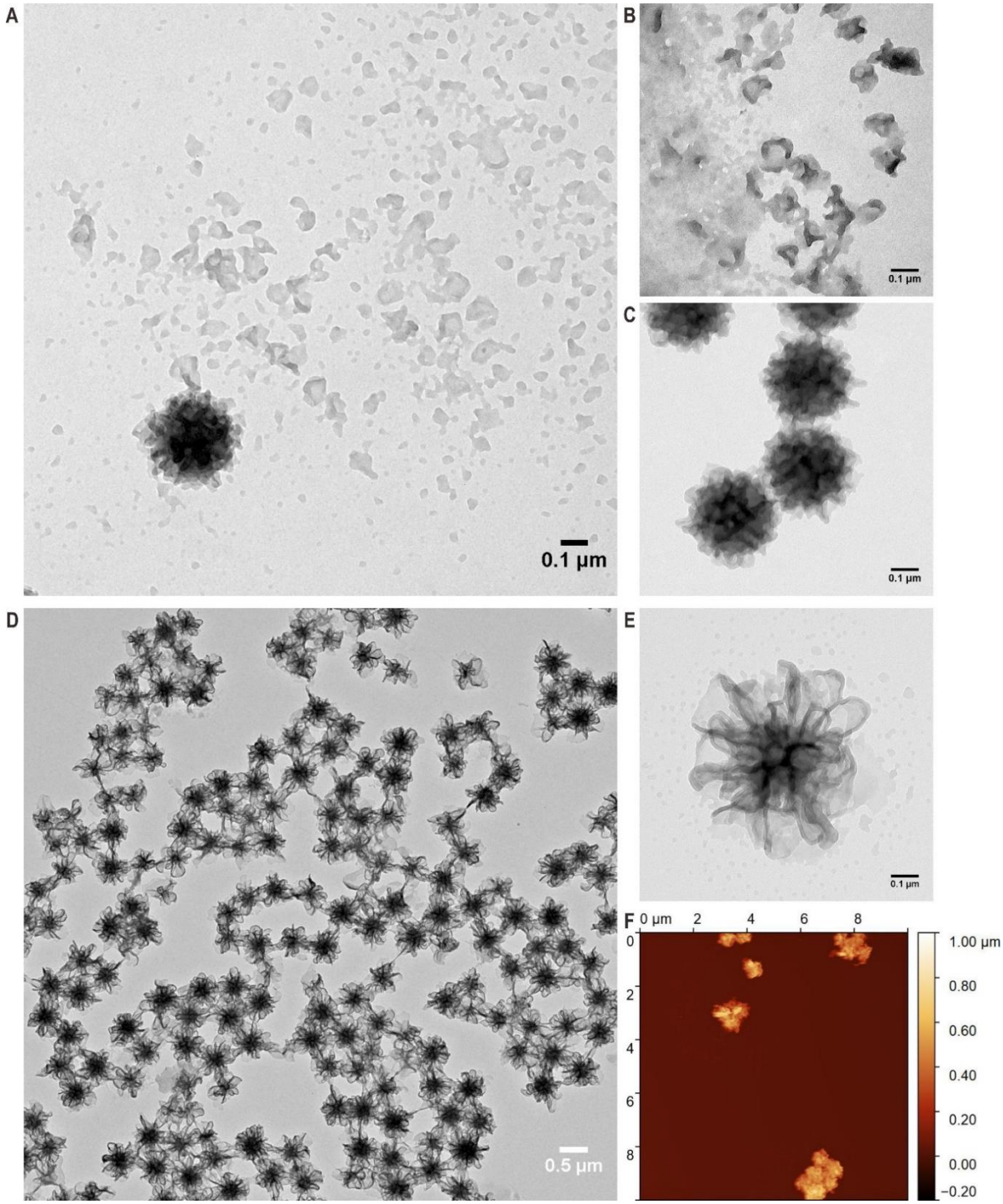

Fig. S50. TEM and AFM images showing the self-assembly of PS_{40}-*b*-PAA_{12} (**BC**) in H_2O at 0.1 mg mL^{-1} (A-C) and 0.4 mg mL^{-1} (D-F). Due to its high weight fraction of hydrophobic PS, the block copolymer mainly self-assembled into lamellae (flat or curved bilayers) and vesicles at 0.1 mg mL^{-1}. When the concentration increased to 0.4 mg mL^{-1}, flower-like large compound vesicles formed by aggregation of simple vesicles were obtained. This observation fits with the results reported by other groups in the literature (*26*).

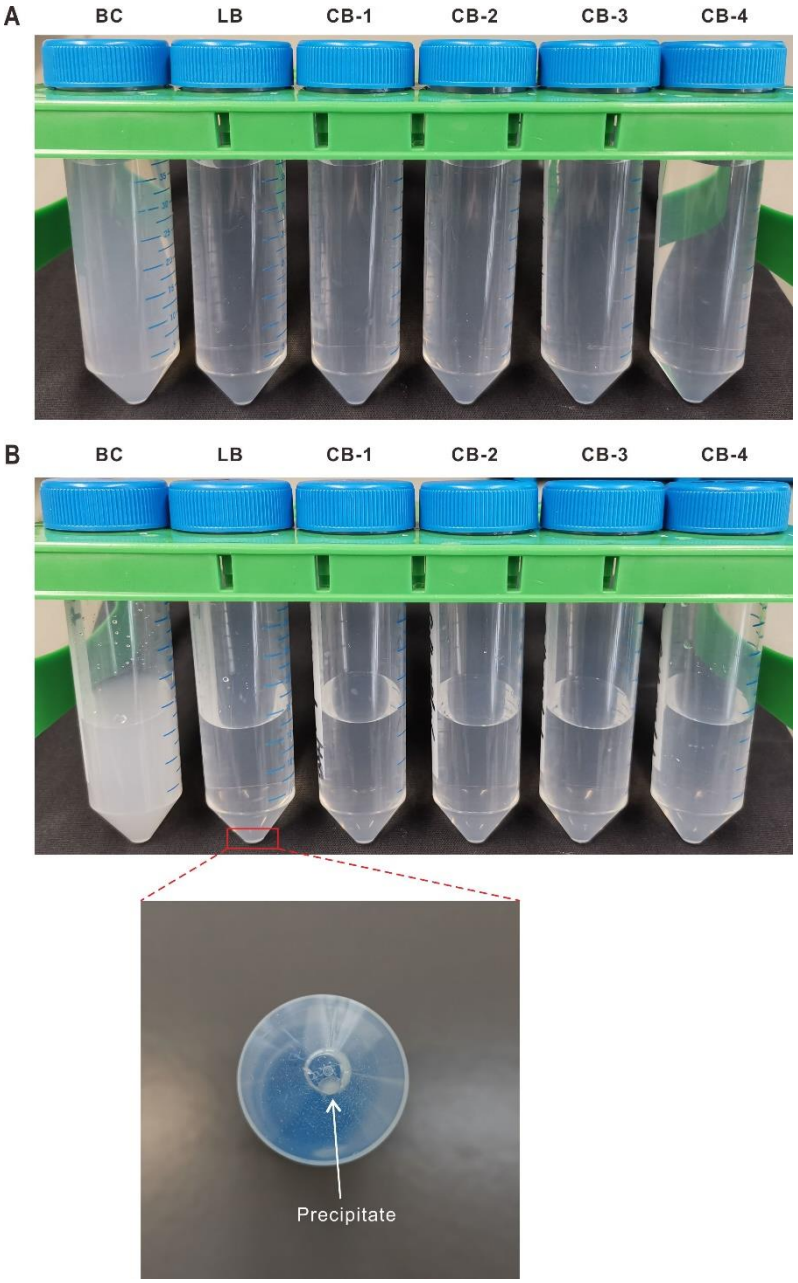

Fig. S51. Self-assembly solutions of block copolymer **BC**, linear brush polymer **LB**, and four cyclic brush polymers **CB-1** to **CB-4** at different concentrations: (A) 0.1 mg mL^{-1}, (B) 0.4 mg mL^{-1}.

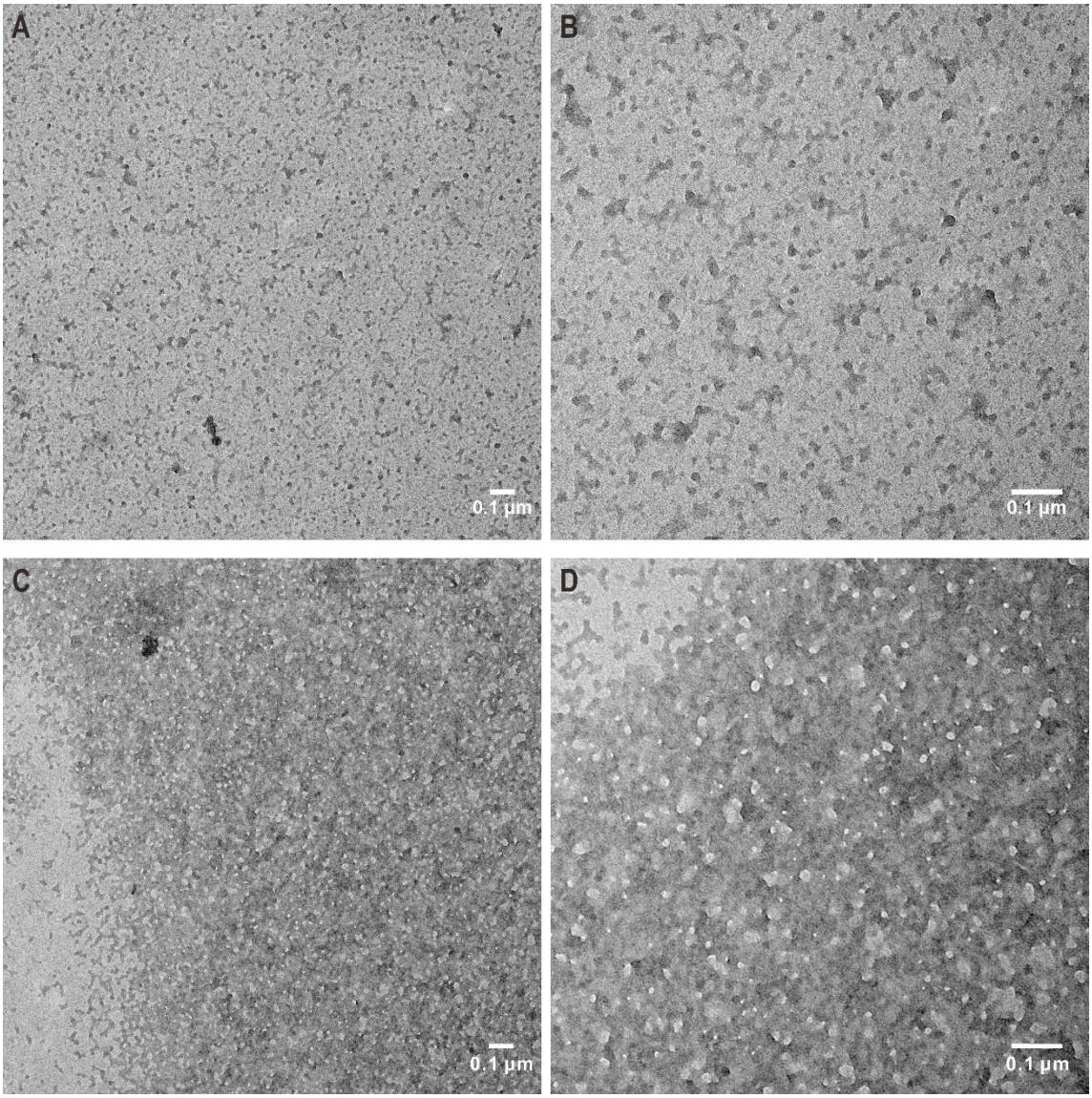

Fig. S52. TEM images showing the formation of irregular aggregates from *l*-P(HEMA-*g*-PS_{40}-*b*-$PAA_{11})_{22}$ (**LB**) in H_2O at 0.1 mg mL^{-1} (A and B) and 0.4 mg mL^{-1} (C and D).

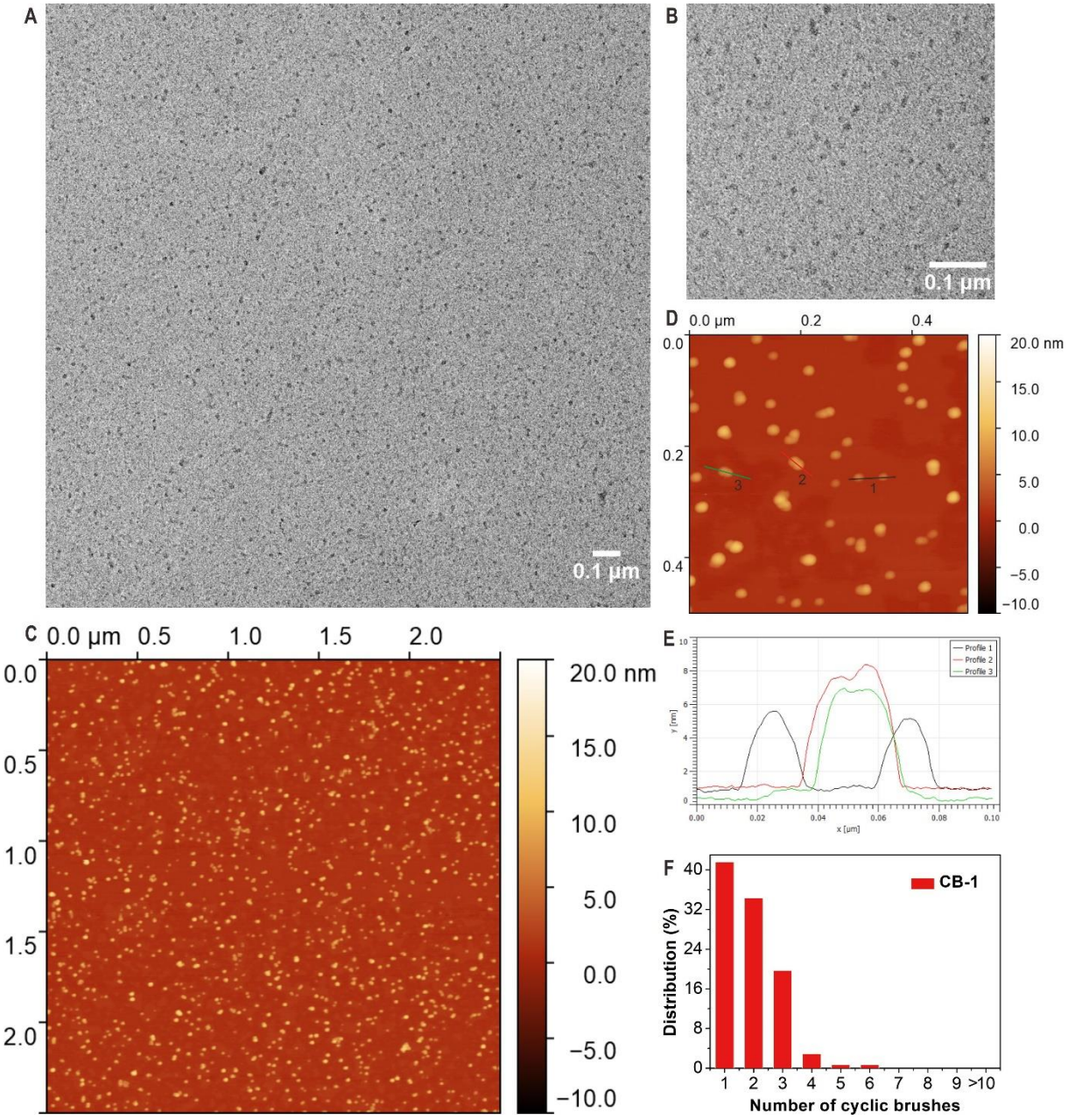

Fig. S53. (A and B) TEM and (C and D) AFM images showing the self-assembly of *f*-P(HEMA-*g*-PS_{22}-*b*-PAA_7)$_{22}$ (**CB-1**) in H_2O at 0.1 mg mL^{-1}. (E) The height profiles of the three lines in (D). Profile 1 indicates two single cyclic brushes. Profile 2 and profile 3 are two dimers. (F) Statistical analysis for the number of cyclic brushes in assemblies based on more than 100 nanoobjects in AFM images.

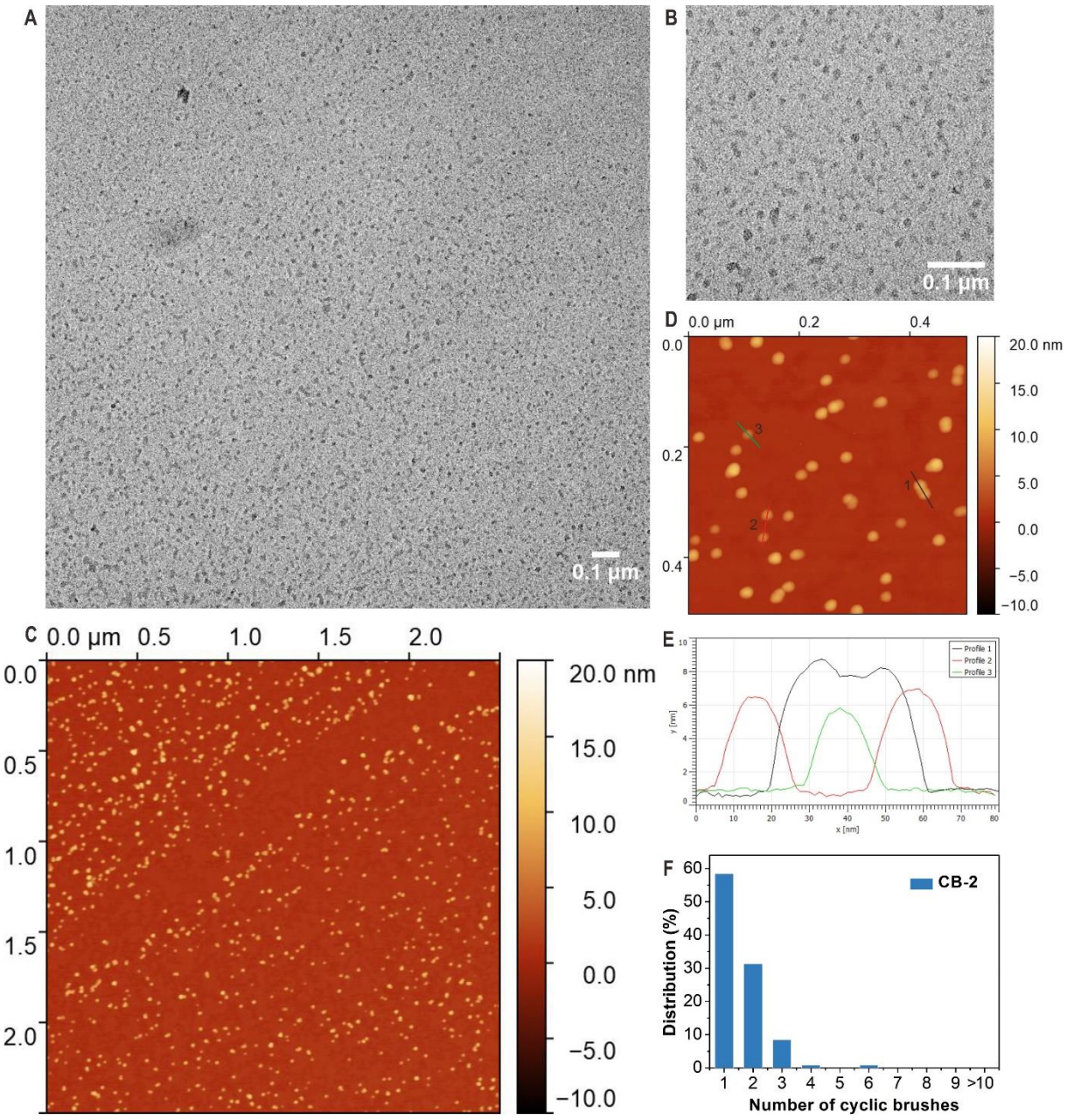

Fig. S54. (A and B) TEM and (C and D) AFM images showing the self-assembly of *f*-P(HEMA-*g*-PS_{40}-*b*-PAA_{12})$_{22}$ (**CB-2**) in H_2O at 0.1 mg mL^{-1}. (E) The height profiles of the three lines in (D). Profile 3 indicates a single cyclic brush polymer and profile 1 indicates a trimer. (F) Statistical analysis for the number of cyclic brushes in assemblies based on more than 100 nanoobjects in AFM images.

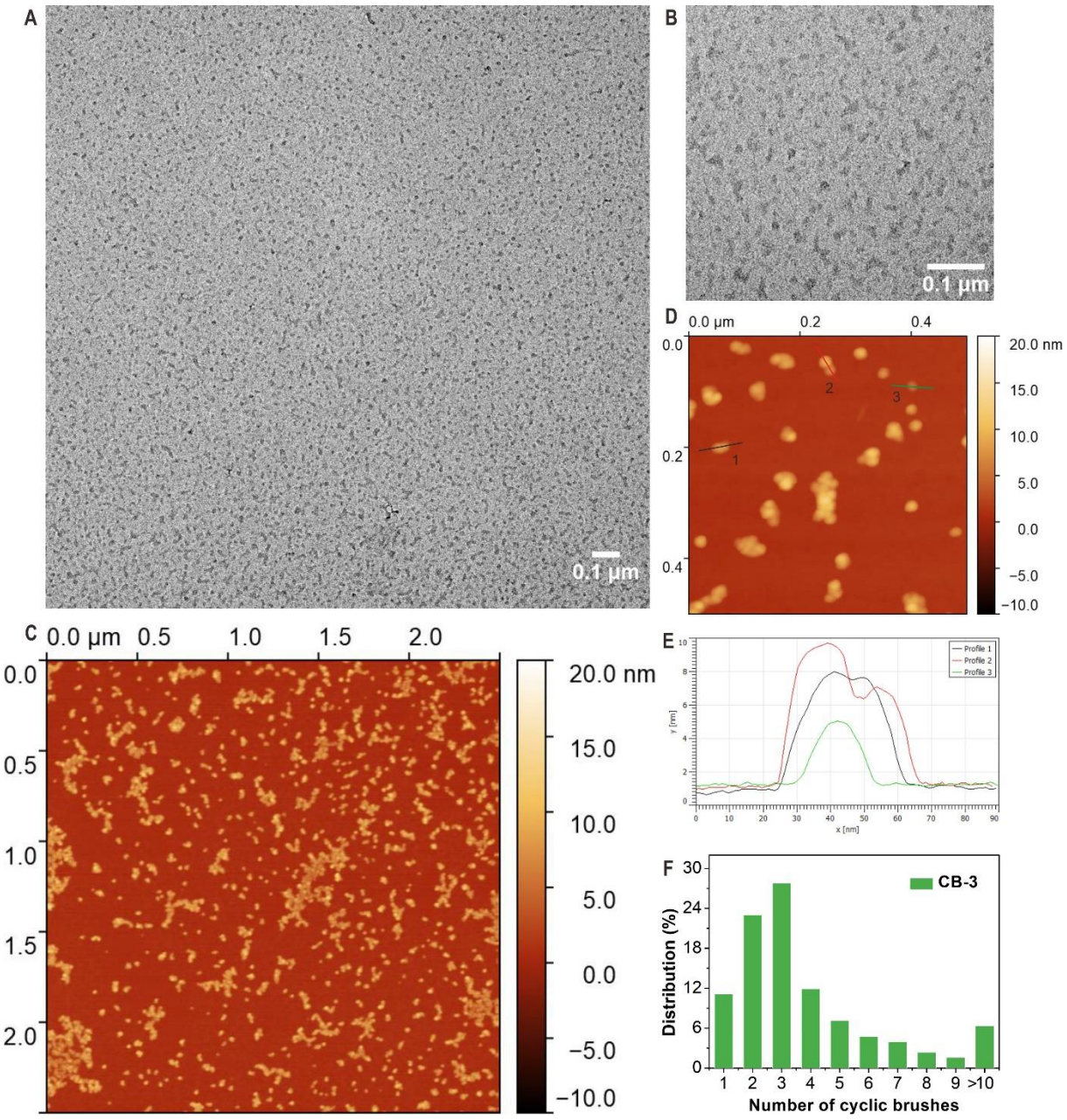

Fig. S55. (A and B) TEM and (C and D) AFM images showing the self-assembly of *f*-P(HEMA-*g*-PS_{40}-*b*-PAA_8)$_{22}$ (**CB-3**) in H_2O at 0.1 mg mL^{-1}. (E) The height profiles of the three lines in (D). Profile 3 indicates a single cyclic brush polymer and profile 2 indicates a dimer. (F) Statistical analysis for the number of cyclic brushes in assemblies based on more than 100 nanoobjects in AFM images.

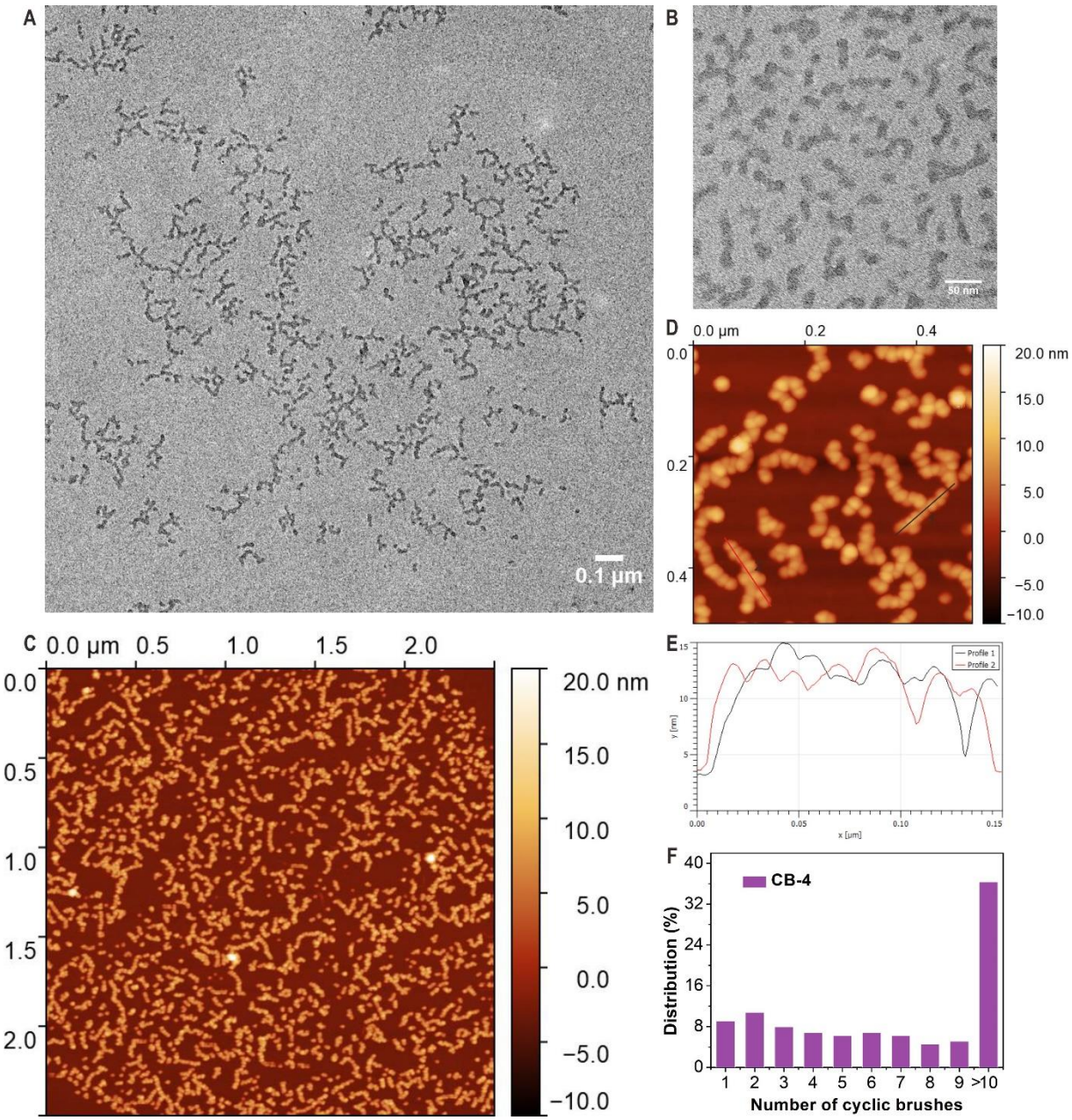

Fig. S56. (A and B) TEM and (C and D) AFM images showing the wormlike structures self-assembled from *f*-P(HEMA-*g*-PS_{42}-*b*-$PAA_5)_{22}$ (**CB-4**) in H_2O at 0.1 mg mL^{-1}. (E) The height profiles of the two lines in (D). (F) Statistical analysis for the number of cyclic brushes in assemblies based on more than 100 nanoobjects in AFM images. The results show that more than 36% of nanoobjects are long wormlike structures assembled by > 10 cyclic brushes.

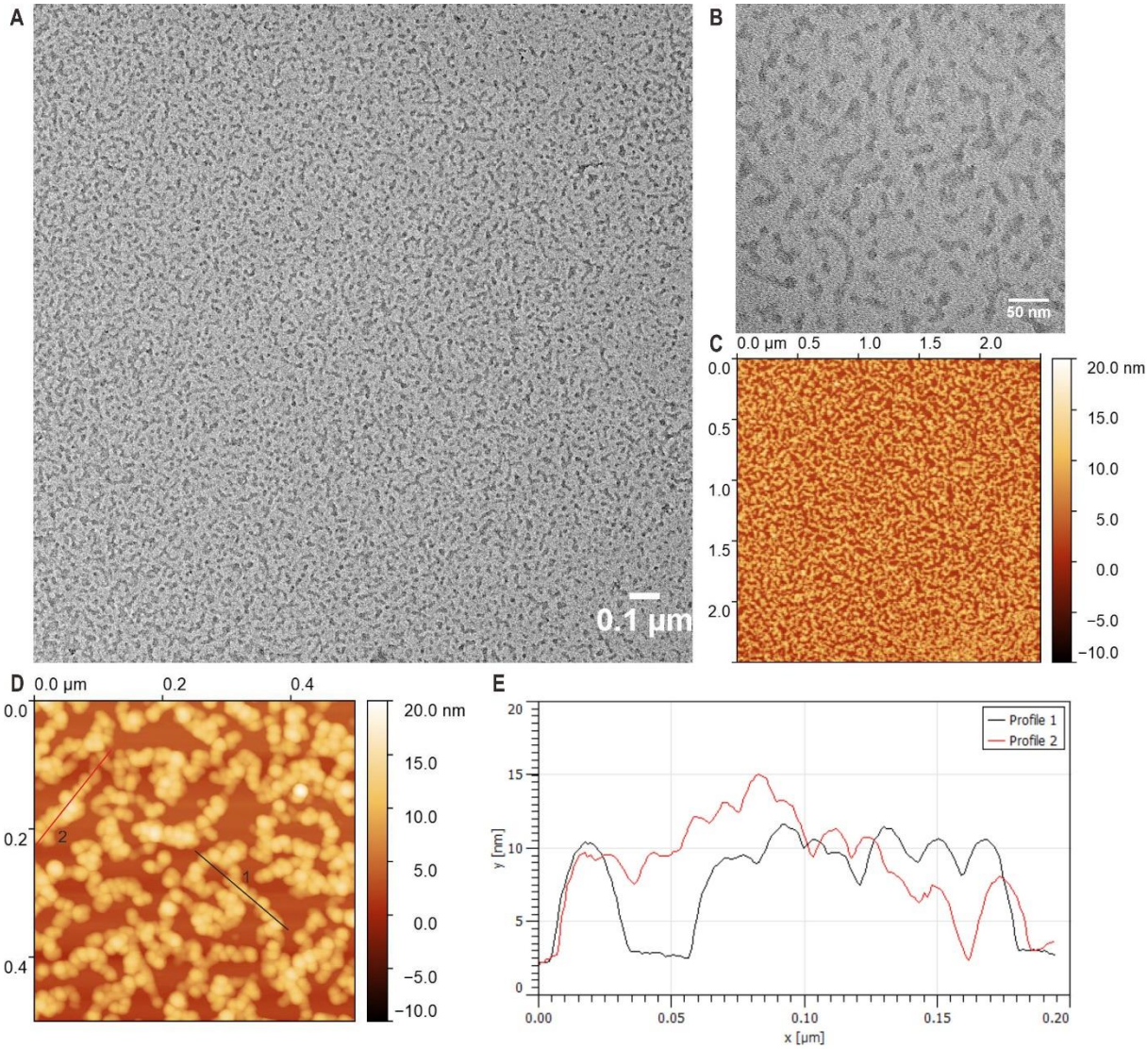

Fig. S57. (A and B) TEM and (C and D) AFM images showing the self-assembly of *f*-P(HEMA-*g*-PS_{22}-*b*-$PAA_7)_{22}$ (**CB-1**) in H_2O at 0.4 mg mL^{-1}. (E) The height profiles of the two lines in (D).

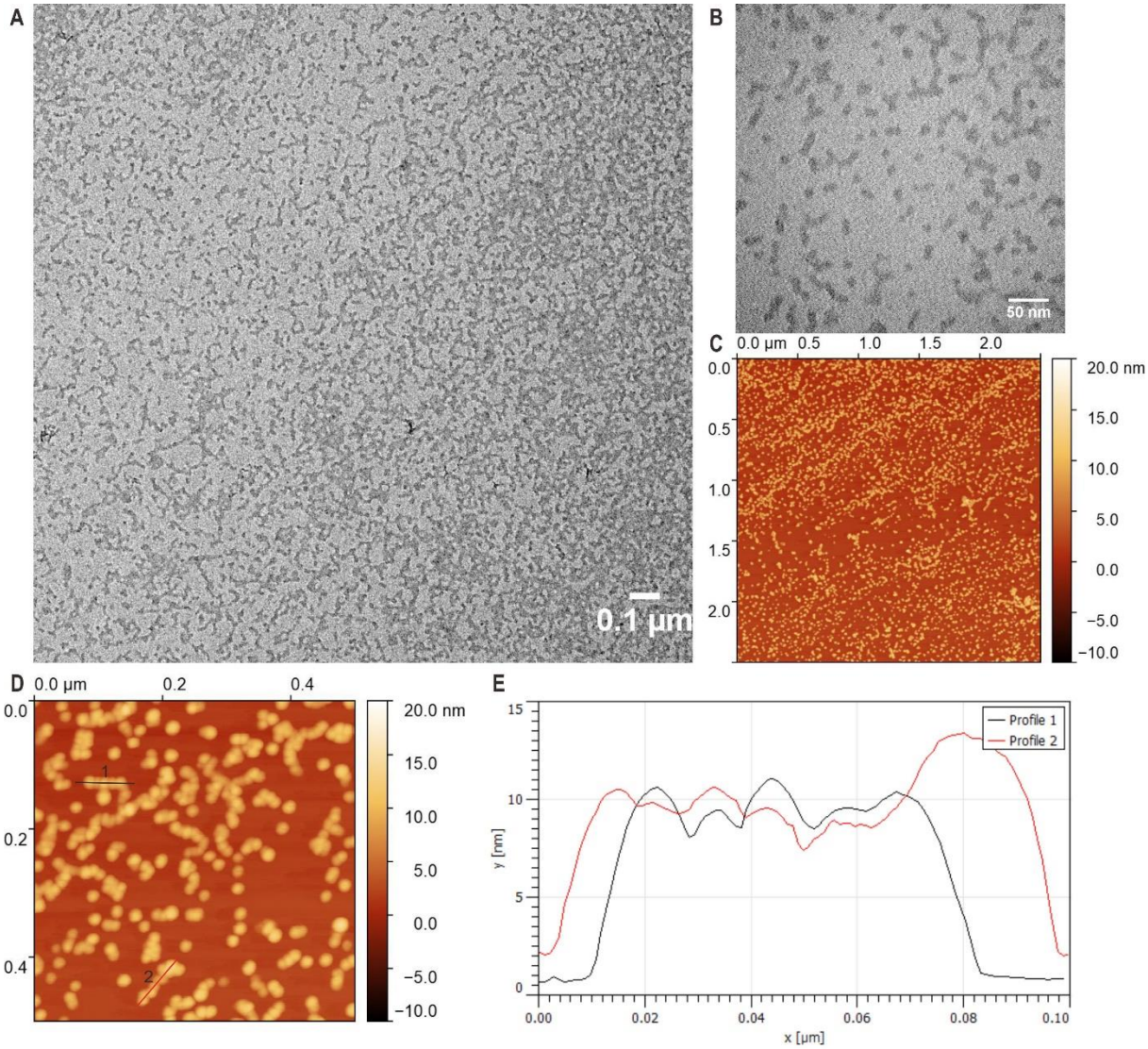

Fig. S58. (A and B) TEM and (C and D) AFM images showing the self-assembly of *f*-P(HEMA-*g*-PS_{40}-*b*-PAA_{12})$_{22}$ (**CB-2**) in H_2O at 0.4 mg mL^{-1}. (E) The height profiles of the two lines in (D).

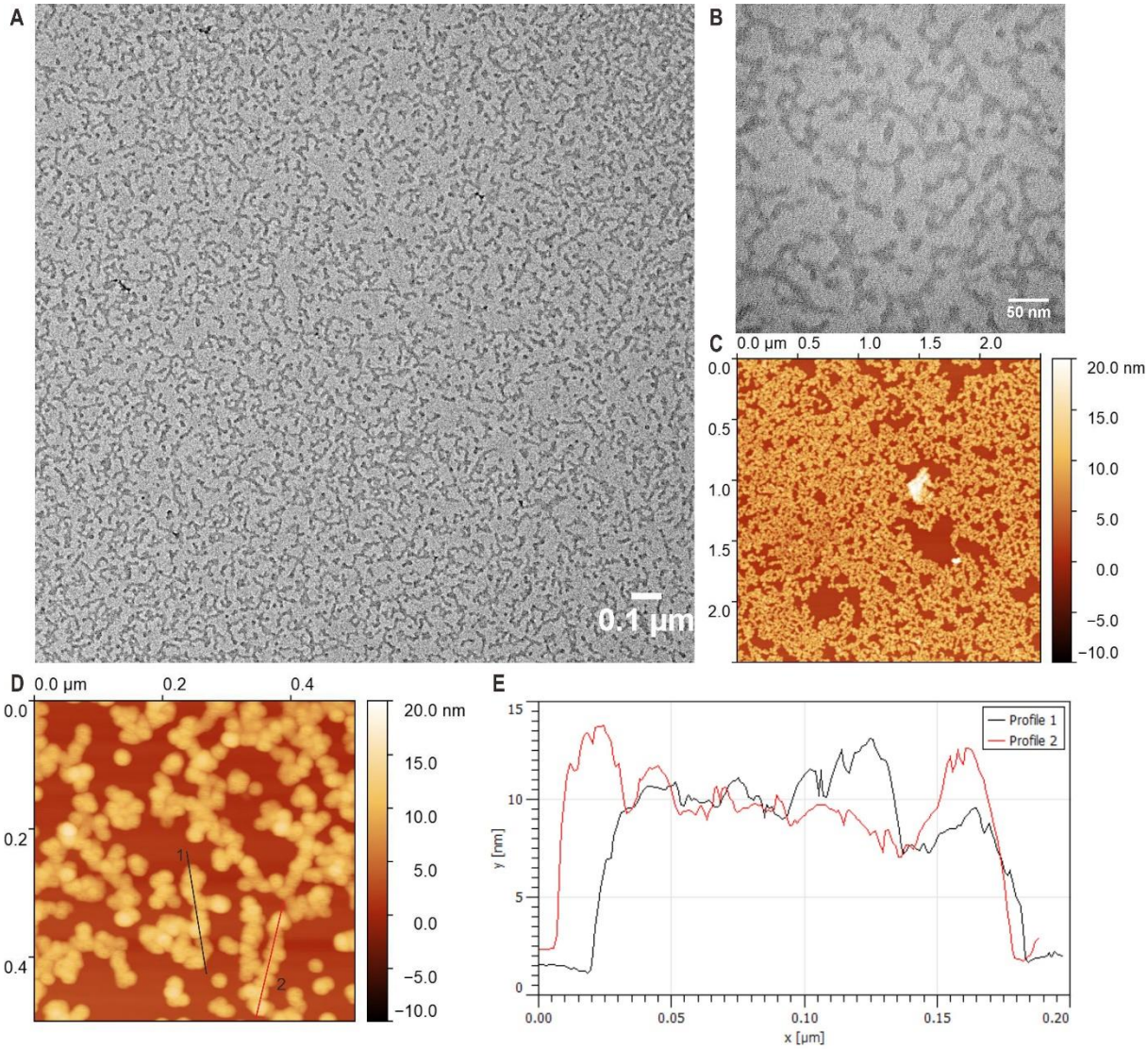

Fig. S59. (A and B) TEM and (C and D) AFM images showing the self-assembly of *f*-P(HEMA-*g*-PS_{40}-*b*-PAA_8)$_{22}$ (**CB-3**) in H_2O at 0.4 mg mL^{-1}. (E) The height profiles of the two lines in (D).

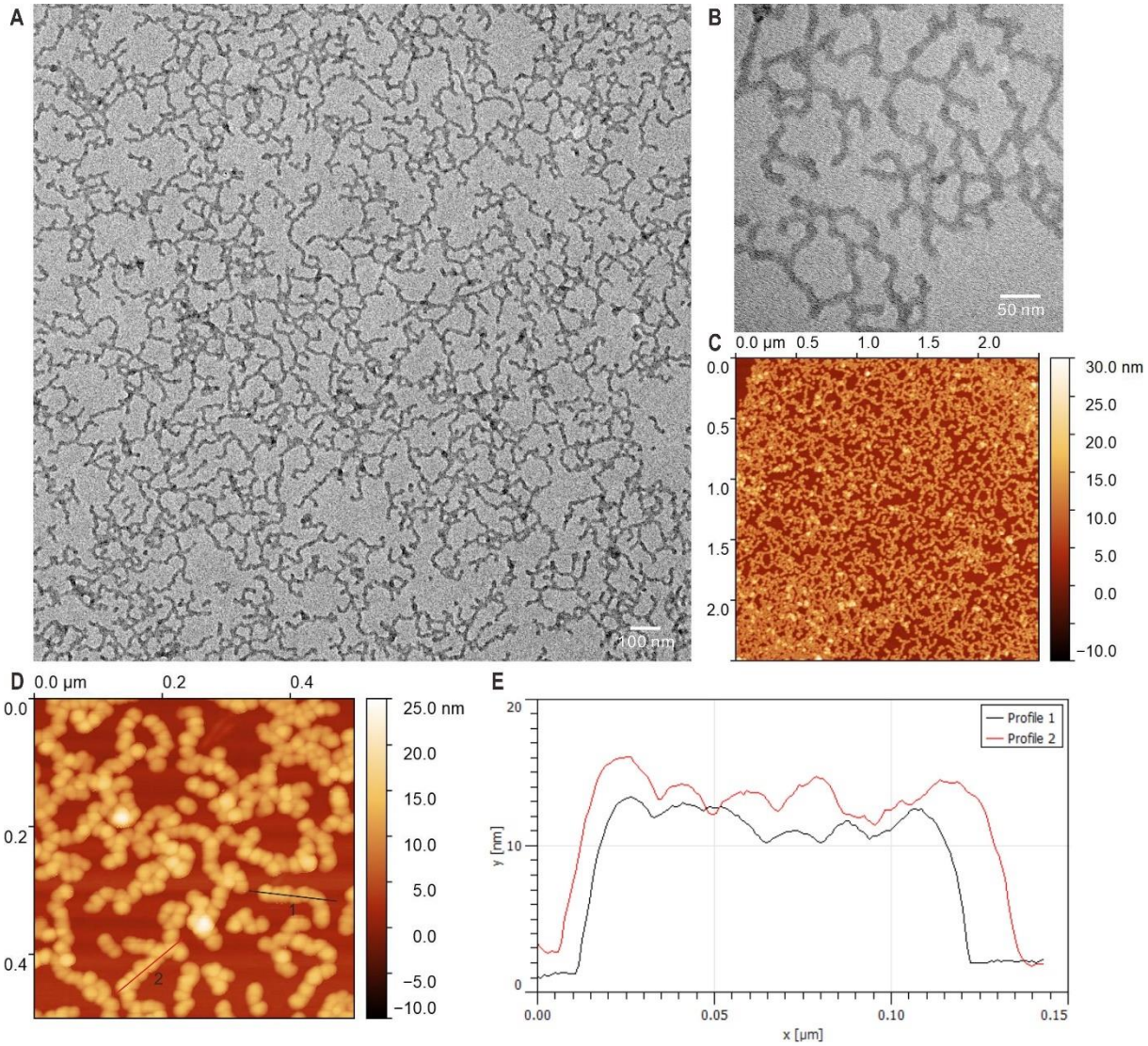

Fig. S60. (A and B) TEM and (C and D) AFM images showing the networks self-assembled from *f*-P(HEMA-*g*-PS_{42}-*b*-$PAA_5)_{22}$ (**CB-4**) in H_2O at 0.4 mg mL^{-1}. (E) The height profiles of the two lines in (D).

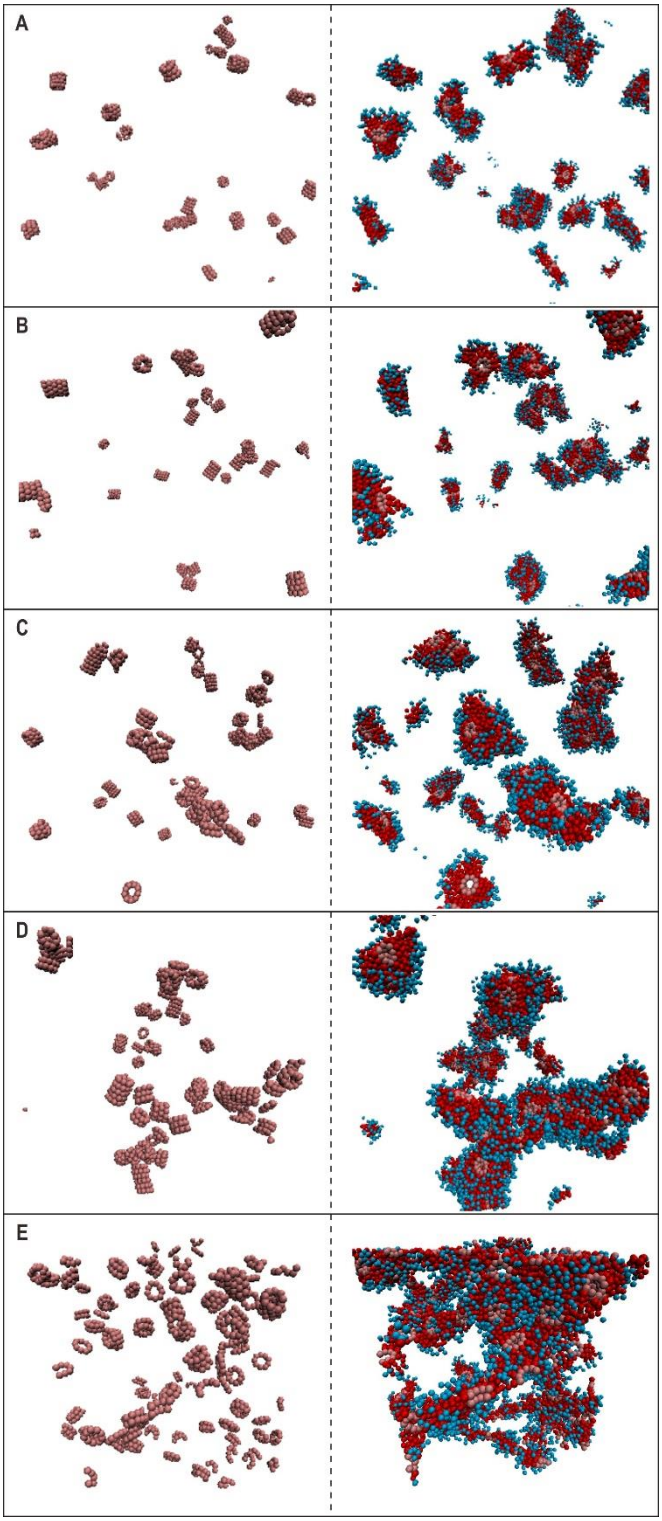

Fig. S61. Molecular simulation snapshots showing the self-assembly of cyclic brush polymers at gradually increased concentrations. The left snapshots show only the hydrophobic cyclic backbones and right the full molecules. The data is shown for the five different concentrations, c = 0.0002σ^{-3} (A), 0.00035σ^{-3} (B), 0.0005σ^{-3} (C), 0.0009σ^{-3} (D), and 0.0017σ^{-3} (E).

Table S1. Characteristics of linear and folded PHEMA samples.

Entry	$M_{n,\ design}$ (g mol^{-1})	$M_{n,NMR}$ [a] (g mol^{-1})	$M_{n,GPC}$ [b] (g mol^{-1})	M_w [b] (g mol^{-1})	V_p [b] (mL)	$Đ$ [b] (M_w/M_n)
l-PHEMA$_{11}$-*Br*	1500	1670	6400	8800	28.30	1.39
l-PHEMA$_{11}$-N_3	/	/	5700	8800	28.21	1.54
f-PHEMA$_{11}$	/	/	4500	6000	29.16	1.33
l-PHEMA$_{15}$-*Br*	2150	2120	8300	11300	27.62	1.36
l-PHEMA$_{15}$-N_3	/	/	8600	12800	27.35	1.49
f-PHEMA$_{15}$	/	/	5000	7400	28.73	1.47
l-PHEMA$_{22}$-*Br*	3450	3040	11400	15900	26.80	1.39
l-PHEMA$_{22}$-N_3	/	/	10900	15900	26.77	1.45
f-PHEMA$_{22}$	/	/	6800	7900	28.09	1.17

[a] Determined by ^{1}H NMR. [b] Determined by GPC using DMF as eluent and PMMA as standards.

Table S2. Synthesis and characterization of linear and cyclic macroinitiators.

Entry	$M_{n,NMR}$ [a] (g mol^{-1})	$M_{n,GPC}$ [b] (g mol^{-1})	M_w [b] (g mol^{-1})	M_p [b] (g mol^{-1})	V_p [b] (mL)	$Đ$ [b] (M_w/M_n)
***l*-P(HEMA-*Br*)$_{22}$**	6300	8700	15200	13200	27.11	1.75
***f*-P(HEMA-*Br*)$_{22}$**	6300	8800	13000	7400	27.95	1.47

[a] Determined by ^{1}H NMR. [b] Determined by GPC using DMF as eluent and PMMA as standards.

Table S3. Synthesis and characterization of PS as well as linear and cyclic brush polymers with PS side chains.

Ratio [a] **I/C/L/M**	**Entry**	$M_{n,NMR}$ [b] (g mol^{-1})	$M_{n,GPC}$ [c] (g mol^{-1})	M_w [c] (g mol^{-1})	M_p [c] (g mol^{-1})	V_p [c] (mL)	$Đ$ [c] (M_w/M_n)
1:1:2:400	PS_{40}-*Br*	4400	3700	5000	4300	29.51	1.34
1:1:2:600	*l*-P(HEMA-*g*-PS_{40}-*Br*)$_{22}$	98000	80300	99200	92900	22.74	1.24
1:1:2:600	*f*-P(HEMA-*g*-PS_{22}-*Br*)$_{22}$	56700	45600	63200	52700	23.77	1.39
1:1:2:600	*f*-P(HEMA-*g*-PS_{40}-*Br*)$_{22}$	98000	59000	79600	71000	23.17	1.35
1:1:2:600	*f*-P(HEMA-*g*-PS_{42}-*Br*)$_{22}$	102500	63300	80800	67700	23.21	1.28

[a] Molar ratio of initiator/catalyst/ligand/monomer. [b] Determined by ^{1}H NMR. [c] Determined by GPC using DMF as eluent and PS as standards.

Table S4. Synthesis and characterization of block copolymer as well as linear and cyclic brush polymers with PS-b-PAA side chains.

Ratio [a] **I/C/L/M**	**Entry**	$M_{n,NMR}$ [b] **(g/mol)**	f_{PAA} **(wt%)**	$M_{n,GPC}$ [c] **(g/mol)**	M_w [c] **(g/mol)**	M_p [c] **(g/mol)**	V_p [c] **(mL)**	$Đ$ [c] **(M_w/M_n)**
1:2:4:400	PS_{40}-*b*-PAA_{12} (**BC**)	5300	16.3	3800	5400	4500	29.41	1.42
1:2:4:400	*l*-P(HEMA-*g*-PS_{40}-*b*-$PAA_{11})_{22}$ (**LB**)	115400	15.1	151900	225500	180300	21.33	1.48
1:2:4:400	*f*-P(HEMA-*g*-PS_{22}-*b*-$PAA_{7})_{22}$ (**CB-1**)	67800	16.4	76200	92800	81200	23.04	1.22
1:2:4:400	*f*-P(HEMA-*g*-PS_{40}-*b*-$PAA_{12})_{22}$ (**CB-2**)	117000	16.3	96400	113300	93600	22.73	1.18
1:2:4:400	*f*-P(HEMA-*g*-PS_{40}-*b*-$PAA_{8})_{22}$ (**CB-3**)	110700	11.5	91000	106200	90800	22.79	1.17
1:2:8:800	*f*-P(HEMA-*g*-PS_{42}-*b*-$PAA_{5})_{22}$ (**CB-4**)	110400	7.2	129300	191600	169700	21.45	1.48

[a] Molar ratio of initiator/catalyst/ligand/monomer. [b] Determined by ^{1}H NMR. [c] Determined by GPC using DMF as eluent and PS as standards.

Movie S1. Molecular simulation animation showing the self-assembly of cyclic brush polymers at $c = 0.0002\sigma^{-3}$. This animation shows only the hydrophobic cyclic backbones.

Movie S2. Molecular simulation animation showing the self-assembly of cyclic brush polymers at $c = 0.0002\sigma^{-3}$. This animation shows the full molecules.

Movie S3. Molecular simulation animation showing the self-assembly of cyclic brush polymers at $c = 0.00035\sigma^{-3}$. This animation shows only the hydrophobic cyclic backbones.

Movie S4. Molecular simulation animation showing the self-assembly of cyclic brush polymers at $c = 0.00035\sigma^{-3}$. This animation shows the full molecules.

Movie S5. Molecular simulation animation showing the self-assembly of cyclic brush polymers at $c = 0.0005\sigma^{-3}$. This animation shows only the hydrophobic cyclic backbones.

Movie S6. Molecular simulation animation showing the self-assembly of cyclic brush polymers at $c = 0.0005\sigma^{-3}$. This animation shows the full molecules.

Movie S7. Molecular simulation animation showing the self-assembly of cyclic brush polymers at $c = 0.0009\sigma^{-3}$. This animation shows only the hydrophobic cyclic backbones.

Movie S8. Molecular simulation animation showing the self-assembly of cyclic brush polymers at $c = 0.0009\sigma^{-3}$. This animation shows the full molecules.

Movie S9. Molecular simulation animation showing the self-assembly of cyclic brush polymers at $c = 0.0017\sigma^{-3}$. This animation shows only the hydrophobic cyclic backbones.

Movie S10. Molecular simulation animation showing the self-assembly of cyclic brush polymers at $c = 0.0017\sigma^{-3}$. This animation shows the full molecules.

References

1. M. Heim, L. Romer, T. Scheibel, Hierarchical structures made of proteins. The complex architecture of spider webs and their constituent silk proteins. *Chem. Soc. Rev.* **39**, 156-164 (2010).
2. N. C. Seeman, H. F. Sleiman, DNA nanotechnology. *Nat. Rev. Mater.* **3**, 17068 (2018).
3. C. J. Chen, D. Y. W. Ng, T. Weil, Polymer bioconjugates: Modern design concepts toward precision hybrid materials. *Prog. Polym. Sci.* **105**, 101241 (2020).
4. C. J. Chen, K. Wunderlich, D. Mukherji, K. Koynov, A. J. Heck, M. Raabe, M. Barz, G. Fytas, K. Kremer, D. Y. W. Ng, T. Weil, Precision Anisotropic Brush Polymers by Sequence Controlled Chemistry. *J. Am. Chem. Soc.* **142**, 1332-1340 (2020).
5. P. W. K. Rothemund, Folding DNA to create nanoscale shapes and patterns. *Nature* **440**, 297-302 (2006).
6. D. Balchin, M. Hayer-Hartl, F. U. Hartl, In vivo aspects of protein folding and quality control. *Science* **353**, aac4354 (2016).
7. B. V. K. J. Schmidt, N. Fechler, J. Falkenhagen, J. F. Lutz, Controlled folding of synthetic polymer chains through the formation of positionable covalent bridges. *Nat. Chem.* **3**, 234-238 (2011).
8. N. Hosono, M. A. J. Gillissen, Y. C. Li, S. S. Sheiko, A. R. A. Palmans, E. W. Meijer, Orthogonal Self-Assembly in Folding Block Copolymers. *J. Am. Chem. Soc.* **135**, 501-510 (2013).
9. P. J. M. Stals, Y. C. Li, J. Burdynska, R. Nicolay, A. Nese, A. R. A. Palmans, E. W. Meijer, K. Matyjaszewski, S. S. Sheiko, How Far Can We Push Polymer Architectures? *J. Am. Chem. Soc.* **135**, 11421-11424 (2013).
10. Y. Tezuka, Topological Polymer Chemistry Designing Complex Macromolecular Graph Constructions. *Acc. Chem. Res.* **50**, 2661-2672 (2017).
11. S. Mavila, O. Eivgi, I. Berkovich, N. G. Lemcoff, Intramolecular Cross-Linking Methodologies for the Synthesis of Polymer Nanoparticles. *Chem. Rev.* **116**, 878-961 (2016).
12. Y. L. Liu, T. Pauloehrl, S. I. Presolski, L. Albertazzi, A. R. A. Palmans, E. W. Meijer, Modular Synthetic Platform for the Construction of Functional Single-Chain Polymeric Nanoparticles: From Aqueous Catalysis to Photosensitization. *J. Am. Chem. Soc.* **137**, 13096-13105 (2015).
13. M. Gonzalez-Burgos, A. Latorre-Sanchez, J. A. Pomposo, Advances in single chain technology. *Chem. Soc. Rev.* **44**, 6122-6142 (2015).
14. M. Schappacher, A. Deffieux, Synthesis of macrocyclic copolymer brushes and their self-assembly into supramolecular tubes. *Science* **319**, 1512-1515 (2008).
15. E. B. Trigg, T. W. Gaines, M. Marechal, D. E. Moed, P. Rannou, K. B. Wagener, M. J. Stevens, K. I. Winey, Self-assembled highly ordered acid layers in precisely sulfonated polyethylene produce efficient proton transport. *Nat. Mater.* **17**, 725-731 (2018).
16. A. H. Groschel, A. Walther, T. I. Lobling, F. H. Schacher, H. Schmalz, A. H. E. Muller, Guided hierarchical co-assembly of soft patchy nanoparticles. *Nature* **503**, 247-251 (2013).
17. H. B. Qiu, Y. Gao, C. E. Boott, O. E. C. Gould, R. L. Harniman, M. J. Miles, S. E. D. Webb, M. A. Winnik, I. Manners, Uniform patchy and hollow rectangular platelet micelles from crystallizable polymer blends. *Science* **352**, 697-701 (2016).
18. H. B. Qiu, Z. M. Hudson, M. A. Winnik, I. Manners, Multidimensional hierarchical self-assembly of amphiphilic cylindrical block comicelles. *Science* **347**, 1329-1332 (2015).
19. M. J. Huang, C. H. Hsu, J. Wang, S. Mei, X. H. Dong, Y. W. Li, M. X. Li, H. Liu, W. Zhang, T. Z. Aida, W. B. Zhang, K. Yue, S. Z. D. Cheng, Selective assemblies of giant tetrahedra via precisely controlled positional interactions. *Science* **348**, 424-428 (2015).

20. B. A. Laurent, S. M. Grayson, An efficient route to well-defined macrocyclic polymers via "Click" cyclization. *J. Am. Chem. Soc.* **128**, 4238-4239 (2006).
21. F. M. Haque, S. M. Grayson, The synthesis, properties and potential applications of cyclic polymers. *Nat. Chem.* **12**, 433-444 (2020).
22. J. V. M. Weaver, I. Bannister, K. L. Robinson, X. Bories-Azeau, S. P. Armes, M. Smallridge, P. McKenna, Stimulus-responsive water-soluble polymers based on 2-hydroxyethyl methacrylate. *Macromolecules* **37**, 2395-2403 (2004).
23. K. L. Robinson, M. A. Khan, M. V. D. Banez, X. S. Wang, S. P. Armes, Controlled polymerization of 2-hydroxyethyl methacrylate by ATRP at ambient temperature. *Macromolecules* **34**, 3155-3158 (2001).
24. C. J. Chen, G. Y. Liu, X. S. Liu, S. P. Pang, C. S. Zhu, L. P. Lv, J. Ji, Photo-responsive, biocompatible polymeric micelles self-assembled from hyperbranched polyphosphate-based polymers. *Polym. Chem.* **2**, 1389-1397 (2011).
25. K. Wunderlich, A. Larsen, J. Marakis, G. Fytas, M. Klapper, K. Mullen, Controlled Hydrogel Fiber Formation: The Unique Case of Hexaphenylbenzene-Poly(ethylene glycol) Amphiphiles. *Small* **10**, 1914-1919 (2014).
26. Y. Y. Mai, A. Eisenberg, Self-assembly of block copolymers. *Chem. Soc. Rev.* **41**, 5969-5985 (2012).
27. C. C. De Silva, P. Leophairatana, T. Ohkuma, J. T. Koberstein, K. Kremer, D. Mukherji, Sequence transferable coarse-grained model of amphiphilic copolymers. *J. Chem. Phys.* **147**, (2017).
28. Y. N. Zhao, M. K. Singh, K. Kremer, R. Cortes-Huerto, D. Mukherji, Why Do Elastin-Like Polypeptides Possibly Have Different Solvation Behaviors in Water-Ethanol and Water-Urea Mixtures? *Macromolecules* **53**, 2101-2110 (2020).
29. D. Mukherji, C. F. Abrams, Microvoid formation and strain hardening in highly cross-linked polymer networks. *Phys. Rev. E* **78**, 050801 (2008).
30. W. Vandesande, A. Persoons, The Size and Shape of Macromolecular Structures - Determination of the Radius, the Length, and the Persistence Length of Rodlike Micelles of Dodecyldimethylammonium Chloride and Bromide. *J. Phys. Chem.* **89**, 404-406 (1985).
31. H. Y. Gao, S. Bettscheider, T. Kraus, M. H. Muser, Entropy Can Bundle Nanowires in Good Solvents. *Nano Lett.* **19**, 6993-6999 (2019).
32. Y. L. Cheng, H. Wei, J. K. Y. Tan, D. J. Peeler, D. O. Maris, D. L. Sellers, P. J. Horner, S. H. Pun, Nano-Sized Sunflower Polycations As Effective Gene Transfer Vehicles. *Small* **12**, 2750-2758 (2016).
33. J. E. Tanner, Use of Stimulated Echo in Nmr-Diffusion Studies. *J. Chem. Phys.* **52**, 2523-2526 (1970).
34. D. H. Wu, A. D. Chen, C. S. Johnson, An Improved Diffusion-Ordered Spectroscopy Experiment Incorporating Bipolar-Gradient Pulses. *J. Magn. Reson., Ser A* **115**, 260-264 (1995).
35. K. F. Morris, C. S. Johnson, Diffusion-Ordered 2-Dimensional Nuclear-Magnetic-Resonance Spectroscopy. *J. Am. Chem. Soc.* **114**, 3139-3141 (1992).
36. S. Pronk, S. Pall, R. Schulz, P. Larsson, P. Bjelkmar, R. Apostolov, M. R. Shirts, J. C. Smith, P. M. Kasson, D. van der Spoel, B. Hess, E. Lindahl, GROMACS 4.5: a high-throughput and highly parallel open source molecular simulation toolkit. *Bioinformatics* **29**, 845-854 (2013).
37. G. Bussi, D. Donadio, M. Parrinello, Canonical sampling through velocity rescaling. *J. Chem. Phys.* **126**, 014101 (2007).
38. M. Parrinello, A. Rahman, Crystal-Structure and Pair Potentials - a Molecular-Dynamics Study. *Phys. Rev. Lett.* **45**, 1196-1199 (1980).

39. U. Essmann, L. Perera, M. L. Berkowitz, T. Darden, H. Lee, L. G. Pedersen, A Smooth Particle Mesh Ewald Method. *J. Chem. Phys.* **103**, 8577-8593 (1995).
40. B. A. C. Horta, P. T. Merz, P. F. J. Fuchs, J. Dolenc, S. Riniker, P. H. Hunenberger, A GROMOS-Compatible Force Field for Small Organic Molecules in the Condensed Phase: The 2016H66 Parameter Set. *J. Chem. Theory Comput.* **12**, 3825-3850 (2016).
41. Y. J. Wu, H. L. Tepper, G. A. Voth, Flexible simple point-charge water model with improved liquid-state properties. *J. Chem. Phys.* **124**, 024503 (2006).
42. K. Kremer, G. S. Grest, Dynamics of Entangled Linear Polymer Melts - a Molecular-Dynamics Simulation. *J. Chem. Phys.* **92**, 5057-5086 (1990).
43. S. Plimpton, Fast Parallel Algorithms for Short-Range Molecular-Dynamics. *J. Comput. Phys.* **117**, 1-19 (1995).

5.6 Polymer bioconjugates: Modern design concepts toward precision hybrid materials

Chaojian Chen, David Yuen Wah Ng,* and Tanja Weil*

* Corresponding authors

Invited review published in *Prog. Polym. Sci.* **2020**, *105*, 101241.

Contribution of the respective authors:

Chaojian Chen: Figure design, chapters 2, 3, and 5.
David Yuen Wah Ng: Introduction, chapter 4, and summary.
Tanja Weil: Acquiring funding for the project, concept, correcting the manuscript.

Progress in Polymer Science 105 (2020) 101241

Contents lists available at ScienceDirect

Progress in Polymer Science

journal homepage: www.elsevier.com/locate/ppolysci

Polymer bioconjugates: Modern design concepts toward precision hybrid materials

Chaojian Chen[a,b], David Yuen Wah Ng[a,*], Tanja Weil[a,b,*]

[a] Max Planck Institute for Polymer Research, Ackermannweg 10, 55128 Mainz, Germany
[b] Ulm University, Institute of Inorganic Chemistry I, Albert-Einstein-Allee 11, 89081 Ulm, Germany

ARTICLE INFO

Article history:
Available online 11 April 2020

Keywords:
Polymer bioconjugates
Peptide–polymer conjugates
Protein–polymer conjugates
DNA–polymer conjugates
Controlled radical polymerization
Site-specific modification
Polymer biohybrids

ABSTRACT

The conjugation of synthetic polymers with various biomolecules provides an easy access to biohybrid materials which combine advantages from both the synthetic world and Nature. Due to the rapid development of synthetic tools and deepening understanding of biomolecule structure and function, these polymer bioconjugates are not only important for biomedical applications, but also can serve as innovative constructs in materials science. This review summarizes a selection of structurally defined polymer bioconjugates and their application as building blocks for preparing hierarchical biohybrid materials. From this perspective, we discuss and illustrate recent breakthroughs, which portray how the field may potentially develop. We first introduce the general synthetic approaches that have been employed for the construction of precision polymer bioconjugates. Various chemistries for site-specific conjugation, different approaches to control the size, distribution, topology, and function of polymers, as well as the versatile manipulation of bioconjugate architecture are presented. Subsequently, recent advances of polymer bioconjugates based on different biological entities including proteins/peptides, nucleic acids, carbohydrates, lipids and even live cells are discussed individually. In particular, we focus on various forms of well-defined constructs at different length scales ranging from precision polymers and nanostructures templated by biomolecules to highly ordered assemblies of polymer bioconjugates in solution, in bulk and on surfaces. Some representative applications of these biohybrids resulting from their high degree of structural precision are also highlighted.

Abbreviations: 2D, two-dimensional; 3D, three-dimensional; 6SL, 6′-sialyllactose; Ad5, adenovirus 5; AEMA, 2-aminoethyl methacrylate; AFM, atomic force microscopy; AIBN, azobisisobutyronitrile; ARGET, activators regenerated by electron transfer; ATRP, atom transfer radical polymerization; bFGF, basic fibroblast growth factor; BSA, bovine serum albumin; BTA, 1,3,5-benzenetricarboxamide; β-CD, β-cyclodextrin; μCP, microcontact printing; cryo-TEM, cryogenic transmission electron microscopy; CTA, chain-transfer agent; CuAAC, copper-catalyzed azide–alkyne cycloaddition; DABCYL, 4-(dimethylaminoazo)benzene-4-carboxylic acid; DMA, dialkyl maleic anhydride; DNA, deoxyribonucleic acid; DNL, dip-pen nanodisplacement lithography; DTT, dithiothreitol; eATRP, electrochemically mediated ATRP; EBL, electron-beam lithography; ELP, elastin-like polypeptide; EQE, external quantum efficiency; FDA, Food and Drug Administration; FITC, fluorescein isothiocyanate; FND, fluorescent nanodiamond; FRET, Förster resonance energy transfer; Gd-DTPA, Gd-diethylene triamine pentaacetic acid; GFP, green fluorescent protein; GOx, glucose oxidase; HPG, hyperbranched polyglycerol; HPMA, 2-hydroxypropyl methacrylate; HSA, human serum albumin; HSP, heat shock protein; ICAR, initiators for continuous activator regeneration; IFN, interferon-α; LCST, lower critical solution temperature; βLG A, β-lactoglobulin A; mPEG, methoxy PEG; MRI, magnetic resonance imaging; NHS, *N*-hydroxysuccinimide; NIPAM, *N*-isopropyl acrylamide; NMP, nitroxide-mediated polymerization; NQMP, 3-(hydroxymethyl)naphthalene-2-ol; NTA, nitrilotriacetic acid; OPG, osteoprotegerin; PAA, poly(acrylic acid); PAMAM, polyamidoamine; PB, phosphate buffer; PBA, poly(*n*-butyl acrylate); PCB, poly(carboxybetaine); PCR, polymerase chain reaction; PDL, α-poly(D-lysine); PE545, phycoerythrin 545; PEG, poly(ethylene glycol); PEGASYS, PEGylated interferon-α; PEGA-1k, methoxy-PEG acrylamide-1k; PG1, poly[3,5-bis(3-aminopropoxy)benzyl methacrylate]; PGMA, poly(glycidyl methacrylate); photo-ATRP, photoinitiated ATRP; PHPMA, poly(2-hydroxypropyl methacrylate); PISA, polymerization-induced self-assembly; PNA, peptide nucleic acid; PNB, polynorbornene; PNIPAM, poly(*N*-isopropylacrylamide); POEGMA, poly[oligo(ethylene glycol) methyl ether methacrylate]; PPEGA, poly(PEG acrylate); PS, polystyrene; PSS, polystyrene sulfonate; p(*SS*-*co*-PEGMA), poly[sodium 4-styrenesulfonate-*co*-poly(ethylene glycol) methyl ether methacrylate]; QD, quantum dot; RAFT, radical addition–fragmentation chain transfer; RBC, red blood cell; RNA, ribonucleic acid; ROMP, ring-opening metathesis polymerization; ROP, ring-opening polymerization; ROS, reactive oxygen species; SEM, scanning electron microscopy; siRNA, small interfering ribonucleic acid; SMA, sodium methacrylate; SNA, spherical nucleic acid; SPL, scanning probe lithography; ssDNA, single-stranded deoxyribonucleic acid; St, styrene; *t*BA, *tert*-butyl acrylate; TCEP, tris(2-carboxyethyl) phosphine; TEM, transmission electron microscopy; VBA, vinylbenzyl adenine; VBT, vinylbenzyl thymine.

* Corresponding authors at: Max Planck Institute for Polymer Research, Ackermannweg 10, 55128 Mainz, Germany.
E-mail addresses: david.ng@mpip-mainz.mpg.de (D.Y.W. Ng), weil@mpip-mainz.mpg.de (T. Weil).

https://doi.org/10.1016/j.progpolymsci.2020.101241

Contents

1. Introduction

Since the seminal work of Hermann Staudinger published in 1920 [1], polymer science has arguably created significant impact on society in various areas with around 400 million tons of plastics produced annually worldwide since 2015 [2]. The emphasis within the field has also significantly evolved over the past 100 years: starting from the creation of these now ubiquitous plastic materials, their tunable properties in improving the standards of living to the present global concern of plastic contamination in the environment. Objectively, these paradigm shifts have brought scientists back to the drawing board to achieve greater understanding towards these materials and rethink strategies aided by modern synthesis technologies unavailable in the past. As the knowledge within polymer science deepens, the molecular consequences how each individual monomer is arranged along the chain, which also has an impact on their spatial organization, become much more apparent and crucial for the design of macromolecules that exhibit complex programmable behavior. Here, the first connection between synthetic polymer chemistry and Nature's macromolecules was made in order to bridge their differences and to find potential synergistic properties.

Molecular precision is the central hallmark among biomacromolecules, i.e. proteins and nucleic acids, where their sequence is coded elegantly serving both as their unique identity and function. This unique feature, alone, accounts for the vast disparity between synthetic polymers and biomolecules in most of their macromolecular properties. Each biomacromolecule has a defined surface contour within a rigid architecture, where each amino acid residue (for proteins) or nucleotide [for deoxyribonucleic acids (DNAs)] has a precise three-dimensional (3D) coordinate within the folded structure, which is a prerequisite to their biological function. In contrast, the position of monomers within a synthetic polymer is largely governed by a statistical distribution, which can be tailored, only to a limited extent, by controlled polymerization techniques [3–5]. Therefore, the inter- and intramolecular interactions within each polymer chain vary from one to the other, producing irregular nanostructures. As a result, on a molecular level, there is a limit in resolution to accurately determine structure–activity relationships for an observed outcome.

Although biomolecules are often perfect in their molecular construction, they do not possess the breadth in chemical design that polymer science allows. The flexibility in monomer synthesis and the repertoire of polymerization technologies available to synthesize novel materials is unquestionable and has demonstrated its solid potential throughout the decades. From this perspective, the community intuitively realized that the properties of polymer chemistry naturally complement the capabilities of biomolecules and vice versa, leading to the first inception of polymer bioconjugates in the 1970s [6,7]. In 1977, Davis et al. reported the first example of poly(ethylene glycol) (PEG) conjugation to a protein [8]. Since the late 1980s, Hoffman and Stayton et al. have intensively studied the conjugation of temperature-responsive polymers to random and specific sites of protein surfaces [9–13]. After that, functional polymer bioconjugates have developed rapidly for broad disciplines, ranging from therapeutics, nanotechnology, biophysics and materials science (Fig. 1). In this regard, several comprehensive reviews have been consolidated summarizing the progress in each theme [14–16].

While the benefits of these conjugates towards application driven areas are unambiguous, there has been a focus in recent years to investigate how biomolecules and synthetic polymers can influence each other on a fundamental level. Some of the raised questions include the possibility of using sequence information

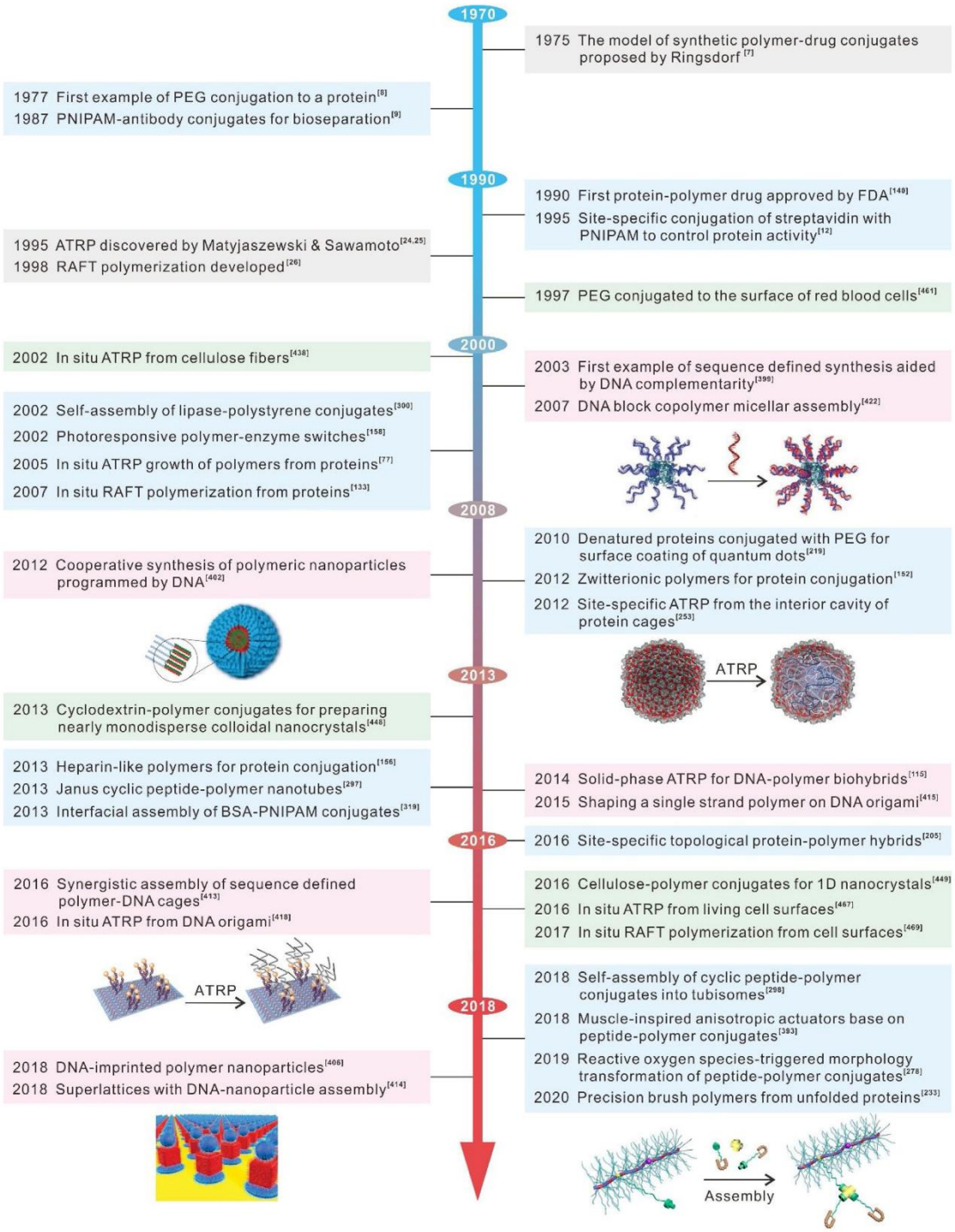

Fig. 1. Timeline of major milestones in the development of polymer bioconjugates. [418,422], Copyright 2016 and 2007. Reproduced with permission from John Wiley and Sons; [253,402], Copyright 2012. Reproduced with permission from Springer Nature; [414], Copyright 2016. Reproduced with permission from the American Association for the Advancement of Science; [223], Copyright 2020. Reproduced with permission from the American Chemical Society.

of biomolecules to guide the precise arrangement of monomers along a synthetic polymer chain, which could not be achieved by state-of-the-art polymer chemistry [17]. Correspondingly, by appending a synthetic polymer onto a biomolecule using modern bioconjugation methods, the stability, bioactivity profile, and self-assembly behavior can be modified and controlled to a large extent by the polymer chain [18]. Within each major class of biomolecules (nucleic acids, proteins/peptides, carbohydrates and lipids), the synthesis strategies to achieve bioconjugates and the impact of the attached synthetic polymer differs greatly as they have different molecular constituents as well as intrinsic 3D structure.

At the molecular level, nucleotides, amino acids, and monosaccharides have their characteristic features that translate separately into the diverse architectures found in Nature. For nucleotides and amino acids, the transformation of these molecules into a defined 3D nano-object is dictated by a set of specific interactions that is predefined among the library of building blocks. Here, the machinations of biology are typically involved in the synthesis, orientation and folding process in a way that the system is funneled and guided through the energy landscape, eventually reaching a precisely defined nano-object. Therefore, it is intriguing for the community whether biomimetic strategies or even biomolecules themselves can be programmed to create the next generation polymeric materials with higher structural definition. Hence, this review provides only a brief background of the synthesis as well as each category of biomolecules while mainly focusing on research highlights that would possibly inspire the development of polymer-bioconjugates in the future.

2. Synthetic approaches for well-defined polymer bioconjugates

The conjugation of synthetic polymers to various biomolecules such as proteins, peptides, and nucleic acids can be realized using one of three synthetic strategies: *grafting to*, *grafting from* and *grafting through* [19,20]. Briefly, *grafting to* is the coupling of a pre-synthesized polymer with a biomolecule, while *grafting from* refers to *in situ* growth of a polymer from a biomolecule or alternatively the synthesis of a biomacromolecule using a pre-formed polymer as the initiator. These two strategies are more frequently used than *grafting through*, which is a strategy to polymerize biomolecule-containing monomers yielding bioconjugates with multiple biofunctional groups along the polymer backbone.

Conventional conjugation of polymers to biomolecules using these strategies may encounter some limitations. For example, the preparation of protein–polymer conjugates through coupling to abundantly presented amines on protein surfaces generates a heterogeneous product mixture with random numbers of polymer chains introduced at arbitrary positions causing significantly reduced biological activity [19]. The isolation and purification of the resultant mixture, including positional isomers, would be daunting and extremely difficult to achieve [21]. In addition, polymers synthesized by traditional polymerization techniques may lack of control over their structure and distribution. Therefore, it is highly desirable to synthesize well-defined polymer bioconjugates, which possess at least the following two characteristics: First, a determined number of polymers are conjugated to specific sites of biomolecules, and second, the polymer chain should have a narrow distribution as well as defined length and architecture.

This chapter aims to summarize the various attempts to meet these two requirements. First, current chemical and biological techniques, such as chemoselective ligations and genetic engineering facilitate the preparation of site-specific and stoichiometric polymer bioconjugates [22,23]. The second requirement has been largely addressed by the rapid development of polymerization techniques including atom transfer radical polymerization (ATRP) [24,25], radical addition–fragmentation chain transfer (RAFT) polymerization [26], nitroxide-mediated polymerization (NMP) [27,28], iniferter radical polymerization [29], ring-opening polymerization (ROP) [30], ring-opening metathesis polymerization (ROMP) [31], and living anionic/cationic polymerization [32,33]. The two most popularly used techniques, ATRP and RAFT polymerization, are discussed in detail in the second section of this chapter. The architecture of polymer bioconjugates is very important for their features and consequent applications. Therefore, an overview of the structural regulation of polymer bioconjugates at the monomer, polymer and conjugate levels is provided in the third section.

2.1. Site-specific polymer conjugation of biomolecules

Due to the large number of lysine residues on the surface of biomolecules, the first-generation methods of polymer conjugation based on the coupling to amines are nonspecific. This type of modification has allowed to reduce the immunogenicity of protein therapeutics as well as increase the stability and circulation time [19]. However, the benefits of preparing site-specific and stoichiometric polymer bioconjugates are obvious, i.e. to purify the product, to provide precise and reproducible control over many properties, particularly their bioactivity [34]. Moreover, well-defined polymer bioconjugates can further be used as precision templates and building blocks for preparing advanced materials with controlled structures.

In order to prepare site-specific polymer bioconjugates, polymers can be directly conjugated to desired locations of biomolecules using various chemoselective interactions. Nevertheless, this strategy often results in low efficiency and conversion due to slow reaction kinetics and the steric effect to connect these high-molecular-weight and sterically demanding macromolecules. Therefore, introduction of functional small molecules in a site-specific manner has been an alternative approach. These small molecules include chemical handles that enable high-efficiency coupling using bioorthogonal chemistries and initiating groups which allow *in situ* polymer growth with controlled polymerization techniques. The site-specific conjugation of polymers and functional small molecules to biomolecules can be achieved through rapidly expanded chemical and bioengineering techniques [35,36].

An effective approach to prepare site-specific polymer bioconjugates is to target specific functional groups at the surface of biomolecule which are less common [19]. For instance, cysteine residues often form disulfide bonds inside the protein structure, and only a limited number of cysteines are accessible providing free thiols on the surface of polypeptides. Therefore, many chemistries, such as disulfide exchange with a pyridyl disulfide and addition reactions with alkenes, alkynes, maleimides or vinyl sulfones to form thioethers, have been employed to target free thiol groups [37]. Among these reactions, the thiol-maleimide interaction under acidic or neutral conditions is one of the most widely used chemistries for preparing site-specific polymer bioconjugates. In addition, disulfide bridges exposed on the surface have also been used as specific sites for the incorporation of polymers [38–42]. Brocchini and Shaunak et al. reported site-specific PEGylation of native disulfide bonds using a bis-thiol alkylating reagent to form a three-carbon bridge [43,44]. Inspired by this work, our group has reported a versatile toolbox of bis-alkylation reagents that re-bridge disulfide bonds of peptides and proteins [45–47]. Tyrosine, which is present in many peptides and proteins represents another possible conjugation site. It reacts with diazonium salts [48] and allows functionalization through a three-component Mannich-type reaction [49]. Due to the lower pK_a than that of amines from lysine, the N-terminal amine is more reactive and can

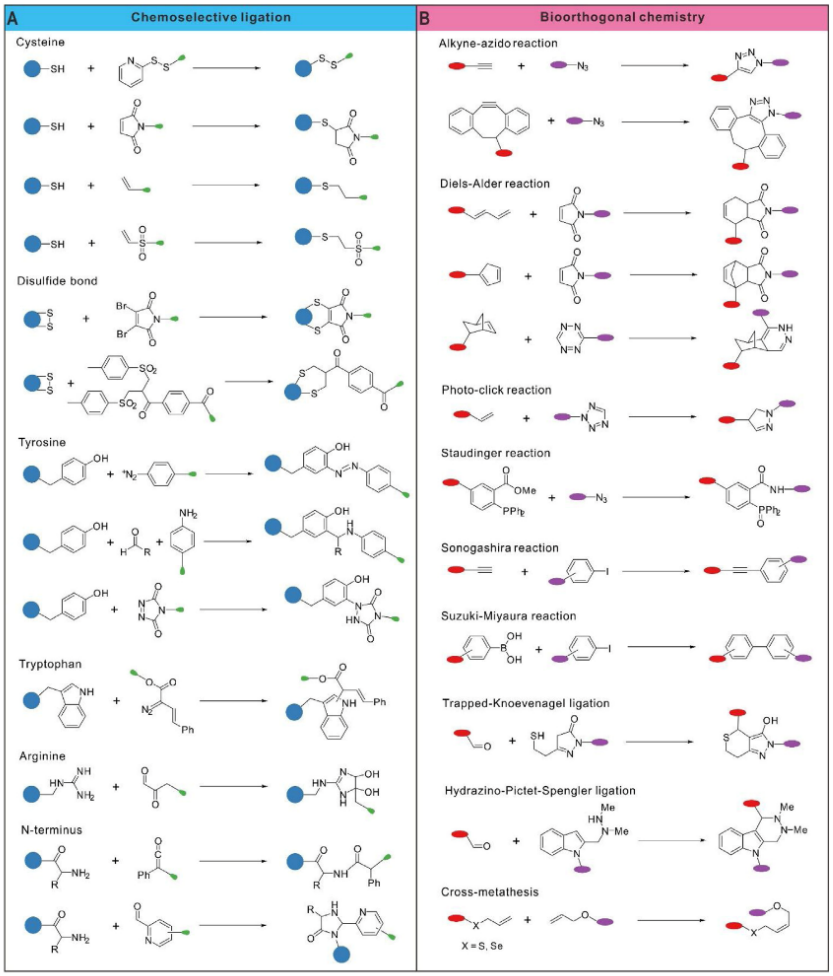

Fig. 2. Representative reactions for site-specific conjugation of biomolecules. (A) Chemoselective ligation with canonical amino acids. (B) Bioorthogonal chemistries available for polymer bioconjugation. The blue circle represents biomolecules and the green pear-shaped symbol indicates polymers or functional small molecules. The red and purple ovals refer to either biomolecules or functional small molecules/polymers, and they are interchangeable. (For interpretation of the references to colour in this figure legend, the reader is referred to the web version of this article.)

therefore also be used for site-specific attachment of polymers and functional small molecules [50–52]. Chilkoti et al. reported the conjugation of an ATRP initiator to myoglobin *via* N-terminal selective transamination, which was further applied for *in situ* ATRP growth of polymers [53]. More examples of the above-mentioned and other natural amino acids for site-specific polymer conjugation are summarized in Fig. 2A and can also be found in other excellent reviews [19,23,54].

In addition to intrinsic reactive groups of native biomolecules, both canonical and non-canonical amino acids can be incorporated at the desired location through bioengineering techniques that provide a platform for site-specific conjugation using chemoselective ligations and a wide range of bioorthogonal chemistries (Fig. 2B). As an example of natural amino acids, cysteine has been genetically introduced into interferon α-2 for site-specific PEGylation, generating well-defined mono-PEGylated proteins with enhanced circulation half-lives and antitumor properties [55,56]. An oligohistidine tag, which binds to a Ni^{2+} complex of nitrilotriacetic acid can be genetically tagged on the C- and N-termini of proteins [57]. Lee et al. demonstrated the site-specific PEGylation of a protein based on a hexahistidine tag, and the polymer bioconjugate provided excellent stability without compromising bioactivity [58]. Non-canonical amino acids with orthogonal chemical reactivity to the 20 canonical amino acids represent a huge toolbox for the preparation of well-defined polymer bioconjugates [59]. For instance, *p*-azidophenylalanine was site-specifically incorporated into proteins enabling a copper-medicated Huisgen [3 + 2] cycloaddition with alkyne end-capped PEG [60]. Matyjaszewski and coworkers incorporated two azide-containing non-canonical amino acids to amino acid residues 134 and 150 on the surface of green fluorescent protein (GFP) by site-directed mutagenesis [61]. These modified proteins were then linked into linear oligomeric strands by PEG with two alkyne ends. A ketone-containing amino acid, *p*-acetylphenylalanine, was also developed for site-specific conjugation of PEG and an aminooxy-derivatized cationic block copolymer to human growth hormone [62] and antibodies [63], respectively. Some reviews have summarized the advances of non-natural amino acids that enable various orthogonal chemistries for site-specific polymer bioconjugation [59,64–66].

Small-molecule initiating groups, which allow *in situ* growth of polymers have also been introduced site-specifically to biomolecules by various techniques. For example, Chilkoti et al. reported two genetic engineering approaches, intein-medicated initiator installation [67] and sortase-catalyzed initiator attachment [68], to introduce an ATRP initiator solely at the C-terminus of proteins and peptides. The sortase-catalyzed initiator attachment was further employed by Gao and coworkers to prepare site-specific protein conjugates with improved stability for cancer therapy [69,70]. Mehl et al. designed the non-canonical amino acid 4-(2′-bromoisobutyramido)phenylalanine, which was used as an initiator for ATRP [71]. It can be genetically engineered at desired sites and therefore represents a general approach to quantitatively encode ATRP initiators to the protein backbone.

Most reported polymer bioconjugates are based on irreversible covalent interactions. However, the conjugation of synthetic polymers and biomolecules with cleavable linkers may provide additional advantages such as more spatiotemporal control over the conjugates and on-demand release of biomolecules [72–75]. By combining enzymatic and chemical bioorthogonal coupling strategies, Meinel et al. demonstrated the site-specific PEGylation of insulin-like growth factor I with a protease-sensitive peptide linker [76]. The growth factor could be released after exposure of the PEGylated conjugate to activated matrix metalloproteinases in inflamed tissues, resulting in the recovery of its bioactivities. In addition, reversible non-covalent interactions such as biotin-streptavidin recognition [77] and host–guest interactions [78,79], have also been used for site-specific polymer conjugation. Anderson and coworkers reported the supramolecular PEGylation of insulin through strong non-covalent binding of cucurbit[7]uril to its N-terminal phenylalanine residue [80]. In comparison to covalent conjugation, this supramolecular approach holds a unique advantage that the authentic therapeutic entity remains unmodified.

Above, we have introduced various strategies for the site-specific polymer conjugation of proteins and peptides. Although many chemical and bioengineering techniques have been established for the site-specific labeling of DNA and ribonucleic acid (RNA) with functional small molecules [81–85], current approaches for polymer conjugation to nucleic acids mainly proceed at the terminus of the oligonucleotide sequence, which results in nucleic acid-containing block copolymers [86,87]. Generally, these methods can be categorized into solution conjugation chemistry and solid-phase synthesis. As amino- and thiol-terminated oligonucleotides are commercially available, functional small molecules and hydrophilic polymers can be easily introduced *via* the formation of an amide or disulfide bond in solution [88–90]. For example, Weil et al. prepared two RAFT agent-terminated single-stranded DNA (ssDNA) sequences *via* *N*-hydroxysuccinimide (NHS) or pentafluorophenyl ester coupling, which were used for photoinduced RAFT polymerization to synthesize well-defined DNA–polymer conjugates [91]. In addition, Michael addition [92] and the copper-catalyzed azide–alkyne cycloaddition (CuAAC) [93] are also popular reactions for the highly efficient conjugation of polymers to nucleic acids. Due to their different solubilities, the coupling efficiencies of hydrophobic polymers with nucleic acids in solution are often much lower. Therefore, solid-phase synthesis approaches were developed. In this regard, the use of 2-cyanoethyl-*N*,*N*-di*iso*propylphosphoramidite groups is a commonly applied method to introduce functional groups to the 5′-end of oligonucleotides *via* solid-phase synthesis [94]. Particularly, fully automated solid-phase synthesis of DNA conjugates based on hydrophobic polymers such as poly(propyleneoxide) in DNA synthesizers is now available [86]. Recently, Matyjaszewski, Das and coworkers reported the automated synthesis of DNA–polymer conjugates by photomediated ATRP using a DNA synthesizer [95]. In addition, molecular biology techniques such as polymerase chain reactions (PCR) have also been successfully used for polymer conjugation to nucleic acids [96]. Previously, two excellent reviews have been published that deliver a comprehensive overview on DNA-containing amphiphilic block copolymers [86,87].

Other small biomolecules such as lipids, monosaccharides, and oligosaccharides could be also connected to polymers in a site-specific fashion. The obtained biohybrids can serve as precision building blocks for the construction of hierarchical structures. For instance, Akiyoshi et al. synthesized amphiphilic carbohydrate-conjugated poly(2-oxzoline)s using a small molecule maltotriose-containing initiator enabling the preparation of polymer vesicles with molecular permeability [97]. Additional examples will be discussed within each class of polymer bioconjugates in chapter 5.

2.2. Controlled radical polymerizations for polymer bioconjugation

2.2.1. Atom transfer radical polymerization

ATRP is a powerful controlled radical polymerization technique, which enables precise synthesis of functional polymers with determined molecular weight and narrow molecular weight distribution [98]. Due to its applicability to various monomers, solvents, catalysts, and reaction conditions, ATRP has been employed for the preparation of a broad range of advanced polymeric materials with controlled architecture and functionality [5,99]. Because it can be carried out at room temperature in aqueous solution, ATRP is particularly useful for the conjugation of polymer chains to biological entities such as proteins, peptides, nucleic acids, viruses, and even live cells. Fig. 3A shows representative ATRP initiators reported in the literature for the synthesis of polymer bioconjugates by ATRP using either *grafting to* or *grafting from* approach.

Maynard et al. reported the preparation of thiol-reactive polymers by ATRP using an initiator functionalized with a pyridyl disulfide group, which were then selectively grafted to the single surface-exposed cysteine group of bovine serum albumin (BSA) [100]. However, the *grafting to* approach often encounters low coupling efficiency especially for high molecular weight polymers due to their steric demand and the challenging removal of unreacted polymers and biomacromolecules. To avoid these limitations, the *grafting from* strategy has become a more popular procedure because ATRP initiators can be easily attached to biomolecules using both chemical means and genetic engineering. As illustrated in Fig. 3B, Maynard et al. reported the first example of *in situ* ATRP synthesis of protein–polymer conjugates using modified streptavidin as a macroinitiator in 2005 [77]. Streptavidin is an intensively studied protein that binds four biotin ligands. Poly(*N*-isopropylacrylamide) (PNIPAM) chains were quantitatively conjugated to the protein at the biotin binding sites only, and the bioactivity of streptavidin remained unaffected. This straightforward approach was also extended by the same group to other proteins including BSA and the enzyme lysozyme [101]. Similarly, chymotrypsin modified with 2-bromoisobutyramide was also used to initiate ATRP of nonionic, cationic, and anionic monomers for the synthesis of near-uniform protein–polymer conjugates while retaining 50–86% of the original enzyme activity [102]. Chilkoti et al. demonstrated the *in situ* ATRP growth of a brush-like polymer, poly[oligo(ethylene glycol) methyl ether methacrylate] (POEGMA), with narrow distribution and high yield, solely from the N-terminus of myoglobin or C-terminus of GFP [53,67]. The resulted site-specific and stoichiometric bioconjugates showed significantly improved pharmacological profiles such as increased blood exposure compared to those unmodified proteins.

With the rapid expansion of different monomers and biomolecules, ATRP as a versatile tool to prepare polymer bioconjugates has also greatly evolved especially under biologically

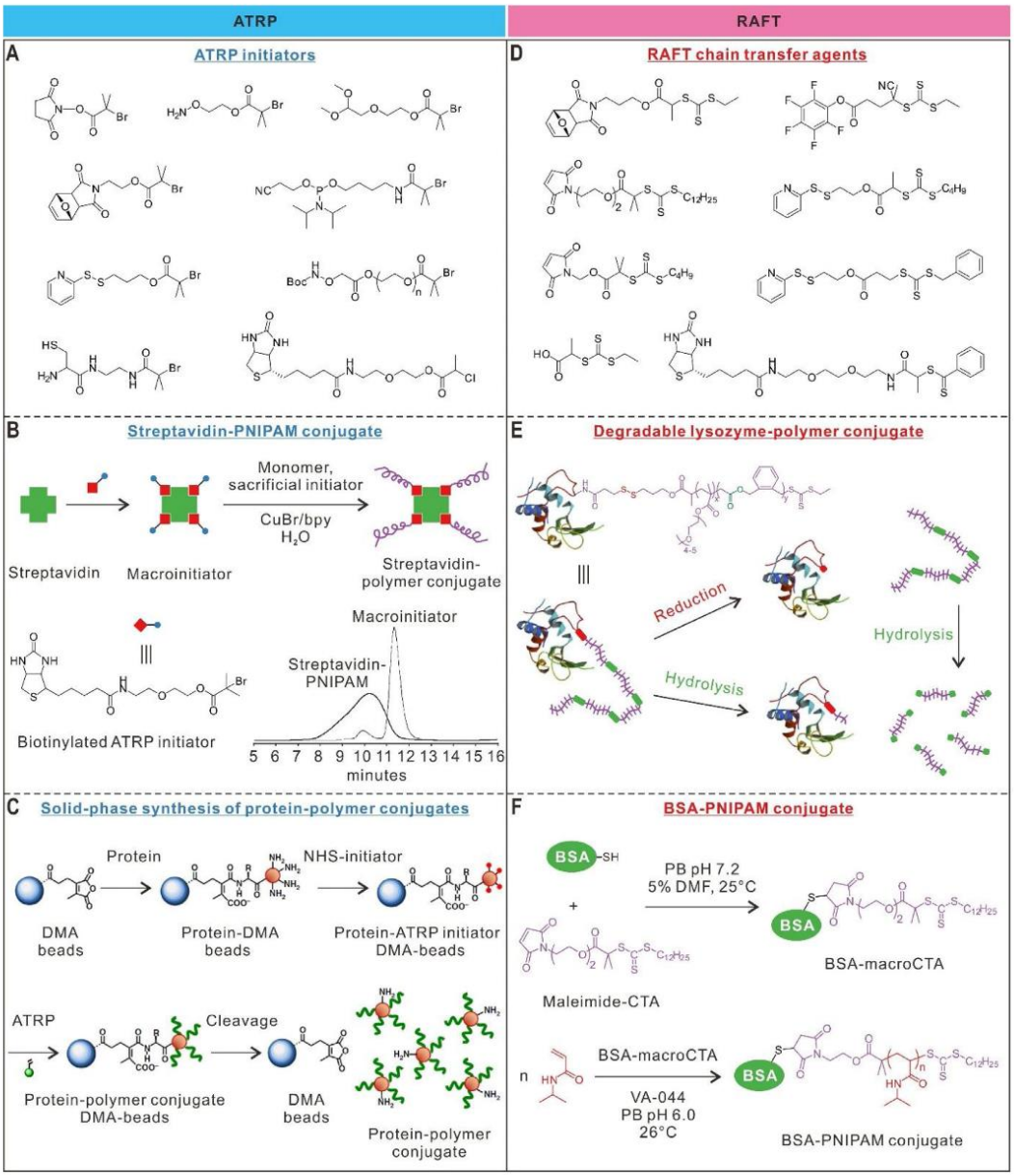

Fig. 3. ATRP and RAFT polymerization for polymer bioconjugation. (A) Selected examples of ATRP initiators reported for polymer bioconjugation; (B) Synthesis of streptavidin-PNIPAM conjugates by *in situ* ATRP; (C) Solid-phase synthesis of protein–polymer conjugates *via* ATRP from protein macroinitiators reversibly immobilized on dialkyl maleic anhydride (DMA)-modified agarose beads; (D) Selected examples of RAFT CTAs reported for polymer bioconjugation; (E) Degradable lysozyme–polymer conjugate synthesized by RAFT polymerization using the *grafting to* approach; (F) Site-specific and *in situ* RAFT polymerization of *N*-isopropylacrylamide (NIPAM) for the synthesis of BSA–PNIPAM conjugate. (B) [77], Copyright 2005. Reproduced with permission from the American Chemical Society. (C) [114], Copyright 2018. Reproduced with permission from Springer Nature. (E) [130], Copyright 2015. Reproduced with permission from Elsevier Ltd. (F) [135], Copyright 2008. Reproduced with permission from the American Chemical Society.

relevant conditions [5]. For example, new ATRP techniques such as activators regenerated by electron transfer (ARGET) ATRP [103–105], initiators for continuous activator regeneration (ICAR) ATRP [106,107], electrochemically mediated ATRP (eATRP) [108–110], and photoinitiated ATRP (photo-ATRP) [111–113] have been developed by continuous regeneration of active catalysts with various external stimuli, which allow the preparation of polymer conjugates with low catalyst loading under biologically benign polymerization conditions. Russell et al. demonstrated the solid-phase synthesis of protein–polymer conjugates by ATRP from protein macroinitiators reversibly immobilized on modified agarose beads (Fig. 3C) [114]. This effective and simple method is readily automated and therefore could dramatically reduce the time for the synthesis and purification of protein–polymer conjugates. Matyjaszewski, Das and coworkers also reported a straightforward method for the solid-phase incorporation of an

ATRP initiator onto a DNA strand, allowing the direct preparation of DNA–polymer conjugates on the solid support [115]. Although ATRP has been successfully employed to grow polymers from biomolecules under aqueous conditions, its oxygen sensitivity is still a vexing challenge. Inspired by aerobic respiration of cells, Matyjaszewski et al. recently demonstrated a fully oxygen tolerant well-controlled ATRP, which used glucose oxidase (GOx) to continuously catalyze the conversion of oxygen to carbon dioxide in the presence of glucose and sodium pyruvate [116]. This "green" ATRP procedure could be conducted under air exposure and it was successfully used for the synthesis of well-defined protein–polymer conjugates. Based on the exciting new development, they further reported an "oxygen-fueled" ATRP using a biocatalytic system composed of GOx and horseradish peroxidase with ppm level of Cu catalyst [117]. This enzymatic cascade polymerization, which requires continuous oxygen supply to generate radicals, was used to prepare BSA–POEGMA and DNA–POEGMA bioconjugates.

2.2.2. Reversible addition–fragmentation chain transfer polymerization

RAFT polymerization is another controlled radical polymerization, which has been popularly used for the preparation of well-defined polymer bioconjugates [118,119]. It tolerates various chemical groups and is applicable for a broad range of solvents and monomers [120]. Similar to ATRP, RAFT polymerization has been employed to synthesize functional polymers of determined molecular weight, low polydispersity, as well as precisely designed architecture and functionality [121]. One distinct advantage of the RAFT approach is that metal catalysts are not needed. Instead, chain-transfer agents (CTAs) such as dithioesters, dithiocarbamates, trithiocarbonates, and xanthates are required because polymers are generated *via* equilibrium between a growing radical and the RAFT CTA [122]. Therefore, the structure of the CTA is of great significance for the controlled growth of polymers. Fig. 3D displays selected RAFT CTAs for the synthesis of polymer bioconjugates.

Similar to ATRP-based systems, polymer bioconjugates can also be prepared by RAFT polymerization using both *grafting from* and *grafting to* approaches [123–128]. For instance, α-chymotrypsin, an enzyme that digests other proteins, was conjugated to well-defined polymers made by RAFT polymerization [129]. These conjugates were able to significantly improve the stability of the protease without affecting its bioactivity. Maynard et al. conducted RAFT copolymerization of cyclic ketene acetal monomer with poly(ethylene glycol methyl ether methacrylate) yielding functional polymers, which were subsequently conjugated to lysozyme through a reducible disulfide linkage [130]. As illustrated in Fig. 3E, the polymer is backbone degradable and also could be easily cleaved off from the lysozyme–polymer conjugate in a reducing environment. For the *grafting from* approach, Börner et al. demonstrated the RAFT polymerization for the synthesis of bioactive oligopeptide–polymer conjugates using a trithiocarbonate-based peptide–CTA [131]. DNA–polymer conjugates on a planar solid support were prepared by covalently attaching CTAs to ends of surface-immobilized oligonucleotides and then initiating RAFT polymerization [132]. The first example of RAFT-mediated *in situ* formation of protein–polymer conjugates was reported by Bulmus, Davis, and coworkers [133]. They synthesized site-specific BSA–poly(PEG acrylate) (PPEGA) conjugates *via* gamma-radiation-initiated RAFT polymerization using a mixture of water and *N*,*N*-dimethylformamide as the solvent. However, the gamma radiation source may cause structural damage on some biological molecules. To avoid this detrimental effect and also the usage of organic solvents, a room temperature azo-initiator and a new water-soluble RAFT CTA were used for the *in situ* generation of well-defined BSA–PNIPAM and BSA–poly(hydroxyethyl acrylate) conjugates in completely aqueous solutions [134]. Importantly, the structural integrity and esterase-like activity of BSA were retained under the polymerization conditions, showing the general applicability of this RAFT approach for the preparation of bioactive protein–polymer conjugates. In these two systems, both RAFT CTAs [general formula Z—C(=S)S—R] were attached to BSA through the "Z-group". As shown in Fig. 3F, the Sumerlin group synthesized a new type of macroCTA by conjugating BSA to the "R-group" of the CTA with thiol–maleimide coupling, which was subsequently applied for room temperature RAFT polymerization of NIPAM in aqueous media [135]. This design provides better polymerization control due to reduced steric hindrance and the labile thiocarbonylthio moiety at the free chain end could be potentially used for further functionalization. In addition, they also prepared well-defined block copolymer conjugates of BSA–PNIPAM-*b*-poly(*N*,*N*-dimethylacrylamide) by two consecutive *grafting from* RAFT polymerizations using this macroCTA [136]. Apart from these two conventional strategies, Thang et al. have recently reported the *grafting through* RAFT polymerization of a methacrylamide monomer containing a pending RGD peptide to afford well-defined peptide–polymer conjugates that were used for enhanced cell adhesion [137].

2.3. Structural design of polymer bioconjugates

2.3.1. Variation of the polymer chain

The conjugation of PEG to peptides and proteins, known as PEGylation, has been widely used in therapeutic fields to improve the stability and biopharmaceutical performance [138]. PEG is regarded as safe and there are many PEGylated protein drugs which have been approved by US Food and Drug Administration (FDA) in the market [139]. However, PEG can also impose a negative impact on the biomolecule such as reduced bioactivity, non-degradability, and immunological responses [140]. Therefore, a variety of alternative functional polymers have been developed for the conjugation of different biomolecules. For example, poly(quaternary ammonium) was grafted from the chymotrypsin surface to afford a dense cationic shell for the modulation of substrate specificity and inhibitor binding [141]. A series of polymers of varying functionality and length was conjugated to lysozyme to investigate the impact of the respective polymer on enzyme stability and activity [142]. Russell, Whitehead and coworkers prepared BSA–polymer conjugates with a phenylpiperazine-containing polymer, which selectively facilitated transepithelial protein transport [143]. Gao et al. have grafted poly(*N*,*N*'-dimethylamino-2-ethyl methacrylate) site-specifically from the N-terminus of GOx to modulate H_2O_2 generation for cancer starvation and H_2O_2 therapy [144]. Reactive water-soluble, azlactone-containing copolymers synthesized by RAFT polymerization were conjugated to holo-transferrin and ovotransferrin forming protein bioconjugates that were internalized by cells via receptor-mediated endocytosis [145].

Biomimetic polymers inspired by biological components found in Nature have also been designed for bioconjugation. Biocompatible, zwitterionic polymers with cell membrane-mimicking characteristics were employed to construct biomaterials minimizing the interactions with proteins and cells [146–151]. Jiang et al. reported the conjugation of zwitterionic poly(carboxybetaine) (PCB) (Fig. 4A) using α-chymotrypsin as a model protein and PCB was found to protect proteins from chemical and thermal denaturation [152]. Remarkably, the PCB conjugates demonstrated superior stability in comparison to the corresponding PEG conjugates of similar molecular weights (Fig. 4B) and similar hydrodynamic size (Fig. 4C). More importantly, enhanced binding affinity with a peptide-based substrate was observed for PCB conjugates which could be attributed to differences on how PEG and PCB affected substrate binding affinities: PEG reduces

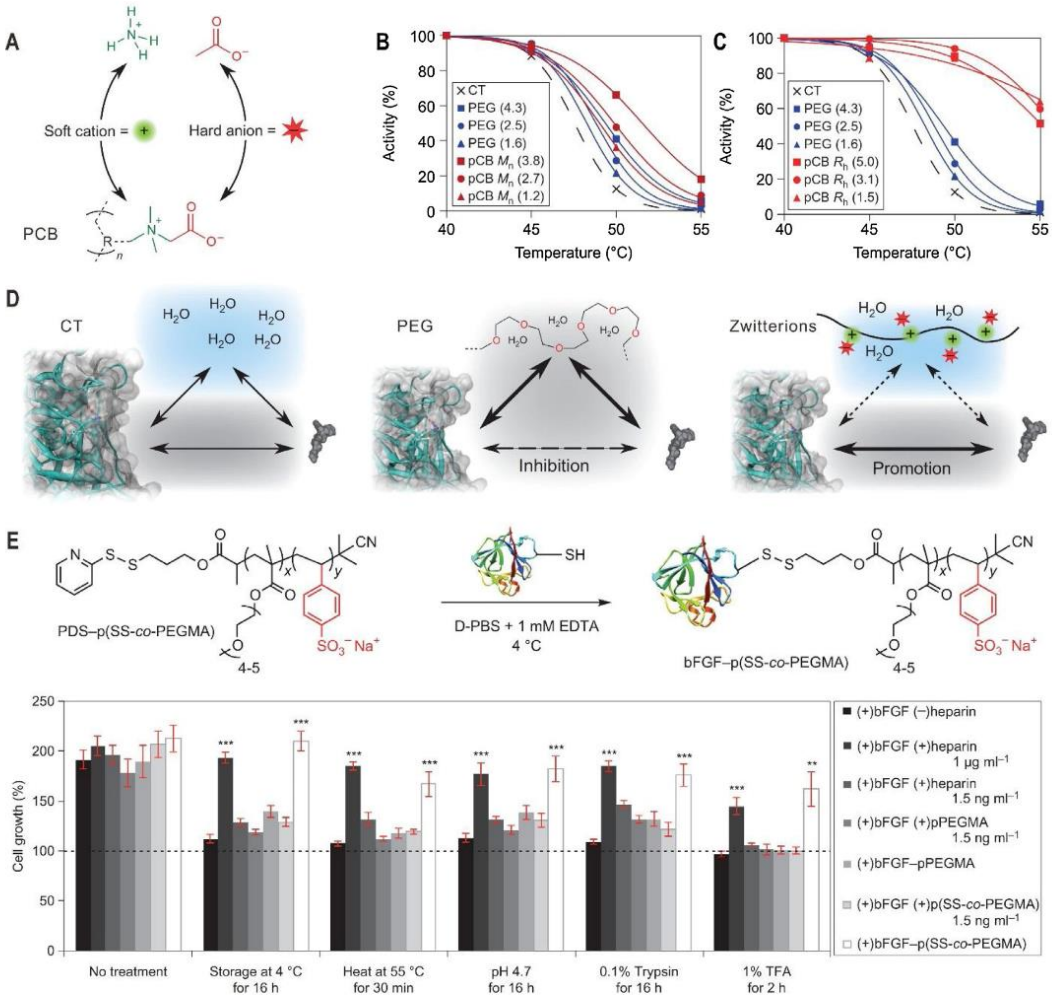

Fig. 4. Biomimetic polymers for protein conjugation. (A) The structure of PCB and its relationship with ammonium acetate. The R group represents a methacrylate backbone. (B and C) Relative activity of PEG and PCB conjugates of similar molecular weight (M_n) and similar hydrodynamic size (R_h). (D) Mechanism of how PEG and PCB polymers affect binding affinity. (E) Structure of a heparin-mimicking polymer, poly[sodium 4-styrenesulfonate-*co*-poly(ethylene glycol) methyl ether methacrylate] [p(SS-*co*-PEGMA)] and its conjugation to protein bFGF. The bottom shows the stability of the resulting polymer bioconjugate bFGF-p(SS-*co*-PEGMA) and its impact on cell growth compared to control samples after different treatments. It is obvious that the bioactivity of the conjugate was comparable to the positive control which had a 700-fold molar excess of heparin, and significantly higher than other control samples, under all environmental stresses. [152,156]. Copyright 2012 and 2013, respectively. Reproduced with permission from Springer Nature.

enzyme–substrate hydrophobic–hydrophobic interactions due to its amphiphilic features while super-hydrophilic PCB promotes these interactions and the binding affinity through strong ionic structuring of water molecules (Fig. 4D). Recently, PCB was also conjugated to insulin *via* amine–NHS ester conjugation and the conjugate showed increased ability to lower *in vivo* glucose compared with native insulin [153]. Gao et al. presented the conjugation of zwitterionic poly(2-methacryloyloxyethyl phosphorylcholine) to the C-terminus of interferon-α, and the resulting polymer bioconjugates showed significantly improved *in vitro* antiproliferative bioactivity and *in vivo* antitumor efficacy compared to those of PEGylated interferon-α [154]. Inspired by the natural disaccharide trehalose, which protects proteins and cells in many plants and animals, well-defined glycolpolymers with pendant trehalose side chains were prepared for stabilization of protein bioconjugates to environmental stressors [155]. Similarly, a heparin-mimicking polymer consisting of styrene sulfonate units and PEG methyl methacrylate units was covalently conjugated to basic fibroblast growth factor (bFGF) [156]. As shown in Fig. 4E, the obtained bioconjugate exhibited significantly improved stability against heat, mild and harsh acidic conditions, storage and proteolytic degradation compared to native and PEGylated bFGFs.

The conjugation of smart polymers, which can respond to various stimuli such as pH, temperature, and light to biomolecules, may allow on-demand regulation of solubility, stability and bioactivity of the resulting conjugate [157]. For instance, light was successfully used to tune enzyme catalytic activity when an azobenzene-containing copolymer was conjugated to a distinct location near the catalytically active site [158]. Thermo-responsive PNIPAM is one of the most famous smart polymers, which has been attached to various biomolecules such as proteins, peptides, nucleic acids, and polysaccharides through different conjugation strate-

gies [159]. Haddleton et al. reported the conjugation of PNIPAM to BSA, lysozyme, bovine hemoglobin, salmon calcitonin, and insulin by aqueous single electron-transfer living radical polymerization [160]. PNIPAM–DNA conjugates were also synthesized and used for preparation of pH and temperature dual-responsive hydrogels, which could find potential applications for sensing and smart drug release [161]. For more examples on the conjugation of stimuli-responsive polymers to biomolecules, the reader can refer to other reviews [157,159].

Because nondegradable polymers may accumulate in biological systems or persist in the environment, the design and synthesis of degradable polymers has received great significance especially for therapeutic applications. For instance, acid-degradable PEG chains were synthesized by introducing a cleavable acetaldehyde acetal into the backbone, which were employed for BSA conjugation [162]. Well-defined and water-soluble polyphosphoesters prepared by living anionic polymerization with chain-end functionalization have also been used for protein conjugation [163]. The resulting bioconjugates exhibited comparable bioactivities compared to PEGylated proteins, and the polymer shell degradation at physiological conditions was proved by online triple detection size exclusion chromatography and gel electrophoresis. Recently, the Maynard group has developed a powerful strategy to prepare a series of degradable polycaprolactones with different side groups including trehalose, lactose, glucose, carboxybetaine, and oligo(ethylene glycol), by combining ROP and thiol–ene post-modification [164]. These degradable polymers were conjugated to protein granulocyte colony-stimulating factor offering enhanced stability against storage and heat stressors.

2.3.2. Alteration of the polymer topology

In addition to functionality and degradability, the polymer topology is also an important factor, which could have a profound influence on the biomolecule and the unique properties of the resulting polymer bioconjugates [139]. This part highlights representative examples on the bioconjugation of synthetic polymers with various controlled topologies such as block copolymers, hyperbranched polymers and dendrimers. Although biomolecule-conjugated polymer networks, particularly hydrogels, have broad applications in the biomedical fields [165,166], these works have not been included because their resulting structures are not clearly defined.

Beside linear homopolymers, functional random and block copolymers have been extensively used for bioconjugation [167,168]. For example, Stayton et al. modulated the activity and aggregation properties of the conjugate of streptavidin with a dual stimuli-responsive block copolymer PNIPAM-*b*-poly(acrylic acid) (PNIPAM-*b*-PAA) [169]. Through two consecutive *grafting from* reactions *via* RAFT polymerization, Sumerlin et al. prepared block copolymer conjugates of BSA [136] and lysozyme [170]. Moreover, block copolymer conjugates of lysozyme were also prepared by combining the *grafting to* and *grafting from* strategies [171].

Synthetic polymers of brush-like, hyperbranched, and dendritic topologies have been widely reported for biomedical applications demonstrating some unique features in comparison to their linear counterparts [172–178]. The conjugation of branched polymers to biomolecules has therefore emerged as an exciting new area to achieve bioconjugates with improved stability and prolonged circulation times *in vivo* [140,179–183]. In order to investigate the impact of the polymer architecture on bioconjugate activity, three polymers with similar molecular weights but different topologies ranging from linear, loosely branched, to densely branched were conjugated to osteoprotegerin (OPG), a protein that can be used for inhibition of bone resorption [184]. The obtained bioconjugates were nontoxic, and *in vivo* studies indicated an increase in the bone mineral density of rats treated by the loosely branched polymer–OPG bioconjugate. Klok et al. reported squaric acid mediated synthesis of functional polymers with varying architectures including linear, midfunctional, hyperbranched, and linear-*block*-hyperbranched polyglycerol copolymers, which yielded a broad range of BSA and lysozyme polymer bioconjugates [185]. Bioactivity of conjugates made from high molecular weight midfunctional polyglycerol copolymers was obviously higher than that of linear polymers of similar molecular weights. Brush-like polymer POEGMA has been demonstrated to significantly improve the circulation time and antitumor effect of myoglobin and GFP [53,67]. Exendin-4, a peptide drug for type 2 diabetes mellitus, was also conjugated by POEGMA site-specifically at the C-terminus, and the resulting bioconjugate demonstrated reduced blood glucose for up to 120 h in fed mice with one single subcutaneous injection [186]. Importantly, the reactivity to anti-PEG antibodies could be completely eliminated by optimizing the length of PEG side chains, showing distinct advantages of these novel bioconjugates compared to those based on linear PEG polymers.

Dendrimers and dendrons are highly branched molecules, which allow the preparation of precisely defined polymer bioconjugates [187,188]. For example, our group demonstrated the dynamic covalent attachment of a positively charged polyamidoamine (PAMAM) dendron to different enzymes including trypsin, papain, and DNase I *via* the pH-responsive interaction between salicyl hydroxamate and boronic acid (Fig. 5A) [189]. The formation of dendronized enzyme constructs was first confirmed by a fluorescence assay, which demonstrated the stoichiometric substitution of fluorogenic Alizarin Red S by the salicyl hydroxamate containing PAMAM dendron (Fig. 5B). At pH 7.4, the functional dendron formed a protective shell on the surface of active enzymes blocking the catalytic sites. Due to the positive charges of the conjugated PAMAM dendrons, these enzyme–dendron conjugates could be efficiently internalized by A549 cells and colocalized in the acidic intracellular compartments (Fig. 5C). The enzyme activity was then recovered causing cytotoxicity and these smart conjugates can therefore serve as structurally defined biotherapeutics. Leroux et al. reported a polycationic dendronized polymer poly[3,5-bis(3-aminopropoxy)benzyl methacrylate] (PG1) for the stabilization of orally administered enzymes in the gastrointestinal tract through covalent conjugation [190]. Specifically, they compared the retention and stabilizing effect of four polymers with different architectures and functional groups (Fig. 5D). Enzymes conjugated to the positively charged dendronized polymer PG1 showed prolonged retention due to the strong mucoadhesive interactions with mucin on the stomach wall (Fig. 5E). In addition, this dendronized polymer could also stabilize the enzyme for over three hours in the stomach of rats while the other three polymers, including α-poly(D-lysine) (PDL), methoxy PEG (mPEG) and PAA, provided little or no retention/protection.

2.3.3. Manipulation of the conjugate architecture

The structural control of polymer bioconjugates is not only focused on the polymer part. Due to the flexibility of using various synthetic tools, the conjugate architecture can also be programmed yielding innovative constructs with superior properties for specific applications [191]. To mimic protein dimerization occurring in Nature, well-defined linear PNIPAM produced by RAFT polymerization was functionalized with protein-reactive maleimide groups at both ends to synthesize homodimeric protein–polymer conjugates using a V131C mutant T4 lysozyme as the model protein [192]. The maleimide–thiol coupling was able to prepare the homodimers in 21% yield after 16 h. To increase the conjugation efficiency, the rapid tetrazine–*trans*-cyclooctene ligation was applied to afford the respective dimers in 38% yield within 1 h [193]. Recently, Bode et al. reported that potassium 2-pyridyl acyltrifluoroborates can be used to construct homodimeric protein–polymer conjugates under near

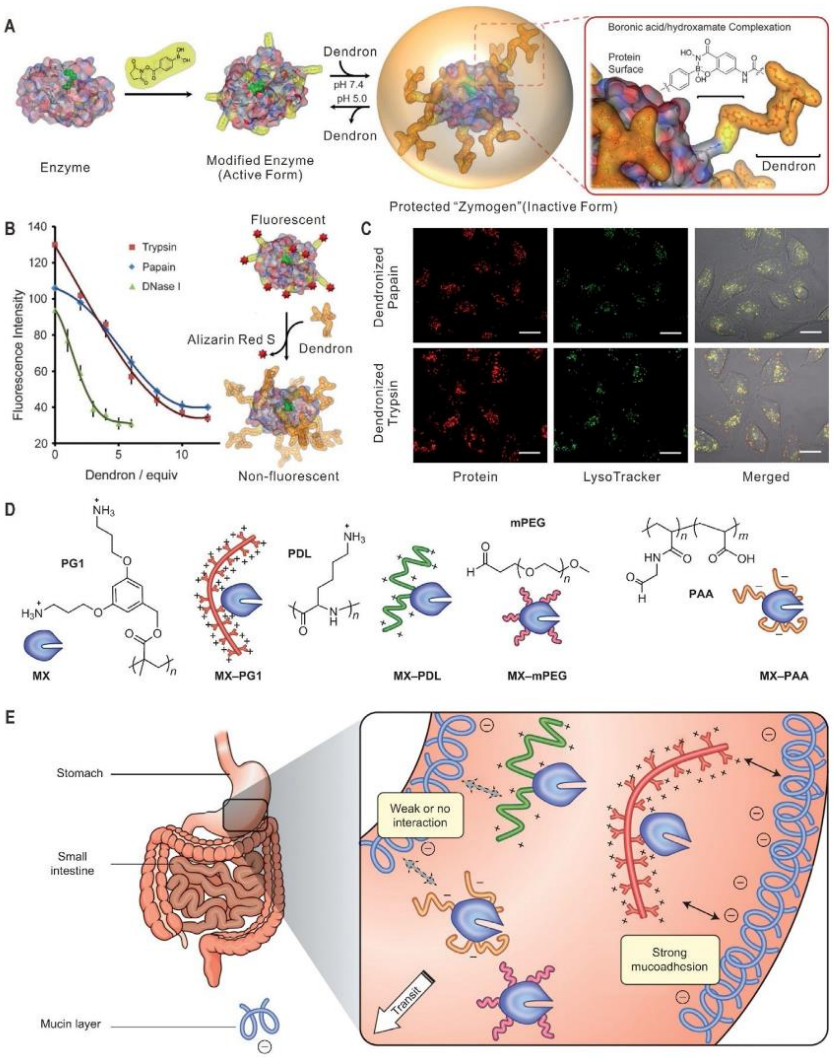

Fig. 5. Branched polymers for bioconjugation. (A) Preparation of supramolecular protein–dendron conjugates based on the pH-controlled interaction between boronic acid and hydroxamate. The residues highlighted in green represent catalytic sites. (B) The quantitative replacement of Alizarin Red S by the PAMAM dendron on protein surfaces revealed by a fluorescence assay. (C) Confocal microscopy images showing the dendron-mediated uptake by A549 cells and colocalization of these dendronized proteins within acidic cellular compartments. Scale bars: 20 μm. (D) Chemical structures of the four polymers used for enzyme conjugation and gastric stabilization. (E) The behavior of enzyme–polymer conjugates in the gastrointestinal tract. [189], Copyright 2014. Reproduced with permission from John Wiley and Sons Inc. [190], Copyright 2013. Reproduced with permission from Springer Nature. (For interpretation of the references to colour in this figure legend, the reader is referred to the web version of this article.)

equimolar conditions with a good yield of 82% [194]. Apart from these examples, heterodimeric protein–polymer conjugates have also been prepared by linking two different proteins with heterotelechelic polymers [195–198].

The conjugation of one polymer with multiple biomolecules, particularly functional peptides, forming multivalent systems is proven to be a successful strategy for enhancing specific molecular recognition in biological systems [199]. As an example, Klok et al. synthesized a series of multivalent side chain peptide–polymer conjugates to inhibit HIV-1 entry into a host cell and improved antiviral activity was achieved by midsized polymer conjugates [200]. To enhance targeting of integrin-expressing cells, a new type of "polymultivalent" polymer–cyclic RGD peptide cluster conjugates with two levels of multivalency were introduced and up to ~2 orders of magnitude potency enhancement was observed in a competitive cell adhesion assay [201].

The architecture of bioconjugate has significant effects on its properties and applications [202–204]. Based on a one-pot, two-step polymerization process, Lu et al. reported the easy synthesis of heterotelechelic poly(amino acid)s offering rapid access to protein–poly(amino acid) conjugates with various topologies (knot-like, dumbbell-like, and circular) under mild conditions [205]. This approach was based on two orthogonal chemical handles, including a thioester for native chemical ligation and a polyglycine for sortase A-mediated ligation, which were *in situ* installed at the C- and N-termini of substrate poly(amino acid)s. Notably, the head-to-tail cyclic conjugates using therapeutic interferon-α as a model protein exhibited dramatically improved

protease resistance and thermostability. In a recent study, they further investigated the antitumor pharmacological activity of the cyclic conjugate in comparison to its linear counterparts [206]. *In vitro* and *in vivo* experiments revealed distinct advantages of the cyclic conjugate in antiproliferative activity, circulation time, tumor retention and penetration, as well as antitumor efficacy.

3. Protein/peptide–polymer conjugates

Peptides and proteins are oligomers and polymers composed of amino acids, which often possess hierarchical structures and specific biological functions. Through conjugation of synthetic polymers, a novel class of soft hybrid materials, namely "protein/peptide–polymer conjugates" can be obtained combing the unique advantages of both natural and synthetic polymers [18,19,191]. One of the most attractive features of natural building blocks is their structure precision in view of sequence, molecular weight, 3D structure and supramolecular complex formation based on precisely defined intra- and intermolecular interactions. In chapter 2, we have discussed the site-specific polymer conjugation at the surface of individual native proteins. The main focus of this chapter is to discuss important advances for the preparation of peptide/protein–polymer conjugates, which have, to some extent, well-defined architectures.

In the first section, we introduce the conjugation of synthetic polymers to precision templates derived from native proteins, focusing on denatured proteins and protein cages. Thereafter, self-assembly of protein/peptide–polymer conjugates into defined architectures such as spherical nanoparticles, fibers, vesicles, and nanotubes are summarized. Moreover, the formation of well-defined structures on surfaces including the covalent immobilization of biomolecules by polymer brushes to gain spatial control over the respective biological activities are also discussed. This wide spectrum of well-defined structures based on protein/peptide–polymer conjugates enables various applications in both biomedical and non-biological areas, ranging from cancer treatment, antibacterial, and antivirus to artificial membrane channels, enzymatic catalysis, and soft actuators. In the last section of this chapter, we highlight selected examples of the most exciting applications, in which structural precision and well-defined structure formation play critical roles for enabling the specific application.

3.1. Proteins as precision templates for polymer conjugation

Proteins are the main components in most biological processes enabling, for example, structure formation, catalysis and transport. These unique features are based on their defined monomer sequence and precise 3D structures. In addition, some proteins are able to form well-defined higher order superstructures under specific conditions [207]. Therefore, proteins represent ideal building blocks to construct well-defined nanomaterials by providing precise structure information at different levels. Here, we highlight recent advances on the construction of well-defined nano-architectures based on protein-derived templates such as the monodisperse polypeptide backbone of denatured proteins as well as highly symmetrical and ordered protein cages.

3.1.1. Precision nanomaterials based on denatured proteins

Globular proteins can be denatured by external stress such as solvents, inorganic salts, exposure to acids or bases, and by heat, which alters their secondary and tertiary structures but retains the peptide bonds of the primary structure between the amino acids [208]. Since all structural levels of the protein determine its function, the protein is usually no longer bioactive once it has been denatured. However, unfolded proteins could be regarded as monodispersed biopolymers providing well-defined contour length and various functional groups at determined positions along the main chain. In 2003, Whitesides et al. pioneered an approach for preparing linear polymers with determined chain lengths and functional groups at defined locations along the chain by acylation of denatured proteins [209]. In the past decade, our group has explored denatured proteins as a unique polymer platform for the construction of defined nano-architectures and nanomaterials for various applications [210]. For protein denaturation, protein aggregation during the denaturation process needs to be strictly avoided as it is very challenging to disaggregate the protein agglomerates once they have precipitated, which reduces yields and makes purification more difficult. Typically, chaotropic agents such as urea to break hydrogen bonds and other supramolecular forces and mild reducing agents such as tris(2-carboxyethyl) phosphine (TCEP) are added. Stabilizing hydrophilic polymer chains can be attached to the polypeptide backbone before or after the denaturation step to prevent aggregation of the denatured polypeptide chains [210]. In our design, PEG chains of different molecular weights (2000–5000 Da) have been covalently linked through either thiol–maleimide chemistry or amine–NHS ester chemistry. PEG chains provide sufficient stability under the denaturing conditions as well as biocompatibility and they alter the hydrophilic–hydrophobic balance of the denatured polypeptide chain consisting of hydrophilic and lipophilic sequence patterns preventing undesirable supramolecular interactions within the chains also due to the steric effect [211]. Fig. 6A shows a typical procedure for PEG conjugation followed by unfolding of the blood plasma protein human serum albumin (HSA, 66 kDa) by 5 M urea–phosphate buffer (PB) in the presence of TCEP. Thiol groups of the unpaired cysteines and reduced disulfide bonds are typically exposed during the denaturation step and they can be capped by different maleimides such as PEG–maleimide and *N*-(2-aminoethyl)maleimide to avoid reformation of disulfide bonds. Noteworthy, the optimal denaturing conditions need to be carefully identified as each protein has a different inherent stability based on its folding as well as the number and location of the disulfide bridges. In this way, hen egg white lysozyme with a molecular weight of 14 kDa requires more drastic denaturation conditions, i.e., 8 M guanidine and excess of the reducing agent dithiothreitol (DTT) for denaturation compared to HSA [212]. By reacting single accessible thiol groups of BSA with PEG–bismaleimide to synthesize a protein-dimer precursor, a giant polypeptide–PEG–polypeptide triblock copolymer of defined structure, composition and a very high molecular weight of about 400 kDa has also been reported *via* the PEGylation and denaturation strategy [213].

The denatured protein–PEG conjugates synthesized by the convenient approach provide several attractive characteristics: (1) biocompatibility; (2) biodegradability by proteases; (3) defined peptide sequence; (4) the final polymers offer narrow molecular weight distributions that can be characterized by mass spectrometry ensuring the quality control of products; (5) various functionalities in specific positions which allow the realization of complex tasks such as cellular uptake and intracellular delivery; and (6) tunable transition between globular, collapsed and extended architectures. In addition, the PEG side chains could reduce protein binding and provide "stealth properties" by shielding the immunogenic recognition sites (epitopes) [214]. Therefore, polypeptide–PEG conjugates based on denatured proteins provide various attractive features for biomedical applications and as precision substrates for templated synthesis of well-defined nanomaterials (Fig. 6).

Because of their unique optical properties, quantum dots (QDs) and fluorescent nanodiamonds (FNDs) are two highly promising probes for tracking biological processes i.e. with super-resolution microscopy and drug delivery applications [215,216]. However,

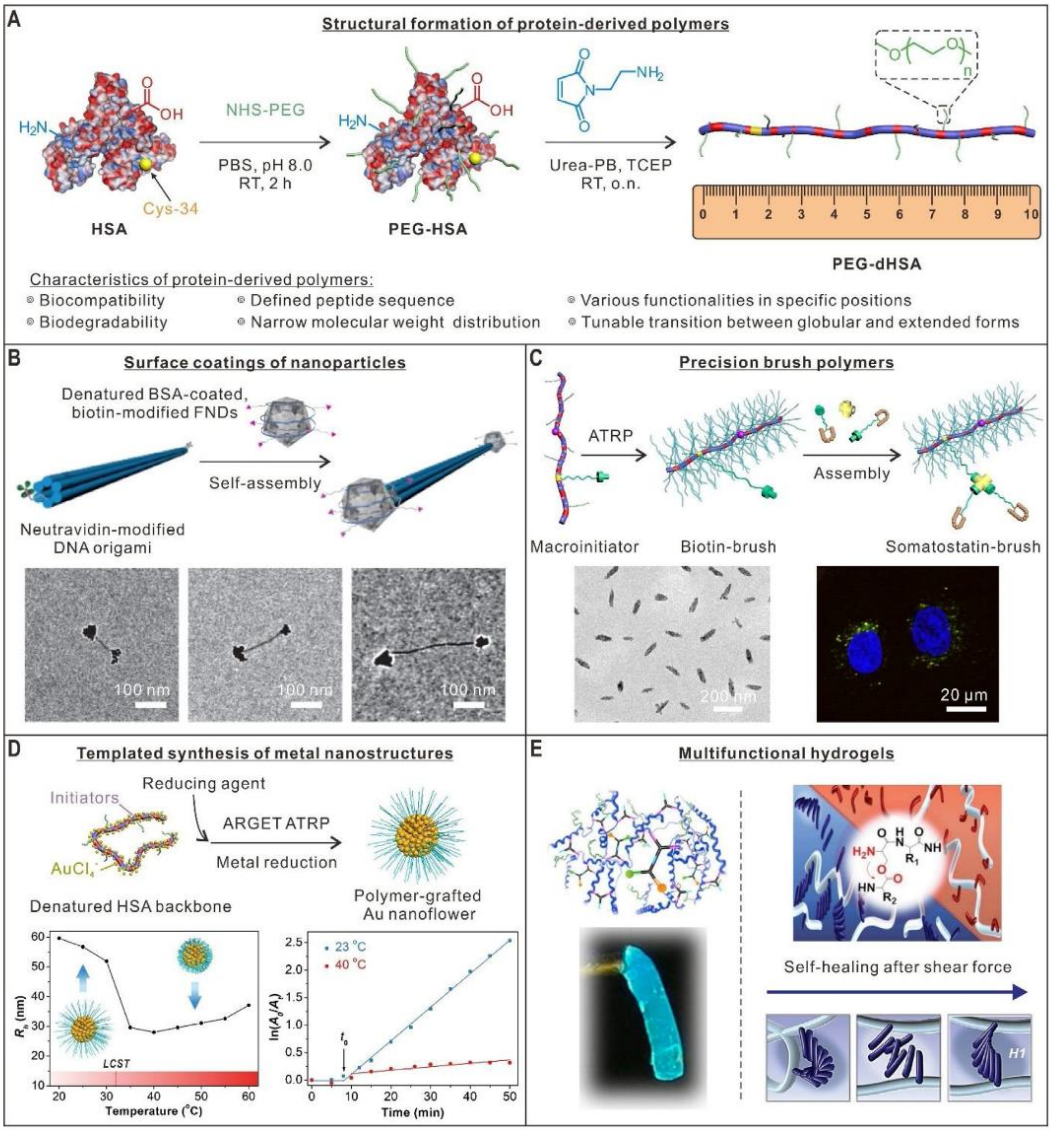

Fig. 6. Synthesis and applications of denatured protein–PEG conjugates. (A) A typical procedure to synthesize protein-derived polymers by PEG conjugation and denaturation of HAS; (B) Surface modification with denatured protein–PEG conjugates and precise assembly of nanodiamonds by DNA origami; (C) Denatured proteins as a precision backbone for the synthesis of anisotropic brush polymers, which allow site-specific functionalization of the main chain and assembly; (D) Templated synthesis of PNIPAM-grafted gold nanoflowers in one pot for temperature-controlled catalysis; (E) Denatured protein–PEG conjugates as multifunctional and degradable backbones to prepare functional hybrid hydrogels. Left: DNA-induced crosslinking of the denatured protein–PEG backbone affording protein–DNA hybrid hydrogels. Right: self-healing hydrogels with inner fibrillar structures by crosslinking of the copolymers with self-assembling peptides as pH-responsive gelators for cell cultivation. (B) [221], Copyright 2015. Reproduced with permission from the American Chemical Society. (C) [223], Copyright 2020. Reproduced with permission from the American Chemical Society. (D) [225], Published by the Royal Society of Chemistry and the Chinese Chemical Society. (E), left [230], Copyright 2014. Reproduced with permission from the Royal Society of Chemistry. (E), right [231], Copyright 2019. Reproduced with permission from John Wiley and Sons Inc.

applications of the "bare" nanoparticles are severely limited by their poor solubility in various biological environments. In addition, other challenges include the toxicity of QDs [217] and the surface modification of FNDs that provide undefined surface functionalities with high batch-to-batch variations [218]. Denatured protein–PEG conjugates serve as attractive nanoparticle coatings due to the availabilities of many reactive amino-, carboxylic acid and thiol groups that could interact with various nanoparticle surfaces though electrostatic interactions or hydrogen bonds as well as the presence of hydrophobic amino acids that bind hydrophobic surfaces by van der Waals interactions. For example, denatured HSA–PEG conjugates functionalized with multivalent thioctic acid groups stabilize the surface of CdSe–CdZnS QDs [219]. The coated QDs gain improved water-solubility and unique pH-responsiveness, which was attributed to conformational rearrangements of the polypeptide coating at different pH. This could alter the capacity of the polymer to efficiently passivate and protect the nanoparticle surface. Based on this strategy, a

polycationic polypeptide–PEG conjugate based on denatured BSA was achieved that encapsulated QDs and enabled their cellular uptake and allowed DNA complexation [220]. In these systems, the QD core served as an *in situ* reporter for pH changes, DNA complexation and ultimately even DNA transfection because its photoluminescence dropped significantly with increasing quantities of complexed DNA. Similarly, the cationized and denatured protein–PEG conjugates could also offer excellent colloidal stability to FNDs so that they remained stable even in the presence of high ionic strength buffers required for DNA origami folding (Fig. 6B). In this way, the first DNA origami-assembled FND nanostructures were formed, which is a critical step to study the coherent coupling of ordered spin arrays [221]. Moreover, the biopolymer-coated FNDs remained stable even after encapsulating high amounts of hydrophobic doxorubicin drug molecules and revealed high uptake into human lung adenocarcinoma A549 cells and *in vivo* efficacy attractive for cancer therapy [222].

In comparison to synthetic polymers, the most prominent advantages of denatured proteins are their monodisperse lengths and defined amino acid sequences. Therefore, the denatured protein–PEG conjugates can be used as precision templates for the preparation of various structurally defined nanomaterials. Very recently, Weil et al. have reported the construction of precision brush polymers using denatured proteins as a monodisperse macromolecular backbone (Fig. 6C) [223]. By introducing ATRP initiators to denatured HSA–PEG conjugates, anisotropic brush polymers with monodisperse contour lengths and narrow distributions were obtained by grafting polymer side chain from the backbone. The size and anisotropy of the brush polymers were tuned by varying polymerization conditions and the initiator density on the polypeptide backbone. Particularly, a distinct functionality can be introduced onto an absolute position located asymmetrically along the polypeptide backbone of these brush polymers. By combining this site-specific functionalization strategy with biotin–streptavidin interactions, various functional entities such as a single fluorescent dye, a gold nanoparticle, the hormone somatostatin, and a model antibody were introduced *via* site-specific assembly to fabricate novel higher ordered constructs, which may find potential applications in both biomedicine and nanoscience [223]. As shown in the confocal laser scanning microscopy image of Fig. 6C, biotin-containing brush polymers self-assemble with biotin-functionalized somatostatin in the presence of streptavidin and the formed construct revealed somatostatin-mediated uptake into cancer cells.

Due to the presence of abundant amino groups in the backbone, denatured protein–PEG conjugates possess strong capability to bind metal ions. Therefore, the biopolymer providing high water solubility was used as an ideal substrate for templated synthesis of metal nanoparticles. For instance, our group has reported a denatured HSA–PEG conjugate functionalized with TAT peptide, and mitochondria targeting triphenyl-phosphonium groups for the synthesis of ultrasmall gold nanoparticles with good biocompatibility and high stability [224]. Recently, the denatured HSA–PEG conjugate has been employed as a precision template for the preparation of polymer-grafted gold nanoflowers by combining ARGET ATRP and metal reduction in a one-pot fashion [225]. The cationized biopolymer with immobilized ATRP initiators serves both as a platform to bind chloroauric anions and as a macroinitiator for ARGET ATRP. Ascorbic acid was then added continuously into the system to activate ATRP catalyst precursors and to reduce gold ions in parallel (Fig. 6D). PNIPAM-grafted gold nanoflowers of controllable sizes, shapes and thermo-responsiveness have been achieved and applied as smart nanoparticle catalysts for the hydrogenation of *p*-nitrophenol to *p*-aminophenol. This convenient approach based on protein-derived templates could be expanded to other functional polymers and noble metal nanoparticles, providing access to various polymer-coated metal nanostructures for broad applications in catalysis, sensing, and biomedicine [225].

The architecture of denatured protein–PEG conjugates responds to changes of the balance of hydrophilic and groups along the polypeptide backbone. These changes could either be lipophilic functionalities that are covalently attached or the presence of hydrophobic guest moieties that interact with the lipophilic amino acid side chains *via* supramolecular interactions. In this way, well-defined core–shell nanostructures were formed suitable for catalysis and delivery of lipophilic molecules into cells. When the cationized and denatured BSA–PEG conjugate was modified with just a few hydrophobic groups such as alkynes, stable nano-sized micelles were formed spontaneously [226]. Complexation with the hydrophobic chromophore perylenetetracarboxydiimide, a denatured HSA–PEG conjugate functionalized with folic acid groups, has been shown to form globular micelles, which were uptaken into cells *via* receptor-mediated endocytosis [227]. The lipophilic drug doxorubicin has also been encapsulated into these micelles by complexation [228] or covalent conjugation [226] and efficient delivery into various cancer cells has been shown. To achieve selectivity and better control over the drug release profile, a pH-responsive hydrazone linker has been introduced to conjugate doxorubicin to the denatured protein backbone that potentially allows release in the acidic microenvironments of tumor tissue as well as in acidic endosomal vesicle [229]. The sophisticated core–shell delivery system composed of a polypeptide core with doxorubicin drug molecules and a PEG shell adopts a two-step drug release based on proteolytic degradation of the backbone and acid-induced drug release. *In vitro* test of the drug-loaded micelles revealed very high cytotoxicities against Hela cells and leukemia cell lines. More importantly, 100% survival rates of mice that received ex vivo transplantation of engrafted leukemic tumor cells after 12 weeks were demonstrated [229].

In combination with various crosslinking chemistries, the denatured protein–PEG conjugate served as biocompatible and biodegradable high molecular weight scaffold to prepare injectable hybrid hydrogels. As crosslinkers, multi-arm DNA [230] as well as self-assembling peptide sequences [231] have been applied. Denatured HSA–PEG conjugates were functionalized with ssDNA sequences that could hybridize with complementary Y-shaped DNA [230]. The formed hydrogel was used to immobilize active proteins including GFP and YFP, which were released by proteases as well as nucleases independently (Fig. 6E). Furthermore, conjugation of a recombinant Rho-inhibiting C3 toxin that inhibits growth and migration of bone degrading osteoclast cells to the multi-arm DNA linker allows the toxin-loaded hydrogel to reduce osteoclast formation and bone resorption without affecting differentiation and mineralization of bone forming osteoblast cells [232]. In another example, self-assembling peptides that spontaneously form cross β-sheet fibrillary structures were grafted to the backbone of denatured HSA–PEG conjugate. To control fibril formation of the peptides, they were masked as depsi-precursor peptides. The depsi peptide sequences do not aggregate at acidic pH until an intramolecular *O,N*-acyl shift occurs at higher pH values affording the formation of peptide nanofibers, which served as pH-responsive gelators (Fig. 6E). The obtained hydrogels are cytocompatible, biodegradable, reveal rapid self-healing abilities and cells migrated into this porous matrix, rendering them attractive for 3D tissue engineering [231].

3.1.2. Protein cages for grafting synthetic polymers

Protein denaturation destroys the 3D structure of native proteins so that nanostructures are mainly formed within the polymer chain by external guests or stimuli. In another class of nanostructures, the self-organizing features of proteins are retained so that distinct and large protein nanostructures are formed. Protein cages

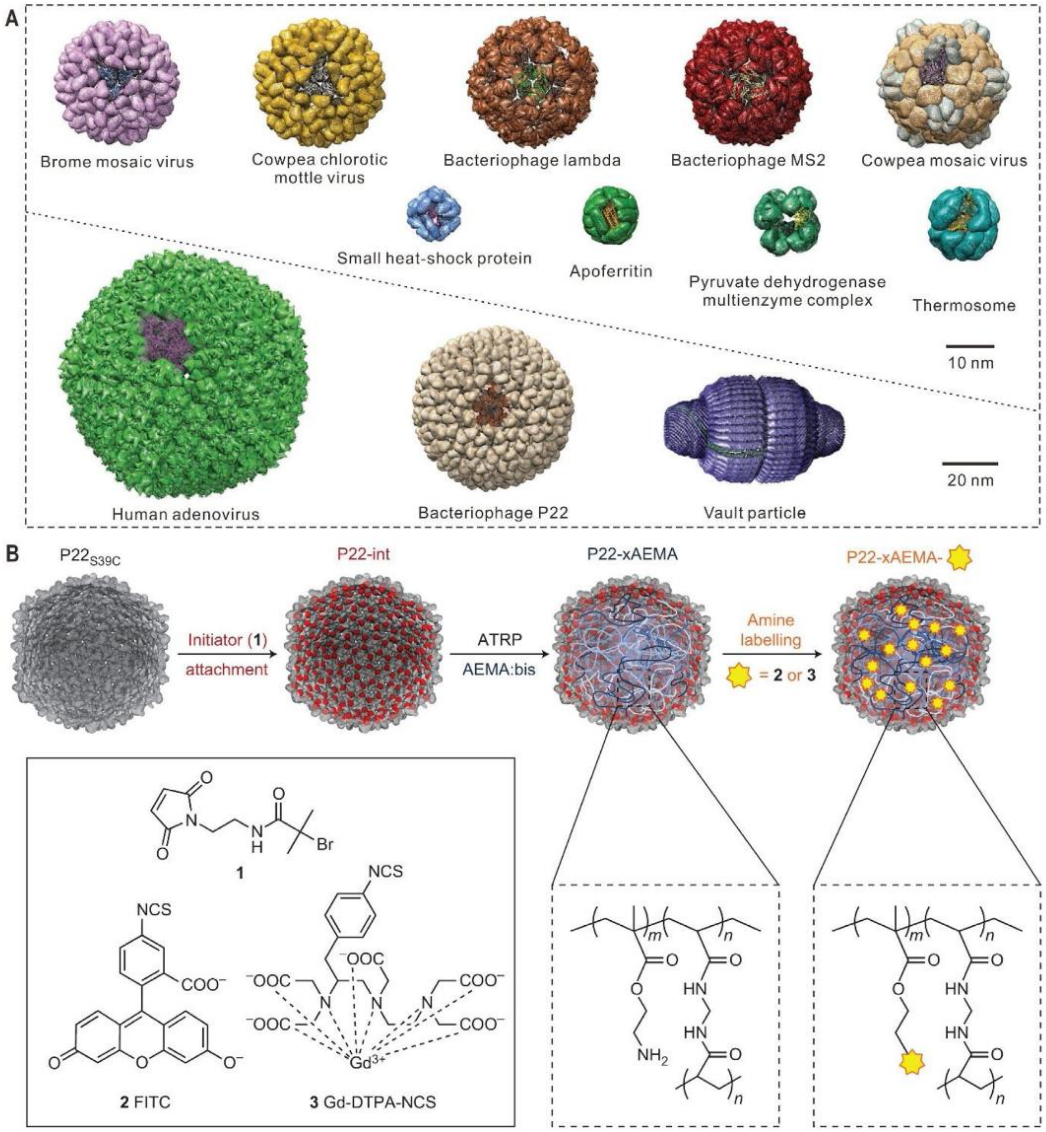

Fig. 7. Protein cages for polymer conjugation. (A) Structures of representative protein cages; (B) Site-specific ATRP growth of functional polymers from the interior cavity of the bacteriophage P22 virus-like particle. The internal functional polymer was subsequently labeled with a fluorophore or a paramagnetic MRI contrast agent. (A) [233], Copyright 2016. Reproduced with permission from the Royal Society of Chemistry. (B) [253], Copyright 2012. Reproduced with permission from Springer Nature.

of different sizes are widely formed in Nature, such as mammalian ferritins with a diameter of 12 nm and virus-derived icosahedral protein cages with diameters from approximately 28 nm (brome mosaic virus and cowpea chlorotic mottle virus) to 95 nm (human adenovirus) and more than 500 nm (megavirus chilensis) (Fig. 7A). These well-defined 3D hollow architectures with symmetric shapes and uniform sizes are formed *via* the self-assembly of individual protein subunits [233]. They have received rapidly growing interests of the materials science community due to their broad applications as nanoscale reactors, as scaffolds for nanomaterial synthesis, and as versatile vehicles to deliver a broad range of drugs, genes, and imaging agents [233,234]. In addition, the subunits of protein cages can be chemically or genetically modified at specific locations, allowing the conjugation of functional moieties within the interior cavity and/or on the exterior surface in a site-selective manner [235]. Polymer conjugation of protein cages give them entirely new properties and expand the range of applications. For instance, PEGylation of protein cages is a very popular and effective strategy to reduce the immunogenic response facilitating their usage for biomedicine [236–238]. In addition, surface engineering with functional polymers offers stimuli-responsiveness [239], increased stability [240,241], and solubility in organic solvents [242,243].

Based on the well-established chemistries to prepare peptide–polymer conjugates, the *grafting to* approach using reactive groups at the surface of these cages is a relatively straightforward modification strategy to decorate protein cages with synthetic polymers. For example, Finn et al. have attached

poly(2-oxazoline)s to the exterior surface of bacteriophage Qβ *via* the CuAAC click reaction [240]. They used a multiple-point conjugation strategy and the polymer-conjugated protein cages showed significantly enhanced thermal stability, surviving at temperatures higher than 100 °C. Thermo-responsive smart polymer PNIPAM has also been conjugated to the surface of vault, a recombinant protein cage with a size of 41 × 41 × 72.5 nm, by coupling the thiol group at N-terminus of the major vault protein [239]. The obtained vault nanoparticles exhibited reversible aggregation behaviors that can be controlled by temperature. Pokorski et al. have attached water-soluble polynorbornene (PNB) chains, which were synthesized by ROMP, to the outer surface of bacteriophage Qβ [244]. Significantly, PNB with brush-like architectures demonstrated better shielding effect from antibody recognition than PEG for the protein cages [245]. In general, the direct conjugation of polymer chains to the interior surface of protein cages is considered more challenging to achieve due to the steric effect. In this regard, dendritic PAMAM has been conjugated into the protein cage thermosome, a group II chaperonin that possesses a large pore size of 7 nm [246]. The thermosome–PAMAM conjugate was successfully used for small interfering ribonucleic acid (siRNA) delivery [246] and templated synthesis of gold nanoparticles inside of the protein cage [247].

In contrast to the *grafting to* approach, it has become a recent trend to conjugate polymers to protein cages *via* the *grafting from* approach [248], which should generate polymer conjugates with better-defined structures. By modifying the exterior surface of horse spleen ferritin nanocage with an ATRP initiator, the polymerization of 2-methacryloyloxyethyl phosphorylcholine and PEG methacrylate has been realized by Russell, Emrick and coworkers [249]. Antibody recognition experiments revealed the "stealth" properties of these hydrophilic coatings. Böker et al. have reported the copolymerization of NIPAM and photo-crosslinkable 2-(dimethyl maleinimido)-*N*-ethyl-acrylamide from the surface of the same protein cage [250]. These bioconjugates have been shown to stabilize emulsions, which allows the formation of thermo-responsive capsules for controlled drug delivery after cross-linking. Finn et al. have polymerized an azido-functionalized oligo(ethylene glycol) methacrylate from the exterior surface of the bacteriophage Qβ by ATRP [251]. This monomer even facilitated post-functionalization of the protein cage *via* the CuAAC reaction, which was demonstrated by conjugation with an alkyne-substituted Alexa Fluor 488 dye, a gadolinium complex (Gd–DOTA) contrast agent for magnetic resonance imaging (MRI), as well as a pH-sensitive and clickable doxorubicin derivative for anticancer therapy.

In addition to the functionalization of the outer surface, Douglas and coworkers pioneered the site-specific growth of both branched [252] and linear [253] polymers from the interior surface of protein cages. They showed stepwise synthesis of a dendritic polymer from heat shock protein (HSP), whose interior cavity has a diameter of 6.5 nm [252]. Here, cysteine reactive sites genetically introduced to the inner side of the protein cage served as the initiation sites. By sequential conjugation of azide and alkyne monomers using click chemistry, the polymer grew to generation 2.5, which formed fully cross-linked network across the protein subunits, rendering the protein cage thermally stable even at 120 °C. In addition, a large number of free amines has been incorporated into the branched polymer chains, which further offers addressable sites to load additional functional components. In their following contributions, the Gd-diethylene triamine pentaacetic acid (Gd-DTPA) contrast agent was attached to the reactive amines of the polymer network [254]. Each protein cage was shown to incorporate up to a maximum of 159 Gd, and the functionalized protein cages demonstrated a per particle relaxivity of 4200 mM^{-1} s^{-1} which was among the highest reported values for protein cage–Gd MRI contrast agents. This strategy was further extended to construct a branched iron–phenanthroline based coordination polymer within the protein cage of HSP [255]. However, the stepwise growth method involves tedious reaction steps, and it is very challenging to achieve polymers with high molecular weights and high densities within the protein cage. To address this issue, the same group has reported the first example of site-specific ATRP growth from the inside cavity of a mutant of the bacteriophage P22 capsid [253]. This P22 protein cage consists of 420 subunits with an interior diameter of 54 nm. ATRP initiators were attached to the only addressable cysteine of each protein subunit, which was mutated to be exposed within the inner cavity, in a near-quantitative manner (Fig. 7B). By copolymerization of 2-aminoethyl methacrylate (AEMA) and bisacrylamide using standard ATRP conditions, cross-linked polymer networks were formed in the interior of the protein cage. Importantly, the reactive primary amines of the polymer chains were still accessible, as confirmed by post-functionalization with small molecules such as fluorescein isothiocyanate (FITC), Gd-DTPA, a photosensitizer (Eosin-Y), and a cobaloxime catalyst [253,256]. Notably, the obtained polymer-conjugated protein cages revealed a high loading capacity of 9100 ± 800 Gd per cage, affording an ultrahigh per particle relaxivity of 200,000 mM^{-1} s^{-1}. In order to obtain nanoreactors for photocatalytic applications, AEMA was also copolymerized with [ruthenium(5-methacrylamido-phenanthroline)$_3$]$^{2+}$ from the inner surface of the P22 capsid [257]. A similar approach have also been demonstrated by Finn and coworkers to polymerize a positively charged monomer *N*,*N*-dimethylaminoethyl methacrylate from the interior surface of Qβ for the delivery of siRNA [258].

Collectively, protein cages constitute well-defined templates for grafting synthetic polymers with defined inner holes and outer surfaces and they receive emerging interest for drug delivery and bioimaging. It should be noted that protein cages can also be combined with synthetic polymers by many other interactions such as electrostatic complexation or non-covalent encapsulation of synthetic polymers into protein cages [233]. For example, the protein corona on adenovirus 5 (Ad5), one of the main vectors in gene therapy, has been mimicked by polyphenylene dendrimers with a distinct amphiphilic surface pattern [259]. These dendrimers coated the surface of Ad5 by distinct non-covalent interactions, which abolished binding of blood coagulation factor X, facilitated uptake into receptor negative cells, which was not possible for Ad5 alone. The dendrimer corona had a significant impact on Ad5 *in vivo* trafficking and the Ad5–dendrimer complexes revealed a new bioactivity profile, which could be attractive to broaden the therapeutic applications of Ad5. In addition, some attention has been paid to the self-assembly of protein–polymer conjugates into protein cages and protein cage-mimicking nanostructures, which are discussed in greater details in section 3.2.2.

3.2. Assemblies of protein/peptide–polymer conjugates

3.2.1. Polymer conjugates based on self-assembling peptides

Polypeptides have been frequently used as building blocks for the preparation of amphiphilic block copolymers. In contrast to proteins, peptides provide shorter chain lengths, lower molecular weights and less complex tertiary structures. In the past two decades, self-assembly of polypeptide-based block copolymers into micelles and vesicles has been intensively explored, particularly for applications in catalysis and drug delivery [260–264]. In contrast to conventional synthetic polymers, peptide sequences can interact with each other *via* different supramolecular interactions such as hydrogen bonding, π-π stacking, and metal ion coordination to form well-defined secondary structures and superstructures. This attractive characteristic offers additional opportunities to control the self-assembly of polypeptide-based copolymers and many unique structures have been achieved [265,266]. For example, Hawker, Knight and coworkers reported the self-assembly of

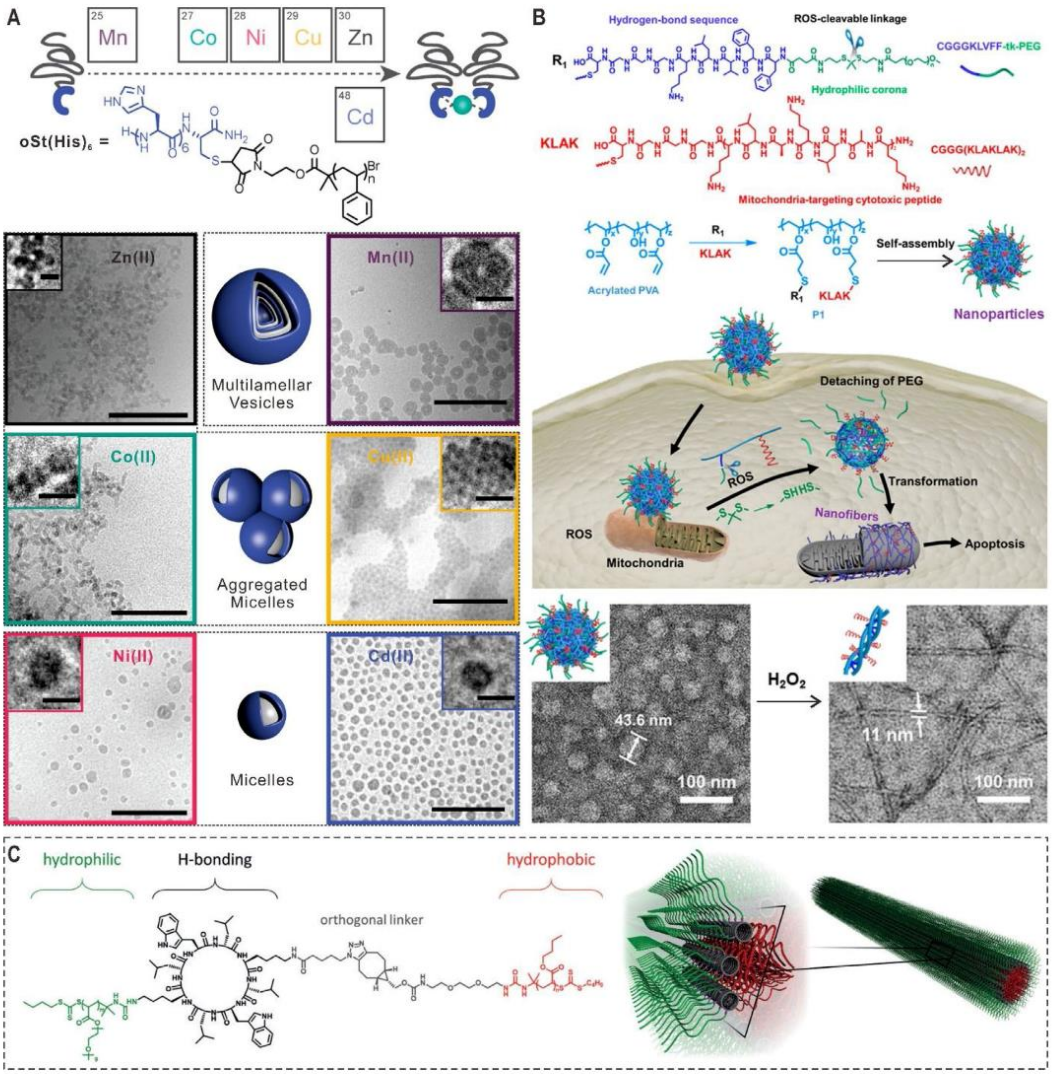

Fig. 8. Self-assembly of peptide–polymer conjugates. (A) Metal ion coordination as driving force for the self-assembly of amphiphile oSt(His)$_6$ into various morphologies. Scale bars in cryogenic transmission electron microscopy (cryo-TEM) images represent 200 nm (larger image) and 20 nm (inset image); (B) Synthesis and self-assembly of ROS-responsive peptide–polymer conjugates and the shape transformation around mitochondria for enhanced antitumor efficacy. Bottom: transmission electron microscopy (TEM) images showing H_2O_2-induced shape change of the peptide–polymer conjugate; (C) Molecular structure of PBA-CP-PPEGA and its hierarchical self-assembly into tubisomes. (A) [267], Copyright 2018. Reproduced with permission from the American Chemical Society. (B) [278], Copyright 2019. Reproduced with permission from the American Chemical Society. (C) [298], Copyright 2018. Reproduced with permission from John Wiley and Sons Inc.

peptide–polymer conjugates based on metal ion coordination of peptides [267]. As shown in Fig. 8A, the amphiphile oSt(His)$_6$ consists a hydrophobic polystyrene block and a hydrophilic block, hexahistidine, which can coordinate with divalent transition metal ions to form dimers. In the absence of metal ions, oSt(His)$_6$ spontaneously self-assembled into vesicles in a noncoordinating buffer (HEPES, 100 mM, pH 7). When different metal ions [Mn(II), Co(II), Ni(II), Cu(II), Zn(II), and Cd(II)] were added during the self-assembly process, the conjugate formed a wide range of new structures including micelles [Ni(II), Cd(II)], aggregated micelles [Zn(II), Co(II), Cu(II)], and multilamellar vesicles [Mn(II)].

Long fibrous structures can be obtained through self-assembly of sequence-controlled oligopeptides that have a tendency to form β-sheet structures [268–270]. Not surprisingly, introducing β-sheet forming peptides into the structure may allow peptide-guided self-assembly of polymer conjugates into well-defined fiber-like structures. For instance, Börner et al. reported the formation of fibers with a maximum length of up to 1 μm by conjugating PEO chains to template pre-organized oligopeptides [271]. These oligopeptides exhibited a high tendency to form β-sheet motifs due to the restriction of conformation freedom. Chen and coworkers investigated the self-assembly behaviors of a series of amphiphilic brush polymers with dendronized oligosaccharide and oligophenylalanine as side chains [272]. Depending on different ratios of sugar units to the oligopeptide, various self-assembled morphologies including compound micelles, nanowires, and nanoribbons were observed. Interestingly, the nanowire was formed *via* a hierarchical self-assembly process driven by the carbohydrate–carbohydrate

interaction of the sugar units and the β-sheet forming tendency of oligophenylalanine.

In biological systems, peptides are dynamic materials and their conformations and biological activities are often regulated by changes in their direct surrounding. Synthetically, the introduction of switchable peptides into polymer bioconjugates would offer vast opportunities for the structural control over their assemblies. The Börner group reported a PEO–peptide conjugate based on a peptide sequence with five repeats of alternating valine and phosphorylated threonine [273]. This conjugate was soluble in aqueous solution. However, fiber formation was triggered by the enzymatic dephosphorylation of the peptide block due to conformation changes of the peptides into β-sheet structures [273]. Recently, *in situ* construction and shape transformation of peptide-based assemblies in specific physiological environments have been demonstrated as promising strategies for biomedical applications [274–277]. Wang, Qiao and coworkers reported reactive oxygen species (ROS)-responsive polymer–peptide conjugates, which undergo morphology changes inside tumor cells [278]. Possessing a mitochondria-targeting peptide KLAK and a β-sheet forming peptide KLVFF conjugated with PEG through a ROS-cleavable linker as side chains, these conjugates were able to self-assemble into spherical nanoparticles and target mitochondria after entering cells (Fig. 8B). Due to the high ROS concentration around mitochondria, PEG chains were detached, which induced *in situ* formation of nanofibers with exposure of KLAK peptides. This shape transformation enhanced the multivalent cooperative interactions between KLAK and mitochondria, leading to improved anticancer effects *in vitro* and *in vivo*.

In addition to linear peptides, β-sheet forming cyclic peptides that can self-assemble into well-defined nanotubes have received special attention in recent years. Polymer conjugation offers many advantages to these nanotubes such as improved solubility, a wide spectrum of functionalities, and additional control over the tube length [279]. This does not only allow for a better understanding of the self-assembly mechanism, but also significantly broadens applications of these nanotubes. Basically, polymer strands can be attached to peptide nanotubes both before and after assembly *via* either the *grafting to* or *grafting from* approach [280–282]. In 2005, Biesalski et al. reported the first example of growing polymer chains from surface-immobilized initiators of cyclic peptide nanotubes *via* ATRP [283]. In addition, they demonstrated that length and diameter of the polymer–peptide nanotubes are highly affected by the molecular weight of grafted polymers [284]. Since the early studies, Perrier and collaborators have made significant contributions in this field by elucidating the tube structure [285,286], tracking their assembly processes [287,288], as well as exploring a wide variety of applications [289–291].

In order to control the self-assembly behavior and tube length, Perrier et al. have introduced different stimuli-responsive polymers to cyclic peptide nanotubes. For example, poly(2-ethyl-2-oxazolin) was successfully used to realize temperature-controlled reversible transformation from nanotubes to microparticles [292]. In addition, a series of pH-responsive polymers including PAA [293], poly(dimethylamino ethyl methacrylate) [294], poly[2-(diisopropylamino)ethyl methacrylate] [295] have also been conjugated into cyclic peptide nanotubes, which allow modulation of their self-assembly upon pH changes. Recently, host–guest interactions were also employed to switch the self-assembly of a cyclic peptide–PEG conjugate [296]. In this system, two phenylalanine groups as binding sites of cucurbit[7]uril were attached to the cyclic peptide, and the nanotube formation could be tuned by reversibly incorporating two bulky cucurbit[7]uril moieties *via* host–guest chemistry.

Cyclic peptide–polymer nanotubes have also been used as building blocks to construct well-defined higher order structures. For instance, Jolliffe et al. reported that hydrophobic cyclic peptide–polymer nanotubes with a Janus corona were able to self-assemble in artificial phospholipid bilayers and form transmembrane channels for a dye [297]. In collaboration with the Perrier group, they further designed an asymmetric cyclic peptide–polymer conjugate (PBA–CP–PPEGA) with a hydrophilic PPEGA chain on one side and on the opposite side, a hydrophobic poly(*n*-butyl acrylate) (PBA) chain [298]. This amphiphilic conjugate demonstrated a hierarchical self-assembly in aqueous solution by first forming amphiphilic Janus nanotubes *via* hydrogen bonds and then generating a superstructure, called tubisome based on terms liposome and polymersome, driven by the hydrophobic interactions (Fig. 8C). These tubisomes were able to fuse into the lipid bilayer of lysosomes in cells forming artificial pores. To identify the key factors to obtain tubisomes, a more detailed study was conducted with varied hydrophilic–hydrophobic ratios of the PBA–CP–PPEGA conjugate [299].

3.2.2. *Self-assembly of protein–polymer conjugates*

As a unique class of polypeptides with fully folded structures and globular shapes, proteins in most cases provide biological functions to protein–polymer conjugates. When hydrophobic polymers are attached to water-soluble proteins, the amphiphilic conjugates self-assemble in a manner similar to that of low molecular weight surfactants and synthetic block copolymers in aqueous solution. Therefore, these protein-based amphiphiles can also serve as building blocks for the construction of a wide range of solution nanostructures. Early examples reported by Nolte and coworkers have demonstrated the self-assembly of protein–polymer conjugates into fibers [300], vesicles [301], and toroids [302]. In recent years, self-assembled nanoparticles based on protein–polymer conjugates have been intensively explored as carriers for delivery of anticancer drugs [303–306]. Due to the presence of proteins, these self-assembled nanostructures possess the special advantage of built-in bioactivity. For example, Thordarson et al. conjugated a maleimide-capped PNIPAM chain to the free cysteine residue of a GFP variant (amilFP497) [307]. The resulting conjugate PNIPAM-*b*-amilFP497 assembled into vesicles in aqueous solution upon heating to 37 °C. Fluorescent characteristics of amilFP497 were not affected during polymer conjugation, which allowed direct observation of vesicle formation using confocal microscopy. These vesicles were used as carriers to encapsulate doxorubicin and a fluorescent light-harvesting protein phycoerythrin 545 (PE545) [307]. Importantly, the location of payloads could be determined by combining fluorescence lifetime imaging microscopy and Förster resonance energy transfer (FRET), showing PE545 protein primarily located inside the vesicle membrane whereas doxorubicin was found both in the core and membrane.

Recently, *in situ* growth of an insoluble polymer block from solvophilic polymers in solution to generate self-assembled nanostructures has become a new trend in macromolecular self-assembly [308–311]. This technique, termed polymerization-induced self-assembly (PISA), has also been expanded to the field of protein–polymer conjugates. As a proof-of-concept experiment, Gao et al. site-specifically attached an ATRP initiator to the only free cysteine group (Cysteine 34) of HSA and then polymerized water-soluble 2-hydroxypropyl methacrylate (HPMA) from the initiator *via* ATRP [312]. The resulting amphiphilic conjugate HSA–poly(2-hydroxypropyl methacrylate) (PHPMA) could self-assemble to well-defined nanostructures with tunable morphologies including micelles, wormlike micelles, and vesicles (Fig. 9A). In order to construct a tumor microenvironment-responsive fluorescence probe, this approach has been used to prepare pH-responsive micelles by polymerizing 2-(diisopropylamino)ethyl methacrylate from HSA [313]. In a similar way, Huang, Liu and coworkers reported photoinitiated RAFT PISA to generate protein–polymer micelles *via*

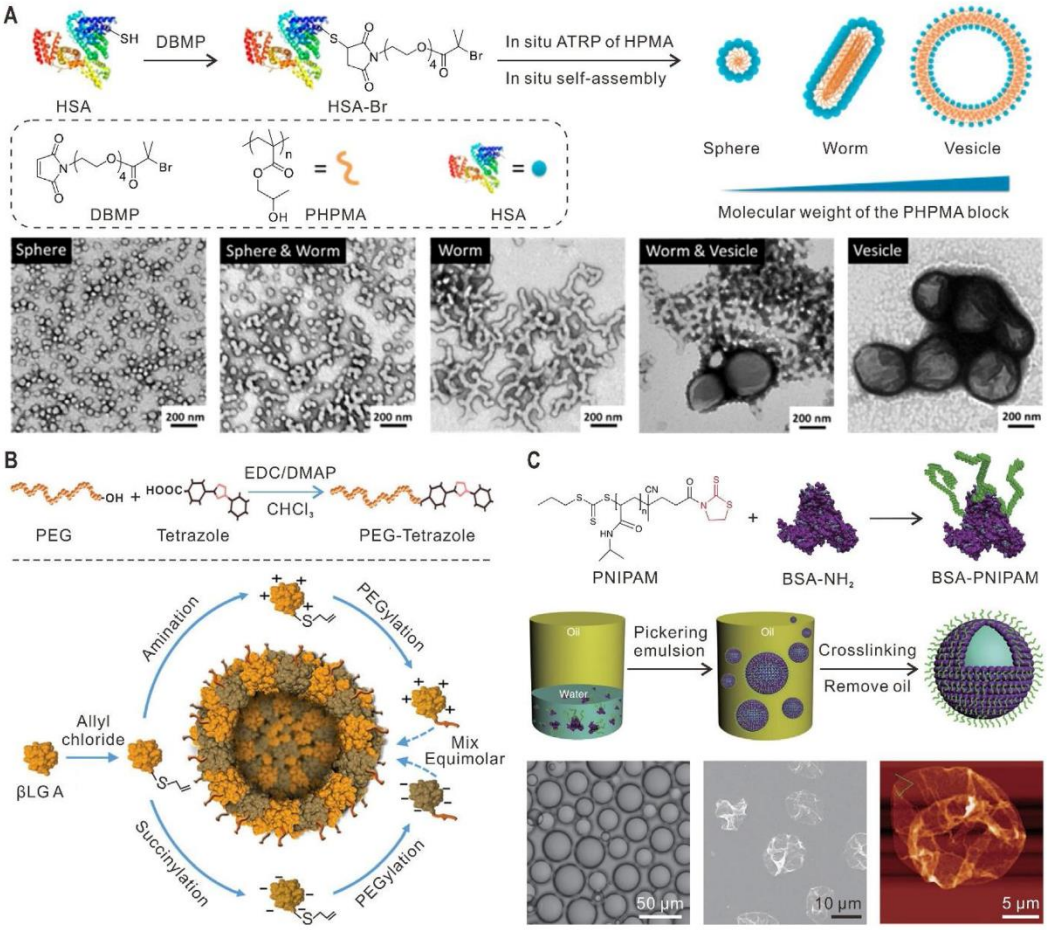

Fig. 9. Self-assembly of protein–polymer conjugates into high order nanostructures. (A) Schematic illustration and TEM images showing the *in situ* site-specific polymerization-induced self-assembly of HSA–PHPMA into tunable morphologies from spheres to worms and vesicles; (B) Synthesis of two oppositely charged βLG A–PEG conjugates and the preparation of nanocapsules by mixing the protein–polymer conjugates at equimolar ratio in solution; (C) Synthesis of BSA–PNIPAM and its self-assembly at the water droplet/oil interface to prepare proteinosomes. Bottom: optical microscopy image (left) of proteinosomes dispersed in oil, as well as SEM (middle) and atomic force microscopy (AFM, right) images of dried proteinosomes. (A) [312], Copyright 2017. Reproduced with permission from the American Chemical Society. (B) [315], Copyright 2017, Reproduced with permission from John Wiley and Sons Inc. (C) [319], Copyright 2013. Reproduced with permission from Springer Nature.

polymerization of HPMA from a multi-RAFT agent modified BSA [314].

As mentioned earlier, protein cages are monodispersed and highly organized protein architectures, which are formed based on the specific and directional interactions between protein subunits. Well-defined protein-based nanostructures can therefore be generated by an alternative approach using interactions between proteins to drive the self-assembly of protein–polymer conjugates. Nallani, Liedberg and coworkers designed and synthesized two oppositely charged β-lactoglobulin A–PEG (βLG A–PEG) conjugates and investigated their co-assembly behaviors [315]. As shown in Fig. 9B, the positively and negatively charged conjugates were obtained by amination or succinylation of βLG A followed by PEGylation *via* photoinduced click chemistry. Driven by electrostatic and hydrophobic interactions between the proteins, spherical capsules with a diameter of 80–100 nm and a narrow size distribution could be obtained by mixing the two charged protein–polymer conjugates at equimolar ratio. These capsules were able to accommodate GFP and FITC-labelled dextran in their interior. On the other hand, the connection between proteins in protein–polymer conjugates could also be created and strengthened by a third component. For example, Cornelissen et al. observed an irreversible dissociation of cowpea chlorotic mottle virus capsids when they were conjugated with PEG chains [316]. However, the resulting protein subunit–PEG conjugates could then reassemble into much more stable virus-like particles in the presence of polystyrene sulfonate (PSS), due to the electrostatic interactions between PSS and the positively charged protein subunits.

In addition to self-assembly in aqueous solution, amphiphilic protein–polymer conjugates have also been reported to organize at water/oil interfaces for emulsion stabilization [250,317,318]. As shown in Fig. 9C, Mann et al. prepared hollow protein capsules termed proteinosomes by interfacial assembly of a protein–polymer conjugate [319]. The conjugate BSA–PNIPAM was synthesized by coupling mercaptothiazoline-capped PNIPAM chains with cationized BSA-NH_2. By emulsifying an aqueous solution of the conjugate in 2-ethyl-1-hexanol, a closely packed and continuous monolayer of protein–polymer conjugates could form at the interface generating proteinosomes with diameters in the range of 20–50 μm. The proteinosomes were stable in oil and were

transferable to aqueous solution after crosslinking, which facilitates their application for guest molecule encapsulation, selective permeability, and as stimuli-responsive micro-reactors.

Owing to their potential applications in biosensors and heterogeneous catalysis, solid-state materials based on protein–polymer conjugates with well-defined nanostructures have attracted much interest in recent years [320,321]. By solvent evaporation from concentrated solutions, protein–polymer conjugates have been observed by Olsen and coworkers to form ordered nanostructures including lamellae, perforated lamellae, and hexagonally packed cylinders [322,323]. Particularly, they have intensively studied effects of various factors such as the chemistry of the polymer block [323,324], protein surface charges [325,326], and molecular topology of the conjugates [327] on the self-assembly behavior. For instance, the electrostatic repulsion of supercharged proteins has been found to severely affect the nanostructure formation and the degree of ordering was reduced in the self-assembled structures [326]. These studies expand our understanding on the bioconjugate self-assembly and may allow the structural control of protein–polymer conjugates in the solid state.

3.3. Well-defined protein/peptide–polymer conjugates on surfaces

Due to their robustness, versatility, and good processability, synthetic polymers have been used extensively to immobilize biomolecules including peptides and enzymes on various surfaces, which could find potential applications in biosensors, biotechnology, and biomedical devices [328,329]. These functional surfaces with attractive biological activities such as antibacterial [330] and cell adhesion properties [331], can be constructed by either direct deposition of polymer bioconjugates or stepwise immobilization of polymers and biomolecules on surfaces. For example, Maynard et al. designed and synthesized a heterotelechelic biotin–maleimide polymer by RAFT polymerization, which site-specifically conjugated proteins and immobilized them onto streptavidin- or neutravidin-functionalized surfaces [197]. Due to the presence of a cleavable disulfide bond in the polymer, the protein–polymer conjugate could be detached from the surfaces under mild reducing conditions.

Similar to those studies in solution and in bulk, surface-deposited protein/peptide–polymer conjugates are able to self-assemble to well-defined nanostructures, forming novel materials combining unique features and bioactivities of polymers and biomolecules, respectively. Early example by Jenekhe et al. showed the self-assembly of triblock copolymers containing a central π-conjugated polymer and two polypeptide end blocks into spherical and fibrillar nanostructures [332]. He et al. reported the hierarchical self-assembly of block copolymers containing PEG and polypeptides with alkyl side chains on graphite [333]. Depending on the block copolymer concentration, diverse morphologies from island-like aggregates and monolayers to monolayers with larger nanorods or ring-shaped aggregates were observed. The self-assembly of globular protein–polymer conjugates into cylindrical nanostructures has been demonstrated by Olsen and coworkers [334]. The conjugate containing fluorescent protein mCherry and poly(oligoethylene glycol acrylate), was flow coated into thin films on PEG-grafted silicon surfaces. Long-range order could be achieved under high humidity in surrounding air with a high coating speed. Polymer bioconjugates can also be co-assembled with synthetic block copolymers leading to hierarchically structured functional biomaterials [335]. Xu et al. reported the simultaneous co-assembly of a PEO-conjugated heme protein and an amphiphilic diblock copolymers, polystyrene-*b*-poly(ethylene oxide) (PS-*b*-PEO), into thin films with macroscale lateral ordering and regular nanoscale morphologies. Importantly, the protein structure and function were not affected during the film processing [335].

In addition to direct deposition of polymer bioconjugates on surfaces, proteins and peptides can be covalently immobilized onto polymer substrates *via* a wide range of conjugation chemistries [336,337]. Polymer brushes, polymer chains covalently anchored to surfaces, are ideal substrates to precisely immobilize biomolecules because they can provide exceptional control over surface properties and functionalities [338]. Various functional groups of polymer brushes such as epoxide, carboxylic acid, hydroxyl, aldehyde and amine groups have been employed to immobilize different biomolecules including peptides, proteins, and enzymes [329]. For instance, Popik, Locklin and coworkers reported functional polymer brushes containing photoreactive 3-(hydroxymethyl)naphthalene-2-ol (NQMP) moieties on silicon oxide surfaces [339]. Upon irradiation with 300 or 350 nm light, NQMP converts efficiently to *o*-naphthoquinone methide, allowing very fast Diels–Alder addition to vinyl ethers such as vinyl ether–biotin conjugate. FITC-functionalized avidin could then be immobilized to the polymer brushes with a significantly higher protein loading amount than that of self-assembled monolayer-based systems. Recently, antifouling polymer brushes containing alkene functional groups have also been used to immobilize cell adhesive peptides *via* thiol–ene radical coupling for the design of cell microarrays [340].

Very important is that patterned polymer brushes [341–344] can be easily prepared by emerging surface patterning techniques including photolithography, colloidal lithography, microcontact printing (μCP), electron-beam lithography (EBL), and scanning probe lithography (SPL), serving as a powerful platform to create well-defined surfaces and biochips with spatial control of biological functions. For example, μCP was successfully used to prepare patterned protein-resistant polymer brushes with nitrilotriacetic acid (NTA) groups that can selectively immobilize histidine-tagged proteins [345]. The protein resistance of NTA-functionalized POEGMA brushes was retained, which allowed the preparation of well-defined binary protein patterns. Yang et al. fabricated protein nanopatterns with different shapes including nanodot arrays, elliptical rings, microdiscs, triangles, and microgrids, by covalently conjugating proteins on hierarchical polymer brush patterns prepared by combining colloidal lithography and photolithography [346–348]. These protein patterns could promote cell adhesion and cell location. In contrast to μCP and colloidal lithography, EBL and SPL are writing techniques that can be used to fabricate arbitrary patterns at the nanometer scale. Maynard et al. employed EBL for the nanoscale arrangement of multicomponent two-dimensional (2D) single-layer or 3D multi-layer protein patterns [349]. Eight-arm PEGs modified with biotin, maleimide, aminooxy, or nitrilotriacetic acid were cross-linked onto Si surfaces using electron beams to form polymer patterns, which could be further used to site-specifically bind proteins with different functional moieties. Dip-pen nanodisplacement lithography (DNL) is a high resolution and program controllable SPL that is particularly suitable for constructing 2D and 3D patterned polymer brushes [350–352]. Zheng et al. employed DNL to create biomimicking nano-micro binary polymer brushes consisting poly(glycidyl methacrylate) (PGMA) and PNIPAM [353]. Gelatin was conjugated to PGMA brush nanolines, which offers the capability to regulate cell orientation.

3.4. Emerging applications based on the well-defined structure

By combining the precision structure and evolved functionality of biomolecules as well as the synthetic flexibility and stimuli-responsiveness of polymers in one platform, protein/peptide–polymer conjugates have demonstrated great

potential for numerous applications particularly in biomedical fields. In addition, these hybrids with well-defined structures are also very promising from a materials perspective [18]. While some examples have been presented during the discussion on synthetic approaches and various structures, we highlight here representative systems in which the conjugate structure plays a critical role for their applications.

3.4.1. Biomedical applications

Protein/peptide–polymer conjugates have been intensively investigated and widely used for therapeutic applications. On one hand, polymer conjugation often imparts increased stability, tunable activity, and prolonged blood circulation time of the therapeutic proteins and peptides [76,354]. For these systems, structural factors including conjugation site, grafting density, and length of polymers may have impact on the bioactivity and therapeutic effects of conjugates [355]. On the other hand, protein–polymer conjugates and their assemblies have also been used as delivery vehicles or coatings for various therapeutic agents and nanoparticles [356–360]. In these cases, the well-defined and hierarchical structure of polymer conjugates is the basis for their respective applications. Alexander et al. synthesized different conjugates of transferrin by grafting polymers either from specific cysteine residues of recombinant transferrin variants or from random amine sites on the surface of native proteins [361]. The self-assembly behavior of these conjugates and their ability to deliver anticancer drugs were investigated. In comparison to the hybrids prepared by nonselective conjugation, the engineered transferrin–polymer conjugates could form better-defined assemblies with enhanced performance in paclitaxel delivery. In addition, the self-assembled nanostructures of the protein–polymer conjugates were found as a key factor to achieve high delivery efficacy. As discussed earlier, PISA has been successfully used to prepare various assemblies from protein–polymer conjugates. To apply this approach for therapy, Gao et al. grafted an amphiphilic block copolymer site-specifically from the C-terminus of a therapeutic protein interferon-α (IFN) (Fig. 10A) [362]. The obtained conjugate IFN–POEGMA-PHPMA could self-assemble into spherical micelles with a diameter of 112 ± 23 nm. Very importantly, these micelles (IFN-micelle) demonstrated significantly enhanced *in vitro* bioactivity and *in vivo* half-life than that of FDA-approved PEGylated IFN (PEGASYS). Moreover, IFN-micelle also showed superior tumor accumulation compared to IFN conjugates modified with hydrophilic PEG or POEGMA chains [362]. Remarkably, tumor growth could be fully inhibited by IFN-micelle and 100% animal survival was achieved after four months in a mouse model of ovarian cancer (Fig. 10A). This example clearly reveals the advantages of self-assembled nanostructures as future therapeutics.

It is well understood that the sizes and shapes of self-assembled nanoparticles are important structural features affecting their pharmacokinetics [363]. Especially, nanostructures with elongated shapes often display longer circulation times in the body and are internalized by cells through different uptake pathways [363,364]. In this regard, Perrier et al. synthesized PHPMA-based cyclic peptide–polymer conjugates, which can self-assemble into well-defined nanotubes as anticancer carriers [365]. By introducing a pyridine-containing comonomer into the polymer, the conjugates could be functionalized with an organoiridium anticancer complex. Compared to free drugs and non-assembling drug-loaded polymers, drug-bearing nanotubes demonstrated higher toxicity toward human ovarian cancer cells. Moreover, cellular accumulation studies indicated that the increased activity could be ascribed to a more efficient action mode of the nanotube through a different drug partitioning profile into the cell organelles. To further explore cyclic peptide–PHPMA nanotubes as an effective drug delivery system, *in vivo* experiments were performed to compare their pharmacokinetics and biodistribution with non-assembling polymers [366]. After intravenous administration of samples to rats, nanotubes were found to circulate for more than 10 h and the plasma exposure was 3-fold higher than that of the polymer control. Importantly, the conjugates could be ultimately cleared from the systemic circulation, which is likely due to the slow disassembly of nanotubes into small entities, making them a promising vector for *in vivo* drug delivery.

Apart from protein and drug delivery for tumor therapy, protein/peptide–polymer conjugates with well-defined structures have also been applied in the construction of other biomaterials such as fluorescence nanoprobes [367–369] and cell matrices [370]. Moreover, proteins and peptides provide a rich library of biofunctions, for example, cell targeting [371,372] and antibacterial properties [373–376], to polymer bioconjugates broadening their application in countless fields. It is well-known that some intractable human diseases, including Parkinson's disease, are associated with the assembly of amyloid β peptides into fibrils. Moore et al. reported multivalent polymer–peptide conjugates as inhibitors to redirect the formation of amyloid β fibrils into discrete nanostructures through specific peptide interactions and multivalent effect [377]. Furthermore, they found that these conjugates of high molecular weights (166–224 kDa) could efficiently break down existing amyloid fibrils [378].

We have introduced above the on-site morphology transformation of nano-assemblies as a novel strategy for *in vivo* tumor therapy [276–278]. This strategy has also been used for bacterial infection treatment. Wang et al. reported shape-transformable nanostructures based on polymer–peptide conjugates containing a chitosan backbone and two peptide side chains, i.e. an antibacterial peptide and a PEG-terminated enzyme-cleavable peptide [379]. This conjugate self-assembled into spherical nanoparticles with diameter of 34 ± 5 nm. After exposure at the bacterial infection site, the nanoparticles underwent morphology transition spontaneously into nanofibers in the presence of gelatinase (Fig. 10B). During this process, the protecting PEG corona was removed through cutting off the cleavable peptide linker and the antibacterial peptide was exposed to the surface, leading to the multisite cooperative electrostatic binding to bacterial membranes. In addition, enhanced accumulation and retention of nanomaterials were demonstrated by *in vivo* experiments, which were ascribed to the formation of fibrous structures. Collectively, the chitosan–peptide conjugates exhibited highly efficient antibacterial activity [379]. In order to address infections caused by multidrug-resistant Gram-negative bacteria, novel well-defined antimicrobial agents with a dendrimer core and determined numbers of peptide side chains have been reported by Qiao, Reynolds and coworkers [380]. These star-shaped nanomaterials, termed "structurally nanoengineered antimicrobial peptide polymers", were synthesized *via* ROP of lysine and valine *N*-carboxyanhydrides from the terminal amines of second- and third-generation PAMAM dendrimers. Remarkably, they exhibited sub-μM antibacterial activity against all tested Gram-negative bacteria and displayed selectivity towards pathogens over mammalian cells.

Well-defined peptide–polymer conjugates were also used as multivalent platforms for virus inhibition. Our group has designed and synthesized a thiol-reactive poly(bis-sulfone) copolymer, which allowed multiple conjugation of an endogenous peptide that targets the C-X-C chemokine receptor type 4 [381]. The resultant polymer–peptide conjugate could self-assemble into narrowly dispersed nanoparticles and demonstrated enhanced antiviral activity on HIV infection. Herrmann and coworkers reported peptide–polymer conjugates based on a dendritic polyglycerol scaffold as non-toxic and high affinity multivalent inhibitors for the influenza A virus [382]. As illustrated in Fig. 10C, the conjugate was

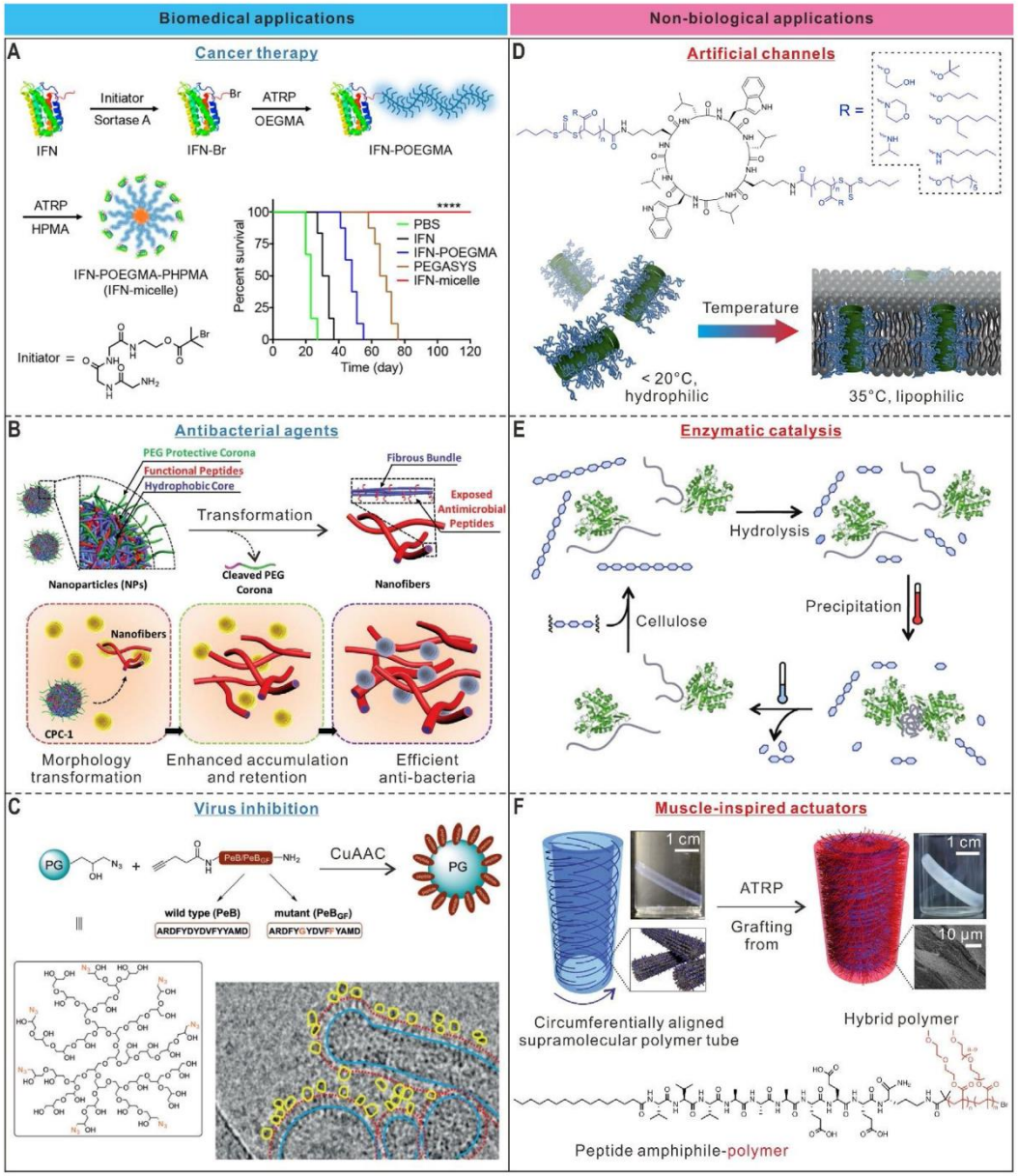

Fig. 10. Representative applications of protein/peptide–polymer conjugates. (A) Preparation of IFN–POEGMA–PHPMA micelle (IFN-micelle) by site-specific *in situ* PISA for cancer therapy. Bottom right: cumulative survival of mice showing the *in vivo* antitumor activity of IFN-micelle; (B) On-site morphology transformation of self-assembled nanoparticles based on a chitosan–peptide conjugate to nanofibers for treatment of bacterial infection; (C) Multivalent peptide conjugation of a dendritic polyglycerol for influenza A virus inhibition. The cryo-TEM image shows the interaction of the conjugate (yellow) with the virus corona (red dashed line); (D) Thermoresponsive cyclic peptide–polymer conjugates for the generation of well-defined phospholipid trans-bilayer channels; (E) Recyclable thermoresponsive polymer–endoglucanase conjugates for the enzymatic hydrolysis of cellulose; (F) Preparation of muscle-inspired anisotropic actuators by grafting thermoresponsive polymers from the surface of a hydrogel tube made of aligned peptide amphiphile nanofibers. (A) [362], Copyright 2018. Reproduced with permission from the American Chemical Society. (B) [379], Copyright 2017. Reproduced with permission from John Wiley and Sons Inc. (C) [382], Copyright 2017. Reproduced with permission from John Wiley and Sons Inc. (D) [289], Copyright 2014. Reproduced with permission from the American Chemical Society. (E) [392], Copyright 2013. Reproduced with permission from the American Chemical Society. (F) [393], Copyright 2018. Reproduced with permission from Springer Nature. (For interpretation of the references to colour in this figure legend, the reader is referred to the web version of this article.)

synthesized by CuAAC coupling of alkyne-containing peptides to an azido-polyglycerol. *In vitro* experiments demonstrated that the viral infection was significantly reduced by increasing the size of polyglycerol scaffold and tuning the peptide density. Binding of the conjugate with virus was directly observed by cryo-TEM (Fig. 10C). More importantly, *in vivo* experiments demonstrated that the conjugate provides the ability to efficiently protect mice from virus infection.

3.4.2. Non-biological applications

Because of their well-defined structures, protein/peptide–polymer conjugates and their assemblies have attracted rapidly growing interest in the materials community for non-biological applications such as nanomaterial synthesis, molecular separation and catalysis [18]. For instance, we have presented that PEG-conjugated denatured proteins can be used for templated synthesis of spherical and flower-like gold nanoparticle catalysts [224,225]. Self-assembled PEG–oligopeptide conjugates have also been used as template for the controlled growth of silver nanoparticle arrays with high particle density [383]. In Nature, the internal interfaces of hierarchical composites are often regulated through peptide-based interface active molecules. Inspired by this, Börner et al. reported the application of peptide–PEG conjugates as specific compatibilizers for a model composite consisting of MgF_2 nanoparticles and PEO matrix, which offers enhanced composite stiffness and toughness at the same time [384]. In addition, Sharma et al. reported BSA–polymer conjugates as a water-less and universal solvent for various dry solutes of different sizes and surface chemistries even including micrometer-sized polystyrene beads [385].

When protein/peptide–polymer conjugates are self-assembled into membranes, they can form specific pores with controlled sizes and shapes for the separation of molecules and particles. Using interfacial self-assembly, Böker et al. fabricated ultra-thin membranes of protein–polymer conjugates with the cage protein ferritin immobilized in the polymer matrix as a sacrificial template [386]. After removal of ferritin by denaturation, uniform pores formed and their diameter was dependent on the protein size. This membrane with a thickness of 7 nm showed good stability when a transmembrane pressure up to 50 mbar was used. Importantly, the membrane was found to have a preferred permeability for gold nanoparticles below 20 nm. As discussed earlier, cyclic peptide–polymer conjugates formed well-defined nanotubes *via* self-assembly. These nanotubes were also introduced into different membranes for the selective transport of small molecules. For example, Xu et al. reported the co-assembly of block copolymers and cyclic peptide–polymer nanotubes forming porous thin films with high-density arrays of channels at the sub-nanometer scale for gas separation [387]. Furthermore, they performed a more detailed study on the kinetic pathway of the co-assembly process pointing out the key factors to increase the membrane quality [388]. Perrier, Jolliffe and coworkers reported the self-assembly of cyclic peptide–polymer conjugates in the phospholipid bilayer of large unilamellar vesicles to form artificial channels (Fig. 10D) [289]. Through synthesis of a series of conjugates based on different hydrophilic and hydrophobic polymers, the channel type and structure-channel formation relationship were elucidated and lipophilicity of the polymer block was found to be important for the formation of unimeric channels. Because the lipophilicity of PNIPAM can be tuned by temperature, thermoresponsive cyclic peptide–PNIPAM conjugates were synthesized for the on-demand control over transbilayer channel formation (Fig. 10D). These transmembrane channels were used to transport cargoes between the cytosol and the extracellular media mimicking natural phospholipid membranes. In their subsequent work, a simple protocol to directly observe proton transport across the bilayer membrane has been developed [290]. Very recently, Perrier et al. reported the synthesis of cyclic peptide–polymer conjugates connected by a cleavable linker between peptide and polymer [291]. These conjugates could prevent undesired and unspecific interactions of self-assembled cyclic peptide–polymer nanotubes with lipid membranes, allowing the on-demand formation of membrane channels triggered by a stimulus in the environment.

Because of its efficiency and selectivity, enzymatic catalysis has been used for industrial productions in many areas such food, medicine, biofuel synthesis and biomass transformation [389]. However, the high cost of enzymes is often a barrier, which restricts the development of these fields. Polymer conjugation is a promising strategy to reduce enzyme costs by providing enhanced activity and recyclability to enzymes [320,390,391]. For example, Mackenzie and Francis reported a library of thermoresponsive polymer–endoglucanase bioconjugates as recoverable catalysts for hydrolysis of cellulose [392]. As shown in Fig. 10E, the bioconjugate is soluble in solution below the lower critical solution temperature (LCST) and can be used for the hydrolysis of cellulose. After the catalytic reaction, the bioconjugate is precipitated out when the temperature is increased above the LCST. By removing the oligosaccharide product and tuning back the temperature, the bioconjugate can be recovered and reused for several cycles of the catalytic depolymerization. Importantly, the authors have demonstrated the easy regulation of the material's LCST in the range of 20–60 °C through polymer structure design, enabling the application and recovery of enzymes at different temperatures.

More complex, hierarchical structures based on self-assembled peptide amphiphile fibers have also been developed by Stupp and coworkers showing interesting actuating properties and potential applications [393]. They firstly fabricated a macroscopic hydrogel tube by circumferentially aligning the supramolecular nanofibers within a tubular mold using weak shear forces, and then grafted thermoresponsive polymer chains from the tube surfaces by ATRP (Fig. 10F). These hybrid supramolecular tubes with different levels of ordered structures exhibited anisotropic contraction along the length of the tube upon heating. Macroscopic alignment of the supramolecular nanofibers and the covalent attachment of polymer chains were identified as two key factors for the anisotropic actuation. This work demonstrates the great opportunities to build smart soft actuators responsive to external stimuli based on well-defined peptide–polymer conjugates to realize complex applications.

4. Nucleic acid-based polymer conjugates

Nucleic acids represent the other class of precision biopolymers, which Nature has evolved specifically as the blueprint of life. In comparison to peptides and proteins, the interaction between the nucleotide pairs (A–T, G–C) are more streamlined in a way where the inter- and intramolecular forces are well-correlated in 3D space. Recognizing this as a powerful tool from the field of biotechnology to guide the structure of polymers and polymeric assemblies, the role of nucleic acids in modern polymer chemistry has recently seen a rising impact.

The combination of nucleic acids and synthetic polymers has shown distinct benefits based on the unique structural features oligonucleotides provide. The first involves the principle of complementarity of nucleic acid hybridization, where any sequence is programmed to recognize its complementary strand selectively. This allows any polymeric or self-assembled structure appended with ssDNA/RNA to possess an intrinsic bio-orthogonal handle coupled with sequence recognition. Secondly, nucleic acids can be bioactive in different forms (i.e. DNAzymes, aptamers, siRNA, etc.), thus imparting both structural and functional features for the design for sophisticated biohybrid materials.

4.1. Nucleic acid-templated synthesis of precision polymers

In DNA, the ubiquitous double helical structure is a pervasive structural component independent of the sequence combination. On the contrary, the macromolecular structure of polymers largely depends on the molecular constituents. In an exemplary situation, a PNIPAM grafted to a DNA oligonucleotide would very likely demonstrate very similar physical (self-assembly, LCST, etc.) and chemical behavior using any non-self-complementary sequence of the same

length. Hence, the flexibility in sequence and the assurance that the oligonucleotide would possess similar physicochemical properties have fueled their widespread application ranging from precision materials, nanorobots, ultrasensitive sensors, molecular computers, medical diagnostics, and therapeutics.

In spite of these advantages, nucleic acids often require stringent conditions to remain stable, with RNA being more susceptible than DNA to hydrolysis due to intramolecular nucleophilic cleavage. For biomedical applications, oligonucleotides have poor pharmacokinetics and *in vivo* stability thus making them unattractive candidates as therapeutics [394]. Similarly, nucleic acids are likewise challenging to be used in materials science due to their limited scalability. However, likewise in protein–polymer conjugates, several of these drawbacks can be addressed by synthetic methods and even made to surpass their individual capabilities within the field of application. Hence, in recent years, nucleic acid bioconjugates have played an emerging role in nanotechnology due to their unique sequence programming capabilities.

The methodologies to link oligonucleotides to polymeric materials have been summarized in Chapter 2 as well as in many excellent reviews [395,396]. Hence, this section adopts a different perspective involving detailed considerations about the special role of oligonucleotides in macromolecular science by guiding precise assemblies at length scales ranging from molecular to nano-objects. On a molecular level, by exploiting the complementary interactions between base pairs, synthetic molecules can be arranged in a sequence specific fashion, coded by the oligonucleotide template. The first examples of this approach using DNA or peptide nucleic acids (PNAs) templates were shown by Liu's and Lynn's groups, respectively [397–399]. Short sequences of DNA/PNA were synthesized to investigate the capabilities of a step-growth oligomerization process that was guided by a continuous DNA template. By selecting the reductive amination as a distance-dependent reaction, these short sequences were shown to ligate spontaneously programmed by the code of the templates. Introduction of errors and mismatch sequences afford only minimal products, demonstrating the regio- and sequence specificity of the concept. In this first proof of concept, the extent of polymerization was accomplished up to a 40-base template, affording a PNA oligomer with a molecular weight of ~10,000.

In addition to sequence precision, oligonucleotides also provide distinct spatial 3D arrangements of two target functionalities to control their interactions. These reactions can take place within the grooves of the DNA double helix or in a micellar system formed by a DNA-*b*-PPO copolymer system [400,401]. Within the minor groove of the double helix, polyamide hairpins find themselves arranged by the "pairing rules", which is presented as the exposed Watson–Crick base pairs for hydrogen bonding (Fig. 11A). This allows the hairpins to be arranged non-covalently according to the sequence of the DNA template, where subsequent click reactions with copper catalyzed azide–alkyne cycloaddition allowed these hairpins to be ligated [400]. While the internal features of the double helix are an attractive avenue to orient the formation of chemical bonds across large oligomeric molecules, spatial programming can be achieved simply by DNA hybridization. The 5′-end of the template strand and 3′-end of the complementary strand are brought in close vicinity, allowing a fluorogenic isoindole reaction to specifically take place [401].

By exploiting how DNA can position interacting molecules in space, one of the first examples using DNA to control synthetic polymer chemistry was reported by the group of O'Reilly [402]. In this seminal work, synthetic analogue of thymine (vinylbenzyl thymine, VBT) was block co-polymerized with styrene (St) to form the template PSt_{115}-*b*-$PVBT_{18}$ (Fig. 11B). This allowed the solubility of the block template in chloroform and thereby promoting the H-bond interaction between the thymine of the template with the target adenine. With the block template, vinylbenzyl adenine (VBA), which was insoluble in chloroform, became soluble through the formation of complementary interactions. Free radical polymerization was conducted on the pre-assembled VBA initiated by azobisisobutyronitrile (AIBN) to form the daughter polymer PVBA. Interestingly, monomodal high molecular daughter PVBA can be formed from just 18 units of PVBT in the block template. The result is a "hopping" feature where propagation of radicals between adjacent strands occurred within the micellar core of the block copolymer template. In contrast, polymerization without the template produced ill-defined, low molecular weight polymers, clearly demonstrating the potential of using DNA based interactions, albeit as a synthetic variant, to direct polymerization processes in a controllable fashion.

While the above methodology provides an elegant approach towards polymer synthesis, it is challenging to incorporate sequence information within the framework. In this respect, Liu's group encoded PEG, α-peptides, and β-peptides onto a "codon" defined by a sequence and arrangement of penta-nucleotide analogues [403]. Using a 5′ hairpin as the DNA template, complementarity allows each codon to hybridize against the template in a sequence specific manner (Fig. 11C). The close vicinity of the codons subsequently facilitates the covalent coupling of the encoded synthetic fragments together into a polymer, preserving the sequence information. The release of the afforded polymer was achieved by installing a stimulus responsive linker, in this case a disulfide, between the coding region and the fragment. Liu's group further refined this strategy to utilize DNA ligase to catalyze the formation of up to 50 consecutive codes along a DNA template, accomplishing a biosynthetic pathway to form a fully customizable nucleic acid based polymeric scaffold [404,405]. On a molecular level, the DNA code can act as a guide to direct polymerization reactions where, as a consequence, confer this information onto the newly created synthetic macromolecule. In another seminal methodology established by the Sleiman group, sequence identity from DNA can be imprinted into polymeric nanoparticles, creating a unique code that programs their assembly [406]. Using a DNA cube scaffold as a template with DNA–polymer amphiphiles flanking the sides, an internal hydrophobic pocket customized by the nature of the polymer can be cross-linked to form an imprinted nanoparticle. Upon hydrolysis of the template, a characteristic polymeric structure comprising of a DNA code ranging from divalent to hexavalent can be precisely constructed. With these coded nanoparticles, self-assembly into various geometries can be exactly defined where features such as interparticle distances, angles and particle junctions are manipulated in a facile way. As a result, nanostructures with identities conferred by the particles were created likewise within a sequence but on a different length scale.

4.2. Precision polymer nanostructures programmed by DNA

While the complementarity and recognition of DNA has enabled programmable features involving the orienting chemical motifs in molecular space, its capabilities extents even further into the nanoscale. DNA sequences can be manipulated to form any arbitrary wire-frame structures as well as continuously folded nanoarchitectures, a collective concept spearheaded by Seeman and Rothemund et al. known as DNA origami [407–409]. The assortments of different DNA shapes and sizes have exponentially grown over the past decade and have since proven to be the pinnacle of synthetic nanotechnology due to its customization potential. Therefore, the sheer possibility of "on-demand" customization and positioning of nanomaterials onto a singular precision platform have brought about new concepts in biophysics, nanomedicine and polymer synthesis.

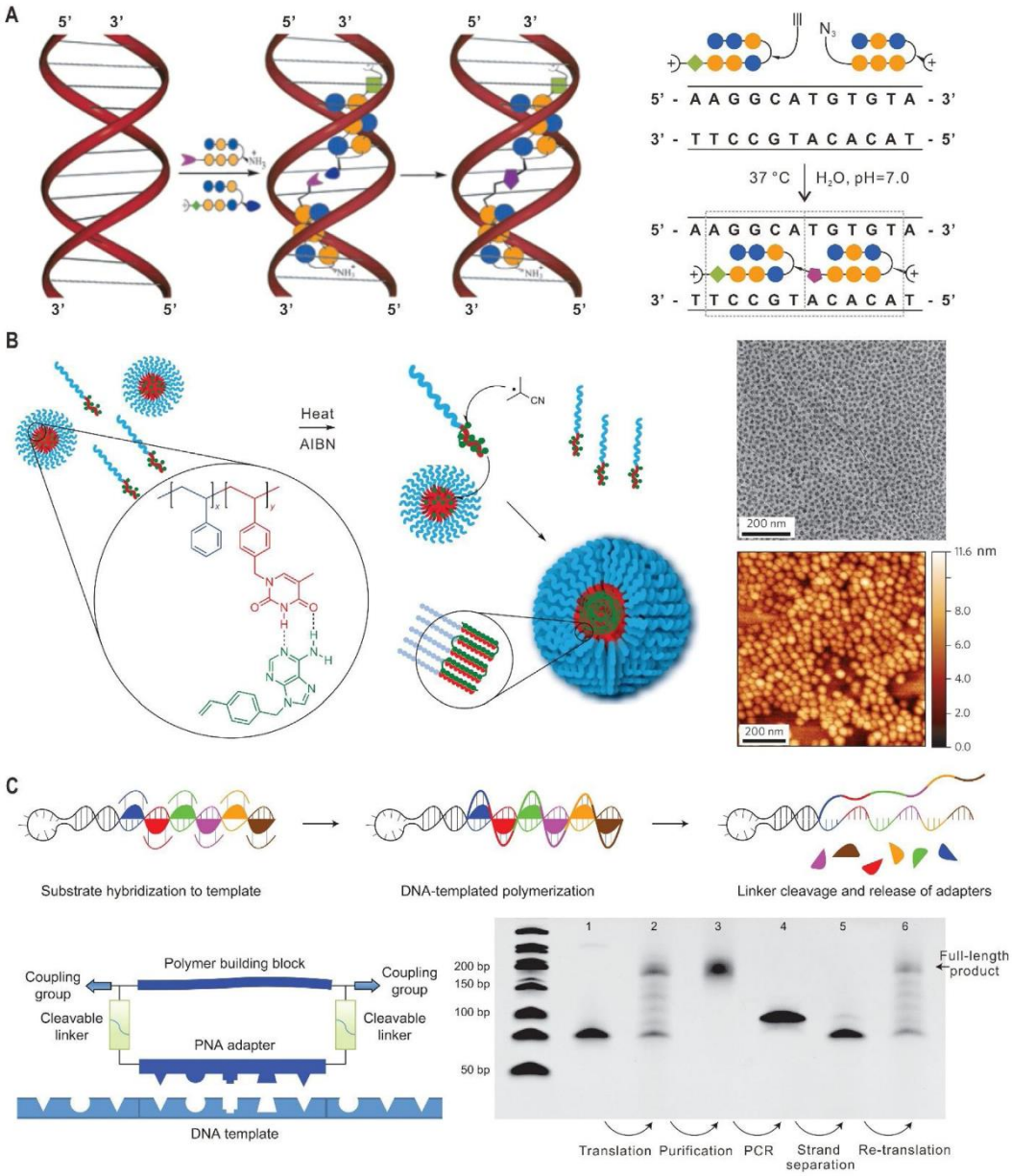

Fig. 11. Nucleic acid-templated synthesis. (A) Schematic illustration of DNA-templated tandem hairpin formation. Polyamides bind to contiguous match sites on DNA and their complementary reactive groups (alkyne and azide) are placed in close proximity forming a covalent triazole linker which is displayed as a purple pentagon; (B) A bioinspired approach to free radical polymerization of a VBA monomer in the presence of a monodisperse block copolymer micellar template with complementary PVBT cores. The right images are TEM and AFM characterization of micelles after the addition and polymerization of VBA; (C) Enzyme-free translation of nucleic acids into sequence-defined non-nucleic acid polymers. The bottom left scheme represents a macrocyclic substrate for the translation system and the bottom right gel image shows a complete cycle of translation, PCR amplification, strand separation and re-translation. (A) [400], Copyright 2003. Reproduced with permission from the American Chemical Society. (B) [402], Copyright 2012. Reproduced with permission from Springer Nature. (C) [403], Copyright 2013. Reproduced with permission from Springer Nature. (For interpretation of the references to colour in this figure legend, the reader is referred to the web version of this article.)

The arrangement of DNA sequences in the assembly of these complex structures is inspired and derived from the way Nature recombines and shuffles genetic information in cells through the formation of Holliday junctions [410]. These junctions are interlocking multi-arm DNA forming the immobile and thus stable connections within most, if not all, DNA-based architectures. As these junctions are rigid with defined distances between each arm, positioning of nanomaterials in 3D space can be accomplished with great precision. At this length scale, the inclusion of polymers into DNA to confer hydrophobicity, stimulus responsiveness and/or synthetic functions within a defined 3D scaffold offers exciting new prospects in nanoscience.

In this context, Sleiman's group constructed minimalistic wire-frame DNA prisms and cubes appended with different hexaethylene glycol units to promote a controlled aggregation process [411,412]. Micellar assemblies containing specific number of cubes and prisms can be tailored according to the polymer length and shape of the initial wire-frame DNA. Superscale assemblies ranging from 1 to 10 μm, containing micelles from these two different shapes, can also be achieved. This strategy was further developed to include hydrophobic 1,12-dodecanediol in both block and alternating format with hexaethylene glycol to better understand the motivation of assembly both inter- and intramolecularly [413]. Using this methodology, a new range of DNA nanostructures can be accessed from the same precursors but with sequence variation of the appended polymeric segment. Separately, the approach of constructing superlattices of DNA to orientate macromolecular objects was further demonstrated by combining different shapes into a three-layer architecture where inter-object distances can be tuned in both nanometer and micrometer scale [414].

As DNA controls structure formation through sequence regularity and specific interconnections into nanometer size objects, its templating effect on the molecular order of synthetic polymers reaches another paradigm. In a seminal study, Gothelf's group demonstrates that a conjugated brush polymer, 2,5-dialkoxy-*p*-phenylene vinylene, can be routed individually on designated patterns of a DNA origami tile [415]. This was achieved through the attachment of ssDNA along the side chains of the polymer, which is complementary to the different patterns (i.e. S-shaped, U-shaped, O-shaped) extending out of the origami tile. The routing procedure was also demonstrated in 3D, by wrapping the single strand polymer around a cylindrical origami. Optical properties were investigated using polyfluorene as an energy transfer donor to poly(*p*-phenylene vinylene), which were both routed in close proximity onto the same origami tile [416]. Efficient inter-polymer energy transfer was observed only upon successful attachment whereas the introduction of a 4-(dimethylaminoazo)benzene-4-carboxylic acid (DABCYL) quencher would block the optical communication between the two polymer strands. Using DNA toehold displacement technology, the alignment of polymers along the origami tile was switched reversibly to form differently oriented tracks [417]. The kinetics of the nanomechanical switching was characterized by time-dependent FRET studies and shown that the complete transformation was achieved in about 30 min.

Beyond directing the conformation changes of synthetic polymers, DNA nanoscale structures can provide an opportunity to guide polymerization reactions to transfer the precise shape profile of DNA onto synthetic polymers. Our group arranged ATRP radical initiators in various shapes (i.e. lines, squares, crosses etc.) on DNA origami tiles, where polymers can subsequently be grafted from [418]. The polymerization reaction includes bis-acrylate cross-linkers to ensure that the growing polymer chains from the origami scaffold were stabilized through the interconnections (Fig. 12A). Degradation of the sensitive origami template was achieved to yield the patterned polymeric structures. The methodology was subsequently expanded to pattern catalytic DNA structures, known as DNAzymes, from which the controlled polymerization of dopamine can be promoted (Fig. 12B) [419]. As polydopamine has a strong propensity to adhere to any neighboring material, it aggregates directly at the catalytic sites and thus takes the shape aspect of the designated pattern. In this way, distinct polydopamine nanostructures were formed at the DNA template. In addition, both polymerization methods were subsequently conducted in sequence on 3D tube origamis to form polymers orthogonally located at the internal and external surfaces of the tube (Fig. 12C) [420]. This opens interesting prospects for cross-sectional engineering of nanoscale objects with synthetic polymers.

4.3. Applications of well-defined nucleic acid–polymer conjugates

Beyond its sequence identity, DNA is a functional molecule from both chemical and biological perspective. Chemically, the complementarity of DNA is essentially a bioorthogonal handle where molecules or materials of interest have been shown to ligate seamlessly [421–423]. This aspect has been exploited liberally in all variations of DNA nanotechnology and applications ranging from photonics, therapeutics, sensing, and nanomaterials. Comparatively, the biological relevance of DNA is more self-explanatory, as nucleic acids often are used to affect genetic information or mediate biological functions through single-stranded DNA or RNA sequences that bind to specific target molecules known as aptamers. The attachment of polymers to such sequences typically takes the stage of increasing the stability of DNA within the biological system, acting as a vehicle to cross cellular membranes and/or as a combinatorial platform for multimodal medical applications [424,425].

Recent advances in this area generally attempt to integrate multiple functions (i.e. stimulus and temporal control, targeting etc.) onto a polymeric scaffold to enhance the bioactivity of DNA and its pharmacological properties. In this respect, the groups of Sumerlin and Tan demonstrated the grafting of DNA aptamers onto a hyperbranched PEG using photo-responsive chemistry [426]. Loaded with the chemotherapeutic, doxorubicin, the drug delivery system exhibited aptamer mediated targeting simultaneously with photo-dependent release (Fig. 13A). Other than aptamers, different classes of biologically attractive nucleic acid sequences such as siRNA have found similar avenues within polymer science. Although RNA is intrinsically more hydrolytically labile, both *grafting to* [427] and *grafting from* [428] strategies work well to form the desired bioconjugates. The groups of Albertazzi and Dankers expanded the possibilities by integrating siRNA into a multicomponent supramolecular polymer platform [429]. The supramolecular polymer is built upon using a 1,3,5-benzenetricarboxamide (BTA) derivative into nanofibrillar architectures (Fig. 13B). By functionalizing the BTA end groups with positively charged amines, siRNA can be complexed along the fiber axis while the hydrophobic core of the fiber provides the possibility to load small organic molecules of interest. The resultant polymeric construct facilitates both intracellular transport and up to 41% gene silencing capabilities against ELAV1, an RNA-binding protein, messenger RNA expression of HK-2 cells after 48 h. Other examples of functionally active DNA include spherical nucleic acids (SNAs) in which the self-assembly into a core–shell architecture is driven by the attachment of a diblock copolymer onto an oligonucleotide [430]. Using different sequences for the SNA formation, cellular internalization, trafficking and gene knockdown effects were elucidated, demonstrating that these assemblies remain highly bioactive through their self-assembly processes.

In certain cases, the interest does not solely lie on the bioactivity of nucleic acids but rather the use of DNA interactions to enhance polymer derived functions i.e. fluorescence, optoelectronics. By conjugating oligonucleotides onto a semi-conducting polymer derivatized from polythiophene, the amphiphilicity of the DNA–polymer conjugate was the driving force for the observed vesicular assembly, and nanoribbons were formed by co-assembly with a PEGylated polythiophene [431]. This concept was also similarly demonstrated in light harvesting polymers where hydrophobic chromophore stacks containing oligo(*p*-phenyleneethynylene) can be directed by DNA interactions to form fibrillar architectures [432]. Bringing such concepts into optoelectronic devices, Wagenknecht's group found that mixed arrays of pyrene

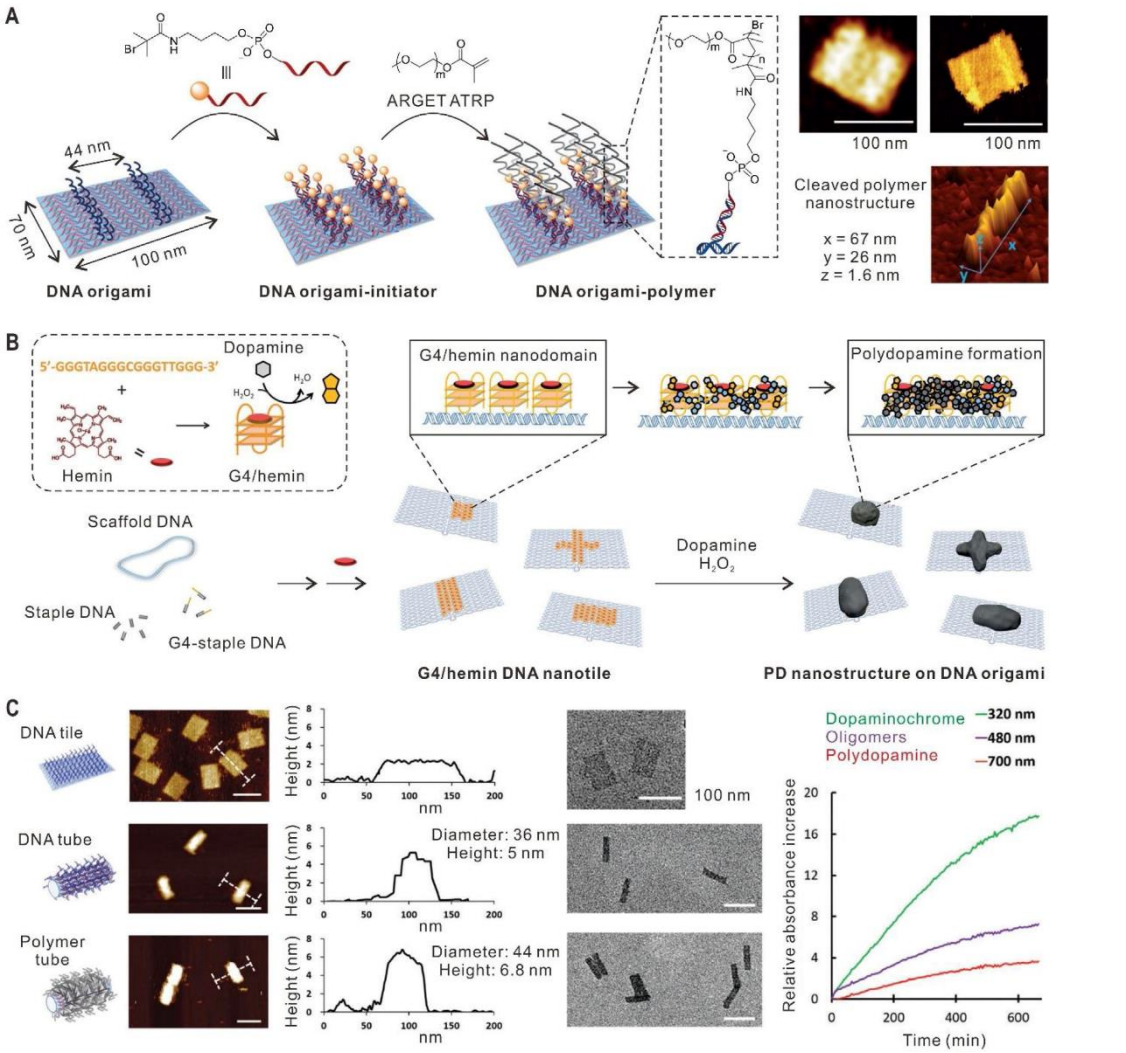

Fig. 12. DNA origami for templated synthesis of precision polymer nanostructures. (A) The fabrication of patterned polymer nanostructures on DNA origami by *in situ* ATRP. The 3D AFM image on the bottom right shows a cross-linked polymer structure extracted from the DNA origami template; (B) Schematic illustration of the process for constructing defined polydopamine nanostructures on DNA origami; (C) A 3D DNA tube transformed from a 2D DNA tile was used as a precise nanotemplate for ATRP from the surface and polydopamine formation in the interior cavity. The rightmost figure shows the kinetics of dopamine polymerization in the DNA–polymer hybrid tube. (A) [418], Copyright 2016, Reproduced with permission from John Wiley and Sons Inc. (B) [419], Copyright 2018, Reproduced with permission from John Wiley and Sons Inc. (C) [420], Copyright 2018, Reproduced with permission from the Royal Society of Chemistry.

and Nile red can be templated along a fullerene functionalized oligonucleotide consisting of 20 repeats of deoxyadenosine [433]. With various pyrene and Nile red ratios, exciton dissociation by electron transfer to the fullerene were manipulated to different extents (Fig. 13C). In addition, the three-component system was incorporated as a photoactive layer in solar cells and charge-carrier generation of the material was demonstrated.

5. Polymer conjugates based on other biotemplates

5.1. Carbohydrate–polymer conjugates

Carbohydrates, also known as saccharides, are composed of monosaccharides, disaccharides, oligosaccharides, and polysaccharides. In contrast to the biomolecules discussed so far, saccharides often reveal complex branching structures, and they interact with various biological target structures. Carbohydrates play many critical roles in living organisms including energy storage and as structural components. Due to their unique features such as biocompatibility, biodegradability, and multifunctionality, carbohydrates have attracted great interest in biomedical and materials fields. The conjugation of functional polymers to carbohydrates is an effective strategy to improve their properties and broaden the applications. For example, cellulose, which is a polysaccharide and the most abundant biopolymer on earth, has been modified by many modern polymerization techniques [434–437]. Malmström et al. conducted ATRP of methyl acrylate from cellulose fibers at ambient temperature, which is the first example of controlled radical polymerizations for polymer growth from cellulose [438]. Using hydroxyl groups on cellulose as initiators, biodegrad-

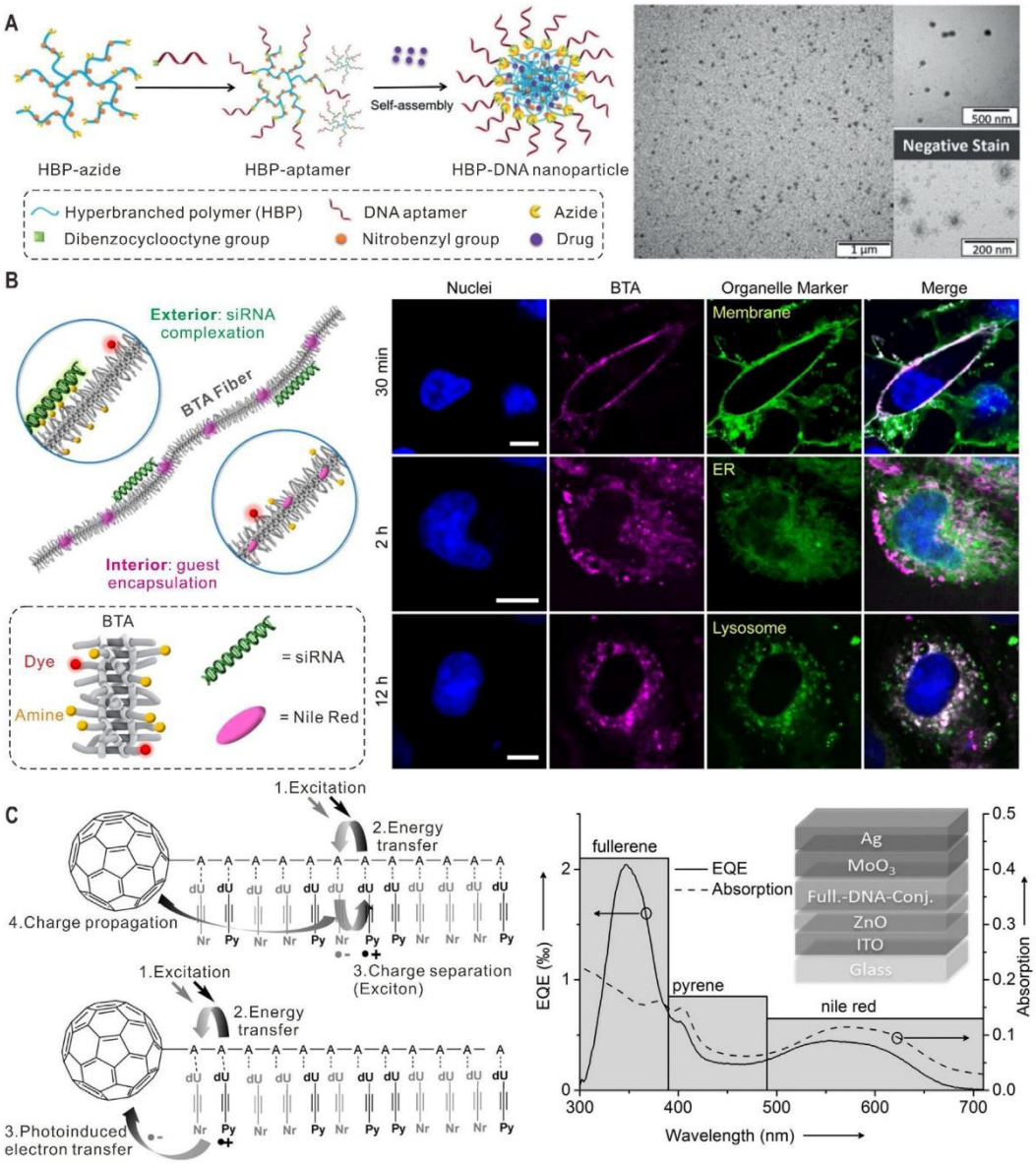

Fig. 13. Representative applications of nucleic acid–polymer conjugates. (A) Self-assembly and TEM images of nanocarriers based on aptamer-grafted hyperbranched polymers for targeted and photo-responsive drug delivery; (B) Multicomponent BTA supramolecular polymers with two functional compartments, small fluorescent molecules loaded in the hydrophobic core and siRNA immobilized on the hydrophilic exterior, were used as a modular platform for intracellular delivery. Confocal microscopy images on the right indicate the intracellular trafficking of BTA polymers. Scale bars: 10 μm; (C) Supramolecular assembly of two different chromophores (pyrene and Nile red) along a fullerene–DNA conjugate scaffold forming ordered and mixed assemblies, which were employed as a photo-active layer in solar cells. The right figure shows the broad spectral absorption of the photoactive layer and respective external quantum efficiency (EQE) of a typical solar cell. (A) [426], Copyright 2018. Reproduced with permission from John Wiley and Sons Inc. (B) [429]. Copyright 2016. Reproduced with permission from the American Chemical Society. (C) [433], Copyright 2016. Reproduced with permission from John Wiley and Sons Inc. (For interpretation of the references to colour in this figure legend, the reader is referred to the web version of this article.)

able polymers such as poly(L-lactic acid) and poly(ε-caprolactone) can also be conjugated *via* ROP [439]. Other carbohydrates including chitosan, pullulan, dextran, starch, and hyaluronan have also been modified by these polymerization methods, yielding functional materials for a variety of applications such as drug and gene delivery [440,441]. Unlike proteins and nucleic acids with absolute structures, most polysaccharides have varied molecular weights and properties. Therefore, this section does not provide a full overview of all carbohydrate–polymer conjugates but some examples with well-defined structures are highlighted.

Well-defined carbohydrate–polymer conjugates can be prepared by introducing monosaccharides or oligosaccharides to a precision polymer scaffold. For instance, functional copolymers with 2-naphthol groups and a narrow molecular weight distribu-

tion were synthesized by ATRP, and α-mannoside was conjugated to the backbone using cucurbit[8]uril-based host–guest inclusion forming supramolecular glycopolymers [442]. Linhardt and Lee et al. prepared a series of well-defined conjugates by attaching 6′-sialyllactose (6SL) to different generation PAMAM dendrimers, which were used to inhibit influenza A viruses [443]. In spherical generation 4 and 5 scaffolds, the interligand spacing was found to be a more important factor than the number of ligands for the antiviral effect. Generation 4 6SL–PAMAM conjugates with a spacing of 3 nm between 6SL ligands demonstrated the highest binding to a hemagglutinin trimer and displayed the best effect to block H1N1 infection. The structure-based design of carbohydrate–polymer conjugates can therefore serve as an effective strategy to improve the antiviral efficacy of the bioconjugates.

Carbohydrates have also been used as precision templates to grow polymers with controlled polymerization techniques, generating carbohydrate–polymer conjugates with well-defined architectures. β-Cyclodextrin (β-CD) is a cyclic oligosaccharide consisting of seven D-glucopyranoside units connected by α-1,4-glucosidic bonds. Each glucopyranoside unit has three hydroxyl groups, which can be functionalized with ATRP initiators. Lin et al. prepared a β-CD macroinitiator by esterification of hydroxyl groups with 2-bromoisobutyryl bromide and pioneered the synthesis of 21-arm, star-like block copolymers using ATRP in combination with click chemistry [444,445]. These star-like polymers can be used as unimolecular micelles for inorganic nanoparticle synthesis, as well as drug and gene delivery [446,447]. In particular, they have demonstrated the preparation of nearly monodisperse colloidal nanocrystals with precisely controlled dimensions, compositions, and architectures by using the well-defined star-like polymers as nanoreactors [448]. Specifically, metallic, ferroelectric, magnetic, semiconductor, and luminescent colloidal nanocrystals with desired sizes and architectures were synthesized following this strategy. Because cellulose forms a rigid backbone, the strategy has been further extended to realize one-dimensional rod-like nanocrystals using cellulose–polymer conjugates as cylindrical unimolecular nanoreactors [449]. As a proof of concept for the preparation of plain nanorods, amphiphilic cellulose-*g*-(PAA-*b*-PS) {cellulose-*graft*-[poly(acrylic acid)-*block*-polystyrene]} was synthesized (Fig. 14A). The PAA blocks can accommodate and coordinate a large volume of inorganic precursors, allowing the nucleation and growth of inorganic nanorods (Fig. 14B). Importantly, the outer PS blocks impart solubility to the obtained nanorods in organic solvents, which facilitates their processing and applications. This approach was readily adaptable to more complex nanostructures such as core–shell nanorods (Fig. 14C and D), and nanotubes (Fig. 14E and F) through rational design and synthesis of functional bottlebrush-like bioconjugates with different triblock copolymer side chains.

5.2. *Lipid–polymer conjugates*

In addition to proteins, nucleic acids and carbohydrates, lipids are the last member of the four major classes of biomolecules. Lipids can be hydrophobic or amphiphilic small molecules. A famous example are amphiphilic phospholipids, which possess unique self-assembly characteristics and are a major component of all cellular membranes. Early studies of lipid–polymer conjugates mainly focus on the PEGylation of lipids to enhance the stability and circulation time of lipid-based drug nanocarriers [450–452]. For example, Farokhzad and coworkers reported a lipid–polymer hybrid nanoparticle platform, which was composed of a biodegradable and hydrophobic polymeric core for drug loading, a lipid monolayer at the interface to promote drug retention, and a hydrophilic PEG layer that was covalently attached to the lipid layer to afford stealth properties [453]. The hybrid nanoparticle combines the advantages of polymeric nanoparticles and liposomes and can be prepared by self-assembly through a single-step nanoprecipitation method. In order to deliver siRNA, the same group later reported a hollow core–shell lipid–polymer–lipid hybrid nanoparticle system consisting of an outer lipid–PEG surface, a middle hydrophobic polymer layer, and a positively charged lipid layer generating the inner hollow core [454]. Besides PEG, a range of other polymers have also been conjugated to lipids through various chemical strategies. Hennink et al. reported the attachment of biodegradable polypeptides to lipids for the design of long-circulating liposomes with drug-targeting capacity [455]. Hawker et al. prepared a variety of lipid–polymer conjugates with controlled molecular weights and narrow molecular weight distributions by photoelectron transfer RAFT polymerization [456].

Bioengineering techniques have also been developed to prepare well-defined lipid–polymer conjugates. Inspired by the post-translational modification of proteins in Nature, Chilkoti et al. reported the high efficiency synthesis of lipid–peptide polymer hybrids through an eukaryotic post-translation modification [457]. Myristic acid as a lipid was conjugated to an elastin-like polypeptide (ELP), and the resulting conjugate self-assembled into tunable micelles that can be applied to deliver anticancer drugs. By further introducing a short β-sheet-forming peptide in between of the lipid and the ELP block, three stimuli-responsive lipid–polypeptide conjugates were prepared, which exhibited temperature-triggered hierarchical self-assembly [458]. Very recently, this genetically encoded approach has also been employed to synthesize cholesterol-conjugated peptide polymers [459].

5.3. *Engineering live cells* via *polymer conjugation*

An exciting new research direction in polymer bioconjugation is direct engineering of living cells with polymers. One could envision that cell–polymer conjugates could provide improved *in vivo* compatibility as well as reduced immune responses and enzymatic degradation can be afforded to modified cells, suggesting entirely new perspectives for fundamental studies in cell biology as well as applications in transfusion, cell-based therapeutics, and tissue engineering [460]. For instance, Scott and coworkers pioneered the covalent conjugation of PEG to the red blood cell (RBC) membrane *via* cyanuric chloride coupling [461]. The conjugated polymer chains could block antibody mediated recognition of RBC surface antigens. Hyperbranched polyglycerol (HPG) has also been conjugated to RBC surfaces *via* an ester–amide linker and the *in vivo* circulation in mice indicated that more than half of HPG-grafted cells were functional and retained a normal circulation behavior [462]. Although the cell surface modification has been achieved in some cases, their low conjugation efficiency due to the repulsion between hydrophilic polymers and cell surfaces represents a major limitation. To address this issue, Kizhakkedathu et al. developed a universal technique to significantly improve cell surface modification by introducing nonreactive and cell-compatible polymers as additives [463]. Unprecedented enhanced polymer grafting by up to 10-fold was demonstrated using four different cell types. Pasparakis et al. synthesized two functional copolymers, which were conjugated to live cells to control cell aggregation behaviors [464]. Recently, Gibson and coworkers reported that telechelic polymers bearing different functional groups prepared by RAFT polymerization can be site-specifically conjugated to metabolic glycans on cell surfaces using strain-promoted azide–alkyne click cycloaddition [465,466].

In situ growth of functional polymers from live cell surfaces by controlled radical polymerizations has also be reported. Choi and Yang et al. selected ARGET ATRP to grow polymers from living cell surfaces because only low concentrations of ATRP catalysts

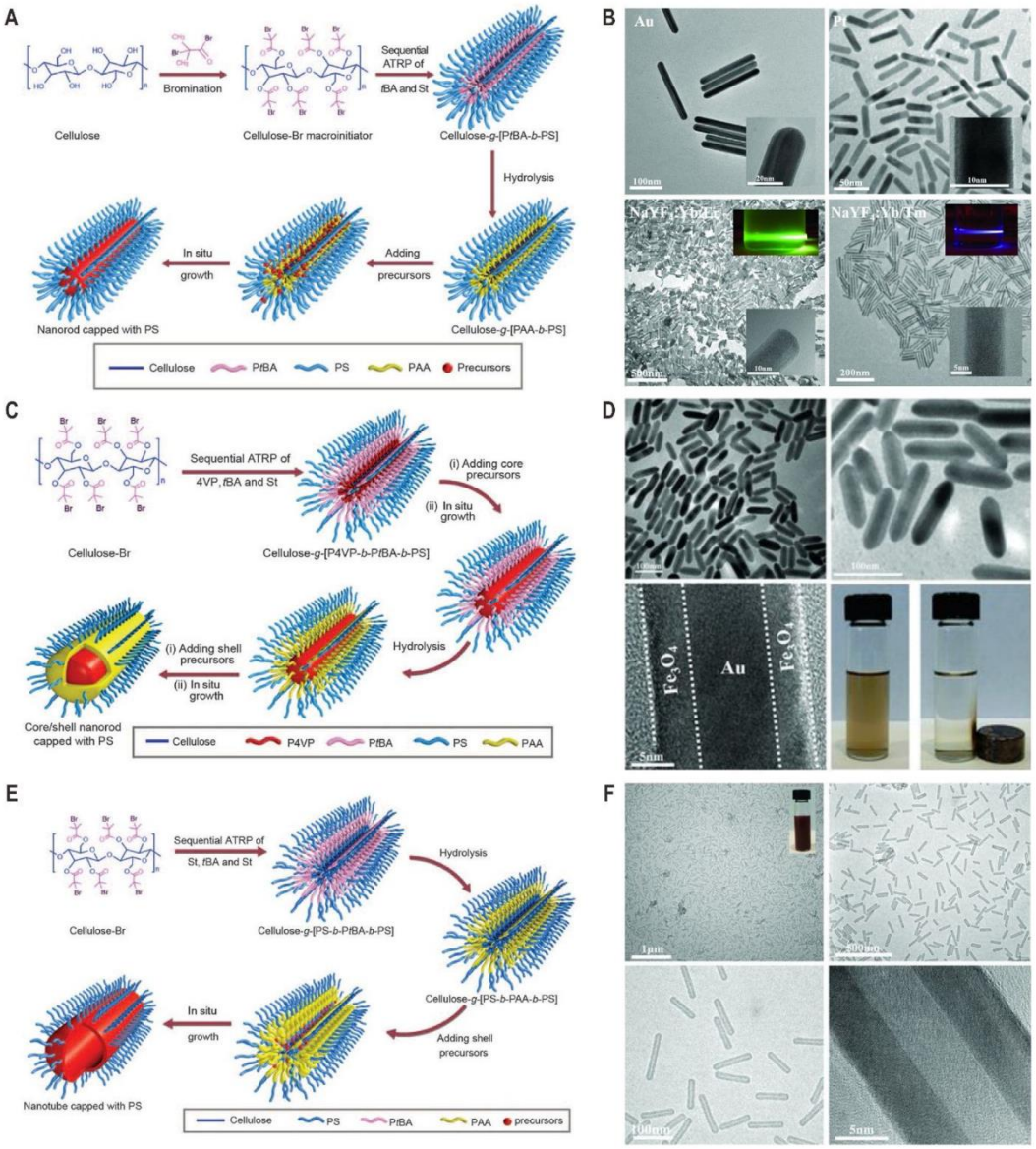

Fig. 14. Preparation of precision 1D nanocrystals by using cylindrical cellulose–polymer conjugates as nanoreactors. (A) Plain nanorods templated by cellulose-*g*-(PAA-*b*-PS). St, styrene; *t*BA, *tert*-butyl acrylate. (B) TEM images of a variety of plain nanorods. (C) Core–shell nanorods templated by cellulose-*g*-(P4VP-*b*-PtBA-*b*-PS). (D) TEM and digital images of Au-Fe_3O_4 core–shell nanorods. (E) Nanotubes templated by cellulose-*g*-(PS-*b*-PAA-*b*-PS). (F) TEM images of Au nanotubes at different magnifications. [449], Copyright 2016, Reproduced with permission from the American Association for the Advancement of Science.

were required, and the reaction was conducted in the aqueous solution under atmospheric conditions [467]. Polydopamine-based ATRP initiators were firstly attached to yeast cells to prevent radical attack during ATRP process (Fig. 15A). A water-soluble and biocompatible monomer, sodium methacrylate (SMA), was then polymerized for a predetermined time. The successful polymer growth was confirmed by scanning electron microscopy (SEM, Fig. 15B) and confocal laser scanning microscopy (Fig. 15C) images. Moreover, poly(SMA)-coated yeast cells did not aggregate when they were mixed with *Escherichia coli*, which indicated that the binding between *E. coli* and yeast cells had been blocked by the polymer layer (Fig. 15D). These results clearly demonstrated that highly dense polymers can be grafted onto live cell surfaces by ARGET ATRP using the *grafting from* strategy. Very recently, the *grafting from* ATRP strategy was also applied to attach thermoresponsive PNIPAM to specific proteins at the surface of living cells for isolation and analysis of membrane proteins [468]. Hawker and coworkers pioneered the *in situ* polymer growth from live yeast and mammalian cells *via* cytocompatible RAFT polymerization (Fig. 15E) [469]. Specifically, a visible light mediated RAFT process was developed, which allowed the polymerization of functional PEG monomers into narrowly distributed polymers ($M_w/M_n < 1.3$)

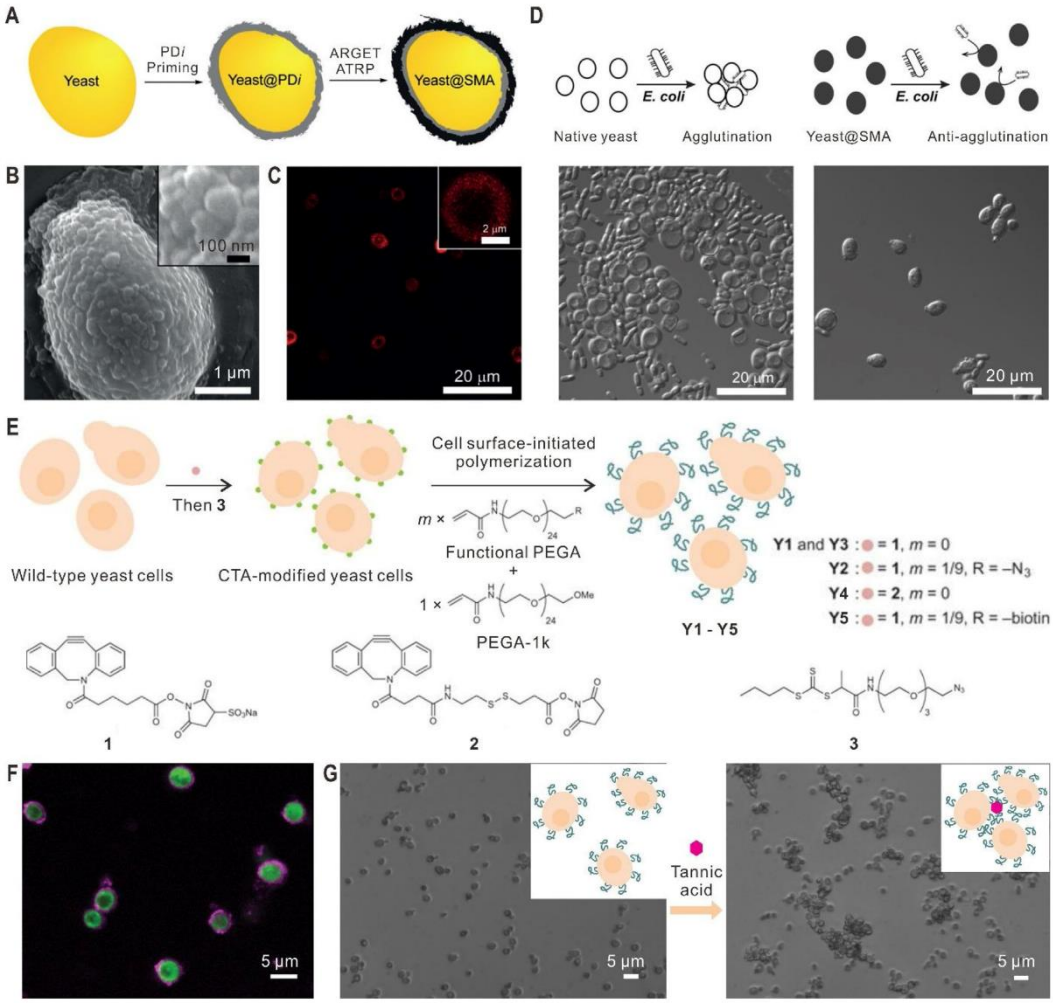

Fig. 15. Polymer grafting from live cell surfaces using cytocompatible controlled radical polymerization techniques. (A) Schematic illustration for polymer grafting from yeast cells *via* surface-initiated ARGET ATRP. (B) SEM images of SMA-coated yeast. (C) Confocal laser scanning microscopy images of azide-functionalized SMA-coated yeast after coupling with alkyne-linked Alexa Fluor 594. (D) Agglutination assay of yeast: (left) native yeast and (right) SMA-coated yeast. (E) Schematic illustration of polymer growth from yeast cells *via* surface-initiated RAFT polymerization. (F) Confocal fluorescent microscopy shows fluorescent labelling of treated yeast cells. Polymers on the surface were labelled with a derivative of Alexa Fluor 647, indicating the successful polymer growth at the cell surface. (G) Tannic acid which binds to PEG through hydrogen bonding was used to manipulate aggregation of polymer-grafted yeast cells. [467], Copyright 2016. Reproduced with permission from John Wiley and Sons; [469], Copyright 2017. Reproduced with permission from Springer Nature.

at room temperature in 5 min. As a proof-of-concept experiment to introduce functional polymers to the surface of cells, copolymerization of methoxy-PEG acrylamide-1k (PEGA-1k) and ω-azido PEG acrylamide with a molar ratio of 9:1 was conducted after introducing RAFT CTAs to the surface of yeast cells. The obtained azide-containing yeast cells were further functionalized with a derivative of Alexa Fluor 647. As shown in Fig. 15F, strong fluorescence of Alexa Fluor 647 was only observed at the surface of yeast cells, indicating the successful surface-initiated growth of reactive polymers. Furthermore, tannic acid, a compound known to bind PEG through hydrogen bonding interactions, was added to a suspension of polymer-modified yeast cells. Considerable aggregation was observed after mild shaking for 1 h (Fig. 15G), indicating that the approach can be used to control cell–cell interactions. These examples impressively indicate the great potential of modern polymerization techniques for directly engineering live cell surfaces. It should be noted that the radical polymerization of biocompatible acrylic and methacrylic monomers inside living cells has also been reported [470]. A light-controlled polymerization method was successfully employed to generate polymers in complex intracellular environments. Therefore, we can expect even more complex and well-defined polymer bioconjugates prepared by conjugating live objects inside cells with synthetic polymers in the near future.

6. Summary and outlook

The development of polymer science and its connection to biology has evolved rapidly in recent years. The field has started as a concept to provide stability to biomolecules and improve their application as therapeutics. However, from the success of the first bioconjugates that moved into clinical phases, the impact of synthetic polymer bioconjugates became apparent not only in

application driven research, but also found its place in newly developed areas of fundamental science such as supramolecular chemistry, precision polymer synthesis and self-organization. Specifically, these are instances where biomolecules have helped to achieve greater heights as well as diversity in macromolecular science. From polymer synthesis, the appreciation of the enzyme degassing system through glucose oxidase/sodium pyruvate has granted the access to *grafting from* controlled radical polymerizations at exceedingly low volumes and in ambient conditions. This important technical progress will enable technologies such as polymerization-induced self-assembly possible with biomolecules such as unnatural peptides or DNA, which have limited scalability. Therefore, it is important to recognize that technical breakthroughs at the synthesis level are essential to provide access to entirely new biohybrid architectures with designed functionalities. With the help of sophisticated enzyme design possibly through directed protein evolution, one could envision that enzymes could be programmed as synthetic polymerases to build polymers on demand.

While the bioactivity of biomolecules often represents the main reason for their applications, their perfect structure could be considered as an equally important feature. There is an emerging interest in the application of biomolecules to direct or template polymer syntheses and assemblies. In this context, the application of DNA has been the main focus where its complementary recognition has an unrivalled specificity. Significant efforts have been made to use DNA base pairs and to arrange a sequence order for synthetic oligomeric or polymeric fragments. While these technologies have already proven success, they are still quite laborious and costly given the quantities that can be fabricated. However, should these templated syntheses achieve directed amplification akin to the polymerase chain reaction, it would immensely broaden the applications DNA-polymer conjugates. To our mind, we are just at the beginning to apply Natures polymers as templates for precision polymer bioconjugates and hybrid materials. Meanwhile, the hierarchical self-assembly of polypeptides into defined nanostructures will create fast access tailored functional nanomaterials by supramolecular copolymerization. In addition, there is also an enormous potential to elucidate the structure of polypeptides and proteins at different levels of order, i.e. in the globular ordered, intrinsically disordered or denatured states. These studies could give entirely new insights into the structures and functions of intrinsically disordered proteins that are just being explored and one could already appreciate many similarities to the behavior of polymers.

Nonetheless, the mainstream applications of biomolecule-polymer conjugates in medicine will remain and we foresee significant developments in the future where treatments and diagnostics may become personalized. As there is typically very limited chemical space available at the target biomolecule, a conjugated polymeric component could impart new features such as enhanced specificity or pharmacokinetics that could be tailored for the individual patient to maximize *in vivo* efficacy. Here, there have been already important discoveries that incorporated synergistic combinations of stimulus responsive chemistry and dynamic self-assemblies to optimize the biological profile of the bioconjugate. We foresee that the evolution of these conjugates moves towards higher complexity and "intelligence" and, at certain stages, show semblance of primitive autonomous behavior. With the advent of modern chemical tools, it would be highly attractive to furnish an autonomous bioconjugate, where it can seemingly decide for itself to solve a targeted biological problem.

Collectively, every aspect of chemistry, from the synthetic tools that enable the bioconjugates to higher ordered assemblies have each found a new lease of life. Every bond formed and its significance will undoubtedly be increasingly featured in the coming years as the community unravels novel possibilities to create greater control of structures and structural complexity. While comparisons to Nature's capabilities are often discussed in the literature, one must not forget that the breadth of synthetic macromolecular chemistry far exceeds those found in the biology. However, what makes Nature unique and seemingly intelligent is the vast network of macromolecules working and communicating within a highly regulated self-sustaining system. Here, although the myriad of conjugates produced by synthetic chemistry has been consistently innovative, relationships between these novel macromolecules are rarely put together and studied within an artificially controlled environment. It could be envisioned that the future of synthetic bioconjugates would greatly lie in establishing the molecular principle of how these macromolecules can be customized to the extent of how an engineer builds a robot.

CRediT author statement

Chaojian Chen: Chapters 2, 3, 5, and figure design. David Y.W. Ng: Introduction, chapter 4, and outlook. Tanja Weil: Concept, structuring, reviewing, and corrections.

Declaration of Competing Interests

The authors declare that they have no known competing financial interests or personal relationships that could have appeared to influence the work reported in this paper.

Acknowledgements

The authors acknowledge financial support from the European Union's ERC Synergy Grant under grant agreement No. 319130 (BioQ) as well as from the Max Planck-Bristol Centre for Minimal Biology. C.C. is grateful for a doctoral fellowship from Promotionskolleg Pharmaceutical Biotechnology of Ulm University funded by the state of Baden–Württemberg. We also thank Nicole Kirsch-Pietz for critically reading the manuscript.

References

[1] Staudinger H. Über polymerisation. Ber Dtsch Chem Ges 1920;53:1073–85.
[2] Geyer R, Jambeck JR, Law KL. Production, use, and fate of all plastics ever made. Sci Adv 2017;3, e1700782/1-5.
[3] Badi N, Lutz JF. Sequence control in polymer synthesis. Chem Soc Rev 2009;38:3383–90.
[4] Lutz JF, Ouchi M, Liu DR, Sawamoto M. Sequence-controlled polymers. Science 2013;341, 1238149/1-8.
[5] Matyjaszewski K. Advanced materials by atom transfer radical polymerization. Adv Mater 2018;30, 1706441/1-22.
[6] Rowland GF, Oneill GJ, Davies DAL. Suppression of tumor-growth in mice by a drug-antibody conjugate using a novel approach to linkage. Nature 1975;255:487–8.
[7] Ringsdorf H. Structure and properties of pharmacologically active polymers. J Polym Sci Polym Symp 1975;51:135–53.
[8] Abuchowski A, Vanes T, Palczuk NC, Davis FF. Alteration of immunological properties of bovine serum-albumin by covalent attachment of polyethylene-glycol. J Biol Chem 1977;252:3578–81.
[9] Monji N, Hoffman AS. A novel immunoassay system and bioseparation process based on thermal phase separating polymers. Appl Biochem Biotechnol 1987;14:107–20.
[10] Chen JP, Yang HJ, Hoffman AS. Polymer protein conjugates. 1. Effect of protein conjugation on the cloud point of poly(N-isopropylacrylamide). Biomaterials 1990;11:625–30.
[11] Chilkoti A, Chen GH, Stayton PS, Hoffman AS. Site-specific conjugation of a temperature-sensitive polymer to a genetically-engineered protein. Bioconjug Chem 1994;5:504–7.
[12] Stayton PS, Shimoboji T, Long C, Chilkoti A, Chen GH, Harris JM, et al. Control of protein-ligand recognition using a stimuli-responsive polymer. Nature 1995;378:472–4.
[13] Ding ZL, Fong RB, Long CJ, Stayton PS, Hoffman AS. Size-dependent control of the binding of biotinylated proteins to streptavidin using a polymer shield. Nature 2001;411:59–62.
[14] Hoffman AS, Stayton PS. Conjugates of stimuli-responsive polymers and proteins. Prog Polym Sci 2007;32:922–32.

[15] Lutz JF, Borner HG. Modern trends in polymer bioconjugates design. Prog Polym Sci 2008;33:1–39.
[16] Messina MS, Messina KMM, Bhattacharya A, Montgomery HR, Maynard HD. Preparation of biomolecule-polymer conjugates by grafting-from using ATRP, RAFT, or ROMP. Prog Polym Sci 2020;100, 101186/1-25.
[17] Li XY, Liu DR. DNA-templated organic synthesis: nature's strategy for controlling chemical reactivity applied to synthetic molecules. Angew Chem Int Ed 2004;43:4848–70.
[18] Shu JY, Panganiban B, Xu T. Peptide-polymer conjugates: from fundamental science to application. Annu Rev Phys Chem 2013;64:631–57.
[19] Canalle LA, Lowik DWPM, van Hest JCM. Polypeptide-polymer bioconjugates. Chem Soc Rev 2010;39:329–53.
[20] Broyer RM, Grover GN, Maynard HD. Emerging synthetic approaches for protein-polymer conjugations. Chem Commun 2011;47:2212–26.
[21] Zhao WG, Liu F, Chen Y, Bai J, Gao WP. Synthesis of well-defined protein-polymer conjugates for biomedicine. Polymer 2015;66:A1–10.
[22] Ekladious I, Colson YL, Grinstaff MW. Polymer-drug conjugate therapeutics: advances, insights and prospects. Nat Rev Drug Discov 2019;18:273–94.
[23] Wang YJ, Wu C. Site-specific conjugation of polymers to proteins. Biomacromolecules 2018;19:1804–25.
[24] Kato M, Kamigaito M, Sawamoto M, Higashimura T. Polymerization of methyl-methacrylate with the carbon-tetrachloride dichlorotris(triphenylphosphine)Ruthenium(II) methylaluminum bis(2,6-di-tert-butylphenoxide) initiating system - possibility of living radical polymerization. Macromolecules 1995;28:1721–3.
[25] Wang JS, Matyjaszewski K. Controlled living radical polymerization - atom-transfer radical polymerization in the presence of transition-metal complexes. J Am Chem Soc 1995;117:5614–5.
[26] Chiefari J, Chong YK, Ercole F, Krstina J, Jeffery J, Le TPT, et al. Living free-radical polymerization by reversible addition-fragmentation chain transfer: the RAFT process. Macromolecules 1998;31:5559–62.
[27] Hawker CJ, Bosman AW, Harth E. New polymer synthesis by nitroxide mediated living radical polymerizations. Chem Rev 2001;101:3661–88.
[28] Nicolas J, Guillaneuf Y, Lefay C, Bertin D, Gigmes D, Charleux B. Nitroxide-mediated polymerization. Prog Polym Sci 2013;38:63–235.
[29] Otsu T. Iniferter concept and living radical polymerization. J Polym Sci Part A: Polym Chem 2000;38:2121–36.
[30] Dechy-Cabaret O, Martin-Vaca B, Bourissou D. Controlled ring-opening polymerization of lactide and glycolide. Chem Rev 2004;104:6147–76.
[31] Bielawski CW, Grubbs RH. Living ring-opening metathesis polymerization. Prog Polym Sci 2007;32:1–29.
[32] Hadjichristidis N, Pitsikalis M, Pispas S, Iatrou H. Polymers with complex architecture by living anionic polymerization. Chem Rev 2001;101:3747–92.
[33] Aoshima S, Kanaoka SA. Renaissance in living cationic polymerization. Chem Rev 2009;109:5245–87.
[34] Ozer I, Chilkoti A. Site-specific and stoichiometric stealth polymer conjugates of therapeutic peptides and proteins. Bioconjug Chem 2017;28:713–23.
[35] Stephanopoulos N, Francis MB. Choosing an effective protein bioconjugation strategy. Nat Chem Biol 2011;7:876–84.
[36] Krall N, da Cruz FP, Boutureira O, Bernardes GJL. Site-selective protein-modification chemistry for basic biology and drug development. Nat Chem 2016;8:102–12.
[37] Stenzel MH. Bioconjugation using thiols: old chemistry rediscovered to connect polymers with nature's building blocks. ACS Macro Lett 2013;2:14–8.
[38] Brocchini S, Godwin A, Balan S, Choi JW, Zloh M, Shaunak S. Disulfide bridge based PEGylation of proteins. Adv Drug Deliv Rev 2008;60:3–12.
[39] Jones MW, Strickland RA, Schumacher FF, Caddick S, Baker JR, Gibson MI, et al. Polymeric dibromomaleimides As extremely efficient disulfide bridging bioconjugation and pegylation agents. J Am Chem Soc 2012;134:1847–52.
[40] Smith MEB, Schumacher FF, Ryan CP, Tedaldi LM, Papaioannou D, Waksman G, et al. Protein modification, bioconjugation, and disulfide bridging using bromomaleimides. J Am Chem Soc 2010;132:1960–5.
[41] Collins J, Tanaka J, Wilson P, Kempe K, Davis TP, McIntosh MP, et al. In situ conjugation of dithiophenol maleimide polymers and oxytocin for stable and reversible polymer-peptide conjugates. Bioconjug Chem 2015;26:633–8.
[42] Zhang LB, Zhao WG, Liu XY, Wang GL, Wang Y, Li D, et al. Site-selective in situ growth of fluorescent polymer-antibody conjugates with enhanced antigen detection by signal amplification. Biomaterials 2015;64:2–9.
[43] Shaunak S, Godwin A, Choi JW, Balan S, Pedone E, Vijayarangam D, et al. Site-specific PEGylation of native disulfide bonds in therapeutic proteins. Nat Chem Biol 2006;2:312–3.
[44] Brocchini S, Balan S, Godwin A, Choi JW, Zloh M, Shaunak S. PEGylation of native disulfide bonds in proteins. Nat Protoc 2006;1:2241–52.
[45] Wang T, Ng DYW, Wu YZ, Thomas J, TamTran T, Weil T. Bis-sulfide bioconjugates for glutathione triggered tumor responsive drug release. Chem Commun 2014;50:1116–8.
[46] Wang T, Wu YZ, Kuan SL, Dumele O, Lamla M, Ng DYW, et al. A disulfide intercalator toolbox for the site-directed modification of polypeptides. Chem Eur J 2015;21:228–38.
[47] Wang T, Zabarska N, Wu YZ, Lamla M, Fischer S, Monczak K, et al. Receptor selective ruthenium-somatostatin photosensitizer for cancer targeted photodynamic applications. Chem Commun 2015;51:12552–5.
[48] Hooker JM, Kovacs EW, Francis MB. Interior surface modification of bacteriophage MS2. J Am Chem Soc 2004;126:3718–9.
[49] Joshi NS, Whitaker LR, Francis MB. A three-component Mannich-type reaction for selective tyrosine bioconjugation. J Am Chem Soc 2004;126:15942–3.
[50] Gilmore JM, Scheck RA, Esser-Kahn AP, Joshi NS, Francis MB. N-Terminal protein modification through a biomimetic transamination reaction. Angew Chem Int Ed 2006;45:5307–11.
[51] Scheck RA, Dedeo MT, Lavarone AT, Francis MB. Optimization of a biomimetic transamination reaction. J Am Chem Soc 2008;130:11762–70.
[52] Obermeyer AC, Jarman JB, Francis MB. N-Terminal modification of proteins with o-aminophenols. J Am Chem Soc 2014;136:9572–9.
[53] Gao WP, Liu WG, Mackay JA, Zalutsky MR, Toone EJ, Chilkoti A. In situ growth of a stoichiometric PEG-like conjugate at a protein's N-terminus with significantly improved pharmacokinetics. Proc Natl Acad Sci U S A 2009;106:15231–6.
[54] Gauthier MA, Klok HA. Peptide/protein-polymer conjugates: synthetic strategies and design concepts. Chem Commun 2008:2591–611.
[55] Rosendahl MS, Doherty DH, Smith DJ, Carlson SJ, Chlipala EA, Cox GN. A long-acting, highly potent interferon alpha-2 conjugate created using site-specific PEGylation. Bioconjug Chem 2005;16:200–7.
[56] Bell SJ, Fam CM, Chlipala EA, Carlson SJ, Lee JI, Rosendahl MS, et al. Enhanced circulating half-life and antitumor activity of a site-specific pegylated interferon-alpha protein therapeutic. Bioconjug Chem 2008;19:299–305.
[57] Ataka K, Giess F, Knoll W, Naumann R, Haber-Pohlmeier S, Richter B, et al. Oriented attachment and membrane reconstitution of his-tagged cytochrome c oxidase to a gold electrode: in situ monitoring by surface-enhanced infrared absorption spectroscopy. J Am Chem Soc 2004;126:16199–206.
[58] Kim TH, Swierczewska M, Oh Y, Kim A, Jo DG, Park JH, et al. Mix to validate: a facile, reversible PEGylation for fast screening of potential therapeutic proteins invivo. Angew Chem Int Ed 2013;52:6880–4.
[59] Jung S, Kwon I. Expansion of bioorthogonal chemistries towards site-specific polymer-protein conjugation. Polym Chem 2016;7:4584–98.
[60] Deiters A, Cropp TA, Summerer D, Mukherji M, Schultz PG. Site-specific PEGylation of proteins containing unnatural amino acids. Bioorg Med Chem Lett 2004;14:5743–5.
[61] Averick S, Karacsony O, Mohin J, Yong X, Moellers NM, Woodman BF, et al. Cooperative, reversible self-assembly of covalently pre-linked proteins into giant fibrous structures. Angew Chem Int Ed 2014;53:8050–5.
[62] Cho H, Daniel T, Buechler YJ, Litzinger DC, Maio ZW, Putnam AMH, et al. Optimized clinical performance of growth hormone with an expanded genetic code. Proc Natl Acad Sci U S A 2011;108:9060–5.
[63] Lu H, Wang DL, Kazane S, Javahishvili T, Tian F, Song F, et al. Site-specific antibody-polymer conjugates for siRNA delivery. J Am Chem Soc 2013;135:13885–91.
[64] Lang K, Chin JW. Cellular incorporation of unnatural amino acids and bioorthogonal labeling of proteins. Chem Rev 2014;114:4764–806.
[65] Tang W, Becker ML. "Click" reactions: a versatile toolbox for the synthesis of peptide-conjugates. Chem Soc Rev 2014;43:7013–39.
[66] Devaraj NK. The future of bioorthogonal chemistry. ACS Cent Sci 2018;4:952–9.
[67] Gao WP, Liu WG, Christensen T, Zalutsky MR, Chilkoti A. In situ growth of a PEG-like polymer from the C terminus of an intein fusion protein improves pharmacokinetics and tumor accumulation. Proc Natl Acad Sci U S A 2010;107:16432–7.
[68] Qi YZ, Amiram M, Gao WP, McCafferty DG, Chilkoti A. Sortase-catalyzed initiator attachment enables high yieldgrowth of a stealth polymer from the C terminus of a protein. Macromol Rapid Commun 2013;34:1256–60.
[69] Hu J, Wang GL, Zhao WG, Liu XY, Zhang LB, Gao WP. Site-specific in situ growth of an interferon-polymer conjugate that outperforms PEGASYS in cancer therapy. Biomaterials 2016;96:84–92.
[70] Hu J, Zhao WG, Gao Y, Sun MM, Wei Y, Deng HT, et al. Site-specific in situ growth of a cyclized protein-polymer conjugate with improved stability and tumor retention. Biomaterials 2015;47:13–9.
[71] Peeler JC, Woodman BF, Averick S, Miyake-Stoner SJ, Stokes AL, Hess KR, et al. Genetically encoded initiator for polymer growth from proteins. J Am Chem Soc 2010;132:13575–7.
[72] Gong YH, Leroux JC, Gauthier MA. Releasable conjugation of polymers to proteins. Bioconjug Chem 2015;26:1172–81.
[73] Zalipsky S, Mullah N, Engbers C, Hutchins MU, Kiwan R. Thiolytically cleavable dithiobenzyl urethane-linked polymer-protein conjugates as macromolecular prodrugs: reversible PEGylation of proteins. Bioconjug Chem 2007;18:1869–78.
[74] Tao L, Liu JQ, Xu JT, Davis TP. Bio-reversible polyPEGylation. Chem Commun 2009:6560–2.
[75] Tao L, Chen GJ, Zhao LX, Xu JT, Huang E, Liu AP, et al. Protein release from biodegradable PolyHPMA-lysozyme conjugates resulting in bioactivity enhancement. Chem Asian J 2011;6:1398–404.
[76] Braun AC, Gutmann M, Mueller TD, Luhmann T, Meinel L. Bioresponsive release of insulin-like growth factor-I from its PEGylated conjugate. J Control Release 2018;279:17–28.
[77] Bontempo D, Maynard HD. Streptavidin as a macroinitiator for polymerization: in situ protein-polymer conjugate formation. J Am Chem Soc 2005;127:6508–9.

[78] Han GD, Wang JT, Ji XT, Liu L, Zhao HY. Nanoscale proteinosomes fabricated by self-assembly of a supramolecular protein-polymer conjugate. Bioconjug Chem 2017;28:636–41.
[79] Biedermann F, Rauwald U, Zayed JM, Scherman OA. A supramolecular route for reversible protein-polymer conjugation. Chem Sci 2011;2:279–86.
[80] Webber MJ, Appel EA, Vinciguerra B, Cortinas AB, Thapa LS, Jhunjhunwala S, et al. Supramolecular PEGylation of biopharmaceuticals. Proc Natl Acad Sci U S A 2016;113:14189–94.
[81] Wang CCY, Seo TS, Li ZM, Ruparel H, Ju JY. Site-specific fluorescent labeling of DNA using Staudinger ligation. Bioconjug Chem 2003;14:697–701.
[82] Lushnikov AY, Potaman VN, Lyubchenko YL. Site-specific labeling of supercoiled DNA. Nucleic Acids Res 2006;34, e111/1-7.
[83] Jahn K, Olsen EM, Nielsen MM, Torring T, MohammadZadegan R, Andersen ES, et al. Site-specific chemical labeling of long RNA molecules. Bioconjug Chem 2011;22:95–100.
[84] Seo YJ, Malyshev DA, Lavergne T, Ordoukhanian P, Romesberg FE. Site-specific labeling of DNA and RNA using an efficiently replicated and transcribed class of unnatural base pairs. J Am Chem Soc 2011;133:19878–88.
[85] Zhao M, Steffen FD, Borner R, Schaffer MF, Sigel RKO, Freisinger E. Site-specific dual-color labeling of long RNAs for single-molecule spectroscopy. Nucleic Acids Res 2018;46, e13/1-8.
[86] Kwak M, Herrmann A. Nucleic acid amphiphiles: synthesis and self-assembled nanostructures. Chem Soc Rev 2011;40:5745–55.
[87] Schnitzler T, Herrmann A. DNA block copolymers: functional materials for nanoscience and biomedicine. Acc Chem Res 2012;45:1419–30.
[88] Oishi M, Hayama T, Akiyama Y, Takae S, Harada A, Yamasaki Y, et al. Supramolecular assemblies for the cytoplasmic delivery of antisense oligodeoxynucleotide: polylon complex (PIC) micelles based on poly(ethylene glycol)-SS-oligodeoxynucleotide conjugate. Biomacromolecules 2005;6:2449–54.
[89] Lee K, Povlich LK, Kim J. Label-free and self-signal amplifying molecular DNA sensors based on bioconjugated polyelectrolytes. Adv Funct Mater 2007;17:2580–7.
[90] Lou XH, Wang CY, He L. Core-shell Au nanoparticle formation with DNA-polymer hybrid coatings using aqueous ATRP. Biomacromolecules 2007;8:1385–90.
[91] Lueckerath T, Strauch T, Koynov K, Barner-Kowollik C, Ng DYW, Weil T. DNA-polymer conjugates by photoinduced RAFT polymerization. Biomacromolecules 2019;20:212–21.
[92] Oishi M, Nagasaki Y, Itaka K, Nishiyama N, Kataoka K. Lactosylated poly(ethylene glycol)-siRNA conjugate through acid-labile ss-thiopropionate linkage to construct pH-sensitive polyion complex micelles achieving enhanced gene silencing in hepatoma cells. J Am Chem Soc 2005;127:1624–5.
[93] Wilks TR, Bath J, de Vries JW, Raymond JE, Herrmann A, Turberfield AJ, et al. Giant surfactants created by the fast and efficient functionalization of a DNA tetrahedron with a temperature-responsive polymer. ACS Nano 2013;7:8561–72.
[94] Beaucage SL, Caruthers MH. Deoxynucleoside phosphoramidites - a new class of key intermediates for deoxypolynucleotide synthesis. Tetrahedron Lett 1981;22:1859–62.
[95] Pan XC, Lathwal S, Mack S, Yan JJ, Das SR, Matyjaszewski K. Automated synthesis of well-defined polymers and biohybrids by atom transfer radical polymerization using a DNA synthesizer. Angew Chem Int Ed 2017;56:2740–3.
[96] Safak M, Alemdaroglu FE, Li Y, Ergen E, Herrmann A. Polymerase chain reaction as an efficient tool for the preparation of block copolymers. Adv Mater 2007;19:1499–505.
[97] Nishimura T, Sumi N, Koda Y, Sasaki Y, Akiyoshi K. Intrinsically permeable polymer vesicles based on carbohydrate-conjugated poly(2-oxazoline)s synthesized using a carbohydrate-based initiator system. Polym Chem 2019;10:691–7.
[98] Siegwart DJ, Oh JK, Matyjaszewski K. ATRP in the design of functional materials for biomedical applications. Prog Polym Sci 2012;37:18–37.
[99] Matyjaszewski K, Tsarevsky NV. Macromolecular engineering by atom transfer radical polymerization. J Am Chem Soc 2014;136:6513–33.
[100] Bontempo D, Heredia KL, Fish BA, Maynard HD. Cysteine-reactive polymers synthesized by atom transfer radical polymerization for conjugation to proteins. J Am Chem Soc 2004;126:15372–3.
[101] Heredia KL, Bontempo D, Ly T, Byers JT, Halstenberg S, Maynard HD. In situ preparation of protein - Šmartpolymer conjugates with retention of bioactivity. J Am Chem Soc 2005;127:16955–60.
[102] Lele BS, Murata H, Matyjaszewski K, Russell AJ. Synthesis of uniform protein-polymer conjugates. Biomacromolecules 2005;6:3380–7.
[103] Jakubowski W, Matyjaszewski K. Activators regenerated by electron transfer for atom-transfer radical polymerization of (meth)acrylates and related block copolymers. Angew Chem Int Ed 2006;45:4482–6.
[104] Jakubowski W, Min K, Matyjaszewski K. Activators regenerated by electron transfer for atom transfer radical polymerization of styrene. Macromolecules 2006;39:39–45.
[105] Dong HC, Tang W, Matyjaszewski K. Well-defined high-molecular-weight polyacrylonitrile via activators regenerated by electron transfer ATRP. Macromolecules 2007;40:2974–7.
[106] Okada S, Park S, Matyjaszewski K. Initiators for continuous activator regeneration atom transfer radical polymerization of methyl methacrylate and styrene with N-heterocyclic carbene as ligands for Fe-based catalysts. ACS Macro Lett 2014;3:944–7.
[107] Krys P, Schroeder H, Buback J, Buback M, Matyjaszewski K. The borderline between simultaneous reverse and normal initiation and initiators for continuous activator regeneration ATRP. Macromolecules 2016;49:7793–803.
[108] Chmielarz P, Fantin M, Park S, Isse AA, Gennaro A, Magenau AJD, et al. Electrochemically mediated atom transfer radical polymerization (eATRP). Prog Polym Sci 2017;69:47–78.
[109] Fantin M, Chmielarz P, Wang Y, Lorandi F, Isse AA, Gennaro A, et al. Harnessing the interaction between surfactant and hydrophilic catalyst to control eATRP in miniemulsion. Macromolecules 2017;50:3726–32.
[110] Sun Y, Lathwal S, Wang Y, Fu LY, Olszewski M, Fantin M, et al. Preparation of well-defined polymers and DNA-polymer bioconjugates via small-volume eATRP in the presence of air. ACS Macro Lett 2019;8:603–9.
[111] Fu LY, Wang ZH, Lathwal S, Enciso AE, Simakova A, Das SR, et al. Synthesis of polymer bioconjugates via photoinduced atom transfer radical polymerization under blue light irradiation. ACS Macro Lett 2018;7:1248–53.
[112] Pan XC, Fang C, Fantin M, Malhotra N, So WY, Peteanu LA, et al. Mechanism of photoinduced metal-free atom transfer radical polymerization: experimental and computational studies. J Am Chem Soc 2016;138:2411–25.
[113] Pan XC, Malhotra N, Simakova A, Wang ZY, Konkolewicz D, Matyjaszewski K. Photoinduced atom transfer radical polymerization with ppm-level Cu catalyst by visible light in aqueous media. J Am Chem Soc 2015;137:15430–3.
[114] Murata H, Carmali S, Baker SL, Matyjaszewski K, Russell AJ. Solid-phase synthesis of protein-polymers on reversible immobilization supports. Nat Commun 2018;9, 845/1-10.
[115] Averick SE, Dey SK, Grahacharya D, Matyjaszewski K, Das SR. Solid-phase incorporation of an ATRP initiator for polymer-DNA biohybrids. Angew Chem Int Ed 2014;53:2739–44.
[116] Enciso AE, Fu LY, Russell AJ, Matyjaszewski K. A breathing atom-transfer radical polymerization: fully oxygen-tolerant polymerization inspired by aerobic respiration of cells. Angew Chem Int Ed 2018;57:933–6.
[117] Enciso AE, Fu LY, Lathwal S, Olszewski M, Wang ZH, Das SR, et al. Biocatalytic öxygen-fueledätom transfer radical polymerization. Angew Chem Int Ed 2018;57:16157–61.
[118] Boyer C, Bulmus V, Davis TP, Ladmiral V, Liu JQ, Perrier S. Bioapplications of RAFT polymerization. Chem Rev 2009;109:5402–36.
[119] Perrier S. 50th anniversary perspective: RAFT polymerization-a user guide. Macromolecules 2017;50:7433–47.
[120] Bulmus V. RAFT polymerization mediated bioconjugation strategies. Polym Chem 2011;2:1463–72.
[121] Le Droumaguet B, Nicolas J. Recent advances in the design of bioconjugates from controlled/living radical polymerization. Polym Chem 2010;1:563–98.
[122] Wallat JD, Rose KA, Pokorski JK. Proteins as substrates for controlled radical polymerization. Polym Chem 2014;5:1545–58.
[123] Shi HT, Liu L, Wang XB, Li JY. Glycopolymer-peptide bioconjugates with antioxidant activity via RAFT polymerization. Polym Chem 2012;3:1182–8.
[124] Sumerlin BS. Proteins as initiators of controlled radical polymerization: grafting-from via ATRP and RAFT. ACS Macro Lett 2012;1:141–5.
[125] Xu JT, Jung K, Corrigan NA, Boyer C. Aqueous photoinduced living/controlled polymerization: tailoring for bioconjugation. Chem Sci 2014;5:3568–75.
[126] Vanparijs N, De Coen R, Laplace D, Louage B, Maji S, Lybaert L, et al. Transiently responsive protein-polymer conjugates via a 'grafting-from' RAFT approach for intracellular co-delivery of proteins and immune-modulators. Chem Commun 2015;51:13972–5.
[127] Yang WK, Zhu LJ, Cui YC, Wang HW, Wang YW, Yuan L, et al. Improvement of site-directed protein-polymer conjugates: high bioactivity and stability using a soft chain-transfer agent. ACS Appl Mater Interfaces 2016;8:15967–74.
[128] Xu GF, Xu YH, Li AH, Chen T, Liu JQ. Enzymatic bioactivity investigation of glucose oxidase modified with hydrophilic or hydrophobic polymers via in situ RAFT polymerization. J Polym Sci Part A: Polym Chem 2017;55:1289–93.
[129] Falatach R, Li SH, Sloane S, McGlone C, Berberich JA, Page RC, et al. Why synthesize protein-polymer conjugates? The stability and activity of chymotrypsin-polymer bioconjugates synthesized by RAFT. Polymer 2015;72:382–6.
[130] Decker CG, Maynard HD. Degradable PEGylated protein conjugates utilizing RAFT polymerization. Eur Polym J 2015;65:305–12.
[131] Hentschel J, Bleek K, Ernst O, Lutz JF, Borner HG. Easy access to bioactive peptide-polymer conjugates via RAFT. Macromolecules 2008;41:1073–5.
[132] He P, He L. Synthesis of surface-anchored DNA-polymer bioconjugates using reversible addition-fragmentation chain transfer polymerization. Biomacromolecules 2009;10:1804–9.
[133] Liu JQ, Bulmus V, Herlambang DL, Barner-Kowollik C, Stenzel MH, Davis TP. In situ formation of protein-polymer conjugates through reversible addition fragmentation chain transfer polymerization. Angew Chem Int Ed 2007;46:3099–103.
[134] Boyer C, Bulmus V, Liu JQ, Davis TP, Stenzel MH, Barner-Kowollik C. Well-defined protein-polymer conjugates via in situ RAFT polymerization. J Am Chem Soc 2007;129:7145–54.

[135] De P, Li M, Gondi SR, Sumerlin BS. Temperature-regulated activity of responsive polymer-protein conjugates prepared by grafting-from via RAFT polymerization. J Am Chem Soc 2008;130:11288–9.
[136] Li M, Li HM, De P, Sumerlin BS. Thermoresponsive block copolymer-protein conjugates prepared by grafting-from via RAFT polymerization. Macromol Rapid Commun 2011;32:354–9.
[137] Chen C, Thang SH. RAFT polymerization of a RGD peptide-based methacrylamide monomer for cell adhesion. Polym Chem 2018;9:1780–6.
[138] Caliceti P, Veronese FM. Pharmacokinetic and biodistribution properties of poly(ethylene glycol)-protein conjugates. Adv Drug Deliv Rev 2003;55:1261–77.
[139] Ko JH, Maynard HD. A guide to maximizing the therapeutic potential of protein-polymer conjugates by rational design. Chem Soc Rev 2018;47:8998–9014.
[140] Pelegri-O'Day EM, Lin EW, Maynard HD. Therapeutic protein-polymer conjugates: advancing beyond PEGylation. J Am Chem Soc 2014;136:14323–32.
[141] Murata H, Cummings CS, Koepsel RR, Russell AJ. Rational tailoring of substrate and inhibitor affinity via ATRP polymer-based protein engineering. Biomacromolecules 2014;15:2817–23.
[142] Lucius M, Falatach R, McGlone C, Makaroff K, Danielson A, Williams C, et al. Investigating the impact of polymer functional groups on the stability and activity of lysozyme-polymer conjugates. Biomacromolecules 2016;17:1123–34.
[143] Cummings CS, Fein K, Murata H, Ball RL, Russell AJ, Whitehead KA. ATRP-grown protein-polymer conjugates containing phenylpiperazine selectively enhance transepithelial protein transport. J Control Release 2017;255:270–8.
[144] Hao HJ, Sun MM, Li PY, Sun JW, Liu XY, Gao WP. In situ growth of a cationic polymer from the N-terminus of glucose oxidase to regulate H_2O_2 generation for cancer starvation and H_2O_2 therapy. ACS Appl Mater Interfaces 2019;11:9756–62.
[145] Kim JS, Sirois AR, Cegla AJV, Jumai'an E, Murata N, Buck ME, et al. Protein-polymer conjugates synthesized using water-soluble azlactone-functionalized polymers enable receptor-specific cellular uptake toward targeted drug delivery. Bioconjug Chem 2019;30:1220–31.
[146] Liu GY, Chen CJ, Ji J. Biocompatible and biodegradable polymersomes as delivery vehicles in biomedical applications. Soft Matter 2012;8:8811–21.
[147] Liu GY, Lv LP, Chen CJ, Liu XS, Hu XF, Ji J. Biocompatible and biodegradable polymersomes for pH-triggered drug release. Soft Matter 2011;7:6629–36.
[148] Blackman LD, Gunatillake PA, Cass P, Locock KES. An introduction to zwitterionic polymer behavior and applications in solution and at surfaces. Chem Soc Rev 2019;48:757–70.
[149] Jin Q, Deng YY, Chen XH, Ji J. Rational design of cancer nanomedicine for simultaneous stealth surface and enhanced cellular uptake. ACS Nano 2019;13:954–77.
[150] Lowe AB, McCormick CL. Synthesis and solution properties of zwitterionic polymers. Chem Rev 2002;102:4177–89.
[151] Jin Q, Chen YJ, Wang Y, Ji J. Zwitterionic drug nanocarriers: a biomimetic strategy for drug delivery. Colloids Surf B Biointerfaces 2014;124:80–6.
[152] Keefe AJ, Jiang SY. Poly(zwitterionic)protein conjugates offer increased stability without sacrificing binding affinity or bioactivity. Nat Chem 2012;4:60–4.
[153] Xie JB, Lu Y, Wang W, Zhu H, Wang ZG, Cao ZQ. Simple protein modification using zwitterionic polymer to mitigate the bioactivity loss of conjugated insulin. Adv Healthcare Mater 2017;6, 1601428/1-5.
[154] Hu J, Wang GL, Zhao WG, Gao WP. In situ growth of a C-terminal interferon-alpha conjugate of a phospholipid polymer that outperforms PEGASYS in cancer therapy. J Control Release 2016;237:71–7.
[155] Mancini RJ, Lee J, Maynard HD. Trehalose glycopolymers for stabilization of protein conjugates to environmental stressors. J Am Chem Soc 2012;134:8474–9.
[156] Nguyen TH, Kim SH, Decker CG, Wong DY, Loo JA, Maynard HD. A heparin-mimicking polymer conjugate stabilizes basic fibroblast growth factor. Nat Chem 2013;5:221–7.
[157] Cobo I, Li M, Sumerlin BS, Perrier S. Smart hybrid materials by conjugation of responsive polymers to biomacromolecules. Nat Mater 2015;14:143–59.
[158] Shimoboji T, Larenas E, Fowler T, Kulkarni S, Hoffman AS, Stayton PS. Photoresponsive polymer-enzyme switches. Proc Natl Acad Sci U S A 2002;99:16592–6.
[159] Trzebicka B, Szweda R, Kosowski D, Szweda D, Otulakowski L, Haladjova E, et al. Thermoresponsive polymer-peptide/protein conjugates. Prog Polym Sci 2017;68:35–76.
[160] Zhang Q, Li MX, Zhu CY, Nurumbetov G, Li ZD, Wilson P, et al. Well-defined protein/peptide-polymer conjugates by aqueous Cu-LRP: synthesis and controlled self-assembly. J Am Chem Soc 2015;137:9344–53.
[161] Guo WW, Lu CH, Qi XJ, Orbach R, Fadeev M, Yang HH, et al. Switchable bifunctional stimuli-triggered poly-N-isopropylacrylamide/DNA hydrogels. Angew Chem Int Ed 2014;53:10134–8.
[162] Dingels C, Muller SS, Steinbach T, Tonhauser C, Frey H. Universal concept for the implementation of a single cleavable unit at tunable position in functional poly(ethylene glycol)s. Biomacromolecules 2013;14:448–59.
[163] Steinbach T, Wurm FR. Degradable polyphosphoester-protein conjugates: PPEylationöf proteins. Biomacromolecules 2016;17:3338–46.
[164] Pelegri-O'Day EM, Paluck SJ, Maynard HD. Substituted polyesters by thiol-ene modification: rapid diversification for therapeutic protein stabilization. J Am Chem Soc 2017;139:1145–54.
[165] Ahadian S, Sadeghian RB, Salehi S, Ostrovidov S, Bae H, Ramalingam M, et al. Bioconjugated hydrogels for tissue engineering and regenerative medicine. Bioconjug Chem 2015;26:1984–2001.
[166] Fisher SA, Baker AEG, Shoichet MS. Designing peptide and protein modified hydrogels: selecting the optimal conjugation strategy. J Am Chem Soc 2017;139:7416–27.
[167] Ho HT, Levere ME, Pascual S, Montembault V, Casse N, Caruso A, et al. Thermoresponsive block copolymers containing reactive azlactone groups and their bioconjugation with lysozyme. Polym Chem 2013;4:675–85.
[168] Zhang QL, Vanparijs N, Louage B, De Geest BG, Hoogenboom R. Dual pH- and temperature-responsive RAFT-based block co-polymer micelles and polymer-protein conjugates with transient solubility. Polym Chem 2014;5:1140–4.
[169] Kulkarni S, Schilli C, Grin B, Muller AHE, Hoffman AS, Stayton PS. Controlling the aggregation of conjugates of streptavidin with smart block copolymers prepared via the RAFT copolymerization technique. Biomacromolecules 2006;7:2736–41.
[170] Li HM, Li M, Yu X, Bapat AP, Sumerlin BS. Block copolymer conjugates prepared by sequentially grafting from proteins via RAFT. Polym Chem 2011;2:1531–5.
[171] Falatach R, McGlone C, Al-Abdul-Wahid MS, Averick S, Page RC, Berberich JA, et al. The best of both worlds: active enzymes by grafting-to followed by grafting-from a protein. Chem Commun 2015;51:5343–6.
[172] Chen CJ, Jin Q, Liu GY, Li DD, Wang JL, Ji J. Reversibly light-responsive micelles constructed via a simple modification of hyperbranched polymers with chromophores. Polymer 2012;53:3695–703.
[173] Chen CJ, Li DD, Wang HB, Zhao J, Ji J. Fabrication of dual-responsive micelles based on the supramolecular interaction of cucurbit[8]uril. Polym Chem 2013;4:242–5.
[174] Chen CJ, Liu GY, Liu XS, Pang SP, Zhu CS, Lv LP, et al. Photo-responsive, biocompatible polymeric micelles self-assembled from hyperbranched polyphosphate-based polymers. Polym Chem 2011;2:1389–97.
[175] Chen CJ, Liu GY, Shi YT, Zhu CS, Pang SP, Liu XS, et al. Biocompatible micelles based on comb-like PEG derivates: formation, characterization, and photo-responsiveness. Macromol Rapid Commun 2011;32:1077–81.
[176] Jiang L, Zhou SS, Zhang XK, Wu W, Jiang XQ. Dendrimer-based nanoparticles in cancer chemotherapy and gene therapy. Sci China Mater 2018;61:1404–19.
[177] Stiriba SE, Frey H, Haag R. Dendritic polymers in biomedical applications: from potential to clinical use in diagnostics and therapy. Angew Chem Int Ed 2002;41:1329–34.
[178] Zhou YF, Huang W, Liu JY, Zhu XY, Yan DY. Self-assembly of hyperbranched polymers and its biomedical applications. Adv Mater 2010;22:4567–90.
[179] Kochendoerfer GG, Chen SY, Mao F, Cressman S, Traviglia S, Shao HY, et al. Design and chemical synthesis of a homogeneous polymer-modified erythropoiesis protein. Science 2003;299:884–7.
[180] Spears BR, Waksal J, McQuade C, Lanier L, Harth E. Controlled branching of polyglycidol and formation of protein-glycidol bioconjugates via a graft-from approach with PEG-likeärms. Chem Commun 2013;49:2394–6.
[181] Zhou XY, Zheng QQ, Wang CY, Xu JK, Wu JP, Kirk TB, et al. Star-shaped amphiphilic hyperbranched polyglycerol conjugated with dendritic poly(L-lysine) for the codelivery of docetaxel and MMP-9 siRNA in cancer therapy. ACS Appl Mater Interfaces 2016;8:12609–19.
[182] Cheng DB, Yang PP, Cong Y, Liu FH, Qiao ZY, Wang H. One-pot synthesis of pH-responsive hyperbranched polymer-peptide conjugates with enhanced stability and loading efficiency for combined cancer therapy. Polym Chem 2017;8:2462–71.
[183] Collins J, Wallis SJ, Simula A, Whittaker MR, McIntosh MP, Wilson P, et al. Comb poly(oligo(2-ethyl-2-oxazoline)methacrylate)-peptide conjugates prepared by aqueous Cu(0)-mediated polymerization and reductive amination. Macromol Rapid Commun 2017;38, 1600534/1-7.
[184] Tucker BS, Stewart JD, Aguirre JI, Holliday LS, Figg CA, Messer JG, et al. Role of polymer architecture on the activity of polymer-protein conjugates for the treatment of accelerated bone loss disorders. Biomacromolecules 2015;16:2374–81.
[185] Wurm F, Dingels C, Frey H, Klok HA. Squaric acid mediated synthesis and biological activity of a library of linear and hyperbranched poly(glycerol)-protein conjugates. Biomacromolecules 2012;13:1161–71.
[186] Qi YZ, Simakova A, Ganson NJ, Li XH, Luginbuhl KM, Ozer I, et al. A brush-polymer/exendin-4 conjugate reduces blood glucose levels for up to five days and eliminates poly(ethylene glycol) antigenicity. Nat Biomed Eng 2016;1, 0002/1-12.
[187] Rendle PM, Seger A, Rodrigues J, Oldham NJ, Bott RR, Jones JB, et al. Glycodendriproteins: a synthetic glycoprotein mimic enzyme with branched sugar-display potently inhibits bacterial aggregation. J Am Chem Soc 2004;126:4750–1.
[188] Kostiainen MA, Szilvay GR, Lehtinen J, Smith DK, Linder MB, Urtti A, et al. Precisely defined protein-polymer conjugates: construction of synthetic DNA binding domains on proteins by using multivalent dendrons. ACS Nano 2007;1:103–13.
[189] Ng DYW, Arzt M, Wu YZ, Kuan SL, Lamla M, Weil T. Constructing hybrid protein zymogens through protective dendritic assembly. Angew Chem Int Ed 2014;53:324–8.

[190] Fuhrmann G, Grotzky A, Lukic R, Matoori S, Luciani P, Yu H, et al. Sustained gastrointestinal activity of dendronized polymer-enzyme conjugates. Nat Chem 2013;5:582–9.
[191] Grover GN, Maynard HD. Protein-polymer conjugates: synthetic approaches by controlled radical polymerizations and interesting applications. Curr Opin Chem Biol 2010;14:818–27.
[192] Tao L, Kaddis CS, Loo RRO, Grover GN, Loo JA, Maynard HD. Synthetic approach to homodimeric protein-polymer conjugates. Chem Commun 2009:2148–50.
[193] Lorenzo MM, Decker CG, Kahveci MU, Paluck SJ, Maynard HD. Homodimeric protein-polymer conjugates via the tetrazine-trans-cyclooctene ligation. Macromolecules 2016;49:30–7.
[194] White CJ, Bode JW. PEGylation and dimerization of expressed proteins under near equimolar conditions with potassium 2-pyridyl acyltrifluoroborates. ACS Cent Sci 2018;4:197–206.
[195] Boyer C, Liu J, Bulmus V, Davis TP, Barner-Kowollik C, Stenzel MH. Direct synthesis of well-defined heterotelechelic polymers for bioconjugations. Macromolecules 2008;41:5641–50.
[196] Heredia KL, Grover GN, Tao L, Maynard HD. Synthesis of heterotelechelic polymers for conjugation of two different proteins. Macromolecules 2009;42:2360–7.
[197] Heredia KL, Tao L, Grover GN, Maynard HD. Heterotelechelic polymers for capture and release of protein-polymer conjugates. Polym Chem 2010;1:168–70.
[198] Roth PJ, Jochum FD, Zentel R, Theato P. Synthesis of hetero-telechelic alpha,omega bio-functionalized polymers. Biomacromolecules 2010;11:238–44.
[199] Fasting C, Schalley CA, Weber M, Seitz O, Hecht S, Koksch B, et al. Multivalency as a chemical organization and action principle. Angew Chem Int Ed 2012;51:10472–98.
[200] Danial M, Root MJ, Klok HA. Polyvalent side chain peptide-synthetic polymer conjugates as HIV-1 entry inhibitors. Biomacromolecules 2012;13:1438–47.
[201] Duret D, Grassin A, Henry M, Jacquet T, Thoreau F, Denis-Quanquin S, et al. Polymultivalentpolymer-peptide cluster conjugates for an enhanced targeting of cells expressing αvβ3 integrins. Bioconjug Chem 2017;28:2241–5.
[202] Wang JT, Wang L, Ji XT, Liu L, Zhao HY. Synthesis of zwitterionic diblock copolymers with cleavable biotin groups at the junction points and fabrication of bioconjugates by biotin-streptavidin coupling. Macromolecules 2017;50:2284–95.
[203] Paloni JM, Miller EA, Sikes HD, Olsen BD. Improved ordering in low molecular weight protein-polymer conjugates through oligomerization of the protein block. Biomacromolecules 2018;19:3814–24.
[204] Suguri T, Olsen BD. Topology effects on protein-polymer block copolymer self-assembly. Polym Chem 2019;10:1751–61.
[205] Hou YQ, Yuan JS, Zhou Y, Yu J, Lu H. A concise approach to site-specific topological protein-poly(amino acid) conjugates enabled by in situ-generated functionalities. J Am Chem Soc 2016;138:10995–1000.
[206] Hou YQ, Zhou Y, Wang H, Wang RJ, Yuan JS, Hu YL, et al. Macrocyclization of interferon-poly(alpha-amino acid) conjugates significantly improves the tumor retention, penetration, and antitumor efficacy. J Am Chem Soc 2018;140:1170–8.
[207] Kuan SL, Bergamini FRG, Weil T. Functional protein nanostructures: a chemical toolbox. Chem Soc Rev 2018;47:9069–105.
[208] Kauzmann W. Some factors in the interpretation of protein denaturation. Adv Protein Chem 1959;14:1–63.
[209] Yang J, Gitlin I, Krishnamurthy VM, Vazquez JA, Costello CE, Whitesides GM. Synthesis of monodisperse polymers from proteins. J Am Chem Soc 2003;125:12392–3.
[210] Kuan SL, Wu YZ, Weil T. Precision biopolymers from protein precursors for biomedical applications. Macromol Rapid Commun 2013;34:380–92.
[211] Ng DYW, Wu YZ, Kuan SL, Weil T. Programming supramolecular biohybrids as precision therapeutics. Acc Chem Res 2014;47:3471–80.
[212] Wu YZ, Pramanik G, Eisele K, Weil T. Convenient approach to polypeptide copolymers derived from native proteins. Biomacromolecules 2012;13:1890–8.
[213] Wu YZ, Weil T. An efficient approach for preparing giant polypeptide triblock copolymers by protein dimerization. Macromol Rapid Commun 2012;33:1304–9.
[214] Veronese FM. Peptide and protein PEGylation: a review of problems and solutions. Biomaterials 2001;22:405–17.
[215] Alivisatos AP, Gu WW, Larabell C. Quantum dots as cellular probes. Annu Rev Biomed Eng 2005;7:55–76.
[216] Kuo Y, Hsu TY, Wu YC, Chang HC. Fluorescent nanodiamond as a probe for the intercellular transport of proteins in vivo. Biomaterials 2013;34:8352–60.
[217] Hardman R. A toxicologic review of quantum dots: toxicity depends on physicochemical and environmental factors. Environ Health Perspect 2006;114:165–72.
[218] Wu YZ, Jelezko F, Plenio MB, Weil T. Diamond quantum devices in biology. Angew Chem Int Ed 2016;55:6586–98.
[219] Wu YZ, Chakrabortty S, Gropeanu RA, Wilhelmi J, Xu Y, Er KS, et al. pH-responsive quantum dots via an albumin polymer surface coating. J Am Chem Soc 2010;132:5012–4.
[220] Wu YZ, Eisele K, Doroshenko M, Algara-Siller G, Kaiser U, Koynov K, et al. A quantum dot photoswitch for DNA detection, gene transfection, and live-cell imaging. Small 2012;8:3465–75.
[221] Zhang T, Neumann A, Lindlau J, Wu YZ, Prarnanik G, Naydenov B, et al. DNA-based self-assembly of fluorescent nanodiamonds. J Am Chem Soc 2015;137:9776–9.
[222] Wu YZ, Ermakova A, Liu WN, Pramanik G, Vu TM, Kurz A, et al. Programmable biopolymers for advancing biomedical applications of fluorescent nanodiamonds. Adv Funct Mater 2015;25:6576–85.
[223] Chen CJ, Wunderlich K, Mukherji D, Koynov K, Heck AJ, Raabe M, et al. Precision anisotropic brush polymers by sequence controlled chemistry. J Am Chem Soc 2020;142:1332–40.
[224] Chakrabortty S, Sison M, Wu YZ, Ladenburger A, Pramanik G, Biskupek J, et al. NIR-emitting and photo-thermal active nanogold as mitochondria-specific probes. Biomater Sci 2017;5:966–71.
[225] Chen CJ, Ng DYW, Weil T. Polymer-grafted gold nanoflowers with temperature-controlled catalytic features by in situ particle growth and polymerization. Mater Chem Front 2019;3:1449–53.
[226] Wu YZ, Wang T, Ng DYW, Weil T. Multifunctional polypeptide-PEO nanoreactors via the hydrophobic switch. Macromol Rapid Commun 2012;33:1474–81.
[227] Eisele K, Gropeanu R, Musante A, Glasser G, Li C, Muellen K, et al. Tailored albumin-based copolymers for receptor-mediated delivery of perylenediimide guest molecules. Macromol Rapid Commun 2010;31:1501–8.
[228] Wu YZ, Shih EK, Ramanathan A, Vasudevan S, Weil T. Nano-sized albumin-copolymer micelles for efficient doxorubicin delivery. Biointerphases 2012;7, 5/1-10.
[229] Wu YZ, Ihme S, Feuring-Buske M, Kuan SL, Eisele K, Lamla M, et al. A core-shell albumin copolymer nanotransporter for high capacity loading and two-step release of doxorubicin with enhanced anti-leukemia activity. Adv Healthcare Mater 2013;2:884–94.
[230] Wu YZ, Li C, Boldt F, Wang YR, Kuan SL, Tran TT, et al. Programmable protein-DNA hybrid hydrogels for the immobilization and release of functional proteins. Chem Commun 2014;50:14620–2.
[231] Gacanin J, Hedrich J, Sieste S, Glasser G, Lieberwirth I, Schilling C, et al. Autonomous ultrafast self-healing hydrogels by pH-responsive functional nanofiber gelators as cell matrices. Adv Mater 2019;31, 1805044/1-7.
[232] Gacanin J, Kovtun A, Fischer S, Schwager V, Quambusch J, Kuan SL, et al. Spatiotemporally controlled release of rho-inhibiting C3 toxin from a protein-DNA hybrid hydrogel for targeted inhibition of osteoclast formation and activity. Adv Healthcare Mater 2017;6, 1700392/1-12.
[233] Rother M, Nussbaumer MG, Renggli K, Bruns N. Protein cages and synthetic polymers: a fruitful symbiosis for drug delivery applications, bionanotechnology and materials science. Chem Soc Rev 2016;45:6213–49.
[234] Maassen SJ, van der Ham AM, Cornelissen JJLM. Combining protein cages and polymers: from understanding self-assembly to functional materials. ACS Macro Lett 2016;5:987–94.
[235] Aumiller WM, Uchida M, Douglas T. Protein cage assembly across multiple length scales. Chem Soc Rev 2018;47:3433–69.
[236] Kovacs EW, Hooker JM, Romanini DW, Holder PG, Berry KE, Francis MB. Dual-surface-modified bacteriophage MS2 as an ideal scaffold for a viral capsid-based drug delivery system. Bioconjug Chem 2007;18:1140–7.
[237] Steinmetz NF, Manchester M. PEGylated viral nanoparticles for biomedicine: the impact of PEG chain length on VNP cell interactions in vitro and ex vivo. Biomacromolecules 2009;10:784–92.
[238] Kim PH, Sohn JH, Choi JW, Jung Y, Kim SW, Haam S, et al. Active targeting and safety profile of PEG-modified adenovirus conjugated with herceptin. Biomaterials 2011;32:2314–26.
[239] Matsumoto NM, Prabhakaran P, Rome LH, Maynard HD. Smart vaults: thermally-responsive protein nanocapsules. ACS Nano 2013;7:867–74.
[240] Manzenrieder F, Luxenhofer R, Retzlaff M, Jordan R, Finn MG. Stabilization of virus-like particles with poly(2-oxazoline)s. Angew Chem Int Ed 2011;50:2601–5.
[241] Holder PG, Finley DT, Stephanopoulos N, Walton R, Clark DS, Francis MB. Dramatic thermal stability of virus-polymer conjugates in hydrophobic solvents. Langmuir 2010;26:17383–8.
[242] Schlick TL, Ding ZB, Kovacs EW, Francis MB. Dual-surface modification of the tobacco mosaic virus. J Am Chem Soc 2005;127:3718–23.
[243] Patil AJ, McGrath N, Barclay JE, Evans DJ, Colfen H, Manners I, et al. Liquid viruses by nanoscale engineering of capsid surfaces. Adv Mater 2012;24:4557–63.
[244] Isarov SA, Lee PW, Pokorski JK. Graft-toprotein/polymer conjugates using polynorbornene block copolymers. Biomacromolecules 2016;17:641–8.
[245] Lee PW, Isarov SA, Wallat JD, Molugu SK, Shukla S, Sun JEP, et al. Polymer structure and conformation alter the antigenicity of virus-like particle-polymer conjugates. J Am Chem Soc 2017;139:3312–5.
[246] Nussbaumer MG, Duskey JT, Rother M, Renggli K, Chami M, Bruns N. Chaperonin-dendrimer conjugates for siRNA delivery. Adv Sci 2016;3, 1600046/1-10.
[247] Nussbaumer MG, Bisig C, Bruns N. Using the dendritic polymer PAMAM to form gold nanoparticles in the protein cage thermosome. Chem Commun 2016;52:10537–9.
[248] Zeng QB, Li T, Cash B, Li SQ, Xie F, Wang Q. Chemoselective derivatization of a bionanoparticle by click reaction and ATRP reaction. Chem Commun 2007:1453–5.

[249] Hu YX, Samanta D, Parelkar SS, Hong SW, Wang QA, Russell TP, et al. Ferritin-polymer conjugates: grafting chemistry and integration into nanoscale assemblies. Adv Funct Mater 2010;20:3603–12.
[250] Mougin NC, van Rijn P, Park H, Muller AHE, Boker A. Hybrid capsules via self-assembly of thermoresponsive and interfacially active bionanoparticle-polymer conjugates. Adv Funct Mater 2011;21:2470–6.
[251] Pokorski JK, Breitenkamp K, Liepold LO, Qazi S, Finn MG. Functional virus-based polymer-protein nanoparticles by atom transfer radical polymerization. J Am Chem Soc 2011;133:9242–5.
[252] Abedin MJ, Liepold L, Suci P, Young M, Douglas T. Synthesis of a cross-linked branched polymer network in the interior of a protein cage. J Am Chem Soc 2009;131:4346–54.
[253] Lucon J, Qazi S, Uchida M, Bedwell GJ, LaFrance B, Prevelige PE, et al. Use of the interior cavity of the P22 capsid for site-specific initiation of atom-transfer radical polymerization with high-density cargo loading. Nat Chem 2012;4:781–8.
[254] Liepold LO, Abedin MJ, Buckhouse ED, Frank JA, Young MJ, Douglas T. Supramolecular protein cage composite MR contrast agents with extremely efficient relaxivity properties. Nano Lett 2009;9:4520–6.
[255] Lucon J, Abedin MJ, Uchida M, Liepold L, Jolley CC, Young M, et al. A click chemistry based coordination polymer inside small heat shock protein. Chem Commun 2010;46:264–6.
[256] Edwards E, Roychoudhury R, Schwarz B, Jordan P, Lisher J, Uchida M, et al. Co-localization of catalysts within a protein cage leads to efficient photochemical NADH and/or hydrogen production. J Mater Chem B 2016;4:5375–84.
[257] Lucon J, Edwards E, Qazi S, Uchida M, Douglas T. Atom transfer radical polymerization on the interior of the P22 capsid and incorporation of photocatalytic monomer crosslinks. Eur Polym J 2013;49:2976–85.
[258] Hovlid ML, Lau JL, Breitenkamp K, Higginson CJ, Laufer B, Manchester M, et al. Encapsidated atom-transfer radical polymerization in q beta virus-like nanoparticles. ACS Nano 2014;8:8003–14.
[259] Wu YZ, Li LJ, Frank L, Wagner J, Andreozzi P, Hammer B, et al. Patchy amphiphilic dendrimers bind adenovirus and control its host interactions and in vivo distribution. ACS Nano 2019;13:8749–59.
[260] Holowka EP, Sun VZ, Kamei DT, Deming TJ. Polyarginine segments in block copolypeptides drive both vesicular assembly and intracellular delivery. Nat Mater 2007;6:52–7.
[261] Carlsen A, Lecommandoux S. Self-assembly of polypeptide-based block copolymer amphiphiles. Curr Opin Colloid Interface Sci 2009;14:329–39.
[262] Castelletto V, McKendrick JE, Hamley IW, Olsson U, Cenker C. PEGylated amyloid peptide nanocontainer delivery and release system. Langmuir 2010;26:11624–7.
[263] Knoop RJI, de Geus M, Habraken GJM, Koning CE, Menzel H, Heise A. Stimuli responsive peptide conjugated polymer nanoparticles. Macromolecules 2010;43:4126–32.
[264] Bacinello D, Garanger E, Taton D, Tam KC, Lecommandoux S. Enzyme-degradable self-assembled nanostructures from polymer-peptide hybrids. Biomacromolecules 2014;15:1882–8.
[265] Hamley IW, Castelletto V. Self-assembly of peptide bioconjugates: selected recent research highlights. Bioconjug Chem 2017;28:731–9.
[266] Machado CA, Smith IR, Savin DA. Self-assembly of oligo- and polypeptide-based amphiphiles: recent advances and future possibilities. Macromolecules 2019;52:1899–911.
[267] Knight AS, Larsson J, Ren JM, Zerdan RB, Seguin S, Vrahas R, et al. Control of amphiphile self-assembly via bioinspired metal ion coordination. J Am Chem Soc 2018;140:1409–14.
[268] Aggeli A, Bell M, Boden N, Keen JN, McLeish TCB, Nyrkova I, et al. Engineering of peptide beta-sheet nanotapes. J Mater Chem 1997;7:1135–45.
[269] Zhang SG. Emerging biological materials through molecular self-assembly. Biotechnol Adv 2002;20:321–39.
[270] Aggeli A, Bell M, Carrick LM, Fishwick CWG, Harding R, Mawer PJ, et al. pH as a trigger of peptide beta-sheet self-assembly and reversible switching between nematic and isotropic phases. J Am Chem Soc 2003;125:9619–28.
[271] Eckhardt D, Groenewolt M, Krause E, Borner HG. Rational design of oligopeptide organizers for the formation of poly(ethylene oxide) nanofibers. Chem Commun 2005:2814–6.
[272] Liu YJ, Zhang YF, Wang ZY, Wang J, Wei KC, Chen GS, et al. Building nanowires from micelles: hierarchical self-assembly of alternating amphiphilic glycopolypeptide brushes with pendants of high-mannose glycodendron and oligophenylalanine. J Am Chem Soc 2016;138:12387–94.
[273] Kuhnle H, Borner HG. Biotransformation on polymer-peptide conjugates: a versatile tool to trigger microstructure formation. Angew Chem Int Ed 2009;48:6431–4.
[274] Qiao SL, Ma Y, Wang Y, Lin YX, An HW, Li LL, et al. General approach of stimuli-induced aggregation for monitoring tumor therapy. ACS Nano 2017;11:7301–11.
[275] Liu FH, Cong Y, Qi GB, Ji L, Qiao ZY, Wang H. Near-infrared laser-driven in situ self-assembly as a general strategy for deep tumor therapy. Nano Lett 2018;18:6577–84.
[276] Qi GB, Gao YJ, Wang L, Wang H. Self-assembled peptide-based nanomaterials for biomedical imaging and therapy. Adv Mater 2018;30:1703444/1-34.
[277] Cong Y, Ji L, Gao YJ, Liu FH, Cheng DB, Hu ZY, et al. Microenvironment-induced in situ self-assembly of polymer-peptide conjugates that attack solid tumors deeply. Angew Chem Int Ed 2019;58:4632–7.
[278] Cheng DB, Zhang XH, Gao YJ, Ji L, Hou DY, Wang ZQ, et al. Endogenous reactive oxygen species-triggered morphology transformation for enhanced cooperative interaction with mitochondria. J Am Chem Soc 2019;141:7235–9.
[279] Chapman R, Danial M, Koh ML, Jolliffe KA, Perrier S. Design and properties of functional nanotubes from the self-assembly of cyclic peptide templates. Chem Soc Rev 2012;41:6023–41.
[280] Loschonsky S, Couet J, Biesalski M. Synthesis of peptide/polymer conjugates by solution ATRP of butylacrylate using an initiator-modified cyclic D-alt-L-peptide. Macromol Rapid Commun 2008;29:309–15.
[281] Poon CK, Chapman R, Jolliffe KA, Perrier S. Pushing the limits of copper mediated azide-alkyne cycloaddition (CuAAC) to conjugate polymeric chains to cyclic peptides. Polym Chem 2012;3:1820–6.
[282] Larnaudie SC, Brendel JC, Jolliffe KA, Perrier S. Cyclic peptide-polymer conjugates: grafting-to vs grafting-from. J Polym Sci Part A: Polym Chem 2016;54:1003–11.
[283] Couet J, Jeyaprakash JD, Samuel S, Kopyshev A, Santer S, Biesalski M. Peptide-polymer hybrid nanotubes. Angew Chem Int Ed 2005;44:3297–301.
[284] Couet J, Biesalski M. Polymer-wrapped peptide nanotubes: peptide-grafted polymer mass impacts length and diameter. Small 2008;4:1008–16.
[285] Chapman R, Koh ML, Warr GG, Jolliffe KA, Perrier S. Structure elucidation and control of cyclic peptide-derived nanotube assemblies in solution. Chem Sci 2013;4:2581–9.
[286] Koh ML, FitzGerald PA, Warr GG, Jolliffe KA, Perrier S. Study of (cyclic peptide)-polymer conjugate assemblies by small-angle neutron scattering. Chem Eur J 2016;22:18419–28.
[287] Mansfield EDH, Hartlieb M, Catrouillet S, Rho JY, Larnaudie SC, Rogers SE, et al. Systematic study of the structural parameters affecting the self-assembly of cyclic peptide-poly(ethylene glycol) conjugates. Soft Matter 2018;14:6320–6.
[288] Rho JY, Brendel JC, MacFarlane LR, Mansfield EDH Peltier R, Rogers S, et al. Probing the dynamic nature of self-assembling cyclic peptide-polymer nanotubes in solution and in mammalian cells. Adv Funct Mater 2018;28, 1704569/1-11.
[289] Danial M, Tran CMN, Jolliffe KA, Perrier S. Thermal gating in lipid membranes using thermoresponsive cyclic peptide-polymer conjugates. J Am Chem Soc 2014;136:8018–26.
[290] Binfield JG, Brendel JC, Cameron NR, Eissa AM, Perrier S. Imaging proton transport in giant vesicles through cyclic peptide-polymer conjugate nanotube transmembrane ion channels. Macromol Rapid Commun 2018;39, 1700831/1-6.
[291] Hartlieb M, Catrouillet S, Kuroki A, Sanchez-Cano C, Peltier R, Perrier S. Stimuli-responsive membrane activity of cyclic-peptide-polymer conjugates. Chem Sci 2019;10:5476–83.
[292] Chapman R, Bouten PJM, Hoogenboom R, Jolliffe KA, Perrier S. Thermoresponsive cyclic peptide - poly(2-ethyl-2-oxazoline) conjugate nanotubes. Chem Commun 2013;49:6522–4.
[293] Chapman R, Warr GG, Perrier S, Jolliffe KA. Water-soluble and pH-responsive polymeric nanotubes from cyclic peptide templates. Chem Eur J 2013;19:1955–61.
[294] Catrouillet S, Brendel JC, Larnaudie S, Barlow T, Jolliffe KA, Perrier S. Tunable length of cyclic peptide-polymer conjugate self assemblies in water. ACS Macro Lett 2016;5:1119–23.
[295] Larnaudie SC, Brendel JC, Jolliffe KA, Perrier S. pH-responsive, amphiphilic core-shell supramolecular polymer brushes from cyclic peptide-polymer conjugates. ACS Macro Lett 2017;6:1347–51.
[296] Song Q, Yang J, Rho JY, Perrier S. Supramolecular switching of the self-assembly of cyclic peptide-polymer conjugates via host-guest chemistry. Chem Commun 2019;55:5291–4.
[297] Danial M, Tran CMN, Young PG, Perrier S, Jolliffe KA. Janus cyclic peptide-polymer nanotubes. Nat Commun 2013;4, 2780/1-13.
[298] Brendel JC, Sanchis J, Catrouillet S, Czuba E, Chen MZ, Long BM, et al. Secondary self-assembly of supramolecular nanotubes into tubisomes and their activity on cells. Angew Chem Int Ed 2018;57:16678–82.
[299] Brendel JC, Catrouillet S, Sanchis J, Jolliffe KA, Perrier S. Shaping block copolymer micelles by supramolecular polymerization: making 'tubisomes'. Polym Chem 2019;10:2616–25.
[300] Velonia K, Rowan AE, Nolte RJM. Lipase polystyrene giant amphiphiles. J Am Chem Soc 2002;124:4224–5.
[301] Boerakker MJ, Hannink JM, Bomans PHH, Frederik PM, Nolte RJM, Meijer EM, et al. Giant amphiphiles by cofactor reconstitution. Angew Chem Int Ed 2002;41:4239–41.
[302] Reynhout IC, Cornelissen JJLM, Nolte RJM. Self-assembled architectures from biohybrid triblock copolymers. J Am Chem Soc 2007;129:2327–32.
[303] Liu ZY, Dong CH, Wang XM, Wang HJ, Li W, Tan J, et al. Self-assembled biodegradable protein-polymer vesicle as a tumor-targeted nanocarrier. ACS Appl Mater Interfaces 2014;6:2393–400.
[304] Jiang YY, Lu HX, Dag A, Hart-Smith G, Stenzel MH. Albumin-polymer conjugate nanoparticles and their interactions with prostate cancer cells in 2D and 3D culture: comparison between PMMA and PCL. J Mater Chem B 2016;4:2017–27.
[305] Jiang YY, Stenzel M. Drug delivery vehicles based on albumin-polymer conjugates. Macromol Biosci 2016;16:791–802.
[306] Jiang YY, Wong S, Chen F, Chang T, Lu HX, Stenzel MH. Influencing selectivity to cancer cells with mixed nanoparticles prepared from albumin-polymer conjugates and block copolymers. Bioconjug Chem 2017;28:979–85.

[307] Wong CK, Laos AJ, Soeriyadi AH, Wiedenmann J, Curmi PMG, Gooding JJ, et al. Polymersomes prepared from thermoresponsive fluorescent protein-polymer bioconjugates: capture of and report on drug and protein payloads. Angew Chem Int Ed 2015;54:5317–22.
[308] Ferguson CJ, Hughes RJ, Pham BTT, Hawkett BS, Gilbert RG, Serelis AK, et al. Effective ab initio emulsion polymerization under RAFT control. Macromolecules 2002;35:9243–5.
[309] Charleux B, Delaittre G, Rieger J, D'Agosto F. Polymerization-induced self-assembly: from soluble macromolecules to block copolymer nano-objects in one step. Macromolecules 2012;45:6753–65.
[310] Warren NJ, Armes SP. Polymerization-induced self-assembly of block copolymer nano-objects via RAFT aqueous dispersion polymerization. J Am Chem Soc 2014;136:10174–85.
[311] Derry MJ, Fielding LA, Armes SP. Polymerization-induced self-assembly of block copolymer nanoparticles via RAFT non-aqueous dispersion polymerization. Prog Polym Sci 2016;52:1–18.
[312] Liu XY, Gao WP. In situ growth of self-assembled protein-polymer nanovesicles for enhanced intracellular protein delivery. ACS Appl Mater Interfaces 2017;9:2023–8.
[313] Li PY, Sun MM, Xu ZK, Liu XY, Zhao WG, Gao WP. Site-selective in situ growth-induced self-assembly of protein-polymer conjugates into pH-responsive micelles for tumor microenvironment triggered fluorescence imaging. Biomacromolecules 2018;19:4472–9.
[314] Ma C, Liu XM, Wu GY, Zhou P, Zhou YT, Wang L, et al. Efficient way to generate protein-based nanoparticles by in-situ photoinitiated polymerization-induced self-assembly. ACS Macro Lett 2017;6:689–94.
[315] Khan AK, Gudlur S, de Hoog HPM, Siti W, Liedberg B, et al. Controlled supramolecular self-assembly of super-charged beta-lactoglobulin A-PEG conjugates into nanocapsules. Angew Chem Int Ed 2017;56:11754–8.
[316] Comellas-Aragones M, de la Escosura A, Dirks AJ, van der Ham A, Fuste-Cune A, Cornelissen JJLM, et al. Controlled integration of polymers into viral capsids. Biomacromolecules 2009;10:3141–7.
[317] van Rijn P, Mougin NC, Boker A. Hierarchical structures via self-assembling protein-polymer hybrid building blocks. Polymer 2012;53:6045–52.
[318] van Rijn P, Park H, Nazli KO, Mougin NC, Boker A. Self-assembly process of soft ferritin-pnipaam conjugate bionanoparticles at polar-apolar interfaces. Langmuir 2013;29:276–84.
[319] Huang X, Li M, Green DC, Williams DS, Patil AJ, Mann S. Interfacial assembly of protein-polymer nano-conjugates into stimulus-responsive biomimetic protocells. Nat Commun 2013;4:2239/1-9.
[320] Huang A, Qin GK, Olsen BD. Highly active biocatalytic coatings from protein-polymer diblock copolymers. ACS Appl Mater Interfaces 2015;7:14660–9.
[321] Obermeyer AC, Olsen BD. Synthesis and application of protein-containing block copolymers. ACS Macro Lett 2015;4:101–10.
[322] Thomas CS, Glassman MJ, Olsen BD. Solid-state nanostructured materials from self-assembly of a globular protein-polymer diblock copolymer. ACS Nano 2011;5:5697–707.
[323] Chang D, Lam CN, Tang SC, Olsen BD. Effect of polymer chemistry on globular protein-polymer block copolymer self-assembly. Polym Chem 2014;5:4884–95.
[324] Chang D, Olsen BD. Self-assembly of protein-zwitterionic polymer bioconjugates into nanostructured materials. Polym Chem 2016;7:2410–8.
[325] Lam CN, Kim M, Thomas CS, Chang D, Sanoja GE, Okwara CU, et al. The nature of protein interactions governing globular protein-polymer block copolymer self-assembly. Biomacromolecules 2014;15:1248–58.
[326] Lam CN, Yao H, Olsen BD. The effect of protein electrostatic interactions on globular protein-polymer block copolymer self-assembly. Biomacromolecules 2016;17:2820–9.
[327] Qin GK, Glassman MJ, Lam CN, Chang D, Schaible E, Hexemer A, et al. Topological effects on globular protein-ELP fusion block copolymer self-assembly. Adv Funct Mater 2015;25:729–38.
[328] Delaittre G, Greiner AM, Pauloehrl T, Bastmeyer M, Barner-Kowollik C. Chemical approaches to synthetic polymer surface biofunctionalization for targeted cell adhesion using small binding motifs. Soft Matter 2012;8:7323–47.
[329] Jiang H, Xu FJ. Biomolecule-functionalized polymer brushes. Chem Soc Rev 2013;42:3394–426.
[330] Muszanska AK, Busscher HJ, Herrmann A, van der Mei HC, Norde W. Pluronic-lysozyme conjugates as anti-adhesive and antibacterial bifunctional polymers for surface coating. Biomaterials 2011;32:6333–41.
[331] Rosenthal A, Mantz A, Nguyen A, Bittrich E, Schubert E, Schubert M, et al. Biofunctionalization of titanium substrates using nanoscale polymer brushes with cell adhesion peptides. J Phys Chem B 2018;122:6543–50.
[332] Kong XX, Jenekhe SA. Block copolymers containing conjugated polymer and polypeptide sequences: synthesis and self-assembly of electroactive and photoactive nanostructures. Macromolecules 2004;37:8180–3.
[333] Gao GZ, Wang T, He JP, Chen XQ, Yang YL. Hierarchical assembly of PEG-b-polypeptide hybrid block copolymers on graphite. Macromolecules 2007;40:2613–9.
[334] Chang D, Huang A, Olsen BD. Kinetic effects on self-assembly and function of protein-polymer bioconjugates in thin films prepared by flow coating. Macromol Rapid Commun 2017;38:1600449/1-6.
[335] Presley AD, Chang JJ, Xu T. Directed co-assembly of heme proteins with amphiphilic block copolymers toward functional biomolecular materials. Soft Matter 2011;7:172–9.
[336] Palacios-Cuesta M, Cortajarena AL, Garcia O, Rodriguez-Hernandez J. Versatile functional microstructured polystyrene-based platforms for protein patterning and recognition. Biomacromolecules 2013;14:3147–54.
[337] Tischer T, Claus TK, Bruns M, Trouillet V, Linkert K, Rodriguez-Emmenegger C, et al. Spatially controlled photochemical peptide and polymer conjugation on biosurfaces. Biomacromolecules 2013;14:4340–50.
[338] Chen WL, Cordero R, Tran H, Ober CK. 50th anniversary perspective: polymer brushes: novel surfaces for future materials. Macromolecules 2017;50:4089–113.
[339] Arumugam S, Orski SV, Locklin J, Popik VV. Photoreactive polymer brushes for high-density patterned surface derivatization using a diels-alder photoclick reaction. J Am Chem Soc 2012;134:179–82.
[340] Colak B, Di Cio S, Gautrot JE. Biofunctionalized patterned polymer brushes via Thiol-Ene coupling for the control of cell adhesion and the formation of cell arrays. Biomacromolecules 2018;19:1445–55.
[341] Zhou XC, Liu XQ, Xie Z, Zheng ZJ. 3D-patterned polymer brush surfaces. Nanoscale 2011;3:4929–39.
[342] Chen T, Amin I, Jordan R. Patterned polymer brushes. Chem Soc Rev 2012;41:3280–96.
[343] Xie Z, Chen CJ, Zhou XC, Gao TT, Liu DQ, Miao Q, et al. Massively parallel patterning of complex 2D and 3D functional polymer brushes by polymer pen lithography. ACS Appl Mater Interfaces 2014;6:11955–64.
[344] Lamping S, Buten C, Ravoo BJ. Functionalization and patterning of self-assembled monolayers and polymer brushes using microcontact chemistry. Acc Chem Res 2019;52:1336–46.
[345] Gautrot JE, Huck WTS, Welch M, Ramstedt M. Protein-resistant NTA-functionalized polymer brushes for selective and stable immobilization of histidine-tagged proteins. ACS Appl Mater Interfaces 2010;2:193–202.
[346] Li YF, Zhang JH, Fang LP, Jiang LM, Liu WD, Wang TQ, et al. Polymer brush nanopatterns with controllable features for protein pattern applications. J Mater Chem 2012;22:25116–22.
[347] Li YF, Zhang JH, Liu WD, Li DW, Fang LP, Sun HC, et al. Hierarchical polymer brush nanoarrays: a versatile way to prepare multiscale patterns of proteins. ACS Appl Mater Interfaces 2013;5:2126–32.
[348] Liu WD, Li YF, Wang TQ, Li DW, Fang LP, Zhu SJ, et al. Elliptical polymer brush ring array mediated protein patterning and cell adhesion on patterned protein surfaces. ACS Appl Mater Interfaces 2013;5:12587–93.
[349] Christman KL, Schopf E, Broyer RM, Li RC, Chen Y, Maynard HD. Positioning multiple proteins at the nanoscale with electron beam cross-linked functional polymers. J Am Chem Soc 2009;131:521–7.
[350] Zhou XC, Wang XL, Shen YD, Xie Z, Zheng ZJ. Fabrication of arbitrary three-dimensional polymer structures by rational control of the spacing between nanobrushes. Angew Chem Int Ed 2011;50:6506–10.
[351] Chen CJ, Xie Z, Wei XL, Zheng ZJ. Arbitrary and parallel nanofabrication of 3D metal structures with polymer brush resists. Small 2015;11:6013–7.
[352] Chen CJ, Zhou XC, Xie Z, Gao TT, Zheng ZJ. Construction of 3D polymer brushes by dip-pen nanodisplacement lithography: understanding the molecular displacement for ultrafine and high-speed patterning. Small 2015;11:613–21.
[353] Chen LN, Xie Z, Gan TS, Wang Y, Zhang GZ, Mirkin CA, et al. Biomimicking nano-micro binary polymer brushes for smart cell orientation and adhesion control. Small 2016;12:3400–6.
[354] Liu XY, Sun JW, Gao WP. Site-selective protein modification with polymers for advanced biomedical applications. Biomaterials 2018;178:413–34.
[355] Kaupbayeva B, Murata H, Lucas A, Matyjaszewski K, Minden JS, Russell AJ. Molecular sieving on the surface of a nano-armored protein. Biomacromolecules 2019;20:1235–45.
[356] Xu X, Cui YC, Bu HX, Chen JM, Li Y, Tang GP, et al. A photosensitizer loaded hemoglobin-polymer conjugate as a nanocarrier for enhanced photodynamic therapy. J Mater Chem B 2018;6:1825–33.
[357] Chakrabortty S, Agrawalla BK, Stumper A, Veg NM, Fischer S, Reichardt C, et al. Mitochondria targeted protein-ruthenium photosensitizer for efficient photodynamic applications. J Am Chem Soc 2017;139:2512–9.
[358] Dong CH, Liu ZY, Wang S, Zheng B, Guo WS, Yang WT, et al. A protein-polymer bioconjugate-coated upconversion nanosystem for simultaneous tumor cell imaging, photodynamic therapy, and chemotherapy. ACS Appl Mater Interfaces 2016;8:32688–98.
[359] Qiao ZY, Hou CY, Zhang D, Liu Y, Lin YX, An HW, et al. Self-assembly of cytotoxic peptide conjugated poly(beta-amino ester)s for synergistic cancer chemotherapy. J Mater Chem B 2015;3:2943–53.
[360] Liu TY, Hussein WM, Jia ZF, Ziora ZM, McMillan NAJ, Monteiro MJ, et al. Self-adjuvanting polymer-peptide conjugates as therapeutic vaccine candidates against cervical cancer. Biomacromolecules 2013;14:2798–806.
[361] Makwana H, Mastrotto F, Magnusson JP, Sleep D, Hay J, Nicholls KJ, et al. Engineered polymer-transferrin conjugates as self-assembling targeted drug delivery systems. Biomacromolecules 2017;18:1532–43.
[362] Liu XY, Sun MM, Sun JW, Hu J, Wang ZR, Guo JW, et al. Polymerization induced self-assembly of a site-specific interferon alpha-block copolymer conjugate into micelles with remarkably enhanced pharmacology. J Am Chem Soc 2018;140:10435–8.
[363] Venkataraman S, Hedrick JL, Ong ZY, Yang C, Ee PLR, Hammond PT, et al. The effects of polymeric nanostructure shape on drug delivery. Adv Drug Deliv Rev 2011;63:1228–46.
[364] Geng Y, Dalhaimer P, Cai SS, Tsai R, Tewari M, Minko T, et al. Shape effects of filaments versus spherical particles in flow and drug delivery. Nat Nanotechnol 2007;2:249–55.

[365] Larnaudie SC, Brendel JC, Romero-Canelon I, Sanchez-Cano C, Catrouillet S, Sanchis J, et al. Cyclic peptide-polymer nanotubes as efficient and highly potent drug delivery systems for organometallic anticancer complexes. Biomacromolecules 2018;19:239–47.
[366] Larnaudie SC, Sanchis J, Nguyen TH, Peltier R, Catrouillet S, Brendel JC, et al. Cyclic peptide-poly(HPMA) nanotubes as drug delivery vectors: in vitro assessment, pharmacokinetics and biodistribution. Biomaterials 2018;178:570–82.
[367] Duro-Castano A, Lim NH, Tranchant I, Arnoura M, Beau F, Wieland H, et al. In vivo imaging of MMP-13 activity using a specific polymer-FRET peptide conjugate detects early osteoarthritis and inhibitor efficacy. Adv Funct Mater 2018;28, 1802738/1-9.
[368] Liu ZY, Chen N, Dong CH, Li W, Guo WS, Wang HJ, et al. Facile construction of near infrared fluorescence nanoprobe with amphiphilic protein-polymer bioconjugate for targeted cell imaging. ACS Appl Mater Interfaces 2015;7:18997–9005.
[369] Gao DY, Zhang PF, Liu YB, Sheng ZH, Chen HJ, Yuan Z. Protein-modified conjugated polymer nanoparticles with strong near-infrared absorption: a novel nanoplatform to design multifunctional nanoprobes for dual-modal photoacoustic and fluorescence imaging. Nanoscale 2018;10:19742–8.
[370] Tsurkan MV, Chwalek K, Prokoph S, Zieris A, Levental KR, Freudenberg U, et al. Defined polymer-peptide conjugates to form cell-instructive starPEG-heparin matrices in situ. Adv Mater 2013;25:2606–10.
[371] Nam HY, Kim J, Kim S, Yockman JW, Kim SW, Bull DA. Cell penetrating peptide conjugated bioreducible polymer for siRNA delivery. Biomaterials 2011;32:5213–22.
[372] Kim HA, Nam K, Kim SW. Tumor targeting RGD conjugated bio-reducible polymer for VEGF siRNA expressing plasmid delivery. Biomaterials 2014;35:7543–52.
[373] Sun H, Hong YX, Xi YJ, Zou YJ, Gao JY, Du JZ. Synthesis, self-assembly, and biomedical applications of antimicrobial peptide-polymer conjugates. Biomacromolecules 2018;19:1701–20.
[374] Kumar P, Takayesu A, Abbasi U, Kalathottukaren MT, Abbina S, Kizhakkedathu JN, et al. Antimicrobial peptide-polymer conjugates with high activity: influence of polymer molecular weight and peptide sequence on antimicrobial activity, proteolysis, and biocompatibility. ACS Appl Mater Interfaces 2017;9:37575–86.
[375] Ji WH, Koepsel RR, Murata H, Zadan S, Campbell AS, Russell AJ. Bactericidal specificity and resistance profile of poly(quaternary ammonium) polymers and protein-poly(quaternary ammonium) conjugates. Biomacromolecules 2017;18:2583–93.
[376] Wang MZ, Zhou CC, Chen J, Xiao YF, Du JZ. Multifunctional biocompatible and biodegradable folic acid conjugated poly(epsilon-caprolactone)-polypeptide copolymer vesicles with excellent antibacterial activities. Bioconjug Chem 2015;26:725–34.
[377] Song Y, Cheng PN, Zhu LJ, Moore EG, Moore JS. Multivalent macromolecules redirect nucleation-dependent fibrillar assembly into discrete nanostructures. J Am Chem Soc 2014;136:5233–6.
[378] Song Y, Moore EG, Guo YS, Moore JS. Polymer-peptide conjugates disassemble amyloid beta fibrils in a molecular-weight dependent manner. J Am Chem Soc 2017;139:4298–301.
[379] Qi GB, Zhang D, Liu FH, Qiao ZY, Wang H. An ön-site transformationstrategy for treatment of bacterial infection. Adv Mater 2017;29, 1703461/1-10.
[380] Lam SJ, O'Brien-Simpson NM, Pantarat N, Sulistio A, Wong EHH Chen YY, et al. Combating multidrug-resistant gram-negative bacteria with structurally nanoengineered antimicrobial peptide polymers. Nat Microbiol 2016;1, 16162/1-11.
[381] Riegger A, Chen CJ, Zirafi O, Daiss N, Mukherji D, Walter K, et al. Synthesis of peptide-functionalized poly(bis-sulfone) copolymers regulating HIV-1 entry and cancer stem cell migration. ACS Macro Lett 2017;6:241–6.
[382] Lauster D, Glanz M, Bardua M, Ludwig K, Hellmund M, Hoffmann U, et al. Multivalent peptide-nanoparticle conjugates for influenza-virus inhibition. Angew Chem Int Ed 2017;56:5931–6.
[383] Diez I, Hahn H, Ikkala O, Borner HG, Ras RHA. Controlled growth of silver nanoparticle arrays guided by a self-assembled polymer-peptide conjugate. Soft Matter 2010;6:3160–2.
[384] Samsoninkova V, Seidt B, Hansske F, Wagermaier W, Borner HG. Peptide-polymer conjugates for bioinspired compatibilization of internal composite interfaces: via specific interactions toward stiffer and tougher materials. Adv Mater Interfaces 2017;4, 1600501/1-5.
[385] Mukhopadhyay A, Das T, Datta A, Sharma KP. Neat protein-polymer surfactant bioconjugates as universal solvents. Biomacromolecules 2018;19:943–50.
[386] van Rijn P, Tutus M, Kathrein C, Mougin NC, Park H, Hein C, et al. Ultra-thin self-assembled protein-polymer membranes: a new pore forming strategy. Adv Funct Mater 2014;24:6762–70.
[387] Xu T, Zhao NN, Ren F, Hourani R, Lee MT, Shu JY, et al. Subnanometer porous thin films by the co-assembly of nanotube subunits and block copolymers. ACS Nano 2011;5:1376–84.
[388] Zhang C, Xu T. Co-assembly of cyclic peptide nanotubes and block copolymers in thin films: controlling the kinetic pathway. Nanoscale 2015;7:15117–21.
[389] Basak S, Punetha VD, Bisht G, Bisht SS, Sahoo NG, Cho JW. Recent trends of polymer-protein conjugate application in biocatalysis: a review. Polym Rev 2015;55:163–98.
[390] Wright TA, Dougherty ML, Schmitz B, Burridge KM, Makaroff K, Stewart JM, et al. Polymer conjugation to enhance cellulase activity and preserve thermal and functional stability. Bioconjug Chem 2017;28:2638–45.
[391] Mukherjee I, Sinha SK, Datta S, De P. Recyclable thermoresponsive polymer-beta-glucosidase conjugate with intact hydrolysis activity. Biomacromolecules 2018;19:2286–93.
[392] Mackenzie KJ, Francis MB. Recyclable thermoresponsive polymer-cellulase bioconjugates for biomass depolymerization. J Am Chem Soc 2013;135:293–300.
[393] Chin SM, Synatschke CV, Liu SP, Nap RJ, Sather NA, Wang QF, et al. Covalent-supramolecular hybrid polymers as muscle-inspired anisotropic actuators. Nat Commun 2018;9, 2395/1-11.
[394] Deleavey GF, Damha MJ. Designing chemically modified oligonucleotides for targeted gene silencing. Chem Biol 2012;19:937–54.
[395] Kundu A, Nandi S, Nandi AK. Nucleic acid based polymer and nanoparticle conjugates: synthesis, properties and applications. Prog Mater Sci 2017;88:136–85.
[396] Sun H, Yang L, Thompson MP, Schara S, Cao W, Choi W, et al. Recent advances in amphiphilic polymer-oligonucleotide nanomaterials via living/controlled polymerization technologies. Bioconjug Chem 2019;30:1889–904.
[397] Kleiner RE, Brudno Y, Birnbaum ME, Liu DR. DNA-templated polymerization of side-chain-functionalized peptide nucleic acid aldehydes. J Am Chem Soc 2008;130:4646–59.
[398] Li ZY, Zhang ZYJ, Knipe R, Lynn DG. DNA-catalyzed polymerization. J Am Chem Soc 2002;124:746–7.
[399] Rosenbaum DM, Liu DR. Efficient and sequence-specific DNA-templated polymerization of peptide nucleic acid aldehydes. J Am Chem Soc 2003;125:13924–5.
[400] Poulin-Kerstien AT, Dervan PB. DNA-templated dimerization of hairpin polyamides. J Am Chem Soc 2003;125:15811–21.
[401] Alemdaroglu FE, Ding K, Berger R, Herrmann A. DNA-templated synthesis in three dimensions: introducing a micellar scaffold for organic reactions. Angew Chem Int Ed 2006;45:4206–10.
[402] McHale R, Patterson JP, Zetterlund PB, O'Reilly RK. Biomimetic radical polymerization via cooperative assembly of segregating templates. Nat Chem 2012;4:491–7.
[403] Niu J, Hili R, Liu DR. Enzyme-free translation of DNA into sequence-defined synthetic polymers structurally unrelated to nucleic acids. Nat Chem 2013;5:282–92.
[404] Hili R, Niu J, Liu DR. DNA ligase-mediated translation of DNA into densely functionalized nucleic acid polymers. J Am Chem Soc 2013;135:98–101.
[405] Chen Z, Lichtor PA, Berliner AP, Chen JC, Liu DR. Evolution of sequence-defined highly functionalized nucleic acid polymers. Nat Chem 2018;10:420–7.
[406] Trinh T, Liao CY, Toader V, Barlog M, Bazzi HS, Li JN, et al. DNA-imprinted polymer nanoparticles with monodispersity and prescribed DNA-strand patterns. Nat Chem 2018;10:184–92.
[407] Seeman NC. Nucleic-acid junctions and lattices. J Theor Biol 1982;99:237–47.
[408] Rothemund PWK. Folding DNA to create nanoscale shapes and patterns. Nature 2006;440:297–302.
[409] Seeman NC, Sleiman HF. DNA nanotechnology. Nat Rev Mater 2017;3, 17068/1-23.
[410] Punatar RS, Martin MJ, Wyatt HDM, Chan YW, West SC. Resolution of single and double Holliday junction recombination intermediates by GEN1. Proc Natl Acad Sci U S A 2017;114:443–50.
[411] McLaughlin CK, Hamblin GD, Hanni KD, Conway JW, Nayak MK, Carneiro KMM, et al. Three-dimensional organization of block copolymers on "DNA-minimal"scaffolds. J Am Chem Soc 2012;134:4280–6.
[412] Serpell CJ, Edwardson TGW, Chidchob P, Carneiro KMM, Sleiman HF. Precision polymers and 3D DNA nanostructures: emergent assemblies from new parameter space. J Am Chem Soc 2014;136:15767–74.
[413] Chidchob P, Edwardson TGW, Serpell CJ, Sleiman HF. Synergy of two assembly languages in DNA nanostructures: self-assembly of sequence-defined polymers on DNA cages. J Am Chem Soc 2016;138:4416–25.
[414] Lin QY, Mason JA, Li ZY, Zhou WJ, O'Brien MN, Brown KA, et al. Building superlattices from individual nanoparticles via template-confined DNA-mediated assembly. Science 2018;359:669–72.
[415] Knudsen JB, Liu L, Kodal ALB, Madsen M, Li Q, Song J, et al. Routing of individual polymers in designed patterns. Nat Nanotechnol 2015;10:892–8.
[416] Madsen M, Christensen RS, Krissanaprasit A, Bakke MR, Riber CF, Nielsen KS, et al. Preparation, single-molecule manipulation, and energy transfer investigation of a polyfluorene-graft-DNA polymer. Chem Eur J 2017;23:10511–5.
[417] Krissanaprasit A, Madsen M, Knudsen JB, Gudnason D, Surareungchai W, Birkedal V, et al. Programmed switching of single polymer conformation on DNA origami. ACS Nano 2016;10:2243–50.
[418] Tokura Y, Jiang YY, Welle A, Stenzel MH, Krzemien KM, Michaelis J, et al. Bottom-up fabrication of nanopatterned polymers on DNA origami by in situ atom-transfer radical polymerization. Angew Chem Int Ed 2016;55:5692–7.
[419] Tokura Y, Harvey S, Chen CJ, Wu YZ, Ng DYW, Weil T. Fabrication of defined polydopamine nanostructures by DNA origami-templated polymerization. Angew Chem Int Ed 2018;57:1587–91.

[420] Tokura Y, Harvey S, Xu XM, Chen CJ, Morsbach S, Wunderlich K, et al. Polymer tube nanoreactors via DNA-origami templated synthesis. Chem Commun 2018;54:2808–11.
[421] Albert SK, Hu XL, Park SJ. Dynamic nanostructures from DNA-coupled molecules, polymers, and nanoparticles. Small 2019;15, 1900504/1-18.
[422] Ding K, Alemdaroglu FE, Boersch M, Berger R, Herrmann A. Engineering the structural properties of DNA block copolymer micelles by molecular recogntition. Angew Chem Int Ed 2007;46:1172–5.
[423] van der Meulen SAJ, Leunissen ME. Solid colloids with surface-mobile DNA linkers. J Am Chem Soc 2013;135:15129–34.
[424] Oh SS, Lee BF, Leibfarth FA, Eisenstein M, Robb MJ, Lynd NA, et al. Synthetic aptamer-polymer hybrid constructs for programmed drug delivery into specific target cells. J Am Chem Soc 2014;136:15010–5.
[425] Jia F, Lu XG, Wang DL, Cao XY, Tan XY, Lu H, et al. Depth-profiling the nuclease stability and the gene silencing efficacy of brush-architectured poly(ethylene glycol)-DNA conjugates. J Am Chem Soc 2017;139:10605–8.
[426] Yang L, Sun H, Liu Y, Hou WJ, Yang Y, Cai R, et al. Self-assembled aptamer-grafted hyperbranched polymer nanocarrier for targeted and photoresponsive drug delivery. Angew Chem Int Ed 2018;57:17048–52.
[427] Heredia KL, Nguyen TH, Chang CW, Bulmus V, Davis TP, Maynard HD. Reversible siRNA-polymer conjugates by RAFT polymerization. Chem Commun 2008:3245–7.
[428] Lin EW, Maynard HD. Grafting from small interfering ribonucleic acid (siRNA) as an alternative synthesis route to siRNA-polymer conjugates. Macromolecules 2015;48:5640–7.
[429] Bakker MH, Lee CC, Meijer EW, Dankers PYW, Albertazzi L. Multicomponent supramolecular polymers as a modular platform for intracellular delivery. ACS Nano 2016;10:1845–52.
[430] Zhang C, Hao LL, Calabrese CM, Zhou Y, Choi CHJ, Xing H, et al. Biodegradable DNA-brush block copolymer spherical nucleic acids enable transfection agent-free intracellular gene regulation. Small 2015;11:5360–8.
[431] Kamps AC, Cativo MHM, Chen XJ, Park SJ. Self-assembly of DNA-coupled semiconducting block copolymers. Macromolecules 2014;47:3720–6.
[432] Albert SK, Thelu HVP, Golla M, Krishnan N, Chaudhary S, Varghese R. Self-assembly of DNA-oligo(p-phenylene-ethynylene) hybrid amphiphiles into surface-engineered vesicles with enhanced emission. Angew Chem Int Ed 2014;53:8352–7.
[433] Ensslen P, Gartner S, Glaser K, Colsmann A, Wagenknecht HA. A DNA-fullerene conjugate as a template for supramolecular chromophore assemblies: towards DNA-based solar cells. Angew Chem Int Ed 2016;55:1904–8.
[434] Roy D, Guthrie JT, Perrier S. Graft polymerization: grafting poly(styrene) from cellulose via reversible addition-fragmentation chain transfer (RAFT) polymerization. Macromolecules 2005;38:10363–72.
[435] Roy D, Semsarilar M, Guthrie JT, Perrier S. Cellulose modification by polymer grafting: a review. Chem Soc Rev 2009;38:2046–64.
[436] Thomas B, Raj MC, Athira KB, Rubiyah MH, Joy J, Moores A, et al. Nanocellulose, a versatile green platform: from biosources to materials and their applications. Chem Rev 2018;118:11575–625.
[437] Roeder RD, Garcia-Valdez O, Whitney RA, Champagne P, Cunningham MF. Graft modification of cellulose nanocrystals via nitroxide-mediated polymerisation. Polym Chem 2016;7:6383–90.
[438] Carlmark A, Malmstrom E. Atom transfer radical polymerization from cellulose fibers at ambient temperature. J Am Chem Soc 2002;124:900–1.
[439] Lonnberg H, Zhou Q, Brumer H, Teeri TT, Malmstrom E, Hult A. Grafting of cellulose fibers with poly(epsilon-caprolactone) and poly(L-lactic acid) via ring-opening polymerization. Biomacromolecules 2006;7:2178–85.
[440] Hu Y, Li Y, Xu FJ. Versatile functionalization of polysaccharides via polymer grafts: from design to biomedical applications. Acc Chem Res 2017;50:281–92.
[441] Seidi F, Salimi H, Shamsabadi AA, Shabanian M. Synthesis of hybrid materials using graft copolymerization on non-cellulosic polysaccharides via homogenous ATRP. Prog Polym Sci 2018;76:1–39.
[442] Geng J, Biedermann F, Zayed JM, Tian F, Scherman OA. Supramolecular glycopolymers in water: a reversible route toward multivalent carbohydrate-lectin conjugates using cucurbit[8]uril. Macromolecules 2011;44:4276–81.
[443] Kwon SJ, Na DH, Kwak JH, Douaisi M, Zhang F, Park EJ, et al. Nanostructured glycan architecture is important in the inhibition of influenza A virus infection. Nat Nanotechnol 2017;12:48–54.
[444] Pang XC, Zhao L, Akinc M, Kim JK, Lin ZQ. Novel amphiphilic multi-arm, star-like block copolymers as unimolecular micelles. Macromolecules 2011;44:3746–52.
[445] Pang XC, Zhao L, Feng CW, Lin ZQ. Novel amphiphilic multiarm, starlike coil-rod diblock copolymers via a combination of click chemistry with living polymerization. Macromolecules 2011;44:7176–83.
[446] Jia T, Huang S, Yang CJ, Wang MF. Unimolecular micelles of pH-responsive star-like copolymers for co-delivery of anticancer drugs and small-molecular photothermal agents: a new drug-carrier for combinational chemo/photothermal cancer therapy. J Mater Chem B 2017;5:8514–24.
[447] Shi XX, Hou ML, Bai S, Ma XQ, Gao YE, Xiao B, et al. Acid-activatable theranostic unimolecular micelles composed of amphiphilic star-like polymeric prodrug with high drug loading for enhanced cancer therapy. Mol Pharm 2017;14:4032–41.
[448] Pang XC, Zhao L, Han W, Xin XK, Lin ZQ. A general and robust strategy for the synthesis of nearly monodisperse colloidal nanocrystals. Nat Nanotechnol 2013;8:426–31.
[449] Pang XC, He YJ, Jung JH, Lin ZQ. 1D nanocrystals with precisely controlled dimensions, compositions, and architectures. Science 2016;353:1268–72.
[450] Zheng MB, Yue CX, Ma YF, Gong P, Zhao PF, Zheng CF, et al. Single-step assembly of DOX/ICG loaded lipid-polymer nanoparticles for highly effective chemo-photothermal combination therapy. ACS Nano 2013;7:2056–67.
[451] Dehaini D, Fang RH, Luk BT, Pang ZQ, Hu CMJ, Kroll AV, et al. Ultra-small lipid-polymer hybrid nanoparticles for tumor-penetrating drug delivery. Nanoscale 2016;8:14411–9.
[452] Date T, Nimbalkar V, Kamat J, Mittal A, Mahato RI, Chitkara D. Lipid-polymer hybrid nanocarriers for delivering cancer therapeutics. J Control Release 2018;271:60–73.
[453] Zhang LF, Chan JM, Gu FX, Rhee JW, Wang AZ, Radovic-Moreno AF, et al. Self-assembled lipid-polymer hybrid nanoparticles: a robust drug delivery platform. ACS Nano 2008;2:1696–702.
[454] Shi JJ, Xiao ZY, Votruba AR, Vilos C, Farokhzad OC. Differentially charged hollow core/shell lipid-polymer-lipid hybrid nanoparticles for small interfering RNA delivery. Angew Chem Int Ed 2011;50:7027–31.
[455] Metselaar JM, Bruin P, de Boer LWT, de Vringer T, Snel C, Oussoren C, et al. A novel family of L-amino acid-based biodegradable polymer-lipid conjugates for the development of long-circulating liposomes with effective drug-targeting capacity. Bioconjug Chem 2003;14:1156–64.
[456] Watanabe A, Niu J, Lunn DJ, Lawrence J, Knight AS, Zhang MW, et al. PET-RAFT as a facile strategy for preparing functional lipid-polymer conjugates. J Polym Sci Part A: Polym Chem 2018;56:1259–68.
[457] Luginbuhl KM, Mozhdehi D, Dzuricky M, Yousefpour P, Huang FC, Mayne NR, et al. Recombinant synthesis of hybrid lipid-peptide polymer fusions that self-assemble and encapsulate hydrophobic drugs. Angew Chem Int Ed 2017;56:13979–84.
[458] Mozhdehi D, Luginbuhl KM, Simon JR, Dzuricky M, Berger R, Varol HS, et al. Genetically encoded lipid-polypeptide hybrid biomaterials that exhibit temperature-triggered hierarchical self-assembly. Nat Chem 2018;10:496–505.
[459] Mozhdehi D, Luginbuhl KM, Dzuricky M, Costa SA, Xiong SN, Huang FC, et al. Genetically encoded cholesterol-modified polypeptides. J Am Chem Soc 2019;141:945–51.
[460] Abbina S, Siren EMJ, Moon H, Kizhakkedathu JN. Surface engineering for cell-based therapies: techniques for manipulating mammalian cell surfaces. ACS Biomater Sci Eng 2018;4:3658–77.
[461] Scott MD, Murad KL, Koumpouras F, Talbot M, Eaton JW. Chemical camouflage of antigenic determinants: stealth erythrocytes. Proc Natl Acad Sci U S A 1997;94:7566–71.
[462] Chapanian R, Constantinescu I, Brooks DE, Scott MD, Kizhakkedathu JN. In vivo circulation, clearance, and biodistribution of polyglycerol grafted functional red blood cells. Biomaterials 2012;33:3047–57.
[463] Rossi NAA, Constantinescu I, Brooks DE, Scott MD, Kizhakkedathu JN. Enhanced cell surface polymer grafting in concentrated and nonreactive aqueous polymer solutions. J Am Chem Soc 2010;132:3423–30.
[464] Amaral AJR, Pasparakis G. Macromolecular cell surface engineering for accelerated and reversible cellular aggregation. Chem Commun 2015;51:17556–9.
[465] Tomas RMF, Gibson MI. Optimization and stability of cell polymer hybrids obtained by ‘clicking’synthetic polymers to metabolically labeled cell surface glycans. Biomacromolecules 2019;20:2726–36.
[466] Tomas RMF Martyn B, Bailey TL, Gibson MI. Engineering cell surfaces by covalent grafting of synthetic polymers to metabolically-labeled glycans. ACS Macro Lett 2018;7:1289–94.
[467] Kim JY, Lee BS, Choi J, Kim BJ, Choi JY, Kang SM, et al. Cytocompatible polymer grafting from individual living cells by atom-transfer radical polymerization. Angew Chem Int Ed 2016;55:15306–9.
[468] Wu YZ, Wu SG, Ma SY, Yan F, Weng ZQ. Cytocompatible modification of thermoresponsive polymers on living cells for membrane proteomic isolation and analysis. Anal Chem 2019;91:3187–94.
[469] Niu J, Lunn DJ, Pusuluri A, Yoo JI, O'Malley MA, Mitragotri S, et al. Engineering live cell surfaces with functional polymers via cytocompatible controlled radical polymerization. Nat Chem 2017;9:537–45.
[470] Geng J, Li WS, Zhang YC, Thottappillil N, Clavadetscher J, Lilienkampf A, et al. Radical polymerization inside living cells. Nat Chem 2019;11:578–86.

Declaration of Originality

Ich versichere hiermit, daß ich die Arbeit selbständig angefertigt habe und keine anderen als die angegebenen Quellen und Hilfsmittel benutzt sowie die wörtlich oder inhaltlich übernommenen Stellen als solche kenntlich gemacht habe.

Ulm, den

…..……..……..

(Chaojian Chen)

I hereby declare that this thesis and the work reported herein was composed by and originated entirely from me. Information derived from the published and unpublished work of others has been acknowledged in the text and references are given in the list of sources.

Ulm, den

…..……..……..

(Chaojian Chen)

Curriculum Vitae

The content on this page has been removed according to personal data protection rules!

The content on this page has been removed according to personal data protection rules!

The content on this page has been removed according to personal data protection rules!

The content on this page has been removed according to personal data protection rules!

Acknowledgements

The content on this page has been removed according to personal data protection rules!

The content on this page has been removed according to personal data protection rules!